frontiers | Research Topics

Advances in basic and applied research in photoplethysmography

Edited by
John Allen and Panicos Kyriacou

Published in
Frontiers in Physiology

ISSN 1664-8714
ISBN 978-2-8325-4809-7
DOI 10.3389/978-2-8325-4809-7

About Frontiers

Frontiers is more than just an open access publisher of scholarly articles: it is a pioneering approach to the world of academia, radically improving the way scholarly research is managed. The grand vision of Frontiers is a world where all people have an equal opportunity to seek, share and generate knowledge. Frontiers provides immediate and permanent online open access to all its publications, but this alone is not enough to realize our grand goals.

Frontiers journal series

The Frontiers journal series is a multi-tier and interdisciplinary set of open-access, online journals, promising a paradigm shift from the current review, selection and dissemination processes in academic publishing. All Frontiers journals are driven by researchers for researchers; therefore, they constitute a service to the scholarly community. At the same time, the *Frontiers journal series* operates on a revolutionary invention, the tiered publishing system, initially addressing specific communities of scholars, and gradually climbing up to broader public understanding, thus serving the interests of the lay society, too.

Dedication to quality

Each Frontiers article is a landmark of the highest quality, thanks to genuinely collaborative interactions between authors and review editors, who include some of the world's best academicians. Research must be certified by peers before entering a stream of knowledge that may eventually reach the public - and shape society; therefore, Frontiers only applies the most rigorous and unbiased reviews. Frontiers revolutionizes research publishing by freely delivering the most outstanding research, evaluated with no bias from both the academic and social point of view. By applying the most advanced information technologies, Frontiers is catapulting scholarly publishing into a new generation.

What are Frontiers Research Topics?

Frontiers Research Topics are very popular trademarks of the *Frontiers journals series*: they are collections of at least ten articles, all centered on a particular subject. With their unique mix of varied contributions from Original Research to Review Articles, Frontiers Research Topics unify the most influential researchers, the latest key findings and historical advances in a hot research area.

Find out more on how to host your own Frontiers Research Topic or contribute to one as an author by contacting the Frontiers editorial office: frontiersin.org/about/contact

Advances in basic and applied research in photoplethysmography

Topic editors

John Allen — Coventry University, United Kingdom

Panicos Kyriacou — City University of London, United Kingdom

Citation

Allen, J., Kyriacou, P., eds. (2024). *Advances in basic and applied research in photoplethysmography*. Lausanne: Frontiers Media SA.

doi: 10.3389/978-2-8325-4809-7

Table of contents

frontiers | Frontiers in Physiology

TYPE Editorial
PUBLISHED 16 May 2024
DOI 10.3389/fphys.2024.1415049

OPEN ACCESS

EDITED AND REVIEWED BY
Raimond L. Winslow,
Northeastern University, United States

*CORRESPONDENCE
John Allen,
ad5325@coventry.ac.uk

RECEIVED 09 April 2024
ACCEPTED 17 April 2024
PUBLISHED 16 May 2024

CITATION
Allen J and Kyriacou PA (2024), Editorial: Advances in basic and applied research in photoplethysmography.
Front. Physiol. 15:1415049.
doi: 10.3389/fphys.2024.1415049

Editorial: Advances in basic and applied research in photoplethysmography

John Allen [1]* and Panicos A. Kyriacou [2]

[1]Research Centre for Intelligent Healthcare, Coventry University, Coventry, United Kingdom, [2]Research Centre for Biomedical Engineering, University of London, London, United Kingdom

KEYWORDS

photoplethysmography, pulse wave analysis, diagnostic, physiology, optical, machine learning, cardiovascular

Editorial on the Research Topic
Advances in basic and applied research in photoplethysmography

Introducing photoplethysmography

Welcome to this Research Topic in Frontiers in Physiology, focusing on Advances in Basic and Applied Research in Photoplethysmography.

Photoplethysmography (PPG) is a low-cost and simple vascular optics technique that can be used to detect blood volume changes in the microvascular bed of tissue with each heartbeat (Allen, 2007; Kyriacou and Allen, 2021). The popularity of this Research Topic area can be attributed to the realization that PPG has important implications for a wide range of applications including assessment of the cardiovascular system, monitoring of vital signs including non-invasive estimation of blood pressure and heart rate, and the study of pain. There is currently a large body of literature contributing new knowledge on the relation of PPG pulse morphology, pulse wave analysis and pulse feature extraction with the physiological status of peripheral blood vessels, such as vascular aging and stiffness, blood pressure and compliance, microvascular disease, autonomic function, and others. There are also significant efforts in the utilization of the PPG for the detection of heart arrhythmias such as Atrial Fibrillation (AF). In addition, the recent significant contributions of PPG to wearable devices have had a major impact on the popularity and usability of PPG. Researchers continue to strive to combine the PPG sensory capabilities of wearables, such as smartwatches, with Artificial Intelligence (AI) machine learning approaches to deliver ubiquitous health monitoring solutions that go beyond currently available consumer devices. PPG and AI have a bright future together for the benefit of patients.

The aim of this Research Topic for Frontiers in Physiology is to bring together the latest cutting-edge basic and applied research in the field of Photoplethysmography. Our Research Topic comes from world-leading authors in the field and showcases 16 original research papers covering a diverse range of contributions in PPG measurement and analysis.

Summary of published papers in this Research Topic

Cardiovascular disease continues to be the leading cause of death globally - this is one of the very important areas where PPG has considerable potential to help impact the burden of disease by allowing us to better understand vascular aging and enable low-cost, accessible monitoring of cardiovascular status. Djurić et al. in "*Using the photoplethysmography method to monitor age-related changes in the cardiovascular system*" collected single-site PPG measurements from above the left common carotid artery in 117 healthy adult participants (up to 70 years of age) and analyzed the data using a non-linear technique (detrended fluctuation analysis, DFA) to produce a ratio of scalar coefficients that were found to decrease exponentially with age–giving a biomarker for monitoring aging. Age-related changes in PPG shape have also been reported in the literature including the classification of the pulse into one of four classes based on the position of the dicrotic notch (Dawber et al., 1973). Zanelli et al. in "*Clustered photoplethysmogram pulse wave shapes and their associations with clinical data*" noted however that when working with real data, labeling waveforms into one of these four classes is no longer straightforward, but correct identification of the PPG shape could improve the precision and reliability of extracted biomarkers. Using a PPG dataset from 300 subjects (aged 19–83 years) the authors employed unsupervised machine learning and deep learning approaches to overcome the limitations of data labeling (including K-medoids-based clustering, a similarity matrix computed with Derivative Dynamic Time Warping, and PPG features extracted with CNN AutoEncoder). The results indicated that PPG waveforms do differ due to their dicrotic notch characteristics. However, there are additional differences such as the width of the systolic peak and the strength of a secondary systolic wave and by investigating the optimal number of clusters they found seven clusters of PPG wave shapes instead of the aforementioned four classes.

PPG provides a valuable way to study the dynamics of the cardiovascular system and key physiological variables such as blood pressure (BP) and heart rate (HR). Xing et al. in "*Temporal complexity in photoplethysmography and its influence on blood pressure*" used the Higuchi fractal dimension (HFD) and the autocorrelation function (ACF) to assess the temporal complexity of the PPG and interpreted the stochastic patterns with a model-based simulation which has the potential to help optimize BP estimation algorithms. The authors adapted the classic four-element Windkessel model to incorporate BP-dependent compliance profiles and simulations generated PPG responses at various time scales. Importantly, the relationship between complexity and hemodynamics predicted by their model aligned well with the experimental analysis of data collected from 40 healthy subjects. HFD and ACF had significant contributions to BP and displayed stability even in the presence of high cardiac output fluctuations. Temporal complexity patterns are essential for single-site PPG-based BP estimation and understanding the physiological implications of these patterns may aid in the development of such algorithms. A study of cardiovascular variability was also reported by Mejía-Mejía and Kyriacou with "*Spectral analysis for pulse rate variability assessment from simulated photoplethysmographic signals*". Pulse rate variability (PRV) has been used as a surrogate for heart rate variability (HRV, measured via ECG) although it has been shown that there are differences that may result from physiological processes or from technical aspects of extracting PRV from PPG. The researchers extracted frequency-domain information from PRV in order to establish the best-performing combination of parameters and algorithms to obtain the spectral representation of PRV. They found that with specific interpolation methods, the Fast Fourier Transform (FFT) and multiple signal classification (PMUSIC) algorithms gave the best results, and considering the lower complexity of FFT over PMUSIC, it was recommended that FFT be considered as the appropriate technique to extract frequency-domain information from PRV signals.

The use of PPG for clinical monitoring was also covered in several leading-edge contributions. Stockwell et al. in "*Forehead monitoring of heart rate in neonatal intensive care*" described pioneering R&D in PPG sensor development for heart rate monitoring in critically unwell infants, with reflection mode measurements advantageously made at the forehead site rather than peripherally on a limb. They reported data comparing heart rates measured with a forehead-based PPG sensor against a wrist-based PPG sensor in 19 critically unwell infants in neonatal intensive care collecting 198 h of data, with good agreement between techniques (Bland-Altman limits of agreement of 8.44 bpm, bias −0.22 bpm) showing that the forehead is a reliable alternative location for measuring vital signs using the PPG. Roldan et al. in "*Non-invasive monitoring of intracranial pressure changes: healthy volunteers study*" aimed to evaluate the possible association between pulsatile near-infrared spectroscopic waveform features at the forehead and induced changes in intracranial pressure (ICP) in healthy volunteers. The authors reported data from 16 healthy volunteers with measurements acquired during changes in body position and during the Valsalva maneuver. The classification model features were extracted and an analysis was carried out to compare the two signals. The results revealed significant differences in the features extracted from these signals, demonstrating a correlation with ICP changes induced by position changes and the Valsalva maneuver. The classification models were able to identify changes in ICP using features from optical signals from the brain, with sensitivities ranging from 63% to 80% and specificities ranging from 60% to 70%; this work represents a first step toward non-invasive monitoring of intracranial pressure. Pettit et al. in "*Photoplethysmogram beat detection using Symmetric Projection Attractor Reconstruction*" presented a novel method that uses the Symmetric Projection Attractor Reconstruction (SPAR) method to generate an attractor in two-dimensional phase space from the PPG signal. A line was defined through the origin of this phase space as a Poincaré section, and beats were detected when the attractor trajectory crossed an optimally defined section. The method was assessed on the Wearable Stress and Affect Detection (WESAD) dataset and achieved median F1 scores of 74.3% in the Baseline phase, 63.0% during Stress, 93.6% during Amusement, and 97.7% during Meditation phases, comparable to one of the best algorithms identified in a recent benchmarking study of 15 beat detection algorithms. Iqbal et al. in "*Deep learning classification of systemic sclerosis from multi-site photoplethysmography signals*" described a pilot study assessing a

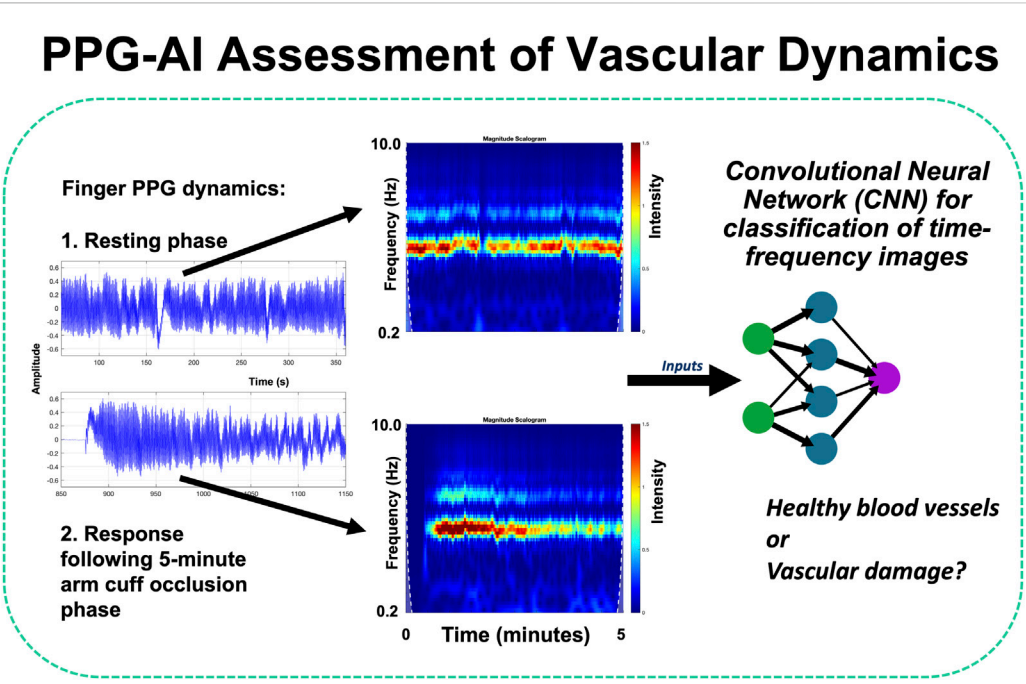

FIGURE 1
Advanced PPG sensing and analysis can give exciting new ways in to assess cardiovascular patients - including the study of vascular dynamics and signal variability (Kyriacou and Allen, 2021). For example, with AI, time-frequency image representations from combined resting and reactive hyperaemia PPG signals can be assessed using a pre-trained convolutional neural network (CNN) image classification system (Iqbal et al.).

novel approach to identify patients with the autoimmune connective tissue disease systemic sclerosis (SSc) using deep learning analysis of RGB scalograms of multi-site PPG waveforms (Figure 1 shows examples of multi-site PPG amplitude variability with illustrative analysis approach). Two different convolutional neural networks (CNNs, namely, GoogLeNet and EfficientNetB0) were trained and evaluated, with EfficientNetB0 showing overall better performance (87.3% accuracy) compared to GoogLeNet (83.1%) - both CNNs were superior to traditional ML methods.

A number of works in this Research Topic focused on non-invasive blood pressure (BP) measurement: "*Intensive care photoplethysmogram datasets and machine-learning for blood pressure estimation: Generalization not guaranteed*" (Weber-Boisvert et al.) studied the differences between the MIMIC waveform dataset and the PPG-BP dataset (an alternative public dataset obtained under controlled experimental conditions) and suggested that BP estimation models based on the MIMIC dataset have reduced predictive power in the general population; "*The identification of blood pressure variation with hypovolemia based on the volume compensation method*" (Chen et al.) studied the blood pressure variation, which is important in continuous blood pressure monitoring, especially in the case of low blood volume, and which is critical for survival; "*Towards continuous non-invasive blood pressure measurements—interpretation of the vasculature response to cuff inflation*" (Loureiro et al.) investigated BP surrogates (e.g., pulse transit or arrival time) and the results provide promising directions to improve the calibration process with cuff inflation toward accurate and robust non-invasive blood pressure estimation; "*Filtering-induced changes of pulse transmit time across different ages: a neglected concern in photoplethysmography-based cuffless blood pressure measurement*" (Liao et al.) showed that filtering-induced PTT changes are significantly influenced by age and PTT definition. These factors deserve further consideration to improve the accuracy of PPG-based cuffless blood pressure measurement using wearable sensors.

Several studies in this Research Topic addressed pain and its objective assessment: "*Induced pain affects auricular and body biosignals: From cold stressor to deep breathing*" (Rapalis et al.) examined targeted biofeedback parameters to close the loop in active pain therapy via auricular vagus nerve stimulation - personalizing pain therapy and increasing patient compliance; "*Photoplethysmography upon cold stress—impact of measurement site and acquisition mode*" (Fleischhauer et al.) systematically investigated the impact of the cold pressor test (CPT), i.e., a painful stimulus, on the morphology of PPG signals in 39 healthy volunteers and compared contact PPG recorded at the finger/earlobe with non-contact PPG (imaging PPG, iPPG) recorded at the face. The authors' findings underlined the importance of the recording setup and physiological in addition to metrological differences related to the measurement protocol; "*Morphological features of the photoplethysmographic signal: a new approach to characterize the microcirculatory response to photobiomodulation*" (Ovadia-Blechman et al.) indicated that post-acquisition analysis of morphological features of the PPG waveform can provide new measures for investigating the microcirculatory response to photobiomodulation such as in the study of peripheral vasodilation, wound healing and pain; "*Contactless photoplethysmography for assessment of small fiber neuropathy*" (Marcinkevics et al.) also considered pain caused by small fiber neuropathy, seeking to develop objective non-invasive assessment methods. The team developed a modular prototype of a contactless

(imaging) photoplethysmography system with three spectral bands (420, 540, and 800 nm) to assess peripheral neuropathy patients via a topical skin heating test and spectral analysis of cutaneous flow motion in 30 subjects, with results showing that neuropathic patients had a significantly lower vasomotor response (50%), flare area (63%), flare intensity index (19%), and neurogenic component (54%) of cutaneous flow motion compared to the control group, independent of photoplethysmography spectral band. iPPG has potential as a cost-effective alternative for the objective and non-invasive assessment of neuropathic patients, but further research is needed to enhance PPG signal quality and establish diagnostic criteria.

Concluding remarks

We, the Editors, hope that this Research Topic will provide you with a deeper appreciation and understanding of PPG technology and its wide range of applications in clinical physiological measurement. We also hope that this Research Topic will help spark fresh ideas and new research collaborations across disciplines, including with biomedical engineering, and scientific and clinical colleagues. With the current trends in PPG-based technologies, sensing and analysis techniques, and clinical applications we can predict with great confidence that PPG will continue to grow and enable the development of further disruptive technologies for use in healthcare and well-being applications.

Author contributions

JA: Conceptualization, Writing–original draft, Writing–review and editing. PAK: Conceptualization, Writing–original draft, Writing–review and editing.

Conflict of interest

The authors declare that the research was conducted in the absence of any commercial or financial relationships that could be construed as a potential conflict of interest.

The author(s) declared that they were an editorial board member of Frontiers, at the time of submission. This had no impact on the peer review process and the final decision.

Publisher's note

References

Allen, J. (2007). Photoplethysmography and its application in clinical physiological measurement. *Physiol. Meas.* 28, R1–R39. doi:10.1088/0967-3334/28/3/R01

Dawber, T. R., Thomas, H. E., and McNamara, P. M. (1973). Characteristics of the dicrotic notch of the arterial pulse wave in coronary heart disease. *Angiology* 24, 244–255. doi:10.1177/000331977302400407

Kyriacou, P. A., and Allen, J. (2021) *Photoplethysmography: technology, signal analysis, and applications*. Netherlands: Elsevier.

frontiers | Frontiers in Physiology

TYPE Original Research
PUBLISHED 09 December 2022
DOI 10.3389/fphys.2022.966130

OPEN ACCESS

EDITED BY
Ahsan H. Khandoker,
Khalifa University, United Arab Emirates

REVIEWED BY
Lin Yang,
Fourth Military Medical University, China
Uldis Rubins,
University of Latvia, Latvia

*CORRESPONDENCE
Elisa Mejía-Mejía,
elisa.mejia-mejia@city.ac.uk

SPECIALTY SECTION
This article was submitted to Computational Physiology and Medicine, a section of the journal Frontiers in Physiology

RECEIVED 10 June 2022
ACCEPTED 29 November 2022
PUBLISHED 09 December 2022

CITATION
Mejía-Mejía E and Kyriacou PA (2022), Spectral analysis for pulse rate variability assessment from simulated photoplethysmographic signals. *Front. Physiol.* 13:966130. doi: 10.3389/fphys.2022.966130

Spectral analysis for pulse rate variability assessment from simulated photoplethysmographic signals

Elisa Mejía-Mejía* and Panicos A. Kyriacou

Research Centre for Biomedical Engineering, City, University of London, London, United Kingdom

Introduction: Pulse rate variability (PRV) refers to the changes in pulse rate through time and is extracted from pulsatile signals such as the photoplethysmogram (PPG). Although PRV has been used as a surrogate of heart rate variability (HRV), which is measured from the electrocardiogram (ECG), these variables have been shown to have differences, and it has been hypothesised that these differences may arise from technical aspects that may affect the reliable extraction of PRV from PPG signals. Moreover, there are no guidelines for the extraction of PRV information from pulsatile signals.

Aim: In this study, the extraction of frequency-domain information from PRV was studied, in order to establish the best performing combination of parameters and algorithms to obtain the spectral representation of PRV.

Methods: PPG signals with varying and known PRV content were simulated, and PRV information was extracted from these signals. Several spectral analysis techniques with different parameters were applied, and absolute, relative and centroid-related frequency-domain indices extracted from each combination. Indices from extracted and known PRV were compared using factorial analyses and Kruskal-Wallis tests to determine which spectral analysis technique gave the best performing results.

Results: It was found that using fast Fourier transform and the multiple signal classification (PMUSIC) algorithms gave the best results, combined with cubic spline interpolation and a frequency resolution of 0.0078 Hz for the former; and a linear interpolation with a frequency resolution as low as 1.22×10^{-4}, as well as applying a fifth order model, for the latter.

Discussion: Considering the lower complexity of FFT over PMUSIC, FFT should be considered as the appropriate technique to extract frequency-domain information from PRV signals.

KEYWORDS

photoplethysmography, pulse rate variability, spectral analysis, fast Fourier analysis, simulation

Introduction

Pulse rate variability (PRV) describes the changes in pulse rate (PR) through time when it is measured from pulsatile signals such as the photoplethysmogram (PPG) (Mejía-Mejía et al., 2020). PRV has been proposed as an alternative to heart rate variability (HRV), which refers to the changes in heart rate (HR) through time, and is obtained from electrocardiograms (ECG) (Task Force of the European Society of Cardiology and The North American Society of Pacing and Electrophysiology, 1996; Schäfer and Vagedes, 2013; Mejía-Mejía et al., 2020). PRV has become more popular recently, mainly due to the widespread use of PPG sensors in wearable devices, and to the non-invasive, cost-effective and non-intrusive nature of acquiring PPGs (Kyriacou, 2021).

PRV and HRV originate from the same physiological process, i.e., the autonomic regulation performed on the sino-atrial node, which controls the pumping rate of the heart (Rangayyan, 2002; Shaffer and Ginsberg, 2017). In fact, HR and PR have been shown to be good surrogates (Schäfer and Vagedes, 2013). However, the relationship between HRV and PRV is not entirely understood, and although they show similar trends, there is evidence of differences between these two variables, especially when measured from non-healthy, non-resting or elderly subjects (Schäfer and Vagedes, 2013; Mejía-Mejía et al., 2020).

Two hypotheses have been proposed to explain these differences. Some authors argue that the differences between HRV and PRV are mainly explained by physiological aspects. It has been observed that stress and diseases affect PRV in a different way than HRV (Giardino et al., 2002; Charlot et al., 2009; Khandoker et al., 2011; Mejía-Mejía et al., 2021), whereas other aspects such as pulse transit time, external forces on the arteries and the different nature of ECG and PPG have also been proposed as physiological differences that may explain the dissimilarity between HRV and PRV (Gil et al., 2010; Trajkovic et al., 2011; Chen et al., 2015). These and the fact that PRV has been observed in the absence of HRV (Constant et al., 1999; Pellegrino et al., 2014) suggest that there are different processes affecting PRV that are not related to HRV.

An alternative hypothesis is that the agreement between HRV and PRV is affected by technical aspects when PRV is extracted from pulsatile signals (Posada-Quintero et al., 2013; Hemon and Phillips, 2016; Choi and Shin, 2017; Béres et al., 2019; Mejía-Mejía et al., 2022). This is a particularly crucial issue, considering that there are no published guidelines for the extraction of PRV from pulse waves and the standardisation of the related analyses. Therefore, most methodologies for PRV studies are based on the guidelines for HRV assessment from ECG signals (Task Force of the European Society of Cardiology and The North American Society of Pacing and Electrophysiology, 1996). Moreover, most studies performed to understand the effects of technical aspects on PRV are based on the comparison between PRV and HRV, which might introduce further biases since PRV is affected differently to HRV by certain physiological processes.

Most studies related with PRV have been based on the extraction of frequency-domain indices, due to their known relationship with sympathetic and parasympathetic activity (Shaffer and Ginsberg, 2017; Mejía-Mejía et al., 2020). However, there is a lack of understanding of how different spectral analysis techniques can affect the obtained results, although it is known that classical and modern approaches for spectral analysis deliver different results and can be affected by several parameters, such as sampling rate, the number of data points used for computing the spectra and the order of the model (Semmlow and Griffel, 2014). Moreover, interbeat intervals are not evenly sampled, which implies that the trends need to be interpolated in order to have an evenly-sampled time-series to which classical and modern methods can be applied to (Clifford, 2006). However, the effects of this interpolation on the measured spectra and the related indices is not clear, and there is no standard approach to apply this interpolation to the data. The aim of this study was then to determine the best combination of parameters for the extraction of frequency-domain indices from PRV, in a first attempt to establish guidelines for the extraction of frequency-domain information from PRV trends. In this first study, this was done using PRV trends extracted from simulated PPG signals with simulated PRV information, which was considered as gold standard. The main advantages of using simulated signals were 1) the availability of larger amounts and more heterogeneous data, and 2) the comparison of obtained results to a known gold standard rather than HRV, which could introduce additional errors and physiologically-induced differences.

Materials and methods

The aim of this study was to determine the best combination of parameters for the extraction of frequency-domain indices from PRV, considering PPG signals simulated with a properly selected sampling rate and applying the best performing combination of inter-beat intervals (IBIs) detection algorithm and fiducial points (Mejía-Mejía et al., 2022). The simulation and processing of photoplethysmographic signals was performed in MATLAB (version 2020b), while statistical analyses were done in RStudio (version 1.4.1717).

Signal simulation

PPG signals were simulated using the model described by Mejía-Mejía et al. (2022). This model is based on the work proposed by Tang et al. (2020b) and Tang et al. (2020a), where each cardiac cycle is simulated using the sum of two

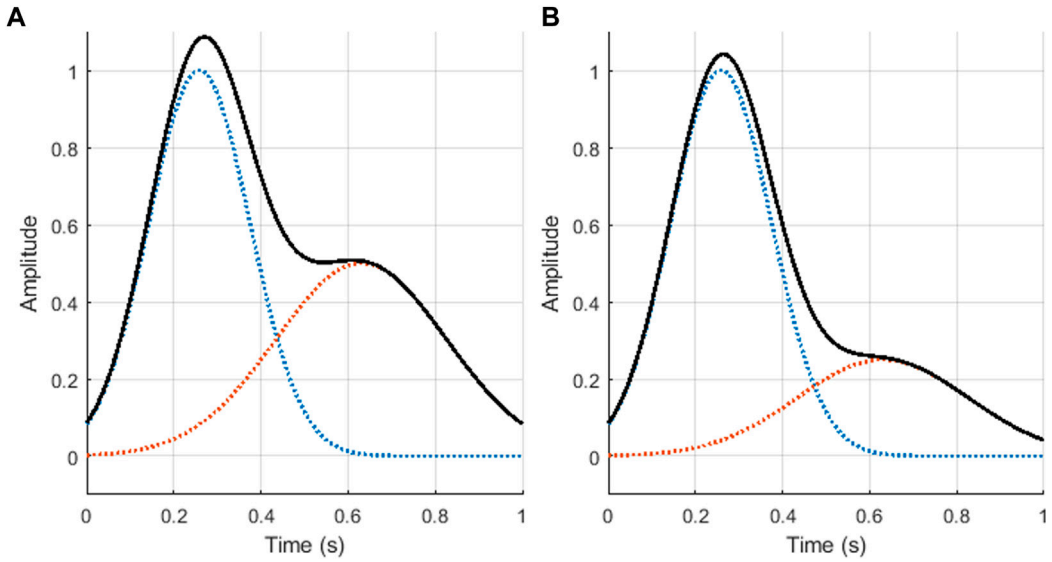

FIGURE 1
Photoplethysmographic cardiac cycles generated using the proposed mode, using ratios of value **(A)** r = 2 (excellent quality), and **(B)** r = 4 (acceptable quality). The blue and orange dotted lines illustrate the two Gaussian functions generated, while the black continuous line shows the result of summing these two Gaussian functions, i.e., z.

Gaussian functions, with parameters set to simulate excellent and acceptable quality PPG signals. The resulting model for a single PPG cycle is shown in Eq. 1, where θ corresponds to the four quadrant inverse tangent of the cosine and sine functions of the duration of the cycle; a_i, b, and μ_i correspond to the height, width and mean values of the Gaussian function; and r is a parameter that can be selected to control the relationship of the amplitudes of both Gaussians. This is the main parameter that differentiates between excellent and acceptable quality PPG cycles, and determines the amplitude of the dicrotic notch. In this study, two groups of PPG signals with different values for the r parameter were simulated. Excellent quality PPG signals were simulated with ratios of r = 2, while acceptable quality PPG signals were considered as those with r = 4. Figure 1 shows the base cardiac cycles used for the simulation of excellent and acceptable quality signals.

$$z = a\left(e^{-\frac{(\theta-\mu_1)^2}{2b_1^2}}\right) + \frac{1}{r}a\left(e^{-\frac{(\theta-\mu_2)^2}{2b_2^2}}\right) \quad (1)$$

The simulated cardiac cycles were then appended to create a PPG signal with a determined length. The duration of each of the cardiac cycles, i.e., the width of the summation of the Gaussians, was modified in order to include PRV information on the PPG signal. The duration of cardiac cycles was randomly generated by simulating PRV information as a sum of sinusoidal waves with parameters that fall inside plausible physiological values for PRV. The ranges for these parameters are shown in Table 1. It is worth mentioning that this is not the only possible way to generate PRV information, and other models could modify the behaviour of the obtained signal.

TABLE 1 Ranges for the Pulse Rate Variability (PRV) parameters and the generation of PRV gold standard values.

Parameter	Range	Units
Low frequency peak location (LF)	0.04–0.15	Hz
High frequency peak location (HF)	0.15–0.40	Hz
Average pulse rate (PR)	40–200	Beats per minute (bpm)
Standard deviation of pulse rate (SD)	0.05–0.08	s

The resulting function for the randomly generated PRV information is shown in Eq. 2. As can be seen, a total of four sinusoidal waves are summed, each of them with different fundamental frequencies, two for each of the main frequency bands in PRV analysis ($LF(i)$ and $HF(i)$). This was done to increase the variability of the frequency spectrum and to alter the area of each of the frequency bands.

$$PRV = PR + SD\sum_{i=1}^{2}\left(\sin\left(2\pi LF\left(i\right)t\right) + \sin\left(2\pi HF\left(i\right)t\right)\right) \quad (2)$$

For this study, a total of 200 excellent quality and 200 acceptable quality PPG signals were simulated, each with 1,200 cardiac cycles and a sampling rate of 256 Hz. An example of these signals is shown in Figure 2.

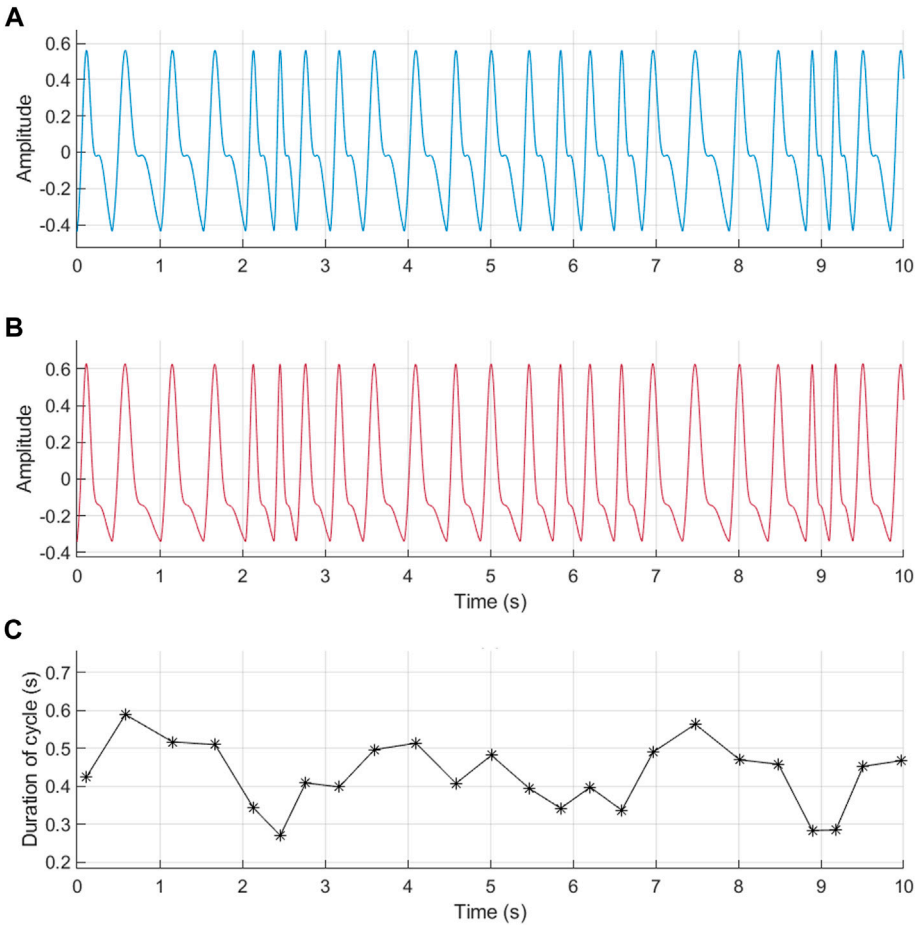

FIGURE 2
Example of photoplethysmographic (PPG) signals simulated using the proposed model and randomly generated pulse rate variability (PRV) information. **(A)** PPG signal with excellent quality (r = 2). **(B)** PPG signal with acceptable quality (r = 4). **(C)** PRV information used for the generation of these signals.

Inter-beat intervals

The cardiac cycles were detected from the simulated signals using the algorithm described by Elgendi et al. ()elg2013, denoted as D2Max, which has been shown to have a good performance for PRV analysis (Mejía-Mejía et al., 2022). This algorithm is based on the generation of blocks of interests based on two moving averages, which are designed based on the expected duration of cardiac cycles and the *a* point in the second derivative of the PPG signal. The location of the systolic peak from the PPG signal is determined as the location of the maximum point in each block of interest.

IBIs were then measured as the time difference between consecutive *a* points detected from each of the identified cardiac cycles. IBIs longer than 1.25 times the median duration of all the IBIs were corrected by looking for additional cardiac cycles in each of these longer windows. IBIs shorter than 0.75 times the median duration of IBIs were also detected and discarded.

Spectral analysis

Several methodologies for spectral analysis were applied to the extracted IBIs. Fast Fourier transform (FFT) and Welch's power spectral density (PWELCH) were used as classical methods. For PWELCH, a Hamming window and a 50% overlap between consecutive segments was considered. Yule-Walker's (PYULEAR), Burg's (PBURG), covariance (PCOV), and modified covariance (PMCOV) autoregressive models were used to obtain model based methods, as well as the multiple signal classification (PMUSIC) algorithm was used to obtain a pseudo-spectrum. Finally, the Lomb-Scargle algorithm (PLOMB) was also applied. In the case of classical and model-based algorithms, the parameters presented in Table 2 were optimized.

From the different combinations of parameters and the different methods for spectral analysis, PRV frequency domain indices were

TABLE 2 Combinations of parameters used for the extraction of frequency spectra from pulse rate variability trends. Frequency resolution: number of samples used to calculate spectrum (nFFT) divided by the sampling rate of the signal.

Methods	Interpolation		Frequency Resolution (Hz)	Order
	Technique	Sampling rate (Hz)		
Classical	Linear or cubic spline	4, 8, 16, 32, 64, 128, 256	0.01, 0.001, 0.0001	—
Model-based	Linear or cubic spline	4, 8, 16, 32, 64, 128, 256 Hz	0.01, 0.001, 0.0001	5, 10, 15, 20, 25, 30, 35, 40, 45, 50

TABLE 3 Mean and standard deviation (SD) values for PRV indices extracted from gold standard PRV.

Index	Mean ± SD
VLF (ms^2)	0.0555 ± 0.1430
LF (ms^2)	1.9781 ± 0.3495
HF (ms^2)	2.0024 ± 0.3639
TP (ms^2)	4.0360 ± 0.6787
nLF	0.4925 ± 0.0489
nHF	0.4941 ± 0.0333
LF/HF	1.0078 ± 0.1833
cLF_x (Hz)	0.0948 ± 0.0235
cLF_y(ms^2)	0.3501 ± 0.0803
cHF_x (Hz)	0.2686 ± 0.0463
cHF_y(ms^2)	0.3313 ± 0.0864
cTP_x (Hz)	0.1799 ± 0.0273
cTP_y(ms^2)	0.3410 ± 0.0445

extracted. The indices considered in this study were: The power of the very low frequency band (VLF); the absolute and relative power of the low frequency band (LF and nLF); the absolute and relative power of the high frequency band (HF and nHF); the total power of the spectrum between 0.0033 and 0.4 Hz (TP); the ratio between LF and HF (LF/HF); and the coordinates of the centroid of LF, HF and TP (cLF_x, cLF_y, cHF_x, cHF_y, cTP_x and cTP_y).

These indices were also extracted from the power spectra obtained from the simulated gold standard PRV signals. These were calculated using FFT with 2^{16} number of points (nFFT). Table 3 summarises the PRV indices extracted from gold standard PRV.

Statistical analysis

Factorial analyses were performed for each independent spectral analysis method. This was done in order to evaluate the effects of interaction among the studied factors, i.e., type of interpolation used (A), the number of data points used for obtaining the spectrum (B), the sampling rate used for interpolation (C), and the order of the model (D). The difference between the indices extracted from measured and gold standard PRV trends were obtained. These differences were then used for the statistical analysis, in which independent factorial analysis were first performed in order to obtain the combination of factors that gave the lowest differences when spectra was obtained using each of the different methods, except for the Lomb-Scargle periodogram, in which no parameters needed to be modified. Then, the best combination of factors was identified for each of the methods and these were compared using a Kruskal-Wallis test, since data did not follow a normal distribution according to the Lilliefors test of normality of data. Using Wilcoxon rank sum tests with Bonferroni correction, *post hoc* analyses were performed for the indices in which the Kruskal-Wallis analysis showed statistically significant differences among methods. The best combination of method, interpolation technique, frequency resolution and model order was then identified. Since data did not comply with ANOVA assumptions for factorial analyses, Box-Cox transformations were applied for the statistical analyses.

Cross-correlation and Pearson (XC Pearson) and Spearman (XC Spearman) correlation analyses were used to compare the frequency spectra obtained from measured and gold-standard PRV. This was done to assess the similarity among spectra extracted with the different combinations of parameters and with the different methods. The cross-correlation was characterized using the maximum value of cross-correlation found (XC max), and the lag at which this maximum occurred (XC lags). A similar process with factorial analyses was performed with these indices, considering that a maximal cross-correlation was desired.

Results

As explained, a factorial analysis was performed for each independent spectral analysis method. This was done in order to evaluate the effects of interaction among the studied factors, i.e., type of interpolation used (A), the number of data points used for obtaining the spectrum, which relates to the frequency resolution (B), the sampling rate used for interpolation (C), and the order of the model (D, for model-based approaches). The

TABLE 4 Summary of results obtained from the Kruskal-Wallis one-way analysis of variance and *post hoc* comparisons for pulse rate variability obtained from excellent quality PPG signals. ×: Significant differences. —: Non-significant differences.

Index	Best results	Significant differences							
		FFT	PWELCH	PYULEAR	PBURG	PCOV	PMCOV	PMUSIC	PLOMB
VLF	PMUSIC	—	—	—	—	—	—	—	×
LF	PWELCH	—	—	×	×	×	×	×	×
HF	FFT	—	×	×	×	×	×	×	×
TP	FFT	—	×	×	×	×	×	×	×
nLF	PMUSIC	×	×	—	×	×	×	—	×
nHF	PMUSIC	×	×	×	×	×	×	—	×
LF/HF	PMUSIC	×	×	×	×	×	×	—	×
cLF_x	PMUSIC	—	—	—	—	—	—	—	—
cLF_y	PCOV	×	×	—	—	—	—	—	×
cHF_x	PMUSIC	—	—	—	—	—	—	—	-—
cHF_y	PYULEAR	×	×	—	×	—	—	—	×
cTP_x	PMUSIC	×	×	—	—	—	—	—	×
cTP_y	PMUSIC	×	×	—	—	—	—	—	×
XC lags	PMUSIC	×	×	×	×	×	×	—	×
XC max	PLOMB	×	×	×	×	×	×	×	—
Spearman	PCOV	×	×	—	—	—	—	—	—
Pearson	PWELCH	×	—	—	—	—	—	×	—

behaviour of indices extracted from excellent and acceptable PPG signals was generally very similar.

In the case of FFT, the interaction between the three factors (A × B × C) was significant for TP and XC lags, whereas it was significant for HF, XC lags and XC Spearman. For both methods, the interaction between the number of data points and sampling rate used for interpolation (B × C) was the most significant, whereas the interactions between the type of interpolation and the other two factors were non-significant in most cases. Centroid related indices were the less affected by the different factors, showing significance on factor A only for cHF_y when measured using FFT and PWELCH, and on factor B for cLF_y when measured using PWELCH.

In the case of modern methods the behaviour was not as clear, since each method showed different significant interactions. In the case of PYULEAR and PMUSIC, the interactions between the type of interpolation used, the number of data points and the order of the model (A × B × D), as well as the interactions between the type of interpolation, the sampling rate used and the order of the model (A × C × D) were significant in the majority of the indices, while for PBURG, PCOV, and PMCOV the maximum level of significance for most of the indices was with two-factor interactions.

The best combination of factors that gave the lowest difference for the measurement of each of the PRV indices, as well as those that delivered maximal cross-correlation to gold-standard spectra were determined for each of the methods that allowed the selection of parameters, both for excellent and acceptable quality PPG signals. Once the best combinations were identified for each of the methods, these and the results obtained using the Lomb-Scargle periodogram were compared using a Kruskal-Wallis one-way analysis of variance for each index. Tables 4, 5 summarize these results for PRV obtained from excellent and acceptable quality PPG signals, respectively.

Figures 3–6 show the mean and standard deviation of the differences of frequency-domain indices obtained between gold-standard and measured PRV trends, considering the best combinations of factors for each spectral analysis method, and Figure 7 summarizes the correlation results after comparing gold-standard and measured PRV spectra. The best spectral analysis should have minimal differences to gold-standard results, while achieving maximal correlation results.

It can be observed that the classical method with better performance was FFT, while MUSIC showed the best performance among modern methods. Both for excellent and acceptable quality PPG signals, PMUSIC was the best performing

TABLE 5 Summary of results obtained from the Kruskal-Wallis one-way analysis of variance and *post hoc* comparisons for pulse rate variability obtained from acceptable quality PPG signals. ×: Significant differences. —: Non-significant differences.

Index	Best results	Significant differences							
		FFT	PWELCH	PYULEAR	PBURG	PCOV	PMCOV	PMUSIC	PLOMB
VLF	PMUSIC	—	—	—	—	—	—	—	×
LF	PWELCH	—	—	×	×	×	×	×	×
HF	FFT	—	×	×	×	×	×	×	×
TP	FFT	—	×	×	×	×	×	×	×
nLF	PMUSIC	×	×	—	×	×	×	—	×
nHF	PMUSIC	×	×	×	×	×	×	—	×
LF/HF	PMUSIC	×	×	×	×	×	×	—	×
cLF_x	PMUSIC	—	—	—	—	—	—	—	—
cLF_y	PBURG	×	×	—	—	—	—	—	×
cHF_x	PBURG	—	—	—	—	—	—	—	—
cHF_y	PYULEAR	×	—	—	—	—	—	—	×
cTP_x	PMUSIC	×	×	—	—	—	—	—	×
cTP_y	PMUSIC	×	×	—	×	×	×	—	×
XC lags	PMUSIC	×	×	×	×	×	×	—	×
XC max	PLOMB	×	×	×	×	×	×	×	—
Spearman	PCOV	×	×	—	—	—	—	—	—
Pearson	PWELCH	×	—	—	—	—	—	×	—

method for 9 and 8 of 17 indices, respectively. In terms of classical methods, FFT showed better behaviour than PWELCH. Also, it was found that the Lomb-Scargle periodogram did not show good reliability for the extraction of frequency-domain indices. Both for excellent and acceptable quality PPG signals, the FFT showed better performances when obtained after applying a cubic spline interpolation and resampling PRV trends to 4 Hz, while an optimal number of samples for measuring the spectrum was 512, which gave a frequency resolution of 0.0078 Hz. In the case of the MUSIC method, resampling PRV trends to 4 Hz using linear interpolation and using a fifth order model gave the best results both for excellent and acceptable quality signals. For excellent quality PPG signals, a resolution frequency of 0.0078 Hz was also found to perform the best, although for acceptable quality PPG signals a number of samples that gave best results increased to 32,768, for a resolution frequency of 1.2207×10^{-4} Hz. Figure 8 exemplifies the behaviour of spectra obtained using these spectral analysis techniques and the corresponding parameters. Since FFT algorithm and application is less complex than PMUSIC, and there were not many significant differences between the best combinations of these two methods, applying FFT with the recommended parameters was found to be the best option for PRV spectral analysis.

Discussion

Frequency-domain indices are probably the most used HRV and PRV features since their relationship with specific processes related to autonomic regulation have been shown in the literature (Task Force of the European Society of Cardiology and The North American Society of Pacing and Electrophysiology, 1996; Billman, 2013; Shaffer and Ginsberg, 2017). However, at least for PRV analysis, there is no consensus regarding how frequency spectra should be derived from PRV time-domain trends, and very little research has been done concerning this issue.

As is mentioned in the guidelines for HRV analysis, the power spectral density (PSD) from HRV can be obtained using non-parametric (classical, such as FFT) and parametric (modern) methods (Task Force of the European Society of Cardiology and The North American Society of Pacing and Electrophysiology, 1996). However, there are multiple algorithms and parameters that can be modified in order to calculate this PSD both from HRV and PRV trends. Also,

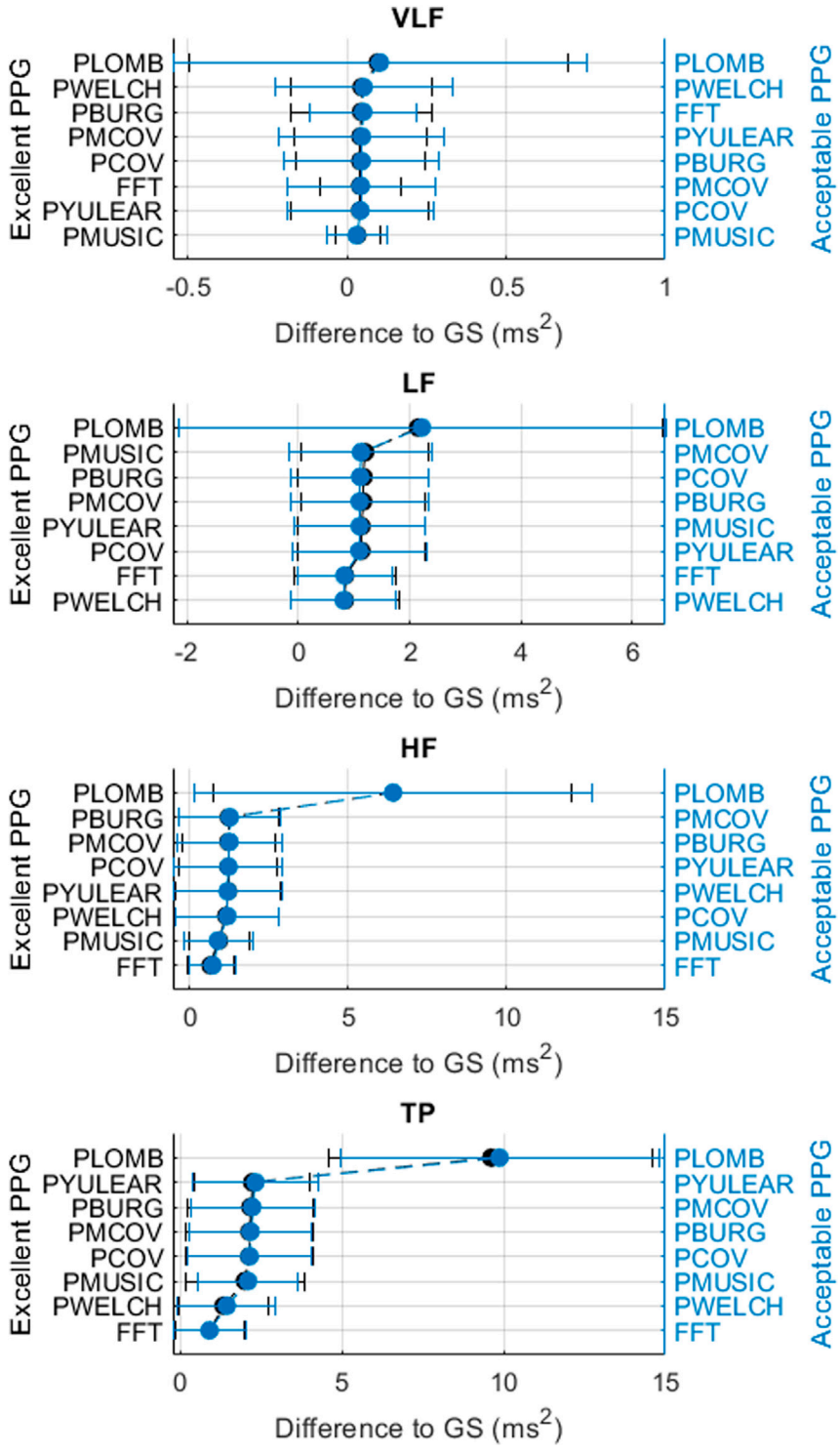

FIGURE 3
Mean and standard deviations of the differences obtained by comparing pulse rate variability absolute power frequency-domain indices obtained from extracted and gold-standard trends.

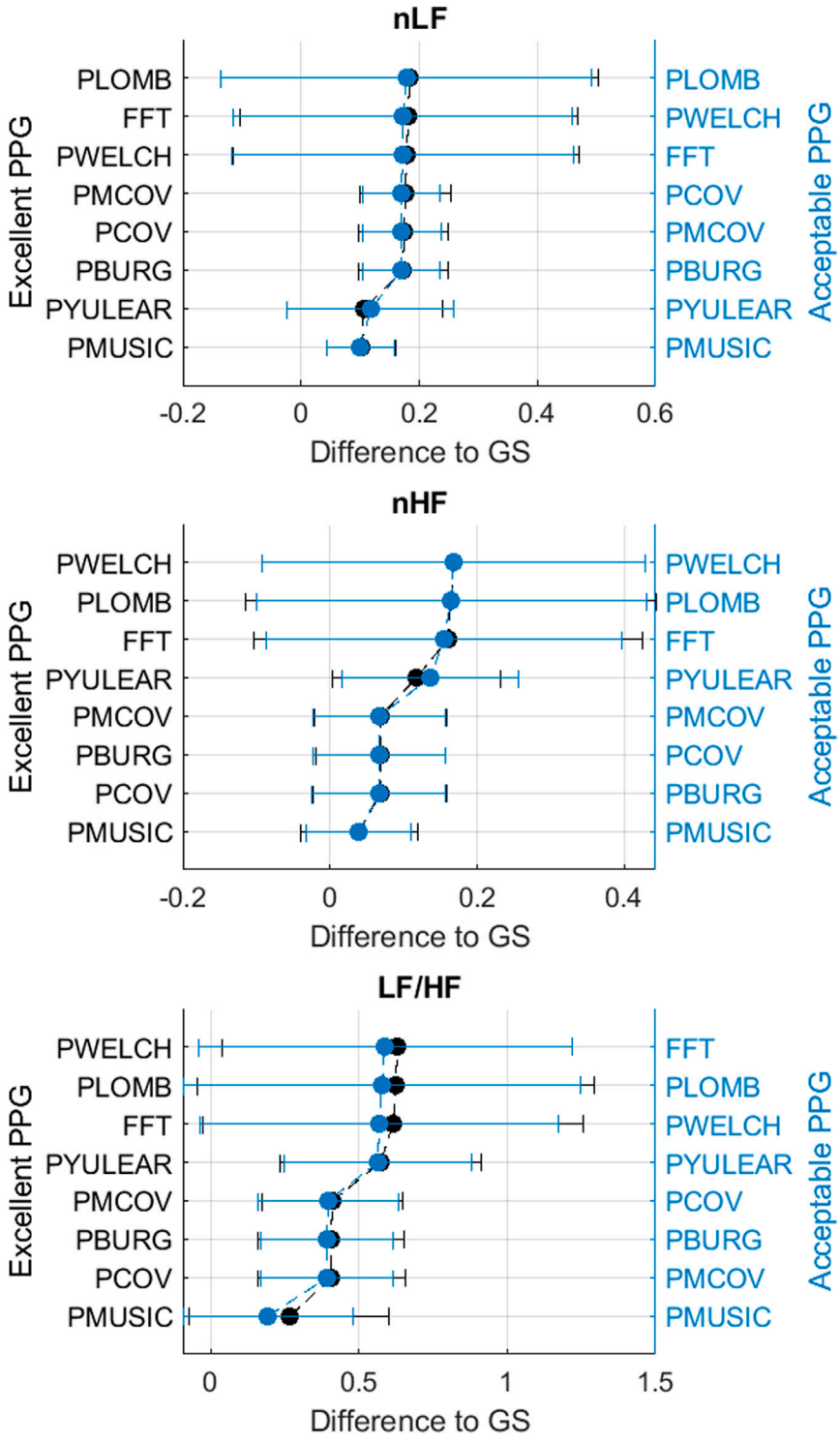

FIGURE 4
Mean and standard deviations of the differences obtained by comparing pulse rate variability relative power frequency-domain indices obtained from extracted and gold-standard trends.

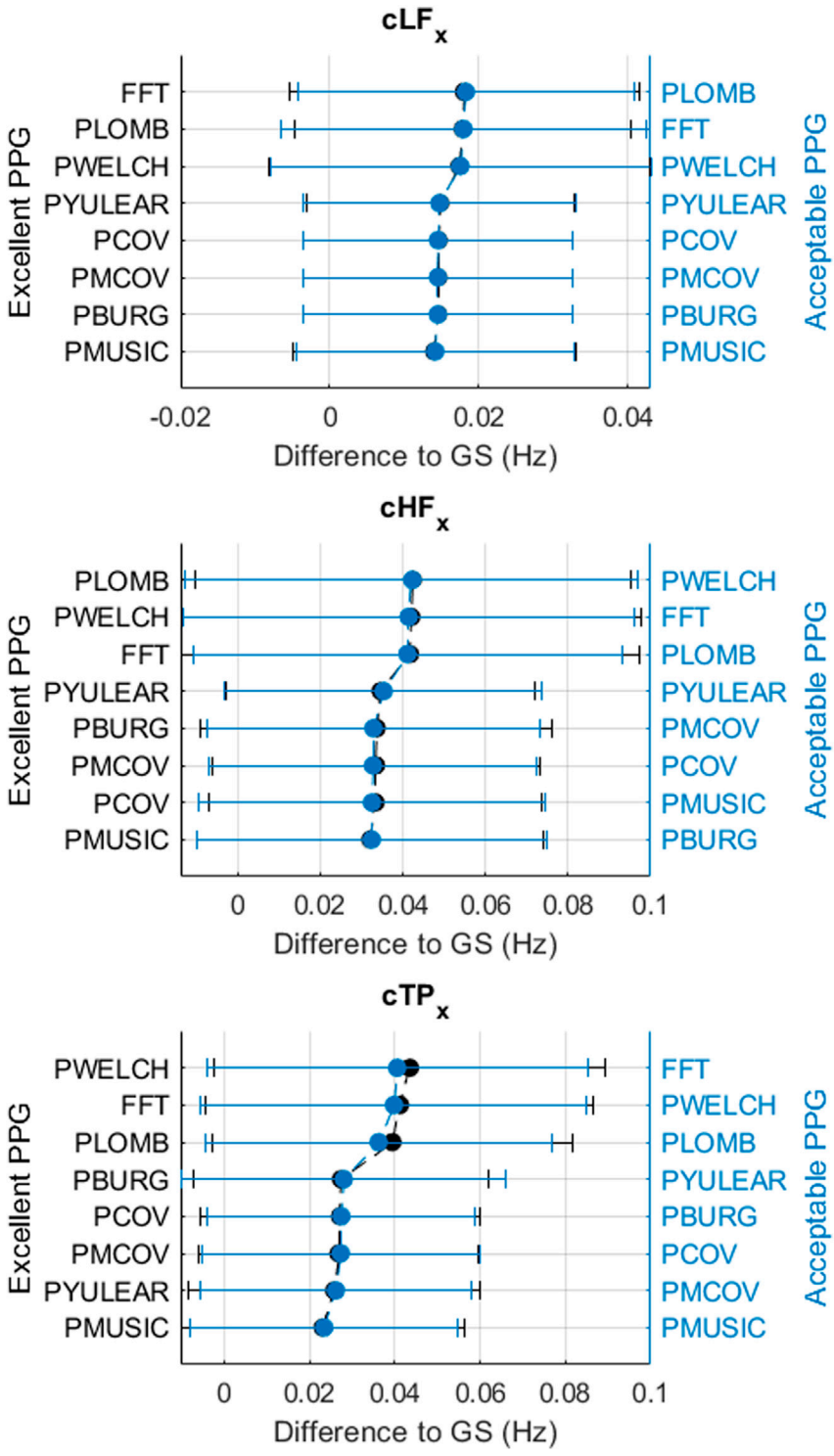

FIGURE 5
Mean and standard deviations of the differences obtained by comparing pulse rate variability *x*-coordinates of centroid-related frequency-domain indices obtained from extracted and gold-standard trends.

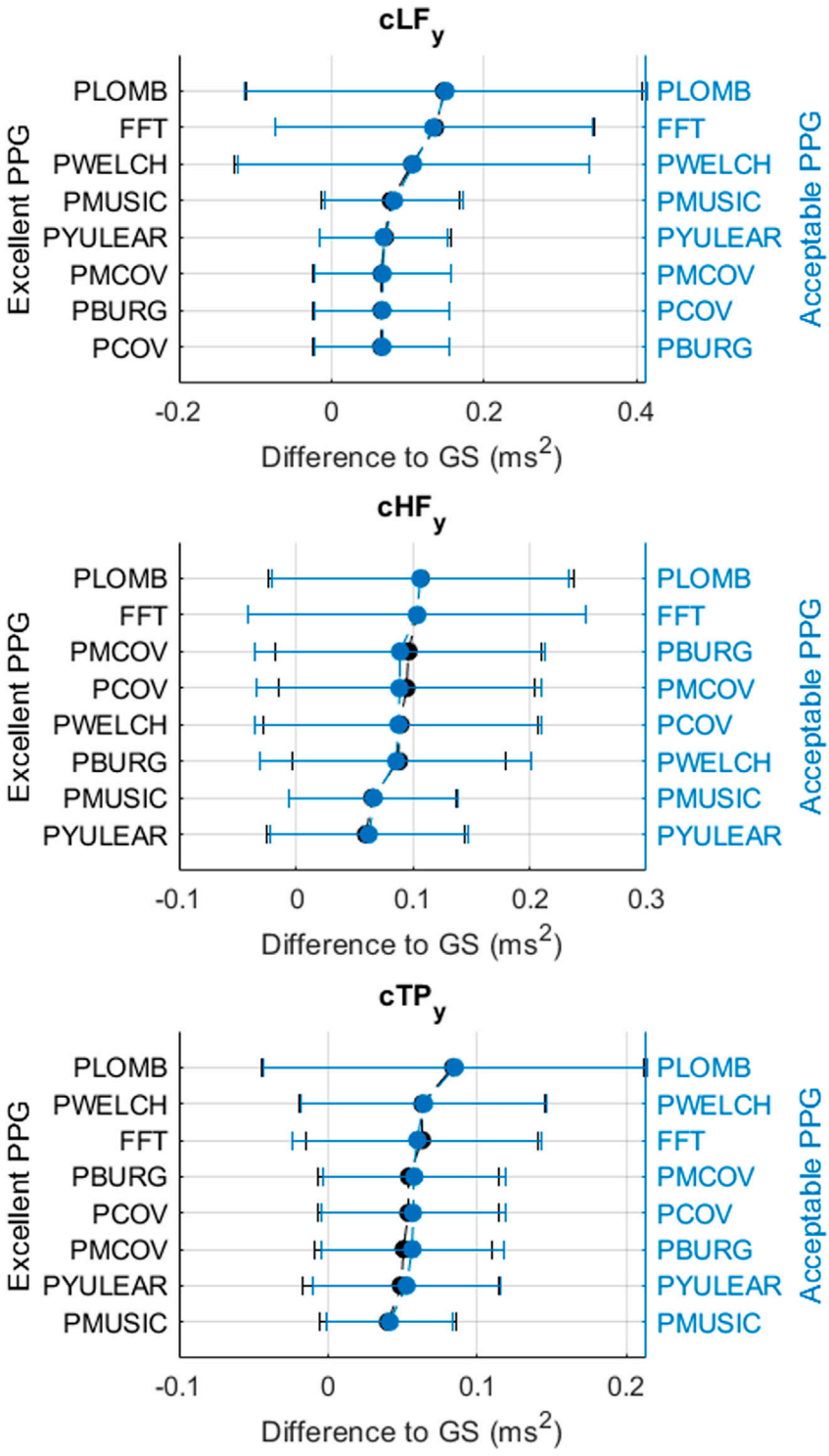

FIGURE 6
Mean and standard deviations of the differences obtained by comparing pulse rate variability *y*-coordinates of centroid-related frequency-domain indices obtained from extracted and gold-standard trends.

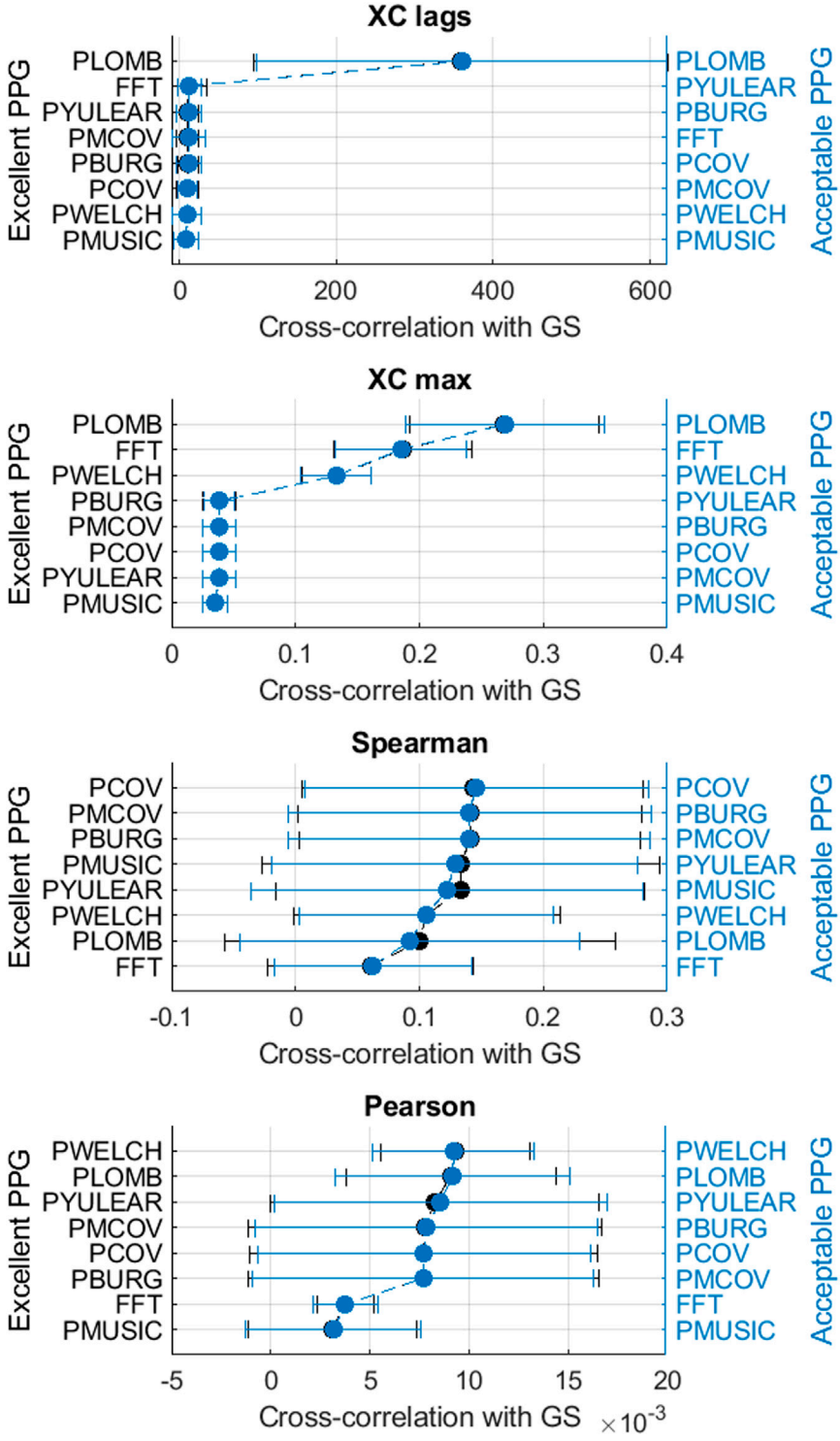

FIGURE 7
Mean and standard deviations of the correlation results obtained by comparing pulse rate variability spectra obtained from extracted and gold-standard trends.

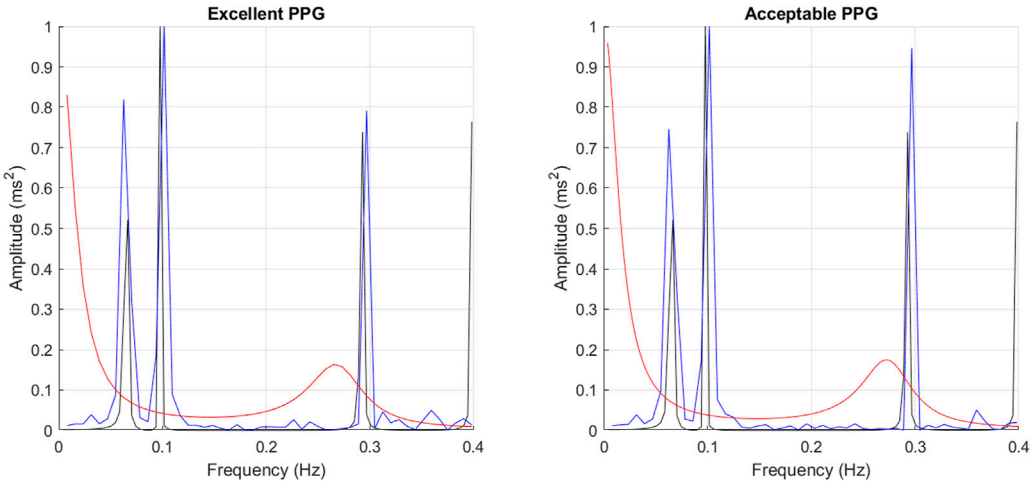

FIGURE 8
Example of spectra obtained from gold standard PRV (black), FFT (blue) and PMUSIC (red), both from excellent and acceptable quality PPG signals.

research related to the optimisation of these parameters and their suitability to obtain frequency domain indices from PRV is scarce, hence reinforcing the need for such research (Li et al., 2019). provided a useful summary of the different methodologies used for spectral analysis from HRV trends. In the case of PRV (Akar et al., 2013), applied several pre-processing techniques for the extraction of PRV indices from PPG signals, and compared the spectra obtained using the periodogram, Welch's and Burg's algorithms. Although qualitative, their results showed differences in the extracted spectra due to the methods used for its extraction (Chen et al., 2018). evaluated the differences between frequency-domain indices extracted from PRV trends re-sampled using different sampling rates, concluding that, from data obtained from wearable devices, better results were obtained using a 1 Hz re-sampling rate for interpolating pulse rate information and extracting frequency-related information. Other studies have also suggested the extraction of frequency-related indices using novel time-frequency techniques, such as empirical mode decomposition (Abeysekera and Jaisankar, 2015; Chuang et al., 2015). In this study, the aim was to determine the best parameters for the extraction of spectral information from PRV trends. It was found that the morphology of the spectra, assessed by measuring cross-correlation indices between spectra obtained from gold-standard and measured PRV trends, is affected, in most cases, by all the factors considered for obtaining the PSD and their interaction. However, PRV indices did not show this behaviour. In the case of classical spectral analysis, indices were mostly affected by the number of data points and the sampling rate used for interpolation before extracting PSD. Both these factors are related to the frequency resolution of the obtained spectra, which was shown to be a critical factor for the assessment of frequency-related information regardless of the algorithm used for obtaining the spectra. The comparison of the behaviour of indices extracted using different modern methods is less straightforward, indicating the variability among the mathematical foundations for each of these algorithms. In the case of Yule-Walker and MUSIC algorithms, three-way interactions including the type of interpolation used and the order of the model showed significant behaviour, while for the remaining methods two-way interactions showed the most significant results.

It is noticeable that, in the case of centroid-related indices, there were more significant interactions for indices related to the *y*-coordinate, particularly for the centroid of the high-frequency band. This could be indicating that the different methods for assessing PRV frequency-content tend to be relatively stable for the distribution of the frequency content, but there are differences in terms of the amplitude of the spectra. Hence, additional care should be taken when amplitude-related indices are of interest. Also of interest is the fact that the Lomb-Scargle algorithm did not show a better performance than the other methods studied. This algorithm is based on probability distributions and does not require a periodically-sampled signal (Clifford, 2006). However, its lower performance might be related precisely to the unpredictability of PRV trends, and the largely variable parameters used for the simulation of PRV information.

In general, it was found that MUSIC and FFT had the best behaviour both for excellent and acceptable quality PPG signals. In the case of MUSIC, the best behaviour was found when PRV trends were resampled to 4 Hz using linear interpolation and when a fifth order model was used, both for excellent and acceptable quality PPG signals, with frequency resolution of 0.0078 and 0.000122 Hz respectively. In the case of FFT, the

best results regardless of quality of the signal were obtained after applying a cubic spline interpolation to obtain a 4-Hz PRV trend, and calculating the spectrum with 512 data points, for a frequency resolution of 0.0078 Hz. Given the simplicity of FFT, the computational load it has, and the easiness to perform it in any platform, including embedded systems, it is recommended to obtain spectral information from PRV trends using this algorithm and these combination of parameters.

It is important to remark that the gold standard measurements were extracted using FFT, hence a bias could be present due to this. Non-etheless, the fact that the MUSIC algorithm also showed a good performance, and that Welch's periodogram showed comparable results to FFT, indicate that the results obtained are reliable. Moreover, the improved results obtained using these algorithms can be explained from their theoretical principles. The MUSIC algorithm, which is based on the identification of eigenvalues and eigenvectors from a signal, has been shown to be a high-resolution method particularly suitable for analysing time series that are a sum of sinusoidal waves, such as PRV, contaminated with Gaussian noise (Fernando et al., 2003; Castanié, 2011). In the case of FFT, this is the most direct and efficient digital implementation of the Fourier transform, and hence is a suitable tool for the spectral analysis of sine wave signals (Castanié, 2011; Semmlow and Griffel, 2014). Also, when FFT is compared to other classical methods, it has a higher resolution than other alternatives such as Welch's method (Semmlow and Griffel, 2014). In general, both MUSIC and FFT could be expected to perform well when the input signal exhibits a sine-like behaviour and when higher resolution is required to observe the behaviour of the signal at lower frequencies, as is the case of PRV.

This study has some limitations. Firstly, simulated PPG signals with simulated PRV information were used in this study. This was done with two main purposes. It is simpler to obtain larger number of samples using simulated data, which gives statistical validity to the experiment. The sample size for this study was estimated to observe differences of 2% in the measurement of the indices, compared to the gold standard. Also, by simulating PRV information it was possible to obtain a gold standard that was not HRV information obtained from the ECG. As mentioned, physiological aspects may explain part of the differences between HRV and PRV, hence comparing them in order to establish methodologies and strategies for obtaining PRV information is not ideal. Regardless of the benefits of using simulated signals, these may not represent the entire variation of the PPG morphology, and the results from these experiments need to be validated using real PPG data. The simulation of PRV information may also affect the results obtained. However, PRV was simulated using physiologically feasible values, which may introduce larger variability of the PRV but also simulate PRV information that could be obtained from most of the healthy population. Future studies should optimise the PRV model to have a better reflection of real PRV information, applying alternative models such as the integral pulse frequency modulation model (Candia-Rivera et al., 2021) or dynamical models such as the one proposed by McSharry et al. (2003). Secondly, the signals simulated were noiseless. This was done to have a controlled way to modify the parameters, but the effect of noise in these results need to be considered in future studies. Also, the agreement between indices was not assessed. Future studies should investigate not only the significance of the difference but also determine how the indices agree using techniques such as Bland-Altman analysis. Finally, the gold standard indices used in this study were extracted from PRV trends using FFT, which could have had a bias on the results. However, this was considered the optimal solution given the response of FFT compared to the rest of the algorithms.

Conclusion

The relationship between PRV and HRV is not straightforward, both due to physiological differences and to effects of technical aspects on the extraction of PRV information from pulsatile signals such as the PPG. The latter has not been thoroughly studied and there is no consensus regarding the methodologies for the extraction of PRV. In this study, a first approach for determining the best combination of factors for the extraction of frequency-domain indices from PRV information from simulated PPG signals was presented. It was found that spectral analysis of PRV information should be performed applying FFT and MUSIC algorithms, each of them with specific parameters for the selection of frequency resolution and interpolation of data. Future studies should aim to validate these results using real data and to evaluate how other technical aspects, such as the length of the recording and the presence of noise may affect frequency-domain analysis from PRV.

Data availability statement

The raw data supporting the conclusion of this article will be made available by the authors, without undue reservation.

Author contributions

Conceptualization, EM-M and PK; methodology, EM-M and PK; formal analysis, EM-M; writing—original draft preparation, EM-M; writing—review and editing, PK; supervision, PK. All authors have read and agreed to the published version of the manuscript.

Conflict of interest

The authors declare that the research was conducted in the absence of any commercial or financial relationships that could be construed as a potential conflict of interest.

Publisher's note

References

Abeysekera, S., and Jaisankar, B. (2015). "Photoplethysmographic signal feature extraction using an empirical mode decomposition approach," in 2015 10th International Conference on Information, Communications and Signal Processing (ICICS) (Singapore: IEEE), 1–5. doi:10.1109/ICICS.2015.7459904

Akar, S., Kara, S., Latifoğlu, F., and Bilgiç, V. (2013). Spectral analysis of photoplethysmographic signals: The importance of preprocessing. *Biomed. Signal Process. Control* 8, 16–22. doi:10.1016/j.bspc.2012.04.002

Béres, S., Holczer, L., and Hejjel, L. (2019). On the minimal adequate sampling frequency of the photoplethysmogram for pulse rate monitoring and heart rate variability analysis in mobile and wearable technology. *Meas. Sci. Rev.* 19, 232–240. doi:10.2478/msr-2019-0030

Billman, G. (2013). The lf/hf ratio does not accurately measure cardiac sympatho-vagal balance. *Front. Physiol.* 4, 26. doi:10.3389/fphys.2013.00026

Candia-Rivera, D., Catrambonea, V., Barbieri, R., and Valenza, G. (2021). Integral pulse frequency modulation model driven by sympathovagal dynamics: Synthetic vs. real heart rate variability. *Biomed. Signal Process. Control* 68, 102736. doi:10.1016/j.bspc.2021.102736

Castanié, F. (2011). *Digital spectral analysis*. 1 edn. London, UK: John Wiley & Sons.

Charlot, K., Cornolo, J., Brugniaux, J., Richalet, J., and Pichon, A. (2009). Interchangeability between heart rate and photoplethysmography variabilities during sympathetic stimulations. *Physiol. Meas.* 30, 1357–1369. doi:10.1088/0967-3334/30/12/005

Chen, H., Hu, Y., and Lin, S. (2018). Methodological considerations in calculating heart rate variability based on wearable device heart rate samples. *Comput. Biol. Med.* 102, 396–401. doi:10.1016/j.compbiomed.2018.08.023

Chen, X., Huang, Y., Yun, F., Chen, T., and Li, J. (2015). Effect of changes in sympathovagal balance on the accuracy of heart rate variability obtained from photoplethysmography. *Exp. Ther. Med.* 10, 2311–2318. doi:10.3892/etm.2015.2784

Choi, A., and Shin, H. (2017). Photoplethysmography sampling frequency: Pilot assessment of how low can we go to analyze pulse rate variability with reliability? *Physiol. Meas.* 38, 586–600. doi:10.1088/1361-6579/aa5efa

Chuang, S., Liao, J., Chou, C., Chang, C., and Fang, W. (2015). "Spectral analysis of photoplethysmography based on eemd method," in 2015 IEEE International Conference on Consumer Electronics - Taiwan, 224–225. doi:10.1109/ICCE-TW.2015.7216867

Clifford, G. (2006). "Ecg statistics, noise, artifacts, and missing data," in *Advanced methods and tools for ECG data analysis*. Editors G. Clifford, F. Azuaje, and P. McSharry. 1 edn. (Norwood, MA: Artech House), 55–99.

Constant, I., Laude, D., Murat, I., and Elghozi, J. (1999). Pulse rate variability is not a surrogate for heart rate variability. *Clin. Sci. (Lond).* 97, 391–397. doi:10.1042/cs19990062

Fernando, K., Mathews, V., Varner, M., and Clark, E. (2003). Robust estimation of fetal heart rate variability using Doppler ultrasound. *IEEE Trans. Biomed. Eng.* 50, 950–957. doi:10.1109/TBME.2003.814528

Giardino, N., Lehrer, P., and Edelberg, R. (2002). Comparison of finger plethysmograph to ecg in the measurement of heart rate variability. *Psychophysiology* 39, 246–253. doi:10.1017/S0048577202990049

Gil, E., Orini, M., Bailón, R., Vergara, J., Mainardi, L., and Laguna, P. (2010). Photoplethysmography pulse rate variability as a surrogate measurement of heart rate variability during non-stationary conditions. *Physiol. Meas.* 31, 1271–1290. doi:10.1088/0967-3334/31/9/015

Hemon, M., and Phillips, J. (2016). Comparison of foot finding methods for deriving instantaneous pulse rates from photoplethysmographic signals. *J. Clin. Monit. Comput.* 30, 157–168. doi:10.1007/s10877-015-9695-6

Khandoker, A., Karmakar, C., and Palaniswami, M. (2011). Comparison of pulse rate variability with heart rate variability during obstructive sleep apnea. *Med. Eng. Phys.* 33, 204–209. doi:10.1016/j.medengphy.2010.09.020

Kyriacou, P. (2021). "Introduction to photoplethysmography," in *Photoplethysmography: Technology, signal analysis, and applications*. Editors P. Kyriacou and J. Allen (London, UK: Elsevier), 1–15. chap. 1.

Li, K., Rüdiger, H., and Ziemssen, T. (2019). Spectral analysis of heart rate variability: Time window matters. *Front. Neurol.* 10, 545. doi:10.3389/fneur.2019.00545

McSharry, P., Clifford, G., Tarassenko, L., and Smith, L. (2003). A dynamical model for generating synthetic electrocardiogram signals. *IEEE Trans. Biomed. Eng.* 50, 289–294. doi:10.1109/TBME.2003.808805

Mejía-Mejía, E., May, J., and Kyriacou, P. (2022). Effects of using different algorithms and fiducial points for the detection of interbeat intervals, and different sampling rates on the assessment of pulse rate variability from photoplethysmography. *Comput. Methods Programs Biomed.* 218, 106724. doi:10.1016/j.cmpb.2022.106724

Mejía-Mejía, E., May, J. M., Elgendi, M., and Kyriacou, P. A. (2021). Differential effects of the blood pressure state on pulse rate variability and heart rate variability in critically ill patients. *npj Digit. Med.* 4, 82. doi:10.1038/s41746-021-00447-y

Mejía-Mejía, E., May, J., Torres, R., and Kyriacou, P. (2020). Pulse rate variability in cardiovascular health: A review on its applications and relationship with heart rate variability. *Physiol. Meas.* 41, 07TR01. doi:10.1088/1361-6579/ab998c

Pellegrino, P., Schiller, A., and Zucker, I. (2014). Validation of pulse rate variability as a surrogate for heart rate variability in chronically instrumented rabbits. *Am. J. Physiol. Heart Circ. Physiol.* 307, H97–H109. doi:10.1152/ajpheart.00898.2013

Posada-Quintero, H. F., Delisle-Rodríguez, D., Cuadra-Sanz, M. B., and Fernández de la Vara-Prieto, R. R. (2013). Evaluation of pulse rate variability obtained by the pulse onsets of the photoplethysmographic signal. *Physiol. Meas.* 34, 179–187. doi:10.1088/0967-3334/34/2/179

Rangayyan, R. (2002). *Biomedical signal analysis*. Calgary, Canada: IEEE Press.

Schäfer, A., and Vagedes, J. (2013). How accurate is pulse rate variability as an estimate of heart rate variability? A review on studies comparing photoplethysmographic technology with an electrocardiogram. *Int. J. Cardiol.* 166, 15–29. doi:10.1016/j.ijcard.2012.03.119

Semmlow, J., and Griffel, B. (2014). *Biosignal and medical image processing*. 3 edn. Boca Raton, Florida: CRC Press.

Shaffer, F., and Ginsberg, J. (2017). An overview of heart rate variability metrics and norms. *Front. Public Health* 5, 258. doi:10.3389/fpubh.2017.00258

Tang, Q., Chen, Z., Allen, J., Alian, A., Menon, C., Ward, R., et al. (2020a). Ppgsynth: An innovative toolbox for synthesizing regular and irregular photoplethysmography waveforms. *Front. Med.* 7, 597774. doi:10.3389/fmed.2020.597774

Tang, Q., Chen, Z., Ward, R., and Elgendi, M. (2020b). Synthetic photoplethysmogram generation using two Gaussian functions. *Sci. Rep.* 10, 13883. doi:10.1038/s41598-020-69076-x

Task Force of the European Society of Cardiology and The North American Society of Pacing and Electrophysiology (1996). Heart rate variability: Standards of measurement, physiological interpretation, and clinical use. *Circulation* 93, 1043–1065. doi:10.1161/01.CIR.93.5.1043

Trajkovic, I., Scholkmann, F., and Wolf, M. (2011). Estimating and validating the interbeat intervals of the heart using near-infrared spectroscopy on the human forehead. *J. Biomed. Opt.* 16, 087002. doi:10.1117/1.3606560

frontiers | Frontiers in Physiology

TYPE Original Research
PUBLISHED 17 January 2023
DOI 10.3389/fphys.2023.1090696

OPEN ACCESS

EDITED BY
John Allen,
Coventry University, United Kingdom

REVIEWED BY
Youngsun Kong,
University of Connecticut, United States
Christopher Austelle,
Medical University of South Carolina, United States

*CORRESPONDENCE
Eugenijus Kaniusas,
eugenijus.kaniusas@tuwien.ac.at

SPECIALTY SECTION
This article was submitted to Computational Physiology and Medicine, a section of the journal Frontiers in Physiology

RECEIVED 05 November 2022
ACCEPTED 06 January 2023
PUBLISHED 17 January 2023

CITATION
Rapalis A, Piartli P, Jankauskaitė L, Marozas V and Kaniusas E (2023), Induced pain affects auricular and body biosignals: From cold stressor to deep breathing.
Front. Physiol. 14:1090696.
doi: 10.3389/fphys.2023.1090696

Induced pain affects auricular and body biosignals: From cold stressor to deep breathing

Andrius Rapalis[1,2], Povilas Piartli[1], Lina Jankauskaitė[3,4], Vaidotas Marozas[1,2] and Eugenijus Kaniusas[5]*

[1]Biomedical Engineering Institute, Kaunas University of Technology, Kaunas, Lithuania, [2]Department of Electronics Engineering, Faculty of Electrical and Electronics Engineering, Kaunas University of Technology, Kaunas, Lithuania, [3]Department of Pediatrics, Faculty of Medicine, Medical Academy, Lithuanian University of Health Sciences, Kaunas, Lithuania, [4]Institute of Physiology and Pharmacology, Medical Academy, Lithuanian University of Health Sciences Kauno Klinikos, Kaunas, Lithuania, [5]Institute of Biomedical Electronics, Faculty of Electrical Engineering and Information Technology, Vienna University of Technology (TU Wien), Vienna, Austria

Pain affects every fifth adult worldwide and is a significant health problem. From a physiological perspective, pain is a protective reaction that restricts physical functions and causes responses in physiological systems. These responses are accessible for evaluation *via* recorded biosignals and can be favorably used as feedback in active pain therapy *via* auricular vagus nerve stimulation (aVNS). The aim of this study is to assess the significance of diverse parameters of biosignals with respect to their deflection from cold stressor to deep breathing and their suitability for use as biofeedback in aVNS stimulator. Seventy-eight volunteers participated in two cold pressors and one deep breathing test. Three targeted physiological parameters (*RR* interval of electrocardiogram, cardiac deflection magnitude Z_{AC} of ear impedance signal, and cardiac deflection magnitude PPG_{AC} of finger photoplethysmogram) and two reference parameters (systolic and diastolic blood pressures BP_S and BP_D) were derived and monitored. The results show that the cold water decreases the medians of targeted parameters (by 5.6, 9.3%, and 8.0% of *RR*, Z_{AC}, and PPG_{AC}, respectively) and increases the medians of reference parameters (by 7.1% and 6.1% of BP_S and BP_D, respectively), with opposite changes in deep breathing. Increasing pain level from relatively mild to moderate/strong with cold stressor varies the medians of targeted and reference parameters in the range from 0.5% to 6.0% (e.g., 2.9% for *RR*, Z_{AC} and 6.0% for BP_D). The physiological footprints of painful cold stressor and relaxing deep breathing were shown for auricular and non-auricular biosignals. The investigated targeted parameters can be used as biofeedback to close the loop in aVNS to personalize the pain therapy and increase its compliance.

KEYWORDS

auricular bioimpedance, auricular vagus nerve stimulation, blood pressure, cold pressor test, deep breathing, physiological biofeedback, photoplethysmography

1 Introduction

Acute or chronic pain is one of the main complaints for seeking medical care. According to the International Association for the Study of Pain, pain is defined as "unpleasant sensory and emotional experience associated with, or resembling that associated with, actual or potential tissue damage" Raja et al. (2020). Pain is a protective reaction restricting physical functions with various physiological parameters, such as heart rate, respiratory rate, and arterial blood

pressure, which are potential indicators of pain intensity Arbour et al. (2014); Cowen et al. (2015); Peters and Schmidt (1991). The specific changes can be observed by the reactivity and reflexivity of the autonomic nervous, cardiovascular, and respirator systems Kyle and McNeil (2014).

Adults and children suffer the pain associated with different medical conditions, undergo different painful procedures, or are referred with acute pain to the emergency department Dahlhamer et al. (2018); Keating and Smith (2011); Mura et al. (2017); Othow et al. (2022). Data suggest that 7 out of 10 patients come to the emergency department due to pain Todd et al. (2007). Meanwhile, chronic pain affects about 20.5% of adults in the United States Yong et al. (2022) and about 10%–30% in Europe Breivik et al. (2006); Reid et al. (2011). The meta-analysis showed that the prevalence of chronic pain ranges between 0% and 24% globally Mansfield et al. (2016).

Different medications, such as non-steroidal anti-inflammatory drugs, opioids, or others, are used daily against pain. Despite various pain medications and strategies, pain treatment faces many adversities Fishman (2007), such as severe side effects, the use of illicit drugs, opioid crisis St. Marie and Broglio (2020), peptic ulcers Tai and McAlindon (2021), and others. All the more, pain management is a fundamental human right Enright and Goucke (2016); Fishman (2007).

Vagal nerve stimulation (VNS)—as a pain neuromodulation technique, as reviewed in Kaniusas et al. (2019a)—has been investigated in humans and animals. VNS can affect the autonomic nervous system and is an approved treatment for pharmacoresistant depression and drug-resistant epilepsy Nemeroff et al. (2006); O'Reardon et al. (2006). Non-invasive transcutaneous modalities of VNS emerge Busch et al. (2013); Nesbitt et al. (2015), such as the electrical stimulation of the external surface of the ear innervated by the afferent auricular branch of the vagus nerve, known as auricular vagus nerve stimulation (aVNS). aVNS is performed using miniature electrodes tightly fixed inside the auricular concha. The current intensity is individually adjusted at the beginning of the aVNS session to a level without evoking pain. However, the initial personalization of the intensity of current alone does not ensure adequate vagus nerve stimulation for the relatively long treatment duration (from days to weeks). Here habituation effects, varying physiology, and deterioration of the electrode-tissue interface contribute to this uncertainty in the treatment Bouton (2017); Kaniusas (2019); Kaniusas et al. (2019b). Therefore, aVNS can be hypothesized to avoid under- or over-stimulation, reduce side effects, and save stimulation energy when based on individual physiological biofeedback.

Biofeedback can be assessed using data from internal (in-the-ear) and external (outside-the-ear) sensors, i.e., auricular and non-auricular biosignals. However, it is not known which biosignals and extracted parameters help estimate the balance between the stimulated parasympathetic system and the complementary sympathetic system, which is generally predominant in chronic ailments such as pain. In the ideal case, this balance should be provided to the aVNS stimulator to avoid the disadvantages of the non-personalized aVNS. Thus, easy-to-access biosignals are of high interest which could estimate this balance in favor of the efficiency of aVNS therapy.

The present study proposes a cold stressor as a sympathetically driven stimulus (usually accompanied by acute pain) and deep breathing as a mainly parasympathetically driven stimulus (with relaxing effects) to manipulate the sympathovagal balance from sympathetic to parasympathetic dominance while recording a set of auricular and non-auricular biosignals. The aim of this study is to assess the significance of diverse parameters of biosignals with respect to their deflection from cold stressor to deep breathing and their suitability for use as biofeedback in aVNS stimulator.

2 Materials and methods

2.1 Study population and data acquisition

Seventy-eight healthy volunteers (36 women), 32.6 ± 10.7 years old (range 20–64 years, with 23 men and 19 women <30 years), with a height of 1.76 ± 0.1 m, a weight of 75.0 ± 13.6 kg, and a body mass index of 24.1 ± 3.7 kg/m^2 participated in the study. All participants met the following criteria: 1) age ≥18 years; 2) no chronic pain; 3) no documented cardiovascular, respiratory, diabetes, and depression diseases; 4) no medication with b-blockers or calcium channel antagonists; and 5) no pregnancy or breastfeeding. Participants were instructed to avoid taking painkillers or anti-inflammatory drugs for at least 24 h and activities that could affect the cardiovascular system (smoking, coffee, alcohol, physical activity, medication, etc.) for at least 4 h before the study.

Data collection took place indoors at the Biomedical Engineering Institute (Kaunas, Lithuania) in a quiet and temperature-controlled (24.0°C ± 1.0°C) laboratory at the same time of the day (08:00–13:00) to minimize the circadian influence. Four synchronous biosignals were recorded in the study, as illustrated in **Figure 1**: 1) a modified bipolar three-lead electrocardiogram (ECG) signal (sampling rate 2 kHz); 2) a red wavelength finger photoplethysmogram (PPG) signal (sampling rate 1 kHz) using a proprietary multimodal signals recording system Nautilus II (Biomedical Engineering Institute, Kaunas, Lithuania); 3) an ear impedance signal (at the frequency of 12.5 kHz, sampling rate 1 kHz) using the data acquisition system Biopac MP150 (Biopac Systems Inc., Aero Camino, Goleta, CA, United States); and 4) arterial blood pressure signal (sampling rate 100 Hz) using the non-invasive arterial blood pressure monitoring system CNAP Monitor 500 (CNSystems, Graz, Austria). The subjective/perceived pain was recorded by a volunteer self-report (announced verbally and aloud to an experimenter) using the numerical rating scale NRS (range 0–100, with 0 for no pain and 100 for unbearable pain) at least every 30 s (or even more often based on a volunteer's initiative).

Well-known and effective pain-causing (the cold pressor test) and relaxation (deep breathing) tests were used in the study. Namely, the study protocol consisted of eight phases, as depicted in **Figure 2A**: 1) the first rest phase (Rest #1) lasting 10 min in the sitting position; 2) the warm water for 1 min (equalization phase), in which the participant immersed his left hand into warm water (32.0°C ± 0.1°C); 3) the first cold water phase (CPT #1), in which the participant immersed his left hand into cold water (7.0°C ± 0.1°C) for 2 min or even shorter if the volunteer felt very uncomfortable and voluntarily resumed; 4) the second rest phase (Rest #2) for 5 min where the participant took his left hand out from cold water and rested in the sitting position; 5) the second cold water phase (CPT #2), in which the participant immersed his left hand into a little less cold water (10.0°C ± 0.1°C) for 2 min or even shorter if the volunteer felt very uncomfortable and voluntarily resumed; 6) the third rest phase (Rest #3) for 10 min in analogy with Rest #2; 7) the deep breathing phase (DB) for 1 min with the paced breathing rate 6 1/min (paced *via* a

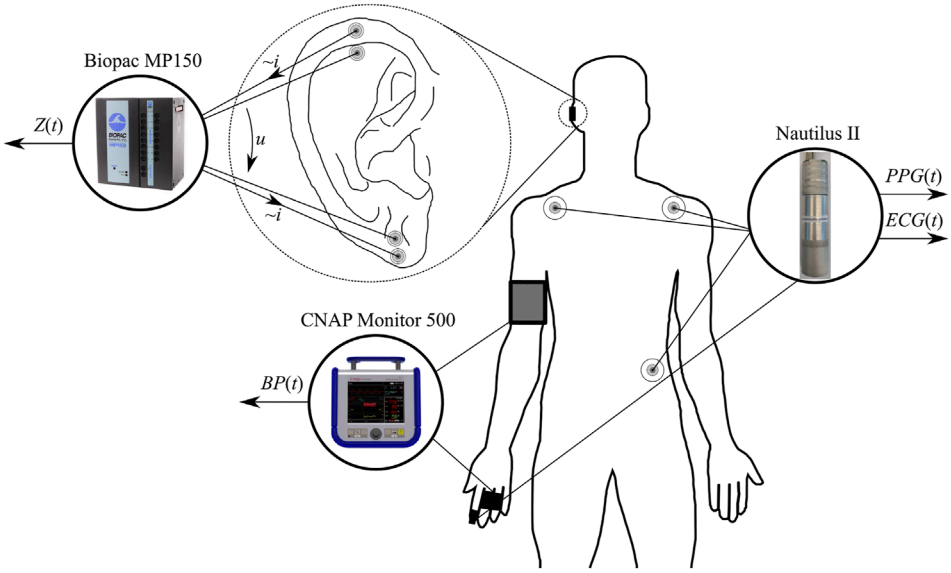

FIGURE 1
Placement of all sensors and electrodes for the recording of electrocardiogram *ECG*(*t*), pulse plethysmogram *PPG*(*t*), auricular impedance *Z*(*t*), and blood pressure *BP*(*t*) signals.

monitor and a bar rising/falling periodically every 10 s); 8) the fourth rest phase (Rest #4) for 5 min in analogy with Rest #2. Participants were verbally instructed to immerse their left hand (up to the middle of the forearm) in warm or cold water, indicate their subjective pain level (in cold water), and take out their hand after 1 min in warm and 2 min in cold water.

The study was conducted following the ethical principles of the Declaration of Helsinki and with ethics approval from the Kaunas Region Biomedical Research Ethics Committee (No. BE-2-24), including informed consent and voluntary participation. Personal information was removed from the collected data to ensure participants' anonymity.

2.2 Signal processing and parameters extraction

ECG was filtered using zero-phase Butterworth high-pass and low-pass filters (cut-off frequencies 0.5 and 35 Hz, respectively), R waves were detected using the modified Tompkins algorithm Hamilton and Tompkins (1986), and *RR* was estimated as the time interval between the successive R peaks. The ear impedance signal reflects local changes in the blood perfusion and blood vessel size, accounting for the local changes in capacitance and resistance. The impedance signal is morphologically similar to PPG so that both *PPG* and *Z* were filtered using high-pass and low-pass zero-phase Butterworth filters (cut-off frequencies 0.5 and 10 Hz, respectively). The associated peak and valley fiducial points in *PPG*, *Z*, and *BP* signals were detected in line with the detected R waves of ECG. Five parameters were extracted out of the four recorded biosignals (**Figure 3**): 1) time interval *RR* between R peaks of ECG; 2) cardiac deflection magnitude PPG_{AC} of PPG; 3) cardiac deflection magnitude Z_{AC} of ear impedance signal; 4) systolic blood pressure BP_S; and 5) diastolic blood pressure BP_D. Please note that the analyzed PPG_{AC} is mainly related to the pulsatile arterial blood, proportional to the local systolic-diastolic deflection of the blood pressure and the arterial compliance of the vascular wall Kaniusas (2015).

The entire periods of stimulation phases CPT #1, CPT #2, and DB were included in the analysis, only the last 4 min of rest phases Rest #1, Rest #2, and Rest #3 were included to avoid the transient influence of the preceding phase (**Figure 2B**). The medians of evaluated parameters from CPT #1, CPT #2, and DB phases were compared with the medians of the respective Rest #1, Rest #2, and Rest #3 phases, without any averaging. The analysis was performed using different pain levels, ages, and gender. The pain level threshold was chosen at 40 points, corresponding to mild pain Karcioglu et al. (2018). The age threshold was selected at 30 years in order to end up with comparably populated groups of men and women.

2.3 Statistical analysis

The Shapiro-Wilk test was used to assess data normality. Because of the non-normal distribution, the results are summarized using boxplots with medians and quartiles. The Wilcoxon signed-rank test with the Bonferroni's adjustment for dependent samples was used to compute the *p*-value, and statistical significance was set at $p < 0.05$.

3 Results

Out of 78 recorded data sets, two *ECG*, thirteen *PPG*, twenty-four *Z*, and six *BP* traces were eliminated from the analysis due to poor quality. Eight participants retreated earlier and did not finish the CPT #1 phase, i.e., two women (age ≤30 years), two women (age >30 years), one man (age ≤30 years), and one man (age >30 years).

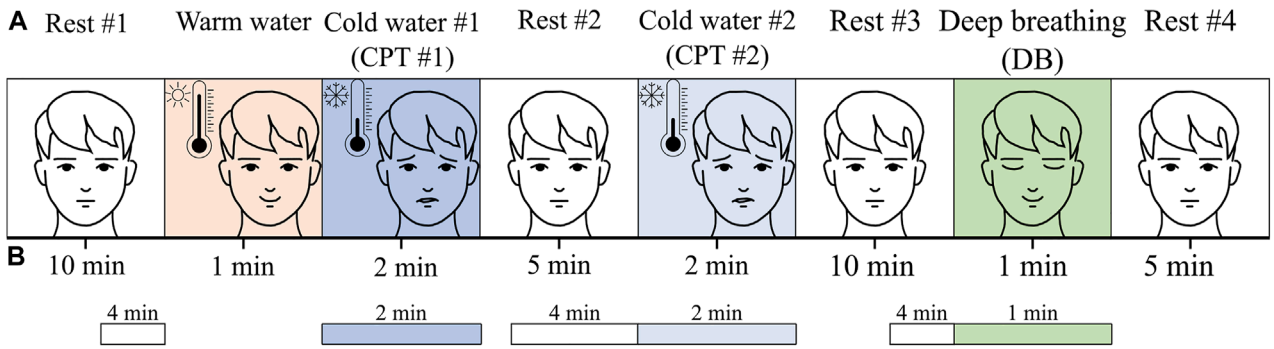

FIGURE 2
(A) The protocol of the study and **(B)** analyzed intervals.

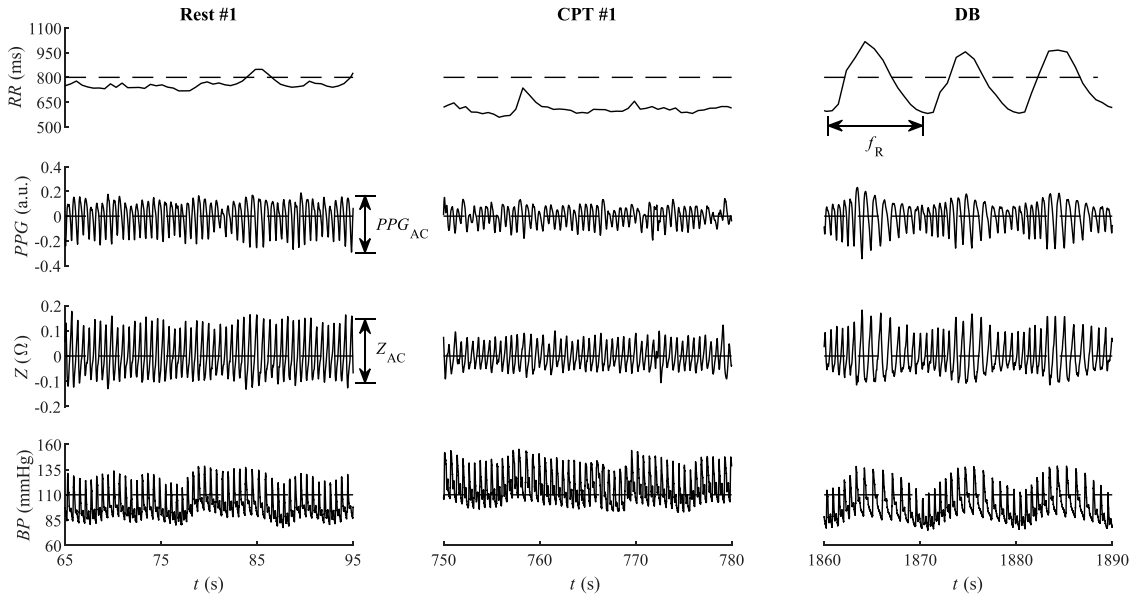

FIGURE 3
Instructive qualitative changes of the interbeat period *RR*, the pulse plethysmography *PPG*, bioimpedance *Z*, and blood pressure *BP* from the first rest phase (Rest #1), the first cold water phase (CPT #1), and the deep breathing phase (DB) of a single participant. The maximum reported NRS value of the CPT #1 was 80.

Two other participants did not finish CPT #2, i.e., one woman and one man, both aged >30 years.

3.1 General tendencies

Figure 3 illustrates the temporal courses of *RR*, *PPG*, *Z*, and *BP* during phases Rest #1, CPT #1, and DB. Compared to Rest #1, the cold stimulus CPT #1 shows reduced both *RR* and its variability, as well as reduced cardiac deflection magnitude PPG_{AC} of *PPG* and reduced cardiac deflection Z_{AC} of *Z*. The associated mean *BP* is larger during CPT #1 than during Rest #1. The subsequent DB phase contrasts CPT #1 in that PPG_{AC} and Z_{AC} increase in DB. The respiration-related variability of all four *RR*, PPG_{AC}, Z_{AC}, and *BP* dominates in DB, with the indicated respiration rate f_R (Figure 3).

3.2 Cold water versus deep breathing

As shown in Figure 4, the first cold water stimulation CPT #1 decreases the median of *RR* (−5.5%) and Z_{AC} (−9.8%) while increasing that of BP_S (+12.6%) and BP_D (+13.4%) of BP, as compared with the first rest phase Rest #1. Here the associated PPG_{AC} remains almost constant (+0.9%). The second cold water stimulation CPT #2 decreases the median of *RR* (−5.6%), PPG_{AC} (−8.0%), and Z_{AC} (−9.3%) while increasing that of BP_S (+7.1%) and BP_D (+6.1%), as compared with the second rest phase Rest #2. The subsequent deep breathing DB produces opposite effects: the median of *RR* (+1.8%), PPG_{AC} (+5.1%), and Z_{AC} (+5.4%) increase, while that of BP_S (−0.9%) and BP_D (−5.6%) decrease, as compared with the third rest phase Rest #3. The observed changes in DB are significantly different compared to CPT #2 in all five parameters.

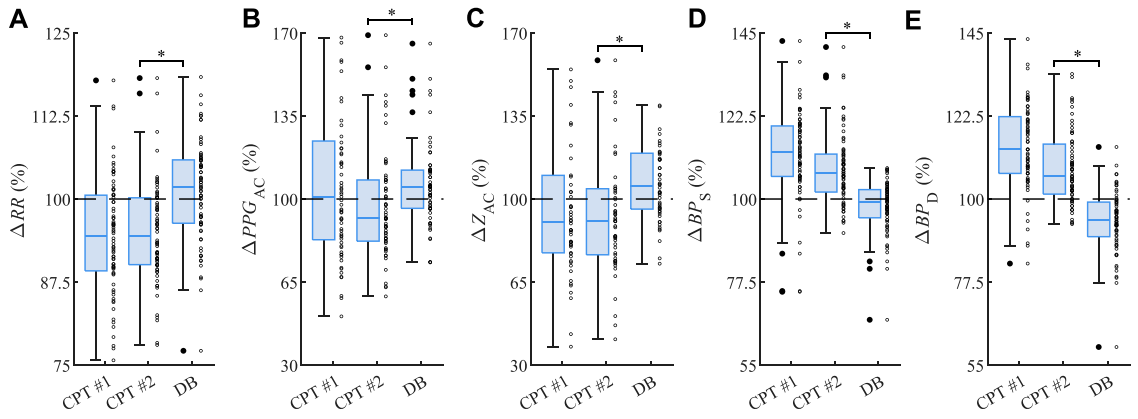

FIGURE 4
Relative changes **(A)** ΔRR of RR, **(B)** ΔPPG_{AC} of PPG_{AC}, **(C)** ΔZ_{AC} of Z_{AC}, **(D)** ΔBP_S of systolic BP values, and **(E)** ΔBP_D of diastolic BP values from CPT #1, CPT #2, and DB as related to the respective Rest #1, Rest #2, and Rest #3. The asterisk "*" indicates significant changes (p <0.05) between CPT #2 and DB.

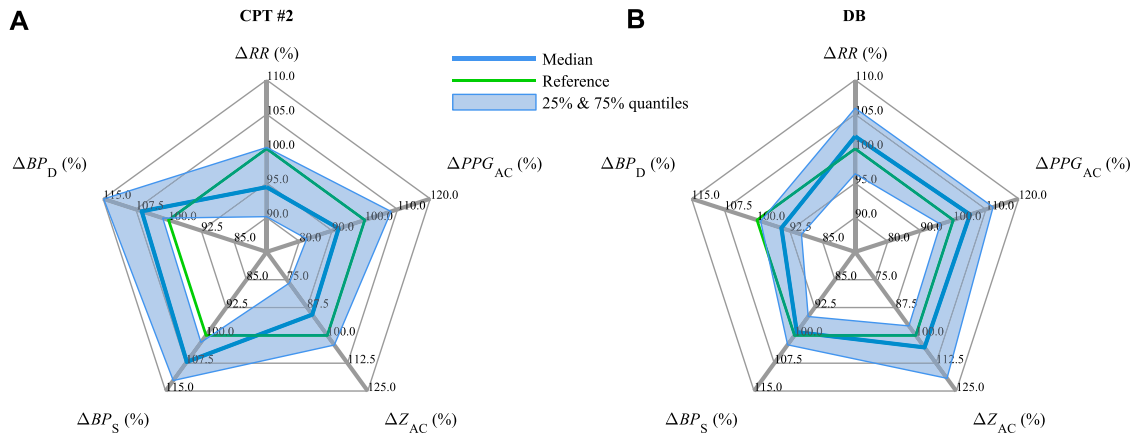

FIGURE 5
Medians and interquartile ranges of ΔRR, ΔPPG_{AC}, ΔZ_{AC}, ΔBP_S, and ΔBP_D (compare **Figure 4**) during **(A)** CPT #2 and **(B)** DB.

Figure 5 summarizes and contrasts the observed changes for all parameters in CPT #2 (**Figure 5A**) versus DB (**Figure 5B**), with the indicated interquartile range from 25% to 75%. In line with **Figure 4**, CPT #2 reduces RR, PPG_{AC}, and Z_{AC} and increases BP_S and BP_D, whereas DB causes physiological processes with reversed tendencies, i.e., RR, PPG_{AC}, and Z_{AC} increase while BP_S and BP_D decrease.

3.3 Pain level differences

Figure 6 illustrates the relative changes in the parameters in CPT #2 for relatively mild pain with the associated NRS ≤40 (**Figure 6A**) in comparison with moderate to strong pain with NRS >40 (**Figure 6B**). It can be observed that the physiological changes for NRS ≤40 are more closely located to the 100% reference line, i.e., to the values in Rest #2, than for NRS >40. Namely, the median ΔRR decreases by −3.8% and −6.7% for NRS ≤40 and NRS >40, respectively; the associated ΔPPG_{AC} decreases by −7.5% and −8.0%, ΔZ_{AC} decreases by −6.5% and −9.4%, ΔBP_S increases by +6.1% and +8.1%, and ΔBP_D increases by +3.4% and +9.4%. When comparing NRS ≤40 and NRS >40, statistically significant changes are observed in BP_D only.

3.4 Gender and age tendencies

The influence of gender and age is depicted in **Figure 7** considering CPT #2 and DB (compare **Figure 5**). In CPT #2, the relative values of ΔRR decrease by 1.5%–8.4%, with a minor decrease for young men (<30 years) and the largest decrease for adult men (≥30 years). Here ΔPPG_{AC} decreases by 8.4%–12.3%, with almost no changes for adult women (≥30 years). ΔZ_{AC} decreases by 3.9%–19.7%, with little changes for adult women and maximum changes for young women (<30 years). ΔBP_S increases by 5.3%–8.2% with minor changes for young women, whereas ΔBP_D increases by 5.1%–9.7%, with the largest changes for adult women.

During DB, in line with **Figure 5**, the observed changes in all gender and age groups mainly follow the opposite behavior. ΔRR increases by 2.1%–4.5% except for adult men (≥30 years); ΔPPG_{AC} increases by 4.5%–12.1% but also except for adult men; ΔZ_{AC} increases

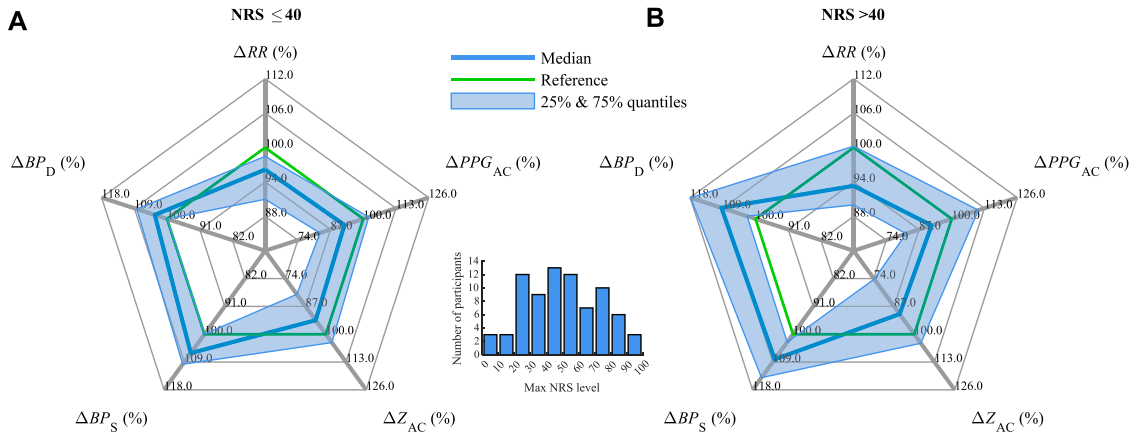

FIGURE 6
Median and interquartile ranges of ΔRR, ΔPPG_{AC}, ΔZ_{AC}, ΔBP_S, and ΔBP_D (compare **Figure 4**) during CPT #2 for **(A)** mild pain with NRS ≤40 and **(B)** moderate to severe pain with NRS >40. The distribution of maximum self-report NRS of the CPT #2 phase is presented in a bar diagram.

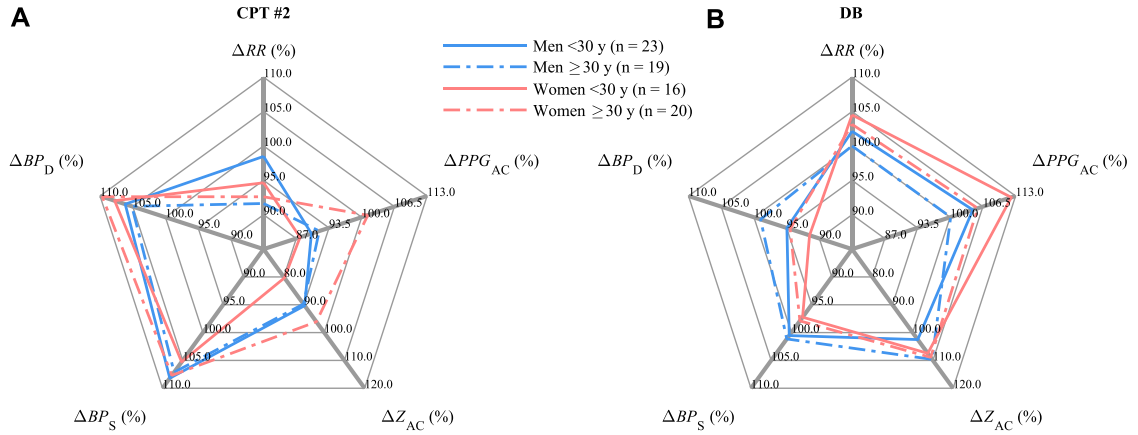

FIGURE 7
Medians of ΔRR, ΔPPG_{AC}, ΔZ_{AC}, ΔBP_S, and ΔBP_D (compare **Figure 4**) differentiated by age and gender during **(A)** CPT #2 and **(B)** DB.

by 2.5%–9.6% with a minor increase for young men (<30 years); ΔBP_S increases very slightly for men (0.5%–1.1%) but decreases more strongly for women (2.1%–2.8%); ΔBP_D decreases in all cases by 1.0%–8.5% with a minor decrease for adult men (≥30 years) and the largest decrease for young women (<30 years).

4 Discussion

The present study investigates the physiological footprints of auricular and non-auricular biosignals in response to a cold stressor and deep breathing. While a cold stressor is a sympathetically driven stimulus (accompanied by acute pain), deep breathing is a mainly parasympathetically driven stimulus (with relaxing effects). Thus, it was investigated how the opposing sympathetic and parasympathetic stimuli are reflected by the auricular biosignals, namely, its parameter Z_{AC}, and by parameters accessible from the auricular biosignals such as RR and PPG_{AC}. All these three parameters can be used as biofeedback to close the loop in aVNS, i.e., in a targeted stimulation of the parasympathetic system. The closed-loop set-up personalizes aVNS with an expected tendency to avoid over and under-stimulation of the vagus nerve/parasympathetic system. Thus, the closed-loop aVNS may minimize both the energy consumption of the aVNS stimulator and potential side effects (no over-stimulation) while optimizing and personalizing the aVNS therapy (no recruitment of pain fibers), e.g., in chronic pain. Here, the non-auricular biosignals with their parameters BP_S and BP_D serve as a necessary reference to monitor stimuli-related vital functions of the body and as an instructive substrate for their comparison with stimuli-related changes in auricular biosignals.

The auricular biosignal Z, namely its parameter Z_{AC} (**Figure 1**), decreases significantly during the sympathetic stimulus (CPT #2) as compared with the parasympathetic one (DB) (**Figures 3–5**), as well as decreases tendentially with increasing pain perception (**Figure 6**). This behavior indicates the potential suitability of Z_{AC} in assessing changes in the balance of the parasympathetic and sympathetic stimuli, or, more generally, in the balance of the parasympathetic and sympathetic systems of the human body (sympathovagal balance). On the other

hand, this balance, especially its normalization from a derailed state, is usually a therapeutic target in aVNS when applied to different chronic ailments Kaniusas et al. (2019a). Thus Z_{AC} can be hypothesized to be reasonable auricular biofeedback for the closed-loop aVNS without using any sensors external to the ear, which may obstruct the patient.

The parameters *RR* and PPG_{AC} also reflect sympathovagal balance. *RR* and PPG_{AC} decrease significantly during the sympathetic CPT #2 compared to the parasympathetic DB (**Figures 3–5**). While *RR* tends to decrease with increasing pain, the level of PPG_{AC} does not (**Figure 6**). Therefore, *RR* and PPG_{AC}, the former to a larger extent, can also be hypothesized to be reasonable auricular biofeedback for the closed-loop aVNS targeting a derailed sympathovagal balance. Please note that *RR* could be estimated from the period of the cardiac oscillation of the auricular *Z* (**Figure 3**), whereas PPG_{AC} from the cardiac deflection of *PPG* from the earlobe Allen (2007). However, limitations in the precision of the estimated *RR* may apply in the former case due to a rather smooth waveform of *Z* in contrast to the spiky R peak of *ECG*. Likewise, limitations in PPG_{AC} may apply in the latter case due to a rather central connection of the ear perfusion in contrast to the peripheral perfusion of the finger (**Figure 1**).

The non-auricular parameters BP_S and BP_D reflect the sympathovagal balance as well. Both increase significantly during the sympathetic CPT #2 as compared with the parasympathetic DB (**Figures 3–5**), while this increase in CPT #2 tends to be larger for stronger pain (**Figure 6**). The level of BP_D appears to depend even stronger on the stimuli-induced sympathovagal balance with the observed changes of 11.7% (from CPT #2 to DB) in contrast to the associated changes in BP_S of 8.0% (**Figure 4**). Likewise, the sympathetically-governed vasoconstriction (governing BP_D) may be more dominant than stroke volume changes (governing BP_S) Kaniusas (2012). This leads to a hypothesis that BP_S and BP_D could be used as non-auricular biofeedback for the closed-loop aVNS when external sensors are used outside the ear.

In terms of gender and age, the largest changes from CPT #2 to DB were shown in *RR* for adult women (≥30 years), PPG_{AC} for young women (<30 years), Z_{AC} for young women (<30 years), BP_S for adult women (≥30 years), BP_D for young women (<30 years). In contrast, the minor changes from CPT #2 to DB were shown in *RR* for young men (<30 years), PPG_{AC} for adult men (≥30 years), Z_{AC} for young men (<30 years), BP_S for adult men (≥30 years), BP_D for adult men (≥30 years). Overall, men seem to show fewer changes from CPT #2 to DB than women. This conclusion is in line with previous studies, which conclude that women are more sensitive to pain Fillingim et al. (2009); Mogil (2012); Popescu et al. (2010), but it depends on the method of pain induction and assessment. In most cases, the study also supports the still controversial claims that older individuals are more tolerant of pain and show fewer physiological effects than younger individuals Edwards et al. (2003); Riley et al. (2010); Rittger et al. (2011). However, these statements are very limited in their validity due to the small sample in this study.

A limitation of the present study is the relatively small database of recordings representing the elder part of the population which has tendentially a larger prevalence of suffering pain. Collecting and analyzing a more representative database is planned as a future research direction in the research of the aVNS stimulator. Since the warm water phase immediately preceding CPT #1 strongly affected the results in CPT #1, we focused our investigations on the comparison of CPR #2 and DB, both preceded by rest phases. Another limitation is that the order of the different phases of the protocol were not randomized, especially the order of CPT and DB. Therefore, the results may have been influenced by other factors such as expectation, adaptation, prolonged exposure.

Lastly, it should be noted that the recorded pain level, in contrast to nociception with its physiological encoding and processing of nociceptive stimuli, is a subjective feeling connected with the emotional experience to impeding or actual harm Loeser and Treede (2008) but also altering autonomic nervous system Woo et al. (2017); Adamczyk et al. (2020); Abdallah and Geha (2017). Thus, the investigated objective characteristics of the autonomic system may be useful for a continuous and objective personalization of aVNS in chronic ailments such as pain.

5 Conclusion

The three parameters *RR*, PPG_{AC}, and Z_{AC} accessible from auricular biosignals reflect the artificially-induced stimuli with sympathetic or parasympathetic dominance and thus the sympathovagal balance derailed in pain and other chronic conditions. Therefore, auricular biosignals can be used as biofeedback to close the loop in auricular vagus nerve stimulation to personalize the strength and timing of the stimulation in favor of therapy, patient compliance, and resourceful energy use.

Data availability statement

The raw data supporting the conclusions of this article will be made available by the authors, without undue reservation.

Ethics statement

The studies involving human participants were reviewed and approved by Kaunas Region Biomedical Research Ethics Committee (No. BE-2-24). The patients/participants provided their written informed consent to participate in this study.

Author contributions

AR contributed to the study design, collected data, developed algorithms, conducted data analysis, interpreted the results, and wrote and revised the manuscript. PP collected data, contributed to algorithm development, and revised the manuscript. LJ interpreted the results and revised the manuscript. VM contributed to the study design and revised the manuscript. EK initiated and designed the study, interpreted the results, and designed, wrote, and revised the manuscript. All authors have read the submitted manuscript and approved the final version.

Funding

This research was funded by the Research and Innovation Fund of Kaunas University of Technology (project grant No. PP2021/5) and the Research Fund of Lithuanian University of Health Sciences (2021-JV-00006). This study received funding from the European Union's Horizon 2020 research and innovation program under grant agreement No. 880603 (SzeleSTIM GmbH). The funder SzeleSTIM GmbH had the following involvement with the study: the study design and collection of data. All authors declare no other competing interests.

Acknowledgments

The authors acknowledge TU Wien Bibliothek for financial support through its Open Access Funding Programme. We thank all the volunteers for their participation in the study.

Conflict of interest

The authors declare that the research was conducted in the absence of any commercial or financial relationships that could be construed as a potential conflict of interest.

The handling editor JA declared a shared research group VascAgeNet WG3 with the author VM at the time of review.

Publisher's note

References

Abdallah, C. G., and Geha, P. (2017). Chronic pain and chronic stress: Two sides of the same coin? *Chronic Stress* 1, 2470547017704763. doi:10.1177/2470547017704763

Adamczyk, A. K., Ligeza, T. S., and Wyczesany, M. (2020). The dynamics of pain reappraisal: The joint contribution of cognitive change and mental load. *Cognitive, Affect. Behav. Neurosci.* 20, 276–293. doi:10.3758/s13415-020-00768-7

Allen, J. (2007). Photoplethysmography and its application in clinical physiological measurement. *Physiol. Meas.* 28, R1–R39. doi:10.1088/0967-3334/28/3/R01

Arbour, C., Choinière, M., Topolovec-Vranic, J., Loiselle, C. G., and Gélinas, C. (2014). Can fluctuations in vital signs be used for pain assessment in critically ill patients with a traumatic brain injury? *Pain Res. Treat.* 2014, 175794. doi:10.1155/2014/175794

Bouton, C. (2017). Cracking the neural code, treating paralysis and the future of bioelectronic medicine. *J. Intern. Med.* 282, 37–45. doi:10.1111/joim.12610

Breivik, H., Collett, B., Ventafridda, V., Cohen, R., and Gallacher, D. (2006). Survey of chronic pain in Europe: Prevalence, impact on daily life, and treatment. *Eur. J. Pain* 10, 287–333. doi:10.1016/j.ejpain.2005.06.009

Busch, V., Zeman, F., Heckel, A., Menne, F., Ellrich, J., and Eichhammer, P. (2013). The effect of transcutaneous vagus nerve stimulation on pain perception-an experimental study. *Brain Stimul.* 6, 202–209. doi:10.1016/j.brs.2012.04.006

Cowen, R., Stasiowska, M. K., Laycock, H., and Bantel, C. (2015). Assessing pain objectively: The use of physiological markers. *Anaesthesia* 70, 828–847. doi:10.1111/anae.13018

Dahlhamer, J., Lucas, J., Zelaya, C., Nahin, R., Mackey, S., DeBar, L., et al. (2018). Prevalence of chronic pain and high-impact chronic pain among adults — United States, 2016. *MMWR. Morb. Mortal. Wkly. Rep.* 67, 1001–1006. doi:10.15585/mmwr.mm6736a2

Edwards, R. R., Fillingim, R. B., and Ness, T. J. (2003). Age-related differences in endogenous pain modulation: A comparison of diffuse noxious inhibitory controls in healthy older and younger adults. *Pain* 101, 155–165. doi:10.1016/S0304-3959(02)00324-X

Enright, A., and Goucke, R. (2016). The global burden of pain: The tip of the iceberg? *Anesth. Analgesia* 123, 529–530. doi:10.1213/ANE.0000000000001519

Fillingim, R. B., King, C. D., Ribeiro-Dasilva, M. C., Rahim-Williams, B., and Riley, J. L. (2009). Sex, gender, and pain: A review of recent clinical and experimental findings. *J. Pain* 10, 447–485. doi:10.1016/j.jpain.2008.12.001

Fishman, S. M. (2007). Recognizing pain management as a human right: A first step. *Anesth. Analgesia* 105, 8–9. doi:10.1213/01.ane.0000267526.37663.41

Hamilton, P. S., and Tompkins, W. J. (1986). Quantitative investigation of qrs detection rules using the mit/bih arrhythmia database. *IEEE Trans. Biomed. Eng. BME-* 33, 1157–1165. doi:10.1109/TBME.1986.325695

Kaniusas, E. (2012). *Biomedical signals and sensors I*. Springer Berlin, Heidelberg. doi:10.1007/978-3-642-24843-6

Kaniusas, E. (2015). *Biomedical signals and sensors II*. Springer Berlin, Heidelberg. doi:10.1007/978-3-662-45106-9

Kaniusas, E. (2019). *Biomedical signals and sensors III*. Springer Cham. doi:10.1007/978-3-319-74917-4

Kaniusas, E., Kampusch, S., Tittgemeyer, M., Panetsos, F., Gines, R. F., Papa, M., et al. (2019a). Current directions in the auricular vagus nerve stimulation i – A physiological perspective. *Front. Neurosci.* 13, 854–923. doi:10.3389/fnins.2019.00854

Kaniusas, E., Kampusch, S., Tittgemeyer, M., Panetsos, F., Gines, R. F., Papa, M., et al. (2019b). Current directions in the auricular vagus nerve stimulation ii - an engineering perspective. *Front. Neurosci.* 13, 772. doi:10.3389/fnins.2019.00772

Karcioglu, O., Topacoglu, H., Dikme, O., and Dikme, O. (2018). A systematic review of the pain scales in adults: Which to use? *Am. J. Emerg. Med.* 36, 707–714. doi:10.1016/j.ajem.2018.01.008

Keating, L., and Smith, S. (2011). Acute pain in the emergency department: The challenges. *Rev. Pain* 5, 13–17. doi:10.1177/204946371100500304

Kyle, B. N., and McNeil, D. W. (2014). Autonomic arousal and experimentally induced pain: A critical review of the literature. *Pain Res. Manag.* 19, 159–167. doi:10.1155/2014/536859

Loeser, J. D., and Treede, R. D. (2008). The kyoto protocol of iasp basic pain terminology. *Pain* 137, 473–477. doi:10.1016/j.pain.2008.04.025

Mansfield, K. E., Sim, J., Jordan, J. L., and Jordan, K. P. (2016). A systematic review and meta-analysis of the prevalence of chronic widespread pain in the general population. *Pain* 157, 55–64. doi:10.1097/j.pain.0000000000000314

Mogil, J. S. (2012). Sex differences in pain and pain inhibition: Multiple explanations of a controversial phenomenon. *Nat. Rev. Neurosci.* 13, 859–866. doi:10.1038/nrn3360

Mura, P., Serra, E., Marinangeli, F., Patti, S., Musu, M., Piras, I., et al. (2017). Prospective study on prevalence, intensity, type, and therapy of acute pain in a second-level urban emergency department. *J. Pain Res.* 10, 2781–2788. doi:10.2147/JPR.S137992

Nemeroff, C. B., Mayberg, H. S., Krahl, S. E., McNamara, J., Frazer, A., Henry, T. R., et al. (2006). Vns therapy in treatment-resistant depression: Clinical evidence and putative neurobiological mechanisms. *Neuropsychopharmacology* 31, 1345–1355. doi:10.1038/sj.npp.1301082

Nesbitt, A. D., Marin, J. C., Tompkins, E., Ruttledge, M. H., and Goadsby, P. J. (2015). Initial use of a novel noninvasive vagus nerve stimulator for cluster headache treatment. *Neurology* 84, 1249–1253. doi:10.1212/WNL.0000000000001394

O'Reardon, J. P., Cristancho, P., and Peshek, A. D. (2006). Vagus nerve stimulation (vns) and treatment of depression: To the brainstem and beyond. *Psychiatry (Edgmont (Pa, Townsh.* 3, 54–63.

Othow, C. O., Ferede, Y. A., Tawuye, H. Y., and Aytolign, H. A. (2022). The magnitude and associated factors of post-operative pain among adult patients. *Ann. Med. Surg.* 81, 104406. doi:10.1016/j.amsu.2022.104406

Peters, M. L., and Schmidt, A. J. (1991). Psychophysiological responses to repeated acute pain stimulation in chronic low back pain patients. *J. Psychosomatic Res.* 35, 59–74. doi:10.1016/0022-3999(91)90007-B

Popescu, A., Leresche, L., Truelove, E. L., and Drangsholt, M. T. (2010). Gender differences in pain modulation by diffuse noxious inhibitory controls: A systematic review. *Pain* 150, 309–318. doi:10.1016/j.pain.2010.05.013

Raja, S. N., Carr, D. B., Cohen, M., Finnerup, N. B., Flor, H., Gibson, S., et al. (2020). The revised international association for the study of pain definition of pain: Concepts, challenges, and compromises. *Pain* 161, 1976–1982. doi:10.1097/j.pain.0000000000001939

Reid, K. J., Harker, J., Bala, M. M., Truyers, C., Kellen, E., Bekkering, G. E., et al. (2011). Epidemiology of chronic non-cancer pain in Europe: Narrative review of prevalence, pain treatments and pain impact. *Curr. Med. Res. Opin.* 27, 449–462. doi:10.1185/03007995.2010.545813

Riley, J. L., King, C. D., Wong, F., Fillingim, R. B., and Mauderli, A. P. (2010). Lack of endogenous modulation and reduced decay of prolonged heat pain in older adults. *Pain* 150, 153–160. doi:10.1016/j.pain.2010.04.020

Rittger, H., Rieber, J., Breithardt, O. A., Dücker, M., Schmidt, M., Abbara, S., et al. (2011). Influence of age on pain perception in acute myocardial ischemia: A possible cause for delayed treatment in elderly patients. *Int. J. Cardiol.* 149, 63–67. doi:10.1016/j.ijcard.2009.11.046

St. Marie, B., and Broglio, K. (2020). Managing pain in the setting of opioid use disorder. *Pain Manag. Nurs.* 21, 26–34. doi:10.1016/j.pmn.2019.08.003

Tai, F. W. D., and McAlindon, M. E. (2021). Non-steroidal anti-inflammatory drugs and the gastrointestinal tract. *Clin. Med. J. R. Coll. Physicians Lond.* 21, 131–134. doi:10.7861/CLINMED.2021-0039

Todd, K. H., Ducharme, J., Choiniere, M., Crandall, C. S., Fosnocht, D. E., Homel, P., et al. (2007). Pain in the emergency department: Results of the pain and emergency medicine initiative (pemi) multicenter study. *J. Pain* 8, 460–466. doi:10.1016/j.jpain.2006.12.005

Woo, C. W., Schmidt, L., Krishnan, A., Jepma, M., Roy, M., Lindquist, M. A., et al. (2017). Quantifying cerebral contributions to pain beyond nociception. *Nat. Commun.* 8, 14211. doi:10.1038/ncomms14211

Yong, R. J., Mullins, P. M., and Bhattacharyya, N. (2022). Prevalence of chronic pain among adults in the United States. *Pain* 163, E328–E332. doi:10.1097/j.pain.0000000000002291

frontiers | Frontiers in Physiology

TYPE Original Research
PUBLISHED 02 March 2023
DOI 10.3389/fphys.2023.1126957

OPEN ACCESS

EDITED BY
Panicos Kyriacou,
City University of London,
United Kingdom

REVIEWED BY
Guanghao Sun,
The University of Electro-Communications, Japan
Leonardo Bocchi,
University of Florence, Italy

*CORRESPONDENCE
Guillaume Weber-Boisvert,
guillaume.weber-boisvert.1@ulaval.ca
Frida Sandberg,
frida.sandberg@bme.lth.se

SPECIALTY SECTION
This article was submitted to Computational Physiology and Medicine, a section of the journal Frontiers in Physiology

RECEIVED 18 December 2022
ACCEPTED 17 February 2023
PUBLISHED 02 March 2023

CITATION
Weber-Boisvert G, Gosselin B and Sandberg F (2023), Intensive care photoplethysmogram datasets and machine-learning for blood pressure estimation: Generalization not guarantied.
Front. Physiol. 14:1126957.
doi: 10.3389/fphys.2023.1126957

Intensive care photoplethysmogram datasets and machine-learning for blood pressure estimation: Generalization not guarantied

Guillaume Weber-Boisvert[1]*, Benoit Gosselin[1] and Frida Sandberg[2]*

[1]Department of Electrical and Computer Engineering, Université Laval, Quebec, QC, Canada, [2]Department of Biomedical Engineering, Lund University, Lund, Sweden

The large MIMIC waveform dataset, sourced from intensive care units, has been used extensively for the development of Photoplethysmography (PPG) based blood pressure (BP) estimation algorithms. Yet, because the data comes from patients in severe conditions—often under the effect of drugs—it is regularly noted that the relationship between BP and PPG signal characteristics may be anomalous, a claim that we investigate here. A sample of 12,000 records from the MIMIC waveform dataset was stacked up against the 219 records of the PPG-BP dataset, an alternative public dataset obtained under controlled experimental conditions. The distribution of systolic and diastolic BP data and 31 PPG pulse morphological features was first compared between datasets. Then, the correlation between features and BP, as well as between the features themselves, was analysed. Finally, regression models were trained for each dataset and validated against the other. Statistical analysis showed significant ($p < 0.001$) differences between the datasets in diastolic BP and in 20 out of 31 features when adjusting for heart rate differences. The eight features showing the highest rank correlation ($|\rho| > 0.40$) to systolic BP in PPG-BP all displayed muted correlation levels ($|\rho| < 0.10$) in MIMIC. Regression tests showed twice higher baseline predictive power with PPG-BP than with MIMIC. Cross-dataset regression displayed a practically complete loss of predictive power for all models. The differences between the MIMIC and PPG-BP dataset exposed in this study suggest that BP estimation models based on the MIMIC dataset have reduced predictive power on the general population.

KEYWORDS

blood pressure estimation, BP estimation, photoplethysmography, mimic, UCI, PPG-BP, PPG datasets, intensive care datasets

1 Introduction

Hypertension is one of the greatest challenges to public health of our time. According to the Centre for Disease Control, 47% of the adult population in the United States suffer from hypertension, and only 24% of those with hypertension have their condition under control (Centers for Disease Control and Prevention, 2022). Hypertension is an independent risk factor for cardiovascular diseases such as heart attack, stroke, and kidney disease, and ranks

second amongst the preventable causes of death in the U.S., trailing cigarette smoking only (US Department of Health and Human Services, 2003; Kochanek et al., 2019; Danaei et al., 2009). It is now widely accepted that home blood pressure (BP) monitoring and ambulatory BP monitoring are much better at predicting risks associated with hypertension than in-clinic BP measurements (Ogedegbe and Pickering, 2010), with night time BP increasingly seen as an important risk determinant (Hansen et al., 2011; Gehring et al., 2018). Devices presently used for home BP monitoring utilize an inflatable cuff, which only provides intermittent readings instead of presenting the entire dynamic range and patterns of BP fluctuations. Moreover, the discomfort caused by cuff inflation is particularly problematic for nocturnal BP measurement, as it can disturb sleep and thereby interfere with measurements (Solà and Delgado-Gonzalo, 2019).

Photoplethysmography (PPG) based BP estimation shows promises to be a low-cost and convenient technique that enables wearable designs and has the potential to replace cuff-based devices (Elgendi et al., 2019). However, the lack of open access, standardized PPG datasets for training and testing BP estimation algorithms is an obstacle to researchers in the field. Most studies are based on private databases where composition of the data and methods of acquisition vary considerably, making a direct comparison between the published BP estimation algorithms impossible (Solà and Delgado-Gonzalo, 2019).

At the time of writing, several public datasets that include BP and PPG signal are available. There are two large datasets sourced from intensive care and surgical units: the Multiparameter Intelligent Monitoring in Intensive Care II (MIMIC) Waveform Dataset (Saeed et al., 2011) from the Massachusetts Institute of Technology, released on PhysioNet (Goldberger et al., 2000) in 2011, and the VitalDB from the Seoul National University Hospital (Lee et al., 2022) released in 2017. Several smaller datasets also exist, often with a focus on a specific condition. A few examples are: The University of Queensland Vital Sign Dataset (Liu et al., 2012), a 32 patient dataset focusing on anaesthesia acquired at the Royal Adelaide Hospital in Adelaide, Australia, released in 2012; the Bed-Based Ballistocardiography Dataset (Carlson et al., 2020), a 40 patient dataset from the Kansas State University, released at the end of 2020; and the PPG-BP dataset (Liang et al., 2018), a 219 patients dataset from the Guilin People's Hospital, released in 2018, with a focus on the screening of cardiovascular diseases (CVD) from PPG.

The PPG-BP dataset can be considered a middle ground among the available datasets. It contains 657 short PPG segments three for each of the 219 patients and recorded at rest under controlled experimental conditions. Each patient is associated with a single BP measurement, as well as patient biometric data and diagnosed CVD, if any. In contrast, MIMIC contains more than 25,000 records of variable length and varying measurement types, at times including PPG and arterial blood pressure (ABP). The data was acquired from bedside monitoring devices at intensive care units (ICU), including surgery and cardiac care units, at the Beth Israel Deaconess Medical Center in Boston, United States. Among all the public datasets, MIMIC has been available the longest and has been used the most extensively in the field of BP estimation. The other datasets have seen little use in comparison, and some are not well suited for developing and validating BP estimation algorithms due to the limited number of subjects, the special conditions of data collection and the sporadicity of BP measurements.

MIMIC has been used in many BP estimation studies. Kachuee et al. used a sample of 3,663 records from 942 subjects to estimate systolic blood pressure (SBP) using 10 PPG and ECG morphological features. Their best results were a mean absolute error (MAE) of 11.17 mmHG without calibration and 8.21 mmHG with calibration, using AdaBoost for regression (Kachuee et al., 2017). In 2020 Hasanzadeh et al. used a sample of about 1,000 subjects to estimate SBP from one spectral and 18 morphological features using PPG only. Their best results were obtained with AdaBoost regression, giving a MAE of 8.22 mmHg (Hasanzadeh et al., 2020). In 2021, a subset of 200 subjects has been used by Esmaelpoor et al. to compare of 56 machine-learned features generated by convolutional neural network (CNN) against a set of 27 frequently used morphological features from PPG and ECG. Eight regression methods were tested and the best results were obtained with squared exponential Gaussian regression or Gaussian process regression depending on the test parameters, providing SBP with a MAE under 6 mmHg using morphological features, and under 3.5 mmHg using machine-learned features (Esmaelpoor et al., 2021). As in this last example, the dataset has been used many times with pulse transit time and pulse arrival time algorithms, despite that variability in the ECG sampling time makes it unsuitable for transit and arrival time calculation (Elgendi et al., 2019). The breadth and variable quality of the dataset also resulted in uneven sampling by researchers, and as such hardly makes performance comparison easier, even between two studies using it. A more serious concern is the frequently mentioned hypothesis that because the data is sourced from ICU, with patients having received medication and being in varied critical conditions, the MIMIC population may exhibit abnormalities or a different relation between PPG and BP than would be seen in a more controlled setting (Kachuee et al., 2017; Hasanzadeh et al., 2020; Chao et al., 2021), casting doubt on the validity of results beyond the dataset itself.

The aim of this study is to evaluate if the relationship between PPG pulse characteristics and BP in MIMIC is truly different from that in data acquired under controlled conditions. To achieve this goal a subset of MIMIC was compared to PPG-BP in a two-step approach. First, a statistical comparison of the datasets was performed. It comprised comparing the distribution of features characterizing PPG pulse morphology, as well as comparing the correlation between features on each dataset. Second, the correlation between BP and features was compared between datasets to see if similar morphological variations could be observed on both datasets in relation to BP changes. To illustrate the implication of the differences between the datasets, Support Vector Regression models were trained on each dataset and their cross-validated performance on the training set were compared to their performance on the other dataset, in order to assert whether predictive powers were retained.

2 Materials and methods

2.1 Datasets

A subset of the MIMIC database, prepared especially for BP estimation by Kachuee. (2015), is used in this study. Because it is hosted by the University of California, Irvine, the subset is sometimes called the "UCI" dataset, which will be used hereafter. This subset, which excludes segments with missing signals and

abnormal values from MIMIC, contains 12,000 records of lengths varying between 8 s and 10 min. Each record is sampled at 125 Hz and contain fingertip PPG, electrocardiogram (ECG), and instantaneous ABP. No additional information about the subjects is provided, and the devices used for data acquisition are not specified.

The PPG-BP dataset contains 657 fingertip PPG segments from 219 subjects of 21–86 years of age with an average of 57 ± 16 years. Each segment has a duration of 2.1 s and a sampling rate of 1 kHz. A single SBP and diastolic blood pressure (DBP) measurement is provided for each subject, as well as the sex, age, height, weight, heart rate, and disease records. The PPG signal was recorded through an SMPLUS SEP9AF-2 sensor connected to a Texas Instrument MSP430FG4618 microcontroller, with a hardware filter bandpass of 0.5–12 Hz. The BP measurements were taken with an Omron HEM-7201 upper arm BP monitor. While also sourced from hospital patients, the PPG-BP data does not come from ICU units and was acquired under controlled conditions following an experimental protocol. Data acquisition was conducted in private, following a relaxation and adaptation period of 10 min, with the patients sitting in an office chair and their arms resting on a desk. The same acquisition devices were used for all subjects. Furthermore, a screening process excluded patients diagnosed with diseases other than cardiovascular diseases and diabetes. The data was also screened for abnormal and missing values, while a consistent signal quality was ensured by computing a signal quality index and excluding subjects with low values (Liang et al., 2018).

2.2 Pre-processing

All signal processing was done in Python and references to functions are, otherwise noted, part of the standard library or of the *SciPy* scientific library (Virtanen et al., 2020).

For UCI, five evenly spaced segments of a duration of 5 seconds were first extracted from each of the records in the dataset. Records shorter than 25 s were rejected. SBP and DBP were extracted from the continuous ABP signal by averaging all the peak values in the sequence, using function *find_peaks*. Records with less than three ABP peaks, due to non-pulsatile ABP segments, were rejected. Even though the UCI dataset had already been pre-processed to eliminate invalid or excessively noisy signals found in MIMIC, signal segments with movement artefacts, as well as sequences with large variations in pulsatile amplitude remained. To eliminate those issues and ensure coherence between the datasets, the following pre-processing steps were applied to both UCI and PPG-BP. First, all segments had their mean removed and were then filtered using a 0.7–12 Hz zero-phase fourth order Butterworth bandpass filter.

Three screening criteria were created to identify the remaining problematic segments. Any segment satisfying one of the conditions was rejected. The first criterion excluded signal segments with very rapid changes associated with signal artefacts such as those caused by body movements or device disconnection:

$$max\left(\left|x'(n)\right|\right) > \mu\left(x'(n)\right) + 5\sigma\left(x'(n)\right) \tag{1}$$

where x(n) is the filtered PPG signal, x'(n) is its first derivative, σ is the standard deviations (STD) and μ the mean. The second criterion ensured pulsatile amplitude was stable throughout each segment:

$$\begin{gathered}\left(max\left(x_i\right) - min\left(x_i\right)\right) > 1.5\left(max\left(x_j\right) - min\left(x_j\right)\right) \\ for\ i, j \in \{1, 2, 3\}\ and\ i \neq j\end{gathered} \tag{2}$$

where $x_1, x_2\ and\ x_3$ are three equally sized subdivisions of $x(n)$. It was not applicable to PPG-BP because of the shorter segment duration. The last criterion removed segments with extreme heart rate or with characteristics interfering with peak detection:

$$PR < 40 \vee PR > 220 \tag{3}$$

where PR is the pulse rate in beat per minute (BPM) estimated as the average first derivative $x'(n)$ peak to peak interval. To avoid false peaks, those with a prominence lower than 60% of the maximum prominence were discarded. The prominence of a peak quantifies the amplitude difference between its apex and its bases, computed by function *peak_prominences*.

Finally, to be able to compare the various time-based features, both datasets were resampled to a matching frequency of 250 Hz.

2.3 Fiducial points extraction

The fiducial points used for feature extraction are shown in Figure 1. The second derivative of the signal was first computed and low-pass filtered with a 12 Hz zero-phase sixth order Butterworth filter to obtain $x''(n)$, after which the third derivative $x'''(n)$ was computed. The PPG pulses peak positions n_p, and their maximum upslope positions n_u were then established by finding the peak positions of $x(n)$ and $x'(n)$ with the *find_peaks* function, considering only peaks with a prominence greater than 60% of the maximum prominence. Boundaries for each pulse were established by finding the pulse onset, n_0, associated with each n_u. The position of n_0 was chosen as the first positive peak of $x'''(n)$ left of n_u, subject to $x'''(n) > 0.4\,max\left(x'''(n)\right)$ to ignore minor peaks. If a positive zero crossing of $x'(n)$ could be found between that point and n_u, it was used instead. This strategy allowed a robust detection of onset even for pulses preceded with a slow rise

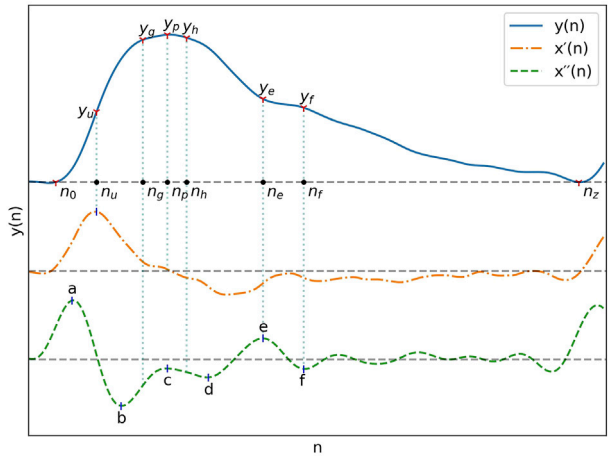

FIGURE 1
A typical PPG signal as well as its first and second derivatives with their most important fiducial points.

TABLE 1 Summary of the features used in this paper.

Feature	Name/Description	Defined in
RI	Reflection index	Sec. 2.4.1, Eq. 4
AI	Augmentation index	Sec. 2.4.1, Eq. 5
AI_{gh}	Augmentation index of early to late systolic peaks	Sec. 2.4.1, Eq. 6
AI_{gf}	Augmentation index of early systolic to diastolic peaks	Sec. 2.4.1, Eq. 7
Y_{gh}	Amplitude ratio or early to late systolic peaks	Sec. 2.4.1, Eq. 8
IPA	Inflection point area ratio	Sec. 2.4.2, Eq. 9
Δn_{ij}	Time span between two fiducial points	Sec. 2.4.3, Eq. 10
HR	Heart rate	Sec. 2.4.3, Eq. 11
N_i	Time ratio between the portion of the pulse duration before and after a fiducial point	Sec. 2.4.4, Eq. 12
AX	Aging index	Sec. 2.4.5, Eq. 13
S_{pe}	Slope between points p and e	Sec. 2.4.6, Eq. 14
S_{pf}	Slope between points p and f	Sec. 2.4.6, Eq. 15
W_{xx}	Width of the pulse at xx% of its amplitude	Sec. 2.4.7

before the onset. The end of the pulse, n_z, was defined as the next pulse onset. Pulses with a marked difference between the amplitude at onset and end point, satisfying $|x(n_0) - x(n_Z)| > 0.12\,(x(n_P) - x(n_0))$, were discarded.

With pulse boundaries and peaks established, the remaining fiducial points were extracted from $x''(n)$. Five of those points are the *a, b, c, d* and *e* points described by Takazawa et al. (1998). Since the *e* point also marks the position of the dicrotic notch, the same nomenclature was kept for the additionnal *f*, *g* and *h* points designating the second derivative estimates of the diastolic peak, early systolic peak and late systolic peak positions. The fiducial points as described by Takazawa asusme an ideal PPG signal with well defined successive waves in the second derivative. To enable extraction from the non-ideal waveforms present in the datasets, the following five step process was developed:

1. Set the position of *a*, n_a, to the point where $x''(n)$ is at its maximum and the position of *b*, n_b, where it is at its minimum, subject to $n < n_P$.
2. Set the position of the dicrotic notch *e*, n_e as the earliest $x''(n)$ peak with n constrained by $n_P < n < \frac{2}{3}(n_z - n_0) \wedge x(n) < 0.7\,x(n_P) \wedge x''(n) > 0.05\,x''(n_a)$.
3. Set the position of the diastolic peak *f*, n_f, as the earliest downward peak satisfying the condition $n_e < n < \frac{2}{3}(n_z - n_0) \wedge x''(n) < 0$.
4. Set the position of *c* and *d*, n_c and n_d, as the $x''(n)$ upward and downward peaks with the greatest difference between them, constrained by $n_b < n < n_e$. For pulses where those peaks did not exist, the positions were estimated as the position of the maximum inflection points of $x''(n)$, that is the maximum downward and upward peaks of the fourth derivative constrained by $n_b < n < n_e$.
5. Estimate the position of the early and late systolic peak by setting $n_g = n_b + \frac{n_c - n_b}{2}$ and $n_h = n_c + \frac{n_d - n_c}{2}$.

All peaks of $x''(n)$ and $x''''(n)$ were extracted by detection of the zero-crossings of the next higher order derivative.

2.4 Features extraction

All features were extracted on a pulse-by-pulse basis. The trend of the signal of each pulse was first removed by subtracting the linear slope connecting the start point of each pulse to its end point, as described in (Xing et al., 2020). Thus, all pulses in the resulting detrended signal, $y(n)$, have value of zero at their starting and ending point. The amplitudes of the detrended signal at various fiducial point are hereafter designated by the form y_i where $y_i = y(n_i)$. The features used in this paper are recapitulated in Table 1.

2.4.1 Amplitude ratios

The reflection index (RI) along with the augmentation index (AI) measure the contribution of the peripheral wave reflections to the overall pulse (Elgendi, 2012). As a measure of reflected waves, AI can also be computed in regards to the early and late systolic peaks as in Eq. 6 and Eq. 7 while Y_{gh} defined in Eq. 8 is an estimate of amplitude ratio of the late to early systolic peak, which has been correlated with changes in systolic pressure (Baruch et al., 2011).

$$RI = \frac{y_f}{y_p} \tag{4}$$

$$AI = \frac{y_p - y_f}{y_p} = 1 - RI \tag{5}$$

$$AI_{gh} = \frac{y_g - y_h}{y_g} \tag{6}$$

$$AI_{gf} = \frac{y_g - y_f}{y_g} \tag{7}$$

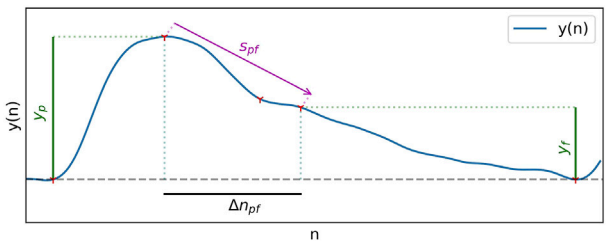

FIGURE 2
Different types of measurements used in feature extraction.

$$Y_{gh} = \frac{y_h}{y_g} \tag{8}$$

2.4.2 Area ratios

The Inflection Point Area ratio (IPA), the ratio of area under the curve until the dicrotic notch to the area under the curve after it, is an indicator of total peripheral resistance (Elgendi, 2012).

$$IPA = \frac{\sum_{n=n_0}^{n_e} y(n)}{\sum_{n=n_e}^{n_z} y(n)} \tag{9}$$

2.4.3 Time spans

Time spans all take the same general form, given in Eq. 10, and can be visualised in Figure 2. The duration of the systolic phase, Δn_{0p}, has been associated with hypertension (Dillon and Hertzman, 1941; Elgendi, 2012) while the duration of the diastolic phase, Δn_{pz}, has been associated with DBP (Yoon et al., 2009). The time spans Δn_{0g}, Δn_{0h}, Δn_{gh}, and Δn_{gf}, are spans between reflected waves components, of which Δn_{gf} has been associated with pulse pressure (PP) (Baruch et al., 2011). Δn_{pf} is the time between the peak and the diastolic peak. Δn_{up}, Δn_{ue}, Δn_{uf} are time spans in relation to the maximum upslope point, of which the last has been shown to have a strong correlation with SBP and DBP (Kim et al., 2008).

$$\Delta n_{ij} = n_j - n_i \tag{10}$$

The HR estimation used as a feature is also, in essence, a time span, and was calculated based on the pulse duration as shown in Eq. 11, where f_s is the sampling rate.

$$HR = \frac{60 f_s}{n_z - n_0} \tag{11}$$

2.4.4 Time ratios

Three different time ratios have been included in this study, each representing the pulse duration ratio before and after a fiducial point, taking the form shown in Eq. 12. Included are N_p in relation to the peak, N_e in relation to the e point, and N_f in relation to the f point. The time ratio of systole to diastole, N_f, was shown to be correlated to SBP (Li et al., 2014).

$$N_i = \frac{\Delta n_{oi}}{\Delta n_{iz}} \tag{12}$$

2.4.5 Acceleration PPG

Acceleration PPG, or second derivative PPG, is a group of features extracted from the fiducial points in the second derivative of the signal. They have been associated with arterial stiffness and vascular aging (Takazawa et al., 1998). The features b/a, c/a, d/a and e/a are amplitude ratios of the second derivative at those fiducial points, while the aging index (AX) is shown in Eq. 13.

$$AX = \frac{b - c - d - e}{a} \tag{13}$$

2.4.6 Slopes

The slopes from the peak to the dicrotic notch, S_{pe}, and to the diastolic peak, S_{pf}, have been investigated as BP predictors. S_{pe} was shown, although with low certainty, to have a weak correlation to DBP (Kim et al., 2008), and has also been associated with peripheral resistance (Lin et al., 2020). Slopes used in this study are normalized, as in (Kim et al., 2008), in relation to the pulse peak value.

$$S_{pe} = \frac{y_e - y_P}{y_P \Delta n_{pe}} \tag{14}$$

$$S_{pf} = \frac{y_f - y_P}{y_P \Delta n_{pf}} \tag{15}$$

2.4.7 Widths

Widths are conceptually the same as time spans, but they are not calculated from specific fiducial points in the pulse. Rather, the span is the width of the pulse at a certain percentage of its amplitude. It has been used as a BP predictor (Ding et al., 2019) and is associated with systemic vascular resistance (Awad et al., 2007). In this study, the pulse width is measured at 30%, 50%, 70% and 90% of y_p for W_{30}, W_{50}, W_{70} and W_{90}, respectively.

2.4.8 Outlier exclusion and feature vector construction

Outlier exclusion was performed on a per-pulse basis. Morphologically abnormal values for IPA were identified first and any values below 0.5, usually caused by an abnormal shape of the diastolic part of the pulse, were rejected. The feature vectors of both datasets were then temporarily joined to compute the global mean and the global STD, σ_{global}, of each feature. Pulses where any feature diverged more than 4 STD from the mean were considered outliers and rejected.

The remaining feature vectors for pulses in the same segment were then averaged and saved. Since only a single BP measurement is provided per subject in the PPG-BP dataset, features extracted from different segments but from the same subject were also averaged together.

2.5 Statistical comparison of the datasets

To characterise the differences between PPG-BP and UCI, the distribution of features and BP data compiled in section 2.4.8 were first examined.

For each feature, as well as SBP and DBP a two sample Kolmogorov–Smirnov (KS) test was performed with α = 0.001 to determine if differences between distributions were significant.

For each dataset, the mean and STD of each feature was calculated. For each feature, the difference between the mean value of the two datasets, was determined as per Eq. 16. The same was also done for the STD value as in Eq. 17. The results were computed as a percentage of σ_{global} to bring them on a comparable scale. This analysis was also done on SBP and DBP.

$$\mu_{\%} = \frac{\mu_{uci} - \mu_{ppg-bp}}{|\sigma_{global}|} \cdot 100 \tag{16}$$

$$\sigma_{\%} = \frac{\sigma_{uci} - \sigma_{ppg-bp}}{|\sigma_{global}|} \cdot 100 \tag{17}$$

Since many features are affected by the pulse duration, those tests were then repeated with HR compensation. That is to say that all time spans (Section 2.4.3) and widths (Section 2.4.7) were multiplied by HR while slopes (Section 2.4.6) were divided by HR before recomputing σ_{global}, Eq. 16 and Eq. 17, yielding $\mu_{adj\%}$ and $\sigma_{adj\%}$.

Finally, the feature correlation matrix was computed: for each feature, the Pearson correlation coefficient (r) was calculated against every other feature. The difference between the correlation matrix of each dataset was then produced to highlight their discrepancies.

2.6 Response to BP variations and shared predictive power

2.6.1 BP correlation test

The Spearman rank correlation coefficient (ρ) was computed to assess correlation between each feature and SBP as well as DBP, respectively. Spearman correlation was selected here instead of Pearson for its ability to identify both linear and non-linear relationships. The difference between the datasets was then computed to reveal any divergence in BP-features relationship.

2.6.2 BP estimation test

For this section, the *Scikit-Learn* machine learning library was used (Pedregosa et al., 2011). Using the *svm.svr* module, a support vector regression (SVR) model with a radial basis function (RBF) kernel was trained for SBP estimation on the PPG-BP dataset and another on UCI, keeping one random sample per subject. Therefore, when splitting a dataset into a training and testing set, data from one subject was never included into both the training and testing set.

To counter the bias caused by the non-uniform sample distribution, sample weights were passed to the model for training and also in subsequent evaluation of performance. Samples were first split into 12 equally spaced bins based on their BP value. The weight g of each sample was $g_i = k_{max}/k_i$ where k_{max} is the number of samples in the bin with the most samples and k_i is the number of samples in the current sample's bin. Because samples were concentrated in the middle of the BP range, the resulting weights increased emphasis on the samples towards the extrema of the BP range, as to approximate training and testing using a uniform distribution.

The features were centered to zero mean and scaled to unit variance before being handed to the model.

The model regularization parameter C, controling penalization of estimation errors during training, and the kernel function scale parameter γ, were optimized first through a coarse then a fine parameter grid search, as described in (Hsu et al., 2016). A leave-one-out cross-validation strategy was used to maximize the ammount of useable data for training.

Backward feature elimination was used to find the optimal feature set for each dataset, following this method:

1. Using 10-fold cross validation, sequentially train and test the SVR using all features but one, until all features have been left out once.
2. Compare the results and save the reduced feature set with the best cross-validated performance.
3. Restart from step one using the reduced feature set until only 4 features remain.
4. Select the optimal feature set, that is the one that had the best performance throughout the entire process.

At every step, performance was evaluated using the weighted coefficient of determination R^2, as defined in Eq. 18, where i is the sample index, g_i is the sample weight, u_i is a sample's true BP, $\hat{u}_i$ is a sample's estimated BP, $\bar{u}$ is the weighted mean of the true BP of all samples defined in Eq. 19, and k is the number of samples.

$$R^2 = 1 - \frac{\sum_{i=1}^{k} g_i (u_i - \hat{u}_i)^2}{\sum_{i=1}^{k} g_i (u_i - \bar{u})^2} \tag{18}$$

$$\bar{u} = \frac{\sum_{i=1}^{k} g_i u_i}{\sum_{i=1}^{k} g_i} \tag{19}$$

The Pearson correlation coefficient between the estimated BP and true BP, as well as the MAE of the estimated BP were used as secondary metrics. In addition to plotting the estimated BP and true BP pairs for each test, Bland-Altman plots (Bland and Altman, 1986) were also produced to allow better interpretation of the results. Final performance evalution with the optimised model parameters was carried out through leave-one-out cross-validation on the training dataset. The models were then retrained separately on their entire respective training dataset without leaving out any samples, but keeping the same set of features as well as the same C and γ values. Those retrained models were then validated against the other dataset to see if the predictive power would be retained.

3 Results

3.1 Pre-processing and feature extraction

For PPG-BP, 16 of the dataset's 657 segments were rejected by criterion 1) before feature extraction. No segments were rejected due to criterion 2) or 3). From the remaining segments, 742 pulses were identified, of which 22 (3%) were rejected as

10.3389/fphys.2023.1126957

outliers based on extracted feature values. Averaging the remaining pulse features per segment yeilded 533 valid segments with complete feature vectors, for an overall segment rejection rate of 19%. After averaging per subject, the dataset had 211 feature vectors.

For UCI, 2,376 records were too short to generate the segments and were ignored. The remaining records yielded 48,120 segments, of which 1791 were rejected due to non-pulsatile ABP signals, 1,228 because criterion 1), 2,663 because of criterion 2) and 78 because of criterion 3). From the remaining segments, 83,903 pulses were identified, of which 7,104 (8%) were rejected as outliers based on extracted feature values. Averaging the valid pulses per segment yeilded 21,698 valid segments with complete feature vectors, for an overall segment rejection rate of 55%.

3.2 Statistical comparison

Results of the statistical comparison of the datasets are aggregated in Figure 3.

According to the KS-test, the differences between feature distributions were significant ($p < 0.001$) for 22 out of 31 features for the original features and 21 out of 31 features for the HR adjusted features.

Looking at μ% the difference in mean original feature values between the datasets, *c/a* stood out among all features, registering a difference of −100% of the standard deviation on UCI compared to PPG-BP. Several other features displayed a large difference, the second highest being Δn_{gh} (−93%), followed by the width features all showing at least −75% difference, S_{pe} (−74%), AI (68%) and RI (−68%). The difference between HR distributions (46%) is worth noting because of its direct physiological implication and its effect on other features. As shown in Figure 4, the UCI HR distribution is bimodal with a first peak positioned around 75 BPM, similar to PPG-BP, and a second peak close to 90 BPM. The average HR was 6.2 BPM higher in UCI and 28% of segments had a HR above 90 compared to 8% in PPG-BP.

Because HR directly affects the value of many features, looking at the HR corrected difference in mean $\mu_{adj\%}$ reveals what part of $\mu_{\%}$ is not explained by the difference in HR distribution, and highlights fundamental differences in the pulse shapes. Values significantly higher on UCI were AI (68%), N_f (68%), AI_{gf} (62%), Δn_{gf} (59%), Δn_{pf} (51%), Δn_{uf} (49%), HR (46%), Δn_{0g} (45%), IPA (31%), AX (28%) and *d/a* (14%). Values significantly lower on UCI were *c/a* (-100%), RI (-68%), Δn_{gh} (−61%), W_{90} (−45%), W_{70} (−42%), S_{pe} (−41%), W_{30} (−40%), W_{50} (−39%) and *b/a* (−30%).

The five features with the highest STD difference were *c*/a (41%), AX (38%), *d*/a (37%), IPA (31%) and S_{pe} (30% or 29% adjusted for HR), all higher on UCI. In fact, STD was higher in UCI for 87% (or 80% adjusted for HR) of features, indicating a greater variability in pulse morphology within the dataset.

The relation of those differences to differences in pulse morphology between UCI and PPG-BP are illustrated in Figure 6. For example, the PPG-BP pulse with typical values (A) had a well defined second derivative peak for the *c* point with *c/a* = −0.15 while the depression at the *c* position for the

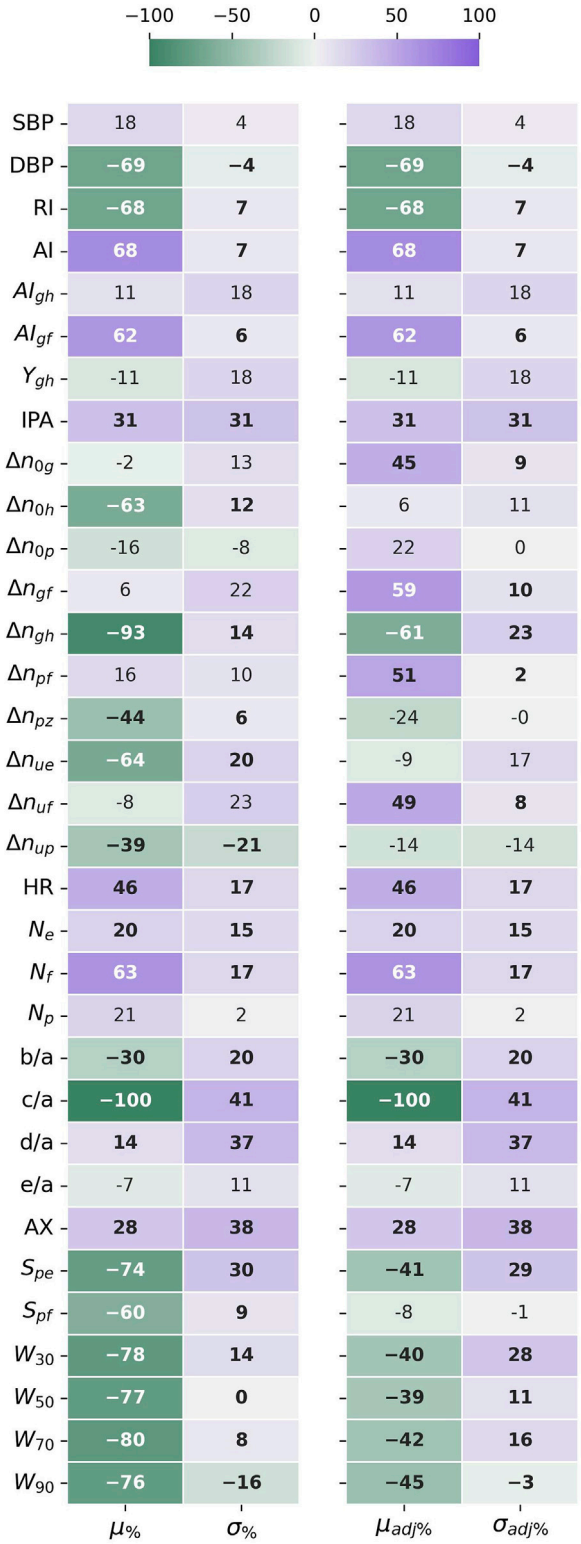

FIGURE 3
The difference in mean (μ%) and standard deviation (σ%) between the datasets, given as a percentage standard deviation of the joined datasets. The HR adjusted forms (μadj%) and (σadj%), compensate for the different HR distributions affecting time sensitive features. Negative values indicate that the mean or std values for UCI are lower than for PPG-BP. Values in bold indicate significantly different distributions ($p < 0.001$) according to the Kolmogorov-Smirnov test.

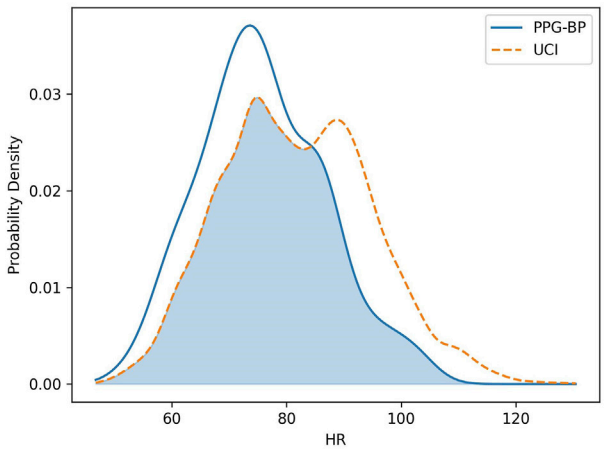

FIGURE 4
Comparison of the HR distribution for the PPG-BP and UCI datasets.

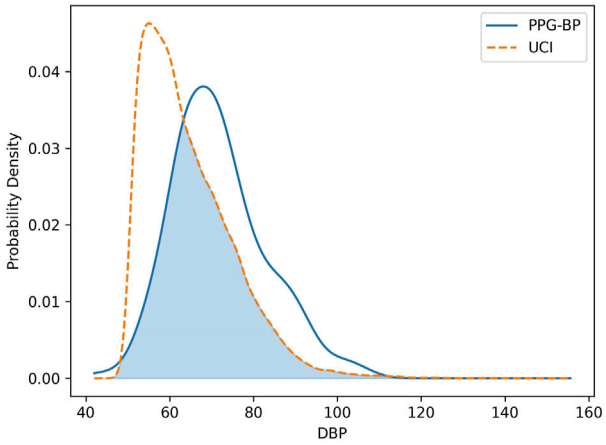

FIGURE 5
Comparison of the DBP distribution of the PPG-BP and UCI datasets.

bottom two pulses, (C) and (D), gave lower values of $c/a = -0.40$ and $c/a = -0.68$. The f point was also positioned later in the pulse for (C) and (D), resulting in larger time spans. Pulse (C) had $S_{pe} = -0.022$, $\Delta n_{0g} = 36$; $\Delta n_{uf} = 83$; $\Delta n_{pf} = 69$ and $N_f = 1.22$ which can be directly compared to the values of (A), $S_{pe} = -0.012$, $\Delta n_{0g} = 32$, $\Delta n_{uf} = 76$, $\Delta n_{pf} = 50$ and $N_f = 0.90$, since both had similar heart rates.

Pulse (C) also had a very narrow peak section with $W_{90} = 14$ while the PPG-BP pulse (A) had a wider one with $W_{90} = 30$. The heart rate of the UCI pulse (B) was 20 BPM lower than the PPG-BP pulse (A) but still only had $W_{90} = 15$. Pulse (B) also had AI = 0.76 because of the larger amplitude difference between p and f as well as a lower $b/a = -1.26$ caused by its more pronounced b peak in the second derivative. In comparison the PPG-BP pulse (A) had AI = 0.50 and $b/a = -0.79$. The variability of c/a in UCI is also illustrated in Figure 6, where the amplitude of c can be seen fluctuating between zero and the amplitude of b in the three UCI pulses. It should be noted that the pulses in Figure 6 are not archetypal pulses of UCI, which includes highly varied pulse shapes. The pulses in Figure 6 were rather selected to illustrate the morphological features that induce some of the largest feature distribution differences observed between the datasets.

In regards to BP, the SBP distribution was similar for both datasets and close to normality. However, the DBP distributions had significant differences. The average DBP value for UCI was lower at 64.3 mmHG, compared to 71.8 mmHG for PPG-BP, or a difference equivalent to -64% of the global sandard deviation. The DBP distribution of UCI was also found to deviate significantly from normality, as shown in Figure 5, with a slightly leptokurtic shape and a significant skew towards lower values.

Overall, the datasets had a similar degree of internal correlation, with $mean(|r|) = 0.36$ compared to $mean(|r|) = 0.35$ for PPG-BP. UCI had 61% of feature pairs with $|r| > 0.25$ and 28% of feature pairs with $|r| > 0.50$, as compared to 57% and 25%, respectively, for PPG-BP.

As for the correlation between features, the largest differences between datasets were observed with S_{pe}, a feature that also displayed a significant mean and STD differences between the datasets. Compared to PPG-BP, the correlation level $|r|$ of S_{pe} increased on average by 0.40 with seven other features in UCI: b/a, d/a, AX, Δn_{up}, Δn_{0p}, Y_{gh} and AI_{gh}. Another important difference was e/a, which had a correlation of r = -0.42 with d/a for PPG-BP, while that correlation fell to r = 0.02 for UCI.

The differences observed between the datasets were in large part associated with the presence of particularily pointed pulses in UCI and rare in PPG-BP. Those pulses hold a different relationship between features compared not only to most pulses in PPG-BP, but also to other types of pulses in UCI, increasing variability. Their caracteristics can be seen in the UCI Pulses of Figure 6. In general their c and d points were not well defined peaks in the second derivative, but inflection points in a curve between b and e. The amplitude of d tended to be higher as e also got higher and the S_{pe} slope became more pronounced. AX, which is calculated from the amplitude of the second derivative fiducial points, was in turn affected. Those pulses were also associated with a quick pulse onset with shorter $\Delta n_{up}, \Delta n_{0p}$ and a proportionnaly narrower pulse wave. Finally the g point also tended to be situated around the peak while the h point came later at a much decreased PPG amplitude, wherea in PPG-BP the amplitude at g and h was not related to S_{pe} due to their more varied positions around a generally flatter pulse peak.

3.3 Response to BP variations and shared predictive power

3.3.1 Correlation to BP

The Spearman rank correlation coefficient (ρ) of each dataset's features against SBP and DBP is presented in Figure 7.

For SBP, significant correlation could be established for 15 features in PPG-BP. The three most correlating features were

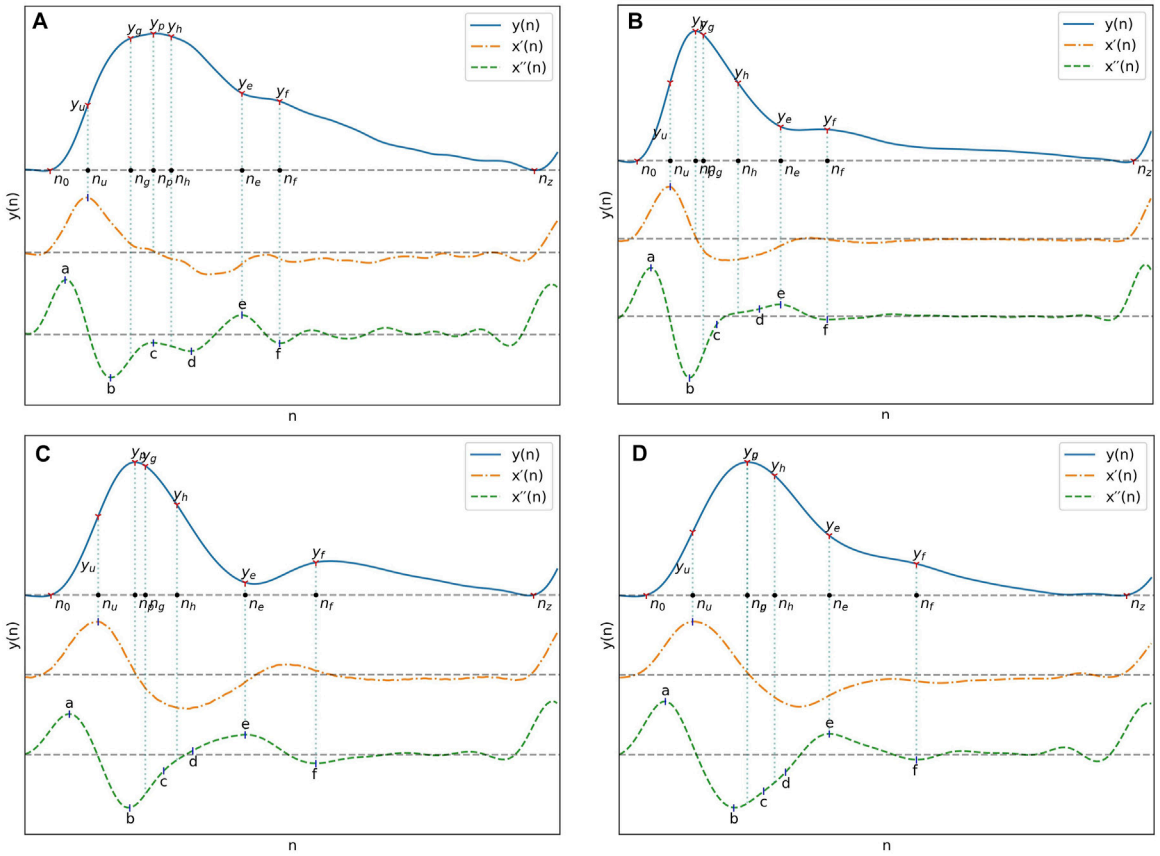

FIGURE 6
(A) Pulse from PPG-BP with characteristics representative of the dataset. **(B)**, **(C)** and **(D)** Pulses from UCI illustrating some of the differences observed with PPG-BP. In general, the pulse shape was more pointed and narrower, dropping sharply after the peak. The amplitude of the PPG signal was usually lower at the e and f points, and the f point was often encountered later in the pulse. The second derivative showed a lot of variability, but compared to PPG-BP, the b point had usually a lower amplitude and the c and d points were often not well-defined peaks in the second derivative and were thus estimated from the inflection points. This resulted in highly variable but general lower amplitude values for the c point especially, compared to PPG-BP where it more consistently appears as a peak with a value closer to zero. Note that the pulse duration is normalized in all four pulses of this figure.

AI_{gh} ($\rho = -0.50$), Y_{gh} ($\rho = 0.50$), S_{pf} ($\rho = -0.48$), and a total of 14 features had a correlation of $|\rho| > 0.25$. For UCI, the three most correlating features were c/a ($\rho = 0.24$), W_{90} ($\rho = 0.22$) and Δn_{gh} ($\rho = 0.20$). It should be noted that those features all had major mean and STD differences with PPG-BP (see Section 3.2). In total, significant correlations with SBP could be established for 22 features in UCI, although coefficients were lower at $|\rho| \leq 0.25$ for all features.

Stronger correlation with SBP in one dataset was not associated to a stronger correlation with SBP in the other dataset. For example, the three most correlating features of PPG-BP, AI_{gh}, Y_{gh} and S_{pf} ($|\rho| \geq 0.48$) were not among the higest in UCI, where their SBP correlation reached at most $|\rho| = 0.09$. As for the most correlating features in UCI, W_{90} obtained $\rho = 0.36$ in PPG-BP, Δn_{gh} was not significant and c/a had a stronger but opposite correlation of $\rho = -0.28$. Two other features showed significant but reversed correlation, although to a lesser degree: S_{pe} with $\rho = -0.23$ for PPG-BP and $\rho = 0.11$ for UCI, and AX with $\rho = 0.42$ for PPG-BP and $\rho = -0.05$ in UCI.

A similar pattern was observed for DBP. Significant correlations were established for ten features for PPG-BP. Those with the highest correlation were Δn_{pf} ($\rho = -0.42$), S_{pf} ($\rho = -0.36$), and d/a ($\rho = -0.35$). For UCI, significant correlations were established for a total of 28 features. Those with the highest correlation were Δn_{pz} ($\rho = -0.25$), HR ($\rho = 0.24$), and N_e ($\rho = 0.23$). In addition, relatively strong correlation (for UCI) was shared with one of the most correlating features of PPG-BP: Δn_{pf} ($\rho = -0.21$). Again for DBP, correlation levels of $|\rho| > 0.25$ were only reached on PPG-BP, and that for nine of the ten features where significance was attained.

3.3.2 BP estimation

Sampling one feature vector per subject in UCI for the BP estimation test yielded a total of 7,087 vectors. Parameter selection for the PPG-BP trained model resulted in $C = 75, \gamma = 0.1$ while selected parameters for UCI were $C = 0.25, \gamma = 0.03$. For PPG-BP, eight features were retained during feature selection: $N_e, S_{pf}, W_{90}, \Delta n_{gf}, \Delta n_{gh}, \Delta n_{pf}$, AX and HR. For UCI, sixteen features were retained: $AI_{gf}, N_f, S_{pf}, W_{30}, W_{50}, W_{90}, \Delta n_{0g}$, Δn_{0h}, Δn_{uf}, $\Delta\ n_{gh}$, HR, AX, RI, b/a, c/a and d/a.

SBP estimation results for the PPG-BP trained model are presented in Figure 8 for cross-validated tests on PPG-BP.

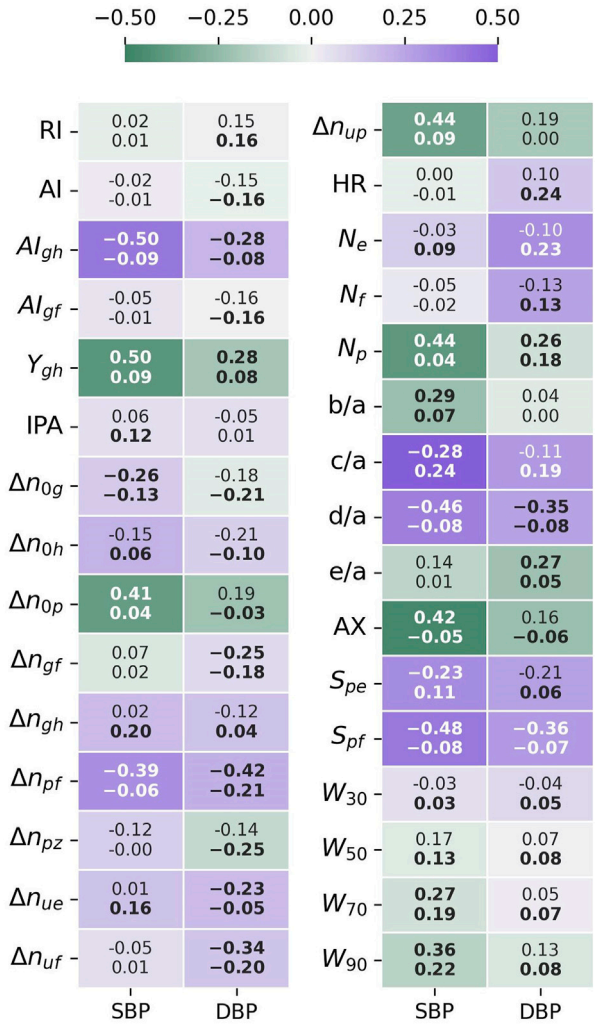

FIGURE 7
Feature-BP Spearman correlation test results. The top value is the correlation coefficient for PPG-BP, the bottom value the correlation coefficient for UCI, while the color and intensity show by how much UCI differs from PPG-BP. Values in bold indicate that the correlation is significant ($p < 0.001$).

During cross-validated tests, the model tended to overestimate samples with low BP values and underestimated samples with high BP. Nonetheless, it showed significant predictive power over the entire range of BP values, as shown by the R^2 score of 0.63. Secondary metrics were $r = 0.63$ and MAE = 13.96 mmHg with an STD of 10.50 mmHg. When applied to predict SBP for the UCI dataset, a model with the same parameters trained with the entire PPG-BP did not retain any predictive power, as shown in Figure 9, giving worse results than a mean predictor, as shown by the R^2 score of -0.07. Secondary metrics were $r = 0.09$ and MAE = 21.03 mmHg with an STD of 16.95 mmHg.

Cross-validated results for UCI, shown in Figure 10 were considerably worse than for PPG-BP, achieving only $R^2 = 0.31$, with secondary metrics $r = 0.42$ and MAE = 16.66 mmHg with an STD of 12.90 mmHg. Applying the UCI trained model to PPG-BP resulted again in a loss of predictive power, as shown in Figure 11, although not as dramatic as for the PPG-BP trained model applied to UCI. It resulted in an R^2 score of 0.12, barely better than a mean predictor. Secondary metrics were $r = 0.45$ and MAE = 16.68 mmHg with an STD of 11.93 mmHg. The model can in fact be said to almost act as a mean predictor, as the produced BP values always remain close to the mean BP, with an STD of 5.74 mmHg.

4 Discussion

Analysis of the BP and features distributions showed fundamental differences between datasets. Because vascular aging plays a role in shaping the pulse wave, it can be hypothesized that differences in the age distribution between the datasets could influence the results. This hypothesis can neither be confirmed nor rejected as age information is not available for UCI. While we can't ascertain that the UCI data is similarly distributed, it can be interesting to look at age data available for 2040 subjects of the MIMIC waveform database that have been matched to the MIMIC clinical database. That information, provided in the MAP-CW file of the dataset, shows an average age of 65 ± 17. It should however be considered a low estimate since age for patients older than 90 years of age is simply noted as "90+".

For several features, the difference can be partly attributed to the higher mean HR in UCI which results in narrower pulses. That characteristic of UCI and more specifically the large portion of data associated with a HR above 90, could be linked with stress or poor health. It supports the idea that differences in the conditions in which the data was obtained, or in the condition of the subject, has an influence on the data.

However, even when scaled by the heart rate, the difference in mean values between the datasets remained significant. That remainder was linked to morphological variations between the datasets, notably to the UCI pulse types illustrated in Figure 6. Those have a more pointed peak, more of their energy concentrated early in their period, and often lack well defined *c* and *d* peaks in the second derivative.

The loss of correlation between *d/a* and *e/a* on UCI may give some insight into the physiological origin behind the differences. The *e/a* ratio is associated with an increased inflection at the dicrotic notch while the *d/a* ratio is associated with inflection at the late systolic peak. A lower *d/a* ratio often equates to a flatter PPG peak with a sharp drop, as compared to a pointier PPG peak with a more progressive decline for higher ratios. In the wave-reflection based PPG model, this can be seen as the effect of timings and amplitude between the main systolic peak and the renal and iliac reflections (Baruch et al., 2011). The correlation between those features in the PPG-BP indicates that relatively uniform parameters in the circulatory system of the subjects define both reflections, while the loss of correlation on UCI indicates less uniformity, since the renal and iliac reflections appear modulated by different parameters. The *d/a* and *e/a* ratios have been shown to change independently with the administration of vasodilators or vasoconstrictors (Takazawa et al., 1998), which hints at possible differences in subject or environmental conditions between UCI and PPG-BP.

The relatively high degree of linear correlation between features was expected, as many features are similar in nature and are influenced in the same way by the pulse characteristics. For example widths and timings are all expected, to a certain degree, to vary together with the pulse duration.

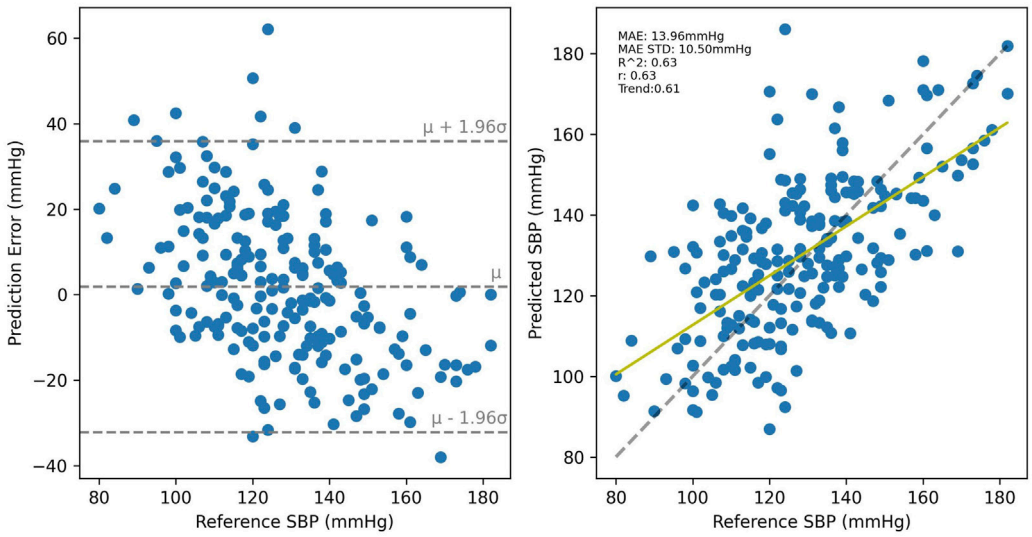

FIGURE 8
Cross validated results for the PPG-BP trained model.

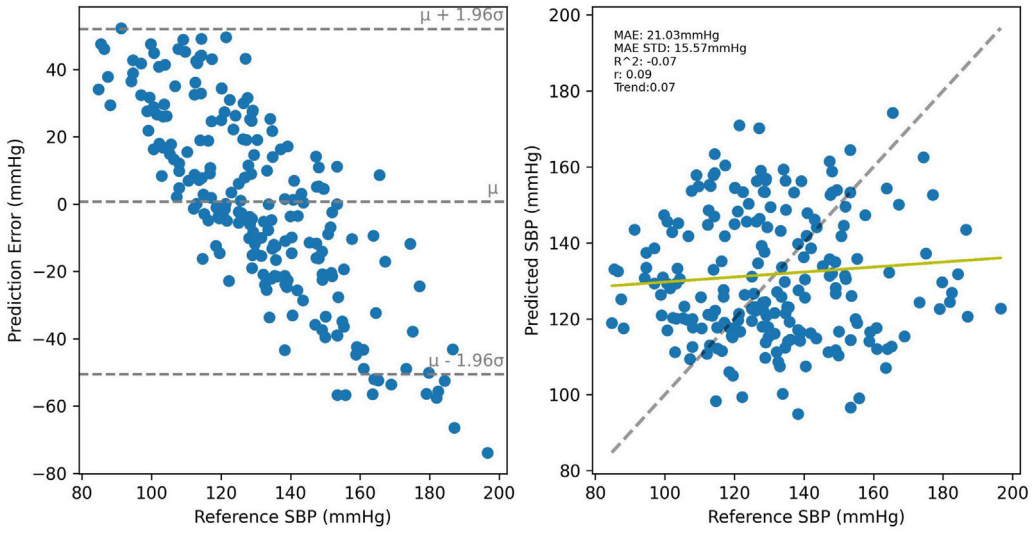

FIGURE 9
Results of the PPG-BP trained model tested with the UCI data. A random sample of the BP estimations are shown but the metrics are for the entire dataset.

The BP correlation test showed a different relationship between features and BP for each dataset. The higher correlation coefficients generaly found on PPG-BP indicated a more uniform response between the subjects, which is coherent with the controlled data collection and subject selection methodology of PPG-BP, whereas the data from UCI lacks any control over environmental and subject conditions. For UCI, two of the features correlating the most with SBP were c/a and Δn_{gh}, features that also had the most difference between the datasets. Since those features had an opposite or null correlation on PPG-BP, the difference points to possible clusters of patients or conditions in UCI where consistant BP changes accompany those morphological changes. In fact, 35% of the pulses had a c amplitude lower than d in UCI, while it is the case for only 5% of pulses in PPG-BP. In UCI, those pulses were associated with an average SBP lower by 10.7 mmHg and average DBP lower by 3.8 mmHg compared to pulses with well defined second derivative peaks where $c > d$.

Of the features retained by the SBP estimation model for PPG-BP, four out of eight ($S_{pf}, W_{90}, \Delta n_{pf}$ and AX) had significant correlation to SBP. Some of the feature that showed among the strongest correlation were not retained, which may be attributed to information redundance due to the generally strong correlation

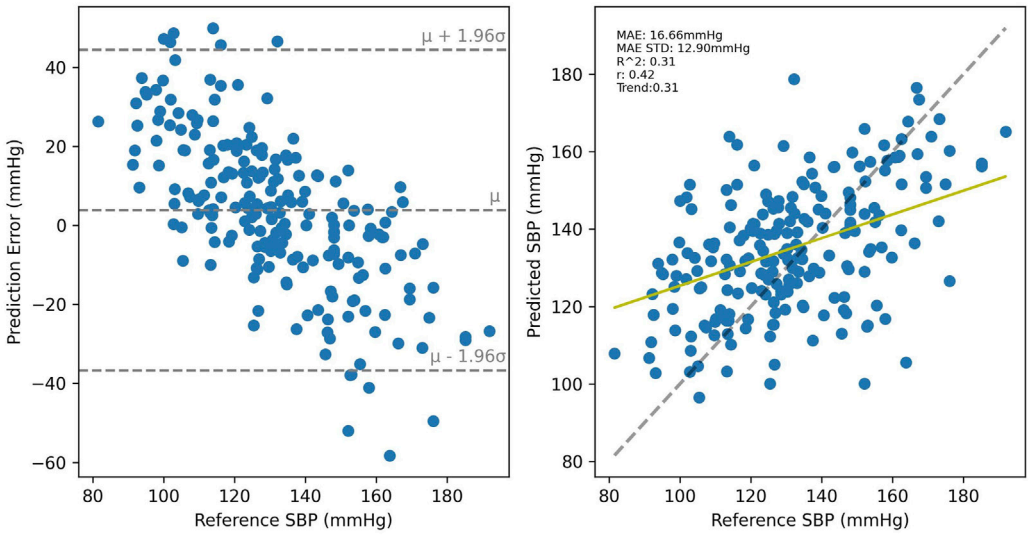

FIGURE 10
Cross validated results for the UCI trained model. A random sample of the BP estimations are shown but the metrics are for the entire dataset.

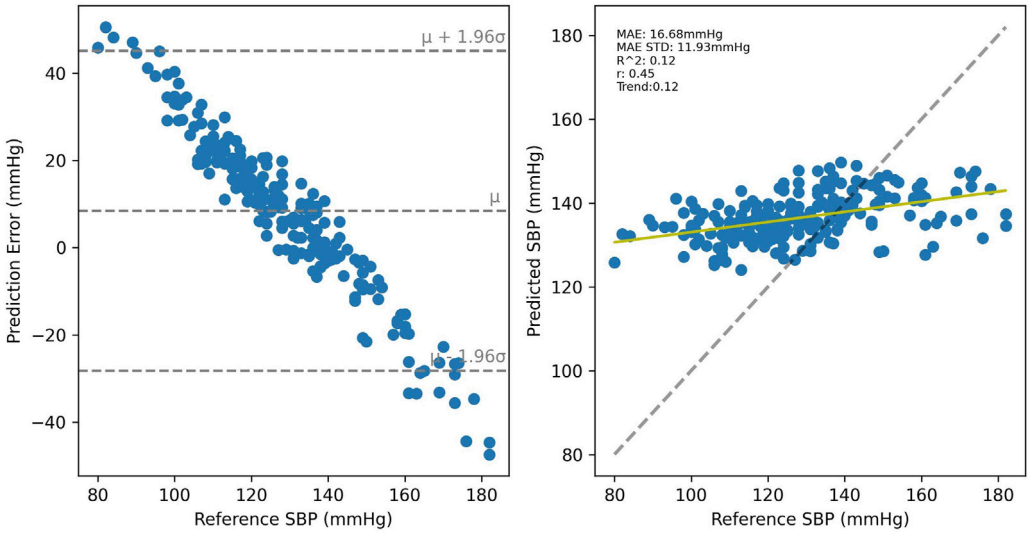

FIGURE 11
Results of the UCI trained model tested with the PPG-BP data.

between features. For UCI, the large sample size allowed establishing significance at lower correlation levels, despite the increased variability of the data. The three features with the highest correlation to SBP ($W_{90}, \Delta n_{gh}$ and c/a) were retained for estimation, the latter two also being the two features with the largest difference in mean value between datasets. Despite significant SBP correlation being present for b/a, c/a and d/a, no second derivative ratios were retained for PPG-BP. The fact that those three ratios were retained for UCI, and especially c/a with its opposite correlation profile compared to PPG-BP, maybe related to the aforementioned presence of clusters of patients with significant differences in the second derivative. It is also interesting to note that HR was retained for both datasets despite the absence of direct correlation to SBP, which suggests that scaling of some features in relation to the pulse duration played an important part in the estimation process.

Performance of BP estimation algorithms are extremely difficult to compare. The absence of a standard test dataset and the tradition of reporting the results in mmHg mean error or MAE make the results very sensitive to sample selection and BP range. Sample size, preprocessing and sampling methods vary widely, and are not always clearly described in published studies. Comparison with a

few other calibration free studies can be made but should not be seen as decisive. Kachuee et al. obtained an MAE of 11.17 ± 10.09 mmHG and $r = 0.59$ on UCI using Adaboost, but also making use of ECG (Kachuee et al., 2017). Slapnicar et al. obtained an MAE of 15.41 mmHg on 510 MIMIC subjects with a deep neural network on the raw PPG signal and the two first derivatives, while 18.34 mmHG was obtained when using a random forest algorithm with hand crafted features (Slapničar et al., 2019). As a last example, Maqsood and al. tested the same algorithms on both PPG-BP and MIMIC (although without cross-dataset tests) and reported an MAE of 5.32 ± 4.26 mmHG for PPG-BP and 5.59 ± 5.92 mmHg for MIMIC with a bidirectional long short-term memory neural network (Bi-LSTM) and time domain features, while they obtained 15.48 ± 3.52 mmHG for PPG-BP and 12.14 ± 6.67 mmHG with an SVR (Maqsood et al., 2021).

While the use of more complex models such as Bi-LSTM may potentially bring uncalibrated BP estimation closer to medical device requirements, optimal performance was not the goal of this study and a simpler model was prefered to illustrate the impact of observed differences. The present results are thus more in line with those of other simpler models. More importantly, the present results clearly show that what was learned on one dataset does not apply, or applies only weakly, to the other. It is interesting to note that with fewer features, the cross-validated model of PPG-BP obtained an R^2 twice as that of UCI. The fact that less features and thus less information is necessary to get those results in PPG-BP indicates a more uniform response in the subjects, which may be due to the more controlled data collection conditions. This would also explain why the PPG-BP trained model retains no predictive power at all with UCI, since it would not cover the wider variety of patients and recording conditions present in UCI, while the UCI trained model, having knowledge of a wider variety of conditions, may be able to retain some power, even though very weak, when applied to PPG-BP.

Absolute values of the PPG signal can vary greatly depending on the recording conditions and equipment calibration. To ensure a consistent comparison between the different records, and especially between datasets possible, no raw amplitudes were used as features, neither was the DC component of the signal. Thus, a part of the signal information, which could potentially improve performance, was not used. The added benefit of this information in the case of UCI is however doubtful, as amplitudes were uneven between segments, with the pulsatile amplitude actually following a strict bimodal distribution with a wide separating gap.

Another factor limiting the comparison was the structure of PPG-BP, which offers three short PPG segments per patient, all associated to a single BP value. In contrast, UCI offers longer segments with continous a contnuous ABP signal. The use of 5 s samples of UCI allows to obtain on average the same number of usable pulses as in three PPG-BP segments, and to reduce the ABP signal to mean SBP and DBP over the period. As a result of those differences, two additional criteria had to be applied to UCI in Section 2.2 to ensure the integrity of the signal. One on the ABP signal to detect non-pulsatile ABP, and one on the PPG signal to ensure consistant pulsatile amplitude throughout the segment. We believe that those additional criteria should not affect the validity of the comparison. They merely ensure the signals are present and usable to the same degree as in PPG-BP, which was already similarily screened for signal integrity prior to its release. However, another aspect of those differences brings uncertainty to the cross-dataset validation. While in UCI the BP measurements are derived from the ABP signal corresponding to the 5 s PPG segment, the BP measurements in PPG-BP are derived from a period of 30 s preceding the acquisition of the PPG signal. Moreover, unknown gaps exist between the three PPG segments, the only guarantee being that the BP measurements and all PPG segments are taken within a period of 3 min. While this is not an idea situation and may ultimately produce a certain degree of decoupling between the PPG signals and the recorded BP value, the simultaneous acquisition of BP and PPG may not be as important for PPG-BP as for UCI, where ABP signals sometimes change rapidely. Indeed, the acquisition protocol of PPG-BP guarantees a rest period as well as a quiet and stable environement, which should provide more stable BP values and PPG signals.

The preprocessing screening criteria were devised to catch the most obvious signal issues, such as artefacts resulting from sudden movements or sensor disconnections, that could be seen in UCI. The exclusion thresholds were adjutsted incrementally to ensure that, through visual inspection of a sample of 100 UCI segments, only those with obvious issues were rejected. Thus, this step should not be seen as an optimized method of eliminating all possible segments with issues, but only those with the most flagrant signal quality issues. The aim was to remove those early in order to have less data to process and have a better baseline for statistical comparison for filtering the remaining, lesser issues, in later stages of processing. Segments are later excluded if fiducial points cannot all be extracted according to the constrains, or if the features produced are outliers.

The larger number of outliers in UCI compared to PPG-BP raises the question of whether those segments could be a result of extreme BP, and should not be rejected as outliers. It is however not the case. The DBP distribution of rejected segments is almost identical to that of retained segments. The SBP distribution is only slightly more skewed towards lower values for rejected segments with a mean and STD of 126.4 ± 21.8 mmHg compared to 131.8 ± 21.4 mmHg for retained segments. The large number of outliers can be explained by the lower signal quality of UCI, where noise and remaining artefacts can result in miss-detection of fiducial points or in abnormal pulse shapes, generating anomalous feature values.

Although not presented here, two pulse decomposition algorithms were evaluated to extract the g and h points: The recursive algorithm described by Kontaxis et al. (2020) and the gaussian fitting algorithm described by Couceiro et al. (2015). The first one gave very inconsistant results for pulses with different shapes, such as more pointed or wider top pulses and may not be appropriate to compare between subjects with such differences. R^2 estimation results were also lower by as much as 0.18 with that method compared to the estimation method based on the second derivative described in Section 2.3. For the gaussian fitting method, R^2 estimation results were similar while computation time for feature extraction was several times larger. The observation that some points in the second derivative were highly correlated with the position of the fitted gaussian components resulted in using those points directly, as described in Section 2.3.

To conclude, the various private datasets used in the indirect BP measurement literature make comparing the published algorithms difficult, and researchers have called for the creation of a standardised dataset suitable to compare and validate BP estimation algorithms (Solà and Delgado-Gonzalo, 2019). MIMIC, and by extension UCI, are publicly available and contain a large quantity of data, which may seem like a good basis for comparison. However, results presented in this paper reinforces suspicions of many researchers: that data sourced in intensive care units, under unknown conditions, may have a skewed response to BP and impair the generalisation of BP estimation algorithms. In fact, the issue of cross-dataset generalization is neither new nor limited to the field of BP estimation, but it is an issue often overlooked. It has been argued that cross-dataset validation of machine learning models developed for the medical field is essential to evaluate their performance (Thambawita et al., 2020). Yet, it is almost never done in the BP estimation literature. Cross-dataset generalisation can be challenging in itself, for example because of differences in equipment calibration, sampling, and recording conditions. Using intensive care data introduces an obvious sampling and recording condition bias. This is reflected in our presented results as significant differences in the relationship between BP and pulse features when comparing the UCI dataset to data obtained under more controlled conditions, which may make generalization more difficult to achieve. Besides using data that better represents the entire population, researchers could turn to data fusion and data augmentation to make their datasets more comprehensive. The latter has been used successfully in computer vision to improve cross-dataset performance, including in the field of imaging photoplethysmography (Nowara, 2021). In any case, we hope that the present paper raises awareness of this issue, replaces the vague suspicions surrounding intensive care data with quantified results that can be referred to, and stimulates better validations of models on different populations in future research.

Data availability statement

Publicly available datasets were analyzed in this study. This data can be found here: The UCI Cuffless Blood Pressure Estimation can be found here: https://archive.ics.uci.edu/ml/datasets/Cuff-Less+Blood+Pressure+Estimation. The PPG-BP dataset can be found here: https://figshare.com/articles/dataset/PPG-BP_Database_zip/5459299. The MIMIC 2 Waveform Database can be found here: https://archive.physionet.org/physiobank/database/mimic2wdb/.

Ethics statement

The studies involving human participants were reviewed and approved by Université Laval human research ethics committee (approval number: 2022-174). Written informed consent for participation was not required for this study in accordance with the national legislation and the institutional requirements.

Author contributions

GW-B wrote the code and algorithms, performed the experiments, and wrote the manuscript. BG and FS provided guidance and ideas, helped develop and validate the methodology, and reviewed the manuscript.

Funding

This research project was supported by the SMAART Program, Sentinel North and by the Canada Research Chair in Smart Biomedical Microsystems. Frida Sandberg was supported by the Swedish Research Council (Grant VR 2019-04272), and the Crafoord Foundation (Grant 20200605).

Acknowledgments

A preprint version of this paper was previously published online as part of a master's thesis (Weber-Boisvert, 2022).

Conflict of interest

The authors declare that the research was conducted in the absence of any commercial or financial relationships that could be construed as a potential conflict of interest.

Publisher's note

References

Awad, A. A., Haddadin, A. S., Tantawy, H., Badr, T. M., Stout, R. G., Silverman, D. G., et al. (2007). The relationship between the photoplethysmographic waveform and systemic vascular resistance. *J. Clin. Monit. Comput.* 21, 365–372. doi:10.1007/s10877-007-9097-5

Baruch, M. C., Warburton, D. E., Bredin, S. S., Cote, A., Gerdt, D. W., and Adkins, C. M. (2011). Pulse Decomposition Analysis of the digital arterial pulse during hemorrhage simulation. *Nonlinear Biomed. Phys.* 5, 1. doi:10.1186/1753-4631-5-1

Bland, J. M., and Altman, D. G. (1986). Statistical methods for assessing agreement between two methods of clinical measurement. *Lancet* 327, 307–310. doi:10.1016/s0140-6736(86)90837-8

Carlson, C., Turpin, V.-R., Suliman, A., Ade, C., Warren, S., and Thompson, D. E. (2020). Bed-based Ballistocardiography: Dataset and ability to track cardiovascular parameters. *Sensors* 21, 156. doi:10.3390/s21010156

Centers for Disease Control and Prevention (2022). Facts about hypertension. Available at: https://www.cdc.gov/bloodpressure/facts.htm (Accessed December 18, 2022).

Chao, P. C.-P., Wu, C.-C., Nguyen, D. H., Nguyen, B.-S., Huang, P.-C., and Le, V.-H. (2021). The machine learnings leading the cuffless PPG blood pressure sensors into the next stage. *IEEE Sensors J.* 21, 12498–12510. doi:10.1109/JSEN.2021.3073850

Couceiro, R., Carvalho, P., Paiva, R. P., Henriques, J., Quintal, I., Antunes, M., et al. (2015). Assessment of cardiovascular function from multi-Gaussian fitting of a finger photoplethysmogram. *Physiol. Meas.* 36, 1801–1825. doi:10.1088/0967-3334/36/9/1801

Danaei, G., Ding, E. L., Mozaffarian, D., Taylor, B., Rehm, J., Murray, C. J. L., et al. (2009). The preventable causes of death in the United States: Comparative risk assessment of dietary, lifestyle, and metabolic risk factors. *PLoS Med.* 6, e1000058. doi:10.1371/journal.pmed.1000058

Dillon, J. B., and Hertzman, A. B. (1941). The form of the volume pulse in the finger pad in health, arteriosclerosis, and hypertension. *Am. heart J.* 21, 172–190. doi:10.1016/s0002-8703(41)90966-3

Ding, X., Yan, B. P., Zhang, Y.-T., Liu, J., Su, P., and Zhao, N. (2019). Feature exploration for knowledge-guided and data-driven approach based cuffless blood pressure measurement. *Electr. Eng. Syst. Sci.* doi:10.48550/arXiv.1908.10245

Elgendi, M., Fletcher, R., Liang, Y., Howard, N., Lovell, N. H., Abbott, D., et al. (2019). The use of photoplethysmography for assessing hypertension. *npj Digit. Med.* 2, 60. doi:10.1038/s41746-019-0136-7

Elgendi, M. (2012). On the analysis of fingertip photoplethysmogram signals. *CCR* 8, 14–25. doi:10.2174/157340312801215782

Esmaelpoor, J., Moradi, M. H., and Kadkhodamohammadi, A. (2021). Cuffless blood pressure estimation methods: Physiological model parameters versus machine-learned features. *Physiol. Meas.* 42, 035006. doi:10.1088/1361-6579/abeae8

Gehring, J., Gesche, H., Drewniok, G., Küchler, G., and Patzak, A. (2018). Nocturnal blood pressure fluctuations measured by using pulse transit time in patients with severe obstructive sleep apnea syndrome. *Sleep. Breath.* 22, 337–343. doi:10.1007/s11325-017-1555-9

Goldberger, A. L., Amaral, L. A. N., Glass, L., Hausdorff, J. M., Ivanov, P. Ch., Mark, R. G., et al. (2000). PhysioBank, PhysioToolkit, and PhysioNet: Components of a new research resource for complex physiologic signals. *Circulation* 101, e215–e220. doi:10.1161/01.CIR.101.23.e215

Hansen, T. W., Li, Y., Boggia, J., Thijs, L., Richart, T., and Staessen, J. A. (2011). Predictive role of the nighttime blood pressure. *Hypertension* 57, 3–10. doi:10.1161/HYPERTENSIONAHA.109.133900

Hasanzadeh, N., Ahmadi, M. M., and Mohammadzade, H. (2020). Blood pressure estimation using photoplethysmogram signal and its morphological features. *IEEE Sensors J.* 20, 4300–4310. doi:10.1109/JSEN.2019.2961411

Hsu, C.-W., Chang, C.-C., and Lin, C.-J. (2016). A practical guide to support vector classification. Available at: https://www.csie.ntu.edu.tw/~cjlin/papers/guide/guide.pdf (Accessed May 19, 2016).

Kachuee, M., Kiani, M. M., Mohammadzade, H., and Shabany, M. (2017). Cuffless blood pressure estimation algorithms for continuous health-care monitoring. *IEEE Trans. Biomed. Eng.* 64, 859–869. doi:10.1109/TBME.2016.2580904

Kachuee, M. (2015). UCI machine learning repository: Cuff-less blood pressure estimation data set. Available at: https://archive.ics.uci.edu/ml/datasets/Cuff-Less+Blood+Pressure+Estimation# (Accessed April 19, 2021).

Kim, J. S., Kim, K. K., Baek, H. J., and Park, K. S. (2008). Effect of confounding factors on blood pressure estimation using pulse arrival time. *Physiol. Meas.* 29, 615–624. doi:10.1088/0967-3334/29/5/007

Kochanek, K. D., Murphy, S. L., Xu, J., and Arias, E. (2019). Deaths: Final data for 2017. *Natl. Vital Stat. Rep.* 68, 1–77.

Kontaxis, S., Gil, E., Marozas, V., Lazaro, J., Garcia, E., Posadas-de Miguel, M., et al. (2020). Photoplethysmographic waveform analysis for autonomic reactivity assessment in depression. *IEEE Trans. Biomed. Eng.* 1, 1273–1281. doi:10.1109/TBME.2020.3025908

Lee, H.-C., Park, Y., Yoon, S. B., Yang, S. M., Park, D., and Jung, C.-W. (2022). VitalDB, a high-fidelity multi-parameter vital signs database in surgical patients. *Sci. Data* 9, 279. doi:10.1038/s41597-022-01411-5

Li, Y., Wang, Z., Zhang, L., Yang, X., and Song, J. (2014). Characters available in photoplethysmogram for blood pressure estimation: Beyond the pulse transit time. *Australas. Phys. Eng. Sci. Med.* 37, 367–376. doi:10.1007/s13246-014-0269-6

Liang, Y., Chen, Z., Liu, G., and Elgendi, M. (2018). A new, short-recorded photoplethysmogram dataset for blood pressure monitoring in China. *Sci. Data* 5, 180020. doi:10.1038/sdata.2018.20

Lin, W.-H., Li, X., Li, Y., Li, G., and Chen, F. (2020). Investigating the physiological mechanisms of the photoplethysmogram features for blood pressure estimation. *Physiol. Meas.* 41, 044003. doi:10.1088/1361-6579/ab7d78

Liu, D., Görges, M., and Jenkins, S. A. (2012). University of Queensland vital signs dataset: Development of an accessible repository of anesthesia patient monitoring data for research. *Anesth. Analgesia* 114, 584–589. doi:10.1213/ANE.0b013e318241f7c0

Maqsood, S., Xu, S., Springer, M., and Mohawesh, R. (2021). A benchmark study of machine learning for analysis of signal feature extraction techniques for blood pressure estimation using photoplethysmography (PPG). *IEEE Access* 9, 138817–138833. doi:10.1109/ACCESS.2021.3117969

Nowara, E. M. (2021). Towards robust imaging photoplethysmography in unconstrained settings. Available at: https://scholarship.rice.edu/handle/1911/110424 (Accessed December 16, 2022).

Ogedegbe, G., and Pickering, T. (2010). Principles and techniques of blood pressure measurement. *Cardiol. Clin.* 28, 571–586. doi:10.1016/j.ccl.2010.07.006

Pedregosa, F., Varoquaux, G., Gramfort, A., Michel, V., Thirion, B., Grisel, O., et al. (2011). Scikit-learn: Machine learning in Python. *J. Mach. Learn. Res.* 12, 2825–2830.

Saeed, M., Villarroel, M., Reisner, A. T., Clifford, G., Lehman, L.-W., Moody, G., et al. (2011). Multiparameter intelligent monitoring in intensive care II: A public-access intensive care unit database. *Crit. Care Med.* 39, 952–960. doi:10.1097/CCM.0b013e31820a92c6

Slapničar, G., Mlakar, N., and Luštrek, M. (2019). Blood pressure estimation from photoplethysmogram using a spectro-temporal deep neural network. *Sensors* 19, 3420. doi:10.3390/s19153420

Solà J., and R. Delgado-Gonzalo (Editors) (2019). *The handbook of cuffless blood pressure monitoring: A practical guide for clinicians, researchers, and engineers* (Cham: Springer International Publishing). doi:10.1007/978-3-030-24701-0

Takazawa, K., Tanaka, N., Fujita, M., Matsuoka, O., Saiki, T., Aikawa, M., et al. (1998). Assessment of vasoactive agents and vascular aging by the second derivative of photoplethysmogram waveform. *Hypertension* 32, 365–370. doi:10.1161/01.HYP.32.2.365

Thambawita, V., Jha, D., Hammer, H. L., Johansen, H. D., Johansen, D., Halvorsen, P., et al. (2020). An extensive study on cross-dataset bias and evaluation metrics interpretation for machine learning applied to gastrointestinal tract abnormality classification. *ACM Trans. Comput. Healthc.* 1, 1–29. doi:10.1145/3386295

US Department of Health and Human Services (2003). *The Seventh Report of the Joint national committee on prevention, detection, evaluation, and treatment of high blood pressure*. United States: US Department of Health and Human Services.

Virtanen, P., Gommers, R., Oliphant, T. E., Haberland, M., Reddy, T., Cournapeau, D., et al. (2020). SciPy 1.0: Fundamental algorithms for scientific computing in Python. *Nat. Methods* 17, 261–272. doi:10.1038/s41592-019-0686-2

Weber-Boisvert, G. (2022). *Cuffless blood pressure estimation*. Québec: Université Laval

Xing, X., Ma, Z., Zhang, M., Gao, X., Li, Y., Song, M., et al. (2020). Robust blood pressure estimation from finger photoplethysmography using age-dependent linear models. *Physiol. Meas.* 41, 025007. doi:10.1088/1361-6579/ab755d

Yoon, Y., Cho, J. H., and Yoon, G. (2009). Non-constrained blood pressure monitoring using ECG and PPG for personal healthcare. *J. Med. Syst.* 33, 261–266. doi:10.1007/s10916-008-9186-0

frontiers | Frontiers in Physiology

TYPE Original Research
PUBLISHED 04 April 2023
DOI 10.3389/fphys.2023.1127419

OPEN ACCESS

EDITED BY
John Allen,
Coventry University, United Kingdom

REVIEWED BY
Haipeng Liu,
Coventry University, United Kingdom
Michael Drinnan,
Newcastle Hospitals, United Kingdom

*CORRESPONDENCE
B. R. Hayes-Gill,
barrie.hayes-gill@nottingham.ac.uk

SPECIALTY SECTION
This article was submitted to Computational Physiology and Medicine, a section of the journal Frontiers in Physiology

RECEIVED 19 December 2022
ACCEPTED 21 March 2023
PUBLISHED 04 April 2023

CITATION
Stockwell SJ, Kwok TC, Morgan SP, Sharkey D and Hayes-Gill BR (2023), Forehead monitoring of heart rate in neonatal intensive care.
Front. Physiol. 14:1127419.
doi: 10.3389/fphys.2023.1127419

Forehead monitoring of heart rate in neonatal intensive care

S. J. Stockwell[1], T. C. Kwok[2], S. P. Morgan[1], D. Sharkey[2] and B. R. Hayes-Gill[1]*

[1]Optics and Photonics Research Group, Faculty of Engineering, University of Nottingham, Nottingham, United Kingdom, [2]Centre for Perinatal Research, Lifespan and Population Health, School of Medicine, University of Nottingham, Nottingham, United Kingdom

Heart rate is an extremely important physiological parameter to measure in critically unwell infants, as it is the main physiological marker that changes in response to a change in infant condition. Heart rate is routinely measured peripherally on a limb with a pulse oximeter. However, when infants are critically unwell, the blood supply to these peripheries is reduced in preference for central perfusion of vital organs such as the brain and heart. Measurement of heart rate with a reflection mode photoplethysmogram (PPG) sensor on the forehead could help minimise this problem and make it easier for other important medical equipment, such as cannulas, to be placed on the limbs. This study compares heart rates measured with a forehead-based PPG sensor against a wrist-based PPG sensor in 19 critically unwell infants in neonatal intensive care collecting 198 h of data. The two heart rates were compared using positive percentage agreement, Spearman's correlation coefficient and Bland-Altman analysis. The forehead PPG sensor showed good agreement with the wrist-based PPG sensor with limits of agreement of 8.44 bpm, bias of −0.22 bpm; positive percentage agreement of 98.87%; and Spearman's correlation coefficient of 0.9816. The analysis demonstrates that the forehead is a reliable alternative location for measuring vital signs using the PPG.

KEYWORDS

photoplethysmogram, PPG, neonatal, heart rate, forehead, reflectance-mode, pulse oximeter Min.5-Max. 8, NICU (neonatal intensive care unit)

1 Introduction

Pulse oximeters are a crucial piece of equipment when monitoring critically unwell newborns in neonatal intensive care units (NICU). They are used to measure vital signs such as heart rate and blood oxygen saturation (SpO_2). These vital signs are obtained by transmitting light through the body and investigating how the signal is modulated by the pulsatile blood flow. This modulation of light can be detected and is referred to as the photoplethysmogram (PPG). The PPG can be measured in two different modes, transmission and reflection (Jubran, 2015). Transmission mode PPG is used on areas where light can be transmitted through, such as the fingers, toes, and earlobes with the detector placed on the opposite side to the light source. Reflection mode PPG can operate on almost all parts of the body with sufficient cutaneous blood flow but with the detector placed alongside the light source.

The PPG signal originates from oscillatory changes in volume of the microvasculature as blood is pumped around the body by the heart. The PPG is regulated by several physiological factors, including but not limited to respiration (Nilsson, 2013), blood pressure (Elgendi et al., 2019) and neural activity (Khalid et al., 2022). These oscillatory changes can enable the

extraction of multiple vital signs, such as heart rate, respiratory rate, and blood pressure. The PPG is used for a range of applications but here we focus on the newborn population. For details of other applications of PPG, we refer the reader to a recent review (Park et al., 2022).

Monitoring of the heart rate provides insight into the infant's condition and how well they are responding to treatment. Although SpO_2 provides oxygen status, heart rate is the first physiological marker to respond when an infant's condition deteriorates or when treatment is successful (Wyckoff et al., 2020). Conventional pulse oximeters rely on the transmission of red and infrared (IR) light through the limb. Since the signal observed is due to pulsatile blood flow, the quality of the signal is reduced in the presence of poor peripheral perfusion. Reduced perfusion is common in the high-risk group of newborns due to a variety of reasons, including iatrogenic causes such as the use of inotropes (Dilli, Soylu, and Tekin, 2019) (Kluckow, 2018) or bloodstream infections (Verstraete et al., 2015). Hence, at a time when accurate heart rate measurement is crucial as the infant becomes critically ill, impaired peripheral perfusion can affect the ability of the conventional pulse oximeter to obtain reliable signals and subsequent heart rate measurements.

The space surrounding an unwell newborn in NICU can be especially limited with many wires and tubes being attached to the newborn and to the respective monitors to display the data. A sensor that uses wireless transmission to the bedside display not only reduces the number of wires around the newborn but also frees up vital space needed for important medical equipment, such as cannulas. Furthermore, the reduction in wires also helps parents establish skin-to-skin bonding (kangaroo care) with their newborn earlier (Bonner et al., 2017).

The new device used in this study is a reflection-based green light PPG probe mounted inside a cap placed on the forehead. This probe benefits from the strong absorption of green light (λ = 525 nm) in both oxygenated and deoxygenated haemoglobin, giving a large pulsatile signal. Furthermore, green light is applicable for heart rate detection since the deeper penetration depths provided by longer wavelengths, such as IR, is not necessary to measure the pulsatile blood flow in the microvasculature required to measure heart rate (Mejía-Mejía et al., 2022). As such, this optimises the measurement of the pulsatile signal of blood flow on the forehead.

The forehead provides a site with haemodynamic stability that allows the heart rate to be determined using the blood supply of the supraorbital artery and superficial temporal artery. These arteries are in turn supplied by the internal and external carotid arteries, which also supply blood to the brain. This makes the site much less susceptible to poor peripheral perfusion since blood flow to the brain is physiologically preserved at the expense of other less important organs and peripheral limbs (Schallom et al., 2007) (Berkenbosch and Tobias, 2006). Previous studies have recommended the forehead for neonatal monitoring due to its haemodynamic stability in comparison to the peripheries (Grubb et al., 2014). The forehead has also shown promise as a suitable location for non-contact PPG monitoring (Allen and Howell, 2014). A further advantage of forehead monitoring is that the wrists of neonates, especially preterm, are extremely small and it is not always possible to place more than one piece of equipment. Should a cannula be required, such as a peripheral venous line, PPG could not be performed on that wrist. By implementing PPG on the forehead, the wrists are available for cannulation where necessary.

We have previously studied a forehead-based PPG (fhPPG), operating in multiple newborn clinical settings (NICU and delivery room), demonstrating strong heart rate correlation with a gold standard device (Henry et al., 2020). The aim of this study is to compare a fhPPG sensor with a traditional, peripherally sited limb-based pulse oximeter for heart rate monitoring in more critically unwell newborns over a much longer study period (198 h compared to 16 h previously).

2 Materials and methods

2.1 Study population

This cohort observation study was conducted at the Nottingham University Hospitals NHS Trust, United Kingdom, following ethical approval (East Midlands - Nottingham 1 Research Ethics Committee 20/EM/0034). Informed parental consent was obtained prior to infants being recruited into the study. One of the aims of this trial was to evaluate the reliability and accuracy of the heart rate algorithm of the fhPPG device in critically unwell infants in the NICU. Infants were only recruited if they had an arterial line as part of routine care and required monitoring of vitals such as heart rate and blood oxygen saturation, the subject of a future publication with the same fhPPG sensor used here. Infants, regardless of gestational age or birthweight, were considered for the trial if they met the aforementioned criteria. The trial was terminated once the arterial line was removed from the infant. A convenience sample of 20 infants was recruited. One infant was excluded as there was no pulse oximeter (PO) data due to a lack of a research compatible monitor from which to collect data.

2.2 Study design

The aim of this study is to compare a forehead-based PPG (fhPPG) sensor with a traditional limb-based pulse oximeter for heart rate monitoring. We have previously shown a device operating in multiple clinical settings (NICU and delivery room) demonstrating strong correlation with a gold standard (Henry et al., 2020). The device has now been further trialed on a much larger sample of data points (198 h compared to 16 h previously) from critically unwell infants in neonatal intensive care to further assess the ability to measure heart rates quickly and accurately over a long continuous period.

For monitoring of the infant, the equipment consisted of an fhPPG device (Surepulse Medical Ltd.) housed inside a cap of appropriate size for the infant's head and connected wirelessly to a data logging system *via* an inbuilt Bluetooth module. The probe has three LEDs of different wavelengths in the green (λ = 525 nm), red (λ = 660 nm) and IR (λ = 950 nm) regions. For the detection and calculation of heart rate, the fhPPG uses a green LED with a photodiode to detect changes in the magnitude of detected light as blood is pumped around the body. As part of routine care, a transmission mode Nellcor MAX-N PO was placed on the infant's right wrist and was attached to a CARESCAPE Monitor B850

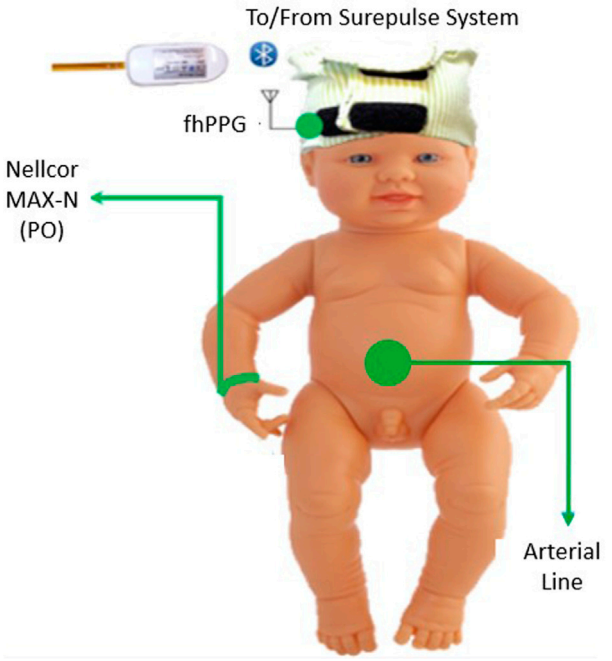

FIGURE 1
Diagram of the placement of the equipment on the subject in the trial. The Nellcor PO was placed on the right wrist and the fhPPG on the forehead.

(General Electric Healthcare). Custom software designed in MATLAB 2021b (MathWorks) was used to collect synchronised data in real-time from the B850 and stored on a laptop (Lenovo Thinkpad L540, Lenovo Group Ltd.) running Windows 10. In accordance with regular practice, if either of the devices presented a poor or no trace, the device was repositioned in an attempt to restore the signal. This was performed by neonatal nurses when the trace observed on either the B850 or fhPPG display was noticeably poor as is normal care practice. A diagram of the equipment used, and site location is illustrated in Figure 1.

Each subject had multiple data recording sessions taken with the fhPPG device with each record approximately 60–90 min long. After each recording, the sensor was removed and placed back on the infant's head. This removal was necessary to check the skin integrity under the sensor regarding redness and intact skin. Minimal redness was observed and importantly, there was no skin damage. The device has already met regulatory requirements for biocompatibility, however, additional safety measures were taken proactively to ensure the health of the subjects.

The raw fhPPG data is initially filtered in hardware by a 30 Hz single pole switched capacitor filter. It is then further filtered in software by a 3rd order linear phase bandpass filter (0.4—9 Hz) to isolate the pulsatile signal of the PPG which has an expected frequency between 1 and 4 Hz (60bpm—240bpm). The linear phase response results in negligible distortion to the shape of the pulse compared to non-linear phase responses (Liu et al., 2021).

Prior to the beginning of each record, the clocks of both the fhPPG and the B850 were aligned to synchronise the two data streams. The B850 monitor generates heart rate data over a 10-s window with an update rate of one second. The fhPPG was set to the same window length as the B850. However, the fhPPG produces a heart rate value every 5 s. As such, the B850 heart rate data was downsampled to match the fhPPG, such that each device observes the same period for each window. Downsampling was chosen so that the time window observed by both devices matched exactly as opposed to averaging the B850 data.

2.3 Data analysis

Data analysis was performed using MATLAB. All continuous variables were tested for normality with the Lilliefors test and presented as mean and standard deviation (SD), median (range), or median (IQR), as appropriate. On occasions, signal integrity errors occurred with the B850 causing the data stream to output constant values for the heart rate for the PO. Where this occurred, or an error code was present, the data were disregarded and not included in the analysis.

For all data pairs (fhPPG and PO), the following output statistical values are calculated.

i) Positive percentage agreement (PPA)
ii) Bland-Altman plots (Limits of Agreement (LOA) and Bias)
iii) Spearman's Correlation Coefficient (ρ)

When calculating the PPA, Spearman's correlation coefficient, and Bland-Altman statistics, *"unsuccessful"* paired data points were removed from the analysis. An unsuccessful paired data point is where either the fhPPG or the PO device: is unable to output a reading due to an inability to calculate a heart rate; or a device presented an error code; or device outputs a heart rate value outside the standard operating ranges of 30–240 bpm. The removal of these data points reduced the total amount of data available to process by 25 h, from 223 h to 198 h of paired data, for a total of 142,567 data points.

For PPA, an fhPPG data point was considered in positive agreement if the data point was within 10% of the paired PO data point. This term provides a reliability indicator with an element of accuracy compared to the PO. Correlation between fhPPG heart rate and PO heart rate is shown with the Spearman's correlation coefficient. Spearman's correlation coefficient was chosen since the two values, fhPPG heart rate and PO heart rate are not independent of each other, as they are both attempting to measure the same signal. Finally, a comparison of fhPPG and PO heart rate values was performed by Bland-Altman analysis (Bland and Altman, 2007) reporting LOA and bias. The modified Bland-Altman analysis was selected due to the differing number of data points for each subject (Bland and Altman, 2007). For Spearman's correlation coefficient, the value of ρ is calculated by taking the entire cohort of data. This is similar to the bias calculation from Bland & Altman, 2007 as it accurately weights the data based on the number of data points collected from each subject. The same cohort technique was also performed for the PPA, such that those subjects contributing the most data points to the analysis were weighted correctly.

TABLE 1 Demographics of the study. All values are either absolute values or median and interquartile ranges (IQR). Primary reason for admission to NICU given.

Demographics and characteristics	Overall cohort (N = 19)
Gestational age at birth (weeks + days)	37^{+2} (27^{+5}–40^{+3})
Chronological age at recruitment (days)	2 (1–12)
Birthweight (g)	2920 (1060–3610)
Male sex, n (%)	7 (37)
Fitzpatrick skin type, n (%)	
II	16 (84)
IV	2 (11)
V	1 (5)
Number of fhPPG records per subject	6 (1–34)
Principal cardiorespiratory diagnosis for neonatal admission, n (%)	
Persistent pulmonary hypertension	9 (47)
Congenital diaphragmatic hernia	3 (16)
Sepsis	2 (11)
Hydrops fetalis	2 (11)
Respiratory distress syndrome	1 (5)
Congenital heart defect	1 (5)
Right pneumothorax	1 (5)
Inotrope requirement, n (%)	12 (63)
Death before neonatal discharge, n (%)	1 (5)

3 Results

The demographics of the 19 subjects are shown in Table 1. A total of 187 recordings were made (median number of records 6/infant, range 1-34). This corresponds to a median total record length/infant of 7.16 h (IQR 4.12–17.05 h) with a minimum of 0.79 h and a maximum of 45.08 h/infant. In total 223 h of recordings were undertaken with a total of 198 h of paired data being analysed.

Figure 2 shows the cohort PPA against PPA thresholds in the range of 2%–10%. At a threshold of 10% (where the fhPPG heart rate was within 10% of the PO heart rate), the cohort had a PPA of 98.87%. Pearson's correlation coefficient had a strong correlation of 0.9816 ($p < 0.001$) between the PO heart rate and fhPPG heart rate. Bland-Altman analysis of the data demonstrated a small negative bias of −0.22 bpm with limits of agreement of 8.44 bpm. All fhPPG and PO pairs used in analysis are shown in a pooled scatter plot and Bland-Altman plot in Figures 3, 4 respectively.

Of the 19 subjects recruited, eight were considered preterm (gestation age (GA) < 37 weeks). Of these eight, five were moderate to late preterm (GA 32–37 weeks), two are very preterm (GA 28–32 weeks) and one is extremely preterm (GA < 28 weeks). Table 2 shows the measurement statistics of two sub-cohorts of the data, term subjects and preterm subjects.

4 Discussion

The aim of this trial was to assess the accuracy and reliability of a head mounted fhPPG heart rate sensor on a large cohort of data from critically ill infants not previously studied (Henry et al., 2020). This was achieved as the dataset collected was over ten times larger, with over 198 h of data compared to 16 h, albeit with only 19 subjects compared to 34 previously. The strongly positive Spearman's correlation coefficient shows that the fhPPG was able to track the changes in the heart rate when compared with the PO. When both devices were working in tandem, a very high PPA was achieved when tested at all thresholds. This suggests that the fhPPG consistently calculates heart rate to within a small tolerance of the PO, with 98.87% of fhPPG heart rate datapoints in positive agreement with the PO at a 10% threshold. Given that the heart rate of the subjects was generally between 100 and 200 bpm, the 81.53% PPA at a 2% threshold shows that the fhPPG was within 2–4 bpm of the PO

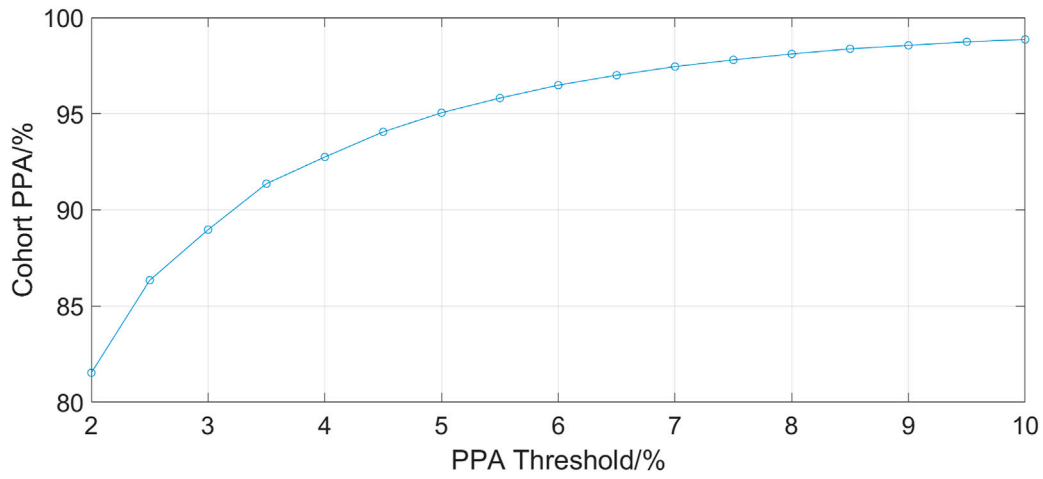

FIGURE 2
A plot of PPA threshold against the cohort PPA value. The PPA threshold was defined as the fhPPG heart rate being within a certain percentage of the PO heart rate.

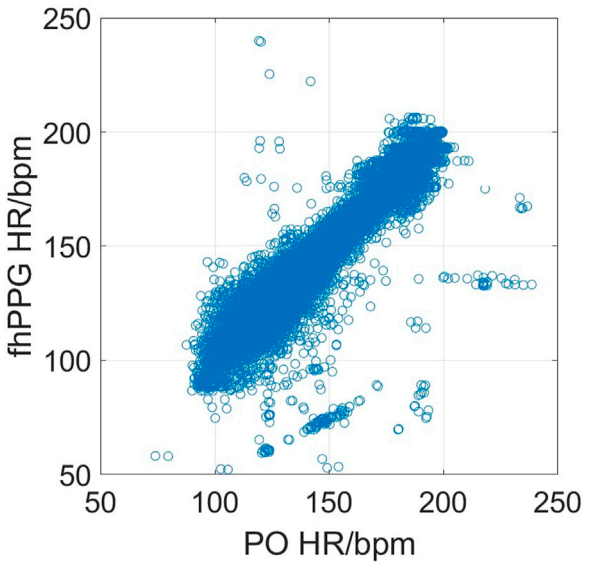

FIGURE 3
Scatter plot of heart rate between PO vs. fhPPG (n = 142,567) for 19 subjects.

TABLE 2 Accuracy results when separated into sub-cohorts of term and preterm infants. Spearman's correlation coefficient (ρ), bias and LOA are presented.

Cohort\Variable	N	ρ	Bias (bpm)	LOA (bpm)
Cohort	19	0.9816	−0.22	8.44
Term	11	0.9819	−0.17	6.99
Preterm	8	0.9750	−0.46	12.41

over 80% of the time. The high PPA, in combination with the strongly positive Spearman's correlation coefficient, suggests that the fhPPG is not only able to track changes in heart rate but also to do so accurately.

Previously, work has been undertaken to find the best location for a pulse oximeter. Longmore et al. found that if only heart rate and SpO_2 is required, then the forehead is the most suitable location with the smallest median error compared to a finger-based PPG sensor (Longmore et al., 2019). Furthermore, Peralta et al. (2017) showed that the forehead provided greater accuracy than the finger when detecting pulse rate variability, a derivative of the heart rate. However, along with most forehead PPG comparison studies, these tests were performed on adults. The previous work on reflection-mode monitoring in newborns compared ECG (Grubb et al., 2014; Henry et al., 2020) or PPG from a non-forehead site such as the thigh (Johansson et al., 1999).

Whilst the magnitude of the bias decreased from the previous trial (Henry et al., 2020) (−0.22 bpm vs. 0.6 bpm) there was an increase in the LOA (8.44 bpm vs. 5 bpm). The aim of this trial was to compare two optical based devices at different locations on the body, forehead and wrist, in critically unwell subjects. However, the use of a wrist-based PO is a limitation as comparison to the more accurate ECG heart rate as suggested by ISO 80601-2 (BS EN ISO 80601-2-61:2019) is recommended. ECG probes were placed on the subject in line with standard care practice, however ECG data for the whole dataset was unavailable for comparison. The previous analysis of accuracy statistics (RMSE and Bland-Altman) was conducted against ECG (Henry et al., 2020) and is a possible reason why the LOA has increased when compared with the previous data. Another potential reason for the increase in the LOA in preterm cohort is that the infants were on multiple vaso-active medications, such as adrenaline and ventilation modalities that could interfere with the PPG signal from either device. As these infants were much sicker than those previously studied (Henry et al., 2020), these data indicate that the fhPPG can still accurately monitor critically ill infants with only small reduction in accuracy.

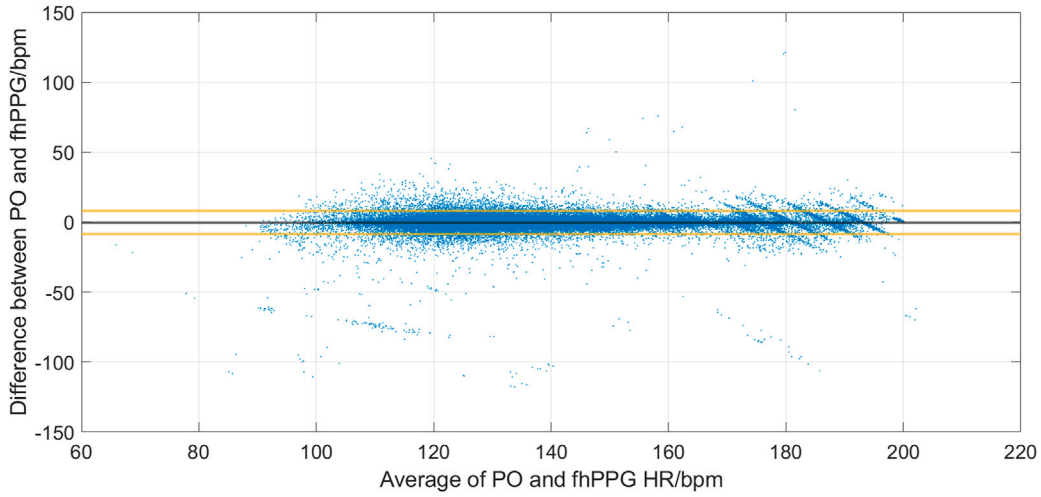

FIGURE 4
Bland-Altman analysis of PO and fhPPG (n = 142,567) for 19 subjects.

This study enrolled subjects of varying gestational age. Of the 19 subjects enrolled, 11 were term and eight preterm infants. For the preterm infants, there was an increase in the bias and LOA when compared with the term infants. The bias remained small, however the LOA increased by 5.42 bpm to 12.41 bpm. This is likely due to a variety of factors including the higher baseline heart rate of preterm infants, often increased further with caffeine treatment, and the differing pathologies between term and preterm infants, such as an underdeveloped respiratory and circulatory system. As a result, the ratio of the noise and motion artefacts compared to the measured PPG signal in newborns is larger compared to adults showing the importance of such a new medical device for paediatricians use and provides a benchmark for future improvements. The Spearman's correlation coefficient remained strongly positive however at 0.975, suggesting that the fhPPG was able to track the changes in heart rate but the fhPPG and PO disagreed on the value of the heart rate more so than in term infants. As discussed previously this could be due in part to errors in the PO as opposed to errors in the fhPPG heart rate, or a combination of errors in both devices.

5 Conclusion

The results presented demonstrate that the forehead is an equally suitable site for measuring reflectance mode PPG for heart rate compared to a peripheral transmission mode PO. The use of the forehead for monitoring PPG signals for heart rate provides benefits when compared with peripheral limbs. The forehead allows a measurement of the core blood supply which is less susceptible to decreases in perfusion during times of stress (Berkenbosch and Tobias, 2006). Additionally, it opens up the possibility to use the wrists or ankles for other interventions, such as cannulas. By coupling these advantages with the ability to wirelessly transmit data to a remote screen, forehead PPG also increases newborn accessibility allowing vital skin to skin parental bonding and easier clinical access to the infant. Further work investigating the effects of different therapies and drugs on neonates would help assess further the benefits of the forehead compared with the wrist for PPG monitoring.

Data availability statement

The datasets presented in this article are not readily available for public access as it will be further used for commercial purposes by Surepulse Medical Ltd. The data will be made publicly available at a future date, please contact the authors. Requests to access the datasets should be directed to Barrie Hayes-Gill, barrie.hayes-gill@nottingham.ac.uk.

Ethics statement

The studies involving human participants were reviewed and approved by East Midlands—Nottingham 1 Research Ethics Committee. Written informed consent to participate in this study was provided by the participants' legal guardian/next of kin. Reference number (20/EM/0034).

Author contributions

BH-G, SM, and DS contributed to the conception and design of the study. DS and TK enrolled the participants and collected the PO and fhPPG sensor data. SS contributed to MATLAB data analysis. SS, BH-G, and SM contributed to data interpretation. All authors revised the article and approved the final version to be published.

Funding

This work was funded by an EPSRC CASE Award EP/R513283/1, a Medical Research Council Confidence in Concept Grant CiC2018045, EPSRC IAA EP/K503800/1 and Surepulse Medical Ltd. for the loan of the fhPPG devices.

Acknowledgments

We are grateful for the support of the University of Nottingham and Nottingham University Hospitals Trust. Also, thank you to all the infants and their families for their participation in this study.

Conflict of interest

Simon John Stockwell is funded *via* the EPSRC and an associated CASE award from SurePulse Medical Ltd. T'ng Chang Kwok is funded by an MRC CiC grant with matched funding from SurePulse Medical Ltd. The following are University of Nottingham employees and shareholders in SurePulse Medical Ltd—Don Sharkey, Barrie Hayes-Gill, and Steve Morgan. Don Sharkey and Barrie Hayes-Gill are non-executive directors of SurePulse Medical Ltd.

Publisher's note

References

Allen, J., and Howell, K. (2014). Microvascular Imaging: Techniques and opportunities for clinical physiological measurements. *Physiol. Meas.* 35 (7), R91–R141. Available at:. doi:10.1088/0967-3334/35/7/r91

Berkenbosch, J. W., and Tobias, J. D. (2006). Comparison of a new forehead reflectance pulse oximeter sensor with a conventional digit sensor in pediatric patients. *Respir. Care* 51 (7), 726–731.

Bland, J. M., and Altman, D. G. (2007). Agreement between methods of measurement with multiple observations per individual. *J. Biopharm. Statistics* 17 (4), 571–582. Available at:. doi:10.1080/10543400701329422

Bonner, O., Beardsall, K., Crilly, N., and Lasenby, J. (2017). 'There were more wires than him': The potential for wireless patient monitoring in neonatal intensive care. *BMJ Innov.* 3 (1), 12–18. Available at:. doi:10.1136/bmjinnov-2016-000145

BS EN ISO 80601-2-61:2019 (2019). *Medical electrical equipment Part 2-61: Particular requirements for basic safety and essential performance of pulse oximeter equipment (ISO 80601-2-61:2017, Corrected version 2018-02)*.

Dilli, D., Soylu, H., and Tekin, N. (2019). Neonatal hemodynamics and management of hypotension in newborns. *Türk Pediatri Arşivi* 53 (1), 65–75. Available at:. doi:10.5152/turkpediatriars.2018.01801

Elgendi, M., Fletcher, R., Liang, Y., Howard, N., Lovell, N. H., Abbott, D., et al. (2019). The use of photoplethysmography for assessing hypertension. *NPJ Digit. Med.* 2 (1). Available at:. doi:10.1038/s41746-019-0136-7

Grubb, M. R., Carpenter, J., Crowe, J. A., Teoh, J., Marlow, N., Ward, C., et al. (2014). Forehead reflectance photoplethysmography to monitor heart rate: Preliminary results from neonatal patients. *Physiol. Meas.* 35 (5), 881–893. Available at:. doi:10.1088/0967-3334/35/5/881

Jubran, A. (2015). Pulse oximetry. *Crit Care.* 19 (1). doi:10.1186/s13054-015-0984-8

Henry, C., Shipley, L., Ward, C., Mirahmadi, S., Liu, C., Morgan, S., et al. (2020). Accurate neonatal heart rate monitoring using a new wireless, Cap Mounted device. *Acta Paediatr.* 110 (1), 72–78. Available at:. doi:10.1111/apa.15303

Johansson, A., Öberg, P. Å., and Sedin, G. (1999). Monitoring of heart and respiratory rates in newborn infants using a new photoplethysmographic technique. *J. Clin. Monit. Comput.* 15 (7/8), 461–467. Available at:. doi:10.1023/a:1009912831366

Khalid, S. G., Ali, S. M., Liu, H., Qurashi, A. G., and Ali, U. (2022). Photoplethysmography temporal marker-based machine learning classifier for anesthesia drug detection. *Med. Biol. Eng. Comput.* 60 (11), 3057–3068. Available at:. doi:10.1007/s11517-022-02658-1

Kluckow, M. (2018). The pathophysiology of low systemic blood flow in the preterm infant. *Front. Pediatr.* 6, 29. Available at:. doi:10.3389/fped.2018.00029

Longmore, S. K., Lui, G. Y., Naik, G., Breen, P. B., Jalaluddin, B., and Gargiulo, G. D. (2019). A comparison of reflective photoplethysmography for detection of heart rate, blood oxygen saturation, and respiration rate at various anatomical locations. *Sens.* 19 (08), 1874. doi:10.3390/s19081874

Liu, H., Allen, J., Khalid, S. G., Chen, F., and Zheng, D. (2021). Filtering-induced time shifts in photoplethysmography pulse features measured at different body sites: The importance of filter definition and standardization. *Physiol. Meas.* 42 (7), 074001. Available at:. doi:10.1088/1361-6579/ac0a34

Mejía-Mejía, E., Allen, J., Buddidha, K., El-Hajj, C., Kyriacou, P. A., and Charlton, P. H. (2022). *Photoplethysmography signal processing and synthesis.* London: Photoplethysmography, 69–146. Available at:. doi:10.1016/b978-0-12-823374-0.00015-3

Nilsson, L. M. (2013). Respiration signals from photoplethysmography. *Anesth. Analgesia* 117 (4), 859–865. doi:10.1213/ane.0b013e31828098b2

Park, J., Seok, H. S., Kim, S., and Shin, H. (2022). Photoplethysmogram analysis and applications: An integrative review. *Front. Physiology* 12, 808451. Available at:. doi:10.3389/fphys.2021.808451

Peralta, E., Lázaro, J., Gil, E., Bailón, R., and Marozas, V. (2017). "Robust pulse rate variability analysis from reflection and transmission photoplethysmographic signals," in *Computing in cardiology conference (CinC)*. [Preprint]. doi:10.22489/cinc.2017.205-286

Schallom, L., Sona, C., McSweeney, M., and Mazuski, J. (2007). Comparison of forehead and digit oximetry in surgical/trauma patients at risk for decreased peripheral perfusion. *Heart and Lung* 36 (3), 188–194. doi:10.1016/j.hrtlng.2006.07.007

Verstraete, E. H., Blot, K., Mehieu, L., Vogelaers, D., and Blot, S. (2015). Prediction models for neonatal health care–associated sepsis: A meta-analysis. *Pediatrics* 135 (4), e1002–e1014. Available at:. doi:10.1542/peds.2014-3226

Wyckoff, M. H., Wyllie, J., Aziz, K., de Almeida, M. F., Fabres, J., Fawke, J., et al. (2020). Neonatal life support: 2020 international consensus on cardiopulmonary resuscitation and emergency cardiovascular care science with treatment recommendations. *Circulation* 142 (16), S185–S221. Available at:. doi:10.1161/cir.0000000000000895

frontiers | Frontiers in Physiology

TYPE Original Research
PUBLISHED 01 June 2023
DOI 10.3389/fphys.2023.1127624

OPEN ACCESS

EDITED BY
John Allen,
Coventry University, United Kingdom

REVIEWED BY
Chenxi Yang,
Southeast University, China
V. N. Du Le,
The University of Alabama in Huntsville, United States

*CORRESPONDENCE
Sebastian Zaunseder,
sebastian.zaunseder@uni-a.de

RECEIVED 19 December 2022
ACCEPTED 15 May 2023
PUBLISHED 01 June 2023

CITATION
Fleischhauer V, Bruhn J, Rasche S and Zaunseder S (2023), Photoplethysmography upon cold stress—impact of measurement site and acquisition mode.
Front. Physiol. 14:1127624.
doi: 10.3389/fphys.2023.1127624

Photoplethysmography upon cold stress—impact of measurement site and acquisition mode

Vincent Fleischhauer[1], Jan Bruhn[1], Stefan Rasche[2] and Sebastian Zaunseder[1,3]*

[1]Laboratory for Advanced Measurements and Biomedical Data Analysis, Faculty of Information Technology, FH Dortmund, Dortmund, Germany, [2]Faculty of Medicine Carl Gustav Carus, TU Dresden, Dresden, Germany, [3]Professorship for Diagnostic Sensing, Faculty of Applied Computer Science, University Augsburg, Augsburg, Germany

Photoplethysmography (PPG) allows various statements about the physiological state. It supports multiple recording setups, i.e., application to various body sites and different acquisition modes, rendering the technique a versatile tool for various situations. Owing to anatomical, physiological and metrological factors, PPG signals differ with the actual setup. Research on such differences can deepen the understanding of prevailing physiological mechanisms and path the way towards improved or novel methods for PPG analysis. The presented work systematically investigates the impact of the cold pressor test (CPT), i.e., a painful stimulus, on the morphology of PPG signals considering different recording setups. Our investigation compares contact PPG recorded at the finger, contact PPG recorded at the earlobe and imaging PPG (iPPG), i.e., non-contact PPG, recorded at the face. The study bases on own experimental data from 39 healthy volunteers. We derived for each recording setup four common morphological PPG features from three intervals around CPT. For the same intervals, we derived blood pressure and heart rate as reference. To assess differences between the intervals, we used repeated measures ANOVA together with paired t-tests for each feature and we calculated Hedges' *g* to quantify effect sizes. Our analyses show a distinct impact of CPT. As expected, blood pressure shows a highly significant and persistent increase. Independently of the recording setup, all PPG features show significant changes upon CPT as well. However, there are marked differences between recording setups. Effect sizes generally differ with the finger PPG showing the strongest response. Moreover, one feature (pulse width at half amplitude) shows an inverse behavior in finger PPG and head PPG (earlobe PPG and iPPG). In addition, iPPG features behave partially different from contact PPG features as they tend to return to baseline values while contact PPG features remain altered. Our findings underline the importance of recording setup and physiological as well as metrological differences that relate to the setups. The actual setup must be considered in order to properly interpret features and use PPG. The existence of differences between recording setups and a deepened knowledge on such differences might open up novel diagnostic methods in the future.

KEYWORDS

imaging photoplethysmography (iPPG), cold pressor test (CPT), pulse wave analysis (PWA), blood pressure, photoplethysmography (PPG)

1 Introduction

Today, photoplethysmography (PPG) is an extremely popular metrological procedure. The technique supports multiple setups, i.e., it applies to various body sites and features different modes of application including finger clips, smart watches and non-contact approaches by cameras denoted as imaging photoplethysmography (iPPG). PPG signals and numerous features that can be derived from them carry wide information on the physiological state Almarshad et al. (2022); Elgendi (2012); Park et al. (2022). Recently, the usage of multiple PPG at a time, sometimes referred to as multisite PPG, has attracted attention as it even extends the possibilities for PPG based analyses Chan et al. (2019). There are, however, still limitations dealing with PPG. Such limitations relate to the origin of PPG signals, local peculiarities of signal acquisition, the interaction of multiple PPG signals, the behavior of features in dependency to influencing factors and features' interpretation. Research on such aspects can deepen the understanding of prevailing physiological mechanisms, help to optimize metrological equipment and pave the way for improved or novel methods for PPG analysis.

This contribution is dedicated to a deeper characterization of PPG considering different measurement sites and acquisition modes. Our comparison includes contact PPG recorded at the finger, contact PPG recorded at the earlobe and iPPG, i.e., non-contact PPG, recorded at the face. Recordings at the finger are the traditional setup and most common way of application. Earlobe PPG is used less frequently but also well known as it can feature advantages, e.g., with respect to motion artifacts. iPPG is a relatively novel approach, which has become extremely popular over the last years. iPPG uses cameras to record the skin. The technique exploits subtle variations in the intensity of reflected light, which varies with blood filling of superficial vessels. Multiple current reviews provide good overviews on the fundamentals and applications of iPPG Molinaro et al. (2022); Selvaraju et al. (2022); Shao et al. (2021); Zaunseder and Rasche (2022). According to them, the vast majority of available works in the field of iPPG direct at heart rate and heart rate variability. However, there is a growing interest on morphological analyses and iPPG usage beyond heart rate.

Within this contribution, we employ PPG in the aforementioned three setups and focus on morphological features during a cold pressor test (CPT), i.e., a painful stimulus. CPT is a common tool in research and carries potential for diagnostics as well. We hypothesize that PPG derived features undergo changes upon CPT in all recording setups but we would expect differences between them. The presented research is worthwhile from two points of view. On the one hand, a more detailed understanding on the behavior of PPG derived features from single PPG signals and research on the interaction between different PPG is highly beneficial as it might contribute to refine existing analysis approaches or develop novel ones Natarajan et al. (2022). Particularly with respect to iPPG, ongoing debates regarding iPPG's origin, a limited knowledge on influence factors and a reduced number of works dedicated to morphological analysis require basic research. On the other hand, further research on the CPT is beneficial as the physiological basics are not yet fully understood and standard values have to be established in order to develop strategies to integrate the CPT for diagnostic or prognostic purposes Lamotte et al. (2021).

The remainder of this work is structured as follows. **Section 2** provides the background on the CPT and contains the results of a literature review concerning PPG usage during CPT. In **section 3** we describe the used data, which originates from own multimodal experiments, the applied processing method and the statistics. **Section 4** and **section 5** provide results and discuss them.

2 Background on PPG during cold stress

2.1 Cold pressor test

Cold is known to elicit multiple physiological reactions. The CPT, i.e., the defined application of a cold stimulus, was firstly described for research purposes by Hines and Brown (1936); Lamotte et al. (2021). Since then, the CPT has become a widely used tool to study the cardiovascular system and autonomous nervous system, most often in terms of blood pressure as well as heart rate and its regulation Bali and Jaggi (2015); Mitchell et al. (2004); Mourot et al. (2009). The most common experimental CPT design requires immersing the hand into cold water. According to published works, water temperatures vary between 0°C and 7°C (even higher temperatures up to 20°C have been considered but then the perception is classified as cold sensation rather than as pain). Duration of immersion also varies, typically between 1 and 6 min while termination upon participant's request is always possible. Immersion generates cold pain triggering sympathetic activation and parasympathetic withdrawal. Sympathetic activation causes a pronounced peripheral vasoconstriction. Positive inotropic and chronotropic effects due to both, sympathetic activation and parasympathetic withdrawal, accompany the peripheral vasoconstriction. Consequently, CPT increases blood pressure and heart rate immediately after immersion. However, heart rate was shown to be affected to a lesser extent or even to decrease again shortly after a first increase. A potential explanation is the baroreceptor reflex. Increased blood pressure triggers the baroreceptors leading to parasympathetic activation and a reduction of heart rate.

As a result, CPT has been consistently shown to yield a rather persistent blood pressure increase during CPT execution. Heart rate, in turn, shows a more indifferent and individual pattern during CPT Bali and Jaggi (2015); Mitchell et al. (2004); Mourot et al. (2009).

2.2 PPG during CPT

As stated before, the CPT is a widely used experimental technique. Many works explored and summarized the effect of CPT on blood pressure and heart rate. PPG during CPT is common but most often it serves to capture heart rate and its variability. The morphological analysis of the photoplethysmographic waveform during CPT is less common. To reflect the current state of knowledge on CPT's effect on the photoplethysmographic waveform, we conducted a systematic literature review using pubmed. The review was done according to the Preferred Reporting Items for Systematic Reviews and Meta-Analyses (PRISMA). Our search considered articles that had the word "cold" and either the word

"PPG", "photoplethysmogra*", "oximet*" or "oxymet*" in their title or abstract. We considered original articles only (reviews were excluded). Further inclusion criteria were the use of finger and/or earlobe PPG and/or iPPG and the examination of features related to the shape of PPG signals (not only heart rate and heart rate variability). In addition, inclusion required that the cold stimulus of the CPT was not applied at the measurement site (cooling the measurement site introduces additional effects beside the effect of painful stimulus). The search was limited to studies that were conducted on or regarding human subjects. Additional exclusion criteria were the unavailability of full texts or articles written in languages other than English or German.

Figure 1 shows the PRISMA flow chart. The initial search resulted in 203 articles. 15 articles were excluded for non-fitting language. 188 works were then further reviewed to exclude works that we deemed unfitting based on titles, abstracts or full texts. After screening the results for unfitting titles we excluded 83 articles. Of the remaining 105 articles we excluded another 62 based on their abstracts. Four additional articles were excluded for missing/non-existent full texts. After review of the full texts of the remaining 39 articles, we excluded 29 of them and finally ended up with ten articles that matched our inclusion criteria. Common reasons to exclude articles during review were, for example, the lack of a CPT, cooling at the measurement site and lacking usage of the PPG waveform.

Table 1 summarizes details on the studies that were finally included. The considered works invoked seven to 33 subjects. Healthy subjects were always considered. Five works also included patients. The way cold stress was induced varied between studies. Besides immersion of the hand into water Awad et al. (2001b), Awad et al. (2006); Hamunen et al. (2012); Jaryal et al. (2009); Cooke et al. (1993); Kurki et al. (1990), finger immersion Suzuki et al. (1994), foot immersion Natarajan et al. (2022) and holding an ice bottle in the hand Lin et al. (2020) were described. Used temperatures to yield a cold response varied in a wide range up to 20°C Cooke et al. (1993). Some works also employed multiple temperatures to investigate the effect of the actual temperature Suzuki et al. (1994); Veluswamy et al. (2020). As PPG measurement site, fingers were most common. Regarding the used features, by far the most often used feature was the amplitude. Besides, features related to the slope and rise time are common. Other features, like areas and derivative features, have also been considered (particularly as some researchers invoked large feature sets Lin et al. (2020); Natarajan et al. (2022)) but are not that common.

The studies rather consistently describe a significant effect of CPT on the amplitude with very few exceptions (concerning the earlobe in PPG Awad et al. (2001b) and the finger in Kurki et al. (1990)). Most other features also show significant changes upon CPT. Changes exist (almost) independently of the actual way of stimulation though effect sizes increase with decreasing stimulus temperature. Only few works directly compare PPG from different sites. Awad et al. (2001b), Awad et al. (2006) describe a much more pronounced response within the finger PPG compared to earlobe PPG visible in multiple features including amplitude and area. Natarajan et al. (2022) make use of PPG features to estimate blood pressure. Dependent on the measurement site, different features can make a valuable contribution. Such a finding also hints at a non-uniform local behavior. With respect to pathology, available works indicate changes Kurki et al. (1990); Veluswamy et al. (2020); Jaryal et al. (2009); Cooke et al. (1993). There is, however, no uniform behavior but the effects caused by CPT can be less or more pronounced according to the specific disease.

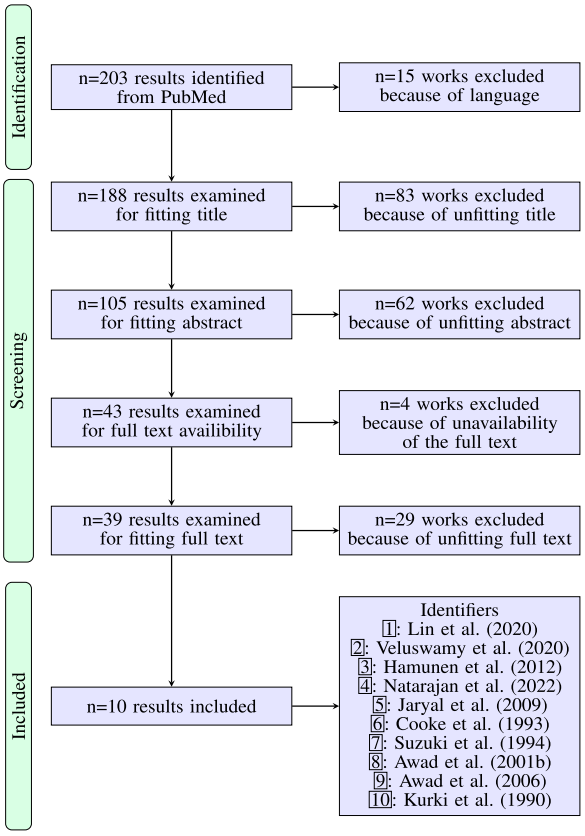

FIGURE 1
PRISMA flow diagram on the literature research regarding the effect of CPT on the waveform of the PPG. **Table 1** contains details for the included works.

3 Materials and methods

3.1 Data

Overview: The used data originates from own multimodal experiments invoking healthy volunteers of Caucasian origin. The whole experimental protocol contained different stimuli, namely, paced deep breathing (PDB), multiple orthostatic maneuvers and CPT. Throughout the experiment, we recorded multiple vital signs and videos. Below we detail the experimental procedure and the technical equipment. All subjects gave written consent. The study was approved by the Ethics Committee at TU Dresden (EK 311082018).

Procedure: **Figure 2** provides an overview on the whole experimental protocol and the part of it that was considered in this contribution. The experiment lasted approximately 49 min. During execution, the tilt-table was alternated between supine and upright position every 7 min defining seven phases. Between orthostatic maneuvers participants had resting epochs and executed CPT or

TABLE 1 Overview on the included works according to Figure 1 (IDs are given there). Column "population" provides details on the cohorts. Age is given in years as provided by the original references. Column "features" contains those features that originate from PPG and carry morphological information. Column "main findings" concern findings directly related to CPT. † "Indices" denote features that are combinations of amplitude and pulse interval. ‡ The study features two parts and invokes patients. As CPT only applies to healthy controls, we restrict the provided information to this part. Note that the population is probably the same as in [8] but other features were considered. RSD - reflex sympathetic dystrophy, RSI - repetitive strain injury, PWHA - pulse width at half amplitude.

Id	Population	Site(s)	Feature(s)	Main finding(s)
[1]	12 (2 f/10 m), healthy, 27.8 ± 5.4 (mean ± std)	finger	amplitudes, slopes, areas, intra-beat time intervals (65 features)	significant changes in almost all features but intra-beat time intervals
[2]	33 (13 f/20 m), sickle cell disease (17)/healthy controls (16), age ≥13	finger	amplitude	significant reduction in amplitude; effect more pronounced (faster, stronger) in sickle cell disease
[3]	29 (0 f/29 m), age 24(18–28) (mean (range)), healthy	finger	amplitude, PPG derived indices† (4 features)	significant changes in all features
[4]	32 (16 f/16 m), age 52 ± 17 (mean ± std), healthy (24)/hypertensive (8)	finger, earlobe, toe	amplitudes, derivative features, areas, time intervals (31 features)	parameters related to fast upstroke provide added value for blood pressure estimation
[5]	21 (9 f/12 m), diabetes mellitus (10)/healthy controls (11), age 47 ± 8 (mean ± std)	finger	amplitude, slope, crest time, decay time	amplitude and slope affected most by CPT (even after termination); reduced effects in patients
[6]	27 (18 f/9 m), RSD (6)/RSI (9)/healthy controls (12)/age 39.0/39.8/30.1 ± 11.7/13.6/8.6 (mean ± std per group)	finger	amplitude	amplitude change in disease less pronounced
[7]	7 (0 f/7 m), healthy, age: 23–29 (range)	finger	amplitude	significant amplitude reduction; strength related to water temperature
[8]	12 (0 f/12 m), healthy, age: 25–50 (range)	finger, earlobe	amplitude	70% reduction in finger amplitude (significant) and 10% reduction in earlobe amplitude (non-significant)
[9]	12 (0 f/12 m), healthy, age: 25–50 (range)	finger, earlobe	amplitude, area, upstroke slope, downstroke slope, PWHA	significant decrease in all finger PPG features; only significant change in earlobe PPG increase of PWHA
[10]	30 (28 f/2 m), Raynaud's phenomenon (15)/healthy controls (15), age 38.4(25–54)/55.0(38–71) (mean (range) per group)	finger	amplitude	decrease (non-significant) in controls and patients

10.3389/fphys.2023.1127624

PDB. Each participant executed at least one CPT (denoted as CPT1), which was randomly assigned to phase one or phase three. A random subset of participants executed another CPT (CPT2) in phase five. The presented investigation uses data from CPT1 (i.e., CPT2, tilting and PDB are not relevant for this contribution). CPT required participants to put their left hand into cold water (temperature was approximately 4°C, which should yield a strong effect according to the literature Suzuki et al. (1994); Veluswamy et al. (2020)). Immersion was intended for 60 s but participants could terminate before that time if they felt (too) uncomfortable. During immersion, participants stayed in supine position and tried to keep the position of their face and right arm as constant as possible. For the analysis, we defined the following three time intervals of 10 s in relation to the time of immersion t_{CPT}: baseline (BL), starting at $t_{CPT} - 30$ s, stimulation 1 (ST1), starting at $t_{CPT} + 20$ s and stimulation 2 (ST2), starting at $t_{CPT} + 40$ s. According to the preceding interval at rest, we assume BL to represent a stable state, which is interchangeable for phase one and phase three. For ST1 and ST2 we expect a notable effect of the pain stimulus. The time interval ST1 was chosen as we assumed the painful stimulus already having caused an effect. ST2 represents the latest possible interval to see if different recording setups diverge over the experiment. As subjects were told shortly before the end of CPT to be prepared for removing their hands, we avoided to use the last 10 s of the record. Note that we do not expect the reaction upon cold stress to be terminated at ST2. However, our investigation does not aim to explore the full temporal behavior upon cold stress but explores the immediate effect of a painful stimulus considering different measurement sites and acquisition modes. According to Hamunen et al. (2012) there seems to be a "saturation of unpleasantness" after approximately 60 s, which renders 60 s a suitable duration.

Equipment: The used equipment is depicted in **Figure 3**. Vital signs and RGB videos were continuously recorded throughout the whole experiment. We used two biosignal amplifiers Biopac MP36 (Biopac; Goleta, United States of America) and reflective photoplethysmographic signal transducer SS4LA (Biopac; Goleta, United States of America) to record (contact) PPG signals from right earlobe and right index finger at a sampling rate of 2000 Hz with an emitter/detector wavelength of 860 ± 60 nm (we also recorded PPG at right antecubital fossa and right shoulder area but they are not relevant to this contribution). In addition, we used the Finapres Nova (Finapres Medical Systems; Enschede, Netherlands) to record continuous non-invasive blood pressure and a single lead electrocardiogram (Einthoven II). Videos were recorded by three UI-3060CP-C-HR Rev 2 RGB cameras (IDS Imaging Development Systems GmbH; Obersulm, Germany). The cameras were mounted on the tilt table with fixed orientation regarding the subject during the experiment. For this work, solely camera 2 is of particular interest. This camera recorded the subject's head at a distance of approximately 40 cm. The recorded area covered the head and a small portion of the shoulders. Videos were captured at a color depth of 12 bit, a frame rate of 25 Hz and a spatial resolution of $1,280 \times 960$ pixel. All videos were stored in a proprietary format with lossless compression. The recordings took place in a controlled environment using indirect artificial illumination by two spotlights Walimex pro LED Sirius 160 Daylight 65 W (color temperature 5,600 K, color rendering index ≥90) (WALSER GmbH & Co. KG; Gersthofen, Germany). Inputs from cameras and Finapres were fed into the Biopac MP36 biosignal amplifiers for synchronization of modalities.

Used data: Overall, 61 recordings were carried out using the setting described above. We excluded 18 recordings which showed intermittent technical problems (early recordings partially suffered from a software issue, which could lead to missing data in at least one video or signal; we completely discarded such recordings for this analysis). We further excluded four recordings, which were stopped upon participant's request owing to malaise from tilting. Overall, we include 39 recordings in our analysis (13 female, 26 male; age: 30.5 ± 12.0 years; body height: 177 ± 7.83 cm; body weight: 76.5 ± 14.9 kg). As stated before, from each recording we only consider CPT1.

3.2 PPG processing

In general, we applied the same approach to process PPG and iPPG signals. However, iPPG processing first requires signal formation including region of interest (ROI) segmentation, ROI tracking and signal extraction. The further processing of all signals - contact and non-contact PPG signals - included filtering, beat detection, template construction and feature extraction by means of pulse wave decomposition (PWD) and using derivatives of the respective signals.

iPPG signal formation: To acquire iPPG signals from our videos, we manually defined polygons for the forehead as our ROIs in the first frame of the first interval (BL). We also defined ROIs for both cheeks and used the combination of all face ROIs as a "super" ROI to mimic common ROIs generated by automatic segmentation. For each of the following intervals ST1 and ST2, we shifted the ROIs to fit slightly changed body positions. The ROIs remained static for the duration of each interval. We spatially smoothed the videos with an averaging filter of 10 pixel width and then obtained iPPG signals by averaging all pixels inside the ROI. The signals were then inverted to resemble the conventional PPG and linear interpolated to a sampling rate of 2000 Hz in order to match the sampling rate of contact PPG. **Figure 4** shows an example of the defined ROIs.

Signal processing: We filtered the PPG and iPPG signals with a bandpass filter (fifth-order Butterworth filter with cut-off frequencies of 0.4 Hz and 8 Hz). Single beats from the PPG signals were detected with the method of Làzaro et al. (2014). The method considers the steepest ascent as the detection point t_i. Around each detection t_i we defined a beat segment in the interval $[t_i - 0.45 \cdot \widetilde{BBI}; t_i + \widetilde{BBI}]$, where $\widetilde{BBI}$ is the median length of beat-to-beat intervals (BBI) within the considered interval. All detected beat segments were correlated pairwise. We discarded beat segments with a mean pairwise correlation lower than 0.3. The remaining segments were ensemble averaged and potential linear trends were removed to form a beat template. **Figure 5** shows exemplary template generations. The median number of usable beats for template generation per measurement site was 10.

Feature extraction: We applied pulse wave decomposition and recomposition to each template for denoising. We used the GammaGaussian2 decomposition algorithm (i.e., decomposition by a Gamma kernel and a Gaussian kernel, see **Figure 6**) that was described previously Fleischhauer et al. (2020). A reconstructed

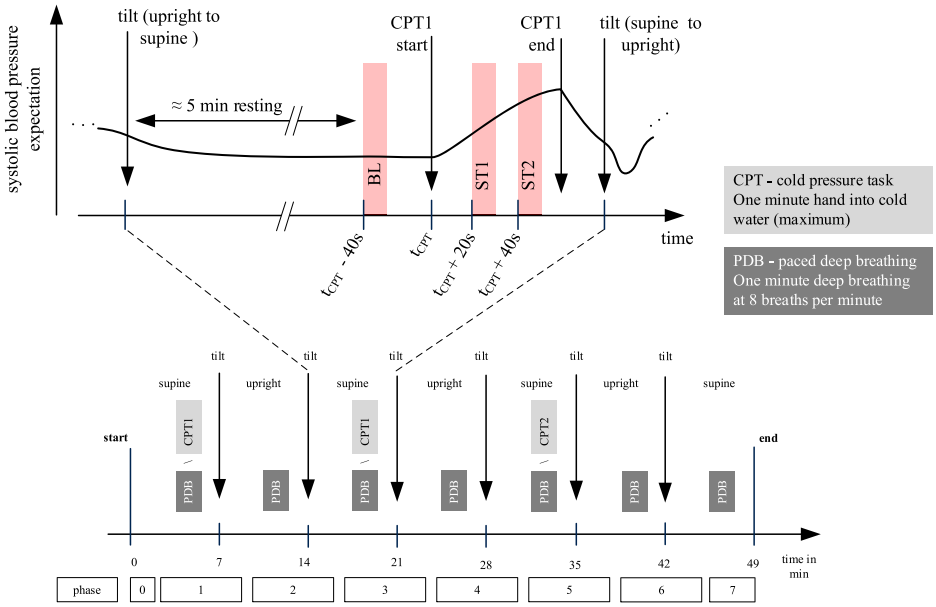

FIGURE 2
Overview on the whole experimental protocol (lower part) and CPT1 (upper part). This work uses data from CPT1 only, which was randomized executed in phase one or phase three. For each subject we define three time windows of 10 s: baseline (BL), stimulation 1 (ST1) and stimulation 2 (ST2). Independently of the CPT execution in phase one or phase three, there was a resting epoch for approximately 5 minutes before the CPT.

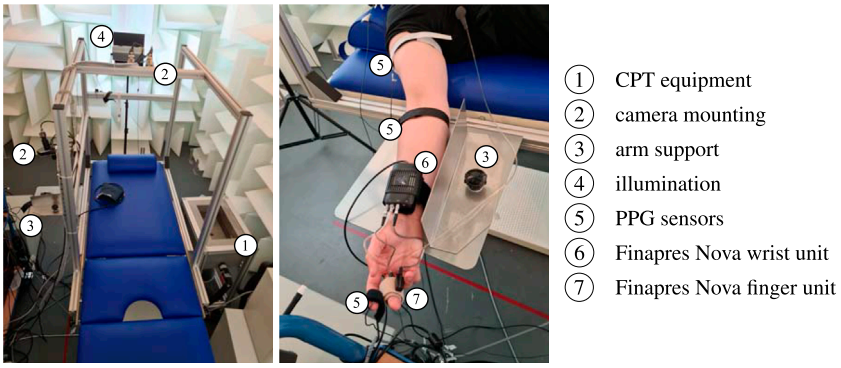

FIGURE 3
Illustration of the used equipment.

beat y for the Gamma-Gaussian algorithm with 2 kernels can be described as:

$$y_{\text{GammaGaussian2}}(t,\theta) = \frac{\beta_1^{\alpha_1}}{s_1 \cdot \Gamma(\alpha_1)} t^{\alpha_1 - 1} e^{-\beta_1 t} + a_2 \cdot e^{\left(\frac{-(t-\mu_2)^2}{2\sigma_2^2}\right)}. \quad (1)$$

Each reconstructed beat is a function of time t and an optimization vector $\theta = [a, \mu, \sigma]$. The interior point optimization algorithm fits the kernels to the template beat using the constraints $a_1 > a_2, \mu_1 < \mu_2$, i.e., the Gamma kernel has to occur before the Gaussian kernel and its amplitude has to be higher. The initial values for the algorithm are explained in detail in Fleischhauer et al. (2020). **Figure 6** displays the processing of the template beats. Considering the literature on PPG during CPT and common procedure in PPG processing, we selected four features for analysis: amplitude (maximum of the template), slope (maximum of the first derivative of the template), area (area under the template) and PWHA (pulse width at half amplitude). **Figure 6** illustrates the definition of these features.

3.3 Reference parameters

In addition to the PPG features under test, we considered blood pressure and heart rate as reference to verify if CPT yielded the expected effect. We used systolic blood pressure (SBP), diastolic blood pressure (DBP) and heart rate by Finapres Nova. The device yields values for such features for each single beat. From SBP and DBP we additionally derived pulse pressure (PP). For each interval

FIGURE 4
Exemplary ROI definition. Shown are three facial ROIs (forehead (blue polygon), right cheek (yellow polygon), left cheek (orange polygon)). To derive an iPPG signal we use the forehead ROI alone and all ROIs in combination as a "super" ROI.

(BL, ST1, ST2) we calculated one single value for each reference parameter by taking the median value of single beats' values in the respective interval.

3.4 Statistical assessment

To evaluate the effect of CPT, we firstly conducted repeated measures ANOVA for each recording setup and feature on a significance level of $\alpha = 0.05$ with no grouping of the subjects. For significant ANOVA results, we conducted paired t-tests as *post hoc* tests for all combinations of intervals (BL vs ST1, BL vs. ST2 and ST1 vs ST2). We tested each of these intervals against each other, thereby creating non-orthogonal contrasts. Thus, we used the Holm-Bonferroni correction to adjust the p values of our *post hoc* tests with the respective correction factor $(k - i + 1)$ (with k being the number of conducted tests and i the rank of the p values sorted in ascending order) Holm (1979). As a measure of effect size we calculated Hedges' g Hedges (1981).

$$g = J(\mathrm{df}) \cdot \frac{\bar{x} - \bar{y}}{s} \tag{2}$$

$$s = \sqrt{\frac{(n_x - 1)s_x^2 + (n_y - 1)s_y^2}{n_x + n_y - 2}} \tag{3}$$

$$J(\mathrm{df}) = \frac{\Gamma(\mathrm{df}/2)}{\sqrt{\mathrm{df}/2}\,\Gamma((\mathrm{df} - 1)/2)} \tag{4}$$

$$\mathrm{df} = n_x + n_y - 2 \tag{5}$$

Hedges g is a modification of Cohens d. It is defined as the difference of the means ($\bar{x}$ and $\bar{y}$) of two groups of sizes n_x and n_y divided by their pooled empirical standard deviation s. The biased estimator is corrected by the factor J (df) that depends on the degrees of freedom df. Effect sizes $g < 0.5$ are considered small, while $g > 0.8$ is considered large Cohen (1988). For visualization purposes, we normalized all response variables, i.e., the PPG features, to the mean of the three intervals for the respective response variable. The same statistical procedure applies to the reference parameters SBP, DPB, PP and heart rate but we omitted normalization as absolute numbers are relevant there.

4 Results

Figure 5 shows templates of one subject from all recording setups and time intervals as example. An overview on templates of all subjects is provided in the **Supplementary Material**. PPG quality should be mentioned here. While iPPG is known for limited signal quality, contact PPG was expected to be of high quality. However, in some cases, even contact PPG showed unstable beat shapes and distortions (e.g., see **Figure 9**). We excluded three subjects as no beat template could be generated in at least one of the analysis intervals. Another subject was excluded because of missing reference data. Those subjects were completely excluded from all analyses. Accordingly, the following results and statistical assessment base on data of 35 subjects.

Figure 7 depicts the behavior of reference parameters (SBP, DBP, PP, heart rate) for all analysis intervals. For better visibility, we omitted outliers in those plots (values are defined as outliers if they are greater than $q_3 + 1.5 \cdot \mathrm{IQR}$ or less than $q_1 - 1.5 \cdot \mathrm{IQR}$, where q_1 is the first quartile, q_3 is the third quartile and IQR is the interquartile range). **Table 2** shows the corresponding number of outliers. Repeated measures ANOVA yielded outcomes of $p < 0.001$ for all reference features. SBP and DBP, both exhibit highly significant ($p < 0.001$) differences in pairwise comparisons of analysis intervals. PP shows a highly significantly increase in ST2 compared to BL and ST1 ($p < 0.001$). There is also a statistically significant increase from BL to ST1 ($p < 0.05$). Heart rate increases significantly between BL and ST1 ($p < 0.001$) and BL and ST2 ($p < 0.01$).

Figure 8 depicts the behavior of PPG features over all analysis intervals for all recording setups. Again, for better visibility, we omitted outliers in those plots. **Table 2** shows the corresponding number of outliers. The repeated measures ANOVA yielded highly significant differences ($p < 0.001$) for all features of all measurement sites and recording setups except the slope of both iPPG measurements. There, the difference was significant with $p < 0.01$.

In all measurement sites, the amplitude shows a statistically significant decrease from BL to ST1. For both contact PPG, the significant decrease can also be observed between BL and ST2. However, this behavior is not found for the iPPG measurements. There, the amplitude exhibits a significant increase between ST1 and ST2 and no significant difference between BL and ST2. The slope also decreases significantly during BL and ST1 on all measurement sites and recording setups. Only in the earlobe PPG a significant decrease between ST1 and ST2 can be observed. The area behaves similarly to the amplitude, though ST2 is significantly lower than BL for both iPPG measurements. Both iPPG and the earlobe PPG show a significant decrease in PWHA from BL to both ST1 and ST2. The finger PPG significantly increases over time.

Tables 3, **4** show the effect sizes of the reference and PPG features over the analysis intervals. We found small to medium increases

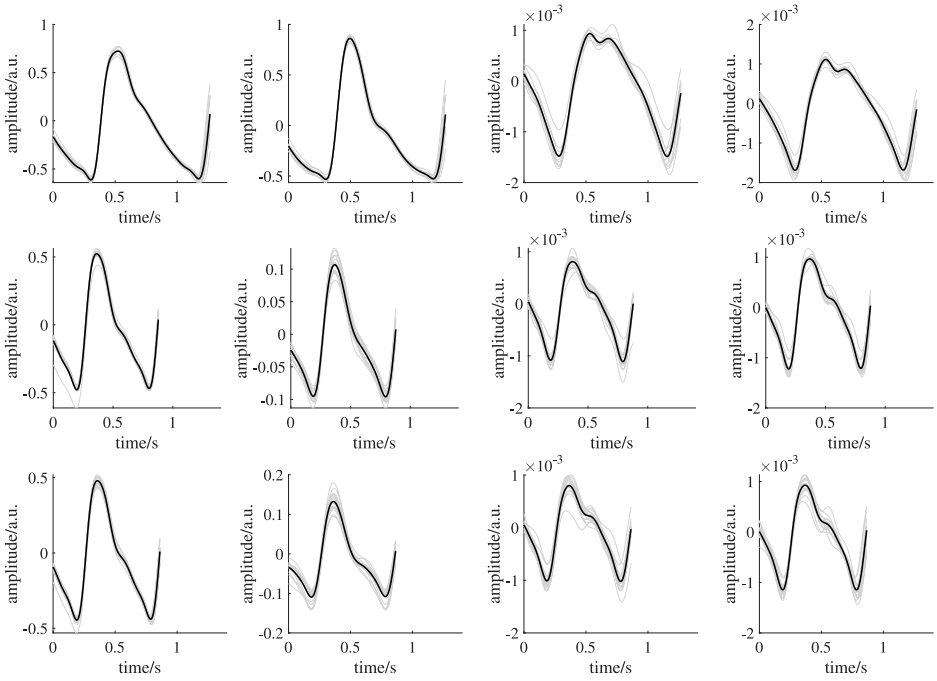

FIGURE 5
Exemplary template generation of one subject. From left to right: earlobe PPG, finger PPG, forehead iPPG, super ROI iPPG. The upper row shows signals during BL. The middle row shows signals during ST1. The lower row shows signals during ST2. Black lines indicate mean beat templates; gray lines indicate the corresponding beat segments.

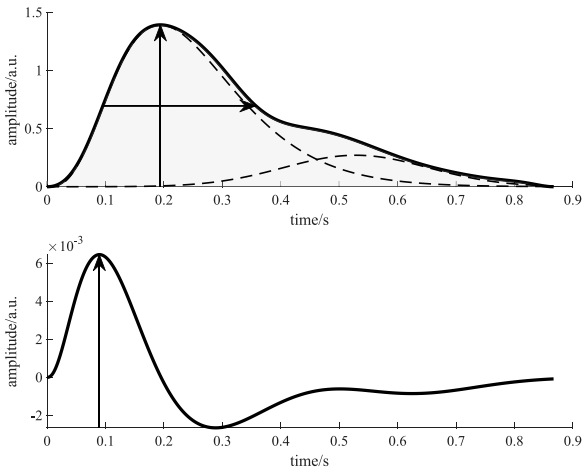

FIGURE 6
Visualization of the features derived from a beat template. The upper figure shows the beat template (solid black line) and the kernels (dashed black lines). The vertical arrow indicates the feature amplitude, while the horizontal arrow shows the feature PWHA. The light gray area marks the feature area. The lower figure shows the first derivative of the recomposed template beat (solid black line). The vertical arrow indicates the maximum of the first derivative, i.e., the feature slope.

for the heart rate and PP and medium to large increases for SBP and DBP. Notably, our analysis indicates large effect sizes in finger PPG for all features except PWHA, which exhibits small to medium increases between all intervals. For all other PPG measurements, the effect sizes are small.

5 Discussion

5.1 Main findings

General response to CPT: In general, the found behavior upon cold stress in our data matches the physiological expectation very well. Immediately after immersion, i.e., at ST1, there is a pain related increase in blood pressure and heart rate. In ST2, both, blood pressure and heart rate, remain increased but heart rate behaves less deterministic (which manifests in an increased standard deviation at ST2, see **Figure 7**). Our observations qualitatively and quantitatively comply to earlier studies. With respect to blood pressure, e.g., Mourot et al. report SBP increases of 14.5 and 18.1 mmHg Mourot et al. (2009), Lin et al. report 14 mmHg Lin et al. (2020), Saab et al. report 14.5 mmHg and Jauregui-Renaud et al. report 11.4 mmHg Jauregui-Renaud et al. (2001). With respect to heart rate, a more indifferent behavior or minor effects were previously reported, e.g., by Mourot et al. (2009) and Lin et al. (2020).

Contact PPG analysis: Our results regarding different PPG features from finger and earlobe PPG are mostly consistent with previous results as derived from our literature review. This concerns, first of all, the amplitude, which undergoes a fundamental decrease upon CPT. Slope and area also decay in finger PPG and earlobe PPG. These features show much more pronounced effects at the finger

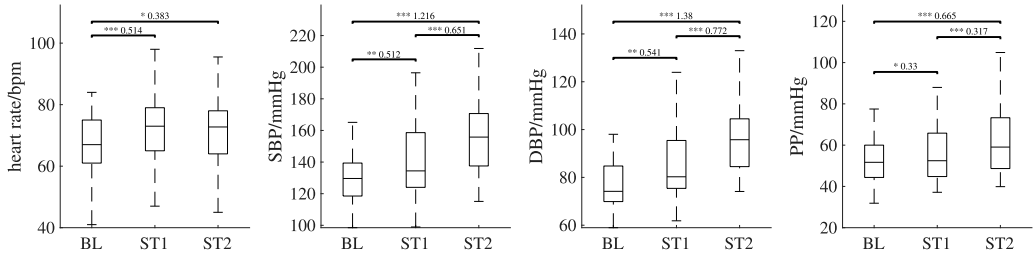

FIGURE 7
Behavior of the reference features (heart rate, systolic blood pressure (SBP), diastolic blood pressure (DBP) and pulse pressure (PP)) over all analysis intervals. If significant, *post hoc* tests' outcome is denoted by * ($p < 0.05$), ** ($p < 0.01$) or *** ($p < 0.001$). The numbers above the lines indicate effect sizes and are provided for significant *post hoc* tests only. Outliers are not shown; the numbers of outliers are provided in **Table 2**.

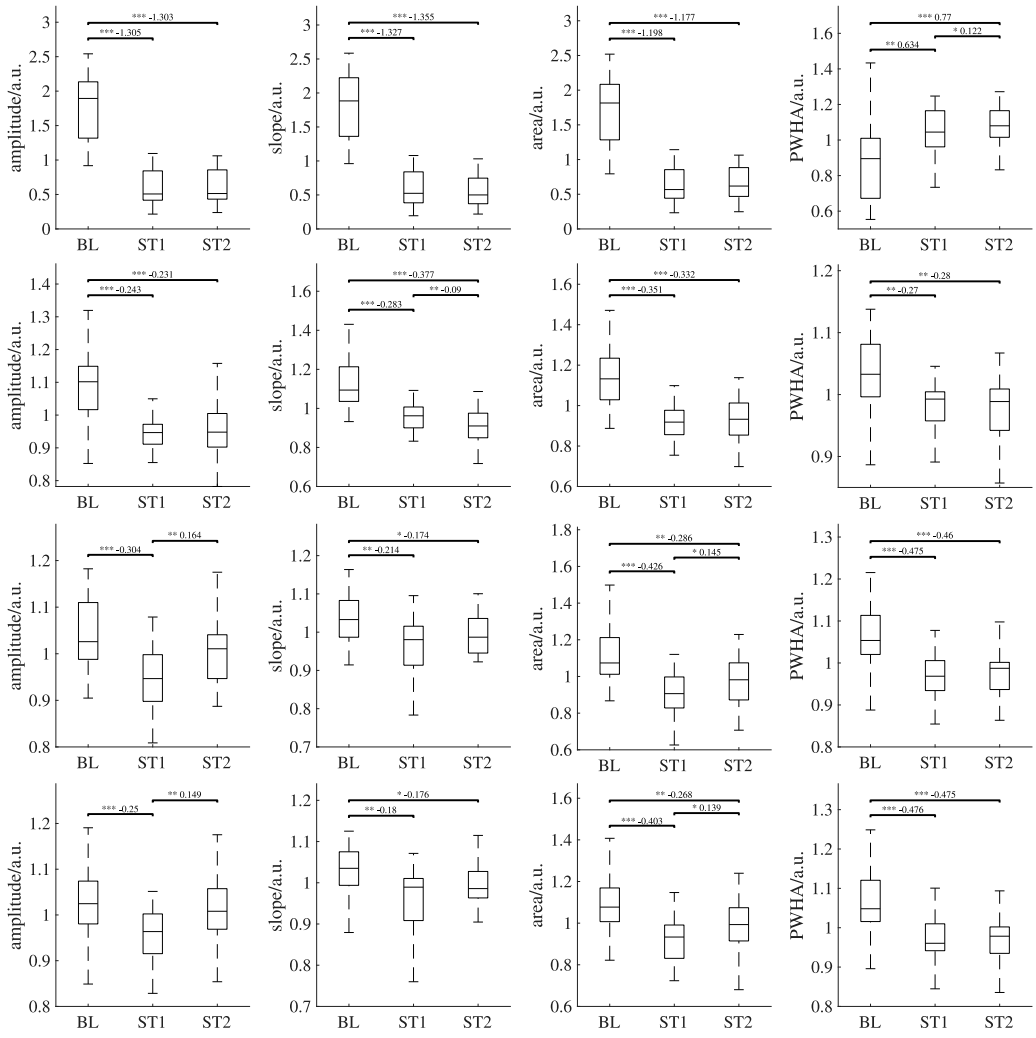

FIGURE 8
Behavior of the features derived from PPG and iPPG (amplitude, slope, area, PWHA) over all analysis intervals. First row: PPG (finger), second row: PPG (earlobe), third row: iPPG (forehead), fourth row: iPPG (super). If significant, *post hoc* tests' outcome is denoted by * ($p < 0.05$), ** ($p < 0.01$) or *** ($p < 0.001$). The numbers above the lines indicate effect sizes and are provided for significant *post hoc* tests only. Outliers are not shown; the numbers of outliers are provided in **Table 2**.

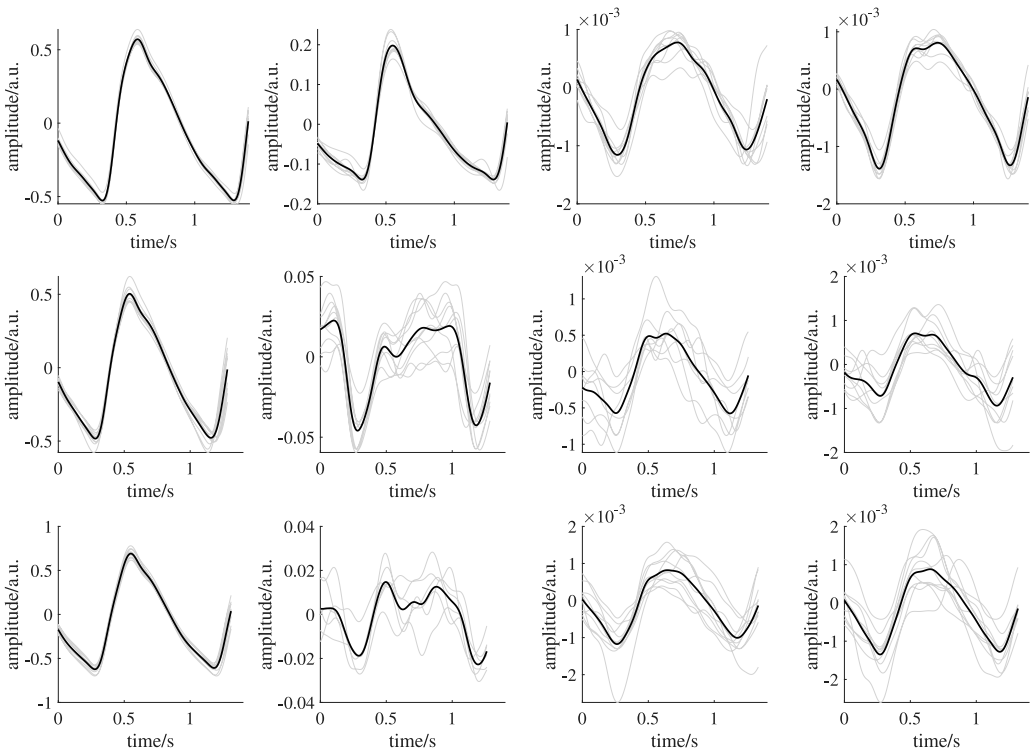

FIGURE 9
Exemplary template generation of one subject showing reduced quality templates. From left to right: earlobe PPG, finger PPG, forehead iPPG, super ROI iPPG. The upper row shows signals during BL. The middle row shows signals during ST1. The lower row shows signals during ST2. Black lines indicate mean beat templates; gray lines indicate the corresponding beat segments. The overall mean pairwise correlation of the beat segments forming the template for the finger PPG, forehead iPPG and super iPPG during ST1 and ST2 is reduced compared to those in **Figure 5**. Reduced quality templates lack distinct features (e.g., completely missing dicrotic notch in forehead iPPG during ST2, overall mean pairwise correlation: 0.71; corresponding overall mean pairwise correlation in **Figure 5**: 0.96) or exhibit unexpected morphologies (e.g., finger PPG during ST2, overall mean pairwise correlation: 0.64; corresponding overall mean pairwise correlation in **Figure 5**: 0.99) due to low correlation of the beat segments forming a template.

than at the earlobe. Such effects of CPT to PPG signals in general and to the considered features in particular was expected. Even local differences were expected. Though only a few studies investigated local differences upon CPT Awad et al. (2001b), Awad et al. (2006), a couple of works describe the variability of PPG features to be dependent on the measurement site indicating local differences Allen and Murray (2000); Bentham et al. (2018); Hernando et al. (2019). The found local behavior, i.e., stronger effects at the finger, reflects the high innervation of the finger vascular bed by α-adrenoceptors and a related responsiveness to sympathetic activation. Blood vessels at the earlobe should be affected by sympathetic activation as well, but to a lesser extend (a decreasing amplitude despite an increasing PP hints at a vascular response at the earlobe as well). The fourth feature, PWHA, turned out to be special. We therefore discuss PWHA in a separate paragraph below.

iPPG analysis: Our results reveal significant differences of morphological features as a response to cold stress. The behavior of the considered ROIs is thereby highly correlated. This is due to the fact that both ROIs include the forehead and forehead as well as cheeks are known to be suitable for signal extraction Lempe et al. (2013). A close look to the quantitative results suggests slightly stronger effects for the forehead ROI. This is reasonable as slightly deviating behavior of forehead and cheeks would introduce some blurring of effects. However, as the results are very similar, the following discussion does not differentiate between such ROIs.

The close relation of iPPG features to earlobe PPG underline the possibility to use iPPG for monitoring purposes beyond heart rate. Though the vast majority of available works on the iPPG focuses on heart rate, a growing number of works invokes morphological analyses. Djeldjli et al. recently presented a comparison of finger and earlobe PPG as well as iPPG Djeldjli et al. (2021). The work analyses several features including amplitude, area and PWHA during normal breathing intervals and during breath hold intervals. As in our study, their results show high correlations between earlobe PPG and iPPG during breath hold intervals for amplitude, area and PWHA[1]. Other related works do not compare iPPG directly to contact PPG but investigate the suitability of morphological features with respect to blood pressure estimation. E.g., Ding et al. showed PWHA to decay with blood pressure Ding et al. (2021). Rong and Li (2021) and Jain et al. (2016) used multiple morphological features to estimate blood pressure. Though not all such works allow statements on the specific behavior of single features, they emphasize the feasibility of morphological iPPG analysis. With

1 Note that normal breathing intervals in Djeldjli et al. (2021) partially suffered from lacking feature variability; as correlation in such cases is misleading, our statements here only relate to results for breath hold intervals.

TABLE 2 Number of outliers not shown in boxplots for reference parameters and PPG features.

Feature	Measurement	BL	ST1	ST2
heart rate	*References*	1	2	3
SBP	*taken from*	1	1	1
DBP	*Finapres*	1	1	1
PP	*Nova*	1	1	1
amplitude	PPG finger	1	1	1
amplitude	PPG earlobe	2	2	1
amplitude	iPPG forehead	2	1	2
amplitude	iPPG super	2	1	1
slope	PPG finger	1	1	1
slope	PPG earlobe	2	2	1
slope	iPPG forehead	2	1	3
slope	iPPG super	3	1	2
area	PPG finger	1	1	1
area	PPG earlobe	1	1	1
area	iPPG forehead	1	1	1
area	iPPG super	2	1	1
PWHA	PPG finger	1	1	1
PWHA	PPG earlobe	2	5	1
PWHA	iPPG forehead	2	1	2
PWHA	iPPG super	1	1	1

TABLE 3 Effect sizes for reference features. Reported are mean effect sizes and their respective confidence interval borders (confidence level of 0.95) in brackets. Effect sizes for non-significant differences are colored grey.

Feature	BL to ST1	BL to ST2	ST1 to ST2
heart rate	0.52[0.03, 1.00]	0.39[−0.09, 0.87]	−0.11[−0.59, 0.37]
SBP	0.53[0.04, 1.02]	1.23[0.71, 1.75]	0.65[0.16, 1.14]
DBP	0.54[0.05, 1.02]	1.38[0.84, 1.90]	0.77[0.27, 1.26]
PP	0.36[−0.12, 0.84]	0.69[0.20, 1.18]	0.32[−0.17, 0.79]

respect to the competing theories on the origin of iPPG - the volumetric model as in contact PPG Moço et al. (2018) *versus* an elastic deformation model Kamshilin et al. (2015) - iPPG's close relation to earlobe PPG in our study as well as the results of related works can be understood as strong hints that signal formation in iPPG corresponds to the volumetric model rather than to tissue compression.

Even if the global behavior of iPPG highly resembles earlobe PPG, it is worth taking a closer look because one can observe differences, which have been rarely discussed before. While features of contact PPG remain reduced at ST2, iPPG shows already an increase. The finding is not that striking as inversion in PWHA (see below), but we observed a similar effect in a different group before Fleischhauer et al. (2019). As in Fleischhauer et al. (2019), the early return to higher amplitudes after CPT in iPPG suggests that iPPG signals are driven by systemic hemodynamics and only to a lesser extent dependent on local vascular effects. Such behavior is reasonable as iPPG signals should be strongly affected by very superficial vessels. Local vasoactive vessels, in turn, contribute less to the signal formation in facial iPPG, at least as it concerns the green channel. Systematic differences between PPG and iPPG as we describe have rarely been addressed before. E.g., Djeldjli et al. (2021) rely on the premise that iPPG should resemble contact PPG. In deep learning approaches, the contact PPG can serve as target function to train deep networks to extract signals from videos Ni et al. (2021). Said premise and the usage for training are certainly valid under a "global view" but they may discard specific information available *via* iPPG. The specific behavior of iPPG renders deepened investigations and combined analyses with contact PPG to exploit their interactions for diagnostic purposes very interesting.

PWHA: PWHA deserves particular attention as it shows an inverse behavior between recording setups in our experiment. While PPG signals from earlobe and face show a significant decrease, finger PPG shows a significant increase in our data. PWHA is commonly related to systemic vascular resistance (SVR) Awad et al. (2007); Park et al. (2022). Marked differences in dependency to the measurement site are thus not intuitive and need detailed consideration.

Table 5 overviews previous works that invoked PWHA. Our results regarding face and earlobe PPG are in line with Ding et al., who recently reported a negative correlation of PWHA from facial iPPG and blood pressure Ding et al. (2021). Awad et al. report differences in PWHA from finger and earlobe in patients undergoing coronary artery bypass grafting Awad et al. (2001a). In contrast to our analysis, however, Awad et al. find PWHA of the earlobe PPG to be positively correlated with SBP while PWHA of the finger PPG exhibits a negative correlation. Even different from our results, Teng and Zhang (2003) describe a negative correlation between PWHA from finger PPG and SBP. Awad et al. also examined morphologic changes of finger and earlobe PPG during CPT for a healthy cohort Awad et al. (2006). They found PWHA to increase significantly during CPT for earlobe PPG and to decrease for finger PPG. Notably, none of the other features (amplitude, area, slope, downslope) of the earlobe PPG changed significantly during immersion. In contrast, the CPT significantly impacted all finger PPG features. Awad et al. explain this behavior with the blood relocating from the finger to other less vasoconstricted sites. The increased blood volume and the assumption of already maximally dilated vessels of the earlobe lead to the increase of PWHA. Again, such observations contradict our findings. An interesting detail that might explain differences in PWHA compared to our work relates to the collective's physiological response to CPT. While blood pressure increased as in our data, pulse rate decreased in Awad et al. (2006). This might be an expression of the indifferent heart rate behavior Mourot et al. (2009) and will obviously impact PWHA. Revision of further literature shows PWHA generally to be controversial. E.g.,; Lin et al. (2020) do not find a significant change in PWHA from finger PPG on cold stress at all; Hickey et al. (2016); Abdullah et al. (2022), both conducted similar studies that invoked arm lowering and elevation. While Hickey et al. describe a significant decrease with lowering and a mild (non-significant) increase with elevation, Abdullah et al. (2022) show a significant decrease with elevation and no effect upon lowering (see **Figure 2** in Abdullah et al. (2022)). Lastly, even in

TABLE 4 Effect sizes for PPG features. Reported are mean effect sizes and their respective confidence interval borders (confidence level of 0.95) in brackets. Effect sizes for non-significant differences are colored grey.

Feature	Measurement	BL to ST1	BL to ST2	ST1 to ST2
amplitude	PPG finger	−1.30[−1.81, −0.79]	−1.30[−1.81, −0.79]	0.00[−0.46, 0.47]
amplitude	PPG earlobe	−0.24[−0.71, 0.22]	−0.23[−0.69, 0.24]	0.01[−0.45, 0.47]
amplitude	iPPG forehead	−0.30[−0.77, 0.16]	−0.14[−0.61, 0.32]	0.16[−0.30, 0.63]
amplitude	iPPG super	−0.25[−0.71, 0.22]	−0.11[−0.57, 0.36]	0.15[−0.32, 0.61]
slope	PPG finger	−1.33[−1.84, −0.81]	−1.36[−1.87, −0.84]	−0.10[−0.57, 0.36]
slope	PPG earlobe	−0.28[−0.75, 0.18]	−0.38[−0.84, 0.09]	−0.09[−0.55, 0.37]
slope	iPPG forehead	−0.21[−0.68, 0.25]	−0.17[−0.64, 0.29]	0.05[−0.41, 0.51]
slope	iPPG super	−0.18[−0.64, 0.28]	−0.18[−0.64, 0.29]	0.02[−0.45, 0.48]
area	PPG finger	−1.20[−1.70, −0.69]	−1.18[−1.68, −0.67]	0.05[−0.41, 0.52]
area	PPG earlobe	−0.35[−0.82, 0.12]	−0.33[−0.80, 0.14]	0.01[−0.45, 0.48]
area	iPPG forehead	−0.43[−0.89, 0.04]	−0.29[−0.75, 0.18]	0.14[−0.32, 0.61]
area	iPPG super	−0.40[−0.87, 0.07]	−0.27[−0.73, 0.20]	0.14[−0.33, 0.60]
PWHA	PPG finger	0.63[0.16, 1.11]	0.77[0.29, 1.25]	0.12[−0.34, 0.59]
PWHA	PPG earlobe	−0.27[−0.73, 0.20]	−0.28[−0.74, 0.19]	−0.00[−0.47, 0.46]
PWHA	iPPG forehead	−0.47[−0.94, −0.00]	−0.46[−0.93, 0.01]	0.02[−0.45, 0.48]
PWHA	iPPG super	−0.48[−0.94, −0.00]	−0.48[−0.94, −0.00]	0.00[−0.46, 0.47]

Djeldjli's work Djeldjli et al. (2021) PWHA stands out. Compared to all other temporal features, PWHA yields a clearly reduced correlation between finger and earlobe PPG during breath hold intervals.

To conclude, the literature on PWHA is not consistent. We thus cannot regard our own results as either plausible or implausible in face of the literature. We tried to rule out problems related to the processing by going through all templates and did not find abnormalities. As stated before, signal quality can cause problems (e.g., see **Figure 9** for an example of low-quality template generation in finger PPG) but is not likely to behave systematically and cause the found inverse effect. Even the existence of a diastolic wave might cause misleading results. Depending on whether it is more or less pronounced, half amplitude could be reached before or after it. But again, a systematic effect as it would be needed to cause our results is not likely. We thus believe that the found behavior reflects a physiological effect in our cohort. Our hypothesis to explain such behavior is as follows. Assuming that the recorded finger PPG integrates contributions of larger vessels, which are less affected by vasoconstriction, a strong increase in arterial vessels downstream to the measurement site could explain an increase in PWHA. Local vasoconstriction in the facial region is less pronounced. The systemically increased blood pressure could lead to higher arterial volumes and vessel tension during systole, which favor the outflow and cause inverse effects on PWHA, i.e., a reduction. The common opinion that PWHA relates to SVR thus might not be generally valid but local factors might have a strong influence. Notably, this finding might have relevance beyond PWHA. If our hypothesis is true, other PPG based features are likely to be similarly affected by local factors but this assumption needs deepened investigations. One approach to deepen the understanding could make use of simulations. Recently, models and simulations of light-tissue interactions in the context of PPG have gained immense interest. Most of these works use Monte Carlo simulations to analyze the impact of contributing factors to the PPG morphology (e.g., sensor geometry Chatterjee and Kyriacou (2019), obesity Ajmal et al. (2021); Boonya-ananta et al. (2021) and skin tone Ajmal et al. (2021)). The used models allow for the simulation of pulsating blood to varying degrees, but they do not incorporate details on interlinked changes of systemic and local hemodynamics (i.e., blood pressure and local vessel properties). While the existing models thus serve to prove some of our experimental findings (e.g., as the lowered quality of red channel Ajmal et al. (2021)), further extensions are required to simulate the behavior of complex parameters like PWHA under varying systemic and local conditions.

5.2 Limitations

Our investigation has some limitations, which we discuss in this section.

First, we have decided to restrict our PPG analyses to finger PPG and earlobe PPG. iPPG analyses were restricted to the green channel and to two ROIs (the forehead and a combination of forehead and cheeks). Our selection was kind of obvious, as finger and earlobe are common choices in PPG. For iPPG, the green channel as a single channel Verkruysse et al. (2008) and the forehead as well as the cheeks Lempe et al. (2013); Kim et al. (2021) are known to yield good results. However, the experimental setup features much more possibilities. Particularly with respect to iPPG,

TABLE 5 Details on selected studies that used PWHA. †More subjects were invoked in another part of the study. ‡The correlation holds if wavelet processing was included. CO - cardiac output.

Reference	Population/experiment	Site	Main finding
Awad et al. (2007)	14, coronary artery bypass grafting	finger	correlation to SVR 0.56
		earlobe	correlation to SVR 0.62
Awad et al. (2006)	12, healthy, reaction upon CPT	finger	significant decrease upon CPT
		earlobe	significant increase upon CPT
	12, coronary artery bypass grafting	earlobe	inverse correlation to CO (−0.761)
Awad et al. (2001a)	10†, coronary artery bypass grafting	finger	negative correlation to SBP (−0.1)
		earlobe	correlation to SBP (0.8)
Teng and Zhang (2003)	15, healthy, reaction upon activity	finger	negative correlation to SBP (−0.732†)
Ding et al. (2021)	12, healthy, deep breathing/exercise	face (iPPG)	negative correlation to SBP (< − 0.7 for 80{%} of subjects)
Lin et al. (2020)	12, reaction upon CPT	finger	no significant change
Hickey et al. (2016)	20, healthy, arm lowering/elevation	finger	significant decrease with lowering
Abdullah et al. (2022)	15, healthy, arm lowering/elevation	finger	significant decrease with elevation

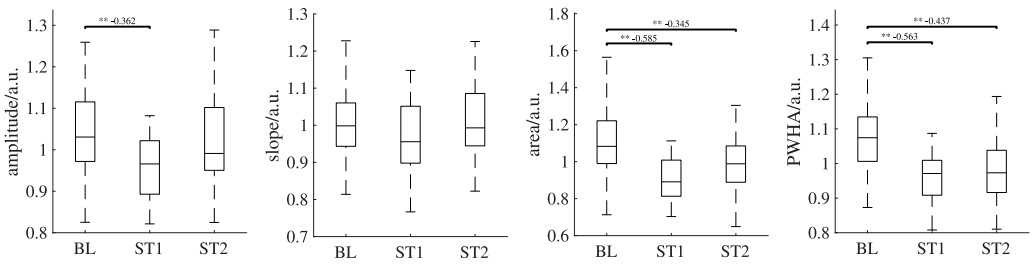

FIGURE 10
Behavior of iPPG features of the forehead using the red channel over all analysis intervals. If significant, *post hoc* tests' outcome is denoted by * ($p < 0.05$), ** ($p < 0.01$) or *** ($p < 0.001$). The numbers above the lines indicate effect sizes and are provided for significant *post hoc* tests only. Outliers are not shown.

alternating ROI definitions including additional constraints, e.g., regarding homogeneity as in Woyczyk et al. (2021), other color spaces Ernst et al. (2021) and combinations of color channels like POS Wang et al. (2017) and CHROM de Haan and Jeanne (2013) are possible and might add valuable insights. We experimentally did some first tests on the red channel. The higher wavelength allows for a deeper penetration offering the potential for further considerations on prevailing physiological mechanisms. **Figure 10** shows the result. According to the expectation from previous works and simulations Ajmal et al. (2021), the red channel generally has reduced signal quality but the found behavior resembles the green channel's behavior. However, in-depth analyses and more sophisticated processing strategies are required to exploit the added value of the red channel. Such tasks should definitely be considered in the future.

Second, we restricted our analysis to a reduced number of features. In fact, multiple other features would be of interest and possible. Owing to their pathophysiological relevance, particularly features from the second derivative seem to be interesting. Deriving such features is possible Fleischhauer et al. (2020) but they are easily affected by distortions as also seen in Djeldjli et al. (2021). In order to avoid distorted features to interfere with the physiological interpretation, we selected the features that are common and that we believe to be robust at the same time. Again, other choices should be considered in the future.

Third, the presented research includes a comparatively high number of subject but healthy volunteers only. In elderly or under pathological conditions, the observed behavior might differ as seen in previous works Cooke et al. (1993); Jaryal et al. (2009); Kurki et al. (1990). Particularly with respect to the idea of combining measurement sites or acquisition modes in order to refine diagnostics, this is of importance and obviously deserves special attention in the future.

5.3 Conclusion and outlook

To summarize, we showed significant changes of PPG signals in all recording setups upon cold stress. Remarkably, even in iPPG, the considered features show an effect. This finding underlines the

opportunity to use iPPG beyond heart rate. Despite the existence of a response in all recording setups, there are differences. Such differences generally relate to the effect sizes. Finger PPG shows the strongest effects, which we attribute to a marked vasoconstriction in the finger. For PWHA, differences do not only concern the effect size but the general behavior. For PWHA, we found an inverse behavior between finger and earlobe. Further, iPPG features tend to an earlier return after a first response than PPG features, which could be an indicator of iPPG's formation to which very small superficial vessels contribute more than in contact PPG.

Taken together, the found differences carry at least three concrete implications for the usage of PPG and future works. First, in multisite PPG, care has to be taken because indifferent shape changes will also affect fiducial points and can thus hamper the analysis as well as interpretation of time delays between PPG signals. Second, care should be taken when earlier findings or even methods, e.g., pretrained machine learning methods, are transferred between recording setups. Third, the existence/absence of differences in recording setups might carry diagnostic information. A future diagnostic usage is of high interest but requires methodological developments and basic research invoking different subject groups.

Data availability statement

The original contributions presented in the study are included in the article/**Supplementary Materials**, further inquiries can be directed to the corresponding author.

Ethics statement

The study was approved by the Ethics Committee at TU Dresden. The patients/participants provided their written informed consent to participate in this study. Written informed consent was obtained from the individual(s) for the publication of any potentially identifiable images or data included in this article.

Author contributions

SZ and SR were responsible for the conception of the experiment. JB and VF were responsible for data recording. SZ and VF were responsible for the conception of the presented analysis. VF and JB were responsible for the data analysis. SZ, VF, and SR were responsible for the discussion of findings. JB, SZ, and VF were responsible for the structured literature review. All authors contributed to the article and approved the submitted version.

Funding

This work was funded by the Deutsche Forschungsgemeinschaft (DFG, German Research Foundation), project 401786308.

Conflict of interest

The authors declare that the research was conducted in the absence of any commercial or financial relationships that could be construed as a potential conflict of interest.

Publisher's note

Supplementary material

The Supplementary Material for this article can be found online at: https://www.frontiersin.org/articles/10.3389/fphys.2023.1127624/full#supplementary-material

References

Abdullah, S. A., Essa, S. I., and Talib, B. (2022). The effect of hand blood flow on the peripheral fingertip plethysmographic waveforms morphology and pulse wave velocity. *Pak. J. Med. Health Sci.* 16, 552–554. doi:10.53350/pjmhs22166552

Ajmal, A., Boonya-Ananta, T., Rodriguez, A. J., Du Le, V. N., and Ramella-Roman, J. C. (2021). Monte Carlo analysis of optical heart rate sensors in commercial wearables: The effect of skin tone and obesity on the photoplethysmography (PPG) signal. *Biomed. Opt. Express* 12, 7445–7457. doi:10.1364/BOE.439893

Allen, J., and Murray, A. (2000). Comparison of regional variability in multi-site photoplethysmographic pulse wave characteristics. *IEE Conf. Publ.* 476, 26–31. doi:10.1049/cp:20000313

Almarshad, M. A., Islam, M. S., Al-Ahmadi, S., and Bahammam, A. S. (2022). Diagnostic features and potential applications of PPG signal in healthcare: A systematic review. *Healthc. Switz.* 10, 547–628. doi:10.3390/healthcare10030547

Awad, A. A., Ghobashy, M. A. M., Ouda, W., Stout, R. G., Silverman, D. G., and Shelley, K. H. (2001b). Different responses of ear and finger pulse oximeter wave form to cold pressor test. *Anesth. Analgesia* 92, 1483–1486. doi:10.1097/00000539-200106000-00026

Awad, A. A., Ghobashy, M. A., Stout, R. G., Silverman, D. G., and Shelley, K. H. (2001a). How does the plethysmogram derived from the pulse oximeter relate to arterial blood pressure in coronary artery bypass graft patients? *Anesth. analgesia* 93, 1466–1471. table of contents. doi:10.1097/00000539-200112000-00022

Awad, A. A., Haddadin, A. S., Tantawy, H., Badr, T. M., Stout, R. G., Silverman, D. G., et al. (2007). The relationship between the photoplethysmographic waveform and systemic vascular resistance. *J. Clin. Monit. Comput.* 21, 365–372. doi:10.1007/s10877-007-9097-5

Awad, A. A., Stout, R. G., Ghobashy, M. A. M., Rezkanna, H. A., Silverman, D. G., and Shelley, K. H. (2006). Analysis of the ear pulse oximeter waveform. *J. Clin. Monit. Comput.* 20, 175–184. doi:10.1007/s10877-006-9018-z

Bali, A., and Jaggi, A. S. (2015). Clinical experimental stress studies: Methods and assessment. *Rev. Neurosci.* 26, 555–579. doi:10.1515/revneuro-2015-0004

Bentham, M., Stansby, G., and Allen, J. (2018). Innovative multi-site photoplethysmography analysis for quantifying pulse amplitude and timing variability characteristics in peripheral arterial disease. *Diseases* 6, 81. doi:10.3390/diseases6030081

Boonya-ananta, T., Rodriguez, A. J., Ajmal, A., Du Le, V. N., Hansen, A. K., Hutcheson, J. D., et al. (2021). Synthetic photoplethysmography (PPG) of the radial artery through parallelized Monte Carlo and its correlation to body mass index (BMI). *Sci. Rep.* 11, 2570. doi:10.1038/s41598-021-82124-4

Chan, G., Cooper, R., Hosanee, M., Welykholowa, K., Kyriacou, P. A., Zheng, D., et al. (2019). Multi-site photoplethysmography technology for blood pressure assessment: Challenges and recommendations. *J. Clin. Med.* 8, 1827. doi:10.3390/jcm8111827

Chatterjee, S., and Kyriacou, P. (2019). Monte Carlo analysis of optical interactions in reflectance and transmittance finger photoplethysmography. *Sensors* 19, 789. doi:10.3390/s19040789

Cohen, J. (1988). *Statistical power analysis for the behavioral sciences*. Oxfordshire: Routledge. doi:10.4324/9780203771587

Cooke, E. D., Steinberg, M. D., Pearson, R. M., Fleming, C. E., Toms, S. L., and Elusade, J. A. (1993). Reflex sympathetic dystrophy and repetitive strain injury: Temperature and microcirculatory changes following mild cold stress. *J. R. Soc. Med.* 86, 690–693. doi:10.1177/014107689308601205

de Haan, G., and Jeanne, V. (2013). Robust pulse rate from chrominance-based rPPG. *IEEE Trans. bio-medical Eng.* 60, 2878–2886. doi:10.1109/TBME.2013.2266196

Ding, X., Wang, W., Chen, Y., Yang, Y., Zhao, Y., and Kong, D. (2021). "Feasibility study of pulse width at half amplitude of camera PPG for contactless blood pressure estimation," in Proceedings of the Annual International Conference of the IEEE Engineering in Medicine and Biology Society, EMBS (IEEE), Mexico, 01-05 November 2021, 365–368. doi:10.1109/EMBC46164.2021.9630964

Djeldjli, D., Bousefsaf, F., Maaoui, C., Bereksi-Reguig, F., and Pruski, A. (2021). Remote estimation of pulse wave features related to arterial stiffness and blood pressure using a camera. *Biomed. Signal Process. Control* 64, 102242. doi:10.1016/j.bspc.2020.102242

Elgendi, M. (2012). On the analysis of fingertip photoplethysmogram signals. *Curr. Cardiol. Rev.* 8, 14–25. doi:10.2174/157340312801215782

Ernst, H., Scherpf, M., Malberg, H., and Schmidt, M. (2021). Optimal color channel combination across skin tones for remote heart rate measurement in camera-based photoplethysmography. *Biomed. Signal Process. Control* 68, 102644. doi:10.1016/j.bspc.2021.102644

Fleischhauer, V., Ruprecht, N., Sorelli, M., Bocchi, L., and Zaunseder, S. (2020). Pulse decomposition analysis in photoplethysmography imaging. *Physiol. Meas.* 41, 095009. doi:10.1088/1361-6579/abb005

Fleischhauer, V., Woyczyk, A., Rasche, S., and Zaunseder, S. (2019). "Impact of sympathetic activation in imaging photoplethysmography," in 2019 IEEE/CVF International Conference on Computer Vision Workshop (ICCVW) (IEEE), Seoul, Korea (South), 27-28 October 2019. 1697–1705. doi:10.1109/ICCVW.2019.00210

Hamunen, K., Kontinen, V., Hakala, E., Talke, P., Paloheimo, M., and Kalso, E. (2012). Effect of pain on autonomic nervous system indices derived from photoplethysmography in healthy volunteers. *Br. J. Anaesth.* 108, 838–844. doi:10.1093/bja/aes001

Hedges, L. V. (1981). Distribution theory for glass's estimator of effect size and related estimators. *J. Educ. Statistics* 6, 107–128. doi:10.3102/10769986006002107

Hernando, A., Peláez-Coca, M. D., Lozano, M. T., Lázaro, J., and Gil, E. (2019). Finger and forehead PPG signal comparison for respiratory rate estimation. *Physiol. Meas.* 40, 095007. doi:10.1088/1361-6579/ab3be0

Hickey, M., Phillips, J. P., and Kyriacou, P. A. (2016). Investigation of peripheral photoplethysmographic morphology changes induced during a hand-elevation study. *J. Clin. Monit. Comput.* 30, 727–736. doi:10.1007/s10877-015-9761-0

Hines, E. A., and Brown, G. E. (1936). The cold pressor test for measuring the reactibility of the blood pressure: Data concerning 571 normal and hypertensive subjects. *Am. Heart J.* 11, 1–9. doi:10.1016/S0002-8703(36)90370-8

Holm, S. (1979). Board of the foundation of the scandinavian journal of statistics A simple sequentially rejective multiple test procedure A simple sequentially rejective multiple test procedure. *Source Scand. J. Statistics Scand J Statist* 6, 65–70.

Jain, M., Deb, S., and Subramanyam, A. V. (2016). "Face video based touchless blood pressure and heart rate estimation," in 2016 IEEE 18th International Workshop on Multimedia Signal Processing (MMSP) (IEEE), Montreal, QC, Canada, 21-23 September 2016. 1–5. doi:10.1109/MMSP.2016.7813389

Jaryal, A. K., Selvaraj, N., Santhosh, J., Anand, S., and Deepak, K. K. (2009). Monitoring of cardiovascular reactivity to cold stress using digital volume pulse characteristics in health and diabetes. *J. Clin. Monit. Comput.* 23, 123–130. doi:10.1007/s10877-009-9174-z

Jauregui-Renaud, K., Hermosillo, A. G., Márquez, M. F., Ramos-Aguilar, F., Hernández-Goribar, M., and Cárdenas, M. (2001). Repeatability of heart rate variability during simple cardiovascular reflex tests on healthy subjects. *Archives Med. Res.* 32, 21–26. doi:10.1016/S0188-4409(00)00255-1

Kamshilin, A. A., Nippolainen, E., Sidorov, I. S., Vasilev, P. V., Erofeev, N. P., Podolian, N. P., et al. (2015). A new look at the essence of the imaging photoplethysmography. *Sci. Rep.* 5, 10494. doi:10.1038/srep10494

Kim, D., Lee, K., and Sohn, C. B. (2021). Assessment of ROI selection for facial video-based rPPG. *Sensors* 21, 7923. doi:10.3390/s21237923

Kurki, T. S., Piirainen, H. I., and Kurki, P. T. (1990). Non-invasive monitoring of finger arterial pressure in patients with raynaud's phenomenon: Effects of exposure to cold. *Br. J. Anaesth.* 65, 558–563. doi:10.1093/bja/65.4.558

Lamotte, G., Boes, C. J., Low, P. A., and Coon, E. A. (2021). The expanding role of the cold pressor test: A brief history. *Clin. Aut. Res. official J. Clin. Aut. Res. Soc.* 31, 153–155. doi:10.1007/s10286-021-00796-4

Làzaro, J., Gil, E., Vergara, J. M., and Laguna, P. (2014). Pulse rate variability analysis for discrimination of sleep-apnea-related decreases in the amplitude fluctuations of pulse photoplethysmographic signal in children. *IEEE J. Biomed. Health Inf.* 18, 240–246. doi:10.1109/JBHI.2013.2267096

Lempe, G., Zaunseder, S., Wirthgen, T., Zipser, S., and Malberg, H. (2013). "ROI selection for remote photoplethysmography," in *Bildverarbeitung für die Medizin 2013*. Editors H.-P. Meinzer, T. M. Deserno, H. Handels, and T. Tolxdorff (Heidelberg: Springer), 99–103.

Lin, W. H., Li, X., Li, Y., Li, G., and Chen, F. (2020). Investigating the physiological mechanisms of the photoplethysmogram features for blood pressure estimation. *Physiol. Meas.* 41, 044003. doi:10.1088/1361-6579/ab7d78

Mitchell, L. A., MacDonald, R. A., and Brodie, E. E. (2004). Temperature and the cold pressor test. *J. Pain* 5, 233–237. doi:10.1016/j.jpain.2004.03.004

Moço, A. V., Stuijk, S., and De Haan, G. (2018). New insights into the origin of remote PPG signals in visible light and infrared. *Sci. Rep.* 8, 8501–8515. doi:10.1038/s41598-018-26068-2

Molinaro, N., Schena, E., Silvestri, S., Bonotti, F., Aguzzi, D., Viola, E., et al. (2022). Contactless vital signs monitoring from videos recorded with digital cameras: An overview. *Front. Physiology* 13, 801709. doi:10.3389/fphys.2022.801709

Mourot, L., Bouhaddi, M., and Regnard, J. (2009). Effects of the cold pressor test on cardiac autonomic control in normal subjects. *Physiological Res./Acad. Sci. Bohemoslovaca* 58, 83–91. doi:10.33549/physiolres.931360

Natarajan, K., Block, R. C., Yavarimanesh, M., Chandrasekhar, A., Mestha, L. K., Inan, O. T., et al. (2022). Photoplethysmography fast upstroke time intervals can Be useful features for cuff-less measurement of blood pressure changes in humans. *IEEE Trans. Biomed. Eng.* 69, 53–62. doi:10.1109/TBME.2021.3087105

Ni, A., Azarang, A., and Kehtarnavaz, N. (2021). A review of deep learning-based contactless heart rate measurement methods. *Sensors* 21, 3719. doi:10.3390/s21113719

Park, J., Seok, H. S., Kim, S.-S., and Shin, H. (2022). Photoplethysmogram analysis and applications: An integrative review. *Front. Physiology* 12, 808451–808523. doi:10.3389/fphys.2021.808451

Rong, M., and Li, K. (2021). A blood pressure prediction method based on imaging photoplethysmography in combination with machine learning. *Biomed. Signal Process. Control* 64, 102328. doi:10.1016/j.bspc.2020.102328

Selvaraju, V., Spicher, N., Wang, J., Ganapathy, N., Warnecke, J. M., Leonhardt, S., et al. (2022). Continuous monitoring of vital signs using cameras: A systematic review. *Sensors* 22, 4097. doi:10.3390/s22114097

Shao, D., Liu, C., and Tsow, F. (2021). Noncontact physiological measurement using a camera: A technical review and future directions. *ACS Sensors* 6, 321–334. doi:10.1021/acssensors.0c02042

Suzuki, J., Maeda, J., and Takemiya, T. (1994). Analysis of microvascular responses in the finger to changes in arm position during cold water stimulation. *Jpn. J. physiology* 44, 181–191. doi:10.2170/jjphysiol.44.181

Teng, X., and Zhang, Y. (2003). "Continuous and noninvasive estimation of arterial blood pressure using a photoplethysmographic approach," in Proceedings of the 25th Annual International Conference of the IEEE Engineering in Medicine and Biology Society (IEEE Cat. No.03CH37439), Cancun, Mexico, 17-21 September 2003. 4, 3153–3156. doi:10.1109/IEMBS.2003.1280811

Veluswamy, S., Shah, P., Khaleel, M., Thuptimdang, W., Chalacheva, P., Sunwoo, J., et al. (2020). Progressive vasoconstriction with sequential thermal stimulation indicates vascular dysautonomia in sickle cell disease. *Blood* 136, 1191–1200. doi:10.1182/blood.2020005045

Verkruysse, W., Svaasand, L. O., and Nelson, J. S. (2008). Remote plethysmographic imaging using ambient light. *Opt. express* 16, 21434–21445. doi:10.1364/oe.16.021434

Wang, W., den Brinker, A. C., Stuijk, S., and de Haan, G. (2017). Algorithmic principles of remote PPG. *IEEE Trans. bio-medical Eng.* 64, 1479–1491. doi:10.1109/TBME.2016.2609282

Woyczyk, A., Fleischhauer, V., and Zaunseder, S. (2021). Adaptive Gaussian mixture model driven level set segmentation for remote pulse rate detection. *IEEE J. Biomed. health Inf.* 25, 1361–1372. doi:10.1109/JBHI.2021.3054779

Zaunseder, S., and Rasche, S. (2022). "Clinical applications for imaging photoplethysmography," in *Contactless vital signs monitoring* (Amsterdam, Netherlands: Elsevier), 149–164. doi:10.1016/B978-0-12-822281-2.00015-9

frontiers | Frontiers in Physiology

TYPE Original Research
PUBLISHED 02 June 2023
DOI 10.3389/fphys.2023.1172688

OPEN ACCESS

EDITED BY
Panicos Kyriacou,
City University of London,
United Kingdom

REVIEWED BY
Ashraf W. Khir,
Durham University, United Kingdom
Branko Celler,
University of New South Wales, Australia

*CORRESPONDENCE
Laura Bogatu,
laura.bogatu@philips.com

RECEIVED 23 February 2023
ACCEPTED 19 May 2023
PUBLISHED 02 June 2023

CITATION
Loureiro J, Bogatu L, Schmitt L, Henriques J, Carvalho P, Noordergraaf GJ, Paulussen I and Muehlsteff J (2023), Towards continuous non-invasive blood pressure measurements—interpretation of the vasculature response to cuff inflation. *Front. Physiol.* 14:1172688. doi: 10.3389/fphys.2023.1172688

Towards continuous non-invasive blood pressure measurements—interpretation of the vasculature response to cuff inflation

João Loureiro[1], Laura Bogatu[2]*, Lars Schmitt[2], Jorge Henriques[1], Paulo Carvalho[1], Gerrit J. Noordergraaf[3], Igor Paulussen[2,3] and Jens Muehlsteff[2]

[1]Centre for Informatics and Systems of the University of Coimbra, University of Coimbra, Department of Informatics Engineering, Coimbra, Portugal, [2]Department of Patient Care and Measurements, Philips Research, Eindhoven, Netherlands, [3]Department of Anesthesiology and Pain Management, Elisabeth-Tweesteden Hospital, Tilburg, Netherlands

Blood pressure (BP) surrogates, such as pulse transit time (PTT) or pulse arrival time (PAT), have been intensively explored with the goal of achieving cuffless, continuous, and accurate BP inference. In order to estimate BP, a one-point calibration strategy between PAT and BP is typically used. Recent research focuses on advanced calibration procedures exploiting the cuff inflation process to improve calibration robustness by active and controlled modulation of peripheral PAT, as measured via plethysmograph (PPG) and electrocardiogram (ECG) combination. Such methods require a detailed understanding of the mechanisms behind the vasculature's response to cuff inflation; for this, a model has recently been developed to infer the PAT-BP calibration from measured cuff-induced vasculature changes. The model, while promising, is still preliminary and only partially validated; in-depth analysis and further developments are still needed. Therefore, this work aims to improve our understanding of the cuff-vasculature interaction in this model; we seek to define potential opportunities and to highlight which aspects may require further study. We compare model behaviors with clinical data samples based on a set of observable characteristics relevant for BP inference and calibration. It is found that the observed behaviors are qualitatively well represented with the current simulation model and complexity, with limitations regarding the prediction of the onset of the distal arm dynamics and behavior changes at high cuff pressures. Additionally, a sensitivity analysis of the model's parameter space is conducted to show the factors that influence the characteristics of its observable outputs. It was revealed that easily controllable experimental variables, such as lateral cuff length and inflation rate, have a significant impact on cuff-induced vasculature changes. An interesting dependency between systemic BP and cuff-induced distal PTT change is also found, revealing opportunities for improved methods for BP surrogate calibration. However, validation via patient data shows that this relation does not hold for all patients, indicating required model improvements to be validated in follow up studies. These results provide promising directions to improve the calibration process featuring cuff inflation towards accurate and robust non-invasive blood pressure estimation.

KEYWORDS

blood pressure, pulse arrival time, oscillometry, blood pressure surrogate calibration, hemodynamic model, pulse transit time, NIBP

1 Introduction

The current standard for clinical Non-Invasive Blood Pressure (NIBP) monitoring is based on sphygmomanometry utilizing a cuff at the upper arm. With the cuff, the transmural pressure across the brachial artery wall is changed, causing the volume of the brachial artery to oscillate with varying amplitude, which is detected as air pressure oscillations inside the cuff. The BP values are then inferred by empirical methods, namely, oscillometry. Depending on the patient's state, this measurement is taken at intervals ranging from a few minutes to multiple hour intervals, implying the risk of not being able to continuously follow the hemodynamic state of a patient undergoing therapeutic intervention, particularly when it comes to not foreseeing (or entirely missing) critical events (hemorrhages, shock, among others), preventing timely and adequate therapy (Vincent et al., 2011).

For this reason, substantial research has been dedicated towards accurate and tendentially continuous NIBP measurement. In particular, the use of Blood Pressure (BP) surrogates, such as Pulse Wave Velocity (PWV), Pulse Transit Time (PTT), and Pulse Arrival Time (PAT), has been extensively explored (Sola et al., 2019). PAT is the time a pulse takes to travel from the heart to a peripheral artery, extracted as the time delay between the R-peak of the electrocardiogram (ECG) signal and a signal feature in a synchronously acquired photoplethysmogram (PPG) signal (e.g., from the finger), PTT is the time between two pulses measured at two artery locations measured with, for example, two PPG devices (Panula et al., 2023). While such measurements are widely available, PAT/PTT-based BP estimation methods are not being implemented in standard practice. A main limitation is the difficulty of estimating the BP surrogate calibration–e.g., an x ms change in PAT/PTT reveals a y mmHg change in BP. A large number of calibration strategies of various levels of complexity have been attempted, e.g., based on demographic data (Chen et al., 2009; Gesche et al., 2012), waveform feature analysis (Yoon et al., 2018), machine learning (Su et al., 2018), among others (Sola et al., 2019). However, there is still an unmet need for accurate and continuous NIBP measurement methods.

Recently, Bogatu et al. (2020) discussed the opportunities in estimating BP-surrogate calibration by utilizing the cuff in combination with other typically available signals such as the electrocardiogram (ECG) and photoplethysmogram (PPG). The cuff actively modulates the blood flow and pulse propagation along the artery distal to the cuff affecting, for instance, pulse arrival time (PAT) or pulse transit time (PTT). The PAT response to cuff inflation may, in principle, be representative of the PAT-BP relationship over a large BP range and, therefore, be used to establish a PAT-BP calibration with improved robustness, allowing for more accurate measurements. However, the correct interpretation of the measured cuff-induced change in PAT poses a challenge. Early models did not correctly explain the dynamics of the PAT response during cuff inflation, e.g., Yan and Zhang (2007) or Bresch et al. (2018). Recent clinical data provided an improved understanding of the true hemodynamic processes measuring the BP dynamics (Bogatu et al., 2021). The cuff decreases the transmural pressure at the brachial artery, causing an increase in PTT for this artery segment. At the same time, the mean arterial pressure (MAP) increases in the distal portion of the arm due to venous collapse, impacting the effective overall observed PAT behavior.

The basic measurement configuration of this work is shown in Figure 1. It includes the simultaneous acquisition of an ECG signal, the pressure within an inflatable cuff at the upper arm, a finger-site PPG, and the invasive measurement of ABP in the radial artery providing an accurate measurement for comparison/validation.

This complex and dynamic PAT response to cuff inflation has been simulated via a hemodynamic model including the cuff and the distal arm by Bogatu et al. (2021), aggregating work from Drzewiecki et al. (1994), Bank et al. (1999), Seagar et al. (1984) and Babbs et al. (2012). This implementation incorporates the dynamic of the BP changes in the distal arm. Preliminary clinical evidence of an improved PAT-BP calibration performance for BP estimation has been reported.

The model, while promising, is still preliminary and only partially validated; in-depth analysis and further developments are still needed. This paper aims at a deeper understanding and critical evaluation of this simulation model in order to strategize possible improvements. Particular attention was given to the underlying dynamics during cuff inflation. For these purposes, we discuss the results of 1) a direct qualitative comparison between simulated and real-life distal BP and PAT data, as well as 2) a sensitivity analysis of the model, identifying and assessing the key variables that affect the distal arm's vasculature response as observed in measurements. These will provide insights on the main factors to explore for future improvements in terms of robustness and performance of BP surrogate calibration.

The remainder of this work is structured as follows.

- In Section 2, the materials and methods employed for this research are described, starting from the simulation model under analysis, followed by the data collection and characterization strategy, as well as the sensitivity analysis that was performed.
- Section 3 encompasses the findings obtained over the course of the various analyses carried out in this work, including a brief description of the results along with their exposition via figure/table. We start by presenting the results of our qualitative comparison between simulated and real data, moving on to the outcomes of the sensitivity analysis.
- Our findings will be subject of discussion in Section 4, where a critical assessment of our work is conducted, highlighting the successes and limitations of our study, as well as their meaning regarding the current hemodynamic monitoring landscape.
- Lastly, Section 5 summarizes and concludes this work.

2 Materials and methods

2.1 Simulation model

An overview of the model analyzed in this work is shown in Figure 2 with input/output parameters and an internal resistor-capacitor (RC) network.

All model variables are listed in Table 1. The inputs of the model are systemic venous pressure, $P_{ven\ sys}$, cuff inflation rate, and the systemic arterial pressure, $P_{art\ sys}$, assumed as a sinusoidal

10.3389/fphys.2023.1172688

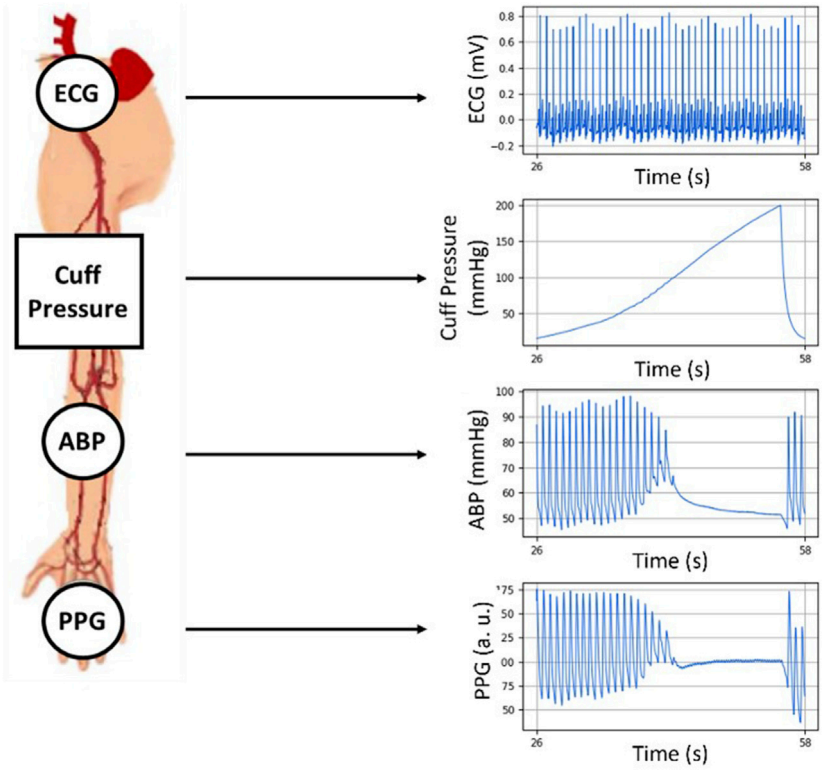

FIGURE 1
The setup utilized in this work acquiring ECG, PPG, the cuff air pressure and the invasively measured radial ABP. All signals are synchronously recorded during a cuff inflation.

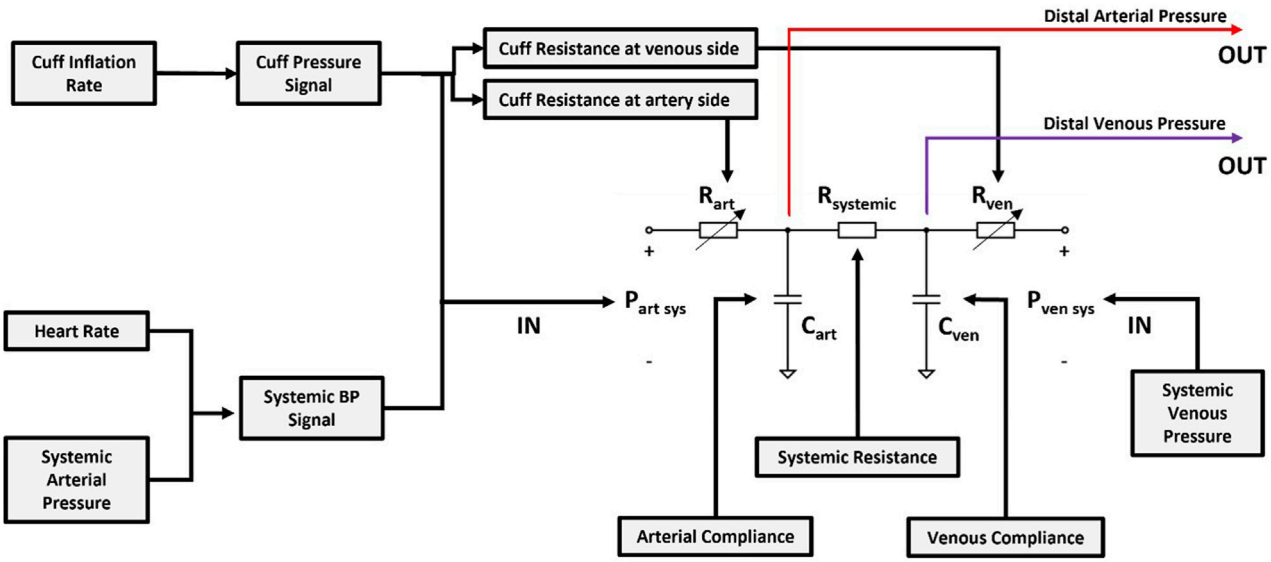

FIGURE 2
Overview of the distal arm circulation model.

signal defined by heart rate and systemic systolic and diastolic pressures. The arterial and venous pressures at the distal portion of the arm are the model's outputs. The behavior of the distal BP signal is characterized by the systolic and diastolic pressure values measured at the superior and inferior peaks of the wave, respectively.

TABLE 1 List of variables and respective reference/control values for the distal arm circulation model.

Parameter	Units	References value
a	$mmHg^{-1}$	0.03
c	$mmHg^{-1}$	0.1
d	cm	0.08
Systolic Pressure	mmHg	120
Pulse Pressure	mmHg	40
Heart Rate	b.p.m	60
Cuff Inflation Rate	mmHg/s	6
Arm length	m	1
Cuff Length	m	0.14

The RC parameters have been modelled as follows: the resistance to blood flow across the portion of the brachial artery occluded by the cuff is represented by R_{art}, estimated using the Poiseuille Formula as stated in (Eq. 1):

$$\boldsymbol{R_{art}(P_{tm}) = \frac{8\eta L_{cuff}}{\pi r(P_{tm})^4}} \quad (1)$$

where η is the blood's viscosity, L_{cuff} is the cuff's length, P_{tm} is transmural pressure, calculated as arterial BP (P_{art}) minus cuff pressure (P_{cuff}), and r (P_{tm}) is the brachial artery's radius as a function of transmural pressure across the arterial wall, which we may obtain from the arterial cross-sectional area given by (Eq. 2), introduced by Drzewiecki et al. (1994):

$$\boldsymbol{A(P_{tm}) = d\frac{ln(aP_{tm} + 3.3)}{1 + e^{-cP_{tm}}}} \quad (2)$$

with a, c, and d as model parameters. The venous resistance, R_{ven}, has been found to be uncritical (Smink et al., 2019)—venous pressure typically ranges between 5 and 15 mmHg (Raju, 2019), being fixed at 10 mmHg for this framework. We can therefore assume that the vein is fully collapsed at a cuff pressure of around 30 mmHg (R_{ven} virtually infinite). For the systemic resistance of the arm, $R_{systemic}$, Alastruey et al. (2006) reported values of about 100 mmHg·s/mL. Arm length is fixed at 1 m.

Two capacitances/compliances were included in the model: C_{art} and C_{ven}, arterial and venous compliance, respectively. C_{art} is defined with a fixed value of 0.03 mL·mmHg-1 (Alastruey et al., 2006) and C_{ven} is defined as approximately 30 times larger than C_{art} (Gelman et al., 2008).

The model illustrated in Figure 2 can be represented via the following equations:

$$\frac{dP_{art\,distal}}{dt} = \left(\frac{P_{art\,sys}}{R_{art}} - P_{art\,distal}\left(\frac{1}{R_{art}} + \frac{1}{R_{systemic}}\right) + \frac{P_{ven\,distal}}{R_{systemic}}\right)\frac{1}{C_{art}} \quad (3)$$

$$\frac{dP_{ven\,distal}}{dt} = \left(\frac{P_{art\,distal}}{R_{systemic}} - P_{ven\,distal}\left(\frac{1}{R_{systemic}} + \frac{1}{R_{ven}}\right) + \frac{P_{ven\,sys}}{R_{ven}}\right)\frac{1}{C_{ven}} \quad (4)$$

The simulation of the interaction between the cuff inflation and pulse propagation at the cuff site is complemented by the modulation of the hemodynamic behavior in the distal portion of the arm. A good agreement between the observations obtained from a limited sample of patient data and model simulations was reported by Bogatu et al. (2021).

2.2 Clinical data acquisition and comparison with model output

Clinical data was collected from four anesthetized and mechanically ventilated patients (ages: 45, 58, 66, and 70 years old), using a sensor arrangement as shown in Figure 1. It consists of an ECG, a brachial blood pressure cuff at the upper arm, a radial intra-arterial line (ABP), and a finger PPG. The patients underwent invasive non-cardiac surgery at the time of the recordings. The data collection process was approved by the MEC-U ethical committee for this study (St. Antonius Ziekenhuis, Koekoekslaan 1, 3430 EM Nieuwegein, NL. Approval W19.046), and it was carried out at the Elisabeth Tweesteden Ziekenhuis hospital in Tilburg, NL. Each patient gave written informed consent. The signals were recorded using a Philips MP50 patient monitor and custom data logging software. The ECG signals were recorded with a sampling frequency of 500 Hz whereas the cuff pressure, ABP, and PPG signals were recorded with a sampling frequency of 125 Hz. All the signals were simultaneously recorded.

The variations in PAT and PTT caused by the inflation of the cuff are calculated over two vascular segments.

- Heart to finger site: $\Delta PAT_{ECG-PPG}$ (P_{cuff}) is calculated as the change in delay between the R-peak of the ECG signal and the foot of the PPG waveform as P_{cuff} increases.
- Radial to finger site: $\Delta PTT_{ABP-PPG}$ (P_{cuff}) is calculated as the change in delay between the foot of the ABP waveform and the foot of the PPG waveform as P_{cuff} increases.

The difficult assessment of the heart's pre-ejection period (PEP) has been characterized as a drawback of the direct application of PAT measurements in BP estimation (Pilz et al., 2023). The presented calibration method eliminates this factor by interpreting the PAT/PTT variations, given that they are generated due to the action of the cuff and PEP remains constant throughout the inflation.

The dynamics taking place in the portion of the arm distal from the cuff are the focus of the model under study. The early venous collapse at the cuff site causes an increase of BP in the distal arm due to continued blood flow at intermediate cuff pressures, which can be measured via invasive methods and is reflected in deviations in the PAT/PTT measurements. With the purpose of describing this distal filling effect, a series of metrics were defined and are explained below and illustrated in Figure 3.

- The maximum drop in distal PTT variations (ΔPTT) caused by the distal filling effect - $\boldsymbol{max|\Delta PTT_{distal}|}$ - measured via the time interval between the pulse detected at the ABP site and

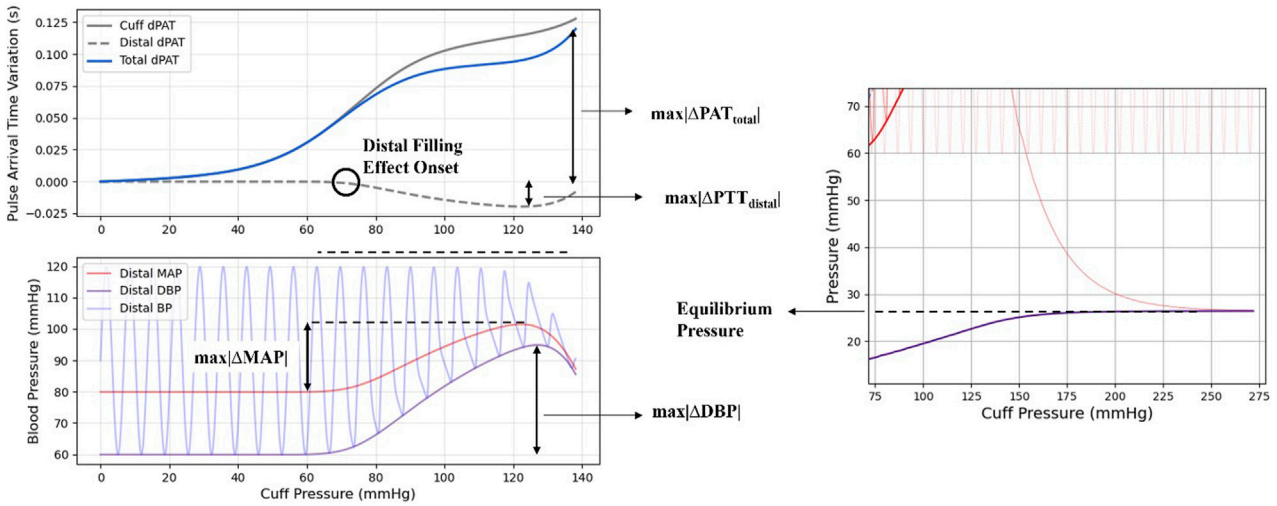

FIGURE 3
Illustration of the metrics as used for this study.

the pulse detected at the finger site through the valleys of the ABP and PPG waveforms.

- The maximum total PAT change (ΔPAT) - $\boldsymbol{max|\Delta PAT_{total}|}$ - measured via the time interval between the R-peak of the ECG signal and the pulse detected at the finger site at the valley of the PPG waveform.
- The maximum change in distal MAP - $\boldsymbol{max|\Delta MAP|}$ - measured as the difference between the maximum measured MAP value during a cuff inflation and the MAP value at the beginning of the cuff inflation.
- The equilibrium pressure - $\boldsymbol{P_{eq}}$–measured as the value to which blood pressure in the distal arm asymptotically tends at cuff pressures that cause arterial and venous occlusion in the upper arm.
- The maximum change in distal Diastolic Pressure (DBP) - $\boldsymbol{max|\Delta DBP|}$ - measured as the difference between the maximum measured DBP value during a cuff inflation and the DBP value at the beginning of the cuff inflation.
- The difference between MAP and cuff pressure at the onset of the distal filling effect - $\boldsymbol{\Delta PTT_{onset}}$–calculated as the difference between systemic MAP and the cuff pressure at the onset of the observed decrease in ΔPTT.

These features have been also investigated in the sensitivity analysis, as discussed in the next section.

2.3 Sensitivity analysis

The sensitivity analysis carried out in this work is based on the variance-based method for Global Sensitivity Analysis (Sobol, 2001; Saltelli et al., 2004), as it is model-independent and allows us to analyze non-linear and non-monotonic functions and models. This method provides a structured approach to identify the most influential parameters of a simulation model via their contribution to the overall model output variance. The technique is based on the decomposition of the model variance into Sobol Indices. These Indices reflect the multiple order contributions to output variance from the various parameter subsets, beginning with the first order Sobol Indices that correspond to the contribution from each individual parameter, moving to the second-order Sobol Indices that reflect interactions between pairs of parameters, and so on. The total-order Sobol indices reflect the overall contribution each parameter has to the variance of the output. Assuming a black-box model with independent input variables represented by an integrable function:

$$Y = f(X) = f(X_1, ..., X_n) \tag{5}$$

where Y is the model output (or objective function) and $(X_1, ..., X_n)$ is the input variable set. We can decompose the function f into summands of increasing dimensionality:

$$\begin{aligned} Y &= f(X_1, ..., X_n) \\ &= f_0 + \sum_{i}^{n} f_i(X_i) + \sum_{i<j}^{n} f_{ij}(X_i, X_j) + \cdots + f_{1,...,n}(X_1, ..., X_n) \end{aligned} \tag{6}$$

and, subsequently, decompose the variance of Y into the summand of the variances of individual parameters and their interactions (Sobol, 1993), as in Eq. 5:

$$V(Y) = \sum_{i}^{n} V_i + \sum_{i<j}^{n} V_{ij} + \cdots + V_{i,...,n} \tag{7}$$

We can then calculate the Sobol indices for a parameter X_i as the ratio of the partial variance which the parameter contributes to the total variance V:

$$\text{First Order Sobol Index: } S_i = \frac{V_i}{V} \tag{8}$$

$$\text{Second Order Sobol Index: } S_{ij} = \frac{V_{ij}}{V} \tag{9}$$

$$\text{Total Order Sobol Index: } S_{Ti} = S_i + \sum_{j \neq i} S_{ij} + \cdots \tag{10}$$

TABLE 2 Assumed parameter constraints; Normal Distribution: N (μ, σ); Uniform Distribution: U (lower limit, upper limit).

Parameters (Units—Type)	Distribution
a (mmHg-1)	U (0.017, 0.035)
c (mmHg-1)	U (0.08, 0.14)
Systolic Pressure (mmHg)	N (125, 15)
Pulse Pressure (mmHg)	N (40, 5)
Cuff Inflation Rate (mmHg/s)	U (4, 8)
Cuff Length (m)	U (0.1, 0.18)

Based on these indices, we draw conclusions on the influence of a parameter on the model. On relative terms.

- If the first order index is high (close to 1), the parameter has a strong influence on the model by itself.
- If the total order index is low (close to 0), the parameter has a weak impact on the model.
- If the first order index is low and the total order index is high, the influence that the parameter has on the model is impacted by interactions with other parameters.

Naturally, the method described above is analytically feasible for simple, analytically trackable models, which is not the case for most. However, for complex and highly non-linear models such as the one at study, the individual variances in Eq. 7 can be estimated via Monte Carlo (or quasi-Monte Carlo) sampling, solely relying on the output of the model, as demonstrated by Sobol (1993).

The list of parameters analyzed in the course of the sensitivity analysis is shown in Table 2 including their respective assumed distributions. There is limited prior information on the arterial collapse parameters *a* and *c*, which have been assigned based on clinical data as found by Bogatu et al. (2021). Regarding the Systolic Pressure (SBP) and Pulse Pressure (PP) distributions, and given that this method assumes independent input parameters, we used Gaussian distributions. For both variables, the means and standard deviations produce realistic samples, in line with the European Society of Hypertension - European Society of Cardiology (ESC) Guidelines for the Management of Arterial Hypertension (Williams et al., 2018). These distributions also provide samples characteristic of hypotensive and hypertensive patients. The sensitivity analysis also evaluates the robustness of these assumptions. Cuff length and inflation rate were set as uniformly distributed given conditions from practice. It must be noted that these settings are treated as variables in this study to assess their value in further experimental protocols, as they were kept constant in the course of the clinical data collection. Remaining constraints and parameters, in particular the internal RC components of the model, were fixed as described in the previous section.

The parameter sets are generated according to a quasi-random, low-discrepancy sampling method (Saltelli, 2002). For each set, the output of the model is computed and its characteristics are registered. The metrics for this quantitative assessment are the same as discussed in Section 2.3 and illustrated in Figure 3.

The implementation of the methods required for this analysis is based on the SALib–Sensitivity Analysis Library in Python (Herman et al., 2017; Iwanaga et al., 2022). The outputs of the model with each parameter set were stored for use in the analysis itself and our own quantitative assessment.

3 Results

3.1 Measured signal vs. model output signal comparison

3.1.1 Distal BP

An example of the qualitative comparison between clinical signal samples and simulated data assuming similar physiological conditions, namely, BP and heart rate, is shown below with a cuff inflation at t = 0 s. The goal is to identify differences in ABP signal behaviors. This comparison is shown in Figure 4.

Visually, the dynamics of BP, the increases in DBP and MAP as well as the decrease in the SBP at the radial location, are well reproduced by the model. However, it is noticeable that the increase in DBP and MAP begins sooner in the simulation than in the clinical data, also reaching higher values (~40 vs. ~25 mmHg, respectively). By contrast, the decrease in SBP seems to be smaller in the model than in the real case. Different dynamics regarding the tendency towards equilibrium pressure are evident between simulation and clinical data. It should be noted that, by design, the model does not take into account difficult to measure or to control parameters such as cardiac output and peripheral resistance.

3.1.2 PAT/PTT

In addition to the distal ABP signals, ΔPAT and ΔPTT behavior is also investigated. The measured ΔPAT/PTT signals obtained from the ECG, ABP and PPG recordings, as well as the simulated ΔPAT/PTT signals are computed as described by Bogatu et al. (2021). Figure 5 provides a side-by-side comparison between an example of a clinical measurement (right diagram) and the equivalent simulation results (left diagram), following the same strategy as before. In this case, the total resulting measurements (ΔPAT_{total}) can be decomposed in two components: ΔPTT_{cuff}, corresponding to the change in PTT cause only by action of the cuff inflation, and ΔPTT_{distal} which is cause by the increase in DBP and MAP due to the filling effect. Key observations include: 1) the distal filling effect starts at lower cuff pressure (~60 mmHg) with higher values of ΔPAT reached in the clinical data compared to the simulation; 2) there is an increase of distal ΔPTT at the end of the inflation, not covered by the simulation; 3) the ΔPAT measurements tend to higher values in the clinical data, compared to the model.

In Figure 6 it is observed that the onset of the MAP increase and the onset of ΔPTT occur simultaneously in the clinical data. This simultaneous onset is observed across the database, confirming that the model represents this process well (in the simulations, onset of MAP and onset of ΔPTT_{distal} are modelled to occur simultaneously).

10.3389/fphys.2023.1172688

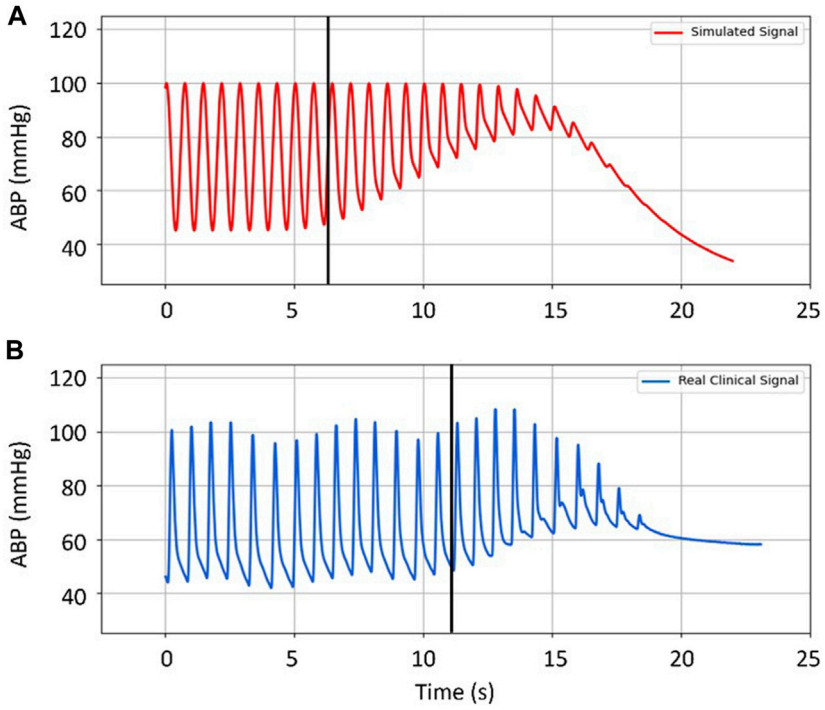

FIGURE 4
Comparison between **(A)** simulated distal arterial BP, and **(B)** real clinical data from a patient. Black vertical lines mark the onset of the filling effect (the moment when distal pressure starts to differ from systemic pressure). Input parameters for the simulated data are the same as the actual patient's: HR: 1.4 Hz (~84 b.p.m.); BP: 100/45 mmHg; Cuff Inflation Rate: 6 mmHg/s; Arterial Collapse Parameters (*a*, *c*, and *d*): reference values, see Table 1.

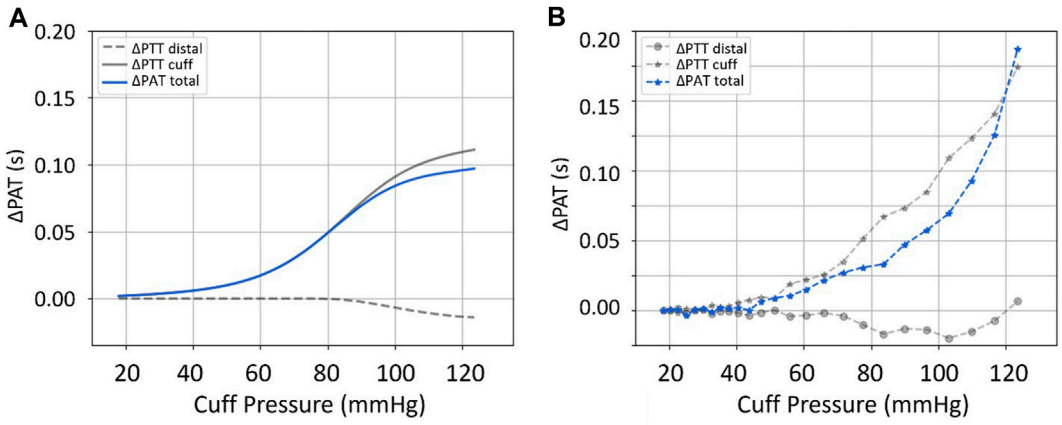

FIGURE 5
Comparison between **(A)** simulated, and **(B)** real measurements of ΔPTT_{cuff}, ΔPTT_{distal}, and ΔPAT_{total}. Input parameters for the simulated data are an approximation of the actual patient's: HR: 1.22 Hz (~73 b.p.m.); BP: 123/75 mmHg; Cuff Inflation Rate: 6.8 mmHg/s; Arterial Collapse Parameters (*a*, *c*, and *d*): reference values, see Table 1.

However, the model cannot be used in the current state to predict when the onset will occur along the cuff inflation. As shown in the example in Figure 4, the onset of the distal effect happens at a different moment in the simulation compared to measured data, whereas in Figure 5 the onset happens later in the simulation. The determinants of this process are explored in the sensitivity analysis.

Overall, the behaviors are qualitatively well represented via the model; the model is an acceptable representation of the core hemodynamic processes happening as result of the cuff inflation. However, significant differences can be observed in amplitudes and timing of signal changes, implying the existence of fundamental inaccuracies/limitations.

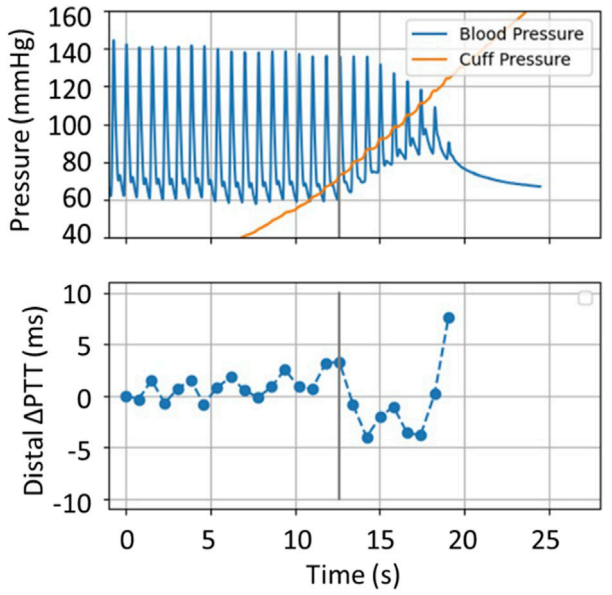

FIGURE 6
Simultaneous recordings of distal BP signal and distal ΔPTT from the clinical dataset. The vertical line marks the onset of the distal filling effect.

3.2 Sobol sensitivity analysis

The sensitivity analysis outputs the Sobol/Sensitivity Indices that reflect the influence of each parameter on the evaluated outcomes. The resulting first and total order Sobol Indices, respectively marked as S1 and ST, are listed below, in Table 3.

The results show that, concerning the model, SBP and PP are responsible for the majority of the variance of the outputs. SBP is the dominant parameter in relation to the equilibrium pressure P_{eq}, individually accounting for over 77% of its variability, and PP is the most influential factor for the observed decrease in distal ΔPTT, and the onset of the distal effect (ΔPTT_{onset}), as well as for increases in DBP and MAP, being individually responsible for ~57%, ~73%, ~82%, and ~82% of their variability, respectively. The magnitude of modelled ΔPAT (represented by $max|\Delta PAT_{total}|$) is mainly driven by cuff length, being more than 75% dependent on it, as compared to other parameters. The results show clearly that parameter *a* is the least influential parameter of the investigated set, never accounting for more than 3.09% for the variability whereas parameter *c* has some influence on $max|\Delta PAT_{total}|$ and ΔPTT_{onset}. P_{eq} is found to also be ~20% dependent on the cuff inflation rate. Finally, the differences between the First and Total Order indices are, albeit existent, not significative when compared to their overall magnitude, suggesting that higher order indices are not relevant for analysis.

Figure 7 illustrates model output characteristics for all simulated parameter ranges. The figure reveals that signals generated via the model fall within realistic physiological ranges; also indicating that model parameter ranges (Table 2) are representative of realistic values.

3.2.1 Effects of cuff length and inflation rate in the simulated response

The results of the sensitivity analysis and the sampled parameter sets allow the analysis of hypotheses regarding dependencies between characteristics of the model outputs and its input variables. First, the dependencies between the experimentally controllable cuff length and inflation rate and the PAT/PTT response of the model are assessed. It is found that cuff length strongly determines the measured ΔPAT and $max|\Delta PAT_{total}|$. Figure 8 illustrates $max|\Delta PAT_{total}|$ as simulated via the model plotted with respect to corresponding cuff length for all parameter sets included in the analysis. A strong linear dependency is found with an $R^2 = 0.76$.

Figure 9 illustrates the expected changes in distal vasculature response to different cuff inflation rates; P_{eq} and $max|\Delta PTT_{distal}|$ are plotted with respect to cuff inflation rate. It is clear that slower inflations induce a more pronounced distal effect in P_{eq}. In terms of $max|\Delta PTT_{distal}|$, the inflation rate can alter the $max|\Delta PTT_{distal}|$ response by 1.5 millisecond; it is a small effect and it might be a challenge to measure.

3.2.2 BP value vs. distal response correlation

The sensitivity analysis (Table 3) reveals that the vasculature response to cuff inflation is considerably influenced by BP; namely, SBP and PP. We therefore investigate a measurement strategy based on the link between the BP value and the expected change in distal PTT, characterized by $max|\Delta PTT_{distal}|$. Figure 10 illustrates this connection - $max|\Delta PTT_{distal}|$ is plotted against the corresponding PP value in a) and against the respective PP and SBP values in b). It is observed that a linear model can be used to characterize this link with good accuracy, particularly in b), as an R^2 of 0.9237 is determined.

The PP value could therefore be used as an index for the expected change in distal ΔPTT during cuff inflation, in this way

TABLE 3 First (S1) and Total (ST) Order Indices from the sensitivity analysis.

Parameter	max|ΔPTTdistal|		max|ΔPATtotal|		max|ΔMAP|		Peq		max|ΔDBP|		ΔPTTonset	
	S1	ST	S1	ST	S1	ST	S1	ST	S1	ST	S1	ST
a	0.0283	0.0352	0.0243	0.0512	0	0	0.0008	0.0009	0	0.0003	0.0309	0.0317
c	0.0023	0.0038	0.0435	0.0881	0.0075	0.0079	0.0079	0.0082	0.0017	0.0021	0.0483	0.0540
Systolic Pressure	0.3519	0.3678	0.0331	0.0599	0.1495	0.1506	0.7729	0.7879	0.1588	0.1612	0.1490	0.1604
Pulse Pressure	0.5857	0.5974	0.0005	0.0138	0.8150	0.8161	0.0047	0.0047	0.8179	0.8190	0.7277	0.7468
Cuff Inflation Rate	0.0153	0.0160	0.0960	0.1330	0.0262	0.0275	0.1988	0.2145	0.0193	0.0214	0.0220	0.0313
Cuff Length	0	0	0.7577	0.7616	0	0	0	0	0	0	0	0

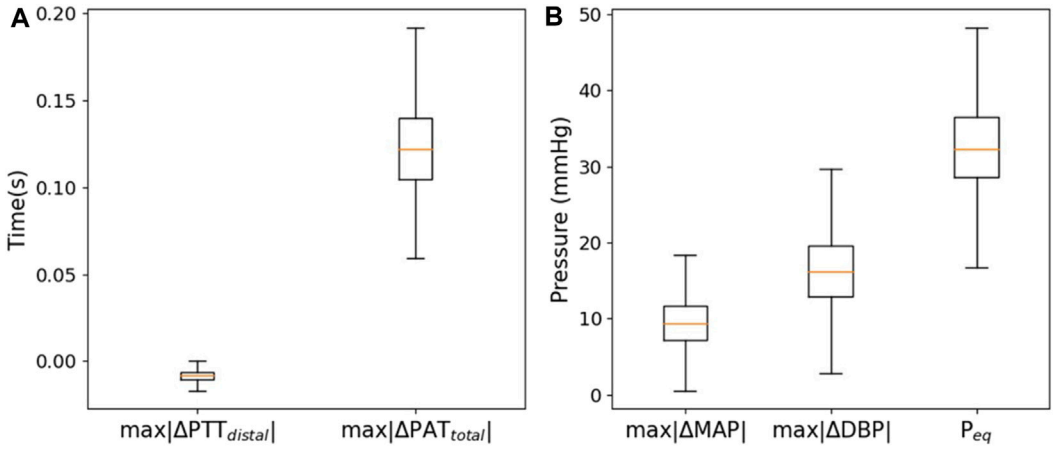

FIGURE 7
Boxplots of the generated **(A)** $max|\Delta PTT_{distal}|$ and $max|\Delta PAT_{total}|$, and **(B)** $max|\Delta MAP|$, $max|\Delta DBP|$, and P_{eq}.

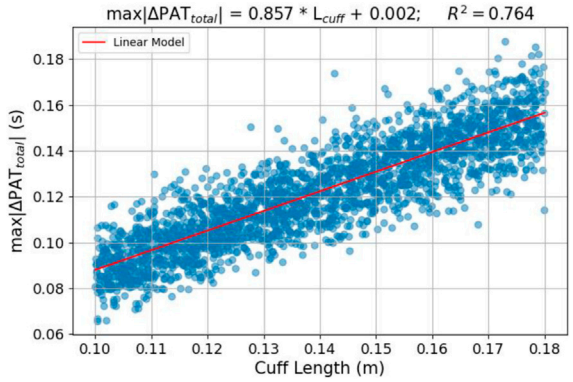

FIGURE 8
Relation between cuff length and $max|\Delta PAT_{total}|$ and cuff length–scatter plot and linear model fit of the sampled simulation sets.

allowing for improved estimation of brachial ΔPTT as measured non-invasively via ECG-PPG combination.

This relationship was also explored in the patient data. The results are present in Figure 11, showing the dependency between $max|\Delta PTT_{distal}|$ and PP as obtained from the recorded signals for the 4 evaluated subjects, S1, S2, S3, and S4. As shown, for S1, S2, and S4, lower PP is associated with lower magnitude measurements of $max|\Delta PTT_{distal}|$. This relationship, however, is not verified for S3, where the opposite seems to happen.

4 Discussion

4.1 Comparison between clinical data and model outputs

4.1.1 Distal BP

Clinical data is compared by visual inspection with simulated data generated with comparable BP and heart rate values and cuff inflation rate and length. We find that the model is an acceptable representation of the core hemodynamic processes happening in the portion of the arm distal to the cuff, which includes the increases in DBP and MAP and the decrease in SBP as observed in the clinical data. From a physiological point-of-view, the observed dynamics are sound. A number of measurement stages can be identified: 1) Cuff pressure value is below systemic venous pressure–no changes occur; 2) Cuff pressure increases beyond systemic venous pressure–vein collapses, flow out of the limb is stopped, buildup of blood begins to occur in the limb from the artery; 3) Cuff pressure approaches systemic systolic pressure–minimal amount of blood flows into the limb at each heart-beat, a decrease in the distal systolic pressure is observed; 4) Eventually, blood flow is stopped–arterial and venous pressures tend towards an equilibrium value. The arterial pressure decreases via an exponential decay function.

However, differences can be observed in amplitudes and timing of signal changes. For example, shifts in DBP and MAP happen earlier and with different magnitude in the model than in the patient data. Such discrepancies may arise from two reasons: 1) the model in this state is not sufficiently complex to represent the full dynamics, such as the venous return, and the outcomes will differ from the patient measurements regardless of the chosen parameters for the simulation; 2) model constraints or incorrect assumptions on parameter ranges, particularly when it comes to the arterial collapse parameters and the distal arm vascular factors (resistances and compliances), both of which were obtained from very limited patient data, may explain differences in morphology of the signals and could be corrected via additional clinical measurements.

4.1.2 PAT/PTT

Observation of ΔPAT and ΔPTT data from the simulation framework and the clinical dataset reveals differences concerning the response to cuff-induced variations in transmural pressure. In the example from Figure 5, we see similar qualitative behaviors observed in the simulation and clinical data, albeit with different timings and magnitudes. However, the model is not able to

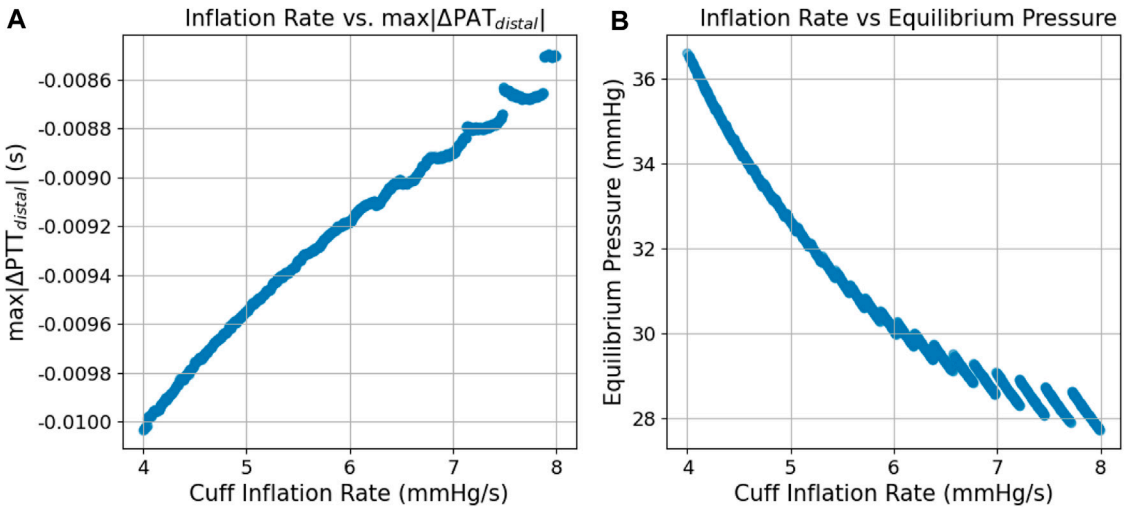

FIGURE 9
Scatter plots of the simulated relation between cuff inflation rate and **(A)** $max|\Delta PAT_{total}|$ and **(B)** P_{eq}.

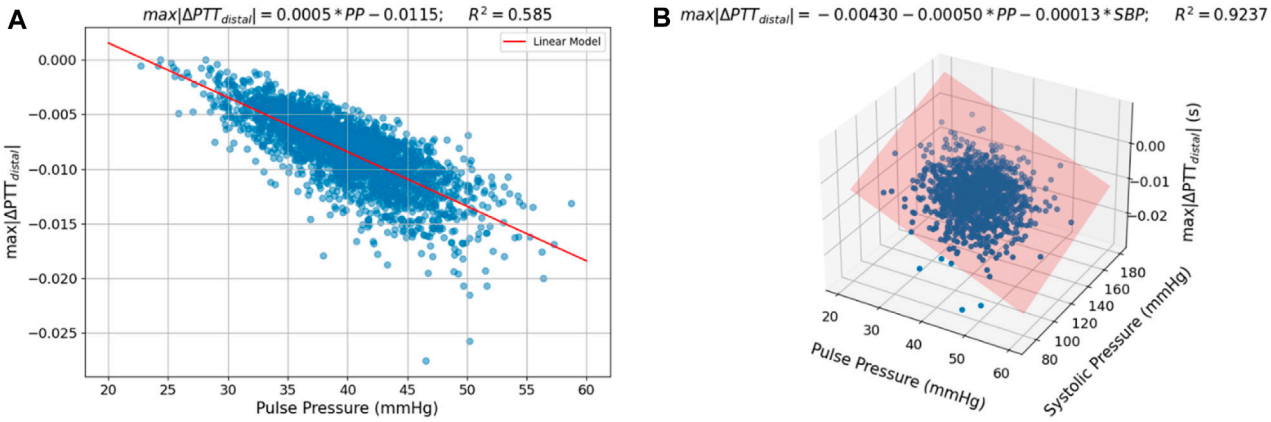

FIGURE 10
Scatter plots of the relation between **(A)** PP and $max|\Delta PTT_{distal}|$ and **(B)** PP and SBP and $max|\Delta PTT_{distal}|$ in the sampled parameter sets with a fitted linear model.

reproduce the clinical data even qualitatively at high cuff pressures, indicating either the need for model improvements and/or possibly inaccurate assumptions regarding constraints and parameter ranges. The PAT-BP calibration depends significantly on the correct understanding of these phenomena, towards accurate and personalized calibration procedure for cuffless and continuous BP measurement.

Upon observation of the complete set of clinical data samples, we find that the onset of the change in BP and the onset of the change in distal ΔPTT happens simultaneously, which is well depicted in the current model. Still, model improvements are needed to better characterize when the onset occurs with respect to cuff pressure. Finally, based on observations from the clinical data, these measurements require improved robustness given their low signal-to-noise ratio (SNR).

4.2 Sensitivity analysis

The results of the sensitivity analysis outline the major influence of SBP and PP. In contrast, the arterial collapse parameter *a* has only a relatively minute effect on the model's behavior. As a consequence, this parameter could probably be set to a constant value when using the Bayesian technique for BP inference as it was introduced by Bogatu et al. (2021). Parameter *c*, despite also not being much influent from a global perspective, still has a noticeable impact under constant cuff length and inflation rate, meaning it should be included in the current estimation framework.

Another relevant finding deals with the impact of cuff length and inflation rate, which both can be easily changed in practice, suggesting a point of optimization of the measurement procedure, discussed more in depth in the following section.

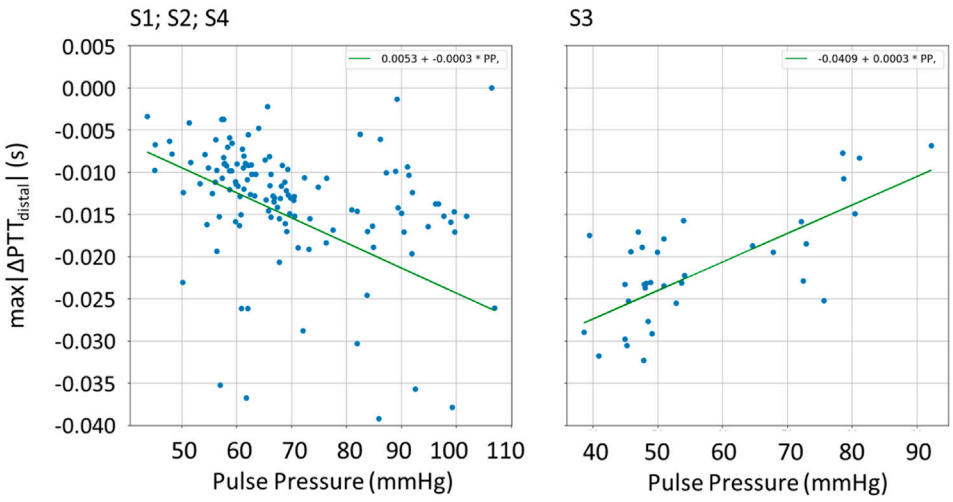

FIGURE 11
Scatter plot of the relation between PP and $max|\Delta PTT_{distal}|$ for the patients S1, S2, S3, and S4, with fitted linear function.

An important result is the global impact of the BP parameters (SBP and PP) across most characteristics of the vasculature response to cuff perturbation.

Overall, we find that the characteristics of the outputs of the simulations are all well determined by one to three parameters each, indicating possibilities for simplified modelling, yet to be verified with clinical data. These results also indicate which parameters we must keep in mind when optimizing particular aspects of the model. It should also be noted that despite the high non-linearity of the simulation, higher order interactions between the parameters are not significant which could be an implication of the relatively low complexity of the framework.

As shown in Figure 7 via boxplots, the results indicate that outputs of the model reflect a realistic behavior over the entire parameter space. This further establishes the model as a useful tool for the representation of the complex hemodynamic processes at play in a global sense, albeit with room for improvement as has been discussed in this work.

4.2.1 Effects of cuff length and inflation rate in the simulated response

The results from the analysis performed on the outputs from the sampled parameter sets reveal dependencies between the cuff length and inflation rate on the behavior of the model. Longer cuff lengths provide larger PAT changes in the course of the cuff inflation. This behavior can be interpreted physiologically–a longer cuff length covers a larger arterial segment. Along this arterial segment the artery is off-loaded and therefore the effective distally measured pulse wave velocity (PWV) is reduced (resulting in an increase in PAT). This result has practical implications on the PAT-BP calibration framework. A longer cuff could be used to increase the changes in PAT caused by the cuff inflation, improving the measurement's SNR.

Clear effects caused by the inflation rate are also visible–on faster inflations, the drop in ΔPTT that characterizes the distal filling effect is smaller, and the theoretical equilibrium pressure is also lower. It should be noted that the scale of these differences (~1 millisecond), despite small, is still significant within the scope of the distal ΔPTT measurements. This behavior is physiologically sound, as a slower inflation translates into more blood pumped in the limb (outflow of blood is stopped via brachial vein collapse, while inflow of blood via artery continues). In practice, slower inflation rates provide more PAT measurement points, as more heartbeats are included in the inflation time window, meaning that a greater amount of data is available for the Bayesian inference of the *a* and *c* parameters, potentially improving its accuracy. However, slower inflation rates also result in the amplification of the distal filling effect, adding uncertainty in a scenario where only non-invasive data sources would be available, which could have possible implications even in standard practice oscillometry. Further work is needed to find the optimal inflation rate for each case, balancing the amount of collected data with the intensity of these effects.

In addition, due to the impact this parameter has on the equilibrium pressure, being responsible for roughly 20% of its variability, its exploration can be useful towards the estimation of mean systemic filling pressure with the circuits time constant, as introduced by Bogatu et al. (2021). As a final remark on this topic, the sensitivity analysis points at cuff length and cuff inflation rate as important determinants of cuff-vasculature interaction, meaning further studies will account for this to observe cuff-induced changes more accurately in PAT/PTT/distal BP oscillations. In addition, parallel studies are seeking to achieve a more direct measurement of the arterial and venous parameters across a broader set of demographics via imaging, while also investigating the mechanisms of pressure transmission via the cuff at brachial site to obtain improved transmural pressure control (Bogatu et al., 2019).

4.2.2 BP value vs. distal response correlation

The results from the simulation indicate a strong linear relationship between distal ΔPTT and PP and SBP. This is an important finding, as PP could indicate the expected change in

distal ΔPTT during cuff inflation, therefore allowing for improved estimation of brachial ΔPTT as measured non-invasively via ECG-PPG combination.

When validating this relationship via patient data, we find that, for subjects S1, S2, and S4, an increase in PP is indeed indicative of an increase in $max|\Delta PTT_{distal}|$. However, this relationship does not hold for S3, where a decrease in $max|\Delta PTT_{distal}|$ is found with an increase in PP. This indicates limitations of the current simulation model. While at first sight, the model represents all signal characteristics well, the in-depth sensitivity analysis highlights specifically which aspects require further investigation via dedicated studies.

4.3 Limitations of the study and future research

There are several factors which may limit the model-clinical data comparison. For example, motion and breathing artifacts, the low number of beats recorded per inflation and the short length of the cuff all affect the SNR, impacting the assessment of amplitude and onset of the response. Nevertheless, qualitative comparisons between model output and measurements are possible. The cuff-induced vasculature response is observed to follow behaviors which are predicted via the model; the trends in signal changes induced via cuff inflation are accurately represented. A more quantitative, one-on-one model-clinical data assessment is not yet possible also due to the difficulty of obtaining all parameter values specific to one patient. However, alternative measurement modalities such as MRI (Bogatu et al., 2022) may enable such research in the future.

In addition, the current work is focused on response of vasculature to relatively short inflations. A more complete model-clinical data comparison relies on design of new clinical studies. This work contributes to planning of such new investigations and definition of study aims; e.g., the sensitivity analysis reveals how cuff length and duration of inflation are expected to impact vasculature response. It is necessary to conduct focused investigations regarding different cuff inflation strategies (e.g., response to inflation/deflation, inflation speed, cuff length, frequency of occlusions, site at which occlusion is applied). Also, the current study highlights inaccuracies in our understanding of the relationship between systemic BP and distal PTT; future studies can be specifically aimed towards the identified effects.

The model representing distal vasculature (Figure 2) also needs to be studied in the context of multi-segment models which describe the entire circulation (e.g., Avolio, 1980), in order to determine the extent to which reflection coefficients, cardiac output, contractility and general waveform characteristics impact the vasculature response to cuff occlusion.

While the dataset utilized for this work includes a substantial amount of cuff inflation segments (the core "unit" of our study), these were recorded from only 4 subjects, implying limited demographic variability, particularly in terms of cardiovascular health status. It should also be considered that the subjects were undergoing invasive surgical procedures and were anesthetized, two factors that may significantly impact their hemodynamic behavior.

Finally, despite popular and powerful, the variance-based Global Sensitivity Analysis has its weaknesses. An important assumption of the employed method is the independence between the parameters. We tackle this via efforts to create a representative and realistic parameter set. Nevertheless, improved analyses may be performed once a more complete understanding of the potential links between the individual model parameters is acquired.

5 Conclusion

Measuring the response of a BP surrogate (PAT/PTT) to transmural pressure modulation controlled via the cuff is a promising approach to improve robustness of calibrations of BP surrogates like PAT and PTT. A detailed understanding of the inflation process and its impact on the hemodynamics distal to the cuff provides insights on how to implement such a calibration strategy.

For that purpose, we investigate a "low complexity" simulation model and compare its performance with real clinical data. Despite its simplicity, the simulation model characteristics agrees qualitatively with experimental findings. The simultaneous onset of distal BP and PTT changes were found to be modelled correctly. However, improved understanding is needed to better model the onset and amplitude of vasculature responses to cuff inflation.

A sensitivity analysis showed that cuff length and cuff inflation rate–both of which can be easily changed in practice - have a significant effect on vasculature response to cuff inflation and may be explored to improve the PAT-BP calibration framework, recommended to be subject of further research. The link between BP and cuff-induced vascular response was also analyzed in depth. A particularly interesting correlation between BP and distal PTT has been revealed, paving the way towards improved BP surrogate calibration. However, a first check with a limited set of patient data gave inconsistent results to be investigated in detail, ideally with an expanded set of patients. While at first sight, the model represents all the signal characteristics well, the in-depth sensitivity analysis highlights specifically which aspects require further investigation via dedicated studies.

Concluding, the model under analysis serves as a valuable tool towards understanding of vascular dynamics occurring during cuff inflation. The model can facilitate the development of monitoring techniques that rely on cuff-based modulation of BP surrogates (PAT/PTT). This study highlighted specifically which effects are/are not well represented via the model, as well as it identified promising avenues via which further investigations can be conducted as well as suggesting improvements of the simulation model.

Data availability statement

The datasets presented in this article are not readily available due to privacy restrictions. Requests to access the datasets should be directed to laura.bogatu@philips.com.

Ethics statement

The studies involving human participants were reviewed and approved by the MEC-U ethical committee (St. Antonius Ziekenhuis, Koekoekslaan 1, 3430 EM Nieuwegein, NL. Approval W19.046). The study was conducted according to the guidelines of the Declaration of Helsinki. The patients/participants provided their written informed consent to participate in this study.

Author contributions

Conceptualization, investigation: JM, PC, JH, LS, JL, and LB; validation, writing—review and editing: all authors; methodology, resources: GN and IP; software: JL and LB.

Conflict of interest

Authors LB, LS, IP, JM are employed by the company Philips LTD.

The remaining authors declare that the research was conducted in the absence of any commercial or financial relationships that could be construed as a potential conflict of interest.

Publisher's note

All claims expressed in this article are solely those of the authors and do not necessarily represent those of their affiliated organizations, or those of the publisher, the editors and the reviewers. Any product that may be evaluated in this article, or claim that may be made by its manufacturer, is not guaranteed or endorsed by the publisher.

References

Alastruey, J., Parker, K. H., Peiró, J., and Sherwin, S. J. (2006). Can the modified allen's test always detect sufficient collateral flow in the hand? A computational study. *Comput. Methods Biomechanics Biomed. Eng.* 9 (6), 353–361. doi:10.1080/10255840600985477

Avolio, A. P. (1980). Multi-branched model of the human arterial system. *Med. Biol. Eng. Comput.* 18 (6), 709–718. doi:10.1007/BF02441895

Babbs, C. (2012). Oscillometric measurement of systolic and diastolic blood pressures validated in a physiologic mathematical model. *Biomed. Eng. online* 11, 56. doi:10.1186/1475-925X-11-56

Bank, A. J., Kaiser, D. R., Rajala, S., and Cheng, A. (1999). *In vivo* human brachial artery elastic mechanics: Effects of smooth muscle relaxation. *Circulation* 100 (1), 41–47. doi:10.1161/01.cir.100.1.41

Bogatu, L., Bresch, E., Muehlsteff, J., Smink, J., and Woerlee, P. (2019). "Insights into oscillometry: An experimental study for improvement of cuff-based blood pressure measurement Technology," in Annual International Conference of the IEEE Engineering in Medicine and Biology Society, Berlin, Germany, 23-27 July 2019, 7068–7071. doi:10.1109/EMBC.2019.8856994

Bogatu, L., Hoppenbrouwers, J., Van Den Bosch, H., Turco, S., Mischi, M., Schmitt, L., et al. (2022). "On the value of MRI for improved understanding of cuff-based oscillometric measurements," in Annual International Conference of the IEEE Engineering in Medicine and Biology Society, Glasgow, Scotland, United Kingdom, 11-15 July 2022, 2898–2901. doi:10.1109/EMBC48229.2022.9871137

Bogatu, L. I., Turco, S., Mischi, M., Schmitt, L., Woerlee, P., Bresch, E., et al. (2021). Modulation of pulse propagation and blood flow via cuff inflation-new distal insights *Sensors* 21 (16), 5593. doi:10.3390/s21165593

Bogatu, L. I., Turco, S., Mischi, M., Woerlee, P., Bouwman, A., Korsten, E. H. H. M., et al. (2020). A modelling framework for assessment of arterial compliance by fusion of oscillometry and pulse wave velocity information. *Comput. methods programs Biomed.* 196, 105492. doi:10.1016/j.cmpb.2020.105492

Bresch, E., Muehlsteff, J., and Schmitt, L. (2018). "Cuff-induced changes of pulse arrival time: Models and experimental results," in EMBEC & NBC 2017. EMBEC NBC 2017 2017. IFMBE Proceedings, Tampere, Finland, 11-15 June, 2017 (Singapore: Springer). doi:10.1007/978-981-10-5122-7_26

Chen, Y., Wen, C., Tao, G., Bi, M., and Li, G. (2009). Continuous and noninvasive blood pressure measurement: A novel modeling methodology of the relationship between blood pressure and pulse wave velocity. *Ann. Biomed. Eng.* 37 (11), 2222–2233. doi:10.1007/s10439-009-9759-1

Drzewiecki, G., Hood, R., and Apple, H. (1994). Theory of the oscillometric maximum and the systolic and diastolic detection ratios. *Ann. Biomed. Eng.* 22 (1), 88–96. doi:10.1007/BF02368225

Gelman, S., Warner, D., and Warner, M. (2008). Venous function and central venous pressure: A physiologic story. *Anesthesiology* 108 (4), 735–748. doi:10.1097/ALN.0b013e3181672607

Gesche, H., Grosskurth, D., Küchler, G., and Patzak, A. (2012). Continuous blood pressure measurement by using the pulse transit time: Comparison to a cuff-based method. *Eur. J. Appl. physiology* 112 (1), 309–315. doi:10.1007/s00421-011-1983-3

Herman, J., and Usher, W. (2017). SALib: An open-source Python library for sensitivity analysis. *J. Open Source Softw.* 2 (9), 97. doi:10.21105/joss.00097

Iwanaga, T., Usher, W., and Herman, J. (2022). Toward SALib 2.0: Advancing the accessibility and interpretability of global sensitivity analyses. *Socio-Environmental Syst. Model.* 4, 18155. doi:10.18174/sesmo.18155

Panula, T., Sirkia, J. P., Wong, D., and Kaisti, M. (2023). Advances in non-invasive blood pressure measurement techniques. *IEEE Rev. Biomed. Eng.* 16, 424–438. doi:10.1109/RBME.2022.3141877

Pilz, N., Patzak, A., and Bothe, T. L. (2023). The pre-ejection period is a highly stress dependent parameter of paramount importance for pulse-wave-velocity based applications. *Front. Cardiovasc. Med.* 10, 1138356. doi:10.3389/fcvm.2023.1138356

Raju, S. (2019). "Venous hemodynamics," in *Atlas of endovascular venous surgery*. Editor J. I. Almeida. Second Edition (Amsterdam: Elsevier), 21–36. doi:10.1016/B978-0-323-51139-1.00002-4

Saltelli, A. (2002). Making best use of model evaluations to compute sensitivity indices. *Comput. Phys. Commun.* 145, 280–297. doi:10.1016/S0010-4655(02)00280-1

Saltelli, A., Tarantola, S., Campolongo, F., and Ratto, M. (2004). "Sensitivity analysis in practice: A guide to assessing scientific models," in *Halsted press eBooks* (Ultimo: Halsted Press). doi:10.1002/0470870958

Seagar, A. D., Gibbs, J. M., and Davis, F. M. (1984). Interpretation of venous occlusion plethysmographic measurements using a simple model. *Med. Biol. Eng. Comput.* 22 (1), 12–18. doi:10.1007/BF02443739

Smink, J., Bogatu, L., Muehlsteff, J., and Bresch, E. (2019). Dynamic MRI visualization of the brachial artery during upper arm air cuff inflations. In Proceedings of the ISMRM 27th Annual Meeting & Exhibition. 11-16 May 2019, Montréal, QC, Canada. 2071.

Sobol, I. (1993). Sensitivity analysis for non-linear mathematical models. *Math. Model. Comput. Exp. (Engl. Transl.)* 1, 407–414.

Sobol, I. (2001). Global sensitivity indices for nonlinear mathematical models and their Monte Carlo estimates. *Math. Comput. Simul.* 55 (1–3), 271–280. doi:10.1016/S0378-4754(00)00270-6

Solà, J., and Delgado-Gonzalo, R. (2019). *Handbook of cuffless blood pressure monitoring*. Cham, Switzerland: Springer.

Su, P., Ding, X., Zhang, Y., Li, Y., and Zhao, N. (2018). "Predicting blood pressure with deep bidirectional LSTM network, arXiv preprint," in 2018 IEEE EMBS International Conference on Biomedical & Health Informatics (BHI), Las Vegas, Nevada, USA, 4-7 March 2018, 323.

Vincent, J. L., Rhodes, A., Perel, A., Martin, G. S., Della Rocca, G., Vallet, B., et al. (2011). Clinical review: Update on hemodynamic monitoring–a consensus of 16. *Crit. care (London, Engl.* 15 (4), 229. doi:10.1186/cc10291

Williams, B. W., Mancia, G., Spiering, W., E, A. R., Azizi, M., Burnier, M., et al. (2018). 2018 ESC/ESH Guidelines for the management of arterial hypertension. *Eur. Heart J.* 39 (33), 3021–3104. doi:10.1093/eurheartj/ehy339

Yan, Y. H., and Zhang, Y. (2007). "A novel calibration method for noninvasive blood pressure measurement using pulse transit time," in 2007 4th IEEE/EMBS International Summer School and Symposium on Medical Devices and Biosensors, Cambridge, UK, 19-22 August 2007. doi:10.1109/issmdbs.2007.4338283

Yoon, Y. Z., Kang, J. M., Kwon, Y., Park, S., Noh, S., Kim, Y., et al. (2018). Cuff-less blood pressure estimation using pulse waveform analysis and pulse arrival time. *IEEE J. Biomed. Heal Inf.* 22, 1068–1074. doi:10.1109/jbhi.2017.2714674

frontiers | Frontiers in Physiology

TYPE Original Research
PUBLISHED 19 July 2023
DOI 10.3389/fphys.2023.1191272

OPEN ACCESS

EDITED BY
Panicos Kyriacou,
City University of London,
United Kingdom

REVIEWED BY
Anton R. Kiselev,
National Research Center for Preventive Medicine, Russia
James Michael May,
City University of London,
United Kingdom

*CORRESPONDENCE
Dejan Žikić,
dzikic@gmail.com

RECEIVED 21 March 2023
ACCEPTED 10 July 2023
PUBLISHED 19 July 2023

CITATION
Djurić B, Žikić K, Nestorović Z, Lepojević-Stefanović D, Milošević N and Žikić D (2023), Using the photoplethysmography method to monitor age-related changes in the cardiovascular system.
Front. Physiol. 14:1191272.
doi: 10.3389/fphys.2023.1191272

Using the photoplethysmography method to monitor age-related changes in the cardiovascular system

Biljana Djurić[1], Katarina Žikić[2], Zorica Nestorović[3], Danijela Lepojević-Stefanović[4], Nebojša Milošević[3] and Dejan Žikić[3]*

[1]Institute of Physiology, Faculty of Medicine, University of Belgrade, Belgrade, Serbia, [2]Faculty of Physics, University of Belgrade, Belgrade, Serbia, [3]Institute of Biophysics, Faculty of Medicine, University of Belgrade, Belgrade, Serbia, [4]Division of Cardiology, Department of Internal Medicine, Belgrade, Serbia

Introduction: Aging is a physiological process characterized by progressive changes in all organ systems. In the last few decades, the elderly population has been growing, so the scientific community is focusing on the investigation of the aging process, all in order to improve the quality of life in elderly. One of the biggest challenges in studying the impact of the aging on the human body represents the monitoring of the changes that inevitably occur in arterial blood vessels. Therefore, the medical community has invested a great deal of effort in studying and discovering new methods and tools that could be used to monitor the changes in arterial blood vessels caused by the aging process. The goal of our research was to develop a new diagnostic method using a photoplethysmographic sensor and to examine the impact of the aging process on the cardiovascular system in adults. Long-term recorded arterial blood flow waveforms were analyzed using detrended fluctuation analysis.

Materials and Methods: The study included 117 respondents, aged 20–70 years. The waveform of the arterial blood flow was recorded for 5 min, with an optical sensor placed above the left common carotid artery, simultaneously with a single-channel ECG. For each cardiac cycle, the blood flow amplitude was determined, and a new time series was formed, which was analyzed non-linearly (DFA method). The values of the scalar coefficients α_1 and α_2, particularly their ratio (α_1/α_2) were obtained, which were then monitored in relation to the age of the subjects.

Result: The values of the scalar ratio (α_1/α_2) were significantly different between the subjects older and younger than 50 years. The value of the α_1/α_2 decreased exponentially with the aging. In the population of middle-aged adults, this ratio had a value around 1, in young adults the value was exclusively higher than 1 and in older adults the value was exclusively lower than 1.

Conclusion: The results of this study indicated that the aging led to a decrease in the α_1/α_2 in the population of healthy subjects. With this non-invasive method, changes in the cardiovascular system due to aging can be detected and monitored.

KEYWORDS

photoplethysmography, sensor, cardiovascular age, blood flow waveform, detrended fluctuation analysis

1 Introduction

Human life has evidently prolonged over the last 50 years, but cardiovascular diseases are still the leading cause of mortality in the modern world (Rudnicka et al., 2020; World Health Organization, 2021). The research that addresses the causes of the disease, age-related changes of blood vessels and the analysis of blood flow waveforms are highly important for patients benefit (Gavrilov and Gavrilova, 2015; Van Leeuwen et al., 2019; Rudnicka et al., 2020).

The cardiovascular system changes through years, particularly it changes its biophysical properties: increase in arterial blood pressure and pulse wave velocity, as well as the appearance of wave reflection (Parikh et al., 2016; Guzik and Touyz, 2017; Allen et al., 2020). Moreover, according to some cardiologists, the older your cardiovascular system is, the older you are (Dantas et al., 2012; Gopcevic et al., 2021; Hamczyk et al., 2022).

The proper medical diagnosis as well as the cardiovascular research, depends from biophysical understanding of arterial hemodynamics, especially from pressure and blood flow waveforms conditions (Willemet and Alastruey, 2015; Jozwiak et al., 2018). More precisely, the blood viscosity, elasticity of the arterial wall, the thickness of the wall, the internal pressure, the blood density, the influence of gravity and body position can be recognized as main biophysical characteristics of blood propagation in vessel (Secomb, 2016; Žikić et al., 2019).

Pulse wave velocity (PWV) measurement is still the primary method for assessing the age of arteries in clinical research (Sutton-Tyrrell et al., 2005; Reference Values for Arterial Stiffness' Collaboration, 2010; Diaz et al., 2018). Previous studies show that the PWV depends on the elasticity of the artery wall, wall thickness, wall diameter and blood density (Avolio, 2013; Messas et al., 2013; Ma et al., 2018).

The main goal of the present study is to find a new biophysical model that could monitor the aging of the cardiovascular system. This idea was created by following the arterial blood flow, with non-invasive measurement of the arterial blood flow waveform. There are two basic techniques of non-invasive blood flow measurement: ultrasonographic and optical. The first method is very sensitive (depending on the experience and skills of medical professionals) and cannot provide reliable signals for wave analysis (Srámek et al., 2000; Loizou, 2014). On the other hand, the second method is independent from the muscle's activity, although there is a problem with the signal calibration (Žikić, 2008; Djuric et al., 2017).

Although the main goal of this study is the analysis of the distribution of wave blood flow with age, the comparison of the mean values of scalar coefficients in three selected age groups can be considered as a secondary goal. Nevertheless, although implicitly presented, the essential goal of this study is to present a non-invasive method of imaging arterial blood flow by photoplethysmography method. In addition, a mathematical model that follows this kind of signal analysis (*Detrended fluctuation analysis - DFA*) can reliably estimate the arterial blood flow waveform in the cardiovascular system during aging.

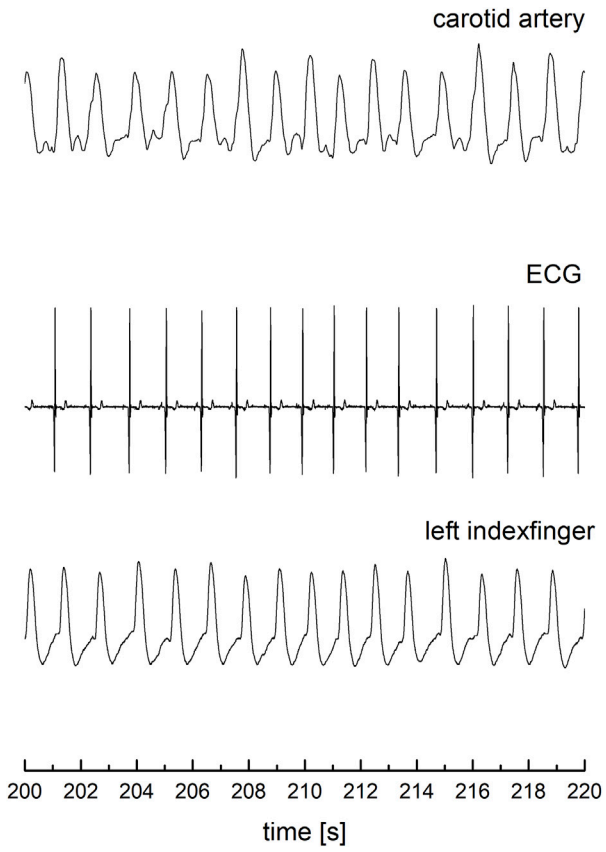

FIGURE 1
Recorded ECG and blood flow waveforms from the left index finger and the carotid artery.

2 Materials and methods

2.1 Subject, groups, and physical examination

The study was conducted at the Faculty of Medicine, University of Belgrade (Serbia), from September 2019 to April 2021 at the Institute of Medical physiology and the Institute of Biophysics. The study was carried out following the recommendations of the Helsinki Committee, which is confirmed by the decision of the Ethics Committee of the Faculty of Medicine.

In total, 117 healthy subjects (58 male and 59 female), aged between 20 and 70 years, have participated in this study. Based on the age in which the frequency of vascular disease symptoms increases markedly, the subjects were divided into two groups (Lloyd-Jones et al., 2006; Wang et al., 2020; Mohanty et al., 2021): younger than 50 years (82) and older than 50 years (35). In addition, subjects have been divided into three age groups (Petry, 2002; Thomas et al., 2018) according to the demographic characteristics. The first group was the younger adults (53) less than 35 years, then middle-aged adults (44) from 35 to 55 years. Finally, the third group was older adults (22) higher than 55 years.

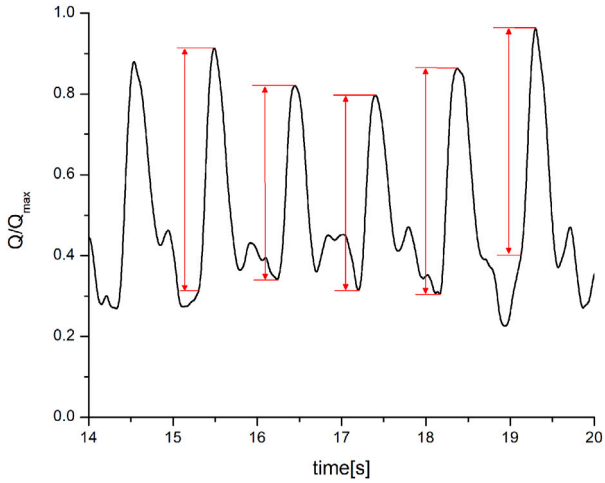

FIGURE 2
Determination of the maximal and minimal value of the arterial blood flow waveform (Q/Q_{max}–flow amplitude normalized in relation to the maximum amplitude.

2.2 Signal recording

For the purposes of this research, the photoplethysmography sensor designed and developed earlier (Žikić, 2008), has been used for continuous and non-invasive recording of the arterial blood flow waveform (Djuric et al., 2017). The sensor was designed in order to eliminate artifacts that were occurring during the phases of respiration, caused by the contraction of the respiratory muscles. In the improved design, the light source was two series-connected IR diodes, and the detector was three series-connected NPN phototransistors. Three serially connected silicon NPN phototransistors were used as light intensity change detectors (Djuric et al., 2017).

The photoplethysmography sensor was placed and secured over the left common carotid artery (Vlachopoulos et al., 2010). Synchronized with the recording of carotid arterial blood flow waveform, a single-lead channel ECG was also recorded, using three electrodes on the surface of the chest, as well as arterial blood flow waveform on the left index finger in order to detect artifacts due to movement of the neck, swallowing or breathing. (Figure 1). Recordings were performed in the supine position for 5–7 min, in order to provide a long-lasting signal suitable for further mathematical analysis (Figure 1).

All the signals from the sensor module and ECG device were digitized in 12-bit resolution (PCI-20428W, data-acquisition board, United States) with a sampling frequency of 1 Khz. After smoothing and normalization of the signal (by dividing the whole signal by the maximum measured value - Q/Qmax), the amplitudes of the arterial blood flow waveform were determined for each cardiac cycle, for a minimum of 256 heartbeats. Amplitudes were calculated as the difference between the maximal reached value of the waveform and the foot-of-the-wave (Figure 2).

Based on the obtained difference values, a new signal, amplitude in function of the heartbeat number N, was constructed (Figure 3).

2.3 Data processing

For each subject, the recording of the arterial flow was analyzed by determining the amplitudes (z_i) for each heartbeat (Peng et al.,

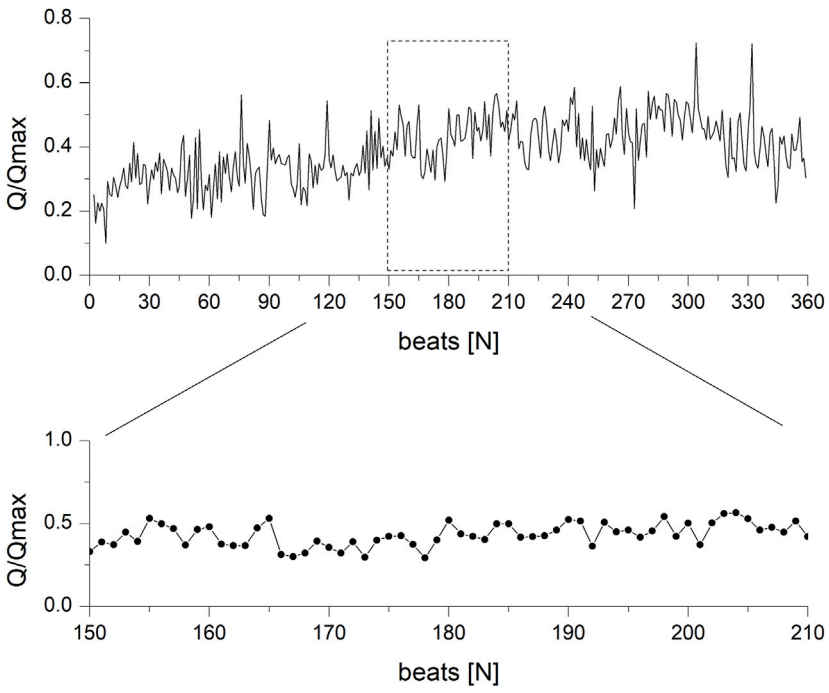

FIGURE 3
Amplitude of the arterial blood flow waveform in the function of the number of heartbeats.

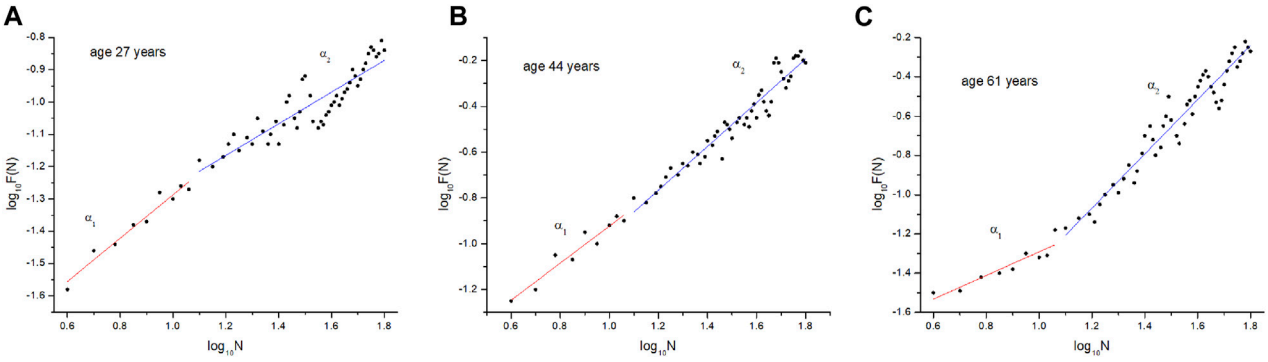

FIGURE 4
Results of arterial blood-flow waveform fluctuations in young **(A)**, middle-aged **(B)**, and elderly **(C)** subject.

TABLE 1 The number of subjects and the corresponding α_1/α_2 statistical parameters (mean, standard deviation *SD*, standard error *SE* and range) in three age groups (A, B and C). Symbol * indicates level of statistical difference between groups.

Group	A	B	C
Number (n)	53	44	22
Mean	1.24	0.87 ***(A)	0.67***(A,B)
SD	0.19	0.18	0.09
SE	0.03	0.03	0.02
Range	0.69	0.94	0.33

1995). Then, on the entire signal, the extracted amplitudes were made as a function of the number of beats (n_i), i.e., $z_i = f(n_i)$. The sequence was further analyzed using the nonlinear dynamics technique, applied to physiological signals, i.e., detrended fluctuation analysis or DFA (Peng et al., 1995; Hausdorff et al., 1996). According to this technique the sequence $y(k)$ was formed (Hardstone et al., 2012) and divided into segments of non-overlapping length n). In each segment the linear local trend ($y_n(k)$) was calculated (Peng et al., 1995; Hardstone et al., 2012).

In the next step, the root mean square of the fluctuations in series y_n on all N segments of length n was calculated (Peng et al., 1995; Bryce and Sprague, 2012). In case when the relationship $F(n)$ vs n is some sort of power function (for instance, const·n^{α}) the graph is shown by a straight line whose direction coefficient is α.

The DFA method applied in this way defines two coefficients: α_1 and α_2. The first refers to correlations over short distances, while the second defines correlations over long temporal distances. In this study, α_1 is the slope of the linear fit between 4 and 15 beats, while α_2 is the slope of the linear fit more than 15 heart beats (Figure 4). At the end, the ratio of the slope α_1/α_2, as the result of the entire signal analysis, was established.

2.4. Statistics

Monitoring and signal registration was performed using the LabView software (National Instruments Corp. United States).

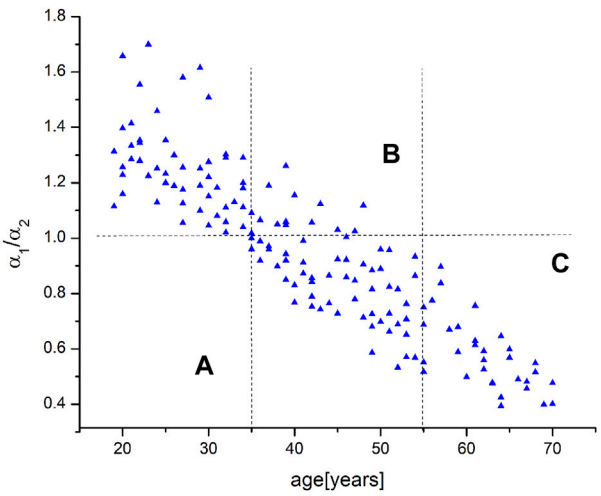

FIGURE 5
The relationship between α_1/α_2 and the age of all subjects who participated in the study. The vertical lines define intervals in the three age groups **(A–C)**.

Further processing of the recorded signal and graphical presentation was done in OriginPro 8.0 (OriginLab). At the end, the statistical evaluation of the measured values was carried out using SPSS 26 (IBM, United States, demo version).

Taking into account the number of values within each age group (Table 1), the statistical evaluation between the mean values was performed using the *t*-test for independent samples (A-B), as well as the Mann-Whitney test between two pairs (A-C and B-C).

3 Results

The DFA analysis was performed after several subjects were measured for over 20 min in order to obtain 1,024 points. However, the preliminary results suggested that the time interval could be shortened for two reasons: 1) after 7–8 min of recording the subjects became uncomfortable and started moving their head/neck

involuntarily, and 2) the same outcome (in the DFA analysis) were obtained with 256 points. Thus, the measurement session lasted 5 min.

Figure 5 shows the distribution of the α_1/α_2 with age, from 20 to 70 years. The vertical lines show the distribution of the α_1/α_2 values across the three age groups of subjects (A, B and C). Qualitative analysis of Figure 5 shows that in the first group, the values of the α_1/α_2 are greater than 1, i.e., they range from 1 to 1.7. At the same time, it can be seen that the α_1/α_2 values for group 2 oscillate around the number 1 (from 0.5 to 1.3). It is possible to conclude that the majority of the α_1/α_2 are below 1, but this was only the case of this study. Finally, the third group of subjects reliably has values of the α_1/α_2 less than 1 (between 0.4 and 1.0).

The next step involved finding the function that most accurately fits the data. The resulting distribution was fitted with four functions: linear ($-a\cdot(\text{age}) + b$), logarithmic ($a\cdot\ln(\text{age}) + b$), exponential ($a\cdot\exp(-b\cdot\text{age})$), and polynomial ($a\cdot(\text{age})^2 - b\cdot(\text{age}) + c$). The quality of fitting was examined by comparing the correlation coefficients R) and comparing the residuals in relation to the fitted curve. The results showed that the polynomial residuals adjust the curve to the data more than they fit it. On the other hand, the exponential function has the highest R (0.841) in comparison with the logarithmic and linear functions (0.813 and 0.809, respectively). Thus, the nature of the distribution should be presented with the exponential function.

Table 1 shows the calculated α_1/α_2 values of the statistical parameters (mean value, standard deviation, standard error, and range) for the three age groups of the subjects. The symbol n indicates the number of subjects in each group, making it clear that comparison of means requires the use of nonparametric statistics. Considering the number of samples, the statistical analysis of the mean values of the first and second groups was performed using the t-test for two independent samples. On the other hand, the comparison of mean values between other pairs (A-C and B-C) was carried out using the Mann-Whitney test. The results showed that the mean values of all pairs showed a convincing statistical significance ($p < 0.001$, Table 1).

4 Discussion

The morphological and functional changes that are occurring in the cardiovascular system during aging are known as the Vascular Health Triad (Townsend et al., 2015). These processes lead to the appearance of arteriosclerosis and atherosclerosis (Diaz et al., 2018). To be precise, an increase in the stiffness of the wall leads to an increase in arterial blood pressure and pulse wave velocity (Ranadive et al., 2021). DFA of signal fluctuation represents the analysis of self-similarity of the fractal structure in relation to the signal as a whole (Peng et al., 1995). This kind of analysis is applicable to various physiological parameters. By using DFA of signal fluctuations, there is a possibility of finding the long-term correlations within the chaotic values in physiological signals (Esen et al., 2009).

Previous studies have shown that the DFA is primarily used in heart-rate analysis (Peng et al., 1995; De Souza et al., 2014; Mizobuchi et al., 2021). However, the existence of amplitude fluctuations for certain parameter, in relation to the time domain, has been only demonstrated in the analysis of continuous EEG recordings (Hardstone et al., 2012; De Souza et al., 2014; Facioli et al., 2021; Mizobuchi et al., 2021). The amplitude of the recorded signal shows large fluctuations (Eke et al., 2002), but the amplitude values can be characterized by the scalar coefficient α). The value of an α value higher than 0.5 shows a positive correlation in fluctuation of the recorded signal. Conversely, the value smaller than 0.5 indicates the absence of correlation, i.e., the existence of small fluctuations (Hardstone et al., 2012).

The present study examines the possibilities of using the DFA technique in the analysis of fluctuations in the amplitude of blood pulse waves. To the best of our knowledge, no study has been reported that analyzes the amplitude fluctuations of arterial blood flow waveforms of subjects of different ages. Therefore, this study represents a novelty in the application of DFA, but considering the number of subjects, the study is still only preliminary. In addition, the study included subjects of different ages (between 20 and 70 years of age) without heart rhythm abnormalities and other cardiac or vascular diseases. The subjects were classified into three age groups (Section 2.1) mostly for the reason of indirectly examining the difference in the morphology of the artery walls (Djuric, 2022). Namely, the difference in the wall morphology with age was quantified through the difference in the fluctuations of the amplitude of the blood flow waveform (Djuric, 2022).

The quantification of the fluctuations of the amplitudes of arterial blood flow waveform was performed by determining the scalar coefficients (α_1 and α_2) over the years, or more precisely their ratio (α_1/α_2). The results of this study clearly show that the ratio of the scalar coefficients decreases with age (Figure 4). This distribution was best represented by the exponential function. Further analysis of the distribution showed that the selected age groups differed significantly from each other (Table 1). In this study, a significant difference between subjects over 55 years (Group C), both in relation other groups (Group A and B) could be seen as expected result. However, the highly significant difference between Group B and C could be seen as a novelty. Subjects with higher values of α_1/α_2 demonstrated the existence of a correlation in waveform amplitude through the entire photoplethysmography signal (Eke et al., 2000; Eke al., 2002; Hardstone et al., 2012). Large fluctuations in the amplitude are most likely occurring due to the high elasticity of the arterial vessels (Zarrinkoob et al., 2016).

Further, the decrease of the α_1/α_2 with age may indicate a decrease in the fluctuation of the waveform amplitude, and this probably occurs because of changes in the elasticity of the wall of the arterial blood vessel (Mitchel, 2021). Finally, observing the distribution of the α_1/α_2 in relation to the age, and comparing the values between different age groups, we can conclude that the mentioned ratio represents a sensitive marker for assessing the age of the vascular system in the population of healthy subjects.

Assessing the age of the cardiovascular system is very difficult to determine with non-invasive measurement methods. With aging, changes occur in the walls of blood vessels, which will certainly affect the waveform of the blood flow. Validation of this method is very difficult. We plan to repeat the measurement of the same subjects after a shorter period and compare the results of the analysis. Another limitation of the method is the impact of hypertension and blood viscosity on the blood flow waveform. These parameters will be included in further studies.

5 Conclusion

Cardiovascular diseases are the leading cause of mortality in Serbia and the rest of the world (Institute of Public Health of Serbia, 2020;

National Center for Health Statistics, 2021; Tsao et al., 2023). The research which addresses age-related changes of blood vessels, particularly the analysis of blood flow waveforms, is highly important for patients' benefit. This becomes especially important knowing that in the last 20 years the number of old people has been growing.

Reviewing the present literature (Charlton et al., 2021), we did not notice a study that analyzes the long-term arterial blood flow waveform within different age ranges. It is usually studied by ultrasonographic analysis of blood flow, so this study represents a novelty by finding that blood flow waveforms recorded by photoplethysmography based sensor can be used for the research of the cardiovascular system aging. However, considering the number of subjects and their age range, we perceive this study as preliminary. As such, this study registers an exponential decrease in the ratio of the scalar coefficients with age and detects differences between the mean values of their ratio in the three selected age groups. In addition, our analysis could indicate certain changes in the cardiovascular system that cannot be detected by standard non-invasive methods.

Therefore, we believe that our new analysis of wave propagation of blood may be very useful for indication of cardiovascular diseases. Our analysis method could contribute to faster diagnosis and adequate therapeutic decision for a better quality of life for older people (American Heart Association, 2019; Lindbohm et al., 2019; Neumann et al., 2022).

Data availability statement

The original contributions presented in the study are included in the article/Supplementary Material, further inquiries can be directed to the corresponding author.

Ethics statement

The studies involving human participants were reviewed and approved by Ethics Committee of the Faculty of Medicine (Permit Number: 1550/IX-8). The patients/participants provided their written informed consent to participate in this study.

Author contributions

BD and DL-S performed all the examination and signal recordings on the subjects. DŽ and KŽ have developed the improved version of photoplethysmograph sensor. DŽ, KŽ, NM, and ZN performed the DFA analysis. NM, DŽ, and BD performed statistical analysis. DŽ initiated, conceived, and supervised the project. All authors contributed to the article and approved the submitted version.

Funding

This study was supported by the Ministry of Education and Science of the Republic of Serbia Grant 200110.

Conflict of interest

The authors declare that the research was conducted in the absence of any commercial or financial relationships that could be construed as a potential conflict of interest.

Publisher's note

All claims expressed in this article are solely those of the authors and do not necessarily represent those of their affiliated organizations, or those of the publisher, the editors and the reviewers. Any product that may be evaluated in this article, or claim that may be made by its manufacturer, is not guaranteed or endorsed by the publisher.

References

Allen, J., O'Sullivan, J., Stansby, G., and Murray, A. (2020). Age-related changes in pulse risetime measured by multi-site photoplethysmography. *Physiol. Meas.* 41 (7), 074001. doi:10.1088/1361-6579/ab9b67

American Heart Association (2019). Heart-Health screenings. Available at: https://www.heart.org/en/health-topics/consumer-healthcare/what-is-cardiovascular-disease/heart-health-screenings.

Avolio, A. (2013). Arterial stiffness. *Pulse (Basel)* 1 (1), 14–28. doi:10.1159/000348620

Bryce, R. M., and Sprague, K. B. (2012). Revisiting detrended fluctuation analysis. *Sci. Rep.* 2, 315. doi:10.1038/srep00315

Charlton, P. H., Paliakaitė, B., Pilt, K., Bachler, M., Zanelli, S., Kulin, D., et al. (2021). Assessing hemodynamics from the photoplethysmogram to gain insights into vascular age: A review from VascAgeNet. *Am. J. Physiol. Heart Circ. Physiol.* 322, H493–H522. doi:10.1152/ajpheart.00392.2021

Dantas, A. P., Jiménez-Altayó, F., and Vila, E. (2012). Vascular aging: Facts and factors. *Front. Physiol.* 10 (3), 325. doi:10.3389/fphys.2012.00325

De Souza, A. C., Cisternas, J. R., De Abreu, L. C., Roque, A. L., Monteiro, C. B., Adami, F., et al. (2014). Fractal correlation property of heart rate variability in response to the postural change maneuver in healthy women. *Int. Arch. Med.* 7, 25. doi:10.1186/1755-7682-7-25

Diaz, A., Tringler, M., Wray, S., Ramirez, A. J., and Cabrera Fischer, E. I. (2018). The effects of age on pulse wave velocity in untreated hypertension. *J. Clin. Hypertens. (Greenwich).* 20 (2), 258–265. doi:10.1111/jch.13167

Djuric, B. (2022). Examination of the aging process influence on the cardiovascular system by the arterial blood flow waveform analysis. dissertation. Belgrade, Serbia: University of Belgrade.

Djurić, B., Suzić, S., Stojadinović, B., Nestorović, Z., Ivanović, M., Suzić-Lazić, J., et al. (2017). An improved design of optical sensor for long-term measurement of arterial blood flow waveform. *Biomed. Microdevices* 19 (3), 48. doi:10.1007/s10544-017-0196-x

Eke, A., Hermán, P., Bassingthwaighte, J. B., Raymond, G. M., Percival, D. B., Cannon, M., et al. (2000). Physiological time series: Distinguishing fractal noises from motions. *Pflugers Arch.* 439 (4), 403–415. doi:10.1007/s004249900135

Eke, A., Herman, P., Kocsis, L., and Kozak, L. R. (2002). Fractal characterization of complexity in temporal physiological signals. *Physiol. Meas.* 23 (1), R1–R38. doi:10.1088/0967-3334/23/1/201

Esen, F., Aydin, G. S., and Esen, H. (2009). Detrended fluctuation analysis of laser Doppler flowmetry time series. *Microvasc. Res.* 78 (3), 314–318. doi:10.1016/j.mvr.2009.07.005

Facioli, T. P., Philbois, S. V., Gastaldi, A. C., Almeida, D. S., Maida, K. D., Rodrigues, J. A. L., et al. (2021). Study of heart rate recovery and cardiovascular autonomic modulation in healthy participants after submaximal exercise. *Sci. Rep.* 11 (1), 3620. doi:10.1038/s41598-021-83071-w

Gavrilov, L. A., and Gavrilova, N. S. (2015). New developments in the biodemography of aging and longevity. *Gerontology* 61 (4), 364–371. doi:10.1159/000369011

Gopcevic, K. R., Gkaliagkousi, E., Nemcsik, J., Acet, Ö., Rosa, M., Bruno, R. M., et al. (2021). Pathophysiology of circulating biomarkers and relationship with vascular aging: A review of the literature from VascAgeNet group on circulating biomarkers, European cooperation in science and technology action 18216. *Front. Physiol.* 12, 789690. doi:10.3389/fphys.2021.789690

Guzik, T. J., and Touyz, R. M. (2017). Oxidative stress, inflammation, and vascular aging in hypertension. *Hypertension* 70 (4), 660–667. doi:10.1161/HYPERTENSIONAHA.117.07802

Hamczyk, M. R., Nevado, R. M., Barettino, A., Fuster, V., and Andrés, V. (2022). Biological versus chronological aging: JACC focus seminar. *J. Am. Coll. Cardiol.* 75 (8), 919–930. doi:10.1016/j.jacc.2019.11.062

Hardstone, R., Poil, S. S., Schiavone, G., Jansen, R., Nikulin, V. V., Mansvelder, H. D., et al. (2012). Detrended fluctuation analysis: A scale-free view on neuronal oscillations. *Front. Physiol.* 3, 450. doi:10.3389/fphys.2012.00450

Hausdorff, J. M., Purdon, P., Peng, C. K., Ladin, Z., Wei, J. Y., and Goldberger, A. L. (1996). Fractal dynamics of human gait: Stability of long-range correlations in stride interval fluctuations. *J. Appl. Physiol.* 80, 1448–1457. doi:10.1152/jappl.1996.80.5.1448

Institute of Public Health of Serbia (2020). Incidence and mortality of acute coronary syndrome in Serbia. Available at: https://www.batut.org.rs/download/publikacije/AKS2019.pdf.

Jozwiak, M., Monnet, X., and Teboul, J. L. (2018). Pressure waveform analysis. *Anesth. Analg.* 126 (6), 1930–1933. doi:10.1213/ANE.0000000000002527

Lindbohm, J. V., Sipilä, P. N., Mars, N. J., Pentti, J., Ahmadi-Abhari, S., Brunner, E. J., et al. (2019). 5-year versus risk-category-specific screening intervals for cardiovascular disease prevention: A cohort study. *Lancet Public Health. Apr* 4 (4), e189–e199. doi:10.1016/S2468-2667(19)30023-4

Lloyd-Jones, D. M., Leip, E. P., Larson, M. G., D'Agostino, R. B., Beiser, A., Wilson, P. W., et al. (2006). Prediction of lifetime risk for cardiovascular disease by risk factor burden at 50 years of age. *Circulation* 113 (6), 791–798. doi:10.1161/CIRCULATIONAHA.105.548206

Loizou, C. P. (2014). A review of ultrasound common carotid artery image and video segmentation techniques. *Med. Biol. Eng. Comput.* 52 (12), 1073–1093. doi:10.1007/s11517-014-1203-5

Ma, Y., Choi, J., Hourlier-Fargette, A., Xue, Y., Chung, H. U., Lee, J. Y., et al. (2018). Relation between blood pressure and pulse wave velocity for human arteries. *Proc. Natl. Acad. Sci. U. S. A.* 115 (44), 11144–11149. doi:10.1073/pnas.1814392115

Messas, E., Pernot, M., and Couade, M. (2013). Arterial wall elasticity: State of the art and future prospects. *Diagn Interv. Imaging* 94 (5), 561–569. doi:10.1016/j.diii.2013.01.025

Mitchel, G. F. (2021). Arterial stiffness in aging: Does it have a place in clinical practice? Recent advances in hypertension. *Hypertension* 77 (3), 768–780. doi:10.1161/HYPERTENSIONAHA.120.14515

Mizobuchi, A., Osawa, K., Tanaka, M., Yumoto, A., Saito, H., and Fuke, S. (2021). Detrended fluctuation analysis can detect the impairment of heart rate regulation in patients with heart failure with preserved ejection fraction. *J. Cardiol.* 77 (1), 72–78. doi:10.1016/j.jjcc.2020.07.027

Mohanty, S. K., Rodgers, J., Singh, R. R., Mishra, R. S., Kim, R., Khan, J., et al. (2021). Morbidity compression or expansion? A temporal analysis of the age at onset of non-communicable diseases in India. *Geroscience* 43 (1), 409–422. doi:10.1007/s11357-020-00296-9

National Center for Health Statistics (2021). Percentage of coronary heart disease for adults aged 18 and over, United States 2019—2021. National Health Interview Survey (Accessed May 23, 2023).

Neumann, J. T., Thao, L. T. P., Callander, E., Chowdhury, E., Williamson, J. D., Nelson, M. R., et al. (2022). Cardiovascular risk prediction in healthy older people. *GeroScience* 44, 403–413. doi:10.1007/s11357-021-00486-z

Parikh, J. D., Hollingsworth, K. G., Kunadian, V., Blamire, A., and MacGowan, G. A. (2016). Measurement of pulse wave velocity in normal ageing: Comparison of vicorder and magnetic resonance phase contrast imaging. *BMC Cardiovasc Disord.* 19, 50. doi:10.1186/s12872-016-0224-4

Peng, C. K., Havlin, S., Stanley, H. E., and Goldberger, A. L. (1995). Quantification of scaling exponents and crossover phenomena in nonstationary heartbeat time series. *Chaos* 5 (1), 82–87. doi:10.1063/1.166141

Petry, N. M. (2002). A comparison of young, middle-aged, and older adult treatment-seeking pathological gamblers. *Gerontologist* 42 (1), 92–99. doi:10.1093/geront/42.1.92

Ranadive, S. M., Dillon, G. A., Mascone, S. E., and Alexander, L. M. (2021). Vascular health Triad in humans with hypertension-not the usual suspects. *Front. Physiol.* 12, 746278. doi:10.3389/fphys.2021.746278

Reference Values for Arterial Stiffness' Collaboration (2010). Determinants of pulse wave velocity in healthy people and in the presence of cardiovascular risk factors: Establishing normal and reference values. *Eur. Heart J.* 31 (19), 2338–2350. doi:10.1093/eurheartj/ehq165

Rudnicka, E., Napierała, P., Podfigurna, A., Męczekalski, B., Smolarczyk, R., and Grymowicz, M. (2020). The World Health Organization (WHO) approach to healthy ageing. *Maturitas* 139, 6–11. doi:10.1016/j.maturitas.2020.05.018

Secomb, T. W. (2016). Hemodynamics. *Compr. Physiol.* 6 (2), 975–1003. doi:10.1002/cphy.c150038

Srámek, A., Bosch, J. G., Reiber, J. H., Van Oostayen, J. A., and Rosendaal, F. R. (2000). Ultrasound assessment of atherosclerotic vessel wall changes: Reproducibility of intima-media thickness measurements in carotid and femoral arteries. *Invest. Radiol.* 35 (12), 699–706. doi:10.1097/00004424-200012000-00001

Sutton-Tyrrell, K., Najjar, S. S., Boudreau, R. M., Venkitachalam, L., Kupelian, V., Simonsick, E. M., et al. (2005). Elevated aortic pulse wave velocity, a marker of arterial stiffness, predicts cardiovascular events in well-functioning older adults. *Circulation* 111 (25), 3384–3390. doi:10.1161/CIRCULATIONAHA.104.483628

Thomas, A. J., Mitchell, E. S., and Woods, N. F. (2018). The challenges of midlife women: Themes from the seattle midlife women's health study. *Womens Midlife Health* 15, 8. doi:10.1186/s40695-018-0039-9

Townsend, R. R., Wilkinson, I. B., Schiffrin, E. L., Avolio, A. P., Chirinos, J. A., Cockcroft, J. R., et al. (2015). Recommendations for improving and standardizing vascular research on arterial stiffness: A scientific statement from the American heart association. *Hypertension* 66 (3), 698–722. doi:10.1161/HYP.0000000000000033

Tsao, C. W., Aday, A. W., Almarzooq, Z. I., Beaton, A. Z., Bittencourt, M. S., Boehme, A. K., et al. (2023). Heart disease and stroke statistics—2023 update: A report from the American heart association. *Circulation* 147, e93–e621. doi:10.1161/CIR.0000000000001123

Van Leeuwen, K. M., Van Loon, M. S., Van Nes, F. A., Bosmans, J. E., De Vet, H. C. W., Ket, J. C. F., et al. (2019). What does quality of life mean to older adults? A thematic synthesis. *PLoS One.* 14 (3), e0213263. doi:10.1371/journal.pone.0213263

Vlachopoulos, C., Aznaouridis, K., O'Rourke, M. F., Safar, M. E., Baou, K., and Stefanadis, C. (2010). Prediction of cardiovascular events and all-cause mortality with central haemodynamics: A systematic review and meta-analysis. *Eur. Heart J.* 31 (15), 1865–1871. doi:10.1093/eurheartj/ehq024

Wang, C., Yuan, Y., Zheng, M., Pan, A., Wang, M., Zhao, M., et al. (2020). Association of age of onset of hypertension with cardiovascular diseases and mortality. *J. Am. Coll. Cardiol.* 75 (23), 2921–2930. doi:10.1016/j.jacc.2020.04.038

Willemet, M., and Alastruey, J. (2015). Arterial pressure and flow wave analysis using time-domain 1-D hemodynamics. *Ann. Biomed. Eng.* 43 (1), 190–206. doi:10.1007/s10439-014-1087-4

World Health Organization (2021). Cardiovascular diseases – overview. Available at: https://www.who.int/health-topics/cardiovascular-diseases#tab=tab_1.

Zarrinkoob, L., Ambarki, K., Wahlin, A., Birgander, R., Calberg, B., Eklund, A., et al. (2016). Aging alters the dampening of pulsatile blood flow in cerebral arteries. *J. Cereb. Blood Flow. Metab.* 36 (9), 1519–1527. doi:10.1177/0271678X16629486

Zikić, D. (2008). An improved reflective photoplethysmograph probe design for detection of an arterial blood flow. *J. Med. Eng. Technol.* 32 (1), 23–29. doi:10.1080/03091900600703529

Žikić, D., Stojadinović, B., and Nestorović, Z. (2019). Biophysical modeling of wave propagation phenomena: Experimental determination of pulse wave velocity in viscous fluid-filled elastic tubes in a gravitation field. *Eur. Biophys. J.* 48 (5), 407–411. doi:10.1007/s00249-019-01376-1

frontiers | Frontiers in Physiology

TYPE Original Research
PUBLISHED 25 July 2023
DOI 10.3389/fphys.2023.1172150

OPEN ACCESS

EDITED BY
Panicos Kyriacou,
City University of London,
United Kingdom

REVIEWED BY
Lin Qi,
Northeastern University, China
Qing Liu,
Xi'an Jiaotong-Liverpool University,
China

*CORRESPONDENCE
Fei Chen,
fchen@sustech.edu.cn

†These authors have contributed equally to this work

RECEIVED 23 February 2023
ACCEPTED 12 July 2023
PUBLISHED 25 July 2023

CITATION
Liao S, Liu H, Lin W-H, Zheng D and Chen F (2023), Filtering-induced changes of pulse transmit time across different ages: a neglected concern in photoplethysmography-based cuffless blood pressure measurement. *Front. Physiol.* 14:1172150. doi: 10.3389/fphys.2023.1172150

Filtering-induced changes of pulse transmit time across different ages: a neglected concern in photoplethysmography-based cuffless blood pressure measurement

Shangdi Liao[1†], Haipeng Liu[2†], Wan-Hua Lin[3], Dingchang Zheng[2] and Fei Chen[1*]

[1]Department of Electronic and Electrical Engineering, Southern University of Science and Technology, Shenzhen, China, [2]Research Centre for Intelligent Healthcare, Coventry University, Coventry, United Kingdom, [3]Chinese Academy of Sciences Key Laboratory of Human-Machine Intelligence-Synergy Systems, Shenzhen Institute of Advanced Technology, Shenzhen, China

Background: Pulse transit time (PTT) is a key parameter in cuffless blood pressure measurement based on photoplethysmography (PPG) signals. In wearable PPG sensors, raw PPG signals are filtered, which can change the timing of PPG waveform feature points, leading to inaccurate PTT estimation. There is a lack of comprehensive investigation of filtering-induced PTT changes in subjects with different ages.

Objective: This study aimed to quantitatively investigate the effects of aging and PTT definition on the infinite impulse response (IIR) filtering-induced PTT changes.

Methods: One hundred healthy subjects in five different ranges of age (i.e., 20–29, 30–39, 40–49, 50–59, and over 60 years old, 20 subjects in each) were recruited. Electrocardiogram (ECG) and PPG signals were recorded simultaneously for 120 s. PTT was calculated from the R wave of ECG and PPG waveform features. Eight PTT definitions were developed from different PPG waveform feature points. The raw PPG signals were preprocessed then further low-pass filtered. The difference between PTTs derived from preprocessed and filtered PPG signals, and the relative difference, were calculated and compared among five age groups and eight PTT definitions using the analysis of variance (ANOVA) or Scheirer–Ray–Hare test with *post hoc* analysis. Linear regression analysis was used to investigate the relationship between age and filtering-induced PTT changes.

Results: Filtering-induced PTT difference and the relative difference were significantly influenced by age and PTT definition ($p < 0.001$ for both). Aging effect on filtering-induced PTT changes was consecutive with a monotonous trend under all PTT definitions. The age groups with maximum and minimum filtering-induced PTT changes depended on the definition. In all subjects, the PTT defined by maximum peak of PPG had the minimum filtering-induced PTT changes (mean: 16.16 ms and 5.65% for PTT difference and relative difference).

The changes of PTT defined by maximum first PPG derivative had the strongest linear relationship with age (R-squared: 0.47 and 0.46 for PTT difference relative difference).

Conclusion: The filtering-induced PTT changes are significantly influenced by age and PTT definition. These factors deserve further consideration to improve the accuracy of PPG-based cuffless blood pressure measurement using wearable sensors.

KEYWORDS

cuffless blood pressure measurement, pulse transit time (PTT), photoplethysmography (PPG), filtering, waveform feature

1 Introduction

Photoplethysmography (PPG) signal reflects the volumetric changes in microcirculation. PPG pulse waveform characteristics contain vital information regarding cardiovascular systems and associated diseases. The PPG technology has been widely used in physiological measurement of important cardiovascular parameters, e.g., heart rate, heart rate variability, and blood pressure (Allen, 2007; Liu et al., 2019; Khalid et al., 2020; Khalid et al., 2022). Nowadays, the development of wearable technology further expanded the application scenarios of PPG-based mobile health monitoring in daily life.

Among many, pulse transit time (PTT) is one of the most important characteristics provided by PPG pulse waveform. PTT refers the time for heart pulse wave (PW) to propagate through a length of the arterial tree. It can be approximated as the interval between the R wave of electrocardiogram (ECG) and the characteristic point of PPG signal (e.g., the end-of-diastolic valley) in the same cardiac cycle. PTT (negatively related to blood pressure) and associated pulse wave velocity (PWV) have been extensively used to develop novel cuffless and continuous blood pressure measurements using wearable PPG sensors (Ding and Zhang, 2019). In early works, several PPG pulse wave characteristics have been extracted to determine PTT, including PPG valley (Babchenko et al., 2000; Nitzan et al., 2002; Allen et al., 2008), PPG peak (Zhang and Zhang, 2006; Allen et al., 2008; Wagner et al., 2010; Kortekaas et al., 2012; Li et al., 2014), peak of the first derivative of PPG (Yoon et al., 2009; Kortekaas et al., 2012; Kim et al., 2013), and peak of the second derivative of PPG (Teng and Zhang, 2006; Kortekaas et al., 2012), etc.

PPG measurement is influenced by many factors, including (but not limited to) body site of measurement, breathing pattern, age, etc. All these factors may affect the waveform quality of the PPG data, and subsequently cause challenges in extracting PPG waveform features. Hartmann et al. found that the PPG signals measured from the fingertip achieved the highest percentage of analyzable waveforms for feature extraction among six measurement sites of finger, wrist under, wrist upper, arm, earlobe, and forehead (Hartmann et al., 2019). In addition, the age-related changes of vascular biomechanical properties, e.g., artery stiffness, can significantly influence the PPG waveform and the location of characteristic points (Allen et al., 2020). It has been reported that PWV, the gold standard for evaluating arterial stiffness, was correlated with age in healthy adults (Koivistoinen et al., 2007; Schwartz et al., 2019). Allen et al. observed multiple age-related changes in PPG pulse shape characteristics measured at different body sites, with small but significant overall elongation of the systolic rising edge (Allen and Murray, 2003). They found a significant correlation between aging and PTT shortening (Allen and Murray, 2002).

In addition to the abovementioned physiological factors, preprocessing of raw PPG signals may also incur some changes on PPG waveform features, particularly the timing information. In many wearable applications, raw PPG signals are filtered before feature extraction. Filtering can change the waveform of PPG signals and the timing of feature points (Liu et al., 2021). At present, the finite impulse response (FIR) and infinite impulse response (IIR) filters are widely applied in PPG signal processing. IIR filters offer a number of advantages over other types of filters, such as their ability to achieve a high degree of signal attenuation and their applicability in digital signal processing systems. Whereas, the nonlinear phase response of the IIR filter can deform PPG signals and affect the timing of PPG waveform feature points (Allen and Murray, 2004). In our previous study, we observed that IIR filtering can significantly change the characteristics of PPG waveforms (e.g., peaks and valleys) with the average time shift over 0.1s (Liu et al., 2021). Hence it was noted that filtering parameters should be quoted to support the reproducibility of PPG-related studies (Liu et al., 2021; Charlton et al., 2022). In this paper, we continue this line of thought and research methodology on IIR filtering which will establish the groundwork for future research on FIR and other filters.

Considering the importance of PTT for measuring important cardiovascular signs (e.g., blood pressure, vascular elasticity), it is valuable to study all possible sources leading to PTT measurement errors. So far, little has been reported on how filtering-induced time shift in PPG signal preprocessing affects PTT measurement, which is largely due the lack of a standardized PPG signal processing workflow. The filtering parameters of many commercial wearable PPG sensors are unrevealed. In early studies, the filtering parameters were not uniform and narrow frequency bands were widely used, e.g., 0.5–4 Hz (Wang et al., 2007; Vogel et al., 2009) and 0.8–4 Hz (Poh et al., 2012).

This work took the first step toward quantitatively assessing the effect of PPG pulse filtering on PTT changes. Specially, eight waveform feature points from PPG signals were used to define 8 types of PPT for studying the PPT definition effect, and PPG signals were collected from a wide range of age for studying the possible aging effect.

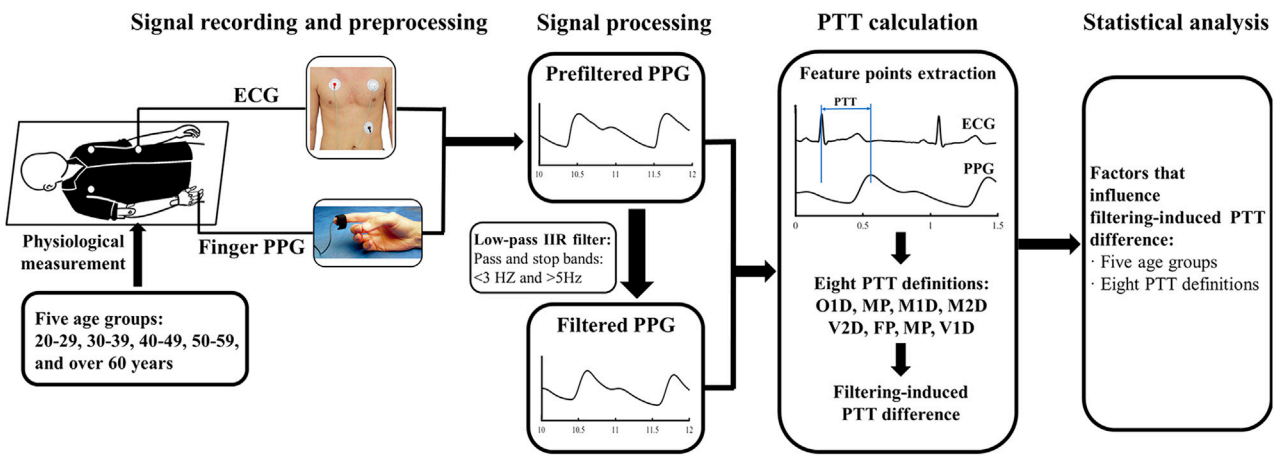

FIGURE 1
Schematic diagram of the measurement system.

2 Materials and methods

2.1 Subjects

A total of one hundred participants (age: 44 ± 14 years, age range: 20–71 years; 48 males and 52 females) were recruited from staff, students and their relatives in Newcastle Hospitals and Newcastle University with written informed consent. The participants were equally distributed in five age groups (i.e., 20–29, 30–39, 40–49, 50–59, and over 60 years old, 20 subjects in each). No participant suffered cardiovascular disease before. This study received ethical permission from the Faculty Research Ethics Panel at Anglia Ruskin University (FMSFREP/17/18205), and all participants provided their written informed consent. The experimental procedures involving human subjects described in this work complied with the principles in the Declaration of Helsinki by World Medical Association in 2000.

2.2 Measurement procedure

Figure 1 illustrates the schematic diagram of the PPG and ECG measurement system. The experiment was performed in a thermostatic room maintaining the temperature at 23°C ± 1°C. In order to stabilize the cardiovascular system, each participant was guided to lie supine on a couch and rest for 5 min. Their arms were placed parallel to the body without any movement. During the experiment, the ECG and PPG signals were recorded, reviewed, and saved using the MP160 data acquisition system with the Biopac AcqKnowledge software. The sensors to measure ECG and PPG signals were attached to thoracic area and right index fingertip, respectively. The participants were informed to keep a normal breathing. When the ECG and finger PPG signals on the monitor screen were stable, they were recorded simultaneously at a sample rate of 2,500 Hz for 120 s. The operator monitored the data during the recording, reviewed the whole data segments after the recording, and then saved the data with adequate quality. If any error or low-quality segment appeared, the data recording was repeated.

2.3 Signal preprocessing and filtering

The recorded data were anonymized and imported to MATLAB (R2021b; MathWorks Inc. Natick, United States) for signal processing. The ECG signals were first pre-processed with a 4th-order Butterworth band-pass filter (passband: 0.05–35 Hz, stopbands: <0.01 Hz and >40 Hz) to remove the baseline drifts (i.e., low-frequency noises) and high-frequency noise, followed by a wavelet transformation to further remove the remaining low-frequency noises due to the slant stopband edges. Specially, the Daubechies 8 wavelet (db8) was used for 11-level decomposition. As compared with a band-pass filter, the discrete wavelet transform could perform better in terms of eliminating high-frequency noise (e.g., electrocardiogram noise, power line noise, etc.) while keeping the morphology feature points of the ECG signal (Zhao et al., 2022). The approximation coefficient of the wavelet decomposition at the 11th level, which contained low-frequency drift component, was replaced by zero. Then, the signal was reconstructed based on the new coefficients to obtain the preprocessed ECG signal.

The raw PPG signals were preprocessed with a high-pass infinite impulse response (IIR) filter (1 zero and 10 poles, passband: >0.5 Hz, stopband: <0.2 Hz) to remove the baseline drifts. A low-pass IIR filter (1 zero and 16 poles, passband: <20 Hz, stopband: >30 Hz) was then used to remove the high-frequency noises which included the 50 Hz power line and electrophysiological noises.

To investigate the effect of filtering on PTT measurement, the preprocessed PPG signals were further filtered with a low-pass IIR filter (1 zero and 13 poles, passband: <3 Hz, stopband: >5 Hz). The details of the PPG signal preprocessing could be found in Figure 2 of (Liu et al., 2021). Figure 2 illustrates the removal of baseline wondering and high-frequency noises (see the enlarged circle) in preprocessing, and further smoothing in the IIR filtering.

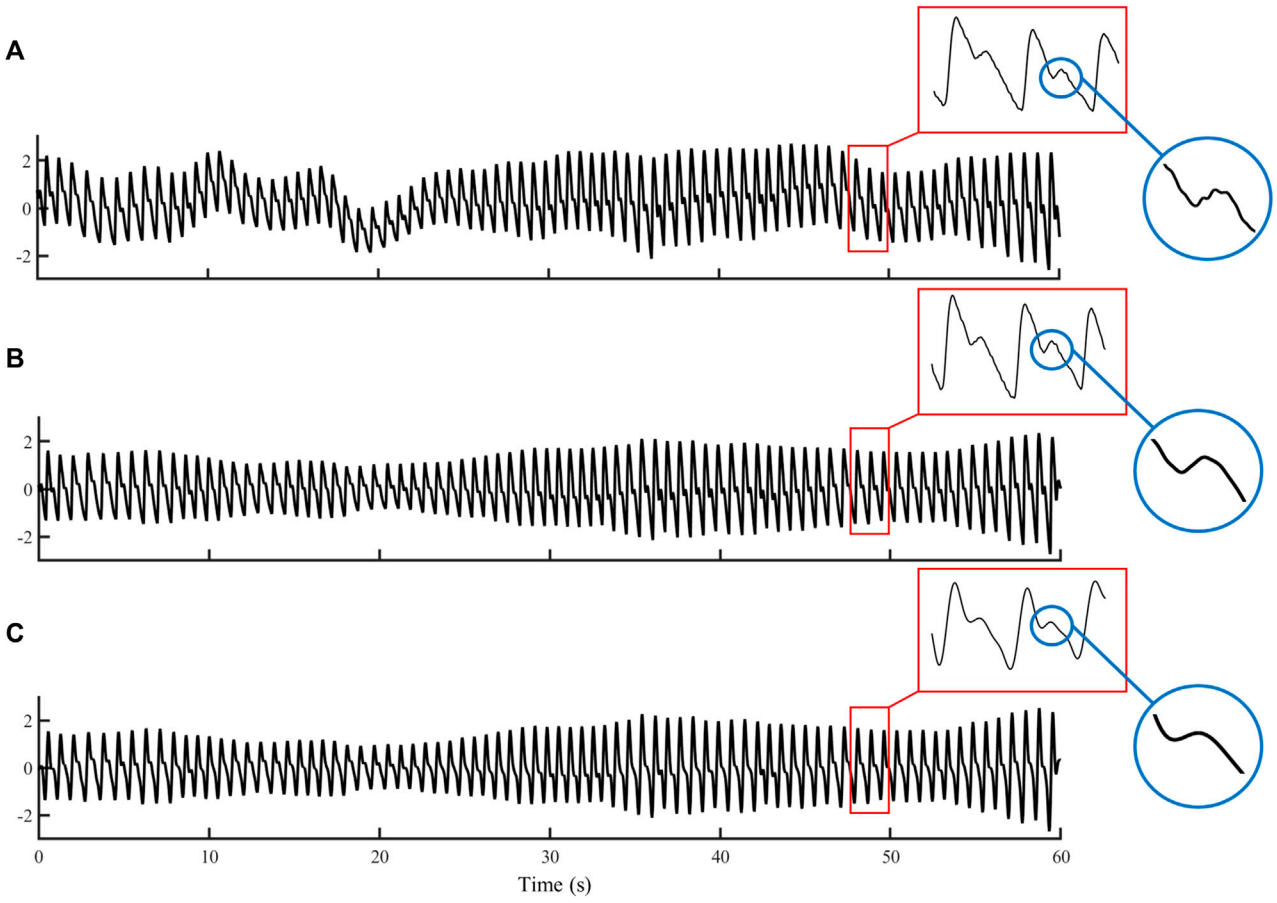

FIGURE 2
Example waveforms of **(A)** raw PPG, **(B)** preprocessed PPG, and **(C)** filtered PPG signals with a duration of 60 s.

2.4 Definition of PTT

PTT is usually defined as the time between the R-peak of the electrocardiogram (ECG) and a reference point on systolic PPG signal segment. The reference point can be derived from different PPG features (e.g., end-of-diastolic valley, systolic peak, see Figure 3), which leads to different PTT definitions.

This work selected eight different PPG pulse waveform characteristics to define eight PTTs. The eight PPG pulse waveform characteristics are (see Figure 4).

(1) Onset point of the first derivative (O1D): the onset of the first derivative of PPG in a cardiac cycle.
(2) Valley point of PPG (VP): the point corresponding to the minimum value of the PPG in a cardiac cycle which is located at the end of diastole.
(3) Maximum second derivative (M2D): the point corresponding to the maximum value of the second derivative of PPG in a cardiac cycle.
(4) Maximum first derivative (M1D): the point corresponding to the maximum value of the first derivative of PPG in a cardiac cycle.

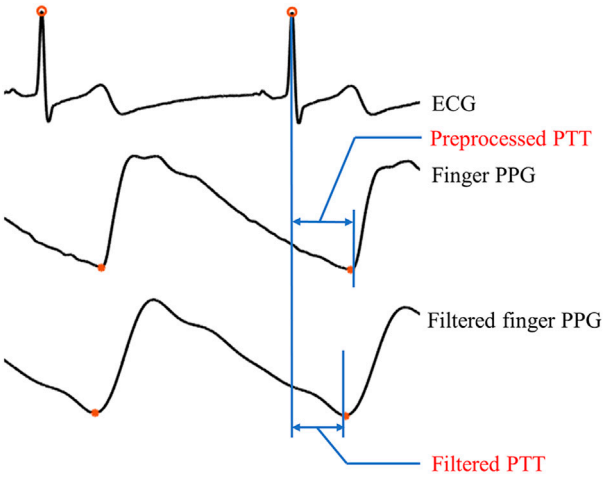

FIGURE 3
Illustration of two types of PTT, i.e., preprocessed PTT and filtered PTT. Here, the preprocessed PTT refers the interval between the ECG R-wave and the end-of-diastolic valley of the preprocessed PPG signal, while the filtered PTT is the interval between the ECG R-wave and the end-of-diastolic valley of the filtered PPG signal.

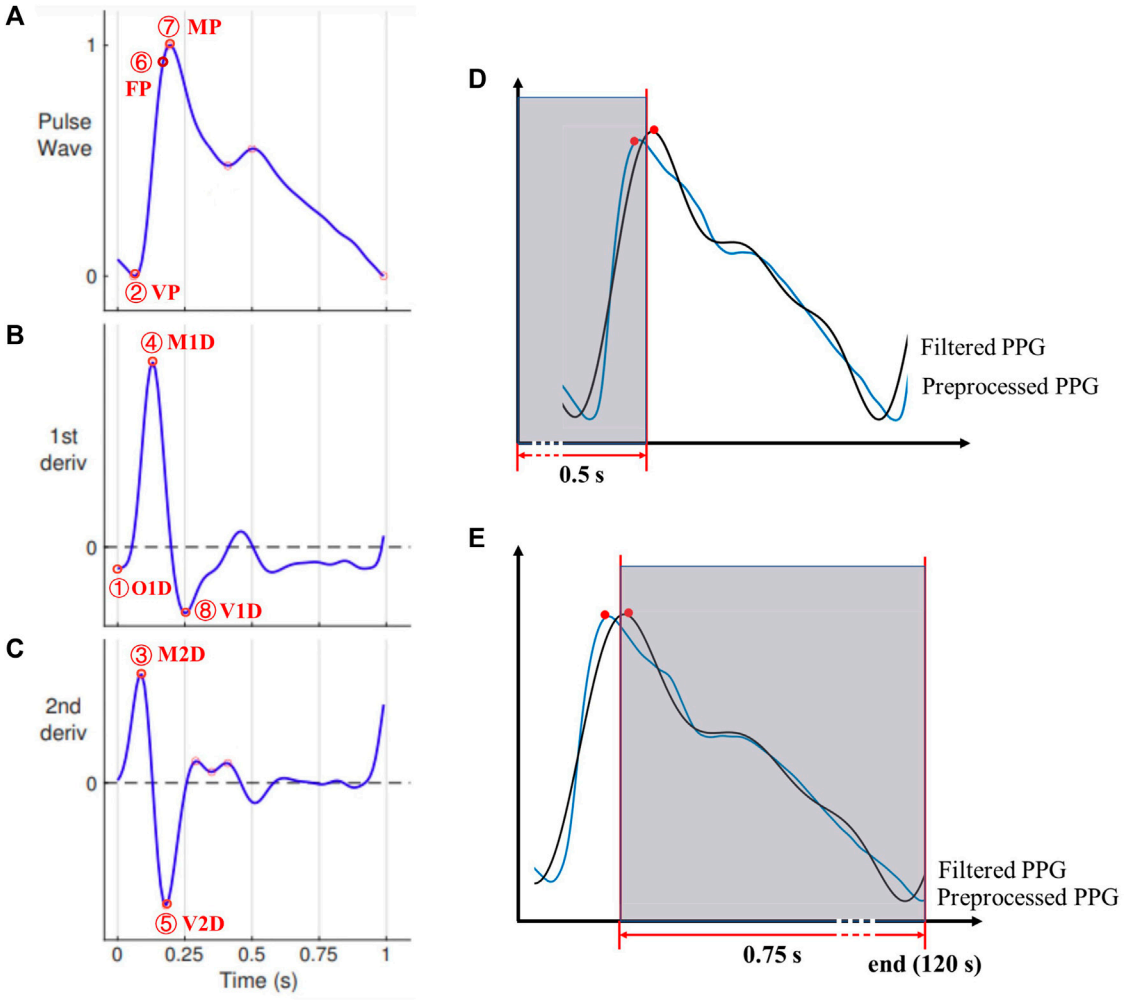

FIGURE 4
The characteristic points on **(A)** the PPG signal and its **(B)** first and **(C)** second derivatives. Points 1-8 denote O1D, VP, M2D, M1D, V2D, FP, MP, and V1D, respectively. Adopted from (Mejia-Mejia et al., 2022). **(D)** and **(E)**: Corresponding PPG waveform characteristics points of both signals (preprocessed and filtered) were excluded from the analysis if any of them falls in the first 0.5s **(D)** or last 0.75s of the recording **(E)**.

(5) Valley point of the second derivative (V2D): the point corresponding to the minimum value of the second derivative of PPG in a cardiac cycle.
(6) Forward peak of PPG (FP): the point that has the maximum value in a cardiac cycle of the forward PPG wave.
(7) Maximum peak of PPG (MP); the systolic peak point that has the maximal PPG value in a cardiac cycle.
(8) Valley point of the first derivative of PPG (V1D): the point corresponding to the minimum value of the first derivative of PPG in a cardiac cycle.

The derivatives were approximated using backward difference calculated from adjacent sampling points. Therefore, the first and second derivatives of the PPG signal started from the second and third sampling points, respectively. Considering the high sampling frequency (i.e., 2,500 Hz), the error caused by the approximation was very limited ($<4 \times 10^{-4}$ s for the timing of any characteristic point). The characteristic points were detected from the extrema (i.e., peak and valley points) of PPG and its derivatives, as well as the decomposition of forward and backward pulse waves. The details of defining and detecting characteristic points can be found in our early works (Liu et al., 2021; Lin et al., 2022).

To prevent inaccurate readings at the immediate start and end of a PPG recording, any characteristic point was excluded from the analysis if it or its 'counterpart' (i.e., any of the preprocessed or filtered one) fell in the first 0.5 s (e.g., in Figure 4D, the pair of peak points are excluded) or the last 0.75 s (Figure 4E). To exclude the missing or erroneous feature points, any detected feature point was excluded if there was no 'counterpart' point within ±0.3 s of the detected feature point. The time axis was unchanged (i.e., no shift of any signal) during signal processing.

As to ECG signals, the R wave peak was detected as the maximal value in a cardiac cycle using the Pan Tompkins method (Sathyapriya et al., 2014). To prevent inaccurate readings at the immediate start and end of an ECG recording, similar as in PPG preprocessing, any R peak point was excluded if it or its counterpart was in the first 0.5 s or the last 0.5 s. When processing the noisy PPG signals in some cardiac cycles, only the valleys within 100–500 ms after the ECG R-peak (i.e., 100 ms≤ PTT ≤500 ms) were selected for

10.3389/fphys.2023.1172150

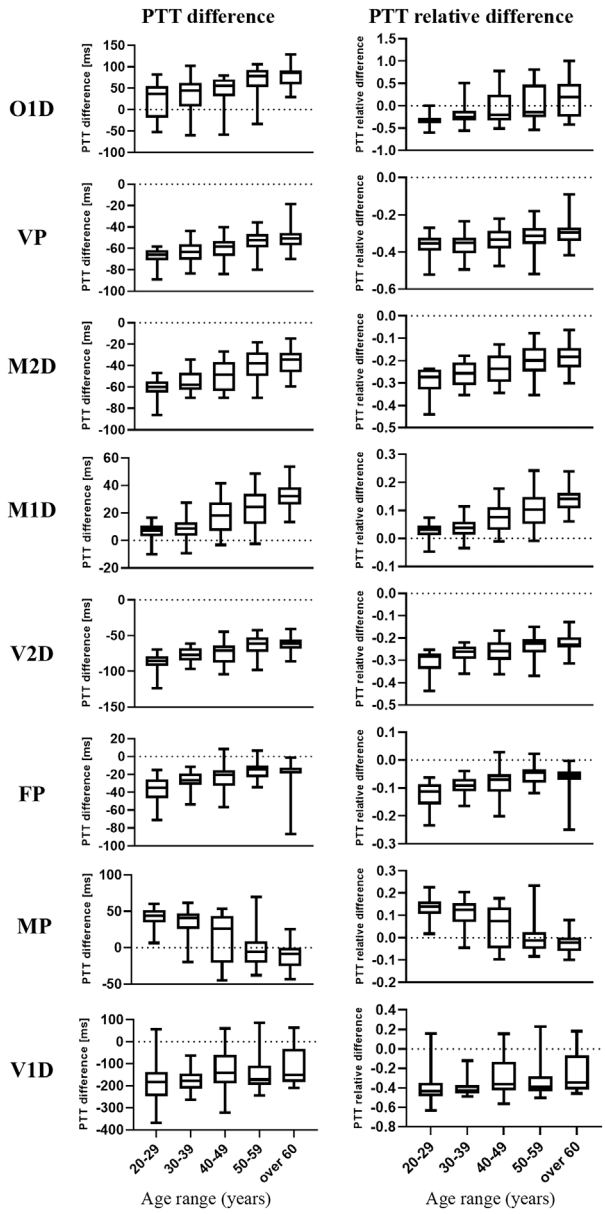

FIGURE 5
Box and whisker plots of the filtering-induced difference and relative difference of PTT in five age groups and eight PTT definitions. The medians are represented by the horizontal lines within the boxes while the first and third quartiles are represented by the box boundaries.

analysis. For each PPG signal (preprocessed or filtered), the PTT was calculated as the mean value of PTTs of all included cardiac cycles.

2.5 Statistical analysis

For each participant, the filtering-induced PTT difference was calculated between the PTT values derived from the filtered and preprocessed PPG signals. The relative PTT difference was calculated as:

$$RD_{PTT} = \left(PTT_{filtered} - PTT_{preprocessed}\right) / PTT_{preprocessed} \quad (1)$$

TABLE 1 Results of Scheirer-Ray-Hare test regarding the PTT difference. Asterisk denotes significant difference.

	H	*p*-value
Age	22.29	<0.001*
PTT Definition	530.37	<0.001*
Age & PTT Definition Interaction	35.89	0.146

TABLE 2 Results of Scheirer-Ray-Hare test regarding the PTT relative difference. Asterisk denotes significant difference.

	H	*p*-value
Age	23.54	<0.001*
PTT Definition	484.48	<0.001*
Age & PTT Definition Interaction	36.87	0.122

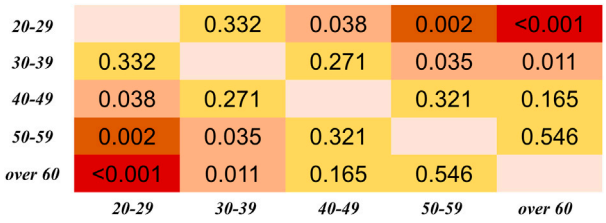

FIGURE 6
Results of Dunn's Kruskal–Wallis multiple comparisons between the five age groups regarding the PTT difference, derived from all PTT definitions. The brightness indicates the statistical significance (i.e., higher significance in red color).

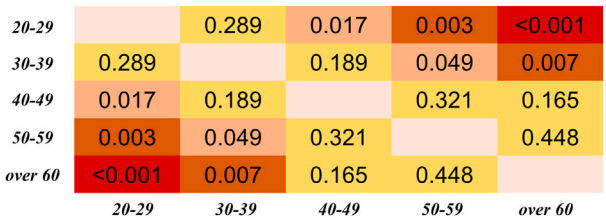

FIGURE 7
Results of Dunn's Kruskal–Wallis multiple comparisons between the five age groups regarding the PTT relative difference (RD_{PTT}). The brightness indicates the statistical significance (i.e., higher significance in red color).

For each subject, the PTT difference and RD_{PTT} were averaged in all included cardiac cycles. The ratio between the mean and standard deviation of RD_{PTT} in all included cardiac cycles was also calculated to estimate the intra-subject variation of filtering-induced PPT changes. Statistical analysis was performed using SPSS (Version 24.0, IBM Corp.; Armonk, NY, United States) and R programming language, version 4.1.0 (R Core Team, 2021). Considering the data size, Shapiro–Wilk test was performed to investigate the normality of

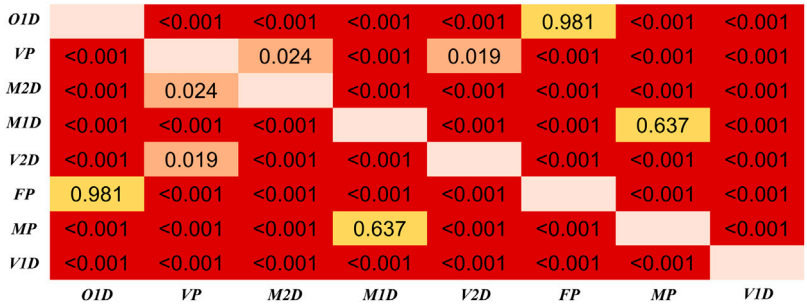

FIGURE 8
Results of Dunn's Kruskal–Wallis multiple comparisons between the eight types of PTT definition regarding the PTT difference. The brightness indicates the statistical significance (i.e., higher significance in red color).

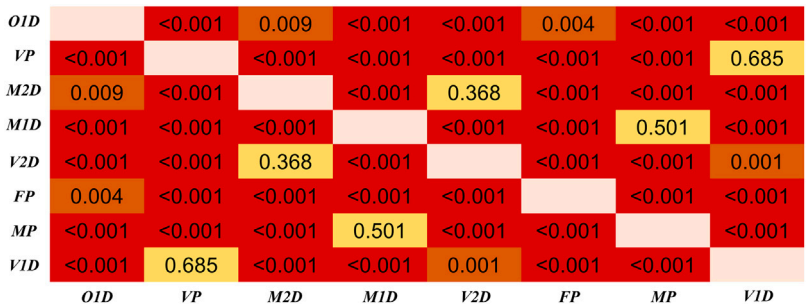

FIGURE 9
Results of Dunn's Kruskal–Wallis multiple comparisons between the eight types of PTT definition regarding the PTT relative difference (RD_{PTT}). The brightness indicates the statistical significance (i.e., higher significance in red color).

data distribution. Normal distribution was defined as $p > 0.05$ in Shapiro–Wilk test.

To investigate if there was any significant effect of age, PTT definition, or their interaction on the filtering-induced PTT difference or RD_{PTT}, the analysis of variance (ANOVA) or Scheirer–Ray–Hare test was performed. ANOVA was performed on normally distributed data where the homogeneity of variance was satisfied (defined as $p > 0.05$ in Levene's test), otherwise the Scheirer–Ray–Hare test was performed as a substitute.

To further investigate the difference between age groups, or between PTT definitions, and to identify the age group and the PTT definition with the highest reliability (i.e., with the least filtering-induced PTT changes), the *post hoc* analysis was performed, i.e., least significant difference tests and Dunn's Kruskal–Wallis multiple comparisons for ANOVA and the Scheirer–Ray–Hare test, respectively. In the Dunn's Kruskal–Wallis multiple comparisons, the *p*-value was adjusted via the Benjamini–Hochberg method (Benjamini and Hochberg, 1995).

Finally, to investigate quantitatively the aging effect on filtering-induced PTT difference and its relative difference, linear regression analysis was performed. The R-squared value was calculated to evaluate the strength of the linear relationship. A significant linear relationship was defined as $r > 0.5$ (R-squared >0.25) and $p < 0.05$. A strong linear relationship was defined as $r > 0.8$ (R-squared >0.64) and $p < 0.05$. Regression analysis of the data and curve plotting were performed using Graphpad Prism (version 9.0.0, GraphPad Software, United States).

3 Results

3.1 Effects of age and PTT definition on filtering-induced PTT differences

The ratio between mean and standard deviation of RD_{PTT} in included cardiac cycles was below 20% for all PTTs in 72 subjects, indicating limited intra-subject variability of filtering-induced PTT difference. Therefore, in this study, the data analysis was focused on the mean values of filtering-induced PTT changes and RD_{PTT}.

Figure 5 shows the distribution of filtering-induced PTT difference and its relative difference in five different age ranges and eight PTT definitions. The distribution of filtering-induced PTT difference and relative difference did not satisfy the homogeneity of variance ($p < 0.05$ in Levene's test for both). Therefore, the Scheirer-Ray-Hare test was performed. As shown in Tables 1, 2, there were significant effects of age and PTT definition ($p < 0.001$ for both) on filtering-induced PTT difference and its relative difference, whereas, the effect of interaction between age and PTT definition is insignificant.

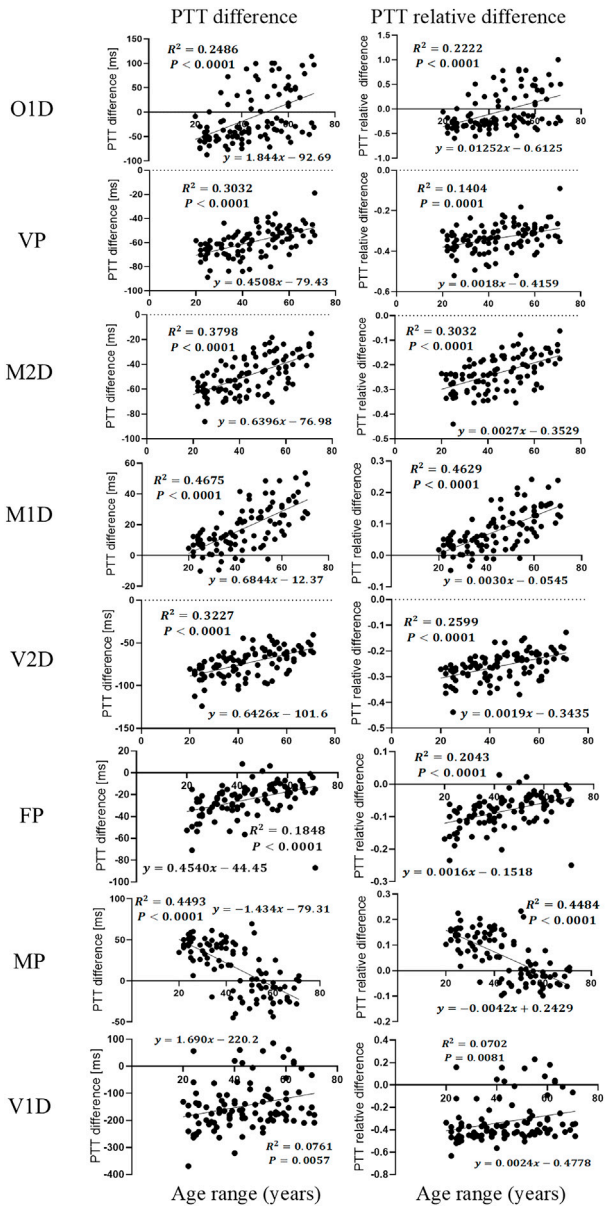

FIGURE 10
Linear regression plot between age and filtering-induced PTT difference and relative difference (RD_{PTT}) under eight definitions of PTT.

3.2 Comparison between age groups and PTT definitions

As shown in Figure 5, in most PTT definitions, there is a consecutive and monotonic trend in filtering-induced PTT difference across different age groups (e.g., increase and decrease with age for M1D in MP, respectively).

In Figures 6, 7, in can be observed that the differences in PTT difference and RD_{PTT} both increase with the gap between age groups, where the difference between the youngest and oldest groups (20–29 and >60 years) is the most significant ($p < 0.001$ for both PTT difference and relative difference). Considering all PTT definitions, the age groups (20–29) and (50–59) had the maximum and minimum filtering-induced changes, respectively (for both PTT difference and relative difference, in mean value). Of note, the age groups with maximal and minimal filtering-induced PTT changes were actually definition-specific (Figure 5).

Regarding the differences among PTT definitions, as shown in Figure 8, significant differences in PTT difference were observed ($p < 0.05$) except between O1D and FP, and between MP and M1D. As shown in Figure 9, significant differences in PTT relative difference were observed ($p < 0.05$) except between V2D and M2D, between V1D and VP, as well as between MP and M1D. Therefore, PTT definition has significant influence on the filtering-induced PTT changes. In all subjects, MP had the minimum filtering-induced changes for both PTT difference and RD_{PTT} (mean in all subjects: 16.16 ms and 5.65%, respectively).

3.3 Quantitative analysis: age and filtering-induced PTT difference

As shown in Figure 10, many filtering-induced PTT changes have linear relationships with age, which is in accordance with the trends in Figure 5. The significant linear relationship between age and PTT difference was found in all types of PTT definition group except O1D, FP and V1D. Overall, M1D had the highest strength of the linear relationship ($r^2 = 0.47$ in PTT difference and $r^2 = 0.46$ in PTT relative difference).

4 Discussion and conclusion

The results in this work showed that IIR filtering considerably influenced PTT values by changing the positions of PPG feature points. We observed that filtering-induced PTT changes depended on age and the definition of PTT. In all PTT definitions, the effect of age was consecutive with a monotonous trend. The age group with the least filtering-induced PTT changes depended specifically on PTT definition. Among different PTT definitions, MP showed the highest robustness against the filtering-induced PTT changes. The MP and M1D exhibited the least filtering-sensitive PTT changes, which may explain the lack of significant difference between them in Figures 8, 9. The performance of difference PTTs deserves further investigation on the underlying physiological mechanisms. The linear trends between age and filtering-induced PTT changes indicated the significance of age-based adjustment in PTT estimation. As far as we know, this work is among the first attempts to investigate the filtering-induced PTT changes.

4.1 Filtering-induced PTT changes: A neglected concern

PPG signals are typically subject to noises and trends. Therefore, a proper preprocessing plays a key role in many applications, e.g., the functional assessment of autonomic nervous system (Akar et al., 2013). However, at present, there is a lack of comprehensive evaluation of the filtering effect on the accuracy of PTT across

different ages. Our results filled this gap and highlighted the importance of age-based adjustment of the filtering-induced inaccuracy in PTT-based applications, e.g., BP estimation.

Currently, despite the increasing diversity in PPG preprocessing techniques, traditional IIR and FIR filers still play an important role because they are easier to design in digital signal processors (Liu et al., 2021; Mejia-Mejia and Kyriacou, 2023). Recently, Mejía-Mejía et al. investigated the effect of PPG filtering strategy in the analysis of pulse rate variability (PRV), and concluded that PRV information can be reliably extracted from PPG signals filtered by elliptic IIR or equiripple or Parks–McClellan FIR filters (Mejia-Mejia and Kyriacou, 2023). We also focused on the IIR filter in this pilot study. Compared with PRV which is measured between consecutive heartbeats, PTT is derived from a much shorter period in a cardiac cycle, and thus can be more sensitive to the filtering-induced time shift of PPG feature points. Our results revealed that the filtering can led to considerable changes in PTT (>39.6%, all age groups in VP), affecting the accuracy in BP estimation. Therefore, filtering-induced PPG waveform deformation deserves further attention in PTT-based BP estimation.

4.2 Beyond age: physiological factors that can influence PTT

It is well known that the PTT-BP relationship depends on age (Allen and Murray, 2002; Foo et al., 2005). Allen et al. found a consistent trend in the effect of age on PTT ($r^2 = 0.48$) (Allen and Murray, 2002), while we further observed similar phenomena in the filtering-induced PTT difference (Figures 5, 10). These observations commonly provide the reference for age-adjusted PTT calculation in the future.

Besides age, many other physiological conditions including measurement site, breathing pattern, and neural activities can significantly influence PPG waveform, therefore change the PTT values (Hartmann et al., 2019; Liu et al., 2020; Khalid et al., 2022). The temperature-induced autoregulation can also influence PTT. Teng et al. found that local cold exposure can influence the PTT defined by MP with negligible effect on the PTT defined by VP (Zhang and Zhang, 2006). Furthermore, vascular stiffness increases with age, which has a significant effect on PPG signal waveform (Allen and Murray, 2002). A recent study on oscillography-based BP estimation concludes that, age, BP, and arterial stiffness have complex interaction (Pan et al., 2022). The effect of these physiological factors in PPG waveform changes deserves further investigation.

4.3 Technological factors in improving the accuracy of PTT estimation

Some technical issues can influence the PTT values. Recently, Chandrasekhar et al. pointed out that the PPG sensor contact pressure might be another factor that influences the reliability of PTT measurement (Chandrasekhar et al., 2020). Teng et al. found that, during the increase of contacting force, the PTT defined by M2D had the largest overall change (from 200.3 ± 20.6 ms to 225.0 ± 19.3 ms) (Teng and Zhang, 2006), whereas the PTT defined by M1D had the minimum 325 changes (from 245.3 ± 20.2 ms to 261.4 ± 14.2 ms) (Teng et al., 2004) which is in accordance with our observations. They also found that the interaction between age and contact force might influence PTT. As the contact force increased to the mean intra-arterial pressure (zero transmural pressure), PTT increased from 155.2 ± 18.5 ms to 164.7 ± 21.6 ms for the group of elderly subjects and from 186.7 ± 21.0 ms to 201.7 ± 19.5 ms for the group of young subjects (Teng and Zhang, 2007). Therefore, more physiological and technical factors, as well as their interactions, need to be considered to improve the accuracy of PTT-based BP estimation. Since MP and M1D exhibited the least filtering-sensitive PTT changes and showed strongest linear relationships, we recommend using M1D in younger subjects and MP in older subjects in calculating PTT to improve its reliability.

4.4 PPG signal preprocessing: towards application-specific standardization

PPG technology provides the possibility of low-cost, non-invasive, and continuous BP measurement for different application scenarios. Recent development of learning-based methods has largely improved the accuracy of BP estimation based on single PPG waveform analysis. PTT-based BP estimation is being considered at a secondary place due to the significant impact of arterial stiffness, individual instability and physical condition on the predetermined hypothetical relationship (Agham and Chaskar, 2021). However, due to its accuracy and reliability, PTT-based BP estimation is still the commonest solution in wearable devices compared with other approaches.

Our results revealed a major limitation of PTT-based methods, i.e., the lack of a framework for standardized filtering and quantitative adjustment of the results. At present, there is a lack of standardized practices in PPG signal acquisition and processing (Charlton et al., 2022). In the majority of PPG studies, there are insufficient details of the settings/parameters of the filters. As summarized in our previous work, the filtering parameters are not uniform, where the lower and upper stop frequencies range around 0.005–0.5 Hz, and 5–20 Hz, respectively, with an inconsistency in key properties such as transition bandwidth and ripples (Liu et al., 2021). Considering the diversity of PPG preprocessing methods, and the interaction between technical with physiological factors in the changes of PTT values, we recommend that the preprocessing of PPG signals can be standardized and tailored to meet different application scenarios, where both technical and physiological factors (e.g., filtering parameters, age, measurement site, etc.) can be considered comprehensively and adjusted quantitatively to improve the accuracy of PTT-based BP estimation.

4.5 Limitations and future directions

This is a small-scale pilot study, where other physiological factors as abovementioned were not included to avoid confounding the results. Another major limitation of the study is

that it did not include the subjects with very low and high ages (<20 and >70 years). Existing studies showed that the relationship between age and arterial stiffness is non-linear (Vlachopoulos et al., 2011; Laurent et al., 2019). Therefore, the results might not reflect the filtering-induced PTT changes in elderly people who are more liable to hypertension. Also, we only included healthy subjects, without considering the effect of pathological changes on PPG signal waveform. Existing evidence showed that PTT was mildly elevated in patients with heart failure compared with healthy subjects (468 ± 12 vs. 430 ± 23 ms, $p = 0.001$) (Wagner et al., 2010).

In future studies, large-scale, multi-center datasets covering a wider range of age and more pathophysiological conditions could be used to improve the accuracy of PTT calculation and enable a fine-grained PTT estimation framework. More filtering metrics and techniques can be explored to develop a panoramic, standardizable PPG preprocessing framework with high robustness against filtering-induced PPG waveform deformation.

In conclusion, the results in this work showed that the filtering-induced PTT difference was significantly different among different types of PTT definite or among different age groups. The physiological factor including age and PTT definition should be considered in PTT-based application using wearable sensors, e.g., blood pressure estimation.

Data availability statement

The raw data supporting the conclusion of this article will be made available by the authors, without undue reservation.

Ethics statement

The studies involving human participants were reviewed and approved by Faculty Research Ethics Panel at Anglia Ruskin University (FMSFREP/17/18205). The patients/participants provided their written informed consent to participate in this study.

Author contributions

SL and HL conceived and planned the study. DZ collected the dataset. SL, HL, and W-HL developed the signal processing algorithms. SL performed the signal processing. SL and HL performed the statistical analysis and drafted the first version of the manuscript. FC supervised the project that led to production of the results. All authors contributed to the article and approved the submitted version.

Funding

This work was supported by Shenzhen Key Technology Program Funding (JSGG20220831103803006).

Acknowledgments

We acknowledge Newcastle University and Anglia Ruskin University for providing convenience in data collection and access.

Conflict of interest

The authors declare that the research was conducted in the absence of any commercial or financial relationships that could be construed as a potential conflict of interest.

Publisher's note

References

Agham, N. D., and Chaskar, U. M. (2021). Learning and non-learning algorithms for cuffless blood pressure measurement: A review. *Med. Biol. Eng. Comput.* 59 (6), 1201–1222. doi:10.1007/s11517-021-02362-6

Akar, S. A., Kara, S., Latifoglu, F., and Bilgic, V. (2013). Spectral analysis of photoplethysmographic signals: The importance of preprocessing. *Biomed. Signal Process. Control* 8 (1), 16–22. doi:10.1016/j.bspc.2012.04.002

Allen, J., and Murray, A. (2002). Age-related changes in peripheral pulse timing characteristics at the ears, fingers and toes. *J. Hum. Hypertens.* 16 (10), 711–717. doi:10.1038/sj.jhh.1001478

Allen, J., and Murray, A. (2003). Age-related changes in the characteristics of the photoplethysmographic pulse shape at various body sites. *Physiol. Meas.* 24 (2), 297–307. doi:10.1088/0967-3334/24/2/306

Allen, J., and Murray, A. (2004). "Effects of filtering on multisite photoplethysmography pulse waveform characteristics," in Computers in Cardiology, 2004: IEEE, Chicago, IL, USA, 19-22 September 2004, 485–488.

Allen, J., O'Sullivan, J., Stansby, G., and Murray, A. (2020). Age-related changes in pulse risetime measured by multi-site photoplethysmography. *Physiol. Meas.* 41 (7), 074001. doi:10.1088/1361-6579/ab9b67

Allen, J., Overbeck, K., Nath, A. F., Murray, A., and Stansby, G. (2008). A prospective comparison of bilateral photoplethysmography versus the ankle-brachial pressure index for detecting and quantifying lower limb peripheral arterial disease. *J. Vasc. Surg.* 47 (4), 794–802. doi:10.1016/j.jvs.2007.11.057

Allen, J. (2007). Photoplethysmography and its application in clinical physiological measurement. *Physiol. Meas.* 28 (3), R1–R39. doi:10.1088/0967-3334/28/3/R01

Babchenko, A., Davidson, E., Adler, D., Ginosar, Y., Kurz, V., and Nitzan, M. (2000). Increase in pulse transit time to the foot after epidural anaesthesia treatment. *Med. Biol. Eng. Comput.* 38 (6), 674–679. doi:10.1007/bf02344874

Benjamini, Y., and Hochberg, Y. (1995). Controlling the false discovery rate: A practical and powerful approach to multiple testing. *J. R. Stat. Soc. Ser. B Methodol.* 57 (1), 289–300. doi:10.1111/j.2517-6161.1995.tb02031.x

Chandrasekhar, A., Yavarimanesh, M., Natarajan, K., Hahn, J. O., and Mukkamala, R. (2020). PPG sensor contact pressure should Be taken into account for cuff-less blood pressure measurement. *Ieee Trans. Biomed. Eng.* 67 (11), 3134–3140. doi:10.1109/tbme.2020.2976989

Charlton, P. H., Pilt, K., and Kyriacou, P. A. (2022). Establishing best practices in photoplethysmography signal acquisition and processing. *Physiol. Meas.* 43 (5), 050301. doi:10.1088/1361-6579/ac6cc4

Ding, X., and Zhang, Y.-T. (2019). Pulse transit time technique for cuffless unobtrusive blood pressure measurement: From theory to algorithm. *Biomed. Eng. Lett.* 9 (1), 37–52. doi:10.1007/s13534-019-00096-x

Foo, J. Y. A., Wilson, S. J., Williams, G., Harris, M. A., and Cooper, D. (2005). Age-related factors that confound peripheral pulse timing characteristics in Caucasian children. *J. Hum. Hypertens.* 19 (6), 463–466. doi:10.1038/sj.jhh.1001846

Hartmann, V., Liu, H. P., Chen, F., Qiu, Q., Hughes, S., and Zheng, D. C. (2019). Quantitative comparison of photoplethysmographic waveform characteristics: Effect of measurement site. *Front. Physiology* 10, 198. doi:10.3389/fphys.2019.00198

Khalid, S. G., Ali, S. M., Liu, H. P., Qurashi, A. G., and Ali, U. (2022). Photoplethysmography temporal marker-based machine learning classifier for anesthesia drug detection. *Med. Biol. Eng. Comput.* 60 (11), 3057–3068. doi:10.1007/s11517-022-02658-1

Khalid, S. G., Liu, H., Zia, T., Zhang, J., Chen, F., and Zheng, D. (2020). Cuffless blood pressure estimation using single channel photoplethysmography: A two-step method. *IEEE Access* 8, 58146–58154. doi:10.1109/access.2020.2981903

Kim, S. H., Song, J. G., Park, J. H., Kim, J. W., Park, Y. S., and Hwang, G. S. (2013). Beat-to-Beat tracking of systolic blood pressure using noninvasive pulse transit time during anesthesia induction in hypertensive patients. *Anesth. Analgesia* 116 (1), 94–100. doi:10.1213/ANE.0b013e318270a6d9

Koivistoinen, T., Kööbi, T., Jula, A., Hutri-Kähönen, N., Raitakari, O. T., Majahalme, S., et al. (2007). Pulse wave velocity reference values in healthy adults aged 26–75 years. *Clin. Physiology Funct. Imaging* 27 (3), 191–196. doi:10.1111/j.1475-097X.2007.00734.x

Kortekaas, M. C., Niehof, S. P., van Velzen, M. H. N., Galvin, E. M., Huygen, F., and Stolker, R. J. (2012). Pulse transit time as a quick predictor of a successful axillary brachial plexus block. *Acta Anaesthesiol. Scand.* 56 (10), 1228–1233. doi:10.1111/j.1399-6576.2012.02746.x

Laurent, S., Boutouyrie, P., Cunha, P. G., Lacolley, P., and Nilsson, P. M. (2019). Concept of extremes in vascular aging. *Hypertension* 74 (2), 218–228. doi:10.1161/hypertensionaha.119.12655

Li, Y. J., Wang, Z. L., Zhang, L., Yang, X. L., and Song, J. Z. (2014). Characters available in photoplethysmogram for blood pressure estimation: Beyond the pulse transit time. *Australas. Phys. Eng. Sci. Med.* 37 (2), 367–376. doi:10.1007/s13246-014-0269-6

Lin, W. H., Zheng, D. C., Li, G. L., Zhou, H., and Chen, F. (2022). Investigation on pulse wave forward peak detection and its applications in cardiovascular health. *Ieee Trans. Biomed. Eng.* 69 (2), 700–709. doi:10.1109/tbme.2021.3103552

Liu, H., Allen, J., Zheng, D., and Chen, F. (2019). Recent development of respiratory rate measurement technologies. *Physiol. Meas.* 40 (7), 07TR01. doi:10.1088/1361-6579/ab299e

Liu, H. P., Allen, J., Khalid, S. G., Chen, F., and Zheng, D. (2021). Filtering-induced time shifts in photoplethysmography pulse features measured at different body sites: The importance of filter definition and standardization. *Physiol. Meas.* 42 (7), 074001. doi:10.1088/1361-6579/ac0a34

Liu, H. P., Chen, F., Hartmann, V., Khalid, S. G., Hughes, S., and Zheng, D. C. (2020). Comparison of different modulations of photoplethysmography in extracting respiratory rate: From a physiological perspective. *Physiol. Meas.* 41 (9), 094001. doi:10.1088/1361-6579/abaaf0

Mejia-Mejia, E., Allen, J., Budidha, K., El-Hajj, C., Kyriacou, P. A., and Charlton, P. H. (2022). Photoplethysmography signal processing and synthesis. *Photoplethysmography* 2022, 69–146. Elsevier. doi:10.1016/B978-0-12-823374-0.00015-3

Mejia-Mejia, E., and Kyriacou, P. A. (2023). Effects of noise and filtering strategies on the extraction of pulse rate variability from photoplethysmograms. *Biomed. Signal Process. Control* 80, 104291. doi:10.1016/j.bspc.2022.104291

Nitzan, M., Khanokh, B., and Slovik, Y. (2002). The difference in pulse transit time to the toe and finger measured by photoplethysmography. *Physiol. Meas.* 23 (1), 85–93. doi:10.1088/0967-3334/23/1/308

Pan, F., He, P., Qian, Y., Gao, H., Chen, F., Liu, H., et al. (2022). Changes of oscillogram envelope maximum with blood pressure and aging: A quantitative observation. *Physiol. Meas.* 43 (11), 115008. doi:10.1088/1361-6579/aca26d

Poh, M. Z., Kim, K., Goessling, A., Swenson, N., and Picard, R. (2012). Cardiovascular monitoring using earphones and a mobile device. *Ieee Pervasive Comput.* 11 (4), 18–26. doi:10.1109/mprv.2010.91

R Core Team (2021). R: A language and environment for statistical computing. Vienna, Austria: R Foundation for Statistical Computing. Available at: https://www.R-project.org

Sathyapriya, L., Murali, L., and Manigandan, T. (2014). "Analysis and detection R-peak detection using modified pan-tompkins algorithm," in International Conference on Advanced Communication Control and Computing Technologies, Ramanathapuram, India, 08-10 May 2014, 483–487. NEW YORK: Ieee.

Schwartz, J. E., Feig, P. U., and Izzo, J. L. (2019). Pulse wave velocities derived from cuff ambulatory pulse wave analysis. *Hypertension* 74 (1), 111–116. doi:10.1161/HYPERTENSIONAHA.119.12756

Teng, X. F., Poon, C. C., Zhang, C., and Zhang, Y. T. (2004). "Study on the effect of contacting force on pulse transit time," in2004 2nd IEEE/EMBS International Summer School on Medical Devices and Biosensors, Hong Kong, China, June 26, 2004–July 02, 2004 IEEE, 111–114. doi:10.1109/ISSMD.2004.1689575

Teng, X. F., and Zhang, Y. T. (2006). The effect of applied sensor contact force on pulse transit time. *Physiol. Meas.* 27 (8), 675–684. doi:10.1088/0967-3334/27/8/002

Teng, X. F., and Zhang, Y. T. (2007). Theoretical study on the effect of sensor contact force on pulse transit time. *Ieee Trans. Biomed. Eng.* 54 (8), 1490–1498. doi:10.1109/tbme.2007.900815

Vlachopoulos, C., Terentes-Printzios, D., and Stefanadis, C. (2011). When the arteries get tough, the tougher do not get going. *Hypertens. Res.* 34 (7), 793–794. doi:10.1038/hr.2011.49

Vogel, S., Hulsbusch, M., Hennig, T., Blazek, V., and Leonhardt, S. (2009). In-ear vital signs monitoring using a novel microoptic reflective sensor. *Ieee Trans. Inf. Technol. Biomed.* 13 (6), 882–889. doi:10.1109/titb.2009.2033268

Wagner, D. R., Roesch, N., Harpes, P., Kortke, H., Plumer, P., Saberin, A., et al. (2010). Relationship between pulse transit time and blood pressure is impaired in patients with chronic heart failure. *Clin. Res. Cardiol.* 99 (10), 657–664. doi:10.1007/s00392-010-0168-0

Wang, L., Lo, B. P. L., and Yang, G. Z. (2007). Multichannel reflective PPG earpiece sensor with passive motion cancellation. *Ieee Trans. Biomed. Circuits Syst.* 1 (4), 235–241. doi:10.1109/tbcas.2007.910900

Yoon, Y., Cho, J. H., and Yoon, G. (2009). Non-constrained blood pressure monitoring using ECG and PPG for personal healthcare. *J. Med. Syst.* 33 (4), 261–266. doi:10.1007/s10916-008-9186-0

Zhang, X. Y., and Zhang, Y. T. (2006). The effect of local mild cold exposure on pulse transit time. *Physiol. Meas.* 27 (7), 649–660. doi:10.1088/0967-3334/27/7/008

Zhao, X. Y., Zhang, J. C., Gong, Y. L., Xu, L. H., Liu, H. P., Wei, S. J., et al. (2022). Reliable detection of myocardial ischemia using machine learning based on temporal-spatial characteristics of electrocardiogram and vectorcardiogram. *Front. Physiology* 13, 854191. doi:10.3389/fphys.2022.854191

frontiers | Frontiers in Physiology

TYPE Original Research
PUBLISHED 27 July 2023
DOI 10.3389/fphys.2023.1180631

OPEN ACCESS

EDITED BY
John Allen,
Coventry University, United Kingdom

REVIEWED BY
Shaoxiong Sun,
King's College London, United Kingdom
Kirk Shelley,
Yale University, United States

*CORRESPONDENCE
Guang Zhang,
zhangguang01@hotmail.com

RECEIVED 06 March 2023
ACCEPTED 17 July 2023
PUBLISHED 27 July 2023

CITATION
Chen R, He M, Xiao S, Wang C, Wang H, Xu J, Zhang J and Zhang G (2023), The identification of blood pressure variation with hypovolemia based on the volume compensation method.
Front. Physiol. 14:1180631.
doi: 10.3389/fphys.2023.1180631

The identification of blood pressure variation with hypovolemia based on the volume compensation method

Ruijuan Chen[1,2], Ming He[1,2], Shumian Xiao[1,2], Cong Wang[1,2], Huiquan Wang[1,2], Jiameng Xu[1,2], Jun Zhang[1,2] and Guang Zhang[3]*

[1]School of Life Sciences, TianGong University, Tianjin, China, [2]Tianjin Key Laboratory of Quality Control and Evaluation Technology for Medical Devices, Tianjin, China, [3]Systems Engineering Institute, Academy of Military Sciences, People's Liberation Army, Tianjin, China

Objective: The purpose of this study is to identify the blood pressure variation, which is important in continuous blood pressure monitoring, especially in the case of low blood volume, which is critical for survival.

Methods: A pilot study was conducted to identify blood pressure variation with hypovolemia using five Landrace pigs. New multi-dimensional morphological features of Photoplethysmography (PPG) were proposed based on experimental study of hemorrhagic shock in pigs, which were strongly correlated with blood pressure changes. Five machine learning methods were compared to develop the blood pressure variation identification model.

Results: Compared with the traditional blood pressure variation identification model with single characteristic based on single period area of PPG, the identification accuracy of mean blood pressure variation based on the proposed multi-feature random forest model in this paper was up to 90%, which was 17% higher than that of the traditional blood pressure variation identification model.

Conclusion: By the proposed multi-dimensional features and the identification method, it is more accurate to detect the rapid variation in blood pressure and to adopt corresponding measures.

Significance: Rapid and accurate identification of blood pressure variation under low blood volume ultimately has the potential to effectively avoid complications caused by abnormal blood pressure in patients with clinical bleeding trauma.

KEYWORDS

hypovolemia, volume compensation method, blood pressure variation, photoplethysmography, non-invasive

1 Introduction

Hemorrhagic shock is a pathophysiological process characterized by reduced effective circulating blood volume and cardiac output, insufficient tissue perfusion, disordered cell metabolism and impaired function due to massive blood loss caused by trauma (Liu et al., 2015). Hemorrhagic shock is often accompanied by concomitant hypotension, which is defined as systolic blood pressure less than 90 mmHg and differential pulse pressure less than 20 mmHg (Chou et al., 2016; Tran et al., 2018). According to World Health Organization

(WHO) statistics, about 10% of global deaths and 16% of disability cases are caused by trauma, which is also the leading cause of death for people under the age of 40 worldwide (World Health Organization, 2019). In trauma patients, the death rate due to excessive blood loss is about 30–40 percent (Edgard et al., 2015; Keane, 2016; Palmer, 2017), and the death rate due to incorrect treatment and inappropriate treatment is 10–20 percent (Küchler et al., 2020).

Arterial blood pressure is critical for adequate tissue perfusion, providing oxygen delivery for energy needs. Continuous and reliable measurements of absolute blood pressure are required for critically ill patients in the ICU, and variations in blood pressure of even a few minutes in patients with hypovolemic blood loss pose unpredictable risks, including hemorrhagic shock (Ameloot et al., 2013). Continuous detection of the blood pressure trend of patients in the state of blood loss and hypovolemia can provide important cardiovascular state supporting data and provide early intervention for corresponding treatment methods. The results of various studies of continuous noninvasive blood pressure monitoring devices versus invasive blood pressure monitoring methods were summarized by Kim et al. They found a significant difference between the non-invasive and invasive blood pressure obtained with the CNAP and ClearSight devices based on the volumetric compensation method. The standard deviations were 5.5 ± 9.3 mmHg and 3.5 ± 6.8 mmHg for CNAP and ClearSight respectively (Kim et al., 2014; Vos et al., 2014; Meidert and Saugel, 2017). This analysis shows that the accuracy and precision of continuous noninvasive devices are not interchangeable with invasive blood pressure measurements.

A method for blood pressure variation identification under hypovolemia based on the volume compensation method and pulse wave morphological characteristics is proposed in this study. Currently, the volume compensation method is a relatively mature blood pressure monitoring technology. This method keeps the blood volume constant in the vessel by applying a pressure value equivalent to the intravascular pressure outside the measurement (ZhangLiuChen and Liu, 2020). Studies have shown that the PPG signal profile of the photoelectric pulse wave signal is mainly controlled by the blood pressure waveform, and contains cardiovascular information, such as blood vessel stiffness and blood pressure. A large number of studies have verified that a large amount of cardiovascular information is contained in the PPG signal, which is strongly correlated to blood pressure (Mukherjee et al., 2018). The morphological analysis of PPG has been applied to vascular assessment (Fedotov, 2019a), providing rich information for cardiovascular analysis (Fedotov, 2019b; Subashini et al., 2021). There were also some studies that use morphological characteristics of not only PPG but also ECG (Electrocardiogram) signals to jointly estimate blood pressure, and to estimate SBP value every 30 s (Sun et al., 2016; Sun et al., 2022). A study that predicted blood pressure by combining various morphologies of Pulse Transit Time and PPG verified that the morphological features of PPG improved the accuracy of blood pressure estimation (Ding and Zhang, 2015; Ding et al., 2016; Lin et al., 2017; Rastegar et al., 2019).

Based on the data set under the experimental model of animal controlled hypovolemia, this study uses the photoelectric pulse signal collected by the volume compensation method to identify the variation of 11-degree blood pressure in the range of 5–15 mmHg. Five models, namely, LightGBM, Random Forest, XGBoost, CatBoost, and Decision Tree, were employed to investigate the advantages of multi-dimensional features compared with single-dimensional features in the identification of blood pressure variation under low blood volume. The accurate prediction of blood pressure variation was realized, which verifies the validity of this research method. Using accurate results of non-invasive blood pressure variation identification under hypovolemia during blood loss can not only help avoid adverse events caused by invasive blood pressure monitoring (Suess and Pinsky, 2015; Minokadeh and Pinsky, 2016), but also provide accurate diagnostic prediction for patients under cardiovascular monitoring to reduce patient tissue hypoxia, mitigate oxidative damage, prevent multiple organ failure, and improve clinical outcomes (Janssen et al., 2017; Nachman et al., 2020).

2 Materials and methods

2.1 Experiment

An animal model of hemorrhagic hypovolemia was designed in this study (The experimental schematic diagram is shown in Figure 1), and five healthy Landrace pigs weighing 23 ± 6 kg were selected as the subjects for a pilot study on blood pressure discrimination with hypovolemia. After Landrace pigs were anesthetized, the pigs were intubated and mechanically ventilated using a ventilator to prevent spontaneous breathing from affecting signal acquisition. Mindray monitor was used to monitor the physiological state and tail PI (Perfusion Index) of pigs in real time. The femoral artery was punctured on the pig, and the IBP signal was collected using the Chengdu Instrument RM6240C multi-channel physiological parameter acquisition device, while the self-developed device and deflatable optoelectronic finger cuff was used to collect the PPG signal on the pig's tail (The light Emitting Diode inside the finger cuff emits infrared light, which is transmitted through the tissues of the pig's tail and the arterial veins, and is received by the Photoelectric Sensor. Due to the flow of blood in the arteries, there is a change in the absorption of the light so that the transmitted light is converted into an electrical signal to form a PPG signal. So the measured PPG signal is opposite to the actual PPG signal waveform of the pig.). The sampling frequency of Chengdu Instrument RM6240C multi-channel physiological parameter acquisition instrument equipment is 1,000 Hz, and the sampling frequency of self-developed device is 500 Hz. Multiple bloodletting operations were performed through the carotid artery until the tail PI (Perfusion Index) was under 0.3, which indicated a state of hypovolemia. which indicates a state of hypovolemia. IBP and PPG signals were collected synchronously during bloodletting. The animal Invasive blood pressure span changed during the blood loss process, where the blood pressure of each animal decreased from different initial baseline blood pressure to blood pressure under hypovolemia. Experiment in this study was approved by the Medical Ethics Committee of Chinese PLA General Hospital (No. S2020-045-01).

2.2 Pressure setting and signal acquisition

2.2.1 Constant pressure setting algorithm

The blood pressure change identification is based on the photoelectric pulse wave signal of the detection site under

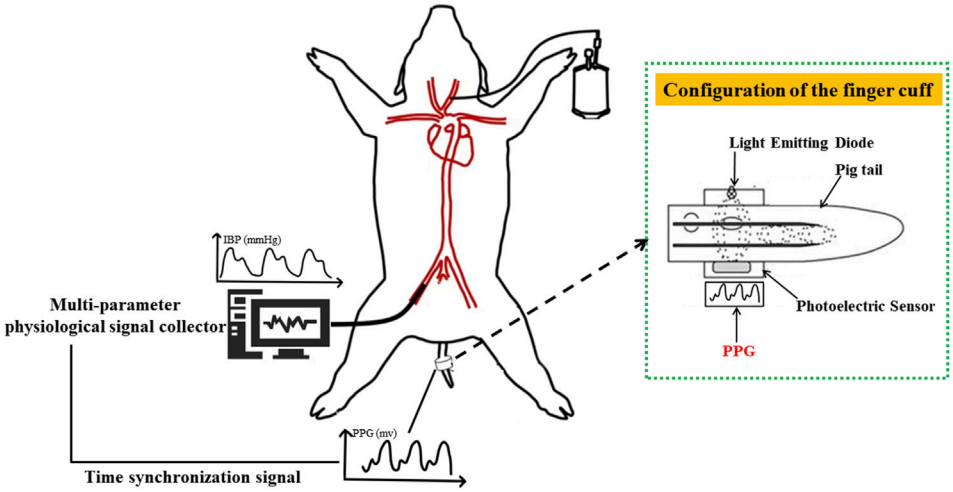

FIGURE 1
Schematic diagram of animal blood loss experiment. PPG signal (human finger probe used) under constant volume and invasive blood pressure were collected based on synchronization level signal sent by the finger cuff to achieve strict time alignment.

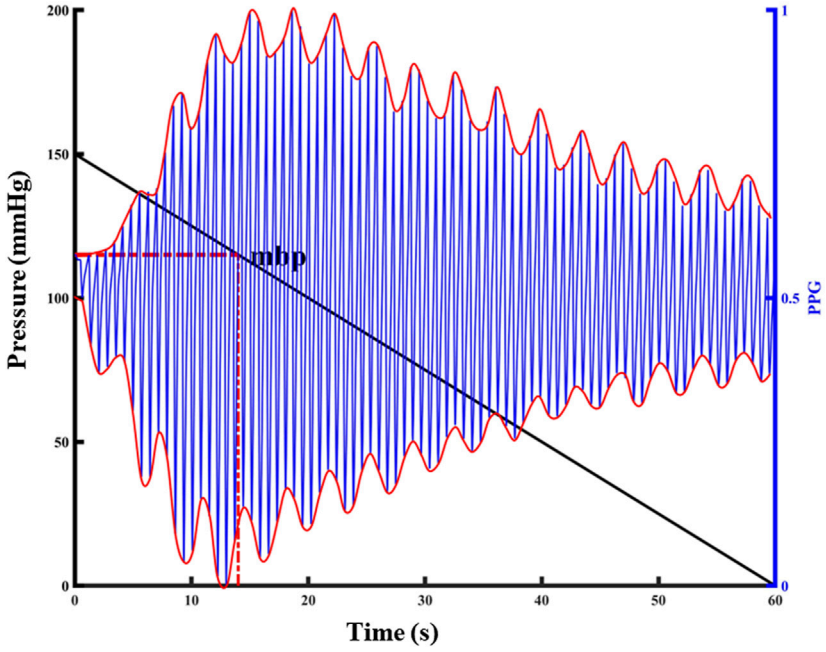

FIGURE 2
Relationship between PPG pulsation and external pressure at the detection site. The left y-label represents the externally applied pressure value, the black diagonal line in the figure represents the pressure change, the right y-label represents the normalized PPG value, the blue line in the figure represents the PPG waveform, and the red curve represents the upper and lower envelopes of the PPG waveform.

constant pressure. In the process of external force change, when the external force applied to the detection site is equal to the average pressure in the artery, pulse wave peak reaches the maximum intensity. As intra-arterial blood pressure changes, the shape of the photoplethysmography wave changes significantly at the constant pressure (Figure 2).

The peak-to-peak value was calculated according to the upper and lower envelopes of the photoelectric pulse wave signal under pressure (Find the function of the PPG signal envelope and the parameters to be set: the function is *envelope*; parameter 1 is set to *250*; parameter 2 is set to "*peak*".). The maximum peak-to-peak value corresponding to the pressure applied to the detection site

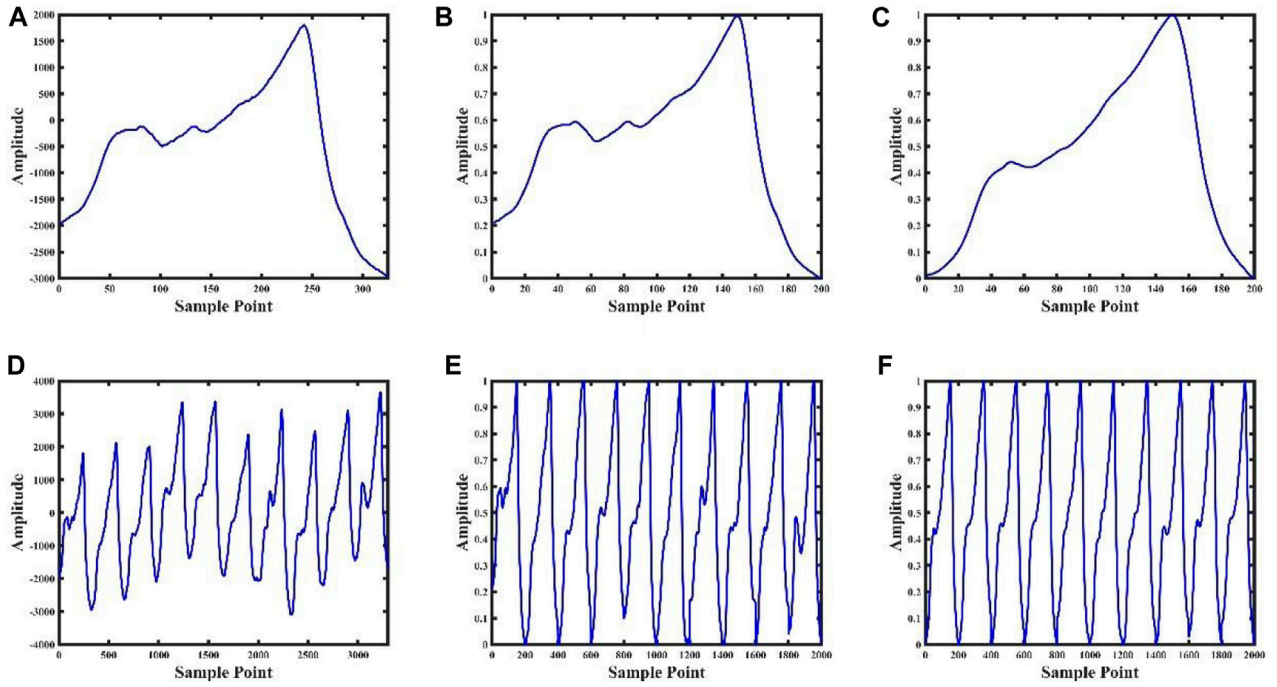

FIGURE 3
Data processing result graph. Figures **(A)**, **(B)**, **(C)** are the pulse wave waveform after single-cycle preprocessing, the pulse wave waveform after single-cycle normalization, and the pulse wave waveform after single-cycle template, respectively; Figures **(D)**, **(E)** and **(F)** are the ten consecutive cycles pulse waveforms after of preprocessing, ten consecutive cycles pulse waveforms after normalizing, and ten consecutive pulse cycles waveforms after templating, respectively.

was the average pressure corresponding to the detection site, and the constant pressure was set at the detection. Repeated application of 150 mmHg finger cuff pressure to the animal tail before the experiment can result in the temporary blood flow blocking effect, in addition to not causing venous congestion damage to the tail. The external force of 150 mmHg was repeatedly applied on the tail, released to 0 mmHg, and the tail photoelectric pulse wave was collected in real time. In this experiment, blood loss and transfusion were performed to change the blood pressure state continuously, and constant pressure value was calculated under a new blood pressure homeostasis. A total of 214 groups of constant pressure sample data were collected, with blood pressure ranging from 52 mmHg to 119 mmHg.

2.2.2 Photoelectric pulse wave data set at constant pressure

Before each blood loss operation in the animal experiment, the constant pressure value that should be applied to the tail of the animal was calculated, and the finger cuff was inflated to this constant pressure value. On a constant pressure, the pressure was maintained for 10 min during a single bloodletting of 200 mL, the pressure was released to zero after 10 min, and the tail was relieved for 10 min. Two photoelectric pulse wave data segments of blood loss process were collected for each animal, and a total of ten blood loss data segments were collected, based on the photoelectric acquisition terminal in the tail finger cuff.

2.3 Data preprocessing

The photoelectric pulse wave signal was collected under constant pressure in the state of continuous blood loss. The experimental subject was accompanied by an accelerated heartbeat and changes in the elasticity of blood vessels during bloodletting. To minimize the influence of factors other than intravascular pressure on the photoelectric pulse waveform, the template processing (Figure 3) for the photoelectric pulse wave was adopted. The templating process consists of five parts:

(1) Preprocessing: Check the original data and remove invalid data segments during convulsions of animals or abnormal device connections. Retain data from 0.3–20 Hz with Butterworth filter to remove baseline drift, low frequency noise and high frequency noise.
(2) Pulse wave single-cycle amplitude normalization: A pulse wave cycle from the pulse wave trough value to the next pulse wave trough value was defined. Amplitude normalization was performed based on the waveform peak and trough value of a single cycle, and the amplitude was fully normalized as [0,1].
(3) Pulse wave single cycle length normalization: A pulse wave cycle from the pulse wave trough value to the next pulse wave trough value was defined, and the length in a single cycle to 200 points was normalized. If the length of a single cycle waveform is greater than two hundred points, the waveform in the cycle will be downsampled, otherwise the

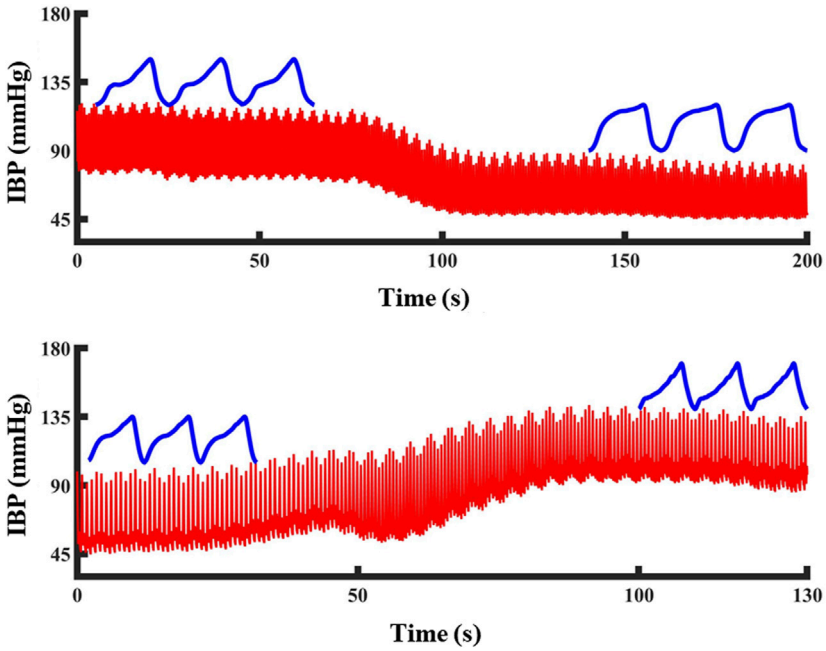

FIGURE 4
The change of PPG waveform shape during blood pressure change: Blood pressure drops and PPG waveform become shorter and wider. Blood pressure increased, PPG waveform became high and narrow. The red line represents the blood pressure and the blue line represents the PPG waveform at that blood pressure.

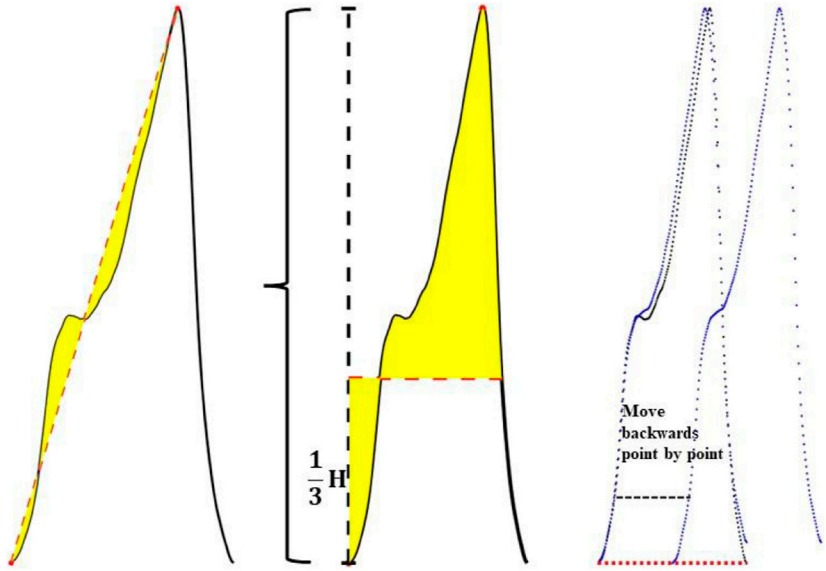

FIGURE 5
Schematic diagram of feature extraction.

waveform in the cycle will be subjected to cubic spline interpolation.

(4) Obtaining the pulse wave template waveform: Based on average of the summation of the normalized waveform PPG_norm for the first n cycles of maintaining a constant pressure, the template formula is shown in (1):

$$\mathbf{PPG\_template} = \frac{\mathbf{PPG\_norm}(1) + \mathbf{PPG\_norm}(2) + \ldots \mathbf{PPG\_norm}(n)}{n} \quad (1)$$

(5) Find the pulse wave sample waveform: Starting from the i-th (i > 2) waveform, the moving average processing is performed

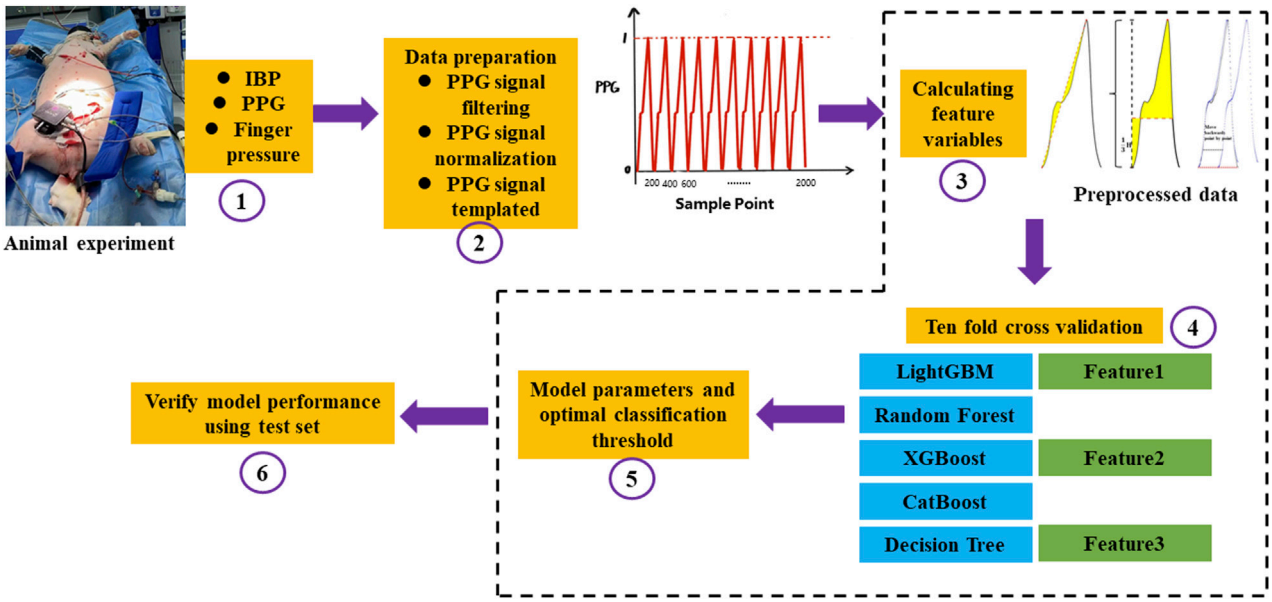

FIGURE 6
The overall flow chart of blood pressure identification. ①Firstly, the animal experiment was carried out. IBP was collected from the left femoral artery, PPG and Finger pressure were collected from the pig tail by self-developed device, and a total of three signals were collected; ②The collected PPG signals were preprocessed, the baseline drift and noise were removed by filtering, the amplitude and length of the signals were normalized, and finally the PPG signals were templated; ③Feature extraction was carried out for the preprocessed PPG signals, and the integral area of the rising edge of the waveform, the integral area of a single cycle of the waveform and the difference between the cross-correlation of the sample waveform and the template waveform and the autocorrelation of the template waveform; ④After feature extraction, the ten-fold cross-validation idea was used to construct the model. The magnitude of a single feature value is used to determine changes in blood pressure and a machine learning model with multiple features is built to identify changes in blood pressure, respectively. Feature 1 represents the integral area of the rising edge of the waveform, Feature 2 represents the integral area of the waveform in one period, and Feature 3 represents the cross correlation between the sample waveform and the template waveform and the difference between the template waveform and the template waveform; ⑤The optimal threshold points were selected by using the Youden's index, Automatic parameter tuning using Bayesian optimization; ⑥Statistical 10-fold cross validation evaluation index.

TABLE 1 Comparison with BHS standard.

Method	Subject	Cumulative error percentage (%)		
		≤5 mmHg	≤10 mmHg	≤15 mmHg
this study	NIMBP	52.8	92.5	100
BHS	Grade A	60	85	95
	Grade B	50	75	90
	Grade C	40	65	85

according to the normalized waveforms of the current n cycles, until the last waveform cycle in the data segment is added to the calculation. The calculation formula is shown in (2):

$$\mathbf{PPG\_sample} = \frac{\boldsymbol{PPG\_norm}(\boldsymbol{i}) + \boldsymbol{PPG\_norm}(\boldsymbol{i}+1) + \ldots \boldsymbol{PPG\_norm}(\boldsymbol{i}+\boldsymbol{n}-1)}{\boldsymbol{n}} \quad (2)$$

2.4 Feature extraction

Three morphological features that are highly correlated with the blood pressure changes during blood loss were extracted based on previous research and the photoelectric pulse wave signal in this experiment. Figure 4 shows the changes of the pulse waveform characteristics and actual blood pressure values in the tail of the

TABLE 2 Identification results of diastolic blood pressure variation under different models (F1 represents the classification model based on the optimal threshold of feature 1, F2 represents the classification model based on the optimal threshold of feature 2, F3 represents the classification model based on the optimal threshold of feature 3, M1 represents the LightGBM model, M2 represents the Random Forest, M3 represents XGBoost model, M4 represents CatBoost model, and M5 represents Decision Tree.).

ΔDBP (mmHg) Model	ACC (%)				AUC (%)			
	5	10	15	Mean	5	10	15	Mean
F1	79	82	90	83	80	86	90	85
F2	66	76	76	73	66	76	76	75
F3	74	80	80	78	75	81	82	79
M1	87	88	90	87	94	94	96	94
M2	83	85	93	87	95	95	97	95
M3	85	87	91	87	93	93	96	93
M4	84	87	92	88	93	95	96	94
M5	88	91	89	88	88	91	89	88

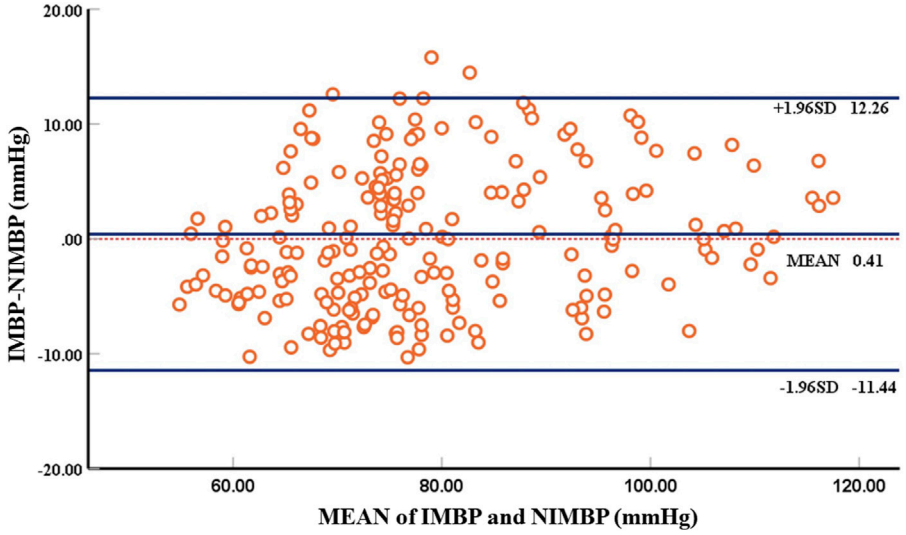

FIGURE 7
Bland-Altman plot comparing non-invasive mean blood pressure and invasive mean blood pressure. There are 214 groups of samples, with each circle representing the mean blood pressure at the beginning of identification of blood pressure.

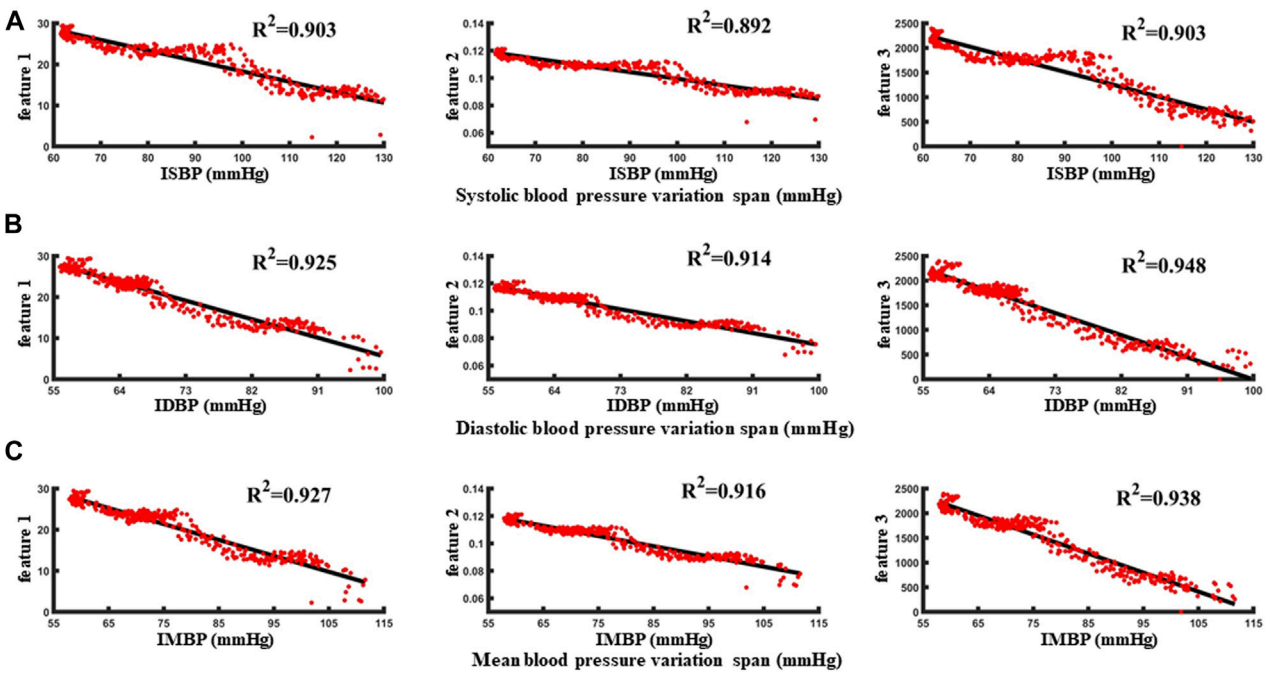

FIGURE 8
(A–C) are the correlation analysis of characteristic parameters with systolic blood pressure, diastolic blood pressure and mean blood pressure, respectively.

animals during blood loss and blood transfusion. In the process of blood pressure change from high to low, the shape of the pulse wave changed from normal to wider and shorter. In the process of blood pressure from small to large, the shape of the pulse wave changed from normal to thinner and taller.

According to the above pulse wave morphological changes, three morphological features in the pulse wave waveform were extracted. It includes the integral area of the rising edge of the waveform, the integral area of a single cycle of the waveform and the difference between the cross-correlation of the sample waveform and the template waveform and the autocorrelation of the template waveform. The feature extraction process is shown in Figure 5.

It includes the integral area of the rising edge of the waveform, the integral area of a single cycle of the waveform and the difference

TABLE 3 Identification results of mean blood pressure variation under different models (F1 represents the classification model based on the optimal threshold of feature 1, F2 represents the classification model based on the optimal threshold of feature 2, F3 represents the classification model based on the optimal threshold of feature 3, M1 represents the LightGBM model, M2 represents the Random Forest, M3 represents XGBoost model, M4 represents CatBoost model, and M5 represents Decision Tree).

ΔMBP (mmHg) Model	ACC (%)				AUC (%)			
	5	10	15	Mean	5	10	15	Mean
F1	82	85	93	86	82	87	93	88
F2	65	75	77	73	67	77	79	75
F3	83	86	90	86	85	84	90	87
M1	78	89	94	89	92	96	98	96
M2	82	91	95	90	92	96	98	96
M3	79	90	94	89	92	96	97	95
M4	77	90	94	89	92	96	98	96
M5	83	91	93	90	83	91	93	90

TABLE 4 Identification results of systolic blood pressure variation under different models (F1 represents the classification model based on the optimal threshold of feature 1, F2 represents the classification model based on the optimal threshold of feature 2, F3 represents the classification model based on the optimal threshold of feature 3, M1 represents the LightGBM model, M2 represents the Random Forest, M3 represents XGBoost model, M4 represents CatBoost model, and M5 represents Decision Tree.).

ΔSBP (mmHg) Model	ACC (%)				AUC (%)			
	5	10	15	Mean	5	10	15	Mean
F1	82	83	86	84	84	84	88	85
F2	64	74	77	73	65	76	79	74
F3	78	82	85	83	80	83	85	84
M1	83	90	91	90	93	96	96	95
M2	80	90	93	89	94	97	96	96
M3	84	90	93	90	92	96	96	95
M4	82	91	90	89	93	96	97	96
M5	86	91	89	90	86	91	89	90

between the cross-correlation of the sample waveform and the template waveform and the autocorrelation of the template waveform.

As shown in Figure 5, the three feature extraction processes were:

Feature 1 extraction:

A linear straight line was fitted in the direction from the pulse trough value to the peak value, and the straight line was used as the baseline to obtain the integral area of the area enclosed between the rising edge curve of the waveform and the baseline.

Feature 2 extraction:

One third of the peak value of the pulse wave was taken as the baseline, and the difference between the integral area of the upper half waveform of the baseline and the lower half waveform of the baseline was calculated.

Feature 3 extraction:

Step1, The cross-correlation matrix of the sample waveform and the template waveform ($R_{t\text{-}s}$) were calculated. Then the sample waveform was multiplied by the point-by-point sliding and then summed. The calculation formula is shown in (3):

$$\boldsymbol{R_{t-s}} = \mathbf{ppg\_template}(\mathbf{n}) * \mathbf{ppg\_sample}^{*}(-\mathbf{n}) \tag{3}$$

Step2, The autocorrelation matrix of the template waveform ($R_{t\text{-}t}$) was calculated. Autocorrelation is a special case of cross-correlation, that is, the correlation between the sequence and itself. The calculation formula is shown in (4):

$$\boldsymbol{R_{t-t}} = \mathbf{ppg\_template}(\mathbf{n}) * \mathbf{ppg\_template}^{*}(-\mathbf{n}) \tag{4}$$

Step3, The difference between the cross-correlation matrix and the auto-correlation matrix was calculated, and this difference was described by the area enclosed by the two matrix curves, as shown in formula (5). When the sample waveform and the template waveform had high similarity, the area enclosed by the two matrix curves was small, otherwise, the difference between the two was considered to be greater.

$$\mathbf{difference} = \sum_{i=1}^{n} |\mathbf{R_{t-s}}(\mathbf{i}) - \mathbf{R_{t-t}}(\mathbf{i})| \tag{5}$$

2.5 Construction of blood pressure variation identification model

2.5.1 Construction of blood pressure variation identification model based on single feature

Three classification models based on the classification thresholds of the three features and ten-fold cross-validation were constructed. In the process of ten-fold cross validation ten sub-data sets were randomly generated from the data set, one sub-data set was selected each time as the test set, and the ten sub-data sets were sequentially used as the test set. Using the traditional single-feature PPG single-cycle integral area as the prediction model index. The minimum and maximum sample values in the model were identified, the value was divided into 100 parts with the maximum and minimum values, and the 100 values were in turn cycled as the classification threshold. According to 10 test results (the intersection of sensitivity curve, specificity curve and accuracy curve), the optimal classification threshold of the model was selected. Finally, the test set was identified based on the optimal classification threshold, and the results were evaluated by the Accuracy (ACC) and Area Under the Curve (AUC) values.

2.5.2 Construction of blood pressure variation identification model based on multiple features

The PPG feature sample dataset and label corresponding to the process of diastolic blood pressure, systolic blood pressure, and mean blood pressure variation of 5–15 mmHg obtained in the blood loss experiment in this study were used as input. Five classic machine learning algorithms, namely, LightGBM, Random Forest, XGBoost, CatBoost, and Decision Tree were used. The learning model performed classification and identification. The following indicators were used to evaluate the ability of five

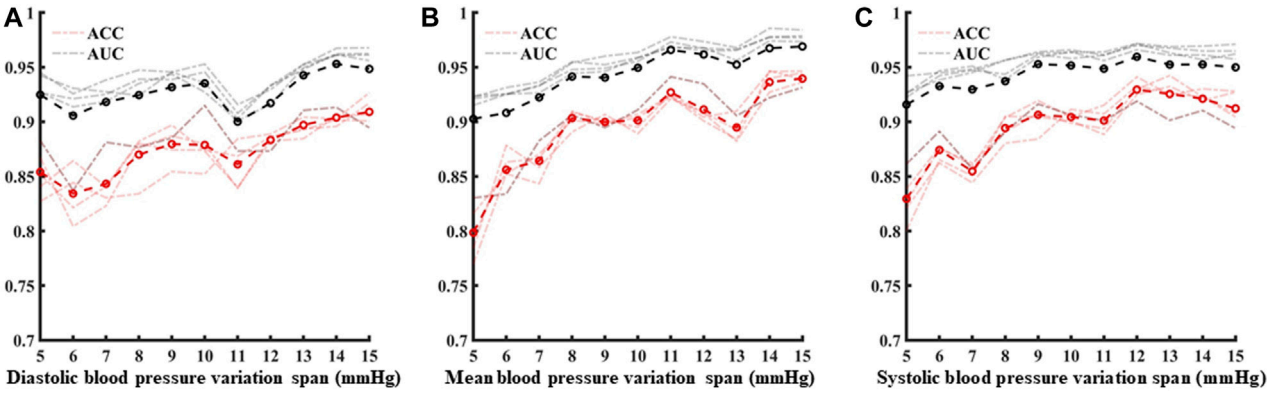

FIGURE 9
(A–C) are the analysis of identification results under different blood pressure variability under diastolic blood pressure, mean blood pressure and systolic blood pressure, respectively.

machine learning models to identify changes in blood pressure under hypovolemia. ACC represents the accuracy of the model, AUC represents the integral area under the Receiver Operating Characteristic (ROC) curve, Matthews correlation coefficient (MCC) represents the consistency of the predicted classification with the actual classification, F1 score (F1_score) considers the accuracy and recall rate of the classification model, Kappa: tests the consistency coefficient, AUPRC: the area under the precision-recall curve. Figure 6 shows the overall flow chart of blood pressure identification.

2.6 Constant pressure setting results

The results of the constant pressure setting algorithm described above showed that the correlation between the non-invasive mean blood pressure of the tail and the invasive mean blood pressure of the left thigh of the animal collected simultaneously was 84%. Table 1 shows the comparison between the error analysis results of the non-invasive mean blood pressure and invasive mean blood pressure and the British Hypertension Society (BHS) standard results. The Bland-Altman analysis results are shown in Figure 7.

Using self-developed device, the mean deviation of non-invasive blood pressure detection and invasive blood pressure detection was 0.41 mmHg, and the 95% confidence of the difference between the two was −11.44 mmHg–12.26 mmHg, which can accurately detect blood pressure. According to the above Bland-Altman diagram, there are 3 samples, namely, 3/214 (1.4%), and less than 5% of the samples exceed the 95% consistency limit. The initial non-invasive mean blood pressure detection is highly consistent with the invasive mean blood pressure, which proves the reliability of the self-developed device.

2.7 Correlation analysis between characteristic parameters and blood pressure

Correlation analysis was performed based on the extracted feature parameters and invasive blood pressure values to evaluate the relationship between the above three pulse wave morphological features and blood pressure. Five periodic waveform periods were used as the sliding window size to perform template processing, and the processed waveforms were the extracted features. A total of 1942 groups of valid feature samples were extracted from five animals. Three characteristic parameters and invasive blood pressure data of an animal under blood loss for 5 minutes were extracted and analyzed (Figure 8). The correlation between the two was 0.892–0.948, and the blood pressure change state under blood loss could be identified based on the characteristic parameters.

With reference to the normal fluctuation range of blood pressure within 12 h and 24 h in humans, the standard of blood pressure change was identified as 5 mmHg–15 mmHg. First, taking the blood pressure change threshold of 5 mmHg as an example, in the blood loss data segment, the samples with invasive blood pressure changes within 5 mmHg were defined as no change in blood pressure and were considered as negative sample data. Conversely, when the blood pressure was greater than 5 mmHg, the samples were identified as the occurrence of individual blood pressure during blood loss and the change was considered as positive sample data. In order to avoid over-fitting caused by the large proportion of category samples, the prediction results would be biased towards the classification with the large number of samples. The positive samples and negative samples for blood pressure change identification classification are 1:1. Taking the data set during the blood loss of a case of an animal as an example, 340 characteristic samples were extracted, and correlation analysis was carried out with the synchronously collected invasive blood pressure data (Figures 8A, B, C). The correlation between the three features and the invasive systolic blood pressure were 0.903, 0.892, and 0.903, respectively, the correlation between the three features and the invasive mean blood pressure were 0.925, 0.914, and 0.948, respectively, and the correlation between the three features and the invasive diastolic blood pressure were 0.927, 0.916, and 0.938, respectively.

2.8 BP variation identification model results

The data set after template processing was analyzed with five waveform periods as the sliding window size, and the blood pressure

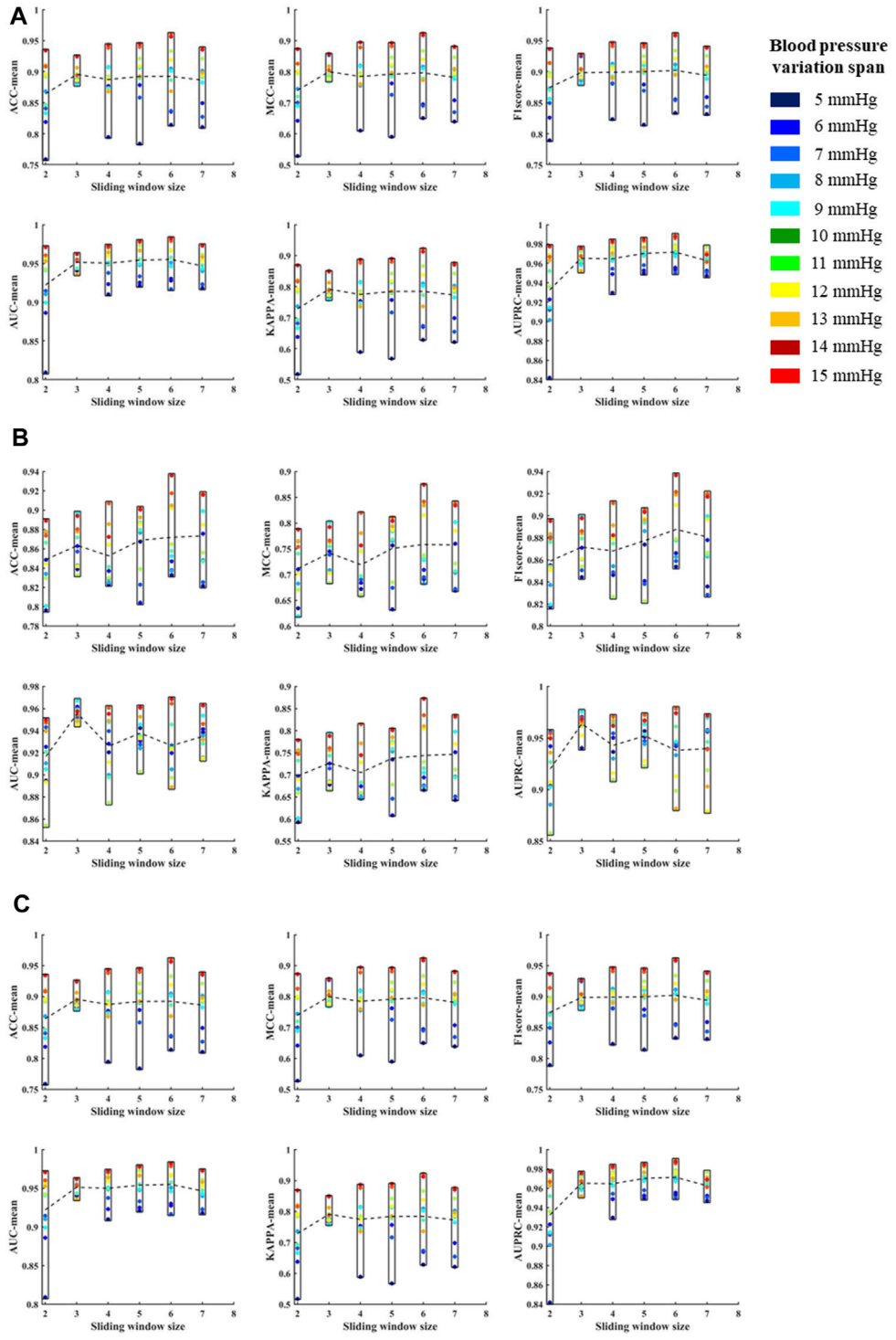

FIGURE 10
(A) is the mean values of ACC, MCC, F1 score, AUC, KAPPA and AUPRC for systolic blood pressure at different sliding window sizes, in models established for blood pressure changes spanning 5–15 mmHg, respectively. **(B)** is the mean values of ACC, MCC, F1 score, AUC, KAPPA and AUPRC for diastolic blood pressure at different sliding window sizes, in models established for blood pressure changes spanning 5–15 mmHg, respectively. **(C)** is the mean values of ACC, MCC, F1 score, AUC, KAPPA and AUPRC for mean blood pressure at different sliding window sizes, in models established for blood pressure changes spanning 5–15 mmHg, respectively. The X label of each graph represents the size of the sliding window and the Y label represents the different evaluation metrics for blood pressure changes across 5–15 mmHg under the current sliding window.

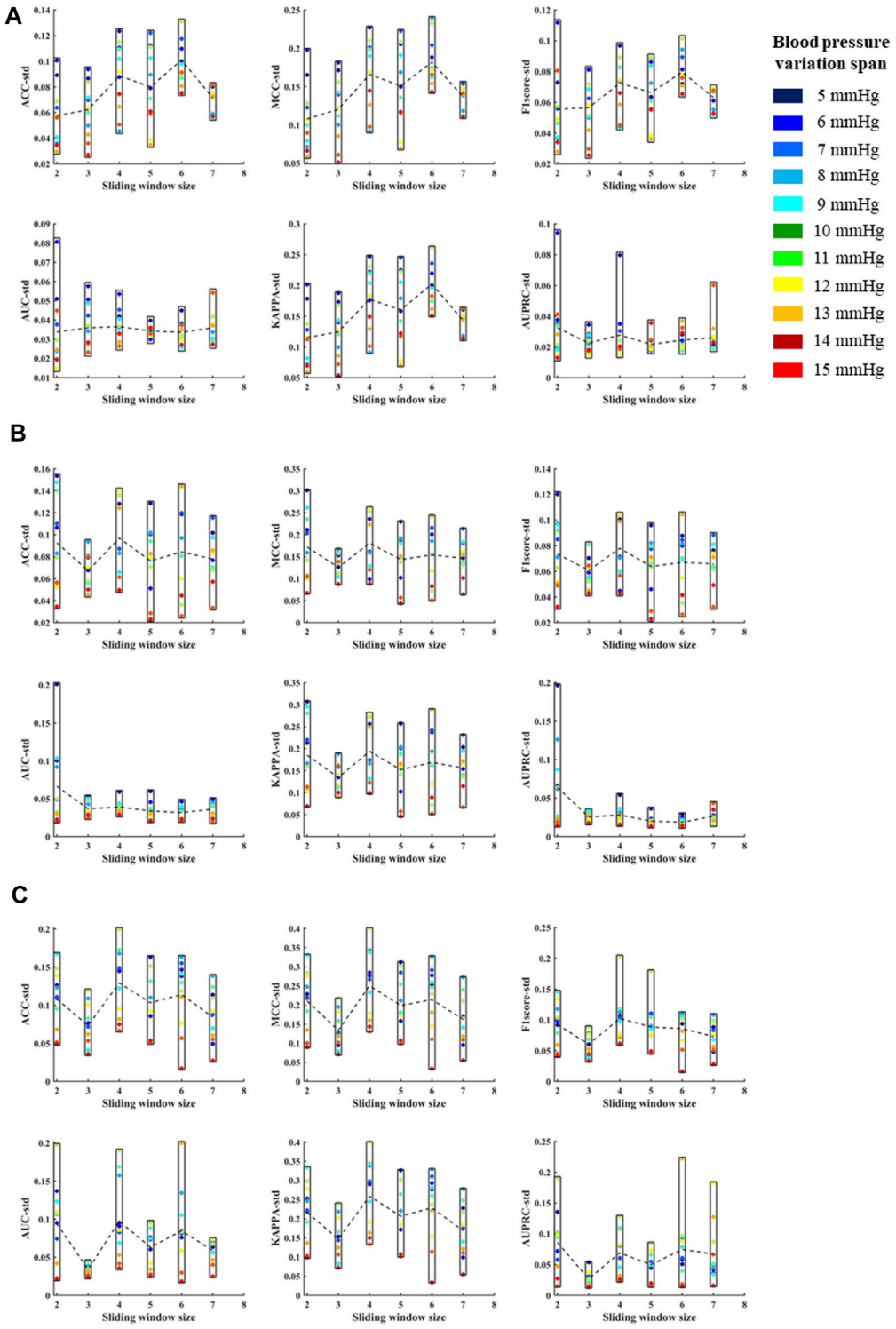

FIGURE 11
(A) is the standard deviations of ACC, MCC, F1 score, AUC, KAPPA and AUPRC for systolic blood pressure at different sliding window sizes, in models established for blood pressure changes spanning 5–15 mmHg, respectively. **(B)** is the standard deviations of ACC, MCC, F1 score, AUC, KAPPA and AUPRC for diastolic blood pressure at different sliding window sizes, in models established for blood pressure changes spanning 5–15 mmHg, respectively. **(C)** is the standard deviations of ACC, MCC, F1 score, AUC, KAPPA and AUPRC for mean blood pressure at different sliding window sizes, in models established for blood pressure changes spanning 5–15 mmHg, respectively. The X label of each graph represents the size of the sliding window and the Y label represents the different evaluation metrics for blood pressure changes across 5–15 mmHg under the current sliding window.

identification range was 5–15 mmHg. Variation identification accuracy and AUC values of blood pressure (diastolic blood pressure, mean blood pressure, systolic blood pressure) at 5 mmHg, 10 mmHg, 15 mmHg and average variation under 5–15 mmHg based on single-feature identification model and five machine learning models based on multi-feature are shown in Tables 2, 3, 4.

As shown in Tables 2, 3, 4: the blood pressure variation identification model under hypovolemia in this study was constructed based on the two newly extracted feature parameters, compared with the traditional Feature 2. The reported ACC and AUC values for diastolic blood pressure increased with the ΔDBP more than 5%, while the ACC and AUC values for mean blood pressure and systolic blood pressure increased with the ΔMBP and ΔSBP more than 10%. The identification model results based on multi-dimensional features compared with the traditional feature 2 blood pressure variation identification model showed that the diastolic blood pressure variation identification ACC and AUC increased with the ΔDBP 14%–15% and 15%–20%, respectively; the mean blood pressure variation average identification ACC and AUC were increased with the ΔMBP 16%–17% and 15%–21%, respectively, and the mean identification of systolic blood pressure variation ACC and AUC were increased with the ΔSBP 16%–17% and 16%–22%, respectively. Comparison of the results of multi-dimensional-based blood pressure variation identification under hypovolemia showed that the features proposed in this study are better for mean blood pressure and systolic blood pressure variation identification than diastolic blood pressure fluctuation identification under hypovolemia. Furthermore, the analysis of the results of the five machine learning models showed that the variation identification accuracy of the mean blood pressure and systolic blood pressure in the range of 5–15 mmHg under the random forest and decision tree machine learning models can reach 90% and all the AUC values exceeding 90%.

3 Analysis and discussion

3.1 Comparative analysis of different blood pressure identification range results

Following template processing, the data set was analyzed with five periodic waveforms as the sliding window size, and blood pressure variation identification was performed for 5 mmHg–15 mmHg in turn. Based on three characteristics of systolic blood pressure, diastolic blood pressure, and average blood pressure variation identification model using the five machine learning models, the average ACC and the average AUC were calculated (Figure 9). With the increase of blood pressure variation range, the ACC values and AUC values show an overall increasing trend.

3.2 Comparison of identification results of blood pressure changes under different template waveforms

According to the above template processing process, five cycles of pulse waves were selected for sliding average processing. In order to compare the optimal sliding window size, this study repeats the above feature extraction process and modeling process for waveforms processed based on two to seven cycles of pulse waves. Based on different template waveforms, blood pressure changes were identified for 5–15 mmHg in turn, and the mean and standard deviation of the systolic blood pressure, diastolic blood pressure, and mean blood pressure variation identification indicators under the above-mentioned multi-feature identification model were used to analyze the mean value and standard deviation, respectively (Figures 10, 11). The results in the two figures show that the average value and standard deviation of the indicators of different template waveforms are comprehensively compared, and the blood pressure change identification effect is the best based when the three-cycle pulse wave was used as the template-processed waveform of the sliding window size.

3.3 Limitation

In this work, we used 1942 samples of 5 pigs to get the result, in the early stage to verify the feasibility of our method, and later experiments with larger samples data will be done to further improve its stability and extensibility.

4 Conclusion

New features and the blood pressure variation identification models under hypovolemia are proposed and established in this study, based on the morphological characteristics of photoplethysmography wave in the tail of animals. The results showed that the morphological characteristic parameters of the volumetric pulse wave under constant pressure can effectively and accurately identify the degree of blood pressure variation under blood loss. Compared with the traditional features, the two new features can further improve the accuracy of the traditional volumetric compensation method to capture blood pressure variation under low perfusion. Compared with single feature models, the classification model based on multi-dimensional features can achieve better identification effect. The feature proposed in this study is more suitable for the variation identification of mean blood pressure and systolic blood pressure, compared with the fluctuation identification of diastolic blood pressure under low blood volume. The results of blood pressure identification at different levels of 5–15 mmHg proposed in this paper can provide information of blood pressure variation for patients with mild blood loss or hemorrhagic shock, and provide non-invasive continuous blood pressure change warning for different clinical application scenarios. Furthermore, the new morphological features proposed in this study can provide an additional new blood pressure tracking method for the continuous non-invasive blood pressure monitoring equipment based on the volume compensation method.

Data availability statement

The raw data supporting the conclusion of this article will be made available by the authors, without undue reservation.

Ethics statement

The animal study was reviewed and approved by Medical Ethics Committee of the General Hospital of the Chinese People's Liberation Army (No. S2020-045-01).

Author contributions

RC, HW, and JZ contributed to conception and design of the study. Experimental data collection and analysis were completed by CW and MH. Machine learning model construction was completed by JX, and paper writing was completed by SX. The thesis proofreading was done by GZ and RC. All authors contributed to the article and approved the submitted version.

Funding

The work described in this manuscript was fully supported by National Key R&D Program of China (Grant Number: 2017YFC0806406) and Science and Technology Program of Tianjin, China (Grant Number: 18ZXJMTG00060) and Science and Technology Plan Project of Tianjin (Grant Number: 21JCYBJC01270) and The Natural Science Foundation of Tianjin (Grant Number: 20JCQNJC00150).

Acknowledgments

The author would like to thank these supporters and all participants for their cooperation in the experiments.

Conflict of interest

The authors declare that the research was conducted in the absence of any commercial or financial relationships that could be construed as a potential conflict of interest.

Publisher's note

References

Ameloot, K., Van, D. V. K., Broch, O., Van, R. N., De, L. I., Schoonheydt, K., et al. (2013). Nexfin noninvasive continuous hemodynamic monitoring: Validation against continuous pulse contour and intermittent transpulmonary thermodilution derived cardiac output in critically ill patients. *Sci. World J.*, 2013, 519080. doi:10.1155/2013/519080

Chou, D., Harada, M. Y., Barmparas, G., Ko, A., Ley, E. J., &Alban, r. f., et al. (2016). Field intubation in civilian patients with hemorrhagic shock is associated with higher mortality. *J. Trauma & Acute Care Surg.* 80, 278–282. doi:10.1097/TA.0000000000000901

Ding, X. R., and Zhang, Y. T. (2015). Photoplethysmogram intensity ratio: A potential indicator for improving the accuracy of PTT-based cuffless blood pressure estimation. *Eng. Med. Biol. Soc.* 2015, 398–401. doi:10.1109/EMBC.2015.7318383

Ding, X. R., Zhang, Y. T., and Tsang, H. K. (2016). A new modeling methodology for continuous cuffless blood pressure measurement. *IEEE.* doi:10.1109/BHI.2016.7455885

Edgard, S., Aya, O. D., Luis, C. A., Tabacchi, F. D., Fernando, D. S., Claudia, I. M., et al. (2015). Heart rate variability analysis in an experimental model of hemorrhagic shock and resuscitation in pigs. *Plos One* 10 (8), e0134387. doi:10.1371/journal.pone.0134387

Fedotov, A. A. (2019a). Noise immunity of pulse wave contour analysis. *Meas. Tech.* 62 (3), 64–67. doi:10.32446/0368-1025it.2019-3-64-67

Fedotov, A. A. (2019b). Techniques for the morphological analysis of the pulse wave. *Biomed. Eng.* 53 (4), 270–274. doi:10.1007/s10527-019-09924-x

Janssen, C., Pathak, A., Grassi, G., and Borne, P. (2017). Endothelin contributes to the blood pressure rise triggered by hypoxia in severe obstructive sleep apnea. *J. Hypertens.* 35 (1), 118–124. doi:10.1097/HJH.0000000000001134

Keane, M. (2016). Triad of death: The importance of temperature monitoring in trauma patients. *Emerg. Nurse J. Rcn Accid. Emerg. Nurs. Assoc.* 24 (5), 19–23. doi:10.7748/en.2016.e1569

Kim, S. H., Lilot, M., Sidhu, K. S., Rinehart, J., Yu, Z., Canales, C., et al. (2014). Accuracy and precision of continuous noninvasive arterial pressure monitoring compared with invasive arterial pressure: A systematic review and meta-analysis. *Anesthesiology* 120 (5), 1080–1097. doi:10.1097/ALN.0000000000000226

Küchler, J., Klaus, S., Bahlmann, L., Onken, N., Keck, A., Ditz, C., et al. (2020). Cerebral effects of resuscitation with either epinephrine or vasopressin in an animal model of hemorrhagic shock. *Eur. J. Trauma Emerg. Surg.* 46 (6), 1451–1461. doi:10.1007/s00068-019-01158-6

Lin, W. H., Wang, H., Samuel, O. W., and Li, G. (2017). "Using a new PPG indicator to increase the accuracy of PTT-based continuous cuffless blood pressure estimation," in 39th Annual International Conference of the IEEE Engineering in Medicine and Biology Society, China, 11-15 July 2017 (IEEE). EMBC 2017).

Liu, H., Xiao, X., Sun, C., Sun, D., Li, Y., and Yang, M. (2015). Systemic inflammation and multiple organ injury in traumatic hemorrhagic shock. *rontiers Bioence* 20 (6), 927–933. doi:10.2741/4347

Meidert, A. S., and Saugel, B. (2017). Techniques for non-invasive monitoring of arterial blood pressure. *Front. Med.* 4, 231. doi:10.3389/fmed.2017.00231

Minokadeh, A., and Pinsky, M. R. (2016). Postoperative hemodynamic instability and monitoring. *Curr. Opin. Crit. Care* 22 (4), 393–400. doi:10.1097/MCC.0000000000000320

Mukherjee, R., Ghosh, S., Gupta, B., and Chakravarty, T. (2018). A literature review on current and proposed technologies of noninvasive blood pressure measurement. *Telemedicine J. e-health official J. Am. Telemedicine Assoc.* 24 (3), 185–193. doi:10.1089/tmj.2017.0068

Nachman, D., Constantini, K., Poris, G., Wagnert-Avraham, L., Littman, R., Gepner, Y., et al. (2020). Wireless, non-invasive, wearable device for continuous remote monitoring of hemodynamic parameters in a swine model of controlled hemorrhagic shock. *Sci. Rep.* 10 (1), 17684. doi:10.1038/s41598-020-74686-6

Palmer, L. (2017). Fluid management in patients with trauma: Restrictive versus liberal approach. *Small Anim. Pract.* 47 (2), 397–410. Epub. doi:10.1016/j.cvsm.2016.10.014

Rastegar, S., GholamHosseini, H., and Lowe, A. (2019). Non-invasive continuous blood pressure monitoring systems: Current and proposed technology issues and challenges. *Australas. Phys. Eng. Sci. Med.* 43, 11–28. doi:10.1007/s13246-019-00813-x

Subashini, V., Janaki, R., Valarmathi, G., Su, S., Kavitha, S., Sivasankari, K., et al. (2021). Survey on regression analysis of photoplethysmography using machine learning. *Mater. Today Proc.* 46 (9), 3743–3748. doi:10.1016/J.MATPR.2021.02.013

Suess, E., and Pinsky, M. (2015). Hemodynamic monitoring for the evaluation and treatment of shock: What is the current state of the art? *Seminars Respir. Crit. Care Med.* 36 (6), 890–898. doi:10.1055/s-0035-1564874

Sun, S., Bezemer, E., Muehlsteff, J., Schmitt, L., Long, X., Bezemer, R., et al. (2022). Systolic blood pressure estimation using ECG and PPG in patients undergoing surgery. *Biomedical signal Process. control* 79 (1), 104040. doi:10.1016/j.bspc.2022.104040

Sun, S., Bresch, R., Long, X., Muehlsteff, J., and Aarts, R. M. (2016). Systolic blood pressure estimation using PPG and ECG during physical exercise. *Physiol. Meas.* 37 (12), 2154–2169. doi:10.1088/0967-3334/37/12/2154

Tran, A., Yates, J., Lau, A., Lampron, J., and Matar, M. (2018). Permissive hypotension versus conventional resuscitation strategies in adult trauma patients with hemorrhagic shock: A systematic review and meta-analysis of randomized controlled trials. *J. Trauma Acute Care Surg.* 84, 802–808. doi:10.1097/TA.0000000000001816

Vos, J. J., Poterman, M., Mooyaart, E., Weening, M., Struys, M., Scheeren, T., et al. (2014). Comparison of continuous non-invasive finger arterial pressure monitoring with conventional intermittent automated arm arterial pressure measurement in patients under general anaesthesia. *Br. J. Anaesth.* 113 (1), 67–74. doi:10.1093/bja/aeu091

World Health Organization (2019). *Global health estimates 2019 summary ta-bles: Deaths by cause, age and sex, 2000 - 2019[eb/ol]*. Gene-va, Switzerland: World Health Organization.

ZhangLiuChen, P. C. H., and Liu, J. (2020). Reconstruction of continuous brachial arterial pressure from continuous finger arterial pressure using a two-level optimization strategy. *IEEE Trans. Biomed. Eng.* 67 (11), 3173–3184. doi:10.1109/TBME.2020.2979249

frontiers | Frontiers in Physiology

TYPE Original Research
PUBLISHED 08 August 2023
DOI 10.3389/fphys.2023.1208010

OPEN ACCESS

EDITED BY
Gunjan Arora,
Yale University, United States

REVIEWED BY
Dipika Nandi,
Takeda Oncology, United States
Faisal Alotaibi,
King Faisal Specialist Hospital and Research Centre, Saudi Arabia
Eberval Figueiredo,
University of São Paulo, Brazil

*CORRESPONDENCE
Maria Roldan,
maria.roldan@city.ac.uk

RECEIVED 18 April 2023
ACCEPTED 06 July 2023
PUBLISHED 08 August 2023

CITATION
Roldan M, Bradley GRE, Mejía-Mejía E, Abay TY and Kyriacou PA (2023), Non-invasive monitoring of intracranial pressure changes: healthy volunteers study.
Front. Physiol. 14:1208010.
doi: 10.3389/fphys.2023.1208010

Non-invasive monitoring of intracranial pressure changes: healthy volunteers study

Maria Roldan*, George R. E. Bradley, Elisa Mejía-Mejía, Tomas Y. Abay and Panayiotis A. Kyriacou

Research Centre for Biomedical Engineering, City University of London, London, United Kingdom

Objective: This research aims to evaluate the possible association between pulsatile near infrared spectroscopic waveform features and induced changes in intracranial pressure in healthy volunteers.

Methods: An optical intracranial pressure sensor was attached to the forehead of 16 healthy volunteers. Pulsatile near infrared spectroscopic signals were acquired from the forehead during body position changes and Valsalva manoeuvers. Features were extracted from the pulsatile signals and analyses were carried out to investigate the presence of statistical differences in the features when intracranial pressure changes were induced. Classification models were developed utilizing the features extracted from the pulsatile near-infrared spectroscopic signals to classify between different body positions and Valsalva manoeuvre.

Results: The presence of significant differences in the majority of the analyzed features ($p < 0.05$) indicates the technique's ability to distinguish between variations in intracranial pressure. Furthermore, the disparities observed in the optical signal features captured by the proximal and distal photodetectors support the hypothesis that alterations in back-scattered light directly correspond to brain-related changes. Further research is required to subtract distal and proximal signals and construct predictive models employing a gold standard measurement for non-invasive, continuous monitoring of intracranial pressure.

Conclusion: The study investigated the use of pulsatile near infrared spectroscopic signals to detect changes in intracranial pressure in healthy volunteers. The results revealed significant differences in the features extracted from these signals, demonstrating a correlation with ICP changes induced by positional changes and Valsalva manoeuvre. Classification models were capable of identifying changes in ICP using features from optical signals from the brain, with a sensitivity ranging from 63.07% to 80% and specificity ranging from 60.23% to 70% respectively. These findings underscored the potential of these features to effectively identify alterations in ICP.

Significance: The study's results demonstrate the feasibility of using features extracted from optical signals from the brain to detect changes in ICP induced by positional changes and Valsalva manoeuvre in healthy volunteers. This represents a first step towards the non-invasive monitoring of intracranial pressure.

KEYWORDS

intracranial pressure, photoplethysmography, near infrared spectroscopy, brain monitoring, machine learning

1 Introduction

Intracranial pressure (ICP) is frequently impaired in neurocritical care patients. There are several conditions which can cause intracranial hypertension, such as, head injury, cerebral haemorrhages, stroke, intracerebral hematomas, meningitis, acute liver failure and hydrocephalus. ICP can also be influenced by surgical interventions such as tumour removal and the repairing of damaged blood vessels (Chiara, 2018). Despite several studies showing that hospital-level ICP monitoring utilisation varies substantially, with some hospitals measuring invasive ICP in as few as 9.5% of their patients, while others monitor up to 83% of their patients (Okazaki et al., 2021; Bennett et al., 2012), it is considered the gold standard in neurocritical monitoring (Evensen and Eide, 2020). Early management of intracranial hypertension decreases the risk of secondary injuries to the brain, poor outcomes and mortality (Chiara, 2018). However, current gold standard monitoring techniques are predominantly measured by invasive methods which rely on neurosurgical expertise, which could potentially delay treatment whilst introducing additional risks for the patient (Roldan et al., 2020). Consequently, numerous authors have searched for non-invasive methods to assess the brain, such as Computerised Tomography Scan, Magnetic Resonance Imaging, Transcranial Doppler and Near-Infrared Spectroscopy (NIRS) (Roldan et al., 2020). The latter has been widely described for cerebral perfusion and brain oxygenation monitoring (Roldan and Kyriacou, 2021). Continuous waveform NIRS and spatially resolved spectroscopy techniques are based on the light absorbance change reflected in the DC component of the optical signal measured by the probe (Roldan and Kyriacou, 2021). However, the information regarding the pulsatile (AC) component of the reflected infrared light has yet to be assessed. This AC component might be associated with changes in intracranial volume, which is highly correlated to ICP. This research aims to evaluate the possible association between pulsatile NIRS waveform features and induced changes in ICP in healthy volunteers.

2 Materials and methods

2.1 Monitoring device

A custom made optical nICP sensor was attached to the subject's foreheadbelow the hairline. This in-house, non-invasive sensor consists of four LEDs at multiple wavelengths and two photodiodes (proximal and distal) arranged as shown in Figure 1. A multiple wavelength sensor allows for multimodal monitoring, however This study exclusively analyzed data at 810 nm as the absorption properties of oxyhemoglobin and deoxyhemoglobin are the same at this specific wavelength. This characteristic enables the extraction of an optical signal that is independent of blood oxygenation (Murkin and Arango, 2009). Montecarlo simulation of the light-tissue interaction has demonstrated that near-infrared (NIR) light travels deeper into the head tissue when the source-detector distance is increased (Roldan et al., 2021). The reflected light from extracerebral tissue reached the proximal photodetector placed 10 mm from the LEDs; and the non-absorbed light from deeper tissues travelled back to the distal photodiode placed 35 mm from the LEDs. This study interrogated the effect of the photodiodes locations under ICP changes, and evaluated the acquisition of pulsatile signals from both distal and proximal photodiodes. The optical probe was driven by a custom made processing system enabling optical signal acquisition, pre-processing, visualization (using LabView) and archiving on a personal computer.

2.2 Healthy subjects

Sixteen healthy volunteers aged 28 ± 6 years (mean ± standard deviation; 6 women) took part in this study. The subjects were recruited through posters in the university where the study took place. The exclusion criteria included existing pathology associated with raised ICP, vasculitis, diabetes, high-risk factor for stroke or heart disease, hypertension, previous traumatic brain injury, meningitis or hydrocephalus, migraine, vertigo, fever, influenza or other infectious diseases. The University Senate Research Ethics Committee approved the study, and all participants signed an informed consent form prior to the study.

2.3 Intervention

Literature has established that tilting body position and the Valsalva manoeuver are effective methods of inducing changes in ICP among healthy volunteers (Haykowsky et al., 2002; Eklund et al., 2016; Watkins et al., 2017). In order to replicate these conditions, the volunteers' body positions were adjusted a tilt-function of the investigation bed. The protocol began with the volunteers in a supine position for 5 min (first supine), followed by a 5-min period in the Tredelenburg position, with the head inclined downward at −30°. The protocol ended with the volunteers returning to a supine position for an additional 2 min (second supine). A transition period of 30–60 s was allowed between each position. During the transition period, data was not recorded. Figure 2 provides a visual summary of this protocol. Similarly, for the Valsalva intervention, volunteers were seated and baseline measurements were recorded before three consecutive Valsalva manoeuvres were performed.

2.4 Analysis

The recorded signals were processed and analyzed using Python (version 3.10). The signal processing began by sectioning the

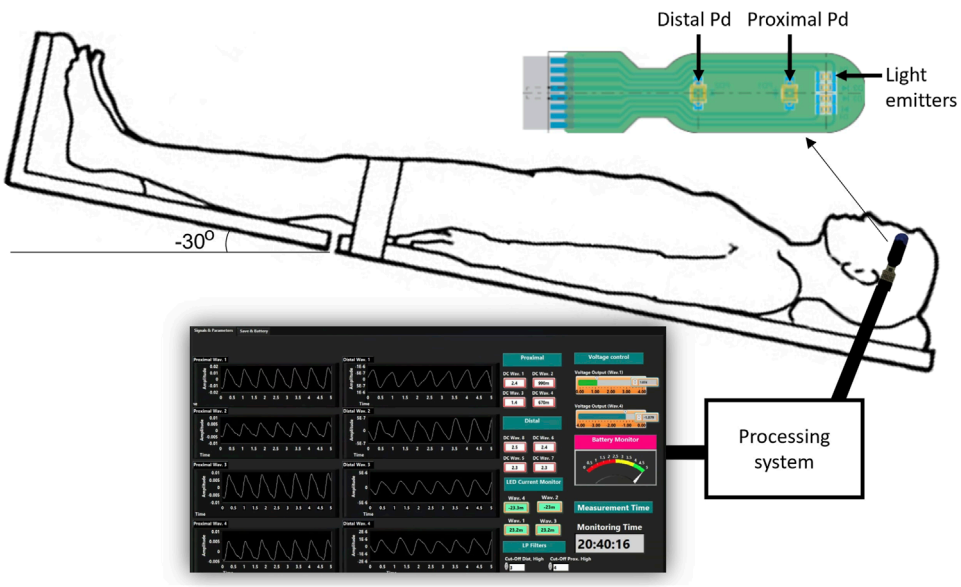

FIGURE 1
Experimental setup for the acquisition of pulsatile optical signals from the forehead. The sensor has a reflectance configuration with four light emitters (770, 810, 855, and 880 nm). The reflected light from extracerebral tissue reached the proximal photodetetor placed 10 mm from the LEDs. Similarly, non-absorbed light from deeper tissues travelled back to the distal photodiode placed 35 mm from the source. The probe is connected to a processing system to acquire the signals, which are finally visualised and recorded in a LabView interface.

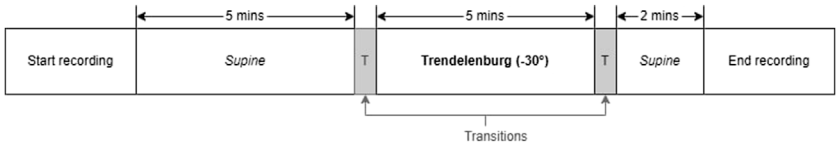

FIGURE 2
Measurement protocol for the body position tilting intervention.

recorded signals based on the corresponding body positions. Additionally, the Valsalva peaks were isolated from the baseline. The signals were filtered using Butterworth filters in order to separate the AC PPG component (2nd order bandpass filter with cutoff frequencies of 0.8 and 10 Hz) from the DC PPG component (2nd order lowpass filter with a cutoff frequency of 0.1 Hz). The data was then normalised by dividing the AC component of the signal by it is DC component, followed by a 10 factor multiplication.

2.5 Sectioning

For the tilting intervention, changes in body position were determined by time. The sectioning algorithm under-sampled the signals to 100 Hz and the total duration of the signal was calculated. From the calculated duration, the time spent in transitions was subtracted to obtain an average transition time. Subsequently, the indices corresponding to each body position window were estimated. To ensure that only relevant data from the body position was included and to exclude transition data, the middle 60{%} of each body position window was extracted. This ensured that the analysis focused on stable body position periods. The flow diagram illustrating this sectioning algorithm can be seen in Figure 3A.

Inversely, the Valsalva manoeuvre peaks were not controlled by time, therefore a different algorithm was required to identify and extract these peaks from the original signal. The first step was calculating the first and second derivative of the PPG signal, which were then filtered using a Savitzky–Golay filter. Then, three maximum peaks were detected from the first derivative envelope, as well as three maximum lows. The algorithm defined where a Valsalva window started when a maximum peak of the first derivative envelope was close to a point where the first and second derivative crossed. Likewise, the Valsalva window ended when a maximum low of the first derivative envelope was close to a point where the first and second derivative crossed. The average time of the three Valsalva peaks was calculated, and a corresponding segment of baseline time was extracted from the signal, representing the period before any Valsalva maneuver occurred. Figure 3B provides a description of the sectioning algorithm used for the Valsalva intervention.

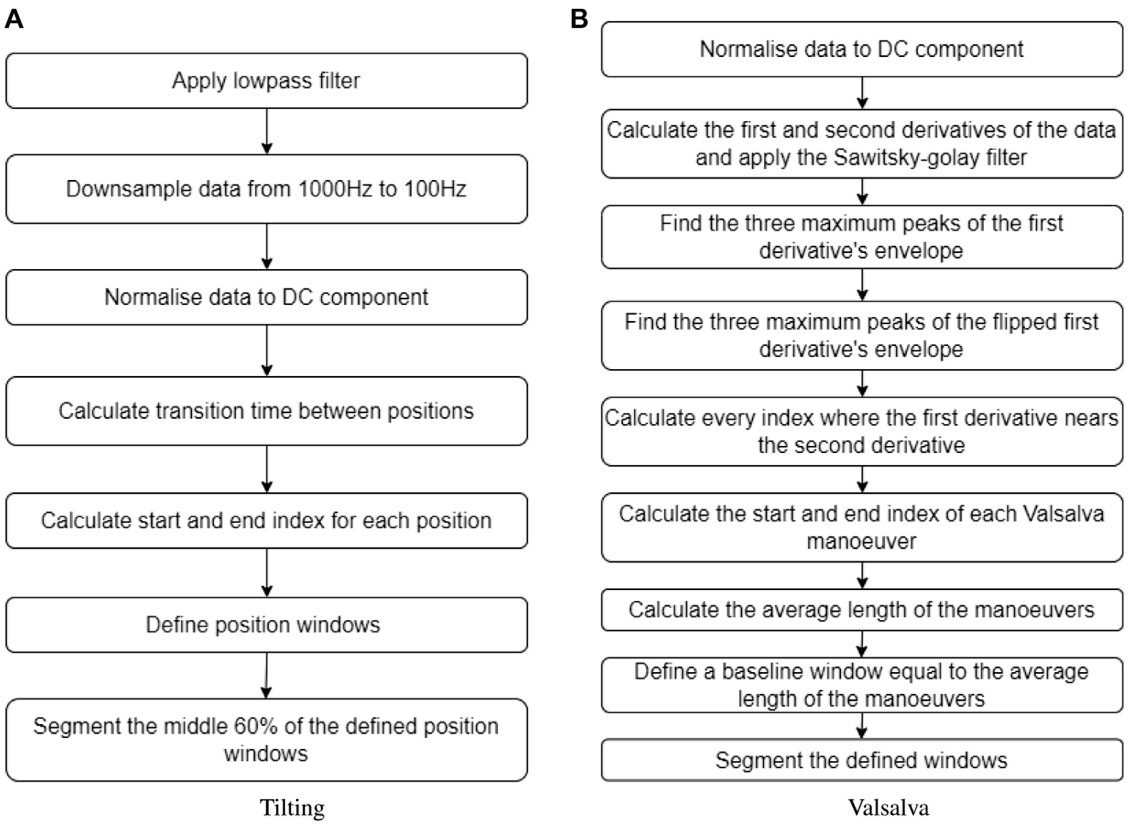

FIGURE 3
Sectioning algorithms applied to segment data obtained during **(A)** the tilting protocol and **(B)** the Valsalva intervention.

2.6 Feature extraction

Several features have been extracted and investigated in the literature to characterise pulsating signals, such as PPG (El-Hajj and Kyriacou, 2021). In this study, nine features were extracted from the optical signals. These features were: the amplitude, pulse width, rise time, decay time, upslope, area under the curve, area of the systolic period, area of the diastolic period and ratio between both systolic and diastolic areas. Figure 4 shows a graphical representation of the figures extracted. The median value of each feature was calculated in a signal window of 15 s for the tilting intervention while a 5 s window was implemented for the Valsalva intervention, where the sectioned signals were shorter. The features from each section (baseline, body position or Valsalva) were compared according to the following statistical analysis.

2.7 Statistical analysis

To assess whether there were any significant differences in the features extracted at different body positions (both proximal and distal measurements), a non-parametric and parametric factorial analysis was undertaken in Python (version 3.10). Utilizing two distinct analytical methods increased the robustness of our investigation and ensured that any significant findings were not reliant upon a particular statistical technique. The significance level was set at 95{%} (α = 0.05) for both analyses. The factors were the body position and the photodetector location.

The ANOVA assumptions were assessed using several statistical tests. Specifically, the normality assumption for each feature was evaluated using the Shapiro-Wilk and Kolmogorov-Smirnov tests, while Bartlett's test was used to evaluate variance homogeneity for each factor. Data independence was assessed through graphical methods. In instances where the assumptions of normality, homoscedasticity, and independence were not met, Box-Cox transformations were applied using an optimal lambda in order to proceed with the factorial analysis. Following the transformation, both factors were incorporated into a linear model to examine any potential interaction effects on the changes in the extracted features.

Lastly, logisitc regression classification models were constructed to predict body position and Valsalva peaks based on the independent variables extracted from the optical signals recorded with the aforementioned probe. The data underwent pre-processing steps prior to model training. Firstly, all instances except for those at the 810 nm wavelength were removed from the original feature dataset, resulting in a dataset containing only instances of extracted features from the 810 nm wavelength. Secondly, to address the issue of class imbalance, the original dataset was randomly undersampled to ensure an equal number of instances for each classification class (body positions/Valsalva peak or baseline) for each volunteer

10.3389/fphys.2023.1208010

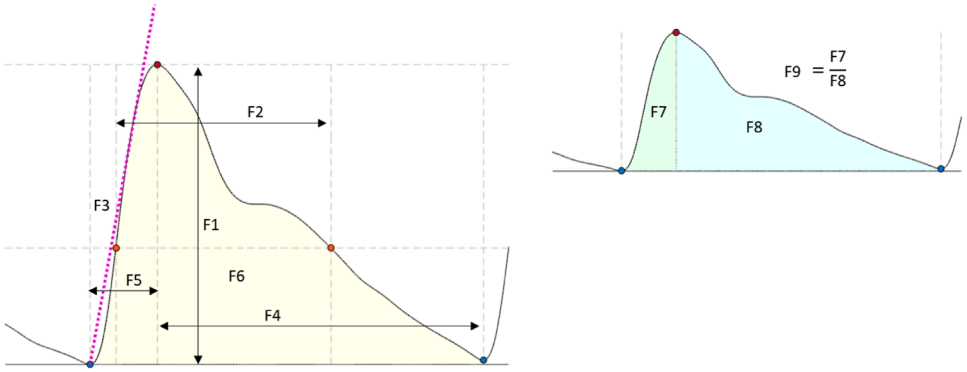

FIGURE 4
Features extracted from the optical signals. F1: Amplitude; F2: Pulse width; F3: Up slope; F4: Decay time; F5: Rise time; F6: Area under the curve; F7: Area of the systolic period; F8: Area of the diastolic period; F9: Ratio between both systolic and diastolic areas.

at each intervention. The independent variables were scaled to a range between 0 and 1. This step was undertaken to help improve the performance and convergence rate of the algorithm, as the features extracted used different ranges. The final pre-processing step for the model involved splitting the tilting and Valsalva datasets by photodetector position (proximal and distal). As distal signals contain cerebral information, the model was trained using the distal photodetector dataset only.

The decision to use a logisitc regression classification model in this study was driven by its suitability for a small labelled dataset and its effectiveness on binary classification tasks. Logistic regression only requires estimation of coefficients associated with each predictor variable, resulting in fewer parameters to estimate compared to more complex models. Consequently, logistic regression is less prone to overfitting. Furthermore, logistic regression takes the form of a sigmoid curve, which ranges between 0 and 1, reflecting the probability of a binary outcome. Therefore, logistic regression is a suitable choice for classification problems where the outcome variable is binary.

To split the data into training and testing datasets, two different approaches were employed. The first approach involved dividing the data into folds, with the number of folds equal to the number of volunteers in the dataset (16 for tilting and 10 for Valsalva). Each fold consisted of all the data from one volunteer. In contrast, the second approach employed a 10-fold cross-validation, where the entire dataset was randomly shuffled and split into 10 folds. In both approaches, the model was trained on the remaining data after holding out the fold and then tested on the held-out data. To evaluate the performance of the models, accuracy measurements, sensitivity and specificity were calculated.

3 Results

3.1 Pulsatile signals from the forehead

Pulsatile signals were successfully recorded from near infrared light from 16 healthy volunteers using a two photodiode probe. Figure 5 presents the first observational proof of brain pulsatile signals obtained at 810 nm. Additionally, the results of the sectioning algorithm, shown in Figure 5, allow for easy identification of changes in the DC component of the optical signals during ICP alterations (i.e., trendelenburg −30 and Valsalva). Differences in the waveform morphology at different body positions or after a Valsalva manoeuvre, were analysed by feature extraction at each section.

3.2 Statistical analysis

To explore the differences in the features extracted at different body positions and between baseline and valsalva manoeuvres, we employed both parametric and non-parametric analyses, the results of which support the hypothesis of this study. Figure 6 shows the boxplots of each feature at the different body positions for both photodiode locations. In the tilting intervention, a non-parametric analysis was conducted using the Mann-Whitney U test. The results indicate significant differences in all features except the rise-time feature. This suggests significant difference between the features across both proximal and distal data.

To complement the non-parametric approach a parametric, factorial analysis using ANOVA was carried out. Although the data did not fit the assumptions of ANOVA in either intervention suggesting that the data were not normally distributed, did not have unequal variances or did not show residual independence a Box-Cox transformation enabled a factorial analysis. After the transformation, the assumptions were evaluated by Q-Q plot, residuals plot and fitted values plot. The results of the ANOVA analysis were consistent with those of the non-parametric analysis. The factorial analysis results indicate significant differences in all features across both proximal and distal measurements. The findings of the comparison between photodiodes showed significant differences between sensor locations across all features, which may be attributed to the fact that the distal photodiode is interrogating mixed brain and extracerebral signals while the proximal photodiode only detects extracerebral signals.

10.3389/fphys.2023.1208010

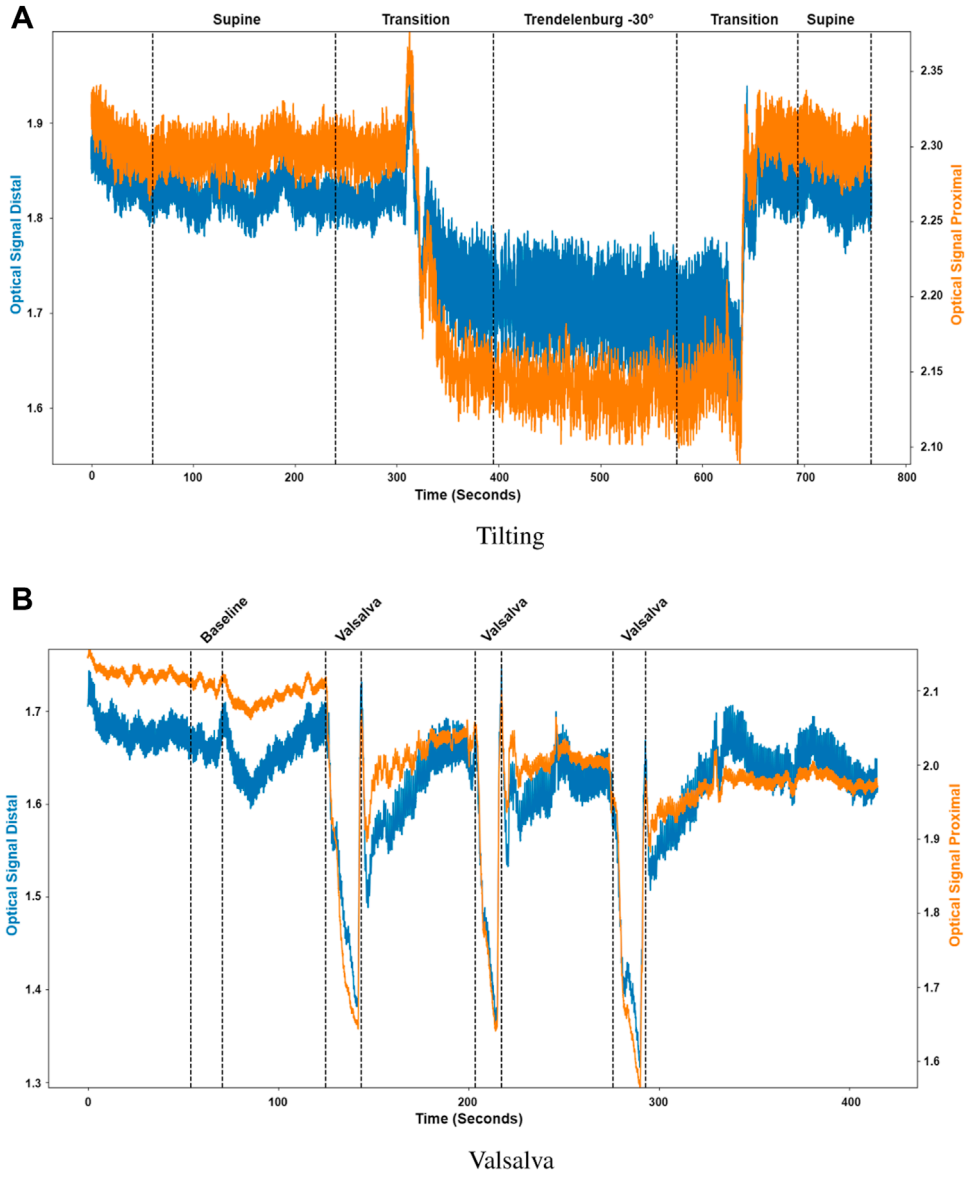

FIGURE 5
Sectioned signals per intervention. **(A)** Tilting, where the distal (blue) and proximal (orange) signals were sectioned to identify initial supine position, the transition from supine to Trendelenburg (−30°), Trendelenburg position, the transition to supine and final supine position. **(B)** Valsalva, where the distal (blue) and proximal (orange) signals were sectioned to identify the baseline condition and the three different Valsalva maneuvers.

The use of both analytical methods allowed us to confirm our findings using two independent statistical techniques. By performing both parametric and non-parametric analyses, we were able to explore the differences in the features extracted at different body positions producing results which were not reliant upon a particular statistical technique. The evidence of both support our hypothesis that there are significant differences in the features extracted at different body positions.

Similarly, in the Valsalva intervention, a non-parametric, Kruskal–Wallis test and a parametric, factorial analysis using ANOVA were conducted to assess the differences between baseline and valsalva for both sensor locations. Due to data quality challenges, data from 10 out of the original 16 volunteers were included in this analysis. Figure 7 presents the boxplots of each feature at baseline and the three Valsalva manoeuvres for both photodiode locations.

The Kruskal–Wallis analysis suggests that the majority of features changed significantly between baseline and Valsalva conditions in the distal dataset, which interrogates mixed brain and extracerebral signals. Conversely, the proximal data revealed that most of the features did not show significant changes between baseline and Valsalva conditions. The ANOVA analysis results were consistent with those of the parametric analysis. The findings indicate significant changes in half of the features analysed between baseline and Valsalva, while the second factor analysis showed significant differences between sensor locations for 70% of the features. These results suggest that the pulsatile signal morphology

10.3389/fphys.2023.1208010

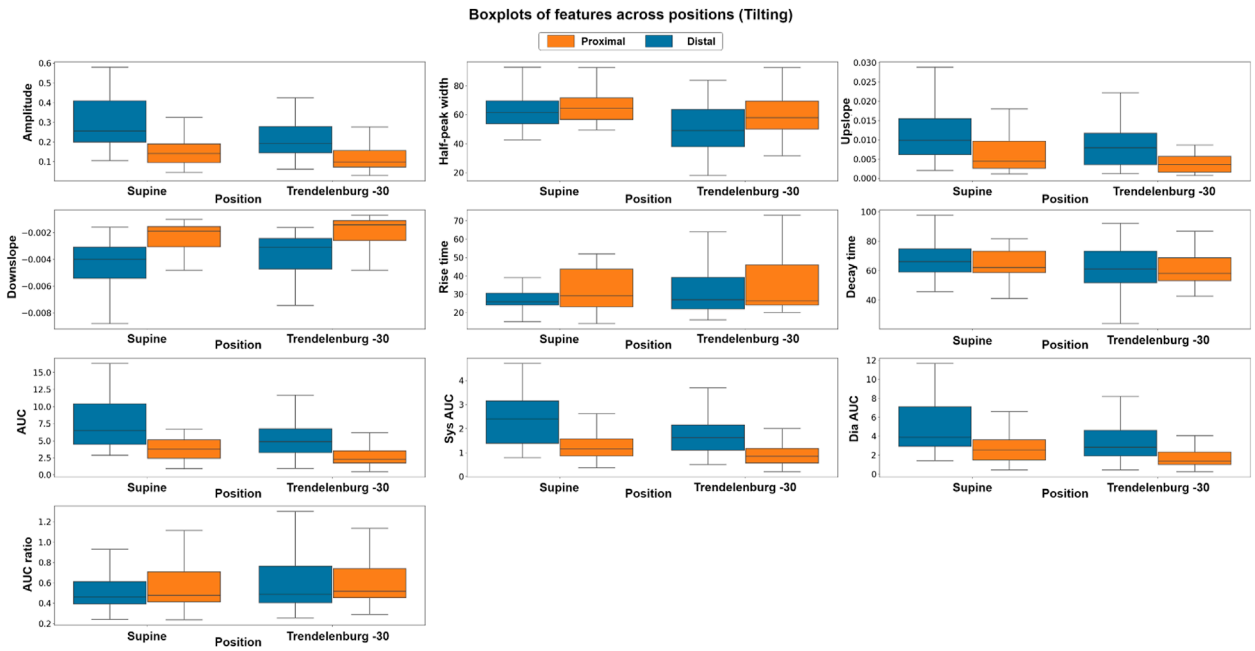

FIGURE 6
Boxplots of pulsatile signal features at different body positions for both distal and proximal photodiode locations. Each box represents the interquartile range (IQR) of the data, with the median value represented by the horizontal line inside the box. Differences in box height between positions and photodiode locations suggest significant variations in the pulsatile waveform morphology.

differs during an instant increase in ICP induced by the Valsalva manoeuvre.

3.3 Classification tasks

The results of the classification models are presented on Table 1. Two training and validation approaches were used: the first approach used a hold-out validation method, while the second approach employed a k-fold cross-validation method.

On the Tilting intervention dataset the results suggest that both approaches achieved a good balance between correctly identifying trendelenburg −30 and supine cases.

The first approach, the hold-out validation method achieved an average sensitivity of 63.07% and an average specificity of 60.23% on the dataset. In contrast, the k-fold cross-validation method demonstrated slightly better performance, with a sensitivity of 68.1% and a specificity of 63.69%. This suggests that the model has a good balance between identifying both positive and negative cases and is effective at identifying patients in the trendelenburg −30 position.

The favourable classification performance of the second approach is also mirrored in the distal Valsalva dataset. The average sensitivity and specificity of the second approach on the Valsalva dataset were 80.0% and 70.0%, respectively, representing a 10% higher sensitivity than that of the first approach.

The results across both datasets demonstrate an encouraging classification performance using both training and validation approaches. The k-fold cross-validation method showed slightly better results than the hold-out validation method.

4 Discussion

This study has proposed the use of a custom optical sensor with multi-distance photodetectors to interrogate pulsatile signals from backscattered light from the brain. The sensor demonstrated its capability to acquire pulsatile signals from extracerebral and cerebral tissue at multiple wavelengths, of which the isosbestic point (810 nm) was selected for further analysis. Volunteers underwent two different interventions, tilting body position and Valsalva manoeuvre, in order to induce changes in the intracranial pressure. Trendelenburg at −30°, lead to the engorgement of the brain, where blood and Cerebrospinal Fluid (CSF) volume increase the total intracranial volume, hence the ICP. Intracranial hypertension decreases the intracranial compliance and results in an enlarged flow pulsatility (Figure 8) (Alperin et al., 2005). The Results from this study demonstrate that both scenarios of enlargement and attenuation of the flow pulsatility due to changes in ICP, correlate to changes in the morphological features of the pulsatile optical signals in healthy volunteers. Similarly, significant changes in the features of the pulsatile signals during Valsalva manoeuvres represent a rise in the intracranial pressure due to the sudden expulsion of blood from the thoracic vessels into the carotid vessels (Prabhakar et al., 2007).

To the knowledge of the authors, there are no previous studies that have analyzed the features of pulsatile optical signals

10.3389/fphys.2023.1208010

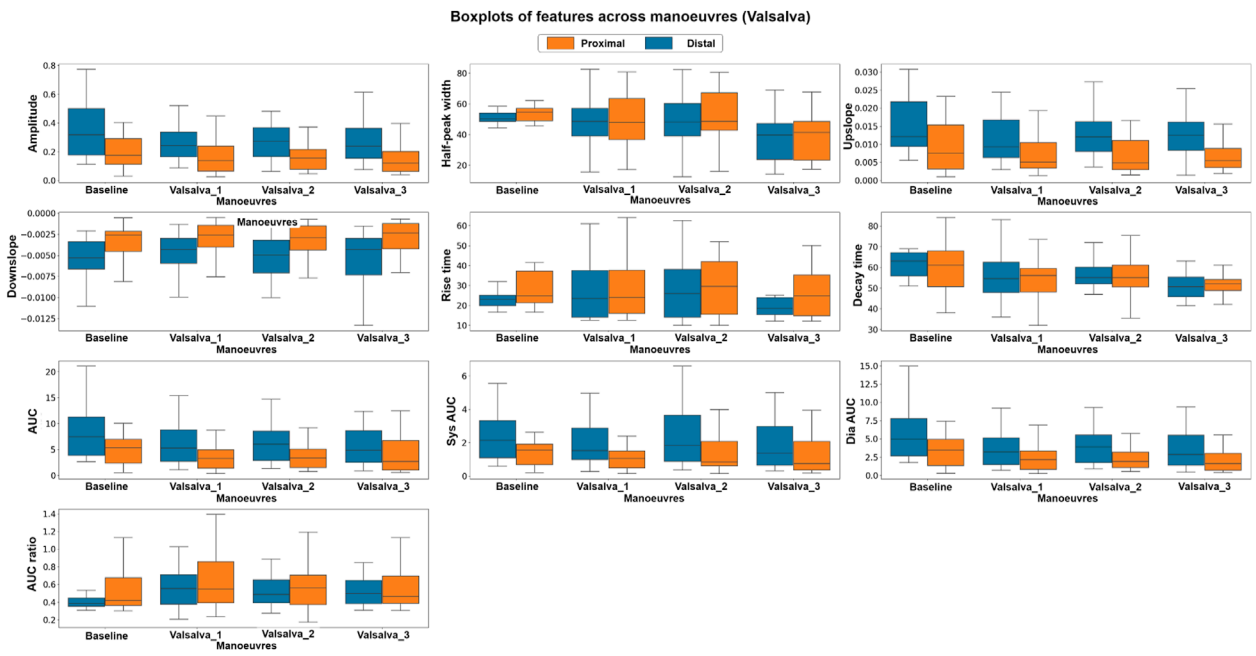

FIGURE 7
Boxplots of pulsatile signal features at baseline and during three Valsalva manoeuvres for both distal and proximal photodiode locations. Each box represents the interquartile range (IQR) of the data, with the median value represented by the horizontal line inside the box. Differences in box height between baseline and Valsalva conditions, as well as between photodiode locations, indicate significant changes in pulsatile waveform morphology during the Valsalva manoeuvre.

to discriminate changes in ICP induced by changes in body position and Valsalva manoeuvers. Literature reports significant changes in ICP when healthy volunteers undergo tilting or Valsalva manoeuvres. Alperin et al. quantified the effect of posture on intracranial physiology using Magnetic Resonance Images (MRI) of the brain, demonstrating that changes in ICP induced by posture alterations strongly affect the dynamics of cerebral blood and CSF flows (El-Hajj and Kyriacou, 2021). Computer tomography scans and MRI are non-invasive technologies used for TBI monitoring; however their accessibility is limited and do not facilitate bedside or continuous monitoring. On the other hand, invasive techniques such as intracranial bolts or neuroendoscopic procedures have also been used to evaluate changes in ICP during Valsalva manoeuvres, showing a significant increase in cerebral dynamics, including intracranial hypertension after the intervention (Alperin et al., 2005). Invasive ICP monitoring is an invasive and expensive procedure which requires a high level of expertise. Increasing the barrier to entry for patients and healthcare systems.

Since the analysis of features of pulsatile optical signals was capable of discriminating changes in ICP in healthy volunteers, this method might be of significant value for the future development of prediction algorithms for non-invasive monitoring of absolute ICP values. From the models developed in this study, a conclusion regarding the hold-out method is that it allows for an accurate measure of the model's performance on each volunteer whilst also giving a representation of the model's performance on unseen data. However, it seems reasonable to suggest that with further research and the collection of a larger dataset we could expect better model performance from approach one. On the other hand, the K-fold classification is a good method of evaluating a model on a limited dataset and provides a good estimate of the model's performance on unseen data.

TABLE 1 Classification results of hold-out Validation and K-fold cross-validation methods on Tilting and Valsalva Datasets. The classification results include average sensitivity and specificity measures for each approach on each dataset.

Tilting dataset			
Approach	Position	Sensitivity (%)	Specificity (%)
One volunteer per fold	Trendelenburg −30	63.07%	60.23%
K-fold cross validation	Trendelenburg −30	68.1%	63.69%
Valsalva dataset			
Approach	Position	Sensitivity (%)	Specificity (%)
One volunteer per fold	Valsalva	70.0%	70.0%
K-fold cross validation	Valsalva	80.0%	70.0%

This study has demonstrated that the morphologies of the signals recorded from the sensor differ between baseline and Valsalva conditions as the analysis found extracted features from the signal changed significantly between the two conditions. In addition to this the results found significant differences within features between body positions supine and trendelenburg −30. In order to further suggest that the sensor is isolating signals from the brain the study could be repeated using data recorded from both the forehead and the finger with the intention to measure and evaluate the

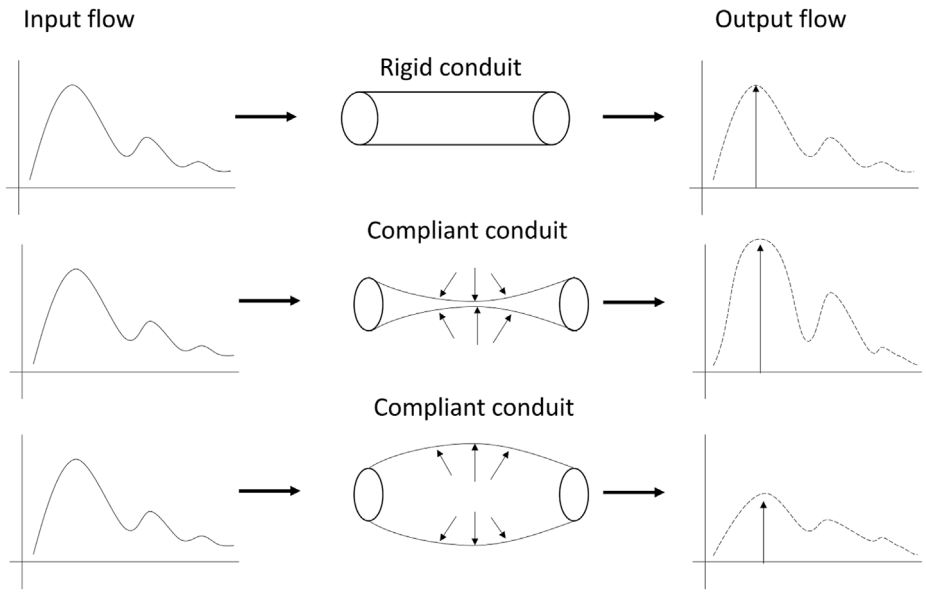

FIGURE 8
Modulation of pulsatile flow through rigid (top) and compliant (bottom) conduits. Outflow waveform from the compliant conduit suffered changes on the pulse morphology compared to outflow from the rigid conduit. Figure adapted from Alperin et al. (2005), with permission from John Wiley and Sons.

changes in extracted features from both during baseline and Valsalva conditions and during the protocol of positions. Additionally this study has found meaningful differences within the features of pulsatile NIRS signals which are correlated with induced changes in intracranial pressure. Given this it seems reasonable to explore the capacity to non-invasively measure intracranial pressure using data collected by the sensor. To determine the efficacy of the sensor's capacity to non-invasively measure intracranial pressure this work could be extended to the simultaneous collection of invasive intracranial pressure data and data from the sensor with the intention to develop a computational approach to calculating intracranial pressure values from the data. The results of which would be measured and compared against the reported gold standard. If it can be demonstrated as being efficacious for the non-invasive measurement of intracranial pressure, the research could be extended to the development of computational approaches for the forecasting of intracranial pressure values at future time points using non-invasively collected data. This would provide a non-invasive and continuous intracranial pressure measurement approach capable of the early detection of intracranial pressure crises.

This study has some limitations. First, and most importantly, gold-standard ICP measurements were not acquired during this study. This was due to the invasive nature of the current ICP monitoring techniques, making it impossible to obtain from healthy volunteers. However, and as has been explained, the effects of the protocols performed in this study have been shown to trigger changes in ICP which was the aim of this study. Future studies should validate the results obtained from this study in critically-ill patients with continuous, invasive ICP monitoring, from which ICP values are available. Secondly, the sample size from this study is relatively small and the characteristics of the subjects were homogeneous, risking overfitting the results of this study to the sample used. Furthermore, only a small subset of features were extracted and analysed from the obtained signals. Future studies should aim to explore more features from pulsatile signals that may be more prone to changes in ICP, such as frequency-domain and nonlinear indices. Additionally only data obtained using light at 810 nm were analysed. This was done due to the importance of this wavelength in the assessment of blood perfusion. However, future studies should evaluate the relationship of signals obtained using other wavelengths to ICP changes. Finally, it has been suggested that the developed sensor acquires pulsatile signals from the extracerebral and cerebral tissues of the brain, from the proximal and distal photodetectors, respectively. This study focused on the distal signal dataset in the classification task, as it is expected to contain cerebral information. However, the proximal data has not been used and the optical subtraction of the data collected from the proximal photodiode from the data acquired from the distal photodiode may isolate the cerebral data by eliminating the noise of extracerebral data, making the results more reliable and resulting in a better performance on the classification task.

5 Conclusion

This study found significant differences in the features extracted from the pulsatile NIRS signals, that correlate to induced changes in intracranial pressure in healthy volunteers. Additionlly this study presented classification models capable of identify changes in ICP induced by changes in body position and Valsalva manoeuvres. This novel method might be of significant value for the future implementation of a non-invasive ICP monitoring tool in neurocritical care.

Data availability statement

The raw data supporting the conclusion of this article will be made available by the authors, without undue reservation.

Ethics statement

The studies involving human participants were reviewed and approved by City University of London, Senate Research Ethics Committee. The patients/participants provided their written informed consent to participate in this study.

Author contributions

Conceptualization, TA and PK; Methodology, TA and MR; Software, GB; Formal Analysis, MR, GB and EM-M; Investigation, MR and TA; Resources, PK; Writing–Original Draft Preparation, MR; Writing–Review and Editing, GB and PK; Visualization, MR and GB; Supervision, PK; Project Administration, MR and PK. All authors contributed to the article and approved the submitted version.

Funding

The project is funded by the National Institute for Health Research (NIHR) [Invention for Innovation (i4i) Product Development (Grant Reference Number II-LA-0216-20005)].

Conflict of interest

The authors declare that the research was conducted in the absence of any commercial or financial relationships that could be construed as a potential conflict of interest.

Publisher's note

All claims expressed in this article are solely those of the authors and do not necessarily represent those of their affiliated organizations, or those of the publisher, the editors and the reviewers. Any product that may be evaluated in this article, or claim that may be made by its manufacturer, is not guaranteed or endorsed by the publisher.

References

Alperin, N., Lee, S., Sivaramakrishnan, A., and Hushek, S. (2005). Quantifying the effect of posture on intracranial physiology in humans by mri flow studies. *J. Magn. Reson. Imaging* 22, 591–596. doi:10.1002/jmri.20427

Bennett, T., Riva-Cambrin, J., Keenan, H., Korgenski, E., and Bratton, S. (2012). Variation in intracranial pressure monitoring and outcomes in pediatric traumatic brain injury. *Arch. Pediatr. Adolesc. Med.* 166, 641–647. doi:10.1001/archpediatrics.2012.322

Chiara, R. (2018). *Neuromonitoring techniques*. Amsterdam, Netherlands: Elsevier Inc.

Eklund, A., Johannesson, G., Johansson, E., Holmlund, P., Qvarlander, S., Ambarki, K., et al. (2016). The pressure difference between eye and brain changes with posture. *Ann. Neurol.* 80, 269–276. doi:10.1002/ana.24713

El-Hajj, C., and Kyriacou, P. (2021). Cuffless blood pressure estimation from ppg signals and its derivatives using deep learning models. *Biomed. Signal Process. Control* 70, 102984. doi:10.1016/j.bspc.2021.102984

Evensen, K., and Eide, P. (2020). Measuring intracranial pressure by invasive, less invasive or non-invasive means: limitations and avenues for improvement. *Fluids Barriers CNS* 17, 34. doi:10.1186/s12987-020-00195-3

Haykowsky, M., Eves, N., Warburton, D., and Findlay, M. (2002). Resistance exercise, the valsalva maneuver, and cerebrovascular transmural pressure. *Med. Sci. Sports Exerc.* 35, 65–68. doi:10.1097/00005768-200301000-00011

Murkin, J., and Arango, M. (2009). Near-infrared spectroscopy as an index of brain and tissue oxygenation. *Br. J. Anaesth.* 103, i3–i13. doi:10.1093/bja/aep299

Okazaki, T., Kawakita, K., and Kuroda, Y. (2021). Hospital-level intracranial pressure monitoring utilization and functional outcome in severe traumatic brain injury: A post hoc analysis of prospective multicenter observational study. *Scand. J. Trauma Resusc. Emerg. Med. l* 29, 5. doi:10.1186/s13049-020-00825-7

Prabhakar, H., Bithal, P., Suri, A., Rath, G., and Dash, H. (2007). Intracranial pressure changes during valsalva manoeuvre in patients undergoing a neuroendoscopic procedure. *Minim. Invasive Neurosurg.* 50, 98–101. doi:10.1055/s-2007-982505

Roldan, M., Abay, T., and Kyriacou, P. (2020). Non-invasive techniques for multimodal monitoring in traumatic brain injury: systematic Review and meta-analysis. *J. Neurotrauma* 37, 2445–2453. doi:10.1089/neu.2020.7266

Roldan, M., Chatterjee, S., and Kyriacou, P. (2021). "Brain light-tissue interaction modelling: towards a non-invasive sensor for traumatic brain injury," in 43rd Annual International Conference of the IEEE Engineering in Medicine and Biology Society (EMBC), Jalisco, Mexico, 1-5 November 2021.

Roldan, M., and Kyriacou, P. (2021). Near-infrared spectroscopy (NIRS) in traumatic brain injury (TBI). *Sensors* 21, 1586. doi:10.3390/s21051586

Watkins, W., Hargens, A., Seidl, S., Clary, E., and Macias, B. (2017). Lower-body negative pressure decreases noninvasively measured intracranial pressure and internal jugular vein cross-sectional area during head-down tilt. *J. Appl. Physiology* 123, 260–266. doi:10.1152/japplphysiol.00091.2017

frontiers | Frontiers in Physiology

TYPE Original Research
PUBLISHED 23 August 2023
DOI 10.3389/fphys.2023.1180288

OPEN ACCESS

EDITED BY
Panicos Kyriacou,
City University of London,
United Kingdom

REVIEWED BY
Haipeng Liu,
Coventry University, United Kingdom
Edik Rafailov,
Aston University, United Kingdom

*CORRESPONDENCE
Zbignevs Marcinkevics,
zbigis@latnet.lv

RECEIVED 05 March 2023
ACCEPTED 02 August 2023
PUBLISHED 23 August 2023

CITATION
Marcinkevics Z, Rubins U, Aglinska A, Logina I, Glazunovs D and Grabovskis A (2023), Contactless photoplethysmography for assessment of small fiber neuropathy.
Front. Physiol. 14:1180288.
doi: 10.3389/fphys.2023.1180288

Contactless photoplethysmography for assessment of small fiber neuropathy

Zbignevs Marcinkevics[1,2]*, Uldis Rubins[2], Alise Aglinska[1], Inara Logina[3], Dmitrijs Glazunovs[3] and Andris Grabovskis[2]

[1]Department of Human and Animal Physiology, Faculty of Biology, University of Latvia, Riga, Latvia, [2]Biophotonics Laboratory, Institute of Atomic Physics and Spectroscopy, University of Latvia, Riga, Latvia, [3]Department of Neurology and Neurosurgery, Riga Stradins University, Riga, Latvia

Chronic pain is a prevalent condition affecting approximately one-fifth of the global population, with significant impacts on quality of life and work productivity. Small fiber neuropathies are a common cause of chronic pain, and current diagnostic methods rely on subjective self-assessment or invasive skin biopsies, highlighting the need for objective noninvasive assessment methods. The study aims to develop a modular prototype of a contactless photoplethysmography system with three spectral bands (420, 540, and 800 nm) and evaluate its potential for assessing peripheral neuropathy patients via a skin topical heating test and spectral analyses of cutaneous flowmotions. The foot topical skin heating test was conducted on thirty volunteers, including fifteen healthy subjects and fifteen neuropathic patients. Four cutaneous nerve fiber characterizing parameters were evaluated at different wavelengths, including vasomotor response trend, flare area, flare intensity index, and the spectral power of cutaneous flowmotions. The results show that neuropathic patients had significantly lower vasomotor response (50%), flare area (63%), flare intensity index (19%), and neurogenic component (54%) of cutaneous flowmotions compared to the control group, independent of photoplethysmography spectral band. An absolute value of perfusion was 20%–30% higher in the 420 nm band. Imaging photoplethysmography shows potential as a cost-effective alternative for objective and non-invasive assessment of neuropathic patients, but further research is needed to enhance photoplethysmography signal quality and establish diagnostic criteria.

KEYWORDS

remote photoplethysmography, imaging photoplethysmography, small fiber neuropathy, vasomotor responses, axon reflex flare, cutaneous vasomotion, optical diagnostic imaging, topical heating

1 Introduction

Pain is an evolutionarily adaptive trait that substantially improves the survival of a species, as it is a product of the nociceptive system that is closely interconnected with reward and motivation mechanisms. This results in the avoidance of potentially dangerous stimuli or activities (Walters and De C Williams, 2019). However, sometimes due to pathological conditions, pain sensations can become spontaneous and chronic, which can substantially impair the functioning and wellbeing of an individual. One particularly debilitating form of

chronic pain is neuropathic pain, which refers to a specific chronic pain syndrome characterized by pain and sensory abnormalities in body parts that have lost their normal peripheral innervation or sensory representation (Costigan et al., 2009). The prevalence of the syndrome is approximately 2.4% globally, and the percentage rises with age, with 5%–7% in those aged 45 and older (Callaghan et al., 2015). This is not entirely clear and can vary in different age populations. Approximately 40% of sufferers never receive appropriate diagnosis, while 21% receive no pain management at all (Carnago et al., 2021). Usually, neuropathic pain occurs as a result of damage to small fibers (A-delta and C nerve fibers) and can be caused by a wide range of disorders (Colloca et al., 2017). Recently, a substantial worsening of the global situation has been observed due to the SarsCov-2 pandemic, which caused a COVID-19 disease burden worldwide (Pires et al., 2022). A growing number of studies have documented a wide variety of neurological manifestations associated with COVID-19 disease, particularly neuropathies, which can account for as much as 36.4% of COVID-19 patients (Ftiha et al., 2020).

The present diagnostics of peripheral neuropathies are primarily based on subjective self-assessment tests or biopsies (Scott et al., 2003). Their results partly depend on the patient's interpretation and feedback to physicians, and therefore may be doubtful for the elderly, who are the main patient group. One such test is Quantitative sensory testing, a measure of perception in response to mechanical, thermal, and painful stimuli of controlled intensity. A more objective alternative is the invasive skin biopsy technique with subsequent histological nerve fiber density determination. However, it is uncomfortable for the patients and therefore not widely used. Nevertheless, after years of research, there is still no affordable non-invasive clinical diagnostic technique for small fiber neuropathy.

In light of the present situation in healthcare and high economic demands (Breivik et al., 2013), the development of alternative techniques for objective and non-invasive diagnostics of neuropathy is of great importance. Recent studies shed light on this issue, suggesting that derangement of small nerve fibers has local manifestation on the adjacent skin and its vasculature (Ando et al., 2021). The skin is the largest human organ, which is extensively vascularized and innervated, manifesting different pathological conditions of local and systemic origin (Leal et al., 2021), such as septic shock, diabetes, hepatitis and rheumatoid arthritis. The skin is easily accessible for optical techniques and has desirable and well-known optical properties (Bashkatov et al., 2011), hence the heterogeneous non-uniform structure possessing sophisticated and not entirely understood regulatory mechanisms (Slominski et al., 2015).

Studies suggest that alterations in dermal blood flow (cutaneous vasomotor responses) evoked by different provocation tests, such as topical skin heating (Minson et al., 2011), cooling, reperfusion during post-reactive hyperemia, or iontophoresis of vasoactive substances into the skin, are promising diagnostic indicators (Lenasi, 2011). Another encouraging but methodologically challenging avenue would be spectral analyses of spontaneous oscillations of cutaneous perfusion, referred to as cutaneous flowmotions (Rossi et al., 2005), which can reflect different local and systemic regulatory mechanisms and might reveal pathology at early stage (Sun et al., 2013). All aforementioned measurements require a simple and reliable, artifact-proof technique for cutaneous perfusion monitoring. Nevertheless, most of the preceding studies on cutaneous blood perfusion were performed by laser Doppler imaging technique (Harrison et al., 1993; Cracowski and Roustit, 2016), which is sophisticated and expensive with relatively low temporal resolution (Merla et al., 2008; Rajan et al., 2009). In recent years, the contactless modality of photoplethysmography has gained popularity as a simpler and cost-effective alternative to Doppler imaging (Hagblad et al., 2010; Mizeva et al., 2015; Rodrigues et al., 2019). It has proven its capability in different diagnostic scenarios, such as monitoring local anesthesia (Rubins et al., 2010), assessing oral mucosa health (Rubins et al., 2019), diagnosing gingivitis (Marcinkevics et al., 2020), and assessing cutaneous vasomotor responses (Trumpp et al., 2016; Marcinkevics et al., 2019). The approach is similar to the conventional contact manner reflection-type photoplethysmography (Hertzman, 1937; Allen, 2007), with the photodetector being replaced by a video camera (Huelsbusch and Blazek, 2002). This allows remote registration of a large area of interest at relatively high spatial and temporal resolution (Cheng et al., 2022) while avoiding any pressure or attachment on the skin, which can prevent tissue compression, capillary blood flow occlusion (Sun and Thakor, 2016), and discomfort during the measurement (Desquins et al., 2022). By using advanced signal processing algorithms, the blood perfusion-related signal can be extracted from the subtle pixel intensity changes in the image sequence even during non-stationary position of body (Maity et al., 2022). The major technical advantages of the contactless plethysmography approach are its flexibility and scalability, which permit its extension to multispectral modality. Over the past decade, several studies have investigated the potential of multispectral modality in different experimental settings (Asare et al., 2011; Trumpp et al., 2016; Chen et al., 2020), including our previous research on the value of multispectral photoplethysmography for the clinical assessment of cutaneous microcirculation at two different depths (Marcinkevics et al., 2016).

Considering the recent evidence and achievements in the field of remote photoplethysmography (Sun and Thakor, 2016; Ryals et al., 2023), and the pressing need for improved healthcare technology in Post-coronavirus pandemic era (Gautam et al., 2020; Jazieh and Kozlakidis, 2020), the present study aims to develop a modular prototype of a contactless photoplethysmography system with three spectral bands and evaluate its potential for assessing peripheral neuropathy via a skin topical heating test. Two hypotheses were formulated. First, we hypothesize that neuropathic patients will exhibit significantly lower perfusion index values during the topical heating-induced vasomotor response than healthy volunteers. Second, we predict that utilizing three spectral bands will yield more valuable diagnostic information for neuropathic patients compared to using a single spectral band.

2 Methods

2.1 Design of contactless photoplethysmography system

The contactless reflection-type photoplethysmography (PPG) system prototype was designed based on our experience in

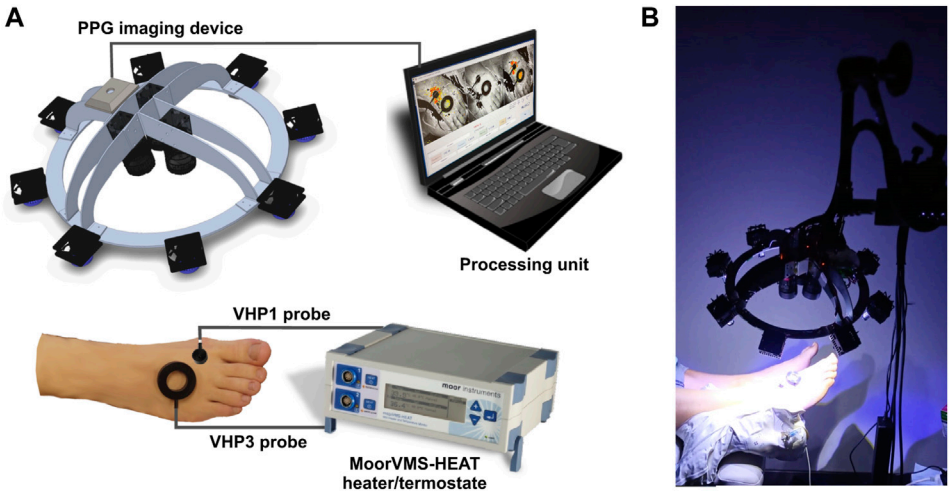

FIGURE 1
The iPPG system for cutaneous perfusion monitoring during the heating tests. **(A)** The experiment setup and major components of the system; **(B)** Photo of imaging system in action.

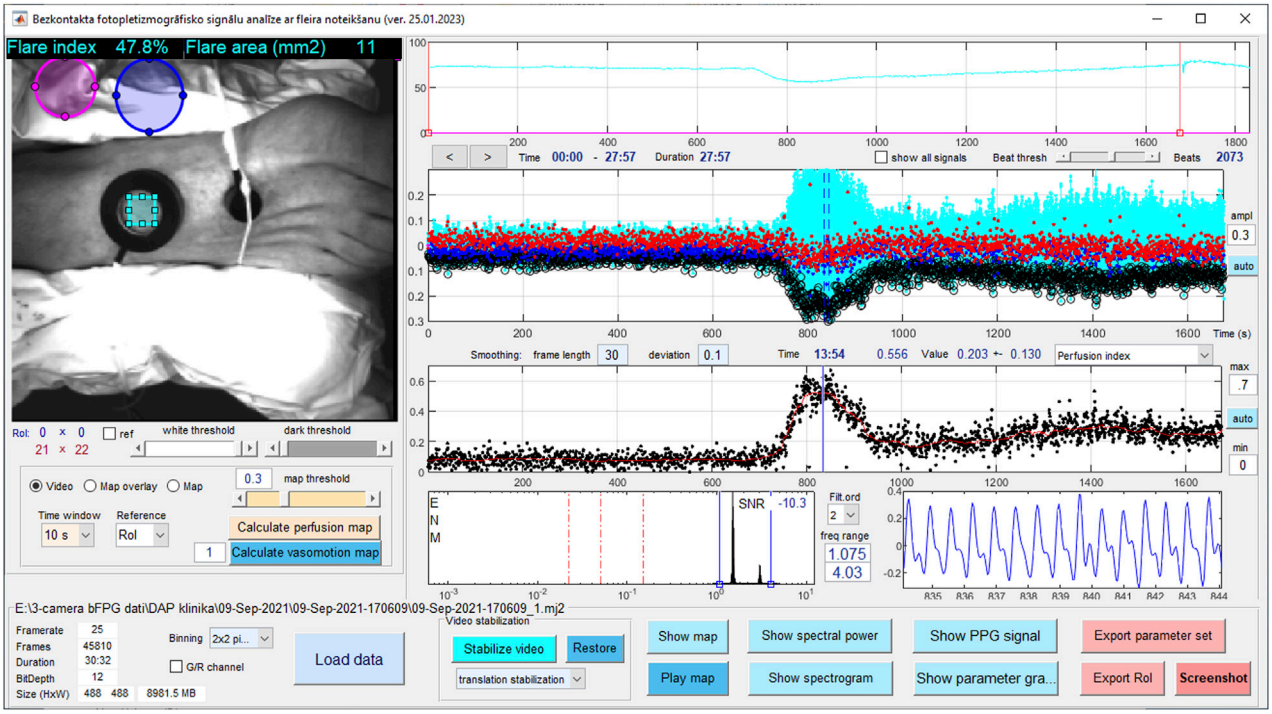

FIGURE 2
The screenshot of custom made dedicated Matlab based software for off-line data analyses.

developing imaging systems, current research, and clinical expert input. The system offers modularity and spectral band flexibility, allowing for customization of spectral bands to optimize measurement conditions for different tissue depths and types of biological tissue. This flexibility makes the system highly adaptable and versatile, suitable for various laboratory and clinical measurement scenarios, including cutaneous perfusion mapping and PPG waveform and phase analysis. The contactless reflection-type photoplethysmography system prototype (Figure 1) consisted primarily of three key components: an imaging device, a signal processing unit, and dedicated software for offline data analysis (Figure 2).

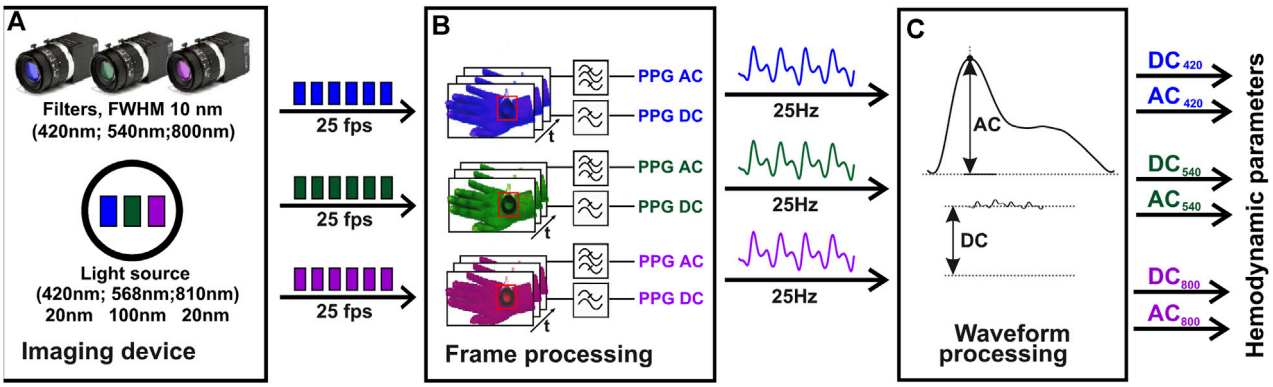

FIGURE 3
The algorithm block chart of iPPG signal analysis. The initial video data acquisition stage, employs a multi-spectral imaging device, including a multi-spectral illuminator and three cameras, each equipped with 420 nm, 540 nm, and 800 nm filters **(A)**. The second stage of the process, where the PPG signal is computed using temporal filtering of the video frames. The frequency range used for AC related to the heartbeat is (0.7–5 Hz), and for slow DC it is (0–0.3 Hz) **(B)**. The final stage, where the hemodynamic parameters, such as the perfusion index, are derived for each spectral channel using the AC and DC values calculated at each heartbeat **(C)**. Z. Marcinkevics, U. Rubins, A. Caica, and A. Grabovskis "Evaluation of nitroglycerin effect on remote photoplethysmogram waveform acquired at green and near infra-red illumination", Proc. SPIE 10592, Biophotonics—Riga 2017, 105920E (7 December 2017); https://doi.org/10.1117/12.2297385.

2.1.1 The imaging device

Comprised three identical cameras (Ximea-xiQ USB-3, ADC 8–12-bits, resolution 648 × 488 pix.) equipped with the lens (Edmund Optics, C-mount f = 25 mm, F1.4, two visible spectra, and one near-infrared lens) which were mounted on the rigid aluminum frame-device chassis at fixed angles to align the visual fields of all three cameras along a single optical axis (Figure 1A). Spectral band changes were achieved by using different sets of optical narrowband interference filters mounted in front of the camera lens, along with an orthogonal polarization system. This system used one linear polarizer in front of the lens and another in front of the light source to prevent reflection from the skin surface and improve image quality. In our measurement setup, the imaging device was equipped with three narrowband filters (CW = 420, 540, and 800 nm, FWHM = 10 nm) based on pilot studies that confirmed the effectiveness of narrowband filters in improving system sensitivity by tuning reflected wavelength to particular hemoglobin absorption maxima, thus reducing biological noise in the signal. The light source consisted of eight custom-made, replaceable illuminator modules of high power LEDs, distributed in a circular arrangement on the device chassis, providing uniform illumination of the measured surface, with the option to replace and customize the desirable illumination wavelength. In the present setup, each module consisted of two blue LEDs (CW = 420 nm, FWHM = 20 nm, max. Electric power 1 W); one green LED (CW = 568 nm, FWHM = 100 nm, max. Power 1 W); and one infrared LED (CW = 810 nm, FWHM = 20 nm, max. Power 0.6 W), which were manufactured by LuxeonZ from LumiLeds (San Jose, CA, United States). Measured irradiance in the skin plane (25 cm from the illuminator) for blue at 420 nm was 1.5 mW/cm^2, for green at 540 nm was 0.3 mW/cm^2 and for infrared at 800 nm was 0.7 mW/cm^2. Advanced active cooling and ultra-stabile LED driver circuit were used to maintain stable irradiation over long measurement sessions, incorporating miniature brushless fans into the back of the illuminator module heatsink plate. universal mounting options are provided by fixing the imaging system frame to the Variable Friction Magic Arm (Manfrotto), which can be attached to the optional tripod stand or any part of the bed or office table if necessary.

2.1.2 The signal processing unit

To ensure high-quality video input and control of illumination modules, the imaging device was connected to a laptop computer (Intel Core i7; 16 GB of RAM) via four USB 3.0 cables. The cables were organized and protected by being enclosed in a flexible spiral tube, which helped to prevent tangling and physical damage during use. The imaging system was operated by custom-developed MATLAB-based software, which allowed for the control of cameras and video storage to 12-bit video files. Following the start of the system, the software operated in preview mode, displaying the 420, 540, and 800 nm spectral videos. When the measurement was started (by pressing the Start button), the software was switched to video recording mode, enabling the viewing of skin blood perfusion maps in each of the images. The software recorded video at 25 frames per second with a resolution of 480 × 480 pixels in 12-bit mode to achieve high dynamic range videos. At the end of the measurement, the software automatically switched back to preview mode and was ready for the next measurement.

2.1.3 The data offline analyses software

The blockchart of iPPG analysis algorithm is shown in Figure 3. The most sophisticated and computationally extensive part of photoplethysmography system is Matlab platform based offline data analyses software, which contains very extensive set of contactless PPG analyses functions, such as signal filtering and frame stabilization, beat detection, estimation of characterizing waveform features, computation of augmentation, reflection and stiffness indexes, perfusion index perfusion mapping, calculation of signal Fourier spectra characteristics and analyses of vasomotor responses. The operation of software was provided by the same

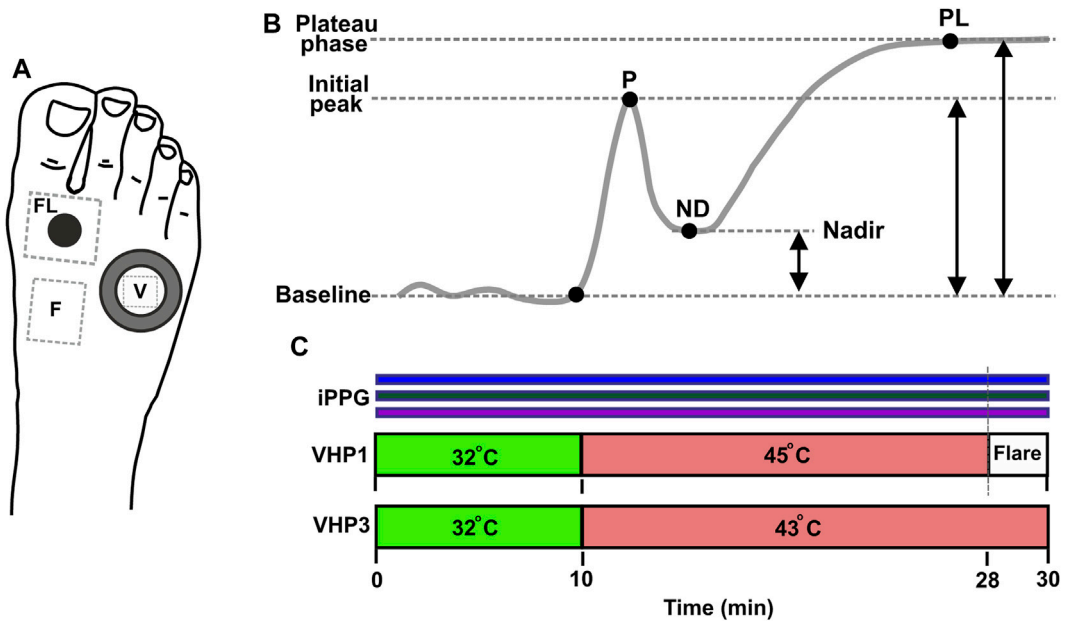

FIGURE 4
Measurement protocol. **(A)** Position of sensors and measurement regions on the dorsal aspect of foot. Water filled VHP3 heating probe is marked with large hollow ring, and the region of signal acquisition for vasomotor response trend is denoted by V; VHP1 heating probe is marked with black filled circle, flare area measurement site is denoted by FL. Flow motion acquisition region is denoted by F. **(B)** Typical trend of topical skin heating induced vasomotor response, comprising baseline, initial peak-P, nadir-ND and plateau phase–PL. Reproduced from Marcinkevics et al. (2021), licensed under CC BY 4.0 **(C)** Topical heating protocol, Simultaneous PPG recording at 420, 540 and 800 nm is marked by horizontal color bar.

signal processing unit (data acquisition Laptop computer). The advantage of software is ability to operate large datasets (Big data) (~25 GB for each measurement set) which is crucial for long, higher framerate recordings. The software is organized with interactive user interface (Figure 2). The further description of the software's signal processing and data analysis functions which are related to vasomotor response, flare and flowmotion analyses is provided in the Signal Processing and Analyses of Cutaneous Perfusion Data sections.

2.2 Subjects

Thirty subjects were enrolled in the study, fifteen neuropathic patients and fifteen similar age (59.33 years vs. 57.20 years, $p > 0.05$), gender proportion (f:67%, m:33% vs. f:67%, m:33%) and body mass index (21.76 kg/m^2 vs. 21.41 kg/m^2) healthy volunteers. The study procedures were approved by both the Ethics Committee of the University of Latvia, Institute of Cardiology and Regenerative Medicine and Riga Stradins University Research Ethics Committee (Prot.Nr: 03.05.2018), and were in accordance with the Declaration of Helsinki (World Medical Association, 2013). Prior to the study, all subjects were informed about the protocol and gave their written informed consent.

An experienced neurologist selected our patient cohort from outpatients based on established clinical guidelines that incorporated the results of both quantitative sensory testing and neurography (sural nerve conduction test.) We applied the referent values for quantitative sensory testing thermal thresholds as proposed by Magerl et al. (2010). According to these guidelines, all patients in our cohort were diagnosed with either probable or definite small fiber neuropathy. The clinical guidelines define probable small fiber neuropathy as the presence of length-dependent symptoms and/or signs of small fiber damage in conjunction with a normal sural nerve conduction test, while the definitive diagnosis of small fiber neuropathy requires the aforementioned criteria to be accompanied by abnormal thermal thresholds detected during quantitative sensory testing at the foot and/or reduced intraepidermal nerve fiber density at the ankle, as ascertained by biopsy (Tesfaye et al., 2010; Terkelsen et al., 2017).

The control group comprised individuals who did not exhibit any length-dependent symptoms or signs of small fiber damage, and were therefore deemed to be healthy.

2.3 Measurement procedure

To evaluate the function of small cutaneous sensory nerve fibers, we employed two modalities of a topical heating test, along with the assessment of cutaneous flow motions. The first modality aimed to produce a heating-induced vasomotor response trend characterized by biphasic changes in cutaneous blood perfusion (Kellogg, 2006). This response consists of a sharp rise (first peak) followed by a decline to a nadir, and then a subsequent increase that remains relatively constant over a longer time course, referred to as the plateau phase as shown in Figure 4B. The second modality was intended to evoke a skin topical heating-induced flare (Weidner et al., 2003), which is an extent of cutaneous reddening beyond the direct contact heating zone. Cutaneous flow motions (Kastrup et al., 1989) were acquired from intact skin regions not influenced by

heating, and comprises three major spectral components (myogenic, neurogenic, and endothelial). Before the procedure, the subject was seated in a reclined position on a comfortable cosmetology seat, with adjustable spinal and leg support angles. The hands were placed on chair arm supports, and the right leg was extended and firmly fixed by a vacuum pillow to eliminate possible movements during the measurement procedure. It was ensured that all subjects were in the same position, so that the foot was approximately 10 cm below heart level. A 10-min adaptation period was allowed for subjects to become accustomed to the laboratory room conditions and the presence of the research staff. The dorsal aspect of the foot was gently wiped with an alcohol pad to remove sweat sediments and the fat layer from the skin. Two different types of heating probes were situated on the skin in the following manner (Figure 4A): the large VHP3 probe was attached to the skin using self-adhesive ring-shaped tape and filled with distilled water, so that perfusion signal can be continuously captured through water from the center of the probe. The small VHP1 probe served for inducing flare response and was gently placed on the skin, securing it with a thin rubber belt, as seen in Figure 1B. The flowmotion acquisition area was selected to avoid different influencing factors of heating-induced responses, or underlying veins and large arteries that might pulsate (Figure 4A). After placement of the probes and all adjustments to the imaging device, which is part of the contactless PPG system, were made, it was fixed to the stand and positioned approximately 25 cm from the skin so that the entire dorsal aspect of the palm fits the visual field, and the illumination is uniform in the regions of interest, providing a sharp, high-quality image.

2.3.1 Heating protocol

The measurement lasted for a total of 30 min. Once the placement of VHP1 and VHP3 heating probes to the skin was complete and the measurement equipment was set up, the recording was started by pressing the record button on the custom-made dedicated software. The video capturing took place at 25 frames per second. During the data acquisition, the external illumination (regular room illumination) was switched off to avoid interference with the imaging device light source. To establish baseline perfusion at 32°C for both probes (VHP1 and VHP3), a 10-min pre-heating period was initiated at the beginning of the protocol. At the 10th minute, the probes were adjusted to 43°C for VHP3 and 45°C for VHP1 respectively as depicted in Figure 4C. The protocol then continued for an additional 18 min with the probes at their respective temperatures. After 28 min, the VHP1 probe was removed to expose the cutaneous flare area. The recording ended 2 min later, and the remaining VHP3 probe was then gently removed from the skin. To provide a visual representation of the protocol, a scheme is provided in Figure 4.

2.4 Signal processing

Data analysis and signal processing of video was performed offline using a dedicated Matlab software (see Figure 2). The process involved opening a previously stored measurement file and performing video pre-processing and iPPG processing. Pre-processing included three steps: 1) loading data into video buffer and spatial downsampling by factor two; 2) alignment of spectral images by estimation of geometric transformation using the "imregtform" function, and applying geometric transformation using the "imwarp" function; 3) video motion stabilization. The stabilized videos can be further analyzed to obtain haemodynamic parameters such as heart rate and perfusion index, or other parameters.

The amplitude of back-scattered light intensity pulsations fast varying component (AC) induced by heart activity is typically very small, usually below 1% from slow varying component (DC) level. Additionally, there is some fraction of biological noise present in the signal which can influence the signal-to-noise ratio and quality of signal. To address these issues, a second-order zero-phase Butterworth bandpass filter was applied within the heartbeat frequency range (0.7–5 Hz) to compute the AC signal, while the DC signal was calculated by low-pass cut-off filtering (0–0.3 Hz). The frequency ranges can be adjusted manually. To obtain hemodynamic parameters, the iPPG AC signal processing was accomplished in several steps. First, the local minima and maxima positions were found in a single PPG waveform using the built-in Matlab "findpeaks" function. If necessary, the sensitivity of the function for localization of extremal points can be adjusted manually. Then, single-period iPPG waveforms were extracted in a beat-per-beat manner, and hemodynamic parameters including pulse rate, DC signal, and AC signal amplitudes were calculated in every beat. The pulse rate was calculated using the formula:

$$Pulse\,rate_i = 60 \cdot (t_{n+1} - t_n)/fs \tag{1}$$

where n is the number of the current heartbeat, t_n is the time of the first local minima of the pulse wave, and f_s is the sampling frequency of the video. Microcirculation is related to the Perfusion Index (PI), which is calculated from the AC amplitude relative to DC level in every heartbeat using the formula:

$$PI_n(\%) = 100 \cdot (ACmax_n - ACmin_n)/DC_n \tag{2}$$

where ACmin and ACmax are the minimum and maximum peak values of the pulsatile component, DC is slow-varying signal, at *n*th beat.

The strength of camera-based contactless plethysmography lies in its high spatial resolution, which is particularly useful for determining topical heating-induced flare-a region of the skin with a substantially increased perfusion above the baseline. The process involves two steps. First, a perfusion map is generated by calculating the pulsatile component in every pixel of the video using the locking-amplification principle as described by Amelard et al. (2017) as the Pearson's linear correlation coefficient between the signal obtained in each image pixel and the ground-truth reference signal in such a way:

$$P(x,t) = \frac{\sum_{t=0}^{T} Y(x,t)R(t)}{\sqrt{\sum_{t=0}^{T} Y(x,t)^2}\sqrt{\sum_{t=0}^{T} R(t)^2}} \tag{3}$$

where P is a perfusion map, x is a pixel coordinate, t is a time, T is a time buffer (10 s) of a pulsatile PPG AC signal Y, and R is the reference signal which is calculated as spatially averaged Y signal from manually selected RoI. Equation 3 represents a spatially-distributed skin blood perfusion, which varies in time. Perfusion map is auto normalized, and its value varies from 0 to 1.

The area of the flare depends on the threshold, which depends on biological zero signal in the skin non-affected by external heat stimuli. The flare area is defined as the sum of the perfusion map pixels where $p >$

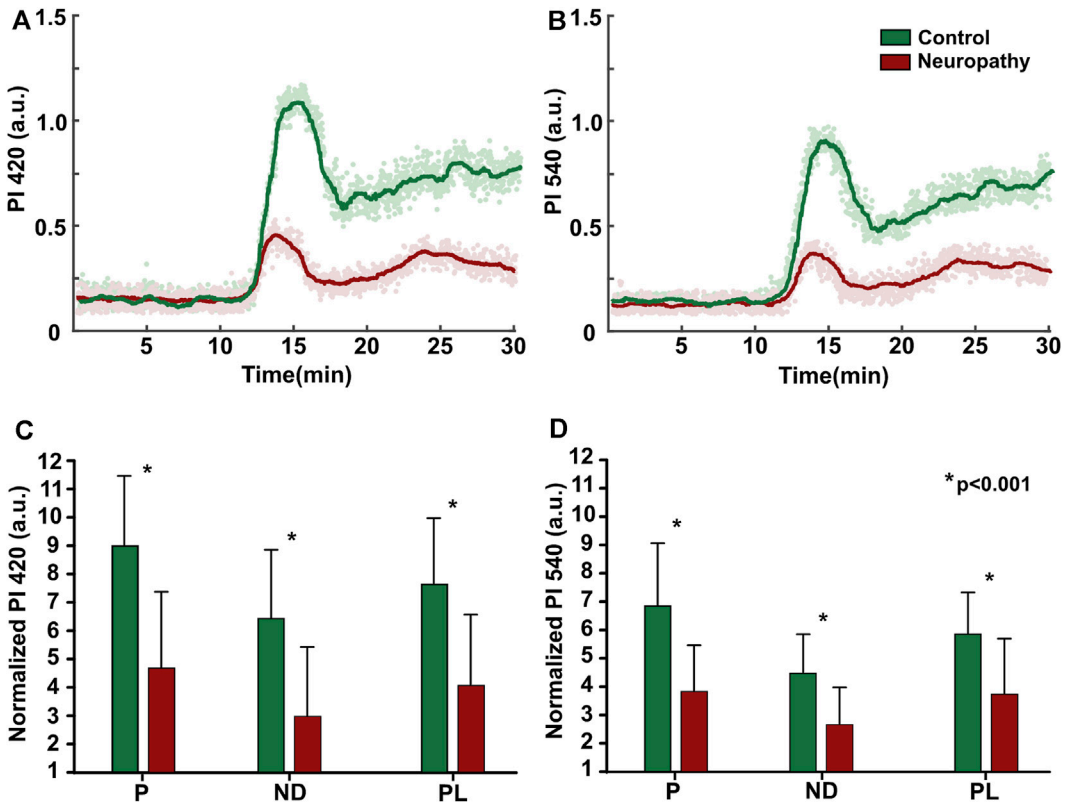

FIGURE 5
Topical heating vasomotor response trend **(A, B)** Individual example from patient and healthy subject at 420 and 540 nm illumination. **(C, D)** Baseline normalized group (patients: n = 15, control: n = 15) mean data of vasomotor response characterizing parameters; P- initial peak, ND-nadir, PL-plateau phase, values presented as mean ± standard deviation, statistically significant difference denoted by asterisk.

0.5, which we assumed as an optimum threshold considering baseline perfusion level. The total flare area (FA) is calculated as the full area minus the area of the VHP1 heater contact surface, which is 100 mm^2. The equation for calculating FA is as follows:

$$FA = a\left(\sum_{x\epsilon S} x - \sum_{x\epsilon H} x\right) \quad (4)$$

where x is a pixel coordinate, a is the area of a single pixel, S refers to the manually selected ellipse region of interest (RoI) that covers the area surrounding the VHP1 probe, and H is the VHP1 probe contact area. The flare intensity index, which has been introduced to characterize the density of the flare, is defined as follows:

$$FD(\%) = \frac{100 \cdot a}{FA}\left(\sum_{x\epsilon S} P(x) - \sum_{x\epsilon H} P(x)\right) \quad (5)$$

where P(x) is a perfusion map values in x pixels belonging to the S and H regions, FD is a flare intensity index.

2.4.1 Analyses of cutaneous perfusion data

The characterization of heating-induced vasomotor response, heating-induced flare, and flowmotions was performed offline using data analysis software that is an integral part of the present contactless photoplethysmography (PPG) system. The relevant regions of interest were manually selected on the preview video screen, and the analyses were performed automatically. Vasomotor response was computed from the region inside the transparent part of the VHP3 heating probe, and the perfusion index changes over time were analyzed using the vasomotor response analysis module which was part of the software. The analyses incorporated perfusion index filtering and trending with the detection of characteristic inflection points that determined the amplitudes of the first peak (P), nadir (ND), and plateau phase (PL), as depicted in Figure 4B. To explore the flare response, two regions of interest were selected. First, a small circular region was selected on the contact zone of the VHP1 probe to fit directly heated skin boundaries, while the second region was placed over the larger area surrounding the VHP1 probe. The analyses were performed on a 1-min duration video fragment just following removal of the heating probe. Offline analyses included the generation of a perfusion map and the determination of the flare area, as described in the signal processing methods section. Cutaneous flowmotions were calculated from flare and heating unaffected skin by selecting a ~40 × 40 pixel region of a 20-min duration video fragment, as depicted in Figure 5. The flowmotions were automatically divided into three spectral ranges representing the influence of myogenic (~0.05–0.15 Hz) (Kastrup et al., 1989), neurogenic (~0.02–0.05 Hz) (Söderström et al., 2003), and endothelial (~0.0095–0.02 Hz) (Kvernmo et al., 1999; Kvandal et al., 2003) activity, as suggested by other studies. The averaged spectral

power density for each spectral range was computed by Fast Fourier Transform using following formula:

$$PSD = \frac{1}{f2 - f1}\sum_{f1}^{f2}|F(f)|^2$$

Where PSD is a averaged power spectral density, F is a Fourier transform of RoI-averaged PPG signal, f1, f2—spectral range of corresponding flowmotion component.

2.5 Statistical analyses

The statistical analyses were conducted using SigmaPlot 12.0 (Systat Software Inc., San Jose, CA, United States). As the majority of the data did not conform to Gaussian distribution, non-parametric statistical tests were employed. To compare the patient group with the control group, the Mann-Whitney Rank Sum Test was utilized. The baseline cutaneous perfusion values for the different wavelengths in both the control and patient groups were compared using Kruskal–Wallis One Way Analysis of Variance on Ranks (ANOVA). To reveal relationship between flare area and flare intensity index Spearman's correlation analyses was utilized. A statistically significant difference was defined as $p < 0.05$. Unless stated otherwise, the values presented in the text and graphs are expressed as the arithmetic mean ± standard deviation.

3 Results

Comparing baseline amplitude of PPG waveform (AC signal) at all three wavelengths, it has been noticed that the infrared channel (800 nm) signal amplitude across all subjects did not significantly differ from the noise. Therefore, these data has been excluded from subsequent analyses, and further results are provided on blue (420 nm) and green channels (540 nm). All fifty subjects (patient group and healthy control group) displayed a reasonable amplitude PPG waveform at both channels during baseline and vasomotor response. The baseline perfusion index amplitude slightly varied among the individuals, with no statistically significant difference observed between subject groups or two PPG channels (420 nm vs. 540 nm). The mean values were as follows: 420 nm - control (0.12 ± 0.04) vs. patients (0.11 ± 0.06) and 540 nm - control (0.13 ± 0.06) vs. patients (0.14 ± 0.07).

The quantification of heating-induced cutaneous response was performed on the two separate modalities as an amplitudes of vasomotor trend and extend of cutaneous reddening area-flare.

3.1 Topical heating vasomotor response trend

Control group subjects exhibited a similar trend of vasomotor response at both 420 and 540 nm, with its characteristic shape comprising sharp, increase of perfusion (P1) with the following decline, nadir, and succeeding elevation, which remained relatively unchanged until the end of recording, known as the plateau phase, as shown in Figure 5. However the signal at 420 nm PPG band was 20%–30% larger, than that of 540 nm, regardless of subjects group. Meanwhile, the neuropathic patient group demonstrated a blunted response (50%), with altered initial peak (P1), nadir (ND), and plateau phase (PL), regardless of the illumination wavelength, Figure 5.

3.2 Topical heating flare response

Topical heating induced the reddening (flare) surrounding the direct contact site of the heating probe in all subjects, with some individual differences in the intensity of flare (flare intensity index) and area noticed among the same group subjects (Figure 6). Similar to vasomotor response amplitude, flare area (63%) and flare intensity index (19%) were significantly decreased in patients compared to healthy volunteers, regardless of the illumination wavelength. The patient group (n = 15) flare intensity index and flare area at 420 nm and 540 nm were as follows: 420 nm illumination 48.74 ± 14.56 a.u. and 248.46 cm^2 ± 198.08 cm^2; 540 nm illumination 45.89 ± 13.69 a.u. and 246.13 cm^2 ± 195.18 cm^2. The control group flare intensity index and flare area were: 420 nm illumination 56.26 ± 5.31 a.u. and 598.07 cm^2 ± 271.89 cm^2; 540 nm illumination 57.92 ± 6.77 a.u. and 673.60 cm^2 ± 275.16 cm^2.

3.3 Cutaneous flowmotions

Acquisition of cutaneous flowmotions was more challenging due to the requirement of long duration artefact-free recording; therefore, moderate substantial variation among the same group subjects was observed for all three components, regardless of illumination wavelength. A noteworthy finding is the significantly larger (54%) neurogenic component of the control group compared to the neuropathic patient group at both wavelengths (Figure 7). The group mean values for healthy volunteers were as follows: at 420 nm illumination-endothelial 0.85 ± 0.68 a.u., neurogenic 0.58 ± 0.49 a. u., myogenic 0.14 ± 0.11a.u.; at 540 nm illumination-endothelial 0.91 ± 0.62a.u., neurogenic 0.55 ± 0.38 a. u., myogenic 0.11 ± 0.08 a. u. Group mean values for neuropathic patients were as follow: at 420 nm illumination-endothelial 0.85 ± 0.68 a. u., neurogenic 0.58 ± 0.49 a. u., myogenic 0.14 ± 0.11 a. u.; at 540 nm illumination-endothelial 0.91 ± 0.62 a. u., neurogenic 0.55 ± 0.38 a. u., myogenic 0.11 ± 0.08 a. u.

4 Discussion

Over decades there were several attempts to use photoplethysmography for assessment on neuropathies, ranging from PPG waveform parameter analyses (Bryce et al., 2022) to spectral analyses of PPG signal fluctuations (Bentham et al., 2018), and using single point PPG recording and multi-channel recording (Kim et al., 2007), alone or in combination with different modalities such as ECG or laser Doppler (Kim et al., 2008). However most of the studies up to date in this field were performed using contact manner conventional transmission type PPG, which is usually applied in the fingers and there are sparse studies assessing function of peripheral nerve fibers by contactless modality of

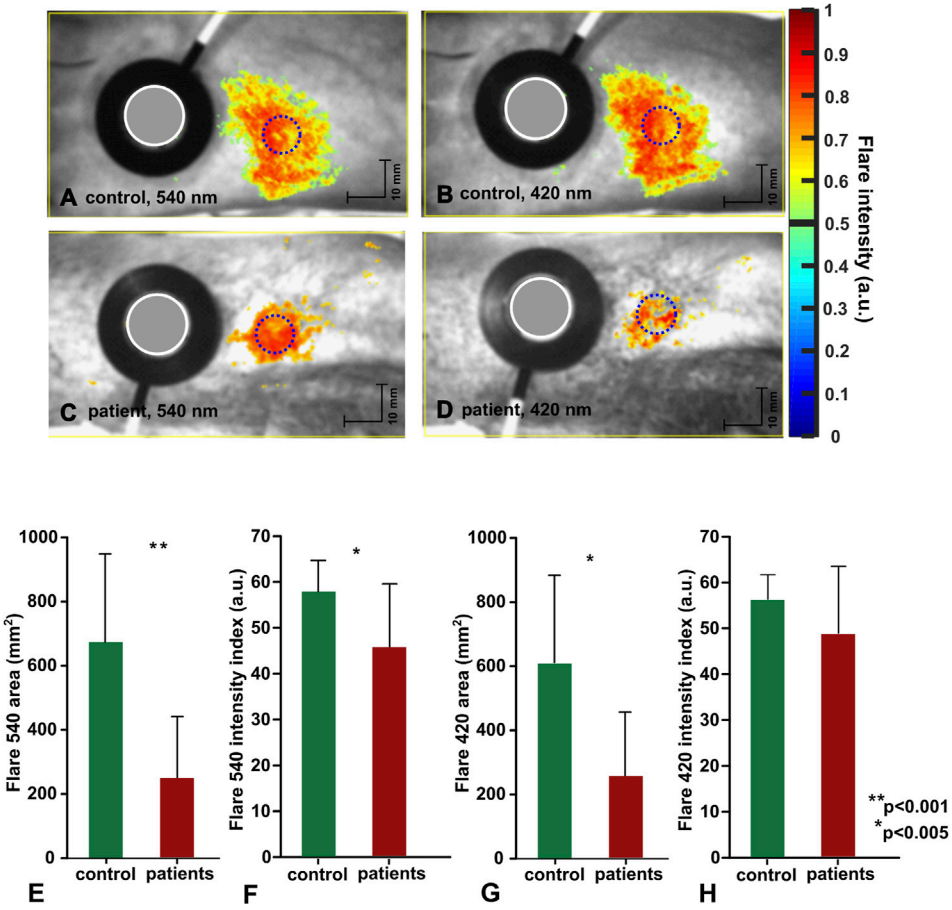

FIGURE 6
Topical heating induced flare response. **(A–D)** representative data from individual subject, flare discrimination threshold is set to 0.5. **(E–H)** Group mean data (control:n = 15, patients:n = 15) mean ± std, statistical significance denoted with asterisks.

PPG. The present study makes a significant contribution to the evaluation of multispectral imaging photoplethysmography for assessing neuropathic patients. By examining cutaneous flow motions and topical heating-induced vasomotor responses, we demonstrate the capability of this method, which to the best of our knowledge is the first of its kind. It was expected that a multispectral approach, comprising three different wavelengths, may provide additional diagnostic information, and therefore was implemented in our present setup. Contrary to our expectations, it was possible to obtain reliable PPG signal only at two (420 and 540 nm) out of three wavelengths during the same test of topical heating, as the signal at 800 nm illumination was extremely noisy and did not significantly differ from the biological zero level. This finding is in contrast to our previous studies where a detectable, hence smaller amplitude signal was obtained from both the dorsal and palmar aspect of the hand at the baseline and during topical heating using similar wavelength illumination (Marcinkevics et al., 2016; Marcinkevics et al., 2017), albeit with approximately four times larger spectral bandwidth, which covers a broader range of chromophores providing absorption in adjacent wavelengths. The possible reasons for the diminished PPG signal at this wavelength are low Hb absorption and lower density of arterio-venous anastomoses in the cutaneous vasculature of the foot's dorsal aspect, which counterweights our initial idea of selecting the Hb isosbestic point, which might be indifferent to alterations of Hb saturation and could provide information regardless of the patient's arterial oxygen content. Noteworthy was finding that baseline perfusion was similar in the blue (420 nm) and green (50 nm) PPG channels and did not differ between neuropathic and control group, which allowed us to normalize cutaneous perfusion to the baseline. Different normalization approaches have been mentioned in the early studies for inter-subject comparison, including normalization to maximal vasodilatory capacity, which is achieved by pharmacological intervention, such as iontophoresis of sodium nitroprusside used or acetylcholine, contributing as an endothelium independent vasodilators (Kellogg et al., 1999), first being an NO dependent, and second acting directly on smooth muscle cells. Or physiological normalization, such as maximal reperfusion during post occlusive reactive hyperemia (Shirazi et al., 2021) and topical heating induced vasodilation (Chaseling et al., 2020). Another option could be normalization to the baseline, which is more non-intrusive but feasible only if constant initial baseline conditions are achieved. All mentioned approaches have its own limitations therefore simpler and less intrusive baseline approach was presently utilized. Its validity can be supported by the fact that all subjects regardless age and health

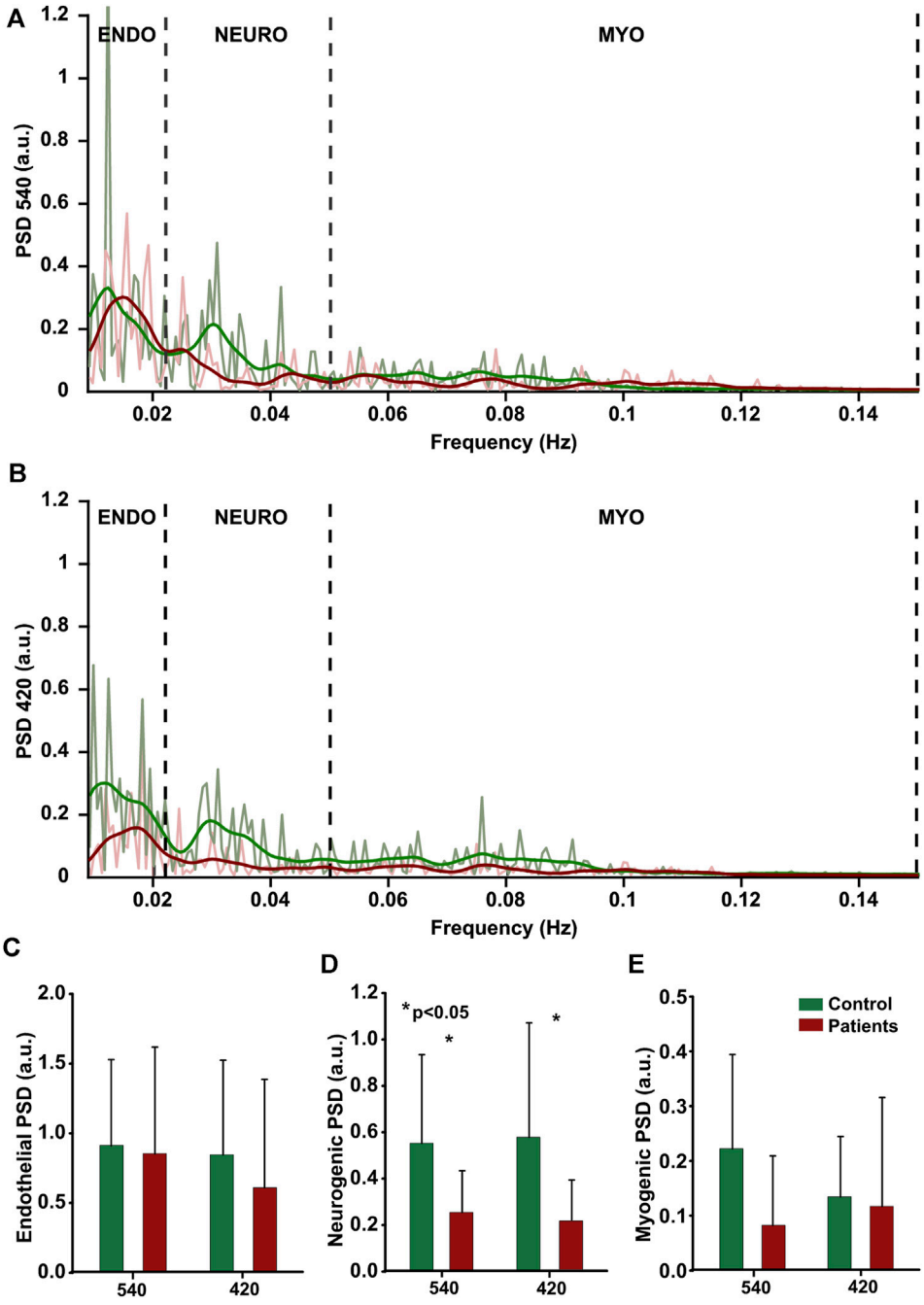

FIGURE 7
Cutaneous flowmotions. Power Spectral Density of endothelial (0.009–0.022 Hz), neurogenic (0.22–0.05 Hz) and myogenic (0.05–0.15 Hz) components at two wavelength, **(A, B)** individual data from one subject. **(C–E)** group mean data (control:n = 15, patients:n = 15), statistically significant data denoted by asterisks.

state exhibited similar absolute values of perfusion index during the baseline, resulted by preconditioning of 32°C preheating.

4.1 Heating induced vasomotor response trend

All subjects responded to topical heating, producing well-known three-phase pattern of cutaneous vasodilation: an initial peak within the first 5–6 min and a subsequent nadir followed by a sustained plateau (Kellogg et al., 1999; Minson et al., 2001). Neuropathic patients showed diverse response with significantly reduced amplitude of cutaneous vasodilation in both PPG channels, particularly in the initial vasodilatory peak (approximately 58%) and to a moderate extent in the plateau phase (approximately 45%). This observation was consistent across all subjects, regardless of the PPG channel, with some individual variations. The interpretation of this phenomenon is particularly challenging, as there is a lack of

studies on contactless PPG assessment of neuropathies. However, our recent study evaluating reversible pharmacological impairment of cutaneous sensory nerve fibers using remote photoplethysmography showed a decrease in the initial vasodilatory peak, but unaltered plateau phase (Marcinkevics et al., 2021), which is contrary to the present finding. Similar were provided from neuropathic patients studies using laser Doppler technique (Kilo et al., 2000; Krishnan and Rayman, 2004; Carter and Hodges, 2011; Obayashi and Ando, 2014; Kubasch et al., 2017), hence the technique substantially differs from PPG. The decreased vasodilatory response in the neuropathic group may be explained by underlying physiological mechanisms of heat induced vasodilation. The literature suggest that major contributor to transient initial vasodilatory peak is a local sensory nerve-mediated axon reflex (Minson et al., 2001), mediated by TRPV1 channel dependent activation of C-fiber afferent nerve fibers that release substance-P and calcitonin gene-related peptide (GCRP) with a modest contribution of NO during early phase (Marche et al., 2017) and therefore may reflect both endothelial and small nerve fiber function. Studies suggest slightly diminishing initial peak due to the aging (Millet et al., 2012), and equally sympathetic-parasympathetic balance along to hormonal level could influence response, potentially accounting to observed variance in our subjects groups. Nevertheless, the substantial effect of age on vasomotor response is excluded, as the patient and control groups have similar age structure, confirmed by statistics. The possible explanations to reduced plateau phase in our patient cohort, is contribution of plethora of mechanisms in its genesis. There is evidence that plateau is only 60%–70% endothelium NO-dependent (Fieger and Wong, 2010; Bruning et al., 2012; Fujii et al., 2014), and could be modulated by other factors such as adenosine receptors, endogenous reactive oxygen species (Huang et al., 2012) and transient receptor potential vanilloid type 1 (TRPV1) channels which are expressed on the membrane of sensory nerve fibers (Wong and Fieger, 2010) and could be deranged in neuropathic patients. In addition etiology of peripheral neuropathies is multifaceted, frequently related to endothelial dysfunction such as in diabetic polyneuropathy. Clinical studies have shown that endothelial function assessed by endothelium-dependent vasodilation is impaired in diabetic patients (McVeigh et al., 1992) although the pathogenesis has not been fully elucidated. Our neuropathic group was etiologically heterogeneous and impairments of endothelial function cannot be ruled out.

4.2 Flare response

Another more robust expression of topical heating is the flare response-a type of localized neurogenic inflammation manifested as the reddening of the skin region which surrounds directly heated site. In our study, the flare response along the vasomotor response trend was employed to evaluate cutaneous nerve fiber function in neuropathic patients. The essential finding of present photoplethysmography study is reduced flare area (approx. 63%) and flare intensity (approx. 19%) in neuropathic patients in comparison to control group regardless of the illumination wavelength. The similar effect have been showed by several laser Doppler studies utilizing different provocation procedures, such as topical skin heating and vasoactive substance iontophoresis in neuropathic patients (Krishnan and Rayman, 2004; Bickel et al., 2009; Green, 2009; Green et al., 2009; Illigens et al., 2013; Namer et al., 2013; Sharma et al., 2015; Abraham et al., 2016; Calero-Romero et al., 2018). However there are also controversial studies, suggesting decreased flare area in neuropathic patients with structurally deranged nerve fibers (Bickel et al., 2009), while others points on flare reliability only for painful neuropathy conditions (Ysihai, 2009). Notably, our present research revealed that the flare intensity index in neuropathic patients remained unchanged regardless of the size of the flare area. What is in line to the laser Doppler study by Alistair et al. suggesting correlation of flare intensity to microvascular function and correlation of flare area to small fiber functions (Arnold et al., 2015). And in the light of this study the slight decrease of flare intensity index might point on moderate microvascular impairments in our neuropathic patient group, which is consisted with findings related to diminished plateau phase of these patients. Hence, it is difficult to interpret the present data due to the lack of relevant studies and sparse evidence regarding photoplethysmography's ability to assess neuropathic patients using quantification of flare response, as this imaging modality differs substantially from Laser Doppler technique and results cannot be directly attributed to other imaging modalities without appropriate investigation. Nonetheless, there is some evidence from our previous research (Marcinkevics et al., 2021) on potential of imaging photoplethysmography for assessment of small fiber functions in the healthy volunteers, which may be extrapolated to the neuropathic patients. Recent evidence suggest that pathophysiology of small fiber neuropathy is related to spontaneous activation of small unmyelinated sensory polymodal nerve fibers which are aimed to detect and transmit temperature and slow pain to the central nervous system; hence, when impaired, can cause chronic neuropathic pain. In the healthy individuals topical skin heating (above 42°C) depolarizes small unmyelinated dermal C-fibers, resulting in afferent action potentials that are conducted toward the spinal cord and, at branching points, antidromically invade peripheral branches adjacent to the initial stimulation point, triggering release of vasoactive substances, such as substance P and calcitonin gene-related peptide (CGRP), from nerve terminals, which leads to arteriolar smooth muscle relaxation and vasodilation at the localized skin area extending outside heated skin region (Weidner et al., 2003). While in the neuropathic patients deranged nerve fibers produce substantially blunted response, which can be detected by imaging photoplethysmography, Laser Doppler imaging, and likely any imaging technique with potential to measure cutaneous blood perfusion.

4.3 Flowmotions

Spectral analysis of photoplethysmography (PPG) signals has long been a desirable technique due to the relative ease of recording and the potential for advanced mathematical tools to yield valuable diagnostic information. In the recent study, we have expanded upon this approach and performed a comprehensive evaluation of the efficacy of contactless PPG in the assessment of patients with small fiber neuropathy using cutaneous flowmotion analyses. The key finding of our present study is a marked reduction in the neurogenic component of vasomotor responses in patients with neuropathy, which is consistent with the observed reductions in flare area, flare intensity, and initial peak pointing on deranged

small nerve fiber function. Surprisingly, there was no statistically significant difference between the endothelial flowmotion component in healthy subjects and neuropathic patients, despite the latter group showing a reduced plateau phase in vasomotor response, which can be partly explained by contribution of systemic factors or insufficiently deranged endothelial function of patients. Overall, our results are consistent with other studies (Bernardi et al., 1997; Lefrandt et al., 2003; Meyer et al., 2003; Quattrini et al., 2007; Sun et al., 2013; Körei et al., 2015) that have used Laser Doppler to evaluate diabetic patients with neuropathy, as well as with our previous study that utilized photoplethysmography to assess small cutaneous nerve fibers in healthy subjects (Marcinkevics et al., 2021). However, the interpretation of our present findings is constrained by the lack of literature on flowmotions studies that utilize the same spectral analysis approach (three major spectral components) and photoplethysmography, as most existing research on this topic are conducted with the Laser Doppler technique, emphasizing the necessity for further research using comparable methodologies to validate and expand our results. Furthermore, the interpretation of our results is limited by incomplete knowledge of the genesis and influencing factors of flowmotions. The precise mechanism underlying these oscillations remains unclear, but prior research suggests a local origin stemming from dynamic interactions between sympathetic vasoconstriction, pressure-dependent vasoconstriction, flow-dependent endothelium-mediated vasodilation, metabolic vasodilation, and spontaneous myogenic activity (Rossi et al., 2006), which can indirectly support our recent findings on alteration on neurogenic component in neuropathic patients.

4.4 Study limitations

While the study was conducted with a commitment to precise methodology and strict adherence to the experimental design, certain limitations were encountered that could impact the reliability of the findings, necessitating careful interpretation of the results.

First, the generalizability of our findings could be affected by the relatively small sample size and the diverse nature of the neuropathic patients we studied. Nevertheless, significant results were still achieved, underscoring the robustness of our photoplethysmographic evaluations.

Second, our study primarily focused on functional assessments of neuropathic patients, without a direct morphologic evaluation of nerve fibers by biopsy to validate clinical diagnoses. However, the intent of our study was not to provide structural assessments, but to showcase a potential functional evaluation technique that could augment existing structural testing methods.

Third, there exists the possibility of parameter drift in the photoplethysmography imaging system during recording, which could potentially affect the recording of vasomotion due to their low frequency. To mitigate this, we assessed the stability of light sources prior to the experiment. Our data showed that for all three channels, the standard deviation did not exceed 0.05% of the mean PPG signal in the 0–5 Hz frequency range. Moreover, the power spectral density (PSD) of the PPG signal, calculated from a white reference video in the 0.0095–0.15 Hz frequency range, was two orders of magnitude lower than the PPG signals obtained from healthy subjects. This indicates that any potential instability of the LED did not significantly influence the flowmotion measurements.

Fourth, the slow respiration rate of subjects could potentially affect the myogenic component of flowmotions (Liu et al., 2020). However, we did not control for this as we assumed subjects were breathing normally in either sitting or resting positions (Rodríguez-Molinero et al., 2013; Miles-Chan et al., 2014; Katz et al., 2018). Further, normal breathing does not interfere with the myogenic frequency range or affect the PPG signal. As corroborated by other studies of vasomotion using laser Doppler, the control of respiratory rate during cutaneous blood perfusion recording is not a critical factor for measuring vasomotion components (Kastrup et al., 1989; Meyer et al., 2003).

Despite these limitations, we believe our study makes valuable contributions to the literature and opens avenues for future research.

4.5 Conclusive remarks

Overall, our study highlights that photoplethysmographic evaluation of the flare response is the most methodically simple and robust technique among all we tested. While the analysis of flowmotions may appear simple and attractive, but is less informative due to its sensitivity to slow fluctuation artifacts and measurement site variations. Taken together, these results suggest that photoplethysmographic evaluation of the vasomotor flare response holds promise as an objective clinically valuable tool for assessing small fiber function in neuropathic patients.

One partially unresolved issue in our study concerns the diagnostic utility of the multispectral approach in photoplethysmography. Our findings suggest that there are no clear indications for any additional diagnostic information gained from the simultaneous use of the green (540 nm) and blue (420 nm) channels, nor are there any strong implications for the preference of the blue channel over the green in assessing neuropathic patients. However, we did observe that in the blue channel, the vasomotor response was numerically larger by approximately 20%–30% in both the patient and control groups, which could be attributed to the higher hemoglobin absorption at this wavelength (Zijlstra et al., 1991) and slightly different penetration depth into the skin, comprising different density of vessels (Finlayson et al., 2022). Nonetheless, despite these differentiating factors, both 420 nm and 540 nm light penetrate only superficially at the epidermal-dermal junction where the majority of vessels are densely situated capillary loops without substantial contractile elements, the two wavelengths provide a similar pattern of vasomotor response. These results suggest that the application of the two band approach in photoplethysmography may not yield significant diagnostic value in the evaluation of neuropathic patients and the usefulness of different PPG bands in diagnostics is highly debatable, while several studies emphasize the contrary (Asare et al., 2011; Chen et al., 2020), such as the study by Labuda et al. (2022) The argument put forth by the authors is that information can be extracted from different depths. At the outset of our study, we hypothesized that simultaneous recording at different illuminations would provide valuable diagnostic information from varying vascular layers within the skin due to the wavelength-dependent penetration depth of light. However, our findings failed to support this hypothesis. An explanation for this may be found in the genesis mechanisms of photoplethysmography, which, despite decades

of research and widespread application varying from heart rate monitors to intensive care pulse oximeters, have not been fully elucidated. Several recent studies have advocated the classical, well-accepted volumetric photoplethysmography model (Moço et al., 2018), which posits that the PPG signal originates from volume variations in the arteriole-arterial network at different depths. According to this model, the depth-origin of PPG using green wavelengths is dermal blood volume variations, while red-IR wavelengths may interact with subcutaneous blood volume variations. Another, the red blood cell aggregation model (Fine and Kaminsky, 2022), suggests that the source of the optical signal pulsation is associated with the modulation of the scattering of RBCs in the blood vessels that is caused by the modulation of blood flow velocity. The change in blood scattering can be explained by the change in the average size of aggregates following the fluctuations of shear forces, which vary during the course of the pulse wave. Recently, an interesting tissue compression model was proposed by Kamshilin et al. (2015), which states that pulse oscillations of the arterial transmural pressure, which occur during every cardiac cycle, deform the connective-tissue components of the dermis. Therefore, further studies using advanced tissue modeling are necessary to reveal a more unified mechanism of PPG signal origin that would fit all existing hypotheses and experimental data.

5 Conclusion

Overall, this study demonstrate the potential of imaging photoplethysmography as a cost-effective and straightforward alternative to existing imaging techniques for the assessment of neuropathic patients, providing novel information to the field of chronic pain diagnostics. However, in order to effectively implement this technology in clinical settings, further extensive research is required to improve provocation methodology, enhance PPG signal quality, and establish diagnostic criteria and referent values for heat-induced vasomotor tests, which can be achieved through the utilization of novel approaches, such as deep learning.

Data availability statement

The raw data supporting the conclusions of this article will be made available by the authors, without undue reservation.

Ethics statement

The studies involving humans were approved by Ethics Committee of the University of Latvia, Institute of Cardiology and Regenerative Medicine and Riga Stradins University Research Ethics Committee (Prot.Nr: 03.05.2018). The studies were conducted in accordance with the local legislation and institutional requirements. The participants provided their written informed consent to participate in this study.

Author contributions

ZM and AG contributed to the design of the experiment, IL and DG collection of data. UR and AA analyses of data. ZM and IL interpretation of data and drafted the article. All authors contributed to the article and approved the submitted version.

Funding

This study was funded by the Latvian Council of Science Fundamental and Applied Research Project "Imaging Photoplethysmography for Chronic Pain Assessment" No. LZP-2018/1-0188.

Acknowledgments

We would like to express our gratitude to the employees of the University of Latvia who participated in this study as subjects. Additionally, we extend our thanks to the staff at the University of Latvia, Institute of Atomic Physics and Spectroscopy, and Professor Janis Spigulis, head of the Biophotonics Laboratory, for their support and valuable discussions throughout the course of this research.

Conflict of interest

The authors declare that the research was conducted in the absence of any commercial or financial relationships that could be construed as a potential conflict of interest.

Publisher's note

References

Abraham, A., Alabdali, M., Alsulaiman, A., Breiner, A., Barnett, C., Katzberg, H. D., et al. (2016). Laser Doppler flare imaging and quantitative thermal thresholds testing performance in small and mixed fiber neuropathies. *PLoS One* 11, e0165731. doi:10.1371/JOURNAL.PONE.0165731

Allen, J. (2007). Photoplethysmography and its application in clinical physiological measurement. *Physiol. Meas.* 28, R1–R39. doi:10.1088/0967-3334/28/3/R01

Amelard, R., Hughson, R. L., Greaves, D. K., Pfisterer, K. J., Leung, J., Clausi, D. A., et al. (2017). Non-contact hemodynamic imaging reveals the jugular venous pulse waveform. *Sci. Rep.* 7, 40150. doi:10.1038/SREP40150

Ando, A., Miyamoto, M., Saito, N., Kotani, K., Kamiya, H., Ishibashi, S., et al. (2021). Small fibre neuropathy is associated with impaired vascular endothelial function in patients with type 2 diabetes. *Front. Endocrinol. (Lausanne).* 12, 1. doi:10.3389/fendo.2021.653277

Arnold, W. D., Kassar, D., and Kissel, J. T. (2015). Spinal muscular atrophy: diagnosis and management in a new therapeutic era. *Muscle Nerve* 51, 157–167. doi:10.1002/MUS.24497

Asare, L., Kviesis-Kipge, E., Rubins, U., Rubenis, O., and Spigulis, J. (2011). "Multi-spectral photoplethysmography technique for parallel monitoring of pulse shapes at different tissue depths," in *Clinical and biomedical spectroscopy and imaging II* Editors N. Ramanujam and J. Popp doi:10.1117/12.889954

Bashkatov, A. N., Genina, E. A., and Tuchin, V. V. (2011). Optical properties OF SKIN, subcutaneous, and muscle tissues: a review. *J. Innov. Opt. Health Sci.* 4, 9–38. doi:10.1142/S1793545811001319

Bentham, M., Stansby, G., and Allen, J. (2018). Innovative multi-site photoplethysmography analysis for quantifying pulse amplitude and timing variability characteristics in peripheral arterial disease. *Diseases* 6, 81. doi:10.3390/DISEASES6030081

Bernardi, L., Rossi, M., Leuzzi, S., Mevio, E., Fornasari, G., Calciati, A., et al. (1997). Reduction of 0.1 Hz microcirculatory fluctuations as evidence of sympathetic dysfunction in insulin-dependent diabetes. *Cardiovasc. Res.* 34, 185–191. doi:10.1016/S0008-6363(97)00017-5

Bickel, A., Heyer, G., Senger, C., Maihöfner, C., Maihoefner, C., Heuss, D., et al. (2009). C-fiber axon reflex flare size correlates with epidermal nerve fiber density in human skin biopsies. *J. Peripher. Nerv. Syst.* 14, 294–299. doi:10.1111/j.1529-8027.2009.00241.x

Breivik, H., Eisenberg, E., and O'Brien, T.OPENMinds (2013). The individual and societal burden of chronic pain in europe: the case for strategic prioritisation and action to improve knowledge and availability of appropriate care. *BMC Public Health* 13, 1229. doi:10.1186/1471-2458-13-1229

Bruning, R. S., Santhanam, L., Stanhewicz, A. E., Smith, C. J., Berkowitz, D. E., Kenney, W. L., et al. (2012). Endothelial nitric oxide synthase mediates cutaneous vasodilation during local heating and is attenuated in middle-aged human skin. *J. Appl. Physiol.* 112, 2019–2026. doi:10.1152/JAPPLPHYSIOL.01354.2011

Bryce, Y., Santos-Martin, E., Ziv, E., Gonzalez-Aguirre, A., Moussa, A., Friedman, A., et al. (2022). Abnormal photoplethysmography waveforms are associated with chemotherapy induced neuropathy. *Vasa* 51, 85–92. doi:10.1024/0301-1526/A000987

Calero-Romero, I., Suter, M. R., Waeber, B., Feihl, F., and Kuntzer, T. (2018). Axon reflex–mediated vasodilation is reduced in proportion to disease severity in TTR-FAP. *Neurol. Genet.* 4, e251. doi:10.1212/NXG.0000000000000251

Callaghan, B. C., Price, R. S., and Feldman, E. L. (2015). Distal symmetric polyneuropathy: a review. *JAMA* 314, 2172–2181. doi:10.1001/JAMA.2015.13611

Carnago, L., O'Regan, A., and Hughes, J. M. (2021). Diagnosing and treating chronic pain: are we doing this right? *J. Prim. Care Community Health* 12, 21501327211008055. doi:10.1177/21501327211008055

Carter, S. J., and Hodges, G. J. (2011). Sensory and sympathetic nerve contributions to the cutaneous vasodilator response from a noxious heat stimulus. *Exp. Physiol.* 96, 1208–1217. doi:10.1113/expphysiol.2011.059907

Chaseling, G. K., Crandall, C. G., and Gagnon, D. (2020). Skin blood flow measurements during heat stress: technical and analytical considerations. *Am. J. Physiol. Regul. Integr. Comp. Physiol.* 318, R57-R69–R69. doi:10.1152/AJPREGU.00177.2019

Chen, S. H., Chuang, Y. C., and Chang, C. C. (2020). Development of a portable all-wavelength PPG sensing device for robust adaptive-depth measurement: a spectrometer approach with a hydrostatic measurement example. *Sensors 2020* 20, *6556* 20, 6556. doi:10.3390/S20226556

Cheng, D., Wang, J., Yokota, T., and Someya, T. (2022). Spatiotemporal processing in photoplethysmography for skin microcirculatory perfusion imaging. *Biomed. Opt. Express* 13, 838–849. doi:10.1364/BOE.442764

Colloca, L., Ludman, T., Bouhassira, D., Baron, R., Dickenson, A. H., Yarnitsky, D., et al. (2017). Neuropathic pain. *Nat. Rev. Dis. Prim.* 3, 17002. doi:10.1038/NRDP.2017.2

Costigan, M., Scholz, J., and Woolf, C. J. (2009). Neuropathic pain: a maladaptive response of the nervous system to damage. *Annu. Rev. Neurosci.* 32, 1–32. doi:10.1146/ANNUREV.NEURO.051508.135531

Cracowski, J.-L., and Roustit, M. (2016). Current methods to assess human cutaneous blood flow: an updated focus on laser-based-techniques. *Microcirculation* 23, 337–344. doi:10.1111/micc.12257

Desquins, T., Bousefsaf, F., Pruski, A., and Maaoui, C. (2022). A survey of photoplethysmography and imaging photoplethysmography quality assessment methods. *Appl. Sci.* 12, 9582. doi:10.3390/APP12199582

Fieger, S. M., and Wong, B. J. (2010). Adenosine receptor inhibition with theophylline attenuates the skin blood flow response to local heating in humans. *Exp. Physiol.* 95, 946–954. doi:10.1113/EXPPHYSIOL.2010.053538

Fine, I., and Kaminsky, A. (2022). Scattering-driven PPG signal model. *Biomed. Opt. Express* 13, 2286–2298. doi:10.1364/BOE.451620

Finlayson, L., Barnard, I. R. M., McMillan, L., Ibbotson, S. H., Brown, C. T. A., Eadie, E., et al. (2022). Depth penetration of light into skin as a function of wavelength from 200 to 1000 nm. *Photochem. Photobiol.* 98, 974–981. doi:10.1111/PHP.13550

Ftiha, F., Shalom, M., and Jradeh, H. (2020). Neurological symptoms due to Coronavirus disease 2019. *Neurol. Int.* 12 (1), 8639. doi:10.4081/NI.2020.8639

Fujii, N., Brunt, V. E., and Minson, C. T. (2014). Tempol improves cutaneous thermal hyperemia through increasing nitric oxide bioavailability in young smokers. *Am. J. Physiol. Heart Circ. Physiol.* 306, H1507–H1511. doi:10.1152/AJPHEART.00886.2013

Gautam, M., Thakrar, A., Akinyemi, E., and Mahr, G. (2020). Current and future challenges in the delivery of mental healthcare during COVID-19. *SN Compr. Clin. Med.* 2, 865–870. doi:10.1007/s42399-020-00348-3

Green, A. Q., Krishnan, S. T., and Rayman, G. (2009). C-fiber function assessed by the laser Doppler imager flare technique and acetylcholine iontophoresis. *Muscle Nerve* 40, 985–991. doi:10.1002/mus.21333

Green, A. Q. M. (2009). Small fibre function assessed using the LDI flare technique in subjects with type 1 diabetes mellitus and impaired glucose tolerance. Available at: http://www.novonordiskfoundation.org.uk/content/dam/NNRF/AFFILIATE/www-novonordiskfoundation-org-uk/en_gb/Homepage/Documents/al-green-md-thesis.pdf.

Hagblad, J., Lindberg, L. G., Andersson, A. K., Bergstrand, S., Lindgren, M., Ek, A. C., et al. (2010). A technique based on laser Doppler flowmetry and photoplethysmography for simultaneously monitoring blood flow at different tissue depths. *Med. Biol. Eng. Comput.* 48, 415–422. doi:10.1007/S11517-010-0577-2

Harrison, D. K., Abbot, N. C., Swanson Beck, J., and McCollum, P. T. (1993). A preliminary assessment of laser Doppler perfusion imaging in human skin using the tuberculin reaction as a model. *Physiol. Meas.* 14, 241–252. doi:10.1088/0967-3334/14/3/002

Hertzman, A. B. (1937). Photoelectric plethysmography of the fingers and toes in man. *Proc. Soc. Exp. Biol. Med.* 37, 529–534. doi:10.3181/00379727-37-9630

Huang, C., Wang, S., and Tsai, Y. (2012). Axon reflex-related hyperemia induced by short local heating is reproducible. *Microvasc. Res.* 84, 351–355. doi:10.1016/j.mvr.2012.07.003

Huelsbusch, M., and Blazek, V. (2002). "Contactless mapping of rhythmical phenomena in tissue perfusion using PPGI," in Proceedings of the SPIE, 110–117. doi:10.1117/12.463573

Illigens, B. M. W., Siepmann, T., Roofeh, J., and Gibbons, C. H. (2013). Laser Doppler imaging in the detection of peripheral neuropathy. *Auton. Neurosci. Basic Clin.* 177, 286–290. doi:10.1016/j.autneu.2013.06.006

Jazieh, A. R., and Kozlakidis, Z. (2020). Healthcare transformation in the post-coronavirus pandemic era. *Front. Med.* 7, 429. doi:10.3389/FMED.2020.00429

Kamshilin, A. A., Mamontov, O. V., Koval, V. T., Zayats, G. A., and Romashko, R. V. (2015). Influence of a skin status on the light interaction with dermis. *Biomed. Opt. Express* 6, 4326–4334. doi:10.1364/BOE.6.004326

Kastrup, J., Bülow, J., and Lassen, N. A. (1989). Vasomotion in human skin before and after local heating recorded with laser Doppler flowmetry. A method for induction of vasomotion. *Int. J. Microcirc. Clin. Exp.* 8, 205–215.

Katz, S., Arish, N., Rokach, A., Zaltzman, Y., and Marcus, E. L. (2018). The effect of body position on pulmonary function: a systematic review. *BMC Pulm. Med.* 18, 159. doi:10.1186/S12890-018-0723-4

Kellogg, D. L. (2006). *In vivo* mechanisms of cutaneous vasodilation and vasoconstriction in humans during thermoregulatory challenges. *J. Appl. Physiol.* 100, 1709–1718. doi:10.1152/japplphysiol.01071.2005

Kellogg, D. L., Liu, Y., Kosiba, I. F., and O'Donnell, D. (1999). Role of nitric oxide in the vascular effects of local warming of the skin in humans. *J. Appl. Physiol.* 86, 1185–1190. doi:10.1152/JAPPL.1999.86.4.1185

Kilo, S., Berghoff, M., Hilz, M., and Freeman, R. (2000). Neural and endothelial control of the microcirculation in diabetic peripheral neuropathy. *Neurology* 54, 1246–1252. doi:10.1212/WNL.54.6.1246

Kim, D. W., Kim, S. W., Kim, S. C., Nam, K. C., Kang, E. S., and Im, J. J. (2007). Detection of diabetic neuropathy using blood volume ratio of finger and toe by PPG. In 2007 29th Annual International Conference of the IEEE Engineering in Medicine and Biology Society 2007, 2211–2214. doi:10.1109/IEMBS.2007.4352763

Kim, S. W., Kim, S. C., Nam, K. C., Kang, E. S., Im, J. J., and Kim, D. W. (2008). A new method of screening for diabetic neuropathy using laser Doppler and photoplethysmography. *Med. Biol. Eng. Comput.* 46, 61–67. doi:10.1007/S11517-007-0257-Z

Körei, A. E., Istenes, I., Papanas, N., Kempler, P., Korei, A. E., Istenes, I., et al. (2015). Small-fiber neuropathy: a diabetic microvascular complication of special clinical, diagnostic, and prognostic importance. *Angiology* 67, 49–57. doi:10.1177/0003319715583595

Krishnan, S. T. M., and Rayman, G. (2004). The LDIflare: a novel test of C-fiber function demonstrates early neuropathy in type 2 diabetes. *Diabetes Care* 27, 2930–2935. doi:10.2337/diacare.27.12.2930

Kubasch, M. L., Kubasch, A. S., Torres Pacheco, J., Buchmann, S. J., Illigens, B. M.-W., Barlinn, K., et al. (2017). Laser Doppler assessment of vasomotor axon reflex responsiveness to evaluate neurovascular function. *Front. Neurol.* 8, 370. doi:10.3389/fneur.2017.00370

Kvandal, P., Stefanovska, A., Veber, M., Kvernmo, H. D., Kirkebøen, K. A., and Kirkebøen, K. A. (2003). Regulation of human cutaneous circulation evaluated by laser Doppler flowmetry, iontophoresis, and spectral analysis: importance of nitric oxide and prostaglandines. *Microvasc. Res.* 65, 160–171. doi:10.1016/s0026-2862(03)00006-2

Kvernmo, H. D., Stefanovska, A., Kirkeboen, K. A., and Kvernebo, K. (1999). Oscillations in the human cutaneous blood perfusion signal modified by endothelium-dependent and endothelium-independent vasodilators. *Microvasc. Res.* 57, 298–309. doi:10.1006/mvre.1998.2139

Labuda, M., Smondrk, M., Babusiak, B., and Borik, S. (2022). System for non-contact and multispectral examination of blood supply to cutaneous tissue. *Electron* 11, 2958. doi:10.3390/ELECTRONICS11182958

Leal, J. M., de Souza, G. H., Marsillac, P. F. de, and Gripp, A. C. (2021). Skin manifestations associated with systemic diseases - Part II. *An. Bras. Dermatol.* 96, 672–687. doi:10.1016/J.ABD.2021.06.003

Lefrandt, J. D., Bosma, E., Oomen, P. H. N., Hoeven, J. H., Roon, A. M., Smit, A. J., et al. (2003). Sympathetic mediated vasomotion and skin capillary permeability in diabetic patients with peripheral neuropathy. *Diabetologia* 46, 40–47. doi:10.1007/S00125-002-1004-5

Lenasi, H. (2011). "Assessment of human skin microcirculation and its endothelial function using laser Doppler flowmetry," in *Medical imaging*. Editor F. Okechukwu Erondu (London, United Kingdom: IntechOpen Limited), 412. Available at: http://www.intechopen.com/books/medical-imaging/assessment-of-human-skin-microcirculation-and-its-endothelial-function-using-laser-doppler-flowmetry.

Liu, H., Chen, F., Hartmann, V., Khalid, S. G., Hughes, S., and Zheng, D. (2020). Comparison of different modulations of photoplethysmography in extracting respiratory rate: from a physiological perspective. *Physiol. Meas.* 41, 094001. doi:10.1088/1361-6579/ABAAF0

Magerl, W., Krumova, E. K., Baron, R., Tölle, T., Treede, R. D., and Maier, C. (2010). Reference data for quantitative sensory testing (QST): refined stratification for age and a novel method for statistical comparison of group data. *Pain* 151, 598–605. doi:10.1016/J.PAIN.2010.07.026

Maity, A. K., Maity, A. K., Wang, J., Wang, J., Wang, J., Sabharwal, A., et al. (2022). RobustPPG: camera-based robust heart rate estimation using motion cancellation. *Biomed. Opt. Express* 13 (10), 5447–5467 13. doi:10.1364/BOE.465143

Marche, P., Dubois, S., Abraham, P., Parot-Schinkel, E., Gascoin, L., Humeau-Heurier, A., et al. (2017). Neurovascular microcirculatory vasodilation mediated by C- fi bers and Transientreceptor potential vanilloid-type-1 channels (TRPV 1) is impaired in type 1 diabetes. *Nat. Publ. Gr.* 7, 44322. doi:10.1038/srep44322

Marcinkevics, Z., Aglinska, A., Rubins, U., and Grabovskis, A. (2021). Remote photoplethysmography for evaluation of cutaneous sensory nerve fiber function†. *Sensors Switz.* 21, 1272. doi:10.3390/s21041272

Marcinkevics, Z., Ilango, K., Balode, P., Rubins, U., and Grabovskis, A. (2020). The assessment of gingivitis using remote photoplethysmography, In Proceedings of the SPIE 11585. doi:10.1117/12.2581969

Marcinkevics, Z., Rubins, U., Aglinska, A., Caica, A., and Grabovskis, A. (2019). Remote photoplethysmography for skin perfusion monitoring using narrowband illumination. in Progress in Biomedical Optics and Imaging - Proceedings of SPIE. doi:10.1117/12.2527221

Marcinkevics, Z., Rubins, U., Caica, A., and Grabovskis, A. (2017). Evaluation of nitroglycerin effect on remote photoplethysmogram waveform acquired at green and near infra-red illumination. *SPIE Proc.* 10592, 18. doi:10.1117/12.2297385

Marcinkevics, Z., Rubins, U., Zaharans, J., Miscuks, A., Urtane, E., and Ozolina-Moll, L. (2016). Imaging photoplethysmography for clinical assessment of cutaneous microcirculation at two different depths. *J. Biomed. Opt.* 21, 35005. doi:10.1117/1.JBO.21.3.035005

McVeigh, G. E., Brennan, G. M., Johnston, G. D., McDermott, B. J., McGrath, L. T., Henry, W. R., et al. (1992). Impaired endothelium-dependent and independent vasodilation in patients with type 2 (non-insulin-dependent) diabetes mellitus. *Diabetologia* 35, 771–776. doi:10.1007/BF00429099

Merla, A., di Donato, L., Romani, G. L., Proietti, M., and Salsano, F. (2008). Comparison of thermal infrared and laser Doppler imaging in the assessment of cutaneous tissue perfusion in scleroderma patients and healthy controls. *Int. J. Immunopathol. Pharmacol.* 21, 679–686. doi:10.1177/039463200802100322

Meyer, M. F., Rose, C. J., Hülsmann, J. O., Schatz, H., and Pfohl, M. (2003). Impaired 0.1-Hz vasomotion assessed by laser Doppler anemometry as an early index of peripheral sympathetic neuropathy in diabetes. *Microvasc. Res.* 65, 88–95. doi:10.1016/S0026-2862(02)00015-8

Miles-Chan, J. L., Sarafian, D., Montani, J. P., Schutz, Y., and Dulloo, A. G. (2014). Sitting comfortably versus lying down: is there really a difference in energy expenditure? *Clin. Nutr.* 33, 175–178. doi:10.1016/J.CLNU.2013.11.009

Millet, C., Roustit, M., Blaise, S., and Cracowski, J. (2012). Aging is associated with a diminished axon reflex response to local heating on the gaiter skin area. *Microvasc. Res.* 84, 356–361. doi:10.1016/j.mvr.2012.06.009

Minson, C. T., Berry, L. T., and Joyner, M. J. (2001). Nitric oxide and neurally mediated regulation of skin blood flow during local heating. *J. Appl. Physiol.* 91, 1619–1626. doi:10.1152/jappl.2001.91.4.1619

Minson, C. T., Tew, G. A., Klonizakis, M., Moss, J., Ruddock, A. D., Saxton, J. M., et al. (2011). Thermal provocation to evaluate microvascular reactivity in human skin Mechanisms and Modulators of Temperature Regulation Thermal provocation to evaluate microvascular reactivity in human skin. *J. Appl. Physiol. (1985)*, 1239–1246. doi:10.1152/japplphysiol.00414.2010

Mizeva, I., Di Maria, C., Frick, P., Podtaev, S., and Allen, J. (2015). Quantifying the correlation between photoplethysmography and laser Doppler flowmetry microvascular low-frequency oscillations. *J. Biomed. Opt.* 20, 037007. doi:10.1117/1.JBO.20.3.037007

Moço, A. V., Stuijk, S., and de Haan, G. (2018). New insights into the origin of remote PPG signals in visible light and infrared. *Sci. Rep.* 8, 8501. doi:10.1038/s41598-018-26068-2

Namer, B., Pfeffer, S., Handwerker, H. O., Schmelz, M., and Bickel, A. (2013). Axon reflex flare and quantitative sudomotor axon reflex contribute in the diagnosis of small fiber neuropathy. *Muscle Nerve* 47, 357–363. doi:10.1002/mus.23543

Obayashi, K., and Ando, Y. (2014). Diagnosis of small-fiber neuropathy using various autonomic function tests. *Rinsho Shinkeigaku* 54, 1044–1046. doi:10.5692/CLINICALNEUROL.54.1044

Pires, S. M., Wyper, G. M. A., Wengler, A., Peñalvo, J. L., Haneef, R., Moran, D., et al. (2022). Burden of disease of COVID-19: strengthening the collaboration for national studies. *Front. public Heal* 10, 907012. doi:10.3389/FPUBH.2022.907012

Quattrini, C., Harris, N. D., Malik, R. A., and Tesfaye, S. (2007). Impaired skin microvascular reactivity in painful diabetic neuropathy. *Diabetes Care* 30, 655–659. doi:10.2337/DC06-2154

Rajan, V., Varghese, B., Van Leeuwen, T. G., and Steenbergen, W. (2009). Review of methodological developments in laser Doppler flowmetry. *Lasers Med. Sci.* 24, 269–283. doi:10.1007/S10103-007-0524-0

Rodrigues, L. M., Rocha, C., Ferreira, H., and Silva, H. (2019). Different lasers reveal different skin microcirculatory flowmotion - data from the wavelet transform analysis of human hindlimb perfusion. *Sci. Rep.* 9, 16951. doi:10.1038/s41598-019-53213-2

Rodríguez-Molinero, A., Narvaiza, L., Ruiz, J., and Gálvez-Barrõn, C. (2013). Normal respiratory rate and peripheral blood oxygen saturation in the elderly population. *J. Am. Geriatr. Soc.* 61, 2238–2240. doi:10.1111/JGS.12580

Rossi, M., Bertuglia, S., Varanini, M., Giusti, A., Santoro, G., and Carpi, A. (2005). Generalised wavelet analysis of cutaneous flowmotion during post-occlusive reactive hyperaemia in patients with peripheral arterial obstructive disease. *Biomed. Pharmacother.* 59, 233–239. doi:10.1016/J.BIOPHA.2004.01.008

Rossi, M., Carpi, A., Galetta, F., Franzoni, F., and Santoro, G. (2006). The investigation of skin blood flowmotion: a new approach to study the microcirculatory impairment in vascular diseases? *Biomed. Pharmacother.* 60, 437–442. doi:10.1016/j.biopha.2006.07.012

Rubins, U., Marcinkevics, Z., Muckle, R. A., Henkuzena, I., Roze, A., and Grabovskis, A. (2019). "Remote photoplethysmography for assessment of oral mucosa," in Progress in Biomedical Optics and Imaging - Proceedings of SPIE. doi:10.1117/12.2526979

Rubins, U., Miscuks, A., Rubenis, O., Erts, R., and Grabovskis, A. (2010). "The analysis of blood flow changes under local anesthetic input using non-contact technique," in 2010 3rd International Conference on Biomedical Engineering and Informatics (IEEE), 601–604. doi:10.1109/BMEI.2010.5640023

Ryals, S., Chiang, A., Schutte-Rodin, S., Chandrakantan, A., Verma, N., Holfinger, S., et al. (2023). Photoplethysmography—new applications for an old technology: a sleep technology review. *J. Clin. Sleep. Med.* 19, 189–195. doi:10.5664/JCSM.10300

Scott, K., Simmons, Z., and Kothari, M. J. (2003). A comparison of quantitative sensory testing with skin biopsy in small fiber neuropathy. *J. Clin. Neuromuscul. Dis.* 4, 129–132. doi:10.1097/00131402-200303000-00006

Sharma, S., Venkitaraman, R., Vas, P. R. J., and Rayman, G. (2015). Assessment of chemotherapy-induced peripheral neuropathy using the LDIFLARE technique: a novel technique to detect neural small fiber dysfunction. *Brain Behav.* 5, e00354. doi:10.1002/brb3.354

Shirazi, B. R., Valentine, R. J., and Lang, J. A. (2021). Reproducibility and normalization of reactive hyperemia using laser speckle contrast imaging. *PLoS One* 16, e0244795. doi:10.1371/JOURNAL.PONE.0244795

Slominski, A. T., Manna, P. R., and Tuckey, R. C. (2015). On the role of skin in the regulation of local and systemic steroidogenic activities. *Steroids* 103, 72–88. doi:10.1016/J.STEROIDS.2015.04.006

Söderström, T., Stefanovska, A., Veber, M., and Svensson, H. (2003). Involvement of sympathetic nerve activity in skin blood flow oscillations in humans. *Am. J. Physiol. Heart Circ. Physiol.* 284, H1638–H1646. doi:10.1152/ajpheart.00826.2000

Sun, P. C., Kuo, C. D., Chi, L. Y., Lin, H. Da, Wei, S. H., and Chen, C. S. (2013). Microcirculatory vasomotor changes are associated with severity of peripheral neuropathy in patients with type 2 diabetes. *Diabetes Vasc. Dis. Res.* 10, 270–276. doi:10.1177/1479164112465443

Sun, Y., and Thakor, N. (2016). Photoplethysmography revisited: from contact to noncontact, from point to imaging. *IEEE Trans. Biomed. Eng.* 63, 463–477. doi:10.1109/TBME.2015.2476337

Terkelsen, A. J., Karlsson, P., Lauria, G., Freeman, R., Finnerup, N. B., and Jensen, T. S. (2017). The diagnostic challenge of small fibre neuropathy: clinical presentations, evaluations, and causes. *Lancet. Neurol.* 16, 934–944. doi:10.1016/S1474-4422(17)30329-0

Tesfaye, S., Boulton, A. J. M., Dyck, P. J., Freeman, R., Horowitz, M., Kempler, P., et al. (2010). Diabetic neuropathies: update on definitions, diagnostic criteria, estimation of severity, and treatments. *Diabetes Care* 33, 2285–2293. doi:10.2337/DC10-1303

Trumpp, A., Schell, J., Malberg, H., and Zaunseder, S. (2016). Vasomotor assessment by camera-based photoplethysmography. *Curr. Dir. Biomed. Eng.* 2, 199–202. doi:10.1515/cdbme-2016-0045

Walters, E. T., and De C Williams, A. C. (2019). Evolution of mechanisms and behaviour important for pain. *Philos. Trans. R. Soc. Lond. B. Biol. Sci.* 374, 20190275. doi:10.1098/RSTB.2019.0275

Weidner, C., Schmidt, R., Schmelz, M., Torebjork, H. E., and Handwerker, H. O. (2003). Action potential conduction in the terminal arborisation of nociceptive C-fibre afferents. *J. Physiol.* 547, 931–940. doi:10.1113/jphysiol.2002.028712

Wong, B. J., and Fieger, S. M. (2010). Transient receptor potential vanilloid type-1 (TRPV-1) channels contribute to cutaneous thermal hyperaemia in humans. *J. Physiol.* 588, 4317–4326. doi:10.1113/JPHYSIOL.2010.195511

World Medical Association (2013). World medical association declaration of Helsinki: ethical principles for medical research involving human subjects. *JAMA* 310, 2191–2194. doi:10.1001/jama.2013.281053

Ysihai, R., Quattrini, C., Jeziorska, M., Malik, R. A., and Rayman, G. (2009). Abnormal LDIflare but normal quantitative sensory testing and dermal nerve fiber density in patients with painful diabetic neuropathy. *Diabetes Care* 32, 451–455. doi:10.2337/dc08-1453

Zijlstra, W. G., Buursma, A., and Meeuwsen-van der Roest, W. P. (1991). Absorption spectra of human fetal and adult oxyhemoglobin, de-oxyhemoglobin, carboxyhemoglobin, and methemoglobin. *Clin. Chem.* 37, 1633–1638. doi:10.1093/clinchem/37.9.1633

frontiers | Frontiers in Physiology

TYPE Original Research
PUBLISHED 31 August 2023
DOI 10.3389/fphys.2023.1187561

OPEN ACCESS

EDITED BY
John Allen,
Coventry University, United Kingdom

REVIEWED BY
Leonardo Bocchi,
University of Florence, Italy
Patrick Celka,
SATHeart SA, Switzerland
Jingyuan Hong,
King's College London, United Kingdom

*CORRESPONDENCE
Xiaoman Xing,
xingxm@sibet.ac.cn
Wen-Fei Dong,
wenfeidong@126.com

†These authors share first authorship

RECEIVED 16 March 2023
ACCEPTED 18 August 2023
PUBLISHED 31 August 2023

CITATION
Xing X, Huang R, Hao L, Jiang C and Dong W-F (2023), Temporal complexity in photoplethysmography and its influence on blood pressure.
Front. Physiol. 14:1187561.
doi: 10.3389/fphys.2023.1187561

Temporal complexity in photoplethysmography and its influence on blood pressure

Xiaoman Xing[1,2*†], Rui Huang[2,3†], Liling Hao[4], Chenyu Jiang[5] and Wen-Fei Dong[2,6*]

[1]School of Biomedical Engineering, Division of Life Sciences and Medicine, University of Science and Technology of China, Suzhou, China, [2]Suzhou Institute of Biomedical Engineering and Technology, Chinese Academy of Sciences, Suzhou, China, [3]Academy for Engineering and Technology, Fudan University, Shanghai, China, [4]College of Medicine and Biological Information Engineering, Northeastern University, Shenyang, China, [5]Jinan Guoke Medical Technology Development Co. Ltd., Jinan, China, [6]Suzhou GK Medtech Science and Technology Development (Group) Co. Ltd., Suzhou, China

Objective: The temporal complexity of photoplethysmography (PPG) provides valuable information about blood pressure (BP). In this study, we aim to interpret the stochastic PPG patterns with a model-based simulation, which may help optimize the BP estimation algorithms.

Methods: The classic four-element Windkessel model is adapted in this study to incorporate BP-dependent compliance profiles. Simulations are performed to generate PPG responses to pulse and continuous stimuli at various timescales, aiming to mimic sudden or gradual hemodynamic changes observed in real-life scenarios. To quantify the temporal complexity of PPG, we utilize the Higuchi fractal dimension (HFD) and autocorrelation function (ACF). These measures provide insights into the intricate temporal patterns exhibited by PPG. To validate the simulation results, continuous recordings of BP, PPG, and stroke volume from 40 healthy subjects were used.

Results: Pulse simulations showed that central vascular compliance variation during a cardiac cycle, peripheral resistance, and cardiac output (CO) collectively contributed to the time delay, amplitude overshoot, and phase shift of PPG responses. Continuous simulations showed that the PPG complexity could be generated by random stimuli, which were subsequently influenced by the autocorrelation patterns of the stimuli. Importantly, the relationship between complexity and hemodynamics as predicted by our model aligned well with the experimental analysis. HFD and ACF had significant contributions to BP, displaying stability even in the presence of high CO fluctuations. In contrast, morphological features exhibited reduced contribution in unstable hemodynamic conditions.

Conclusion: Temporal complexity patterns are essential to single-site PPG-based BP estimation. Understanding the physiological implications of these patterns can aid in the development of algorithms with clear interpretability and optimal structures.

KEYWORDS

photoplethysmography, blood pressure, single-site, Windkessel model, temporal patterns

1 Introduction

Blood pressure (BP) is one of the most important vital signs and is closely related to the prognosis of cardiovascular disease, which ranks first in all-cause mortality (Chobanian et al., 2003). Although the office blood pressure measurement (OBPM) is still the recommended diagnostic tool, ambulatory blood pressure monitoring (ABPM) can offer more details about BP fluctuation and help improve the diagnosis (Force et al., 2021). A lightweight and easy-to-use ambulatory BP monitor could help promote the long-term management of hypertension (Agarwal et al., 2011).

The use of photoplethysmography (PPG) for estimating BP has gained popularity in recent years due to its affordability and convenience (Martínez et al., 2018; Elgendi et al., 2019; Josep Solà and Josep Solà, 2019; Cosoli et al., 2020). However, several drawbacks prevented its widespread usage. The first problem is that current theoretical models may lead to unstable BP prediction in practice. The most well-known pulse transition time (PTT) methods assumed correlations between PTT and arterial compliance (C) (Mukkamala et al., 2015; Ding et al., 2016; Mukkamala and Hahn, 2018). But cardiac output (CO) and peripheral resistance (R) to blood flow also had considerable contributions to BP changes. Calibrations must be done frequently, and sudden failures may occur (Butlin et al., 2018; Finnegan et al., 2021; Avolio et al., 2022). Another theoretical proposal used the four-element Windkessel (WK4) model to estimate major lump hemodynamic properties (Wang et al., 2017; Xing et al., 2021), which could be used to stabilize the measurement. However, this model only used PPG morphological features, making it susceptible to environmental disturbances such as contact pressure, sensor placement, and temperature fluctuations (Hsiu et al., 2011; Hsiu et al., 2012; Grabovskis et al., 2013). Therefore, obtaining reliable BP estimations from PPG morphology alone, even after calibration, remains challenging (Xing et al., 2019; Hosanee et al., 2020). Another problem with single-site PPG-derived BP is associated with instability in ambulatory measurement. Most of the studies required the subjects to stay motionless in a supine or sitting position. The performance of BP estimation may deteriorate quickly in motion because PTT and PPG morphology are sensitive to noise and posture changes (Allen and Murray, 1999; Pour Ebrahim et al., 2019).

Although the "black-box" encoding in machine learning algorithms lacks clear interpretability, they have achieved remarkable performance in practice. Some were deployed in continuous BP measurement and showed improvement in both accuracy and stability (Radha et al., 2019; El-Hajj and Kyriacou, 2021; Yen et al., 2021). Most of them used time-dependent information, such as the long- and short-term memory (LSTM) network (Monte-Moreno, 2011; Radha et al., 2019; Harfiya et al., 2021; Li et al., 2021; Pu et al., 2021; Wang et al., 2021; Ali and Atef, 2022; Meng et al., 2022), system identification (Allen and Murray, 1999), auto-regression (Acciaroli, 2018), multi-stage feature extraction (Ali and Atef, 2022; Jiang et al., 2022), dynamic compliance (Gupta et al., 2022), or simple heart rate variability(HRV) (Mejía-Mejía et al., 2022). These algorithms performed better than those without dynamic features (Radha et al., 2019; Harfiya et al., 2021). In this study, we aim to give a plausible explanation of the system's temporal complexity. With this knowledge, optimizing the structure of the machine learning algorithms would be easier.

Physiological model-based PPG simulations may help decode this "black box". However, current PPG synthesis methods have limitations, with some being overly complicated (Charlton et al., 2019; Mazumder et al., 2022) and others overly simplistic (Tang et al., 2020a; Tang et al., 2020b). The complex physiological models often require human anatomical data and intricate coupling between vascular segments. While they serve as excellent approximations of real PPG signals and are valuable for disease diagnosis, studying rapid hemodynamic changes becomes challenging due to their high computational cost. On the other hand, simple PPG synthesis models combine forward and reflected waves, aiding in PPG event detection. However, these models lack essential hemodynamic details, such as compliance dependent on BP (Tang et al., 2020a). In this study, our aim is to develop a user-friendly simulation tool by modifying the classic four-element Windkessel model. By updating the simulation per heartbeat, we can generate stimuli with varying timescales and observe subsequent PPG responses. This approach enables the simulation of fast-changing CO, R, and compliance, allowing us to investigate unstable hemodynamic conditions. Through this simulation tool, we can gain insights into the stochastic behavior of PPG and evaluate their potential contribution to BP estimation.

This study introduces several key novelties and findings, including.

(1) A novel *in silico* simulation method is proposed to generate dynamic PPG signals with time- and BP-dependent compliance profiles.
(2) The variation of central vascular compliance (C_1) throughout a cardiac cycle, along with CO and R, collectively determine the time delay, amplitude overshoot, and phase lag of the PPG response to a pulse stimulus.
(3) Continuous simulations showed that complicated temporal PPG patterns could be generated by random stimuli, which means that the "passive" buildup of phase lags and amplitude fluctuations are related to hemodynamic fluctuations.
(4) The complexity of stimuli directly influences the complexity of the resulting signal.
(5) The addition of temporal complexity features increased the stability and accuracy of BP estimation, especially at high CO fluctuations.

The rest of this paper is organized as follows. Section 2 provides a detailed description of the modified four-element Windkessel model, pulse and continuous simulation procedures, experimental dataset, validation procedure, and complexity measures. Section 3 presented the simulation results and the complexity feature distribution, which were validated using multi-modal experimental data. The contribution of complexity and morphological features to BP estimation under stable and unstable cardiac conditions were calculated and compared. Section 4 discussed the physiological implication of these findings and the potential advantages of using complexity features in BP estimation. Section 5 concludes the paper.

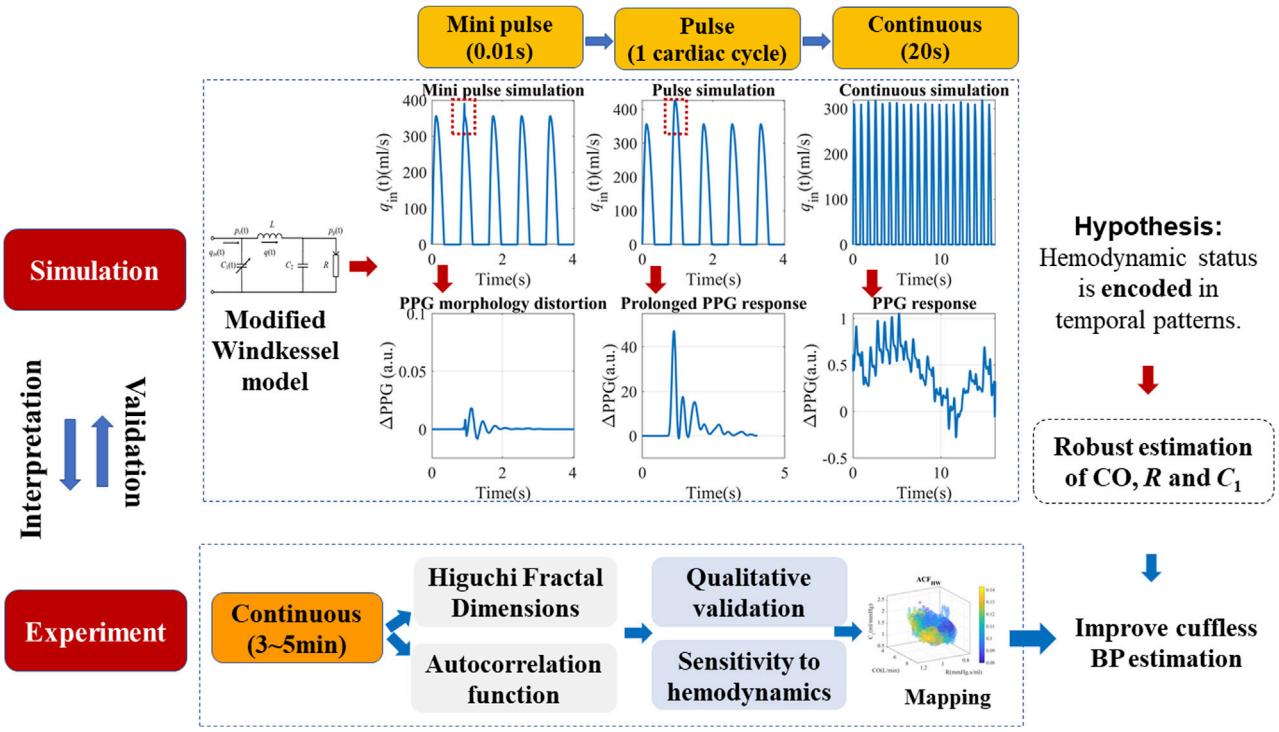

FIGURE 1
Schematics of the proposed simulation method, hypothesis, and experimental verifications. The modified Windkessel model is introduced in detail in Section 2.1, with a simplified assumption of the left ventricular ejection (q_{in}). Pulse and continuous simulations with different timescales were carried out to locate the origin of complexity patterns.

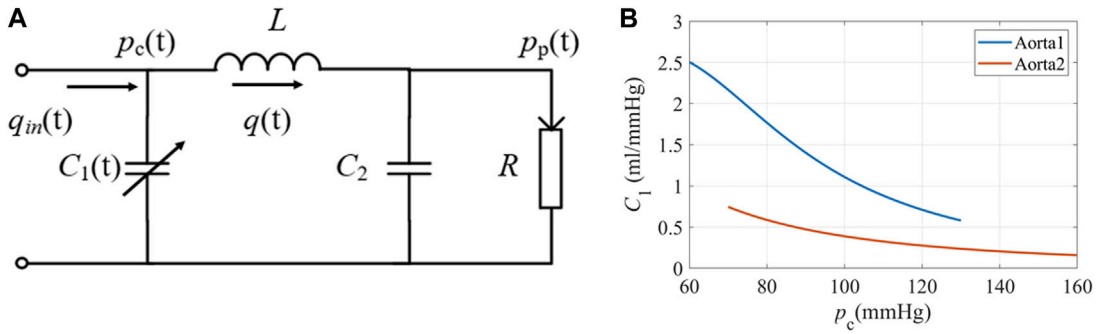

FIGURE 2
(A) The equivalent circuit of the modified WK4 model. $q(t)$ represents blood flow. C_1 is time-dependent and varies with central BP. **(B)** The elastic property of the aorta under different pressures (Langewouters et al., 1984). Aorta1: Am = 3.5 cm^2, P0 = 50.4 mmHg, P1 = 42.3 mmHg; Aorta2: Am = 6.18 cm^2, P0 = −2.3 mmHg, P1 = 21.6 mmHg.

2 Materials and methods

This section mainly describes the *in silico* simulation and experimental verification procedures, as illustrated in Figure 1. For simulation, a modified WK4 model with BP-dependent compliance was introduced. PPG responses to both pulse and continuous stimuli at various timescales were simulated and quantified. Temporal complexity and correlation measures such as HFD and ACF are proposed to describe the PPG responses. Their contribution to BP was calculated and compared to morphological features. Multi-modal continuous experimental recordings were used to verify the simulation results.

2.1 The modified WK4 model with time- and BP-dependent compliance

To get a rough idea of the PPG response to stimuli, we did a series of simulations using a modified WK4 model with time- and BP-dependent compliance, as shown in Figure 2A. In this model, the

heart is represented as a current source q_{in}. The arterial tree system is modeled by four major parameters. Unlike traditional WK4 models (Wang et al., 2017), C_1 is designed to vary within a cardiac cycle, which depends on central BP (p_c), as shown in Figure 2B. R reflects the peripheral resistance, which mainly comes from small arteries, arterioles, and capillaries. BP changes induce corresponding arteriolar resistance changes to keep capillary pressure constant and maintain tissue fluid equilibrium (Nicolaas Westerhof and Noble, 2010). Although R also varies during a cardiac cycle, the overall fluctuation is smaller during a heartbeat. Thus, R is treated as a constant or slowly changing parameter. To reduce the complexity of the model, compliance of the distal arteries (C_2), and inertance (L) are set to be time-invariant, which are added to increase the PPG waveform fitting accuracy (Westerhof et al., 2009). The blood pressure at the peripheral site (p_p) could be obtained if the cardiovascular and hemodynamic parameters are known. Since the amplitude of PPG depends on the tissue substrate, microvasculature, and the coupling coefficient of the sensor and skin, personalized transfer functions were considered to convert BP to PPG (Millasseau et al., 2000).

In the time-dependent WK4 model, $C_1(t)$, $p_c(t)$, and $p_p(t)$ are strongly interdependent, as shown in equations (1a)–(1c).

$$\begin{cases} \dfrac{dq(t)}{dt} = \dfrac{1}{L}\left(p_c(t) - p_p(t)\right) \cdots\cdots\cdots (1a) \\ \dfrac{dp_c(t)}{dt} = \dfrac{1}{C_1(t)}\left(q_{in}(t) - q(t)\right) \cdots\cdots\cdots (1b) \\ \dfrac{dp_p(t)}{dt} = \dfrac{1}{C_2}\left(q(t) - \dfrac{p_p(t)}{R}\right) \cdots\cdots\cdots (1c) \end{cases} \quad (1)$$

In this study, $q_{in}(t)$ is assumed to have the flow profile described by Equation (2), where q_0 is the maximum $q_{in}(t)$. T_s is the left ventricle ejection duration and T is the cardiac cycle; α determines the peak time of $q_{in}(t)$, which is set as 1/3. Note that it is a simplified approximation used to facilitate the simulation. For a more realistic simulation, $q_{in}(t)$ could be replaced by a numeric array obtained by *in-vivo* experiments. q_0 is closely related to stroke volume (SV) and CO, as the integral of $q_{in}(t)$ within a cardiac cycle gives SV. Multiplied by heart rate and we can obtain CO.

$$q_{in}(t) = \begin{cases} q_0 \sin\left(\dfrac{\pi t}{2\alpha T_s}\right) & (0 \le t \le \alpha T_s) \\ q_0 \cos\left(\dfrac{\pi t}{4\alpha T_s}(t - \alpha T_s)\right) & (\alpha T < t \le T_s) \\ 0 & (T_s < t \le T) \end{cases} \quad (2)$$

$C_1(t)$ oscillates in a wide range for subjects with elastic blood vessels (Hallock and Benson, 1937). Langewouters *et al.* proposed a model to describe the cross-sectional compliance of the aorta, which used three independent parameters (Langewouters et al., 1984). In this study, we used volume compliance. $C_1(t)$ is modified by adding a unit length l, as shown in Equation 3.

$$C_1(t) = \frac{A_m l}{\pi P_1\left[1 + \left((p_c(t) - P_0)/P_1\right)^2\right]} \quad (3)$$

A_m is the maximum cross-sectional area of the aorta, and P_0 is the transmural pressure when compliance reached its maximum. P_1 represents the steepness of the compliance rise. We chose two representative sets of values from the published dataset and illustrated the compliance-pressure relationship in Figure 2B.

Our ultimate goal is to estimate $p_p(t)$ and generate corresponding PPG signals. By analyzing Eqs. 1–3, we found that they could be combined to yield a differential equation with only one unknown variable. The procedure is as follows:

(1) Combine Eqs 1a–1c and eliminate $p_c(t)$ and $q(t)$. The resulting equation has only two unknown variables $C_1(t)$ and $p_p(t)$, as shown in Equation (4). All the other parameters were assumed to be known.

$$\frac{d^3p_p(t)}{dt^3} + \frac{1}{RC_2}\frac{d^2p_p(t)}{dt^2} + \left(\frac{1}{LC_1(t)} + \frac{1}{LC_2}\right)\frac{dp_p(t)}{dt} + \frac{1}{LRC_1(t)C_2}p_p(t) = \frac{1}{LC_1(t)C_2}q_{in}(t) \quad (4)$$

(2) Combining Equations (1a), (1c), we could obtain Equation (5) by eliminating $q(t)$. Then $C_1(t)$ in Equation (3) becomes an expression that depends solely on variable $p_p(t)$, as shown in Equation (6).

$$p_c(t) = \left(\frac{d^2p_p(t)}{dt^2} + \frac{1}{C_2R} \times \frac{dp_p(t)}{dt}\right)C_2L + p_p(t) \quad (5)$$

$$C_1(t) = \frac{A_m l}{\pi P_1\left[1 + \left(\dfrac{\left[\left(\frac{d^2p_p(t)}{dt^2} + \frac{1}{C_2R} \times \frac{dp_p(t)}{dt}\right)C_2L + p_p(t) - P_0\right]}{P_1}\right)^2\right]} \quad (6)$$

(3) By replacing $C_1(t)$ in Equation (4) with the expression in Equation (6), the resulting differential equation has only one unknown variable $p_p(t)$, which could be solved with the Runge-Kutta (4,5) formula (ODE45) in Matlab 2021b.

(4) When $p_p(t)$ is obtained, PPG could be subsequently calculated by using the *P-V* relationship (Millasseau et al., 2000). For this study, we conducted simulations with a time resolution of 0.01 s. Although a higher resolution could potentially handle more complex $q_{in}(t)$ profiles, a step size of 0.01 s is sufficient given that we primarily employed an analytical description of $q_{in}(t)$.

Although the modified WK4 model provided realistic PPG waveforms, caution should be taken to interpret the simulation results. Firstly, the original WK4 model was proposed to explain the formation of peripheral BP waveforms at different frequencies (Nicolaas Westerhof and Noble, 2010). The hemodynamic parameters must be constant to yield a reasonable impedance explanation. In this study, we let the compliance be time-dependent, which is physiologically sound, but the simulation results should not be used to modify the characteristic impedance. Secondly, the simulated PPG waveforms may deviate from *in-vivo* measurements due to the oversimplified $q_{in}(t)$ and cardiovascular system. This modified time-dependent WK4 model is used to qualitatively explore the stochastic patterns of PPG, which must be verified using experimental data. Thirdly, WK4 is an open-loop model, which assumes that $q_{in}(t)$ is known and does not depend on cardiovascular feedback. For a more realistic model, the influence on $q_{in}(t)$ should be considered to form a more complex closed-loop model. As a result, the change in blood flow can have much longer impact than an open-loop model.

TABLE 1 Subjects' demographics.

Number of subjects	Age (years)	Height (cm)	Weight (kg)	BMI (kg/m^2)	Sex (M/F)	SBP (mmHg)	DBP (mmHg)
40	34 ± 15	171 ± 11	76 ± 18	26 ± 5.7	17/23	120 ± 14	69 ± 13

*SBP: systolic BP; DBP: diastolic BP.

Considering the complexity of the topic, we have chosen to commence our study with simpler models before gradually advancing to more intricate and realistic ones. By initially employing an open-loop model, we were able to establish a preliminary dynamic relationship between PPG and BP. This approach not only facilitates easier comprehension but also enhances safety during the research process.

To sum up, the *in silico* simulation provided guidance, while experimental data must be used to refine the details.

2.2 Experimental data

To generate realistic simulation data, we used some of the experimentally measured data as the model input. For example, we used 45 different C_1 profiles from Langewouters *et al* (Langewouters et al., 1984). Multi-modal continuous vital recordings are from a publicly available database by Charles Carlson et al. (Carlson et al., 2020), which consists of short PPG-BP measurements from 40 healthy subjects. The original study involving human participants was reviewed and approved by the Kansas State University Institutional Review Board (protocol number 9386, approved 5 July 2019). Informed consent was obtained from all subjects involved in the study. The more popular Medical Information Mart for Intensive Care (MIMIC) database is not used due to its lack of PPG amplitude information (Johnson et al., 2016).

The subjects took a supine position and each measurement lasted for around 5 min. Finger PPG was acquired using a GE patient monitor (Datex CardioCap 5). Continuous brachial BP waveforms and stroke volume (SV) were derived from Finometer PRO (Finapres Medical Systems). The raw data were resampled to 100 Hz and lowpass filtered with a cut-off frequency of 10 Hz. For temporal pattern calculation, data with sufficient length is required. We used a window of 20 s and moved one cardiac cycle each time to increase the sample size. A total of 17,476 measurements were obtained from 40 subjects. The subjects' demographics are listed in Table 1.

The hemodynamic status of each measurement is estimated to help understand the underlying physiological mechanism. N Stergiopulos *et al.* found that C_1 and R could be accurately estimated by the Windkessel model (Stergiopulos et al., 1994; Nicolaas Westerhof and Noble, 2010). In this study, we used a similar approach to estimate C_1 and R (Xing et al., 2021), except that C_1 had to be chosen from the 45 published profiles, as in Equation (3) (Langewouters et al., 1984). We performed individual test on each subject and each C_1 profile using the time-dependent Windkessel models, taking into account the variability of BP within the cardiac cycle. For each pair, we adjusted R, L, and C_2 to minimize the discrepancy between the simulated and measured BP waveforms. On a per-subject basis, the C_1 profile that exhibited the best match (as indicated by the lowest root mean square error, RMSE) to the measured BP waveform was selected. Alternative approaches were used to ensure the validity of hemodynamic estimation. For example, R is also estimated by calculating the ratio of the mean arterial pressure (MAP) and CO (Nicolaas Westerhof and Noble, 2010). C_1 is also estimated by calculating the ratio of the peak-to-peak PPG amplitude and the pulse pressure (PP) of BP (Allen and Murray, 1999). We found that the Windkessel model derived C_1 and R linearly correlated with the alternative methods in this dataset. If different models yielded considerably different estimations, we discard the corresponding samples.

2.3 Pulse stimuli and the corresponding PPG responses

Real hemodynamic stimuli are complicated, as shown in Figures 3A,E. However, they could be decomposed into continuous pulse simulations with different timescales, which may help to understand the physiological mechanism. We designed pulse *in silico* simulations with long and short durations to investigate the corresponding PPG responses, as shown in Figures 3B,F. Firstly, a simulation with a 20% q_0 increase that lasted a single cardiac cycle was built, hereby referred to as SV stimuli. It is the easiest to model, understand and quantify. Then very short stimuli with a 10% increase of $q_{in}(t)$ that lasted for 0.01s was simulated, hereby referred to as "mini" stimuli.

For the *in silico* SV stimuli simulation, cardiovascular systems with different C_1 and R were used. Two indices were proposed to describe the recovery time from a single stimulus, as shown in Figure 3C. Half width (HW) is defined as the width at 50% of the peak response, which measures the recovery time for a single stimulus. Longer HW may lead to overlaps of responses and complex signal fractal structures. The height of the overshoot (OS) is associated with the maximum magnitude of BP or PPG fluctuations. The PPG distortions are defined as the difference between PPG signals with and without stimuli, as illustrated in Figures 3D,H. "Mini" stimuli caused similar but much smaller amplitude responses (~10^{-3} of the response from SV stimuli), which were more pronounced in the derivatives of the PPG signal.

To gain a thorough understanding of the time-dependent PPG responses to stimuli, we used all the 45 C_1 profiles from the published dataset (Langewouters et al., 1984) and varied the peripheral resistance from 0.7 to 1.3 mmHg s/ml, with a step size of 0.2 mmHg s/ml. Three CO levels were tested at 4.25L/min, 5.1 L/min, and 5.95 L/min. Simulations with SBP higher than 220 mmHg or lower than 80 mmHg were discarded, since these out-of-range SBPs did not match our experimental data and may potentially deviate from the simplified model.

The result from SV stimuli simulations could be extrapolated to more complicated situations. For example, q_{in} contour irregularity

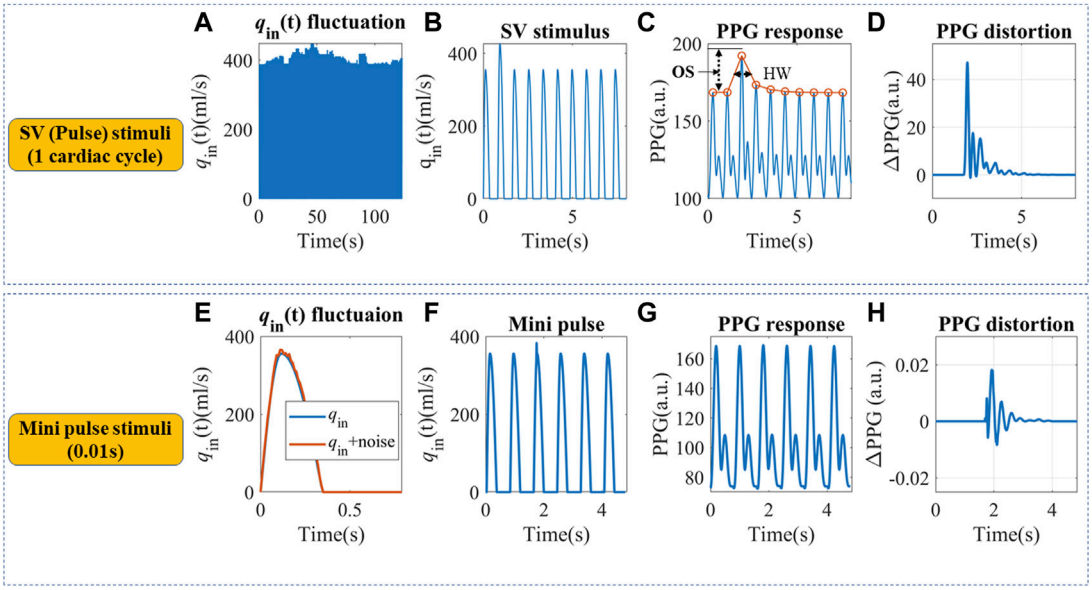

FIGURE 3
(A) Continuous q_{in} fluctuation with SV variation. **(B)** Definition of an SV pulse stimulus that lasted a cardiac cycle. **(C)** The simulated PPG response and definition of half width (HW) and overshoot (OS). Simulation parameters were set as follows: A_m = 3.5 cm^2, P_0 = 50.4 mmHg, P_1 = 42.3 mmHg, T = 0.8 s, α = 1/3, T_s = 0.35 s, CO = 5.95 L/min, C_2 = 0.1 mL/mmHg, R = 1.4 mmHg s/ml, L = 0.03 mmHg s^2/ml. **(D)** The SV pulse-induced PPG changes. **(E)** q_{in} fluctuation within a cardiac cycle. **(F)** Definition of a "mini" pulse stimulus that lasted for 0.01 s. **(G)** The simulated PPG response to a "mini" pulse. **(H)** The "mini" pulse induced PPG changes.

could also be decomposed into an infinite number of "mini" stimuli (Nicolaas Westerhof and Noble, 2010), similar to Figures 3E,F. These "mini" stimuli mainly influence the C_1 trajectory during a cardiac cycle and lead to small phase shifts, as in Figures 3G,H. We assumed PPG responses to "mini" stimuli were similar to SV stimuli, but at a smaller scale.

2.4 Continuous stimulation and experimental validation

2.4.1 Continuous stimulation: Random stimuli

In a real-life application, the cardiovascular system constantly adjusts CO, heart rate (HR), C_1, R, and q_{in} contour depending on the metabolic need and hemodynamic feedback from the entire body. In addition, autocorrelation patterns can also be observed in the fluctuations of SV and R, as depicted in Supplementary Figures S1, S2, which may lead to longer cardiovascular responses. The accumulated PPG responses may form long- and short-term temporal patterns. For simplicity, we chose CO and R perturbation to study longer-term complexities, and assumed q_{in}-caused short-term complexities have similar behavior. To isolate the origin of complexity, random stimuli were used. Peripheral BP signals (p_p(t)) were generated by the modified WK4 model, and PPG is translated from BP by personalized pressure-volume translations. Each simulation contained 20 cardiac cycles.

To build a more realistic simulation, the hemodynamic status of the 40 healthy subjects was estimated and used as simulation inputs. The mean CO and R of each subject were used as baselines, and random perturbations were added. We used a white noise randomly chosen from −5% to 5% of the baseline, with a mean of 0 and standard deviation of 2.83%. To increase sample sizes, CO and R baselines were also shifted by ±10%. An example simulation is shown in Figure 4. This test is to investigate the possibility of forming complexity patterns just from "passive" hemodynamic responses.

In real-life scenarios, stimuli like SV and R may exhibit autocorrelation owing to cardiovascular auto-regulation, as demonstrated in Supplementary Figures S1, S2. The experimental BP and PPG complexity measures exhibit combined impact of the stimuli and vascular response.

2.4.2 Experimental validation: Distribution map and contribution evaluation

For experimental validation, complexity measures such as HFD and ACF were calculated for each 20s sampling window, and their correlation with hemodynamic status is used to investigate the agreement between model prediction and experimental data. For practical usage, three-dimensional maps of complexity measures and their gradients were generated for experimental data.

Furthermore, to assess the influence of temporal patterns to BP under stable and unstable cardiac conditions, we calculated the Pearson correlation coefficient (PCC) of each temporal feature and BP. Additionally, we employed Bayesian neural network to evaluate their collective nonlinear contributions, as explained in Section 2.7. Comparisons were made with commonly-used single-site morphological features, as defined in Table 2 and documented in Supplementary Figure S3 (Elgendi, 2012). Biometric input was not permitted to prevent information leakage. In order to maintain consistency with temporal features, we performed a median averaging of the morphological features, resulting in one reading

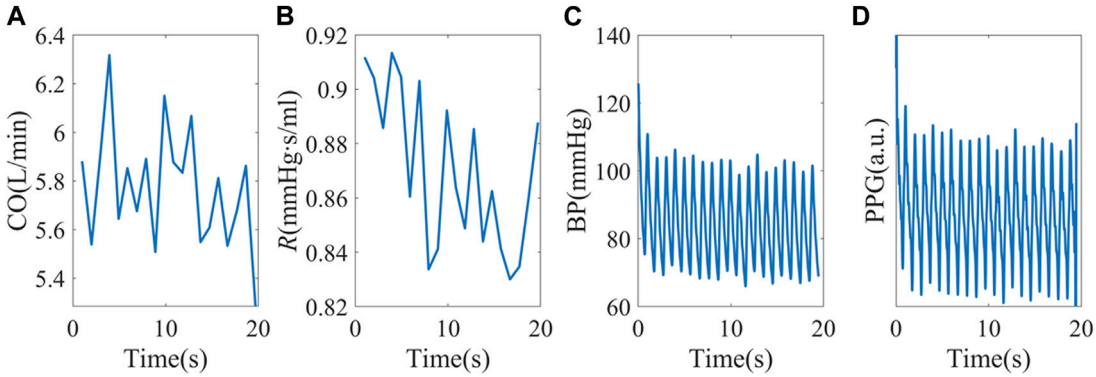

FIGURE 4
(A, B) Random CO and *R* stimuli using baseline hemodynamic status from subject X1047. **(C)** Simulated peripheral BP. **(D)** PPG signals were obtained from personalized *P-V* translations.

TABLE 2 Definition of selected morphological features.

Features	Definition
AC	The pulsating amplitude of PPG
DC	Mean of PPG baseline
Area	The area under the normalized PPG waveform
Notch index (NI)	Notch index. The waveform value at the dicrotic notch over the systolic peak
SPMEAN	Mean upstroke slope during the systolic period
SPVAR	Variation of upstroke slope (standard deviation) during the systolic period
DPMEAN	Mean downstroke slope during the diastolic period
DPVAR	Variation of downstroke slope (standard deviation) during the diastolic period

per 20-s epoch. This approach enables us to simultaneously evaluate the contributions from both morphological and temporal features. By considering these aspects together, we gain a comprehensive understanding of the characteristics under analysis.

2.5 Complexity measures

We also introduced two main categories of parameters to describe the dynamic patterns: autocorrelation and fractal dimension. Autocorrelation Function (ACF) measures the correlation between data points in a time series and their preceding data points (Box et al., 2015; Tunnicliffe Wilson et al., 2015). It provides insights into the translation invariance of the signal across different delay times (τ). A commonly used measure derived from the ACF is known as ACF_{HW}, representing the time when the ACF reaches 0.5, as depicted in Figure 5A.

Fractal dimension analysis is highly sensitive in uncovering hidden information within physiological time series (Higuchi, 1988; Kesić and Spasić, 2016a; Rubega et al., 2020). Most fractal measures require a long recording time of the signals (~hours), which may not be suitable for BP estimation (Baumert et al., 2005). Since BP fluctuations occur on a shorter timescale (minutes), HFD proves to be a favorable choice for capturing the complexity and dynamic patterns in the data.

In this study, we used the HFD of PPG waveforms (HFD_{wave}), baseline (HFD_{DC}), and pulsatile amplitude (HFD_{AC}) to measure complexity at different timescales. PPG signals could be simplified as time sequences $x(1)$, $x(2)$,. . ., $x(N)$. x is sampled at 100 Hz for HFD_{wave}, as a short-timescale fractal measure proposed by Cymberknop *et al.* (Cymberknop et al., 2011). HFD_{DC} and HFD_{AC} are calculated when x is sampled per cardiac cycle, representing longer timescale complexity (Colovini et al., 2019). From the starting time, a new self-similar time series is used to calculate curve length $L_m(k)$, as in Equation 7. N is the length of the original time series x, m is the initial time and k is the time interval. $int[\frac{N-m}{k}]$ is the integer part of the real number $\frac{N-m}{k}$. In this study, k_{max} is set to 5.

$$L_m(k) = \frac{1}{k}\left[\left(\sum_{i=1}^{int\left[\frac{N-m}{k}\right]} |x(m+ik) - x(m+(i-1)k)|\right)\frac{N-1}{int\left[\frac{N-m}{k}\right]k}\right]; k = 1, 2, \ldots, k_{max} \quad (7)$$

$L_m(k)$ is averaged for all m. The mean value of the curve length $L(k)$ is defined as

$$L(k) = \frac{1}{k}\sum_{m=1}^{k} L_m(k) \quad (8)$$

The $\ln(L(k))$ and $\ln(1/k)$ relationship for DC and AC is sometimes nonlinear, as shown in Figures 5B,C. The fitting parameters contain rich information about hemodynamics. To describe the relationship between $\ln(L)$ and $\ln(1/k)$, a cubic fitting is employed, resulting in the following expression: $\ln(L) = a_0 + a_1\ln(1/k) + a_2\ln(1/k)^2 + a_3\ln(1/k)^3$. Notably, the higher-order fitting coefficients ($a_{1\text{-}3}$) demonstrated fractal property of the "active" stimuli at longer timescales, as demonstrated in Supplementary Figure S4. In this study, our focus is on examining the accumulation of "passive" responses, resulting in the usage of the intercept(a_0) as HFD_{AC} or HFD_{DC}. It is important to note that a_0 is more closely related to stochastic signal fluctuation, while a_1

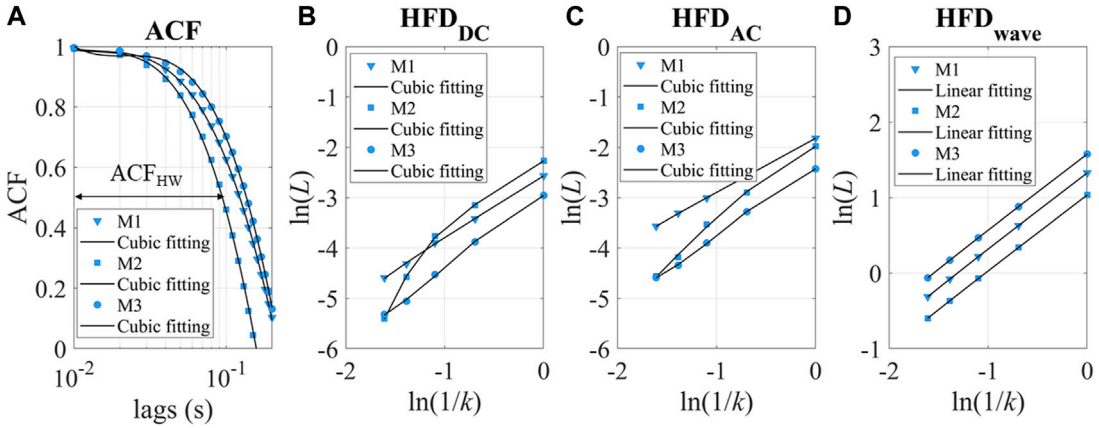

FIGURE 5
(A) ACF of three experimental measurements as examples. M1-3 refers to measurements 1–3. ACF$_{HW}$ refers to the time lag taken to reach 0.5. **(B, C)** ln(L) *versus* ln(1/k). The intercept of the cubic fitting is used for HFD$_{DC}$ and HFD$_{AC}$ calculation. **(D)** ln(L) *versus* ln(1/k) for HFD$_{wave}$ calculation.

represents the traditional definition of fractal dimensions. Conversely, we found that the linear slope of HFD$_{wave}$ had enhanced robustness and correlated with the individual's hemodynamic status. Therefore, the linear slope (a_1) is used as the HFD$_{wave}$ in our study.

2.6 Robustness of temporal patterns and their sensitivity to BP

Typically, fractal dimensions are calculated using longer signals (Baumert et al., 2005; Kesić and Spasić, 2016b). In our study, we chose 20 s to be the window size. It is necessary to evaluate the uncertainty of complexity measure calculation in this specific application. To address this, we undertook two approaches.

Firstly, we simulated a change in the coupling between the sensor and skin by multiplying the experimental PPG amplitudes by factors of 120% and 80%, respectively. We then recorded and analyzed the resulting variations in complexity measures. This evaluation allowed us to assess the sensitivity of the chosen measures to changes in the skin-sensor coupling coefficient.

Secondly, we estimated the error in slope(a_1) and intercept(a_0) estimation caused by cubic fitting of ln(L) *versus* ln(1/k) using experimental data. The errors were calculated by using variance-covariance matrix for the fitted coefficients (Seber, 1989). This analysis provided us with insights into the potential estimation errors caused by the fitting process.

As the goal of our study is to estimate the contribution of temporal patterns to blood pressure (BP) estimation, we evaluated their sensitivity to BP using the partial derivative $\partial f/\partial h$. Here, f represents the chosen complexity measure, and h can be underlying hemodynamic parameters such as SV, R and C_1. Measurements were divided into low and high CO variations according to their beat-to-beat CO fluctuations (|∂CO/∂t|). The threshold is set to be the median of the CO variations.

2.7 Enhancing BP estimation performance with temporal features

To evaluate the impact of temporal complexities on BP, we constructed a straightforward Bayesian neural network(BNN) (Kesić and Spasić, 2016b). Morphological and temporal features, including HRV, were tested as standalone features and feature combinations. The resulting BNN performance may help understand the non-linear side of the relative contribution.

The BNN consisted of a single layer with 15 neurons. To address any imbalances in the input data and improve overall BP estimation performance, we utilized the EasyEnsemble technique (Liu, 2009). This technique effectively balances the data, leading to improved estimation accuracy. To ensure robust testing and training, we implemented a leave-one-subject-out procedure, allowing us to separate the training and testing data. In terms of the testing data, they were fitted and then calibrated using the first 10 data points. We assessed the MAP and PP under high and low CO fluctuation situations. Median absolute errors (MAE) and Pearson's correlation coefficient (r) are used as indicators of accuracy and correlation. These evaluation measures provide valuable insights into the effectiveness of the BP estimation algorithm and its ability to accurately predict BP values.

Please be noted that this neural network structure or feature combination may not be the optimal for real-life deployment. The purpose is to showcase the added value of temporal features.

3 Results

This section presents the analysis of the *in silico* simulation results, which were further examined and verified using experimental data. The distributions of HFD and ACF are visualized, allowing for a thorough estimation of their respective contributions to BP. Additionally, comparisons with morphological

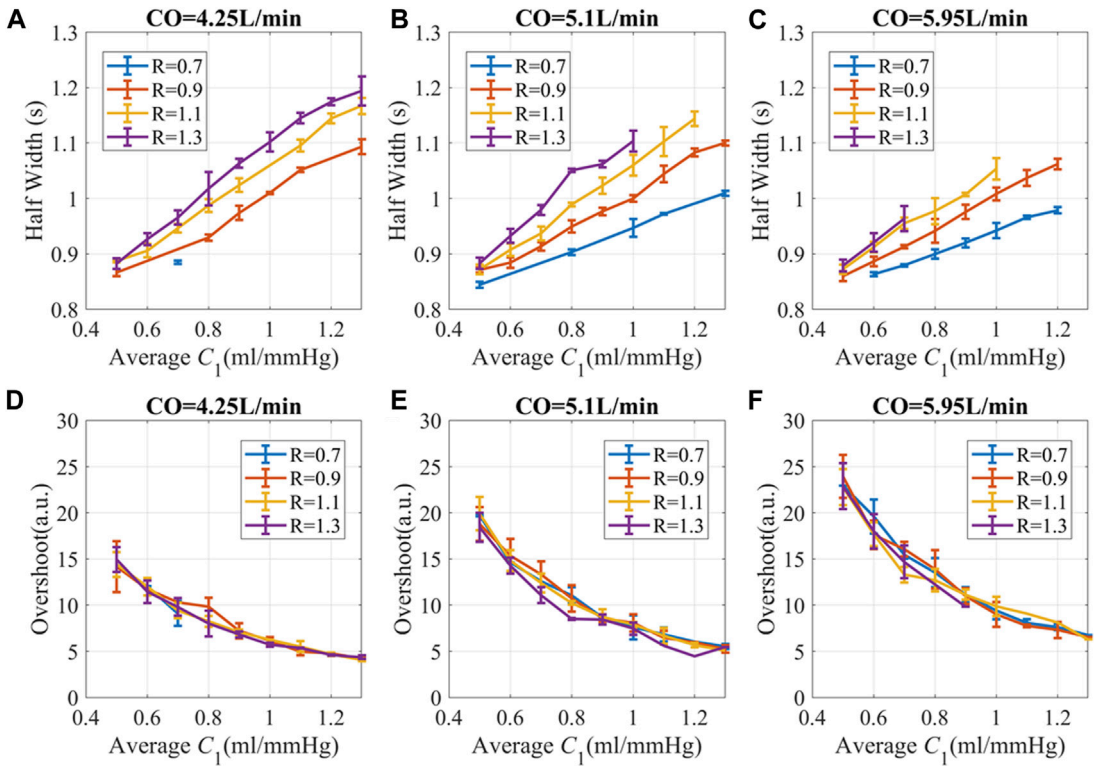

FIGURE 6
PPG recovery parameters *versus* hemodynamic status at different CO. **(A–C)** Half width (HW) of PPG response **(D–F)** Overshoot of PPG amplitude. The unit for *R* is "mmHg.s/ml". The simulation data is presented as "mean ± SD" to accommodate the variations attributed to different C_2 and *L*. Here, SD refers to the standard deviation of the data in each bin.

features under both stable and unstable cardiac conditions were conducted to provide further insights.

3.1 Pulse simulation

Since C_1(t) changes rapidly during a cardiac cycle, to simplify the illustration, C_1(t) is averaged and binned to suppress C_1-profile-related fluctuations. To ensure a consistent comparison of amplitudes, a generalized transfer function was used to convert BP to PPG (Millasseau et al., 2000). We found that at a given peripheral resistance, PPG with higher C_1 had a longer HW or slower recovery time after perturbation, as shown in Figures 6A–C. Lower peripheral resistance reduces the recovery time and narrows the HW differences for different C_1. Smaller CO leads to longer recovery time and lower overshoot, which is probably due to lower BP and hysteresis. Generally speaking, subjects with stiffer blood vessels, lower peripheral resistance, and high CO had a more instantaneous response to stimuli. Subjects with very elastic blood vessels, high peripheral resistance, or low CO have prolonged responses, which may lead to complex overlap patterns.

The overshoot of PPG caused by the pulse stimulus is higher for subjects with lower C_1 and high CO, as shown in Figures 6D–F. Since C_1 becomes smaller with age (Brandfonbrener et al., 1955; Van Bortel and Spek, 1998), older subjects with hypertension are more likely to have high fluctuation of BP during the day, which is consistent with previous publications (Chobanian et al., 2003; Force et al., 2021; Guirguis-Blake et al., 2021).

Similar patterns exist for "mini" pulse simulations, except that PPG responses are much smaller. Pulse simulation with other hemodynamic conditions might be extrapolated from existing results. Another notable point is that all the possible hemodynamic combinations were used as long as the resulting BP is in the desired range. Experimental data showed overall higher C_1 since the participants were young and healthy.

3.2 Continuous simulation

Continuous simulation showed that temporal patterns could be generated by random stimuli, as in Figures 7A–D. Experimental results are similar but not the same as the simulation prediction, due to the autocorrelation patterns of stimuli, perturbation strength, and noise.

We used HFD_{DC} and ACF_{HW} to demonstrate the PPG temporal responses to continuous stimuli. HFD_{DC} showed a significantly positive correlation with *R*. Steiger's z-test showed no statistical difference between the HFD_{DC}-*R* slopes of the simulation and experiments. Experimental data had overall more negative $\partial HFD_{DC}/\partial CO$ slope compared to the simulation, but the slope is not smooth with locally positive gradients in the 6–8L/min subregion. The correlation between HFD_{DC} and C_1 is non-significant in both simulation and experimental data.

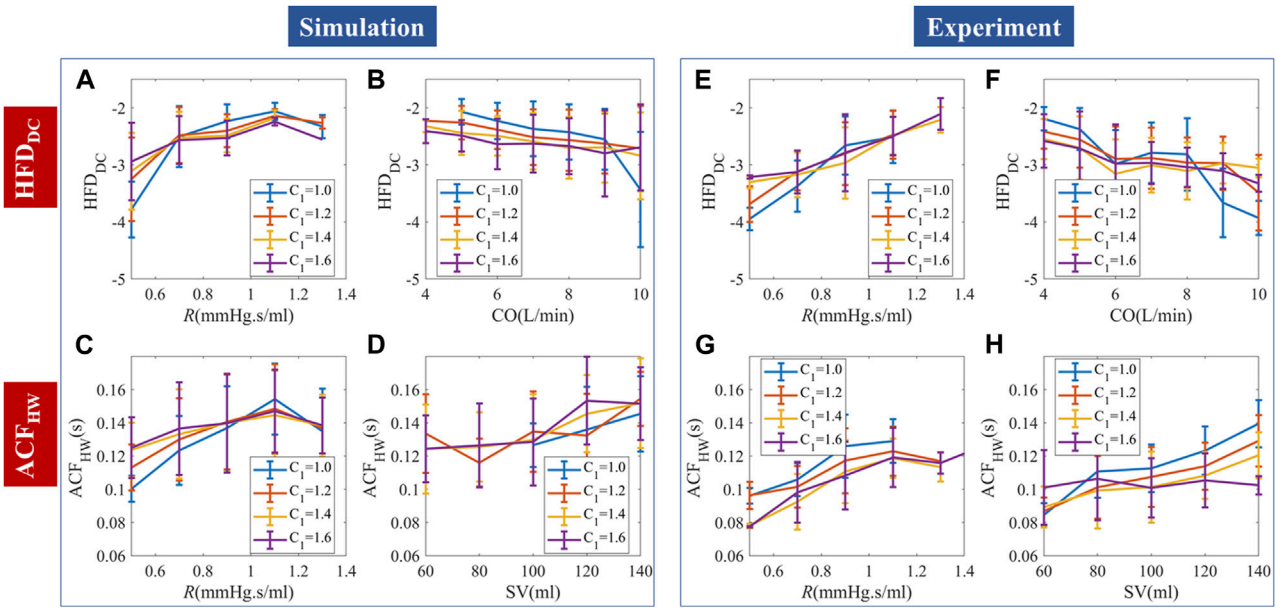

FIGURE 7
Comparison of continuous PPG simulation and experimental results. **(A–D)** Random stimuli caused complexities and their dependence on hemodynamic status. **(E–H)** Measured complexities and their dependence on hemodynamic status. The simulation and experimental data are binned and presented as "mean ± SD".

For random stimuli, ACF_{HW} significantly and positively correlated with R and SV. Experimental data had significantly more positive $\partial ACF_{HW}/\partial R$ and $\partial ACF_{HW}/\partial SV$ slopes. We used SV instead of CO, because the correlation between ACF_{HW} and CO is positive but much weaker. Since the timescale of ACF_{HW} is small (~0.1s), the inherent ACF dynamics likely correlate more with SV than CO. The correlation between ACF_{HW} and C_1 changed with R in simulation, while experimental data showed a consistent negative correlation with C_1. The difference is probably caused by q_{in}-irregularity-induced phase lags. The minimum experimental ACF_{HW} (~0.08s) is lower than the simulated ACF_{HW} (~0.1s), probably due to the deviation from WK4 models caused by structural heterogeneity. The comparative analysis of the average slopes between temporal features and hemodynamics can be found in Supplementary Table S1. To enhance the quality of regression, a robust fitting approach was employed.

The relationship between HFD_{AC}, HFD_{wave}, and hemodynamics is shown in Supplementary Figure S5. For both simulation and experimental data, HFD_{AC} negatively correlated with R and positively correlated with CO. Experimental analysis showed similar trends with weaker C_1 reliance. Experimental HFD_{wave} showed stratified but mixed correlations with C_1. The correlation between HFD_{wave} and CO or R is also nonlinear, while simulations with random stimuli per heartbeat showed no corresponding trends. This result agreed with our hypothesis that HFD at a much shorter timescale (~0.01s) may be caused by q_{in} irregularity and buildup of "mini" stimuli. Due to the high computational cost of adding random q_{in} irregularity and the difficulty of obtaining clinical q_{in} measurements, we think this explanation is plausible, but could not confirm this hypothesis at this stage.

3.3 Robustness of temporal patterns and their multi-dimensional mapping

To investigate the practical usage of temporal patterns in BP estimation, we tested their robustness to scaling factors. Three-dimensional distribution and sensitivity maps were generated, so that machine learning algorithms could use them as references.

3.3.1 Sensitivity to PPG amplitude

The experimental PPG amplitudes were multiplied by 120% and 80% respectively to mimic the changed coupling between the sensor and skin. All the complexity measures are robust to PPG scaling factors, as shown in Figure 8. HFD_{wave} is the most influenced by the scaling factors. But the magnitude (5%) is still much smaller than the disturbances (±20%).

3.3.2 Influence of data segment length

The intercept(a_0) of HFD calculation reveals a small relative uncertainty even with a signal length of 20 s. However, the uncertainty of the slope(a_1) is more influenced by the signal length, showing stabilization around 100 s. It is worth noting that the intercept and slope of the $\ln(L)$ *versus* $\ln(1/k)$ values can fluctuate by 50% and 200% respectively, during a 5-min measurement. Thus, the uncertainty of the HFD calculation remains relatively small.

In this study, our primary focus is on the accumulation of delayed cardiovascular response to stimuli, which is more related to the intercept of the HFD calculation. Supplementary Figure S4 demonstrates that the higher-order fitting coefficients of $\ln(L)$ *versus* $\ln(1/k)$ exhibit a strong correlation with the corresponding fractal dimensions of stroke volume (SV) only when signal lengths

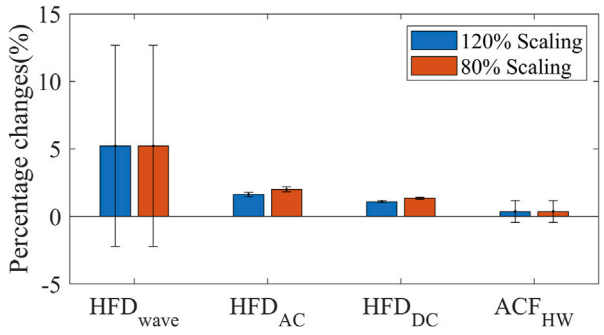

FIGURE 8
Scaling factor-induced HFD and ACF changes (mean ± SD).

reach 100 s or longer. Hence, it is crucial that future studies, which incorporate a closed-loop model and consider CO or SV complexities, utilize longer signal lengths to ensure accurate and reliable calculations. This would enable a more comprehensive understanding of the relationship between the higher-order coefficients, fractal dimensions, and physiological parameters.

3.3.3 Distribution of complexity measures and their sensitivity to hemodynamics

Experimental data were used to generate a three-dimensional map of complexity measures based on CO, *R*, and C_1, as shown in Figure 9. To ascertain the sensitivity of complexity measures to hemodynamic changes, the partial differentiation technique was employed while controlling the effects of the remaining variables. Although the presence of autocorrelation in stimuli, perturbation strength, and noise may cause non-smooth sensitivities, their distribution and differentiability still provide valuable information for analysis.

Knowing the underlying hemodynamic properties of the subject would help build more robust and accurate BP estimation algorithms. Self-similarity and stochastic patterns could encode the hemodynamics-related information in PPG temporal series, which may help stabilize BP estimation and improve the overall performance.

3.4 Contribution to BP: Linear correlation

As shown in Figure 10, temporal complexity features are less influenced by CO fluctuation, and some even had increased correlation at high CO variation. Most morphological features had a significantly decreased or small correlation with MAP at high CO variation. A simple multiple linear regression algorithm was built with these features. The PCC of estimated MAP and PP with reference is shown in Figures 10C,D. BP estimation performance is not affected if morphological features and temporal features are combined, while the morphology-only algorithm has a significantly worse MAP estimation performance at higher CO fluctuations.

3.5 Evaluation of nonlinear correlations with BP

Nonlinearity exists in the PPG-BP relationship. To further investigate the impact of different features on BP estimation performance, a BNN algorithm was employed, as described in Section 2.6. Notably, the combination of morphological features, HRV, and complexity measures such as HFD and ACF exhibited the highest correlation with the reference for BP prediction, although it did not yield the lowest MAE. Upon closer

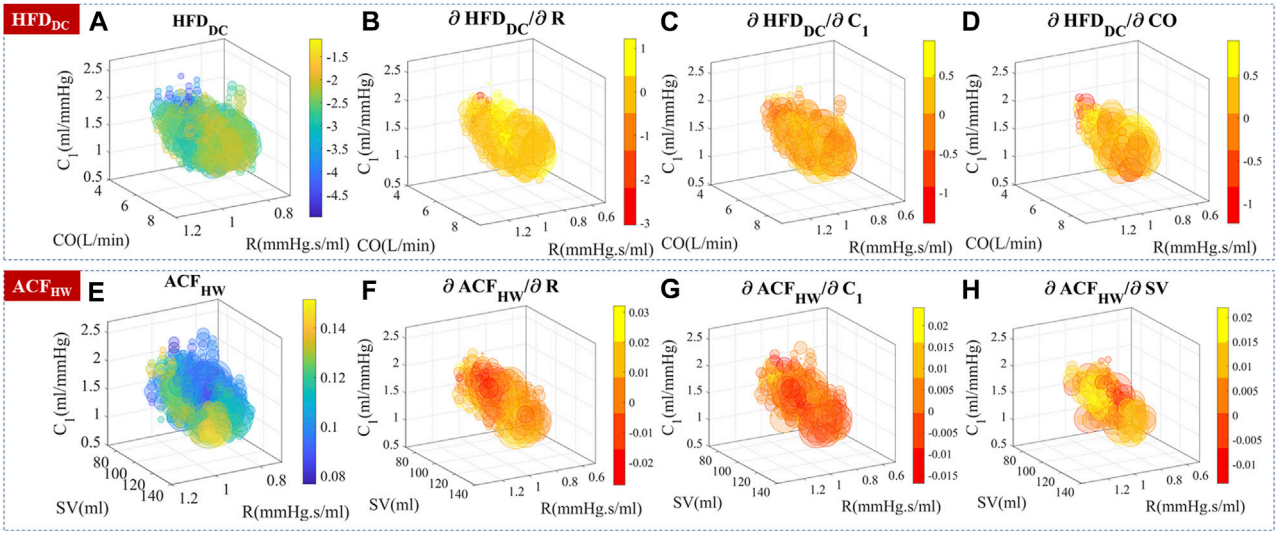

FIGURE 9
Experimental temporal complexity measure distributions and their sensitivity to CO, *R*, and C_1. The size of the bubble represented the relative number of measurements. The color represented the complexity measure or gradient value. **(A–D)** HFD_{DC} distribution and its sensitivity to hemodynamic parameters. $\partial HFD_{DC}/\partial CO$ is locally positive in the 6–8 L/min subregion. **(E–H)** ACF_{HW} distribution and its sensitivity to hemodynamic parameters.

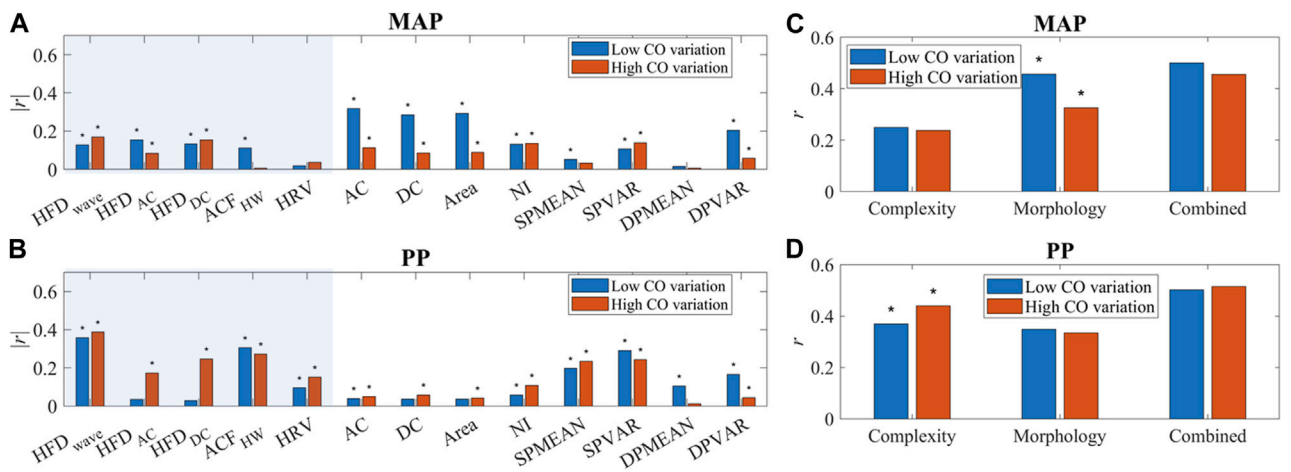

FIGURE 10
(A, B) The correlation of PPG features and BP (MAP and PP). "*" indicated a significant difference between groups. Temporal features are in the shaded area. **(C, D)** Correlation of BP (MAP and PP) estimation and reference with complexity features only, morphology features only, and combined features. "*" indicated a significant difference between low and high CO variation.

examination, it was found that the inclusion of complexity measures introduced more outliers compared to the morphology only method, as shown in Supplementary Figure S6, S7. This finding can be attributed to the inherent uncertainties associated with HFD calculations, which should be carefully considered. To address this issue, implementing a thorough outlier removal or quality check procedure would prove beneficial.

The addition of HRV played a significant role in scenarios with high CO fluctuations. However, it was observed that the incorporation of HRV negatively impacts BP estimation performance when CO fluctuations are low. These findings underscore the importance of considering the specific context and characteristics of the dataset when selecting and combining features for BP estimation. Table 3 Table 4.

TABLE 3 Uncertainty of HFD calculation caused by length selection.

	HFD of DC		HFD of AC	
	Intercept(a_0)	Slope (a_1)	Intercept(a_0)	Slope (a_1)
20	0.60%	20.0%	0.42%	27.0%
60	0.31%	9.6%	0.23%	13.5%
100	0.27%	8.0%	0.19%	10.8%

4 Discussion

4.1 Novelty of the study

Single-site PPG-based BP estimation has raised a lot of interest in both academia and the industrial world. Previous studies showed that PPG morphological information may not be enough to estimate BP, but the dynamic process is too complex to build a precise model. Machine learning algorithms such as LSTM produced better results. But it is difficult to know the exact mechanism.

In this study, we designed a novel *in silico* simulation to provide insight into the hemodynamic process. Pulse simulations showed that CO, R, and C_1 are the main determinants of prolonged PPG fluctuations. Continuous simulation with random stimuli confirmed that the buildup of prolonged vascular responses could generate certain stochastic patterns, which had a strong dependence on hemodynamics. Experimental data agreed well with the prediction. Real-life stimuli could have different levels of autocorrelation and perturbation strengths. The multi-scales and nonlinearity of complexity should be utilized to capture the hemodynamics-related information.

In addition to providing more information about hemodynamics, HFD, and ACF features are more robust. For repetitive measurement, the coupling coefficient of skin and sensor, and the sensor location difference may cause large errors in PPG amplitude measurement. Complexity patterns are less sensitive to PPG amplitude, which may help stabilize BP estimation. At unstable conditions when CO variation is higher, more and more information go into temporal complexity features. The contribution of morphological features to BP significantly decreased. BP estimation algorithms could only have the same performance when temporal features were added, showing the inherent information flow when cardiac stability changes.

4.2 Comparison with previous studies

Very few studies have used explicit stochastic temporal features to estimate BP (Hosanee et al., 2020). Colovini, T. *et al.* reported that HFD of the continuous DBP recordings had a significantly positive correlation with average DBP in hypertensive patients (Colovini et al., 2019). Cymberknop *et al.* found that HFD of arterial pressure morphology decreased with increasing blood flow, which correlated

TABLE 4 Calibrated BP estimation by BNN.

		High CO fluctuation		Low CO fluctuation	
		MAP	PP	MAP	PP
Correlation coefficient (r)	M	0.50	0.61	0.58	0.66
	M + HRV	0.62	0.66	0.42	0.57
	M + HRV + complexity	0.65	0.71	0.61	0.74
MAE (mmHg)	M	4.47	6.78	4.23	6.82
	M + HRV	5.12	8.08	5.18	8.38
	M + HRV + complexity	4.97	7.45	4.61	7.51

with arterial stiffness (Cymberknop et al., 2011). Gomes, R. *et al.* reported acutely decreased HFD of heart rate after exercise (Gomes et al., 2017). The fractal dimension of signals as short as 50 heartbeats is useful (Peña et al., 2009). To our knowledge, ACF has not been studied as a contributing factor to BP estimation. Although HRV is a well-studied dynamic feature, its impact on BP improvement primarily relates to the assessment of neurological activity (Mejía-Mejía et al., 2020a; Mejía-Mejía et al., 2020b; Mejía-Mejía et al., 2022), representing the "active" stimuli and not encompassing all aspects of the dynamic process.

In our study, we gave explicit disclosure about the temporal PPG patterns and their potential physiological meanings. Their relative contribution to BP depended on hemodynamic properties. By mapping the distribution of temporal complexity features, the application scope could be defined.

4.3 Limitations of the study

The database we used contained 40 healthy subjects. Most of them were young and healthy. The same procedure should be tested in datasets with wider coverage of subjects. Human beings are not perfect stochastic systems, and the approximation of HFD and ACF calculations may not be accurate enough. Although sex is unlikely to influence PPG-BP correlation, its role in cardiovascular health deserves to be explored further with PPG technology. Finally, we used estimated blood vessel compliance and peripheral resistance to generate the complexity feature distribution map. Validation from medical ultrasound and total peripheral resistance (TPR) measurements should be necessary.

We proposed a plausible explanation of the stochastic patterns in the PPG signal. The simulation results agreed with experimental observations and previous publications. However, the exact origin should be explored further, and the cardiovascular modeling should be more detailed to account for the closed-loop interaction, vascular tree structure, flow distribution, cardiac activity variation, *etc.*

4.4 Suggestions for future work

Temporal complexities contain rich information about hemodynamics. Our study only showed a fraction of its potential due to limited space. Previous studies mostly used HFD of BP instead of PPG signals. The impact of *P-V* translation and measurement location on the HFD of PPG should be fully investigated. For example, simulating PPG signals in peripheral areas *versus* within the arterial network may yield distinct results due to variations in the volume of arterial blood within the tissues. It would be intriguing to extend the application of the time-dependent model to incorporate multi-site PPG measurements, allowing for a more comprehensive investigation. We have shown that the nonlinearity of $\ln(L)$ and $\ln(1/k)$ relationship contained stimuli information. The role of other fitting coefficients should be thoroughly investigated. The incorporation of these coefficients will further improve the BP estimation accuracy. We found a significant contribution of HFD_{wave} to BP. However, its correlation with hemodynamic parameters is nonlinear. Collection of clinical q_{in} and corresponding simulations should be done to elucidate its influence on HFD_{wave}.

It is possible that we only found one source of temporal PPG complexity. A more detailed simulation including cardiovascular tree structure should be carried out to confirm the origin of the fractal pattern. In addition to SV or CO variations, the influence of breathing should be taken into account, considering its impact on the parasympathetic and sympathetic nervous systems. Furthermore, conducting simulations with different patterns of HRV may provide valuable insights. By using a larger dataset and employing finer grids, more accurate and comprehensive heatmaps of temporal features in relation to BP can be generated. Incorporating these adjustments and considerations will contribute to a more holistic understanding of the intricate relationship between PPG and BP.

We employed a simple BNN to estimate BP, which, although explicit, may not yield optimal performance. Moving forward, it is crucial for future studies to consider the temporal properties of the algorithm and fine-tune parameters in alignment with the specific context, such as stimuli strength, hemodynamic status, and physiological constrains related to temporal interactions. These refinements will contribute to enhancing the performance and accuracy of BP estimation algorithms.

Although we obtained decent BP estimation performance from single-site PPG alone, it is important to note that relying solely on single-site PPG or a simple combination of PPG and ECG may not provide sufficient information for reliable BP estimations (Mieloszyk et al., 2022; Mukkamala et al., 2023). Therefore, adopting a multi-modal approach that integrates multiple sensing modalities is crucial to enhance the reliability of the algorithm. This entails extracting valuable information from each modality and evaluating their respective contributions. By improving data integration and analysis

across various physiological measurements, we can achieve more accurate and robust BP estimation outcomes.

5 Conclusion

Signal fluctuation is not merely a nuisance but also valuable information. In this study, we have demonstrated that the temporal complexity patterns of PPG are correlated with hemodynamic status and make a substantial contribution to BP estimation, particularly in the presence of high CO variations. The integration of these temporal complexity features has the potential to enhance the accuracy and interpretability of single-site PPG-based BP estimation methods, thereby facilitating the development of more advanced algorithms in the future.

Data availability statement

The original contributions presented in the study are included in the article/Supplementary Material, further inquiries can be directed to the corresponding authors.

Ethics statement

The original study involving human participants was reviewed and approved by the Kansas State University Institutional Review Board (protocol number 9386, approved 5 July 2019). Informed consent was obtained from all subjects involved in the study.

Author contributions

XX conceived the study and wrote the main manuscript text. RH did the literature research and curated the data. LH checked the validity of the theoretical model. CJ helped with the experimental design. W-FD supervised the project. All authors contributed to the article and approved the submitted version.

Funding

This work was supported by the National Key R&D Program of China (2022YFC3601003, 2021YFC2501500, 2020YFC2003600), the National Natural Science Foundation of China (62001470), the Natural Science Foundation of Shandong Province, China (ZR2020QF021), and Youth Innovation Promotion Association CAS.

Acknowledgments

We sincerely thank Charles Carlson et al. for the great multi-modal dataset. The proposed model was also described in a preprint (DOI:10.21203/rs.3.rs-2430236/v2). Xu Lisheng provided valuable suggestions.

Conflict of interest

CJ is employed by Jinan Guoke Medical Technology Development Co., Ltd. W-FD is employed by Suzhou GK Medtech Science and Technology Development (Group) Co., Ltd.

The remaining authors declare that the research was conducted in the absence of any commercial or financial relationships that could be construed as a potential conflict of interest.

Publisher's note

Supplementary material

The Supplementary Material for this article can be found online at: https://www.frontiersin.org/articles/10.3389/fphys.2023.1187561/full#supplementary-material

References

Acciaroli, G. (2018). "Non-Invasive continuous-time blood pressure estimation from a single channel PPG signal using regularized ARX models," in 2018 40th Annual International Conference of the IEEE Engineering in Medicine and Biology Society (EMBC).

Agarwal, R., Bills, J. E., Hecht, T. J. W., and Light, R. P. (2011). Role of home blood pressure monitoring in overcoming therapeutic inertia and improving hypertension control: A systematic review and meta-analysis. *Hypertension* 57 (1), 29–38. doi:10.1161/HYPERTENSIONAHA.110.160911

Ali, N. F., and Atef, M. (2022). LSTM multi-stage transfer learning for blood pressure estimation using photoplethysmography. *Electronics* 11 (22), 3749. doi:10.3390/electronics11223749

Allen, J., and Murray, A. (1999). Modelling the relationship between peripheral blood pressure and blood volume pulses using linear and neural network system identification techniques. *Physiol. Meas.* 20 (3), 287–301. doi:10.1088/0967-3334/20/3/306

Avolio, A., Cox, J., Louka, K., Shirbani, F., Tan, I., Qasem, A., et al. (2022). Challenges presented by cuffless measurement of blood pressure if adopted for diagnosis and treatment of hypertension. *Pulse* 10, 34–45. doi:10.1159/000522660

Baumert, M., Baier, V., and Voss, A. (2005). Long-term correlations and fractal dimension of beat-to-beat blood pressure dynamics. *Fluctuation Noise Lett.* 05 (04), L549–L555. doi:10.1142/s0219477505003002

Box, G. E., Jenkins, G. M., Reinsel, G. C., and Ljung, G. M. (2015). *Time series analysis: forecasting and control*. John Wiley & Sons.

Brandfonbrener, M., Landowne, M., and Shock, N. W. (1955). Changes in cardiac output with age. *Circulation* 12 (4), 557–566. doi:10.1161/01.cir.12.4.557

Butlin, M., Shirbani, F., Barin, E., Tan, I., Spronck, B., and Avolio, A. P. (2018). Cuffless estimation of blood pressure: importance of variability in blood pressure dependence of arterial stiffness across individuals and measurement sites. *IEEE Trans. Biomed. Eng.* 65 (11), 2377–2383. doi:10.1109/TBME.2018.2823333

Carlson, C., Turpin, V. R., Suliman, A., Ade, C., Warren, S., and Thompson, D. E. (2020). Bed-based ballistocardiography: dataset and ability to track cardiovascular parameters. *Sensors (Basel)* 21 (1), 156. doi:10.3390/s21010156

Charlton, P. H., Mariscal Harana, J., Vennin, S., Li, Y., Chowienczyk, P., and Alastruey, J. (2019). Modeling arterial pulse waves in healthy aging: A database for

in silico evaluation of hemodynamics and pulse wave indexes. *Am. J. Physiology-Heart Circulatory Physiology* 317 (5), H1062–H1085. doi:10.1152/ajpheart.00218.2019

Chobanian, A. V., Bakris, G. L., Black, H. R., Cushman, W. C., Green, L. A., Izzo, J. L., Jr, et al. (2003). The seventh report of the joint national committee on prevention, detection, evaluation, and treatment of high blood pressure: the JNC 7 report. *Jama* 289 (19), 2560–2572. doi:10.1001/jama.289.19.2560

Colovini, T., Facciuto, F., Cabral, M., Parodi, R., Spengler, M., and Piskorz, D. (2019). Application of Higuchi's algorithm in central blood pressure pulse waves and its potential association with hemodynamic parameters in hypertensive patients. *J. Hypertens.* 37, e234. doi:10.1097/01.hjh.0000573004.23278.99

Cosoli, G., Spinsante, S., and Scalise, L. (2020). Wrist-worn and chest-strap wearable devices: systematic review on accuracy and metrological characteristics. *Measurement* 159, 107789. doi:10.1016/j.measurement.2020.107789

Cymberknop, L., Legnani, W., Pessana, F., Bia, D., Zócalo, Y., and Armentano, R. L. (2011). Stiffness indices and fractal dimension relationship in arterial pressure and diameter time series *in-vitro*. *J. Phys. Conf. Ser.* 332 (1), 012024. doi:10.1088/1742-6596/332/1/012024

Ding, X. R., Zhao, N., Yang, G. Z., Pettigrew, R. I., Miao, F., et al. (2016). Continuous blood pressure measurement from invasive to unobtrusive: celebration of 200th birth anniversary of carl ludwig. *IEEE J. Biomed. Health Inf.* 20 (6), 1455–1465. doi:10.1109/JBHI.2016.2620995

El-Hajj, C., and Kyriacou, P. A. (2021). Cuffless blood pressure estimation from PPG signals and its derivatives using deep learning models. *Biomed. Signal Process. Control* 70, 102984. doi:10.1016/j.bspc.2021.102984

Elgendi, M., Fletcher, R., Liang, Y., Howard, N., Lovell, N. H., Abbott, D., et al. (2019). The use of photoplethysmography for assessing hypertension. *npj Digit. Med.* 2 (1), 60. doi:10.1038/s41746-019-0136-7

Elgendi, M. (2012). On the analysis of fingertip photoplethysmogram signals. *Curr. Cardiol. Rev.* 8 (1), 14–25. doi:10.2174/157340312801215782

Finnegan, E., Davidson, S., Harford, M., Jorge, J., Watkinson, P., Young, D., et al. (2021). Pulse arrival time as a surrogate of blood pressure. *Sci. Rep.* 11 (1), 22767. doi:10.1038/s41598-021-01358-4

Force, U. P. S. T., Krist, A. H., Davidson, K. W., Mangione, C. M., Cabana, M., Caughey, A. B., et al. (2021). Screening for hypertension in adults: US preventive services task Force reaffirmation recommendation statement. *JAMA* 325 (16), 1650–1656. doi:10.1001/jama.2021.4987

Gomes, R., Vanderlei, L. C. M., Garner, D. M., Vanderlei, F. M., and Valenti, V. E. (2017). Higuchi fractal analysis of heart rate variability is sensitive during recovery from exercise in physically active men. *Med. Express* 4. doi:10.5935/medicalexpress.2017.02.03

Grabovskis, A., Marcinkevics, Z., Rubins, U., and Kviesis-Kipge, E. (2013). Effect of probe contact pressure on the photoplethysmographic assessment of conduit artery stiffness. *J. Biomed. Opt.* 18, 27004. doi:10.1117/1.JBO.18.2.027004

Guirguis-Blake, J. M., Evans, C. V., Webber, E. M., Coppola, E. L., Perdue, L. A., and Weyrich, M. S. (2021). Screening for hypertension in adults: updated evidence report and systematic review for the US preventive services task Force. *Jama* 325 (16), 1657–1669. doi:10.1001/jama.2020.21669

Gupta, S., Singh, A., and Sharma, A. (2022). Dynamic large artery stiffness index for cuffless blood pressure estimation. *IEEE Sensors Lett.* 6 (3), 1–4. doi:10.1109/lsens.2022.3157060

Hallock, P., and Benson, I. C. (1937). Studies on the elastic properties of human isolated aorta. *J. Clin. Invest.* 16 (4), 595–602. doi:10.1172/JCI100886

Harfiya, L. N., Chang, C.-C., and Li, Y.-H. (2021). Continuous blood pressure estimation using exclusively photopletysmography by LSTM-based signal-to-signal translation. *Sensors* 21 (9), 2952. doi:10.3390/s21092952

Higuchi, T. (1988). Approach to an irregular time series on the basis of the fractal theory. *Phys. D. Nonlinear Phenom.* 31 (2), 277–283. doi:10.1016/0167-2789(88)90081-4

Hosanee, M., Chan, G., Welykholowa, K., Cooper, R., Kyriacou, P. A., Zheng, D., et al. (2020). Cuffless single-site photoplethysmography for blood pressure monitoring. *J. Clin. Med.* 9 (3), 723. doi:10.3390/jcm9030723

Hsiu, H., Hsu, C. L., and Wu, T. L. (2011). Effects of different contacting pressure on the transfer function between finger photoplethysmographic and radial blood pressure waveforms. *Proc. Inst. Mech. Eng. H.* 225 (6), 575–583. doi:10.1177/0954411910396288

Hsiu, H., Huang, S. M., Hsu, C. L., Hu, S. F., and Lin, H. W. (2012). Effects of cold stimulation on the harmonic structure of the blood pressure and photoplethysmography waveforms. *Photomed. laser Surg.* 30 (2), 77–84. doi:10.1089/pho.2011.3124

Jiang, H., Zou, L., Huang, D., and Feng, Q. (2022). Continuous blood pressure estimation based on multi-scale feature extraction by the neural network with multi-task learning. *Front. Neurosci.* 16, 883693. doi:10.3389/fnins.2022.883693

Johnson, A. E. W., Pollard, T. J., Shen, L., Lehman, L. W. H., Feng, M., Ghassemi, M., et al. (2016). MIMIC-III, a freely accessible critical care database. *Sci. Data* 3 (1), 160035. doi:10.1038/sdata.2016.35

Josep Solà, R. D.-G. (2019). in *The handbook of cuffless blood pressure monitoring*. Editor R. D.-G. Josep Solà (Cham: Springer).

Kesić, S., and Spasić, S. Z. (2016a). Application of higuchi's fractal dimension from basic to clinical neurophysiology: A review. *Comput. Methods Programs Biomed.* 133, 55–70. doi:10.1016/j.cmpb.2016.05.014

Kesić, S., and Spasić, S. Z. (2016b). Application of higuchi's fractal dimension from basic to clinical neurophysiology: A review. *Comput. Methods Programs Biomed.* 133, 55–70. doi:10.1016/j.cmpb.2016.05.014

Langewouters, G. J., Wesseling, K. H., and Goedhard, W. J. A. (1984). The static elastic properties of 45 human thoracic and 20 abdominal aortas *in vitro* and the parameters of a new model. *J. Biomechanics* 17 (6), 425–435. doi:10.1016/0021-9290(84)90034-4

Li, Y.-H., Harfiya, L. N., and Chang, C.-C. (2021). Featureless blood pressure estimation based on photoplethysmography signal using CNN and BiLSTM for IoT devices. *Wirel. Commun. Mob. Comput.* 2021, 1–10. doi:10.1155/2021/9085100

Liu, T. Y. (2009). "EasyEnsemble and feature selection for imbalance data sets," in 2009 International Joint Conference on Bioinformatics, Systems Biology and Intelligent Computing.

Martínez, G., Howard, N., Abbott, D., Lim, K., Ward, R., and Elgendi, M. (2018). Can photoplethysmography replace arterial blood pressure in the assessment of blood pressure? *J. Clin. Med.* 7 (10), 316. doi:10.3390/jcm7100316

Mazumder, O., Banerjee, R., Roy, D., Bhattacharya, S., Ghose, A., and Sinha, A. (2022). Synthetic PPG signal generation to improve coronary artery disease classification: study with physical model of cardiovascular system. *IEEE J. Biomed. Health Inf.* 26 (5), 2136–2146. doi:10.1109/JBHI.2022.3147383

Mejía-Mejía, E., Budidha, K., Abay, T. Y., May, J. M., and Kyriacou, P. A. (2020a). Heart rate variability (HRV) and pulse rate variability (PRV) for the assessment of autonomic responses. *Front. Physiol.* 11, 779. doi:10.3389/fphys.2020.00779

Mejía-Mejía, E., Budidha, K., Kyriacou, P. A., and Mamouei, M. (2022). Comparison of pulse rate variability and morphological features of photoplethysmograms in estimation of blood pressure. *Biomed. Signal Process. Control* 78, 103968. doi:10.1016/j.bspc.2022.103968

Mejía-Mejía, E., May, J. M., Torres, R., and Kyriacou, P. A. (2020b). Pulse rate variability in cardiovascular health: A review on its applications and relationship with heart rate variability. *Physiol. Meas.* 41 (7), 07tr01. doi:10.1088/1361-6579/ab998c

Meng, Z., Yang, X., Liu, X., Wang, D., and Han, X. (2022). Non-invasive blood pressure estimation combining deep neural networks with pre-training and partial fine-tuning. *Physiol. Meas.* 43 (11), 11NT01. doi:10.1088/1361-6579/ac9d7f

Mieloszyk, R., Twede, H., Lester, J., Wander, J., Basu, S., Cohn, G., et al. (2022). A comparison of wearable tonometry, photoplethysmography, and electrocardiography for cuffless measurement of blood pressure in an ambulatory setting. *IEEE J. Biomed. Health Inf.* 26 (7), 2864–2875. doi:10.1109/JBHI.2022.3153259

Millasseau, S. C., Guigui, F. G., Kelly, R. P., Prasad, K., Cockcroft, J. R., Ritter, J. M., et al. (2000). Noninvasive assessment of the digital volume pulse. Comparison with the peripheral pressure pulse. *Hypertension* 36 (6), 952–956. doi:10.1161/01.hyp.36.6.952

Monte-Moreno, E. (2011). Non-invasive estimate of blood glucose and blood pressure from a photoplethysmograph by means of machine learning techniques. *Artif. Intell. Med.* 53 (2), 127–138. doi:10.1016/j.artmed.2011.05.001

Mukkamala, R., Hahn, J. O., Inan, O. T., Mestha, L. K., Kim, C. S., Töreyin, H., et al. (2015). Toward ubiquitous blood pressure monitoring via pulse transit time: theory and practice. *IEEE Trans. bio-medical Eng.* 62 (8), 1879–1901. doi:10.1109/TBME.2015.2441951

Mukkamala, R., and Hahn, J. O. (2018). Toward ubiquitous blood pressure monitoring via pulse transit time: predictions on maximum calibration period and acceptable error limits. *IEEE Trans. Biomed. Eng.* 65 (6), 1410–1420. doi:10.1109/TBME.2017.2756018

Mukkamala, R., Shroff, S. G., Landry, C., Kyriakoulis, K. G., Avolio, A. P., and Stergiou, G. S. (2023). The microsoft research aurora project: important findings on cuffless blood pressure measurement. *Hypertension* 80 (3), 534–540. doi:10.1161/HYPERTENSIONAHA.122.20410

Nicolaas Westerhof, N. S., and Noble, M. I. M. (2010). *Snapshots of hemodynamics*.

Peña, M. A., Echeverría, J. C., García, M. T., and González-Camarena, R. (2009). Applying fractal analysis to short sets of heart rate variability data. *Med. Biol. Eng. Comput.* 47 (7), 709–717. doi:10.1007/s11517-009-0436-1

Pour Ebrahim, M., Heydari, F., Wu, T., Walker, K., Joe, K., Redoute, J. M., et al. (2019). Blood pressure estimation using on-body continuous wave radar and photoplethysmogram in various posture and exercise conditions. *Sci. Rep.* 9 (1), 16346. doi:10.1038/s41598-019-52710-8

Pu, Y., et al. (2021). *Cuff-less blood pressure estimation from electrocardiogram and photoplethysmography based on VGG19-LSTM network*.

Radha, M., de Groot, K., Rajani, N., Wong, C. C. P., Kobold, N., Vos, V., et al. (2019). Estimating blood pressure trends and the nocturnal dip from photoplethysmography. *Physiol. Meas.* 40 (2), 025006. doi:10.1088/1361-6579/ab030e

Rubega, M., Scarpa, F., Teodori, D., Sejling, A. S., Frandsen, C. S., and Sparacino, G. (2020). Detection of hypoglycemia using measures of EEG complexity in type 1 diabetes patients. *Entropy (Basel, Switz.* 22 (1), 81. doi:10.3390/e22010081

Seber, G. A. F. (1989). *Wiley series in probability and statistics*. Wiley.Nonlinear Regression

Stergiopulos, N., Meister, J. J., and Westerhof, N. (1994). Simple and accurate way for estimating total and segmental arterial compliance: the pulse pressure method. *Ann. Biomed. Eng.* 22 (4), 392–397. doi:10.1007/BF02368245

Tang, Q., Chen, Z., Allen, J., Alian, A., Menon, C., Ward, R., et al. (2020b). PPGSynth: an innovative toolbox for synthesizing regular and irregular photoplethysmography waveforms. *Front. Med. (Lausanne)* 7, 597774. doi:10.3389/fmed.2020.597774

Tang, Q., Chen, Z., Ward, R., and Elgendi, M. (2020a). Synthetic photoplethysmogram generation using two Gaussian functions. *Sci. Rep.* 10 (1), 13883. doi:10.1038/s41598-020-69076-x

Tunnicliffe Wilson, G. (2015). in *Time series analysis: Forecasting and control*. Editors E. P. B. George, G. M. Jenkins, G. C. Reinsel, and G. M. Ljung 5th Edition (Hoboken, New Jersey: Published by John Wiley and Sons Inc), 712. ISBN: 978-1-118-67502-1. Journal of Time Series Analysis, 2016. 37: p. n/a-n/a.

Van Bortel, L. M., and Spek, J. J. (1998). Influence of aging on arterial compliance. *J. Hum. Hypertens.* 12 (9), 583–586. doi:10.1038/sj.jhh.1000669

Wang, D., Yang, X., Liu, X., Ma, L., Li, L., and Wang, W. (2021). Photoplethysmography-based blood pressure estimation combining filter-wrapper collaborated feature selection with LASSO-LSTM model. *IEEE Trans. Instrum. Meas.* 70, 1–14. doi:10.1109/tim.2021.3109986

Wang, L., Zhao, L. J., Ma, W. H., Wang, H., Yao, Y., et al. (2017). Design and implementation of a pulse wave generator based on Windkessel model using field programmable gate array technology. *Biomed. Signal Process. Control* 36, 93–101. doi:10.1016/j.bspc.2017.03.008

Westerhof, N., Lankhaar, J.-W., and Westerhof, B. E. (2009). The arterial Windkessel. *Med. Biol. Eng. Comput.* 47 (2), 131–141. doi:10.1007/s11517-008-0359-2

Xing, X., Ma, Z., Xu, S., Zhang, M., Zhao, W., Song, M., et al. (2021). Blood pressure assessment with in-ear photoplethysmography. *Physiol. Meas.* 42 (10), 105009. doi:10.1088/1361-6579/ac2a71

Xing, X., Ma, Z., Zhang, M., Zhou, Y., Dong, W., and Song, M. (2019). An unobtrusive and calibration-free blood pressure estimation method using photoplethysmography and biometrics. *Sci. Rep.* 9 (1), 8611. doi:10.1038/s41598-019-45175-2

Yen, C.-T., Chang, S.-N., and Liao, C.-H. (2021). Deep learning algorithm evaluation of hypertension classification in less photoplethysmography signals conditions. *Meas. Control* 54 (3-4), 439–445. doi:10.1177/00202940211001904

frontiers | Frontiers in Physiology

TYPE Original Research
PUBLISHED 13 September 2023
DOI 10.3389/fphys.2023.1242807

OPEN ACCESS

EDITED BY
Rajesh Kumar Tripathy,
Birla Institute of Technology and Science, India

REVIEWED BY
Guanghao Sun,
The University of Electro-Communications, Japan
Jan Kubicek,
VSB-Technical University of Ostrava, Czechia

*CORRESPONDENCE
John Allen,
john.allen@ncl.ac.uk

RECEIVED 19 June 2023
ACCEPTED 18 August 2023
PUBLISHED 13 September 2023

CITATION
Iqbal S, Bacardit J, Griffiths B and Allen J (2023), Deep learning classification of systemic sclerosis from multi-site photoplethysmography signals. *Front. Physiol.* 14:1242807. doi: 10.3389/fphys.2023.1242807

Deep learning classification of systemic sclerosis from multi-site photoplethysmography signals

Sadaf Iqbal[1,2], Jaume Bacardit[3], Bridget Griffiths[4] and John Allen[1,2,5]*

[1]Faculty of Medical Sciences, Newcastle University, Newcastle Upon Tyne, United Kingdom, [2]Northern Medical Physics and Clinical Engineering, Freeman Hospital, Newcastle Upon Tyne, United Kingdom, [3]School of Computing, Newcastle University, Newcastle Upon Tyne, United Kingdom, [4]Department of Rheumatology, Freeman Hospital, Newcastle Upon Tyne, United Kingdom, [5]Research Centre for Intelligent Healthcare, Coventry University, Coventry, United Kingdom

Introduction: A pilot study assessing a novel approach to identify patients with Systemic Sclerosis (SSc) using deep learning analysis of multi-site photoplethysmography (PPG) waveforms ("DL-PPG").

Methods: PPG recordings having baseline, unilateral arm pressure cuff occlusion and reactive hyperaemia flush phases from 6 body sites were studied in 51 Controls and 20 SSc patients. RGB scalogram images were obtained from the PPG, using the continuous wavelet transform (CWT). 2 different pre-trained convolutional neural networks (CNNs, namely, GoogLeNet and EfficientNetB0) were trained to classify the SSc and Control groups, evaluating their performance using 10-fold stratified cross validation (CV). Their classification performance (i.e., accuracy, sensitivity, and specificity, with 95% confidence intervals) was also compared to traditional machine learning (ML), i.e., Linear Discriminant Analysis (LDA) and K-Nearest Neighbour (KNN).

Results: On a participant basis DL-PPG accuracy, sensitivity and specificity for GoogLeNet were 83.1 (72.3–90.9), 75.0 (50.9–91.3) and 86.3 (73.7–94.3)% respectively, and for EfficientNetB0 were 87.3 (77.2–94.0), 80.0 (56.3–94.3) and 90.1 (78.6–96.7)%. The corresponding results for ML classification using LDA were 66.2 (53.9–77.0), 65.0 (40.8–84.6) and 66.7 (52.1–79.2)% respectively, and for KNN were 76.1 (64.5–85.4), 40.0 (19.1–63.9), and 90.2 (78.6–96.7)% respectively.

Discussion: This study shows the potential of DL-PPG classification using CNNs to detect SSc. EfficientNetB0 gave an overall improved performance compared to GoogLeNet, with both CNNs performing better than the traditional ML methods tested. Our automatic AI approach, using transfer learning, could offer significant benefits for SSc diagnostics in a variety of clinical settings where low-cost portable and easy-to-use diagnostics can be beneficial.

KEYWORDS

deep learning, machine learning, photoplethysmography, pulse, Raynaud's, scleroderma, systemic sclerosis

1 Introduction

1.1 Background

Systemic Sclerosis (SSc, aka Scleroderma) is a complex, rare, connective tissue disease (CTD) involving the collagen, major organs, the blood vessels and the immune system (van den Hoogen et al., 2013; Di Battista et al., 2021), in which extensive fibrosis and vascular alterations take place. It has significant morbidity and mortality (van den Hoogen et al., 2013),

and in the UK an estimated prevalence of 307 per million (95% CI: 290–323), with the highest occurrence in the 70–84 years age group (Royle et al., 2018). SSc (the two most common variants are limited cutaneous variant (lcSSc), and diffuse cutaneous (dcSSc)) is often associated with Raynaud's phenomenon (RP), a condition in which recurrent, reversible vasospasm of the digital small arteries, arterioles, pre-capillary and post-capillary venules occurs on exposure to cold or emotional stress (Hughes and Herrick, 2016; Silva et al., 2016). RP is common and in the UK is reported to affect up to 10 million people (SRUK, 2023). About 1 in 16 women and 1 in 50 men with Raynaud's develop SSc, usually between the ages of 25 and 55 (NHSinform, 2023; Haque, 2020; Belch, 2017). It is usually sub-categorised into: a) Primary RP (PRP) when no underlying cause condition is known (idiopathic); b) Secondary RP when RP is linked to an underlying disease such as SSc or dermatomyositis or to the intake of certain drugs. Secondary RP is typically seen in approximately 90%–96% of patents with SSc and often precedes the development of SSc by an average time of 10.4 years (Spencer-Green, 1998; Pauling et al., 2019). Clinical specialists differentiate secondary RP from PRP by checking for symptoms associated with secondary RP such as the age at onset (secondary RP is usually after 30 years of age), detecting abnormal immunology e.g., certain autoantibodies, observing nailfold capillaries, ulceration of digits, checking for fibrosis in the lungs or other organs, and skin thickening which is the hallmark of SSc. However, diagnosing SSc is not always easy as its symptoms resemble other conditions such as PRP and early symptoms of diseases such as systemic lupus erythematous (where 10% and 45% of patients show Raynaud's phenomenon). Early detection and management of the disease is a must, to improve the morbidity and mortality in patients (Walker et al., 2007). This in turn requires a multi-disciplinary and collaborative effort involving clinical specialists and testing. It can take more than one visit to an expert Rheumatology specialist to diagnose the disease, especially in the early stages. Identification of internal organ involvement and its severity is also important.

1.2 Current methods of SSc diagnosis

These involve extensive and costly testing for autoantibodies and markers of organ involvement. Sometimes, it is difficult to distinguish between SSc and non-SSc cases as patients have overlap conditions. Nailfold capillaroscopy (NFC) is another key technique used to help diagnose SSc. NFC is a non-invasive, optical imaging technique (Allen and Howell, 2014; Eriksson et al., 2014) that is used by an expert operator to visually inspect the microcirculation in the nailfold capillaries of the distal papillae and hence assess pathological/morphological changes associated with SSc such as capillary "dilatation", distribution and density (for "drop-out"), bushing (for "angiogenesis") and microhaemorrhage (extravasation). Tests such as NFC, however, are usually currently performed in specialist hospitals and are not at all readily available to all patients.

There is huge scope to look for alternative, low-cost technologies to assess SSc. Photoplethysmography (PPG) is one such technique, which is non-invasive and optically assesses the circulation. The working principle of a PPG-based system uses a suitable light source such as infrared or near-infrared light to study the heart-synchronous changes in blood volume in the microvascular bed of tissues such as skin (Allen, 2007; Elgendi, 2012; Kyriacou and Allen, 2021). Additional key advantages of PPG are its portability and its versatility to be used in a range of settings such as measurement labs as well as ambulatory assessments (wearable sensors, Charlton et al., 2023). PPG is currently widely used in different clinical applications (Johnson et al., 2020) including for pulse oxygen saturation measurement (SpO2) (Ma et al., 2018), cardiovascular health (heart rate, blood pressure, blood vessel and arterial stiffness) monitoring (Castaneda et al., 2018), and for studying hypertension (Liang et al., 2018).

1.3 Recent works

The potential of PPG for detecting patients with SSc has already been explored using conventional optical pulse wave analysis techniques but the literature here appears to be limited to date. The largest SSc PPG study reported to date is by Rosato et al. (2010) with 105 SSc (compared to 96 PRP and 85 healthy controls) using a Termoflow type PPG instrument. The authors found that the mean amplitude of the PPG sphygmic wave was significantly lower in the PRP group than in the SSc group (mean ± standard deviation = 11 ± 10, given in arbitrary units (a.u.) vs. 24 ± 24 a.u. for SSc). The mean amplitude was also significantly lower in SSc than in HC (56 ± 19 a.u. for HC). A further study by Rosato et al. (2011) using bilateral PPG measurements found a homogeneous pattern (meaning uniformity of morphology and amplitude of sphygmic PPG wave across all 10 fingers) for 95% of the HCs and 93% of the PRPs but was only 28% for the SSc group. McKay et al. (2014) investigated multi-site PPG in 19 SSc, 19 PRP and 23 HC by studying measures of arterial, endothelial and peripheral autonomic dysfunction under a dynamic 3 phase testing protocol. The authors found that measures attributed to endothelial function were significantly impaired in SSc ($p < 0.02$), but with no difference between the HCs and PRPs. The authors reported that the Receiver Operating Characteristic (ROC) based classification accuracy was 81% (sensitivity 90%, specificity 74%) for separating SSc from HCs, and 82% (sensitivity 84%, specificity 79%) for separating SSc from PRPs. Mamontov et al. (2020) employed imaging PPG (iPPG) and studied 19 SSc and 21 HC participants (with age- and sex-matched balanced classes) and from the pulse arrival time (PAT) showed a significant increase in its variability in SSc patients as compared to HCs (52 ± 47 ms vs. 24 ± 13 ms, $p = 0.01$). These earlier works show the potential of PPG as a tool to help investigate SSc but such approaches from the literature have relied on extracting a range of pulse features based on domain knowledge, and then performing specific feature selection to try and improve classification performance. To the authors' best knowledge, there are no papers on contact type PPG measurements using analysis based on deep learning (DL) for the assessment of SSc patients. The aim of this pilot study was to utilise DL in a novel way by applying it to automatically identify the presence (or absence) of SSc from multi-site PPG measurements collected under a dynamic 3-phase test protocol.

2 Materials and methods

2.1 Study participants

Consecutive patients were approached by specific autoimmune connective tissue disease rheumatologists or the connective tissue disease nurse specialist from the Rheumatology outpatient population attending Freeman Hospital, Newcastle upon Tyne. The SSc participants were each diagnosed by an expert consultant Rheumatologist at Freeman Hospital, using the 1980 American College of Rheumatology (ACR) preliminary criteria for the classification of systemic sclerosis (Subcommittee for Scleroderma Criteria, 1980). PRP patients were diagnosed by the same clinical team, as having vasospastic symptoms for >2 years, with routine practice assessments and no other underlying medical or mechanical cause. SSc and PRP participants were recruited from the Rheumatology outpatient clinic at Freeman Hospital, Newcastle upon Tyne. Healthy Control (HC) participants were recruited from volunteers - largely from the University of the Third Age (U3A, Wearside Branch), and from staff and students of Newcastle Hospitals and Newcastle University. The HC participants had no known underlying health condition (e.g., diabetes mellitus and hypertension). For each patient a range of clinical and demographic data were collected for the study, including participants' pertinent medical history, and the tests done in the hospital to assess and diagnose SSc patients. All participants were permitted to continue their regular medication, including vasodilator treatment, at the time of their recruitment and informed consent was taken. Ethics approval for the original study data collection was granted by the National Research Ethics Service (NRES) Committee Northeast (County Durham and Tees Valley 1 REC, 07/H0905/72 2008). Ethics permission for re-analysis of the anonymised PPG waveform data for Sadaf Iqbal's PhD studentship project was obtained from Newcastle University (Reference 7273/2018, with an extension to the study 17138/2021).

2.2 Multi-site PPG measurements and pre-processing

The PPG data set measurements were originally collected by Dr Neil McKay, Rheumatologist, between 2009 and 2011 at Freeman Hospital's microvascular research facility, with 3-phase measurement protocol developed and physiological measurement training supported by expert PPG operator JA. Participants were firstly asked to lay comfortably in a symmetrical supine position for a period of at least 15 min whilst acclimatising in a warm normothermic temperature-controlled (23°C ± 1°C) clinical measurement room. Multi-site PPG waveforms were then collected simultaneously for 20 min from 6 symmetrical, body sites namely: right and left earlobes, index finger pads and great toe pads respectively, using optically and electronically matched amplifiers (bandwidth 0.5–20 Hz) and captured to computer at a sampling frequency (Fs) of 2000 Hz. The 3 phases of measurement were: subject resting supine (10 min, Baseline phase); an arm pressure cuff inflated at 300 mmHg to stop the arterial blood flow into the left arm (for 5 min, Occlusion phase); then at 15 min the cuff pressure was quickly but carefully released, and the degree of reactive hyperaemia monitored for a further 5 min (Flush phase). Figure 1 shows examples of 3-phase PPG beat-to-beat amplitude data for the left finger measurement site of a Control participant and a SSc participant.

For this study involving advanced analysis of the data, a visual analysis of the PPG data was carried out by operator SI to check for the presence of unexpected artifacts (such as that caused by unreliable PPG probe skin contact or when a study did not follow protocol) or a distorted flush response was evident. Some of the 92 participants originally entered into the study had to be excluded: original PPG data collected using too high a manual gain setting causing a high flush which saturated i.e., electronically clipping and making unusable a PPG trace for the left study arm (N = 3); participants not following the 20-min protocol (N = 7). In total, PPG and ECG data from a total of 20 SSc, 22 PRP and 29 HC participants were included and analysed using the techniques described in the next section. Figure 2 shows a participant flowchart summary for the included and excluded subjects in our pilot study.

Healthy controls and patient controls (i.e., PRP) participants were combined in a single control group as they both belong to clinical class of non-life-threatening conditions as opposed to SSc group which needs clinical attention and early identification and management. Also, noting here that although pulse amplitudes can be different between the groups and from the same subject if tested on different days, the literature suggests that PPG pulse measures are similar across the two groups. The study by Rosato et al. (2011) had shown that PPG shows a homogeneous pattern, i.e., a uniformity in morphology as well as amplitude of PPG sphygmic waves across the fingers, in 95% of the healthy control subjects and 93% of the PRP patients as opposed to this being present in only 28% of the SSc patients. McKay et al. (2014) also had found no differences between healthy controls and PRP for the case of dynamic physiological testing i.e., the derived PPG median flush response slope and flush response value.

In this study a PPG signal was pre-processed with only a normalisation stage, with each of the 6 PPG signals divided by their respective PPG amplifier channel gain setting. There was no additional signal filtering performed by the computer.

2.3 Deep learning classification

This data analysis was carried out on a 64-bit Windows 10 and 14 Core PC fitted with a single NVIDIA GeForce RTX 2080 Ti GPU card which used MATLAB software. Here, the PPG time series was converted into scalogram images for the study subjects using continuous wavelet transform (CWT). Scalograms give a time-frequency (T-F) image representing the percentage of signal energy contained in different frequency bands (Gandhi et al., 2014), with the *x*-axis representing time and *y*-axis representing frequency and a signal varying in colour intensity over the T-F plane.

Each PPG channel's gain normalised time series was divided into consecutive 30 s non-overlapping windows and for each 1D time window, a 2D scalogram image along with its label was then generated using continuous wavelet transform (CWT) methods. The Morse mother wavelet was used in CWT as this type of analytic

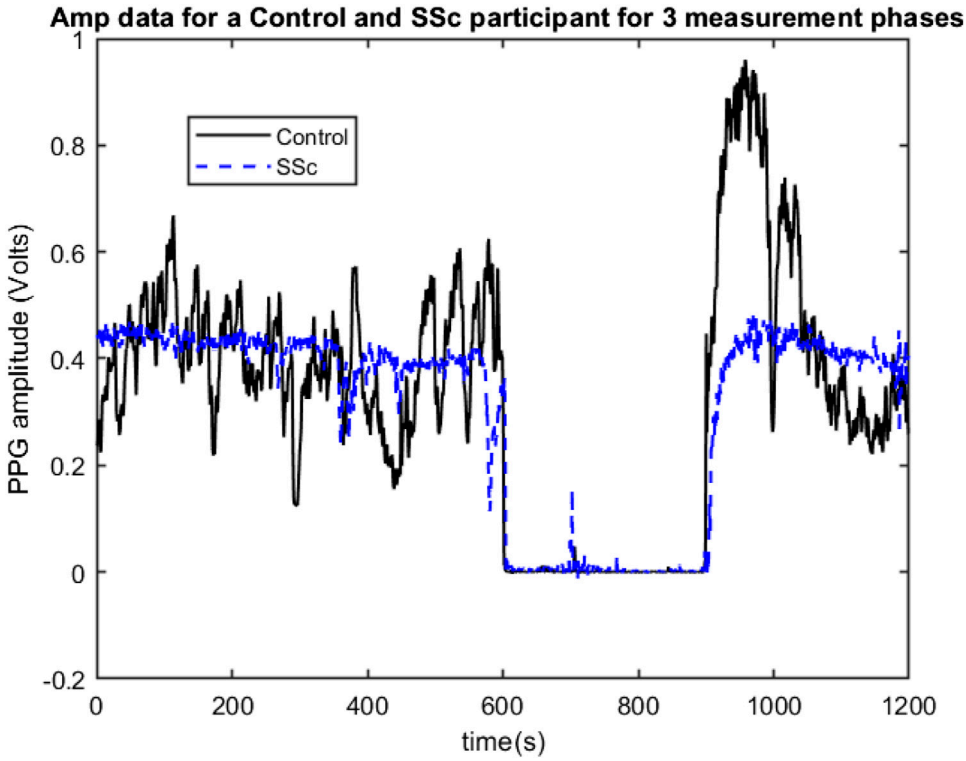

FIGURE 1
Example 3-phase PPG Amp data recordings for a Control (black line) and for a SSc participant (Blue line) showing beat-to-beat amplitude changes for the left finger site, with 0–600 s = Baseline phase, 600–900 s = Occlusion phase, and 600–1200 s = Flush phase.

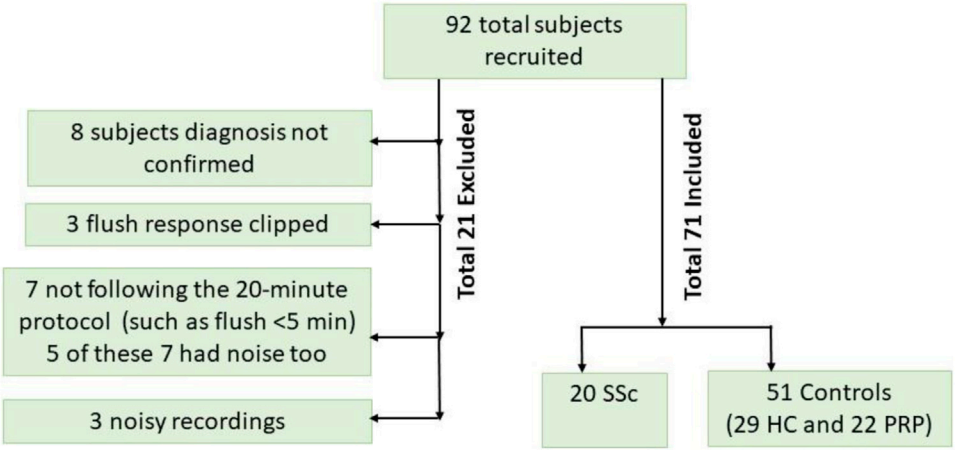

FIGURE 2
Participant flowchart showing included and reasons for the excluded subjects.

wavelet is very useful to analyse signals with time-varying amplitude and frequency (PPG here) (Wachowiak et al., 2018) and Voices per Octave was selected as 12 to keep the computational complexity low (Wachowiak et al., 2018). The 30 s period for plotting scalograms was selected based on initial exploratory scalogram plotting to select meaningful T-F resolution and hence extract meaningful features from the scalogram images. Noting that with the uncertainty principle, the greater length of time window means that frequency resolution is higher but time resolution is lower, and *vice versa*. Hence, for the data under consideration a 30 s epoch provided a reasonable trade-off between the time and frequency resolutions. Figure 3 shows a 30 s sample scalogram with frequencies ranging from 0–20 Hz (noting each PPG was already bandpass filtered in this range using analogue electronics

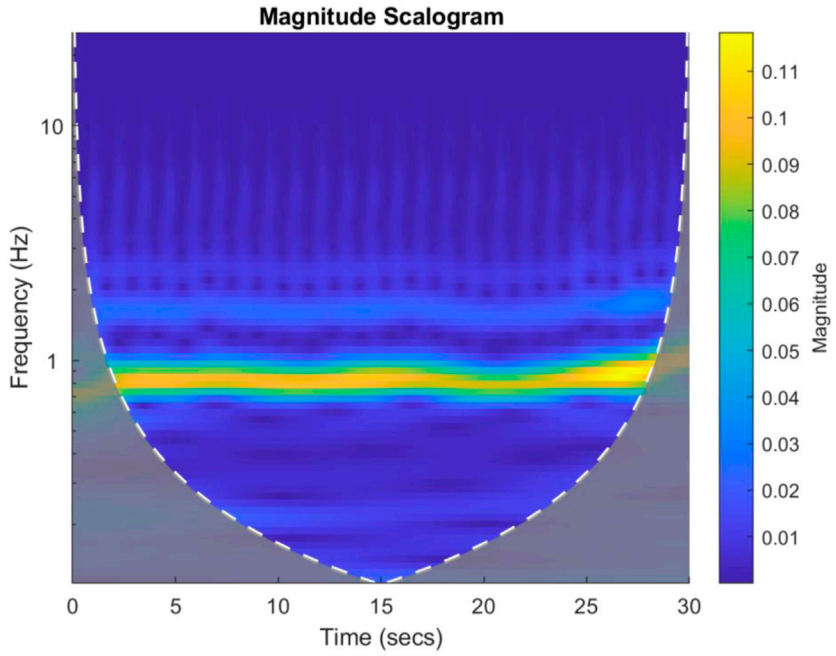

FIGURE 3
An example 30 s scalogram from a Control subject. The magnitude of the scalogram is shown in the colour bar to the right of the image. The brighter colours represent higher signal energy at a particular frequency.

during physiological data acquisition). The scalogram was calculated using Eqs 1, 2 below:

$$S = |coef.*coef| \text{where coef are the CWT coefficients over a time window} \quad (1)$$

$$\text{Scalogram} = (100 \times S)/\left(\sum S\right) \quad (2)$$

In the first stage, the results were calculated using the number of images that were classified into SSc *versus* Control ('image-based performance'). Two pretrained convolutional neural networks (CNN) from MATLAB were used (GoogLeNet (Szegedy et al., 2015) and EfficientNetB0 (Tan et al., 2019)) to learn the PPG T-F features and then perform the classification. These networks have already been previously trained on millions of high-resolution images from the ImageNet database (Krizhevsky et al., 2017). GoogLeNet (structure comprising 144 layers) was the winner of 2014 ImageNet competition and had least number of parameters (~6.9 million) as compared to other pretrained models available in MATLAB at the time of study. EfficientNetB0 (290 layers) which was introduced in 2019 (parameters ~5.3 million) represents a newer generation of CNNs, based on ResNet design, and had been designed to work better and faster than the hitherto available CNNs (Tan and Le, 2019), giving 2 key types of CNN to implement and explore respective performances. Figure 4 shows the basic building blocks for these two types of CNN network. Figures 5, 6 respectively show the network architectures of GoogLeNet (Szegedy et al., 2015) and EfficientNetB0 (Tan et al., 2019; Tan and Le, 2019).

For the PPG dataset, 16,188 labelled scalogram images were generated for the 71 participants covering all 6 PPG sites, i.e., channels of the multi-site PPG system. The scalogram images were rescaled to 224 × 224 × 3 size to match input dimensions of GoogLeNet and EfficientNetB0 using a standard MATLAB function "imresize" which applies a simple scale transformation to the original image using bicubic interpolation which is a standard algorithm used in image resizing (Hashemi et al., 2015). Data were divided into 10 mini batches (batch size 1620 images) to reduce computational time. The learning rate was 0.005. Optimisation utilised the stochastic gradient descent method (Tian et al., 2023) as this is computationally faster and can converge quicker than other optimisation algorithms. The loss function used was cross-entropy loss. Ten-fold stratified cross validation was carried out on 71 participants wherein 9/10 of the participants' images were used in training and 1 mutually exclusive (1/10 of the participants' images) were used for its testing, this process was repeated 10 times. The image wise combined confusion matrix obtained after 10-fold CV was used to calculate measures of classification performance. The two networks train on the input training data and adapt their weights, to learn the features of the data. The approximate training time in any fold of training was about 240–300 min. The approximate testing time for any test fold was between 20–30 min.

The SSc *versus* Control classification was performed based on number of images and this is called as image-based classification throughout. A post-processing step was also applied which calculated the number of images classified in each category per each individual test participant, to provide SSc *versus* Control classification based on number of participants. In this case, the majority class of images in each test participant was considered as the class of the output label. This was compared against the ground truth label (i.e., SSc diagnosis) which was clinically determined beforehand. The steps and methodology of the DL analysis are summarised in the block diagram in Figure 7.

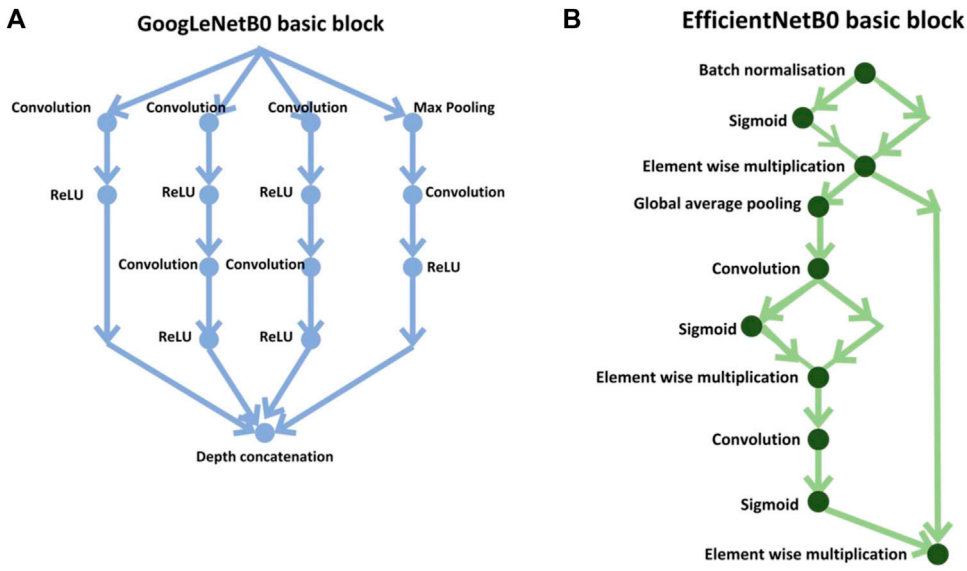

FIGURE 4
Basic building blocks of GoogLeNet and EfficientNetB0 are shown in diagrams **(A,B)**, respectively. The small nodes represent a layer each specified by its name.

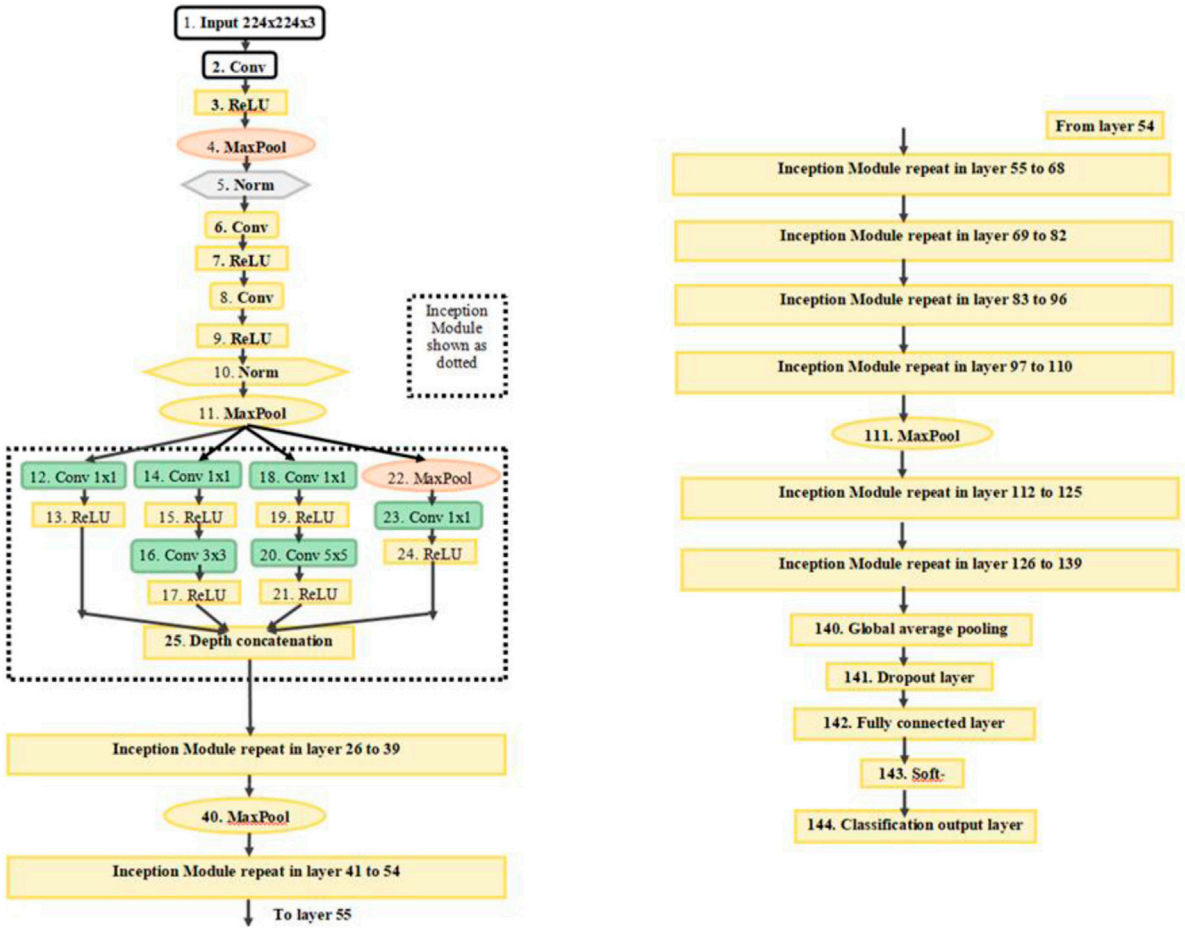

FIGURE 5
The architecture of GoogLeNet. Conv, convolution; Norm, normalization; MaxPool, maximum pooling. The inception modules repeat but filter depth is different in different modules (Szegedy et al., 2015).

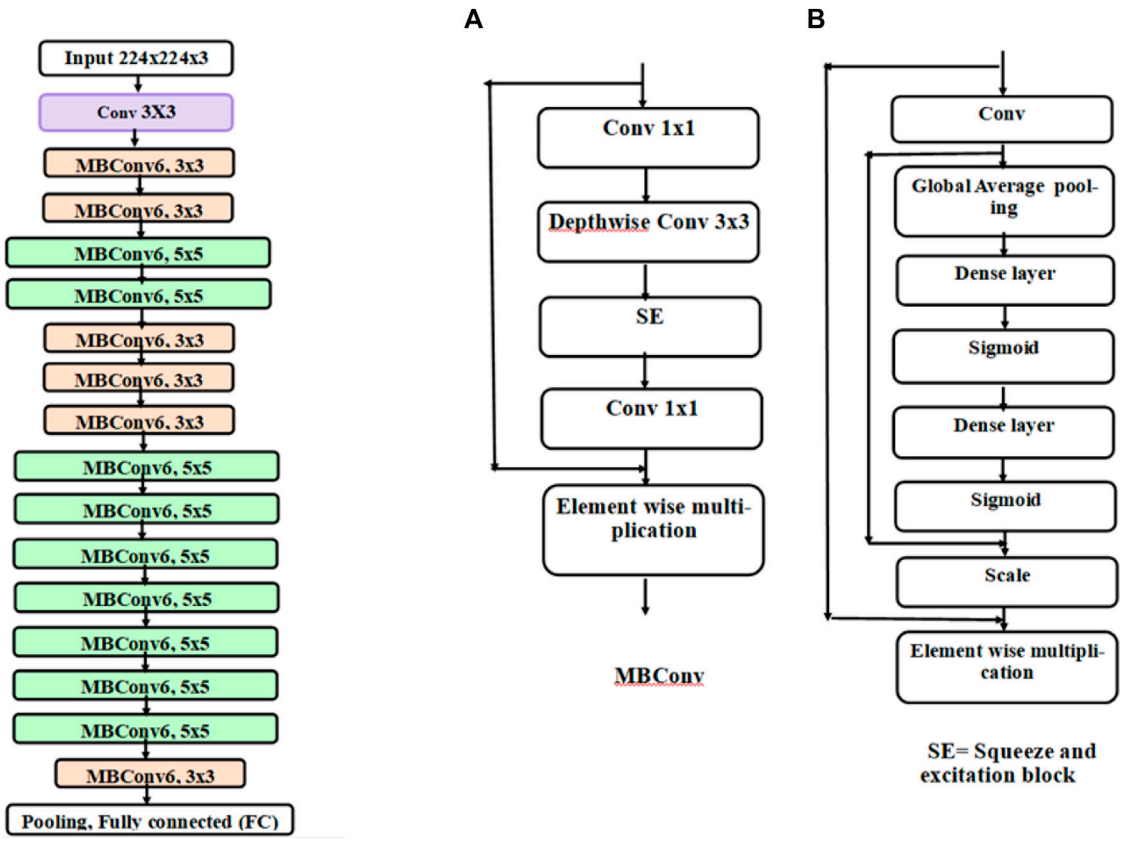

FIGURE 6
Architecture of EfficientNetB0. Each block represented by different colours is made up of different layers. The basic block of EfficientNetB0 is an inverted mobile bottleneck (MBConv) and its structure is shown in diagram **(A)** and the structure of squeeze and excitation (SE) block is shown in diagram **(B)**

2.4 Comparator ML method using wavelet time-frequency classification

This is a comparator ML method using the discrete wavelet transform (DWT) to compare with the performance of the T-F based DL classification. DWT method has advantages over other T-F methods such as CWT such in being computationally faster and the ability to analyse the input signal into desired constituent frequency bands. The same participant-wise partitions of the training/test data sets were used as for the DL classification work to allow a fair inter-comparison between methods.

Ten-level DWT decomposition (Mohamed and Deriche, 2014) was carried out per channel PPG using Daubechies 4 (db4) mother wavelet thereby producing 10 levels of detailed coefficients (d1, d2, ... , d10) and approximate coefficients (shortened as ap in this work) for each channel. The mother wavelet db4 was chosen as it matches the shape of the PPG pulse more than any other wavelet, and hence is the best choice to calculate the wavelet transform of the signal. Since the PPGs had already been bandpass filtered (i.e., 0.5–20 Hz) at data acquisition then only the detailed coefficients containing these relevant frequencies namely, d6 (frequency range 15.63–31.25 Hz), d7 (7.81–15.63 Hz), d8 (3.91–7.81 Hz), d9 (1.95–3.91 Hz), d10 (0.98–1.95 Hz) and ap (0.49–0.98 Hz) were selected for further analysis. To make the computational complexity less and thus the algorithm faster, 4 features were extracted from each of the 6 frequency bands for each channel, thereby giving 6*6*4 = 144 features per participant. PPG features extracted were Energy, Entropy, Mean absolute value and Skewness, as defined in Eqs 3–5.

Energy: Energy of the PPG DWT coefficients is calculated as the sum of the squares of all the sampled amplitudes for a single channel and is defined by Eq. 3:

$$\text{Energy} = \sum_{i=0}^{N} x_i^2 \tag{3}$$

Where x_i, the i^{th} data instance and N are the total number of sample values.

Entropy: Entropy describes the irregularity, complexity, or unpredictability characteristics of a signal. In this work entropy was used as a feature to quantify the irregularity of the PPG time series and hence Shannon entropy was calculated as given by Eq. 4:

$$\text{Entropy} = \sum_{i=1}^{N} \{x_i * log_2(1/x_i)\} \tag{4}$$

Mean absolute value: The absolute value of the average of each channel within the data matrix.

Skewness: Skewness can be used as a measure to describe the asymmetry around the mean of the data sample. If the value of skewness is less than zero, the data has more spread around the left-hand side of the mean, if greater than zero, it is more towards the right-hand side of the mean and if equals to zero, the data can be considered as symmetrically distributed. For a dataset, skewness can be described by Eq. 5:

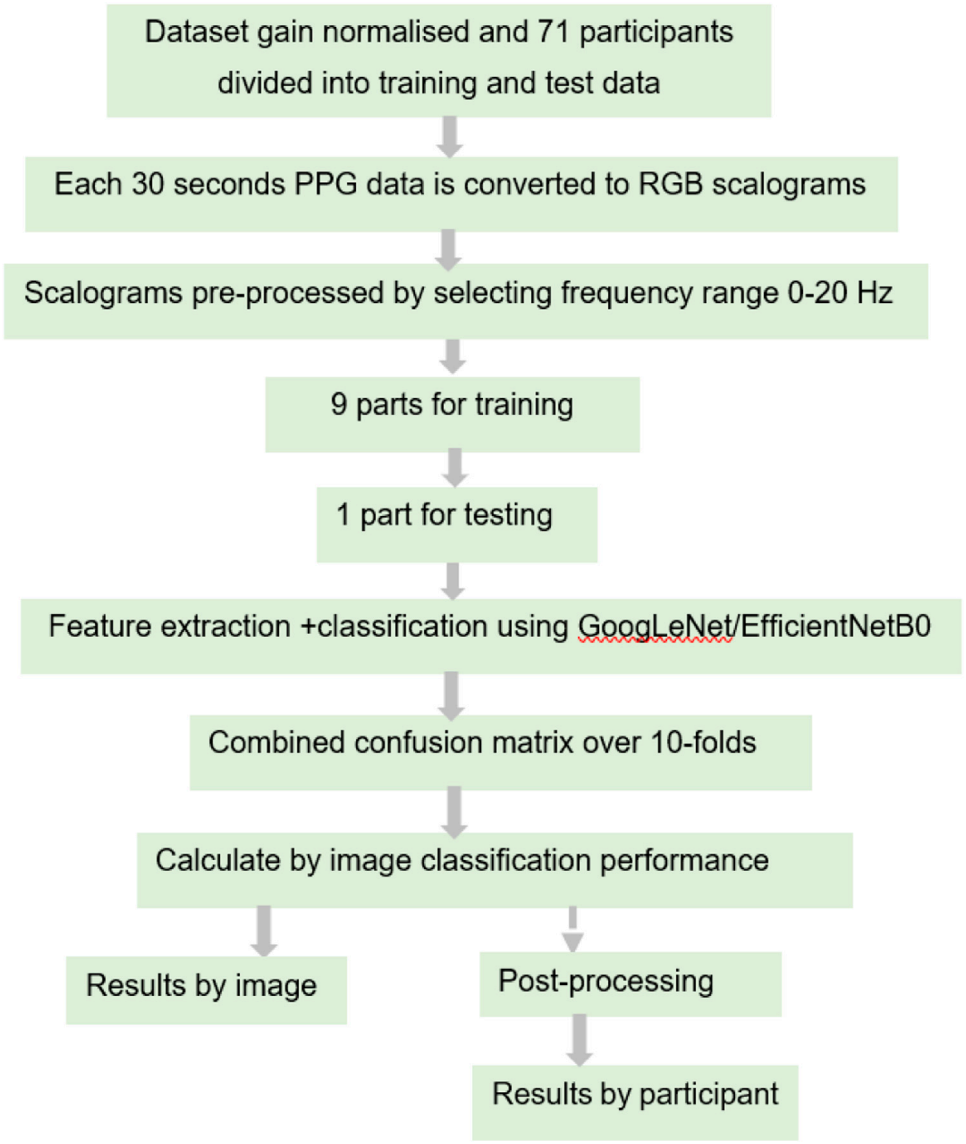

FIGURE 7
Block diagram of the steps and methodology for the DL analysis.

$$\text{Skewness} = \frac{E(x_i - \mu)^3}{\sigma^3} \quad (5)$$

Where μ is the mean of x, σ is the standard deviation of x, and E(t) represents the expected value of the quantity t.

The extracted features were then fed into the linear discriminant analysis (LDA) and into the K-Nearest Neighbour (KNN, set at K = 9) analysis to classify SSc *versus* Control.

2.5 Statistical analysis

Demographic data were expressed using mean (±standard deviation, SD) values. Since the subjects are grouped into 2 distinct SSc and Control classes with each group having independent and different participants, hence unpaired Student's t-test was used to study the mean values of SSc and Control groups. A p-value <0.05 was the level of statistical significance. A crosshair plot illustrating a meta-analysis overview of classifier performance (test sensitivity *versus* False Positive Rate i.e., 1-specificity) was produced using the *mada* command from R (RStudio version 1.4.1106).

3 Results

Table 1 overviews the demographic details for the study participants. Clearly, there were more females than males in the study (18 out of 20 in the SSc group and 45 of 51 in the Control group), but with no significant difference between the groups (p = 0.83). Noting, this is representative as SSc is more prevalent in females than males (van den Hoogen et al., 2013). There was a significant but modest difference for age (p = 0.007) with SSc [62

TABLE 1 Demographic details of the study participants.

Key demographics, with mean (SD values)						
Mean ± SD	Sex	Age (years)	BMI (kg/m^2)	SBP (mmHg)	DBP (mmHg)	Immunology: Specific SSc autoantibodies
HC	23F, 6M	47 (18)	24.1 (3.8)	135 (21)	84 (6)	All presumed negative
PRP	22F, 0M	54 (16)	23.7 (4.0)	138 (16)	84 (7)	All negative
All Controls (HC + PRP)	45F, 6M	50 (18)	23.9 (3.9)	136 (19)	84 (7)	All negative
SSc	18F, 2M	62 (11)	26.4 (4.1)	134 (24)	80 (9)	10 positive
p-value between SSc and Control	Proportion of males between the classes, $p = 0.83$	**0.007**	**0.020**	0.712	0.050	

SD, standard deviation; BMI, body mass index, D/SBP, diastolic/systolic blood pressure, M = male, F = female. Note: the bold numbers in *p* values represent statistically significant levels between Controls and SSc.

TABLE 2 Combined confusion matrix obtained in this analysis for number of image-based classification for GoogLeNet and EfficientNetB0 CNNs.

Number of images classified				
GoogLeNet		SSc	Controls	True class
	SSc	3359 (TP)	1201 (FN)	
	Controls	1517 (FP)	10,111 (TN)	
	Predicted class			
EfficientNetB0	SSc	3666	894	True class
	Controls	989	10,639	
	Predicted class			

TP, true positive; TN, true negative; FP, false positive; FN, false negative.

TABLE 3 Combined confusion matrix of participant-based classification for GoogLeNet and EfficientNetB0 CNNs.

Numbers of participants classified				
GoogLeNet	Number of participants	SSc	Controls	True class
	SSc	15	5	
	Controls	7	44	
	Predicted class			
EfficientNetB0	SSc	16	4	True class
	Controls	5	46	
	Predicted class			

(18) years] older than Controls [50 (11) years] overall. There was a marginally higher BMI for the SSc patient group [26.4 (4.1) kg/m^2] compared to Controls [23.9 (3.9) kg/m^2 ($p = 0.020$). There was no significant difference found for SBP ($p = 0.712$) and borderline significance for the DBP ($p = 0.050$) between the groups.

The key diagnostic test related results (in %) and the respective 95% CI ranges for image based and participant based SSc *versus* Control classification analyses are summarised in Tables 2–5. For image-based classification the diagnostic test accuracy for GoogLeNet was 83.2 (95% CI range 82.6–83.8) %, sensitivity 73.7 (72.4–74.9) and specificity 86.9 (86.3–87.6). Performance was improved for EfficientNetB0 with 88.4 (87.8–88.8) %, 80.4 (79.2–81.5) and 91.5 (90.9–91.9), respectively. For participant-based classification the diagnostic test accuracy for GoogLeNet was 83.1 (72.3–90.9) %, sensitivity 75.0 (50.9–91.3) and specificity 86.3 (73.7–94.3), and once again the performance was improved for EfficientNetB0 with 87.3 (77.2–94.0) %, 80.0 (56.3–94.3), and 90.1 (78.6–96.7), respectively.

DL was also compared against traditional ML T-F wavelet classification using the KNN and LDA classifiers. The results of the T-F ML analysis in terms of diagnostic test accuracy, sensitivity and specificity are shown in Table 6. Using the LDA classifier the diagnostic test accuracy obtained for subject based classification was 66.2 (53.9–77.0) %, sensitivity 65.0 (40.8–84.6) % and specificity 66.7 (52.1–79.2) %. Using the KNN classifier the diagnostic test accuracy obtained for subject based classification was 76.1 (64.5–85.4) %, sensitivity 40.0 (19.1–63.9) and specificity 90.2 (78.6–96.7) %. The 95% CI range for accuracy, sensitivity and specificity for participant-based classification in DL was 72.3%–94.0%, 50.9%–94.3% and 73.7%–96.7% respectively, whereas the corresponding performance range for the ML experiment was 53.9%–85.4%, 19.1%–84.6%, and 52.1%–96.7% respectively.

4 Discussion

This pilot study has shown that AI analysis, i.e., using 2 different types of deep learning classifier, can differentiate between the PPG recordings from Controls and SSc on a participant-basis and give approximate test accuracies of 83% (for GoogLeNet, released circa 2014) and 87% (for EfficientNetB0, released circa 2019). Figure 8 shows crosshair plot showing the comparison of performance of the four classifiers used. The overall test performance of EfficientNetB0 is marginally better overall than GoogLeNet but both CNNs were clearly better than the conventional ML classification approaches (i.e., LDA and KNN, accuracies were only 66% and 76%, respectively).

Previous published research studies on SSc diagnostics using PPG data, particularly Rosato et al. (2010), Rosato et al. (2011), McKay et al. (2014) and Mamontov et al. (2020), had each relied on statistical and manual analysis approaches to differentiate between

TABLE 4 Performance of image-based classification and participant-based classification for GoogLeNet in terms of diagnostic test accuracy, sensitivity and specificity (95% CI range estimates shown).

GoogLeNet CNN model diagnostic test performance (%) along with their 95% CI ranges		
	Image-based	Participant-based
Accuracy (%)	83.2 (82.6–83.8)	83.1 (72.3–90.9)
Sensitivity (%)	73.7 (72.4–74.9)	75.0 (50.9–91.3)
Specificity (%)	86.9 (86.3–87.6)	86.3 (73.7–94.3)

TABLE 5 Performance of image-based classification and participant-based classification for EfficientNetB0 in terms of diagnostic test accuracy, sensitivity and specificity (95% CI range estimates shown).

EfficientNetB0 CNN model diagnostic test performance (%) along with their 95% CI ranges		
	Image-based	Participant-based
Accuracy (%)	88.4 (87.8–88.8)	87.3 (77.2–94.0)
Sensitivity (%)	80.4 (79.2–81.5)	80.0 (56.3–94.3)
Specificity (%)	91.5 (90.9–91.9)	90.1 (78.6–96.7)

TABLE 6 Performance of LDA and KNN comparator machine learning classifiers on a participant-basis in terms of diagnostic test accuracy, sensitivity and specificity (95% CI range estimates shown).

Machine learning (ML) model diagnostic test performance (%) along with their 95% CI ranges for participant-based classification		
	LDA	KNN
Accuracy (%)	66.2 (53.9–77.0)	76.1 (64.5–85.4)
Sensitivity (%)	65.0 (40.8–84.6)	40.0 (19.1–63.9)
Specificity (%)	66.7 (52.1–79.2)	90.2 (78.6–96.7)

subject groups. Manual analysis limits the ability of these techniques to be implemented in practical clinical test settings and for larger datasets. To the best of the authors' knowledge (literature search made to January 2023), there are no studies on contact-based PPG measurements for the study of SSc using DL analytics. In our work we also aimed to fill in the gaps found in the earlier SSc PPG literature. SSc is also a growing area of interest using deep learning and skin histology type imaging, for example, the recent pilot study by Akay et al., 2021.

Advantages with our measurement and analysis approach: This DL-PPG proof-of-concept study presents a straightforward and effective method using deep learning as compared to conventional ML and statistical analysis approaches of differentiating between subject groups. The transfer learning ability of CNNs previously trained on thousands to millions of non-medical images allows quicker retraining on the disease specific dataset, thereby saving time and computational cost. DL eliminates the need to collect an ECG signal to give a cardiac timing reference as in conventional analysis of the PPG features on a beat-by-beat basis. CNNs can learn hundreds of features automatically from the data, thereby eliminating the need to extract key PPG features by domain experts.

Two different CNN architectures, namely, GoogLeNet and EfficientNetB0, have been employed in this research as they both have been trained on the same ImageNet database (Krizhevsky et al., 2017) and have same input dimension of 224 × 224 × 3. However, the 2 structures are different with GoogLeNet having 144 layers and approximately 6.9 million parameters (Tan and Le, 2019) and EfficientNetB0 having 290 layers but a smaller number (i.e., ~5.3 million) parameters. The initial layers of a CNN learn low level features from the input images such as edges whilst the deeper level layers learn advanced features of input images such as constituent parts (LeCun et al., 2015). The CNN acts as a classifier too and the last layer namely, the output layer contains as many output nodes as the number of classes of data fed into the network. In this work, the 71 participants were first partitioned into 10-folds using stratified CV, wherein 9 folds of subjects are used for training the network and the remaining 1-fold of subjects were used for its testing. The participant-based division we employed ensured that the data from same subject does not fall into training and testing simultaneously which could have led to testing the same type of images as in training and hence falsely exaggerated the performance.

In this work, first T-F image-based classification of SSc from Controls was carried out. This was done because the PPG recordings were converted into a series of images and the classifiers trained using these. Then using post-processing, the classification was performed using the participants classified into SSc and Control classes, which is clinically and practically the desired case. Figure 6 shows that more recent CNN EfficientNetB0 has higher sensitivity

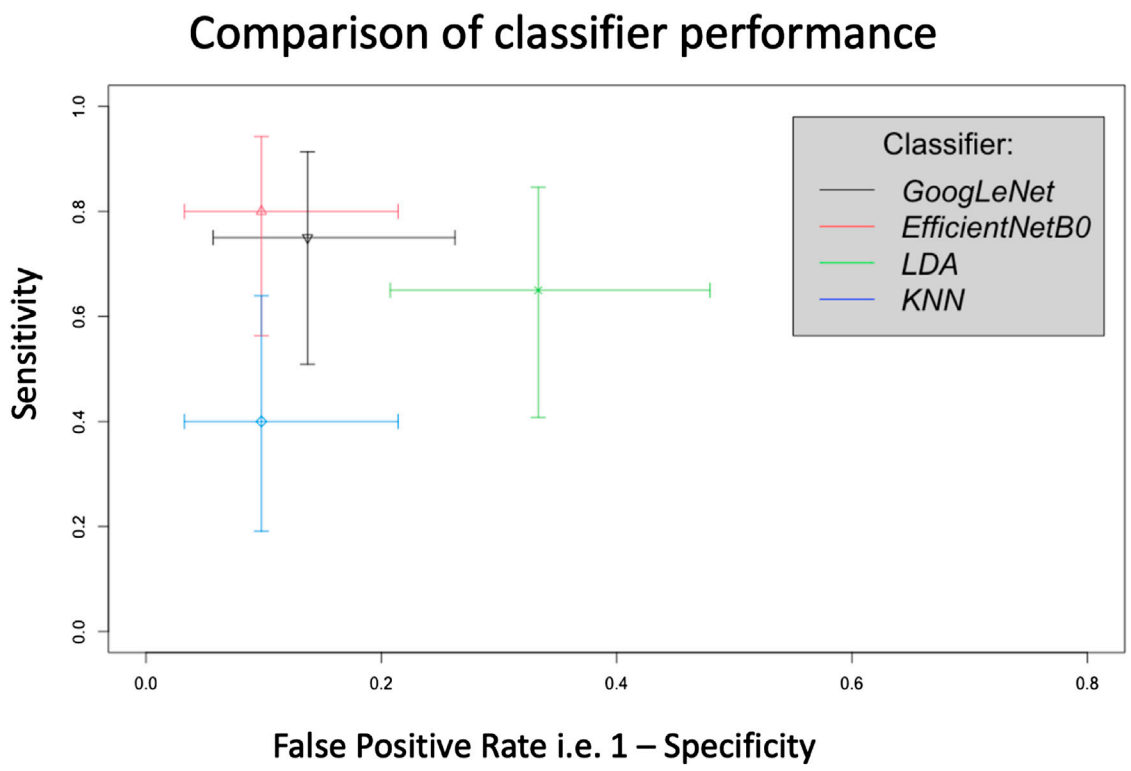

FIGURE 8
Crosshair plot giving a comparison of classifier performance using test sensitivity *versus* false positive rate (i.e., 1-specificity) for SSc *versus* Control on a participant basis. In this representation a sensitivity of 1 = 100% and similarly for the false positive rate.

and specificity and hence produced a better classification performance as compared to GoogLeNet. This could be due to EfficientNetB0 having more layers than other CNN GoogLeNet and hence learning more features from the input data, whilst computing faster (Tan et al., 2019). Future studies could investigate the effects of changing the network parameters to study effects on classification performance. It also shows that both DL architectures, namely, GoogLeNet and EfficientNetBo, can give higher performance in terms of sensitivity and specificity as compared to ML classifiers namely, LDA and KNN. This is because both types of CNN extract several hundreds of features from inputs thereby learning the inherent details of the data, as compared to tens of features chosen manually for the traditional ML classification techniques.

Another point to mention is the good sensitivities (in percent for participant based) of DL architectures namely, GoogLeNet having 75.0 (95% CI 50.9–91.3) % and EfficientNetB0 having 80.0 (56.3–94.3) %. These could be considered better than for the specific antibody blood tests performance summarised in Table 7 since only 10 of the 20 (50%) SSc participants were positive for either the ACA or Scl-70 autoantibodies. It is noted that there is now easier access to extended scleroderma autoantibody panels but at the time of the original PPG data collection only 2 antibody tests were available (ACA and Scl70). High accuracy is of course very important to help make this PPG-based SSc classification technique clinically relevant. Clinically because of the morbidity and mortality involved in SSc, it is particularly important to identify all such patients and therefore the sensitivity of the test should be high. Specificity should also be high as falsely labelling a person who has not got the disease could lead to unnecessary further testing (inefficient use of time and resources) as well as likely significant anxiety for the patient. The ultimate gold standard of diagnosing SSc remains the expertise of the clinicians but this work shows the potential of DL-based classification using PPG to help screen SSc patients in the future. In future this study could be carried out on a bigger dataset comprising a greater number of SSc and control participants to further validate our initial findings. The pilot work also helps in the design of advanced analysis sub-systems of PPG technology for SSc diagnostics.

Limitations and Future Work: In this pilot study there were 20 SSc and 51 Control participants analysed and thus had a degree of imbalance between the classes. The groups were not fully-age-matched either although the age difference here could be considered modest in terms of vascular ageing. Future wider studies, involving more patients should explore the impact of matching across age, BMI and blood pressure. Our study was sufficient though to show the capability of the DL-PPG approach as well as highlight its opportunities and challenges. Stratified cross validation had been used to ensure equal division of minority class cross the different training folds. In this work the patient control PRP participants have been grouped with HC to form the combined Control class because of the clinical relevance of finding life threatening disease cases against the non-life-threatening control cases. The sensitivity or accuracy of classification had also not been maximised. Future studies will address these limitations to study the

TABLE 7 Clinical summary for the 20 SSc participants included in the study.

1	Disease subtype, number (% out of total participants)	11 diffuse cutaneous SSc (55%) 9 limited cutaneous SSc (45%)
2	Disease phase, n (%)	Early: 5 (25%)
		Intermediate/late: 13 (65%), 2 missing data
3	SSc specific autoantibodies, n (%)	Scl70 positive 4 (20%)
		ACA positive 6 (30%)
4	MRSS for the 17 sites (maximum possible score 51)	
	Median (IQR)	4 (11)
	Range	(1–33)
5	Finger digital ulcers, n (%)	6 (30%)
6	Ulcers (foot), n (%)	3 (15%)
7	Capillaroscopy abnormal, n (%)	9 (45%)
8	Thermography abnormal, n (%)	7 (35%)
9	Patients with CRP >5 mg/L, n (%)	4 (20%)
10	SHAQ, mean (range)	9 (2–22)

ACA, anticentromere antibody; MRSS, modified rodnan skin score; IQR, interquartile range, CRP = C-Reactive Protein, SHAQ, Scleroderma Health Assessment Questionnaire.

effect on classification performance by including a balanced study population and with greater SSc participant numbers. Noting though that SSc is a rare disease and it is not straightforward to recruit patients and collect very large data sets except perhaps across multiple clinical centres specialising in the condition. (Mitchell, 2006; Fagerland, 2012; Goodfellow et al., 2016; Allen et al., 2020; Huthart et al., 2020; Dong et al., 2021; Kyriacou and Allen, 2021; Phillips, 2022; Iqbal, 2023).

5 Summary

We have demonstrated in this first proof-of-concept study that GoogLeNet and EfficientNetB0 DL-PPG analytics can detect SSc with an accuracy of 83.1 (95% CIs 72.3–90.9) % and 87.3 (77.2–94.0) % for participant-based classification, respectively. The results from our novel DL-PPG classification technique appear better than for conventional ML methods. The DL-PPG sensitivity (75.0% and 80.0% for GoogLeNet and EfficientNetB0, respectively) is clearly better than for the standard immunological biomarkers for SSc available at the time our original PPG data collection for the research. DL-PPG has shown promise and should be developed further to become an accessible test for the benefit of patients with Systemic Sclerosis as well as for those with Raynaud's.

Data availability statement

The data analyzed in this study is subject to the following licenses/restrictions: The datasets presented in this article are not readily available because the participants involved at the time of the original data collection did not consent to their PPG measurements being shared openly such as in a public repository. Requests to access these datasets should be directed to Not applicable.

Ethics statement

The studies involving humans were approved by National Research Ethics Service (NRES) Committee Northeast (County Durham and Tees Valley 1 REC, 07/H0905/72 2008), consented also for a future reanalysis of the data. Permission obtained then for re-analysis of the anonymised PPG waveform data for Sadaf Iqbal's PhD studentship project from Newcastle University (Reference 7273/2018 plus with Covid-19 situation/delays an extension to the study 17138/2021). The studies were conducted in accordance with the local legislation and institutional requirements. The participants provided their written informed consent to participate in this study.

Author contributions

JA, JB, and SI contributed to the conception and design of the study. JA and BG made significant contributions to the data collection which stems from an earlier published study. SI performed the experimental analysis. SI and JA wrote the first draft of the manuscript. BG contributed her clinical expertise and guided the writing of the manuscript in this respect. All authors contributed to the article and approved the submitted version.

Funding

This research study was funded by the NIHR Newcastle Biomedical Research Centre (BRC) awarded to the Newcastle upon Tyne Hospitals NHS Foundation Trust and Newcastle University [RES/0100/7528/345, project PI (JA)]. This funding specifically supported the PhD studentship of SI and also

resourced a high-performance computer and software for the work.

Acknowledgments

For the data collection originally used in an earlier study focusing on conventional PPG analysis we acknowledge Dr Neil McKay (Rheumatologist) and the wider clinical rheumatology team including Sister Karen Walker (Connective Tissue Disease nurse specialist), the SSc and Raynaud's participants from the Rheumatology department at Newcastle's Freeman Hospital, as well as the healthy control participants recruited from volunteers from the University of the Third Age (U3A, Wearside Branch) and staff and students from Newcastle Hospitals and Newcastle University.

Conflict of interest

The authors declare that the research was conducted in the absence of any commercial or financial relationships that could be construed as a potential conflict of interest.

Publisher's note

References

Akay, M., Du, Y., Sershen, C. L., Wu, M., Chen, T. Y., Assassi, S., et al. (2021). Deep learning classification of systemic sclerosis skin using the MobileNetV2 model. *IEEE Open J. Eng. Med. Biol.* 2, 104–110. doi:10.1109/OJEMB.2021.3066097

Allen, J., and Howell, K. (2014). Microvascular imaging: techniques and opportunities for clinical physiological measurements. *Physiol. Meas.* 35 (7), R91–R141. doi:10.1088/0967-3334/35/7/R91

Allen, J., O'Sullivan, J., Stansby, G., and Murray, A. (2020). Age-related changes in pulse risetime measured by multi-site photoplethysmography. *Physiol. Meas.* 41 (7), 074001. doi:10.1088/1361-6579/ab9b67

Allen, J. (2007). Photoplethysmography and its application in clinical physiological measurement. *Physiol. Meas.* 28 (3), 1–39. doi:10.1088/0967-3334/28/3/R01

Allen, J., Zheng, D., Kyriacou, P. A., and Elgendi, M. (2021). Photoplethysmography (PPG): state-of-the-art methods and applications. *Physiol. Meas.* 42 (10), 100301. doi:10.1088/1361-6579/ac2d82

Belch, J., Carlizza, A., Carpentier, P. H., Constans, J., Khan, F., Wautrecht, J. C., et al. (2017). ESVM guidelines-the diagnosis and management of Raynaud's phenomenon. *Vasa* 46 (6), 413–423. doi:10.1024/0301-1526/a000661

Castaneda, D., Esparza, A., Ghamari, M., Soltanpur, C., and Nazeran, H. (2018). A review on wearable photoplethysmography sensors and their potential future applications in health care. *Int. J. Biosens. Bioelectron.* 4 (4), 195–202. doi:10.15406/ijbsbe.2018.04.00125

Charlton, P. H., Allen, J., Bailon, R., Baker, S., Behar, J. A., Chen, F., et al. (2023). The 2023 wearable photoplethysmography roadmap. *Physiol. Meas* [In press]. doi:10.1088/1361-6579/acead2

Di Battista, M., Barsotti, S., Orlandi, M., Lepri, G., Codullo, V., Della Rossa, A., et al. (2021). One year in review 2021: systemic sclerosis. *Clin. Exp. Rheumatol.* 39 (131), S3–S12. doi:10.55563/clinexprheumatol/izadb8

Dong, S., Wang, P., and Abbas, K. (2021). A survey on deep learning and its applications. *Comput. Sci. Rev.* 40, 100379. doi:10.1016/j.cosrev.2021.100379

Elgendi, M. (2012). On the analysis of fingertip photoplethysmogram signals. *Curr. Cardiol. Rev.* 8 (1), 14–25. doi:10.2174/157340312801215782

Eriksson, S., Nilsson, J., and Sturesson, C. (2014). Non-invasive imaging of microcirculation: A technology review. *Med. Devices Evid. Res.* 7, 445–452. doi:10.2147/MDER.S51426

Fagerland, M. W. (2012). t-tests, non-parametric tests, and large studies—a paradox of statistical practice? *BMC Med. Res. Methodol.* 12 (1), 78. doi:10.1186/1471-2288-12-78

Gandhi, P. G., and Rao, G. H. (2014). The spectral analysis of photoplethysmography to evaluate an independent cardiovascular risk factor. *Int. J. General Med.* 7, 539–547. doi:10.2147/IJGM.S70892

Goodfellow, I., Bengio, Y., and Courville, A. (2016). *Deep learning*. MIT press. Cambridge, CA, USA,

Haque, A., and Hughes, M. (2020). Raynaud's phenomenon. *Clin. Med.* 20 (6), 580–587. doi:10.7861/clinmed.2020-0754

Hashemi, S. M. R., Mohammadalipour, S., and Broumandnia, A. (2015). Evaluation and classification new algorithms in Image Resizing. *Int. J. Mechatronics, Electr. Comput. Technol.* 5 (18), 2649–2654.

Hughes, M., and Herrick, A. L. (2016). Raynaud's phenomenon. *Best Pract. Res. Clin. Rheumatology* 30 (1), 112–132. doi:10.1016/j.berh.2016.04.001

Huthart, S., Elgendi, M., Zheng, D., Stansby, G., and Allen, J. (2020). Advancing PPG signal quality and know-how through knowledge translation—From experts to student and researcher. *Front. Digital Health* 2, 619692. doi:10.3389/fdgth.2020.619692

Iqbal, S. (2023). *Multi-site photoplethysmography waveform analysis using machine learning for the detection of systemic sclerosis*. United Kingdom: Newcastle University.

Johnson, M. S. S., and Eklund, J. M. (2020). "A review of photoplethysmography-based physiological measurement and estimation, Part 2: multi-input methods," in 2020 42nd annual international conference of the IEEE engineering in medicine & biology society (EMBC) (IEEE), 863–866. Montreal, Canada,

Krizhevsky, A., Sutskever, I., and Hinton, G. E. (2017). Imagenet classification with deep convolutional neural networks. *Commun. ACM* 60 (6), 84–90. doi:10.1145/3065386

Kyriacou, P. A., and Allen, J. (Editors) (2021). *Photoplethysmography: Technology, signal analysis and applications* (Academic Press). Cambridge, MA, USA

LeCun, Y., Bengio, Y., and Hinton, G. (2015). Deep learning. *Nature* 521 (7553), 436–444. doi:10.1038/nature14539

Liang, Y., Chen, Z., Ward, R., and Elgendi, M. (2018). Photoplethysmography and deep learning: enhancing hypertension risk stratification. *Biosensors* 8 (4), 101. doi:10.3390/bios8040101

Ma, G., Zhu, W., Zhong, J., Tong, T., Zhang, J., and Wang, L. (2018). "Wearable ear blood oxygen saturation and pulse measurement system based on PPG,"2018 IEEE SmartWorld, Ubiquitous Intelligence & Computing, Advanced & Trusted Computing, Scalable Computing & Communications, Cloud & Big Data Computing (IEEE), 111–116. Guangzhou, China.

Mamontov, O. V., Krasnikova, T. V., Volynsky, M. A., Anokhina, N. A., Shlyakhto, E. V., and Kamshilin, A. A. (2020). Novel instrumental markers of proximal scleroderma provided by imaging photoplethysmography. *Physiol. Meas.* 41 (4), 044004. doi:10.1088/1361-6579/ab807c

McKay, N. D., Griffiths, B., Di Maria, C., Hedley, S., Murray, A., and Allen, J. (2014). Novel photoplethysmography cardiovascular assessments in patients with Raynaud's phenomenon and systemic sclerosis: A pilot study. *Rheumatology* 53 (10), 1855–1863. doi:10.1093/rheumatology/keu196

Mitchell, T. M. (2006). *The discipline of machine learning*, 9. Pittsburgh, PA, USA: Carnegie Mellon University, School of Computer Science, Machine Learning Department.

Mohamed, M., and Deriche, M. (2014). An approach for ECG feature extraction using daubechies 4 (DB4) wavelet. *Int. J. Comput. Appl.* 96 (12), 36–41. doi:10.5120/16850-6712

NHSinform (2023). NHSinform. https://www.nhsinform.scot/illnesses-and-conditions/heart-and-blood-vessels/conditions/raynauds-phenomenon#complications-of-raynaud-s-phenomenon.

Pauling, J. D., Saketkoo, L. A., Matucci-Cerinic, M., Ingegnoli, F., and Khanna, D. (2019). The patient experience of Raynaud's phenomenon in systemic sclerosis. *Rheumatology* 58 (1), 18–26. doi:10.1093/rheumatology/key026

Phillips, R. (2022). Evaluating early diagnostic criteria for SSc. *Nat. Rev. Rheumatol.* 18 (2), 62. doi:10.1038/s41584-021-00745-5

Rosato, E., Molinaro, I., Rossi, C., Pisarri, S., and Salsano, F. (2011). The combination of laser Doppler perfusion imaging and photoplethysmography is useful in the characterization of scleroderma and primary Raynaud's phenomenon. *Scand. J. Rheumatology* 40 (4), 292–298. doi:10.3109/03009742.2010.530293

Rosato, E., Rossi, C., Borghese, F., Molinaro, I., Pisarri, S., and Salsano, F. (2010). The different photoplethysmographic patterns can help to distinguish patients with primary and sclerodermic Raynaud phenomenon. *Am. J. Med. Sci.* 340 (6), 457–461. doi:10.1097/MAJ.0b013e3181eecfad

Royle, J. G., Lanyon, P. C., Grainge, M. J., Abhishek, A., and Pearce, F. A. (2018). The incidence, prevalence, and survival of systemic sclerosis in the UK Clinical Practice Research Datalink. *Clin. Rheumatol.* 37, 2103–2111. doi:10.1007/s10067-018-4182-3

Silva, I., Teixeira, G., Bertão, M., Almeida, R., Mansilha, A., and Vasconcelos, C. (2016). Raynaud phenomenon. *Rev. Vasc. Med.* 4, 9–16. doi:10.1016/j.rvm.2016.03.001

Spencer-Green, G. (1998). Outcomes in primary Raynaud phenomenon: A meta-analysis of the frequency, rates, and predictors of transition to secondary diseases. *Archives Intern. Med.* 158 (6), 595–600. doi:10.1001/archinte.158.6.595

SRUK, (2023). Sruk. https://www.sruk.co.uk/raynauds/.

Subcommittee for Scleroderma Criteria of the American Rheumatism Association Diagnostic and Therapeutic Criteria Committee, (1980). Preliminary criteria for the classification of systemic sclerosis (scleroderma). Subcommittee for scleroderma criteria of the American Rheumatism Association Diagnostic and Therapeutic Criteria Committee. *Arthritis Rheum.* 23, 581–590. doi:10.1002/art.1780230510

Szegedy, C., Liu, W., Jia, Y., Sermanet, P., Reed, S., Anguelov, D., et al. (2015). "Going deeper with convolutions," in Proceedings of the IEEE conference on computer vision and pattern recognition, 1–9. Boston, MA, United States.

Tan, M., Chen, B., Pang, R., Vasudevan, V., Sandler, M., Howard, A., et al. (2019). "Mnasnet: platform-aware neural architecture search for mobile," in Proceedings of the IEEE/CVF conference on computer vision and pattern recognition, 2820–2828. Long Beach, CA, USA.

Tan, M., and Le, Q. (2019). "Efficientnet: rethinking model scaling for convolutional neural networks," in International conference on machine learning, 6105–6114. Long Beach, CA, USA,.

Tian, Y., Zhang, Y., and Zhang, H. (2023). Recent advances in stochastic gradient descent in deep learning. *Mathematics* 11 (3), 682. doi:10.3390/math11030682

van den Hoogen, F., Khanna, D., Fransen, J., Johnson, S. R., Baron, M., Tyndall, A., et al. (2013). 2013 classification criteria for systemic sclerosis: an American College of rheumatology/European league against rheumatism collaborative initiative. *Arthritis Rheum.* 65 (11), 2737–2747. doi:10.1002/art.38098

Wachowiak, M. P., Wachowiak-Smolíková, R., Johnson, M. J., Hay, D. C., Power, K. E., and Williams-Bell, F. M. (2018). Quantitative feature analysis of continuous analytic wavelet transforms of electrocardiography and electromyography. *Philosophical Trans. R. Soc. A Math. Phys. Eng. Sci.* 376 (2126), 20170250. doi:10.1098/rsta.2017.0250

Walker, U. A., Tyndall, A., Czirjak, L., Denton, C., Farge-Bancel, D., Kowal-Bielecka, O., et al. (2007). Clinical risk assessment of organ manifestations in systemic sclerosis: A report from the EULAR scleroderma trials and research group database. *Ann. Rheum. Dis.* 66 (6), 754–763. doi:10.1136/ard.2006.062901

frontiers | Frontiers in Physiology

TYPE Original Research
PUBLISHED 25 September 2023
DOI 10.3389/fphys.2023.1175470

OPEN ACCESS

EDITED BY
John Allen,
Coventry University, United Kingdom

REVIEWED BY
Haipeng Liu,
Coventry University, United Kingdom
Shaoxiong Sun,
King's College London, United Kingdom

*CORRESPONDENCE
Zehava Ovadia-Blechman,
zehava@afeka.ac.il

RECEIVED 27 February 2023
ACCEPTED 11 September 2023
PUBLISHED 25 September 2023

CITATION
Ovadia-Blechman Z, Hauptman Y, Rabin N, Wiezman G, Hoffer O, Gertz SD, Gavish B and Gavish L (2023), Morphological features of the photoplethysmographic signal: a new approach to characterize the microcirculatory response to photobiomodulation. *Front. Physiol.* 14:1175470. doi: 10.3389/fphys.2023.1175470

Morphological features of the photoplethysmographic signal: a new approach to characterize the microcirculatory response to photobiomodulation

Zehava Ovadia-Blechman[1]*, Yermiyahu Hauptman[2], Neta Rabin[3], Gal Wiezman[1], Oshrit Hoffer[4], S. David Gertz[5,6], Benjamin Gavish[7] and Lilach Gavish[5,6]

[1]School of Medical Engineering, Afeka Tel-Aviv Academic College of Engineering, Tel Aviv, Israel, [2]ACLP—The Center for Language Processing, Afeka Tel-Aviv Academic College of Engineering, Tel Aviv, Israel, [3]Department of Industrial Engineering, The Iby and Aladar Fleischman Faculty of Engineering, Tel-Aviv University, Tel Aviv, Israel, [4]School of Electrical Engineering, Afeka Tel-Aviv Academic College of Engineering, Tel Aviv, Israel, [5]Faculty of Medicine, Institute for Research in Military Medicine (IRMM), The Hebrew University of Jerusalem and the Israel Defense Forces Medical Corps, Jerusalem, Israel, [6]The Saul and Joyce Brandman Hub for Cardiovascular Research and the Department of Medical Neurobiology, Faculty of Medicine, Institute for Medical Research (IMRIC), The Hebrew University of Jerusalem, Jerusalem, Israel, [7]Yazmonit Ltd, Jerusalem, Israel

Introduction and Objectives: Advanced analysis of the morphological features of the photoplethysmographic (PPG) waveform may provide greater understanding of mechanisms of action of photobiomodulation (PBM). Photobiomodulation is a non-ionizing, red to near-infrared irradiation shown to induce peripheral vasodilatation, promote wound healing, and reduce pain. Using laser Doppler flowmetry combined with thermal imaging we found previously in a clinical study that PBM stimulates microcirculatory blood flow and that baseline palm skin temperature determines, at least in part, why some individuals respond favorably to PBM while others do not. "Responders" (n = 12) had a skin temperature range of 33°C–37.5°C, while "non-responders" (n = 8) had "cold" or "hot" skin temperature (<33°C or >37.5°C respectively). The continuous PPG signals recorded from the index fingers of both hands in the original clinical study were subjected to advanced post-acquisitional analysis in the current study, aiming to identify morphological features that may improve the accuracy of discrimination between potential responders and non-responders to PBM.

Methods: The PPG signals were detrended by subtracting the lower envelope from the raw signal. The Root Mean Square (RMS) and Entropy features were extracted as were two additional morphological features -- Smoothness and number of local extrema per PPG beat (#Extrema). These describe the signal jaggedness and were developed specifically for this study. The Wilcoxon test was used for paired comparisons. Correlations were determined by the Spearman correlation test (r_s).

Results: The PPG waveforms of responders to PBM had increased amplitude and decreased jaggedness (Baseline vs. 10′ post-irradiation: Entropy, 5.0 ± 1.3 vs. 3.9 ± 1.1, $p = 0.012$; #Extrema, 4.0 ± 1.1 vs. 3.0 ± 1.6, $p = 0.009$; RMS, 1.6 ± 0.9 vs. 2.3 ± 1.2, $p = 0.004$; Smoothness, 0.10 ± 0.05 vs. 0.19 ± 0.16, $p = 0.016$). In addition, unilateral irradiation resulted in a bilateral response, although the response of the

contralateral, non-irradiated hand was shorter in duration and lower in magnitude. Although subjects with 'cold,' or 'hot,' baseline skin temperature appeared to have morphologically distinct PPG waveforms, representing vasoconstriction and vasodilatation, these were not affected by PBM irradiation.

Conclusion: This pilot study indicates that post-acquisitional analysis of morphological features of the PPG waveform provides new measures for the exploration of microcirculation responsiveness to PBM.

KEYWORDS

photoplethysmography, waveform, photobiomodulation, low-level laser, entropy, signal processing, peripheral microcirculation

1 Introduction

Photoplethysmography (PPG) is a non-invasive, inexpensive optical technique that can detect relative changes in the quantity of red blood cells (RBC) in the peripheral microcirculation (Allen, 2007; Nitzan and Ovadia-Blechman, 2022). PPG is widely accepted for monitoring pulsations associated with local blood volume changes assuming a constant RBC concentration (Ovadia et al., 1995; Kyriacou and Chatterjee, 2022). Previous studies have shown that PPG can detect compensatory changes in local blood flow as well as predict changes in systemic hemodynamic variables during a variety of physiological and pathological conditions (Ovadia et al., 1995; Allen, 2007; Ovadia-Blechman et al., 2015a; Ovadia-Blechman et al., 2015b; Ovadia-Blechman et al., 2017; Ovadia-Blechman et al., 2018; Ahmed et al., 2022). Moreover, using PPG monitoring, changes in peripheral blood supply following a unilateral clinical intervention can exert significant contralateral effects, the characterization of which may be further elucidated by advanced post-acquisitional analysis of the PPG signals (Ahmed et al., 2022; Allen, 2022; Mejia-Mejia et al., 2022).

In recent years, advanced morphological analysis of the PPG signal has contributed to a better understanding of the underlying physiological mechanisms associated with various normal and pathological conditions with particular effort seen in various fields of cardiovascular medicine (Hickey et al., 2015; Goshvarpour and Goshvarpour, 2020; Qawqzeh et al., 2020; Vasyltsov and Lee, 2020; Ahmed et al., 2022; Allen, 2022; Mejia-Mejia et al., 2022; Roy et al., 2022). Alterations in features such as entropy, that reflects the level of signal disorder, allow for more precise characterization of the morphology of the signals that may improve clinical diagnosis (Wei et al., 2020; Hauptman et al., 2019).

Photobiomodulation (PBM) is a non-ionizing, red to near-infrared optical irradiation that stimulates and/or stabilizes mitochondrial membrane potential and ATP production, reduces pro-inflammatory mediators, and increases cell proliferation (Pastore et al., 1996; Gavish et al., 2004; Gavish et al., 2008; Passarella and Karu, 2014; Hamblin, 2018; Gavish et al., 2021). It is widely used clinically to reduce pain and accelerate wound healing (Avci et al., 2013; Chow, 2016; Oyebode et al., 2021). PBM was shown to stimulate vasodilatation and increase peripheral blood flow (Schindl et al., 1998; Schindl et al., 2002; Samoilova et al., 2008a; Samoilova et al., 2008b). This effect is based at least in part on the upregulation by PBM of synthesis and secretion of nitric oxide (NO) and modification of reactive oxygen species (Vladimirov et al., 2000; Chen et al., 2008; Gavish et al., 2008; Chen et al., 2022; Keszler et al., 2022). In a previous study using laser Doppler flowmetry and thermal imaging, PBM was found to increase microvascular flow (Gavish et al., 2020) and that those that did not respond were found to have either 'hot' or 'cold' hand with skin temperature at baseline being >37.5°C or <33°C respectively (Gavish et al., 2020).

The current pilot study involves advanced post-acquisitional analysis of PPG signal recordings collected from the index fingers of both hands in the previous study (Gavish et al., 2020). This post-acquisitional study will interrogate previously validated as well as novel morphological features of the PPG signal. Its purpose is to identify morphological features of the PPG signal that may increase the accuracy of prediction of those likely to respond favorably to PBM treatment and those who may not respond and to quantify the bilateral response using these features.

2 Methods

2.1 Study overview

This study is a subgroup analysis consisting of advanced post-acquisitional processing of PPG signals collected previously (Gavish et al., 2020), NCT03357523). The study analyses and compares PPG recordings of responders and non-responders (NR) to PBM. The criterion for dividing the participants into responders (n = 12) and non-responders (n = 8) in the original study was an increase of ≥0.5°C which is accepted as a deviation from the normal symmetrical thermal distribution between sides of the body extremities (Ammer, 2012; Garcia Becerra et al., 2022) and was found to indicate underlying pathologies (Suominen and Asko-Seljavaara, 1996; Selfe et al., 2008). In the original study (Gavish et al., 2020), this criterion was used as a threshold for dynamic changes in thermal response to PBM.

This created 3, non-overlapping subgroups according to baseline skin temperature. "Responders" to PBM had a range of skin temperature from 33°C to 37.5°C, while "non-responders" to PBM had "cold" or "hot" skin temperature (<33°C or >37.5°C respectively). The original study was approved by the Afeka Institutional Ethics Review Board (05.04.2017-1-AFK), and all participants signed an informed consent form prior to inclusion.

The study population included 20, healthy, adult, non-smoking volunteers (10:10 males: females, 30 ± 8 years old) that were randomized to receive either red or near infrared PBM irradiation (633 nm, power density = 70 mW/cm^2; total energy per session 21 J/cm^2; 830 nm, 55 mW/cm^2; 16.5 J/cm^2) using a commercial light emitting diode (LED) cluster (Omnilux new-U,

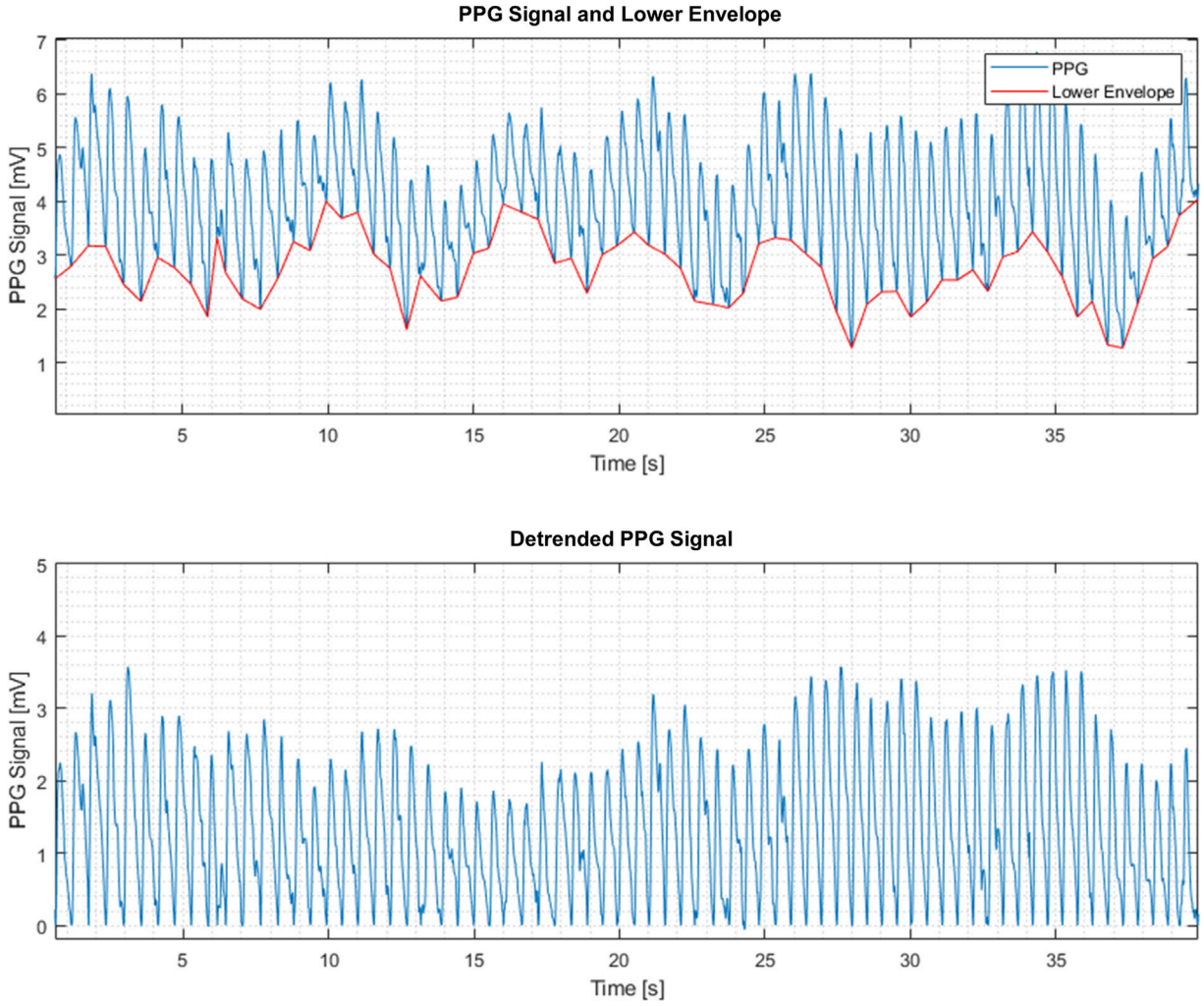

FIGURE 1
Raw (top) and detrended (bottom) PPG signals.

Photomedex United States). The LaserMate power-meter (Coherent, Auburn group, Coherent-Europe, Utrecht, Holand) was used to confirm the power density at the plane of irradiation.

Subjects were requested not to consume any beverages that contained caffeine (coffee, tea, cola, etc.) or alcohol at least 3 h prior to the session. The subjects sat relaxed in a quiet room with constant temperature (25°C ± 1°C) for at least 15 min with exposed hands before data collection. The LED cluster was positioned over the left wrist and switched on for 5 min, while the right hand was protected from the light.

The PPG optical reflective sensors (model SS4LA, wavelength—860 nm) were placed on the index finger of both hands using Velcro® strip (Biopac™ System Inc., Goleta, CA). Both PPG and electrocardiographic (ECG) signals were monitored continuously and sampled at 200 Hz using the Biopac™ software. Skin temperature was measured in the center of the palm by an infrared thermal imaging camera (emissivity = 0.98, Sensitivity = 50 mK) that was positioned above the hands (FLIR A35, FLIR Systems Inc., OR, United States). The thermal camera calibration has undergone factory calibration to be within the manufacturer's accuracy. Signals were collected before PBM irradiation and during irradiation and continued for 20 min after the end of irradiation. The signal processing was performed at the following time periods: half a minute before the irradiation (baseline), the last 3 min of the irradiation, and at follow-up–during 5–10 min, 10–15 min, and 15–20 min after the end of irradiation.

2.2 Signal processing and feature extraction

In general, PPG signals have beats reflecting local blood volume variations in response to the blood pressure fluctuations during the cardiac cycle. PPG maximum and minimum reflect the systolic and diastolic pressures respectively (Figure 1). The PPG beats are superimposed on slower signal variations generated by other dynamic processes, e.g., respiratory activity ("lower envelope" in Figure 1). In addition, the PPG signal contains local minima and maxima that may be physiologically meaningful and that can be studied by the presently described extraction of PPG-signal features.

The PPG signal processing was performed as follows:

10.3389/fphys.2023.1175470

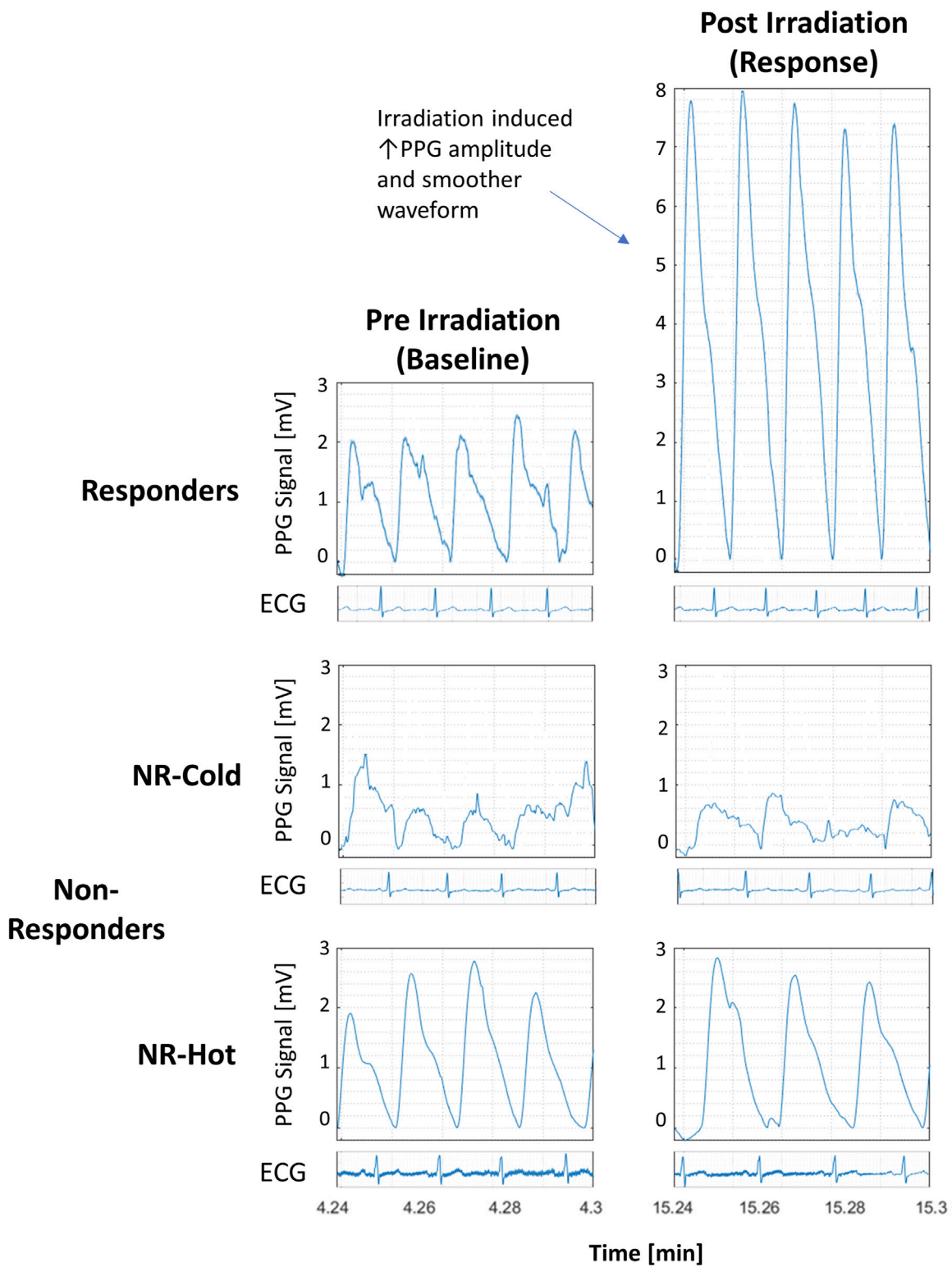

FIGURE 2
Detrended PPG signals from responders and non-responders (NR) to photobiomodulation (PBM) before and 10 min after PBM from 3 participants with accompanying electrocardiographic strips to show synchronicity with the pulse. All graphs are at the same scale.

a. Sampling the PPG signal at 200 Hz and dividing it into consecutive frames. The frame size was 120 s with 3 s stride (97.5% overlap). Thus, each frame consists of N = 24000 samples.

b. Restricting the analysis to the PPG beats by subtracting the lower envelope from the raw PPG signal resulted in a detrended PPG signal, denoted by x(n), where n = 1,2, . . . N as the sample

number (Figure 1). The lower envelope is constructed by finding the lowest point in each PPG beat and connecting these points consecutively by a piecewise linear function.

c. Extracting the following features from each frame of detrended PPG signals:

2.2.1 RMS

RMS stands for the Root Mean Square of a frame of N samples and calculated by Eq. 1 from the detrended PPG signal.

$$RMS = \sqrt{\frac{1}{N}\sum_{n=1}^{N} x^2(n)} \quad (1)$$

2.2.2 Entropy

Entropy is a statistical measure of the randomness of data. This feature indicates the extent of disorder of the signal. Entropy is calculated by Eq. 2, where the Probability Mass Function (PMF), p(i), is the normalized histogram (using 256 bins—i.e., dividing the signal level range into 256 equal parts) of the detrended PPG signal *x(n)*.

$$Entropy = -\sum_{i=1}^{256} p(i) * log_2(p(i)) \quad (2)$$

2.2.3 Smoothness

The average of High Frequency Components (HFC) of the signal is obtained by averaging the absolute values of the differences between the detrended PPG signal $x(n)$ and a filtered signal $x'(n)$ given by Eq. 3.

$$Smoothness = \frac{1}{N}\sum_{n=1}^{N} |x(n) - x'(n)| \quad (3)$$

A moving-average filter given by Eq. 4 is used, where the value of k was set to 30, and x is the detrended PPG signal.

$$x'(n) = \frac{1}{2k+1}\sum_{l=-k}^{+k} x(n+l) \quad (4)$$

2.2.4 Local extrema

This feature counts the number (#) of Extrema points (local maxima or minima) in each beat. The calculation was performed as follows:

(1) The derivative of the detrended PPG signal was calculated using the local polynomial method (De Brabanter et al., 2013).
(2) The sign of the derivative of the detrended PPG signal was calculated. Positive values were set to 1 and negative values were set to −1.
(3) The time index of the sign changes (i.e., from −1 to 1 or *vice versa*) was marked as an extremal point.
(4) If two Extrema points were detected in a time interval that was smaller than 50 ms, only one point was accounted.
(5) The number of Extrema was counted in the calculation frame.
(6) The number of Extrema was divided by the mean heart-rate to obtain the average number per PPG beat.

(See Discussion for additional points related to the morphological features defined in this section.)

2.3 Study outcomes

Study outcomes included the average feature values and the average change from baseline during irradiation and 10, 15, and 20 min during the follow up period.

2.4 Statistics

All participants of the original trial were included. Variables are presented as mean ± SD. Statistical analysis pertained only to the "responders" in view of the sample size. Normality of the data was determined with the Shapiro-Wilk test with a cutoff of $p = 0.1$. The Friedman's test with multiple comparisons was used to compare baseline to other time points (and Holm's modification of Bonferroni's correction for 4 comparisons [HMBC]) and the exact Wilcoxon signed rank test was used to compare irradiated to non-irradiated hands (ratio to baseline) per time point also with HMBC. The Spearman correlation test was used to determine the level of correlation between hands. In order to determine if the improvement in correlation between pre- and post-irradiation was significant, Spearman correlation coefficients (r_s) were computed twice between the right and left hands for each PPG feature—once for pre-irradiation and once for post-irradiation. These were compared using a special adaptation of Fisher's z-transformation (Dunn and Clark, 1969) that can be assumed to be normally distributed in such cases (Silver et al., 2004) and which is suitable for Spearman coefficients (Zar, 2010; Wilcox, 2016) (See supplement). $p < 0.05$ was considered significant.

3 Results

Representative examples of the distinctive PPG waveform for each group before and after irradiation are depicted in Figure 2, and the extracted morphological features, including Entropy, Root Mean Square (RMS), Smoothness, and the number of Extrema per beat (#Extrema) for each time period (baseline, irradiation, and follow up), are presented in Table 1 and Figures 3A–D).

Following irradiation, responders (n = 12) had increased amplitude and decreased jaggedness displaying an increase in RMS and smoothness of 80% and 107% respectively. They had a decrease in Entropy and #Extrema of 21% and 27% respectively (Baseline vs- 10' post-irradiation: Entropy, 5.0 ± 1.3 vs. 3.9 ± 1.1, $p = 0.012$; #Extrema, 4.0 ± 1.1 vs. 3.0 ± 1.6, $p = 0.009$; RMS, 1.6 ± 0.9 vs. 2.3 ± 1.2, $p = 0.004$; Smoothness, 0.10 ± 0.05 vs. 0.19 ± 0.16, $p = 0.016$) (Table 1).

Non-responders (n = 8) with "cold," or "hot," baseline skin temperature appeared to have PPG waveforms that were morphologically distinct from responders. Those with "cold" hands (n = 3) appeared to have the highest Entropy and #Extrema, and the lowest RMS and Smoothness, reflecting a noisy and low-amplitude PPG waveform. By contrast, the signal of those with hot' hands (n = 5) appeared noiseless with the lowest number of Extrema. However, the numbers of subjects in each of these two extreme groups (on the high versus

TABLE 1 Effect of photobiomodulation on the morphological features of the photoplethysmographic waveform.

PPG feature	Irradiated (PBM)				Non-irradiated				Correlation r_s	
	Pre	Post	%	*p**	Pre	Post	%	*p**	Pre	Post
Entropy	5.0 ± 1.3	3.9 ± 1.3	−21%	0.012	5.6 ± 1.6	4.9 ± 1.5	−11%	0.008	0.706	0.853
#Extrema	4.0 ± 1.1	3.0 ± 1.6	−27%	0.009	3.6 ± 1.36	2.87 ± 1.34	−19%	<0.001	0.566	0.923†
RMS	1.57 ± 0.89	2.25 ± 1.22	+80%	0.00	0.97 ± 0.5	1.26 ± 0.74	+31%	<0.001	0.469	0.811
Smoothness	0.10 ± 0.05	0.19 ± 0.16	+107%	0.016	0.07 ± 0.04	0.11 ± 0.06	+61%	<0.001	0.860	0.797

PBM = photobiomodulation (low level laser irradiation), Pre = baseline; Post = 10 min after irradiation; % = Change over baseline; RMS = root mean square; Data = mean ± SD; by Spearman correlation test; *$p < 0.05$ by Friedman's test with multiple comparisons with Holm's modification of Bonferroni's correction; †by modified Fisher's z-transformation.

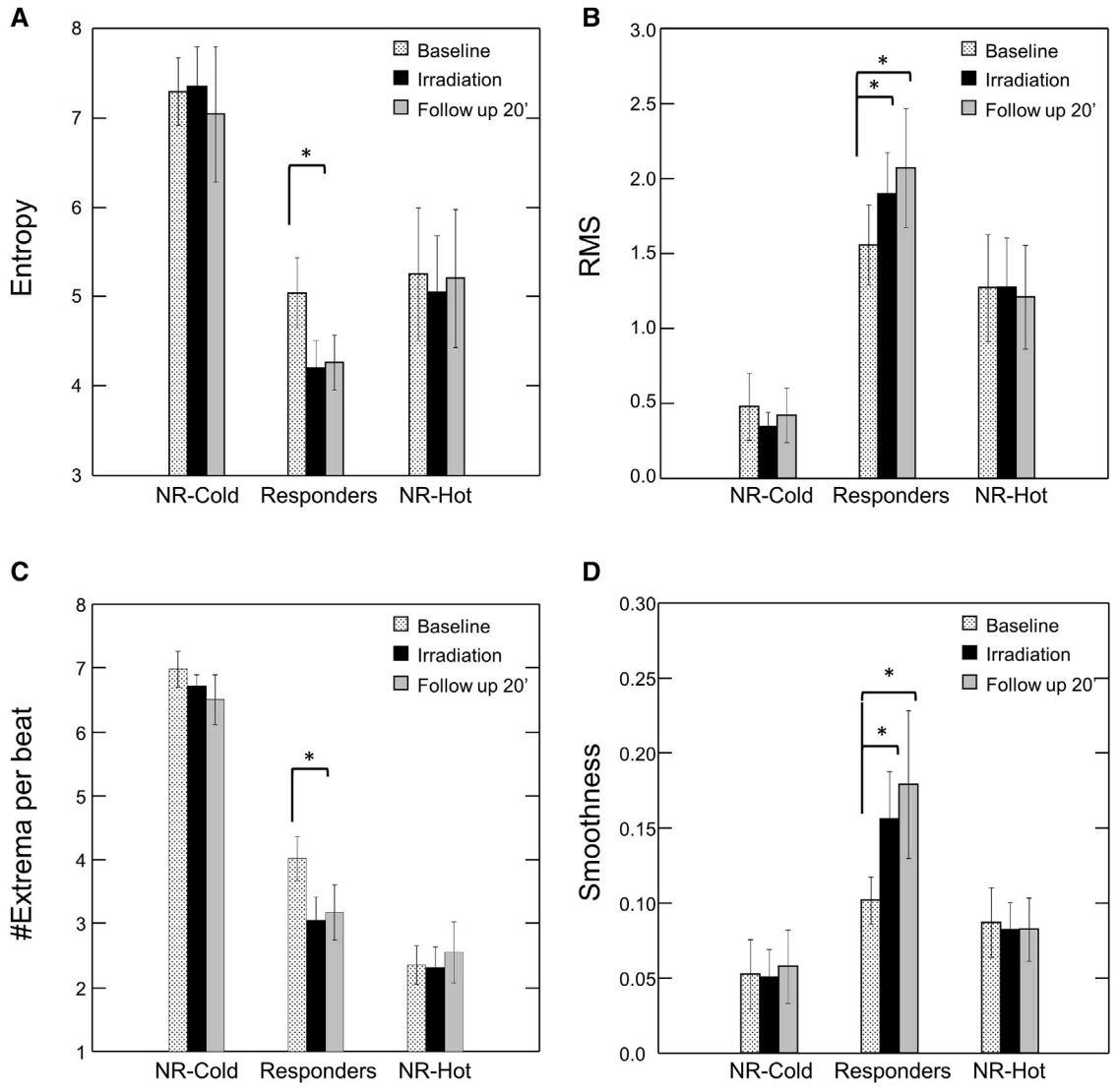

FIGURE 3
Effect of Photobiomodulation on Morphological Features of the PPG Waveform by Subgroup. Bars represent mean ± SEM for each subgroup at baseline (dots), after irradiation (black), and at the end of the follow up period (20' post-irradiation) (grey) for **(A)** Entropy; **(B)** Root Mean Square (RMS); **(C)** #Extrema per beat; and **(D)** Smoothness. Note significant change in each of the features post-irradiation for the "responders". *$p < 0.05$ by Friedman's test with multiple comparisons and Holm's modification of Bonferroni's correction. NR = non-responders.

the low end of baseline skin temperature) were too small to reach definite conclusions regarding the differences between these two groups of non-responders. Nonetheless, it should be noted that the morphological features of the PPG in these two extreme groups of non-responders were not affected by PBM irradiation.

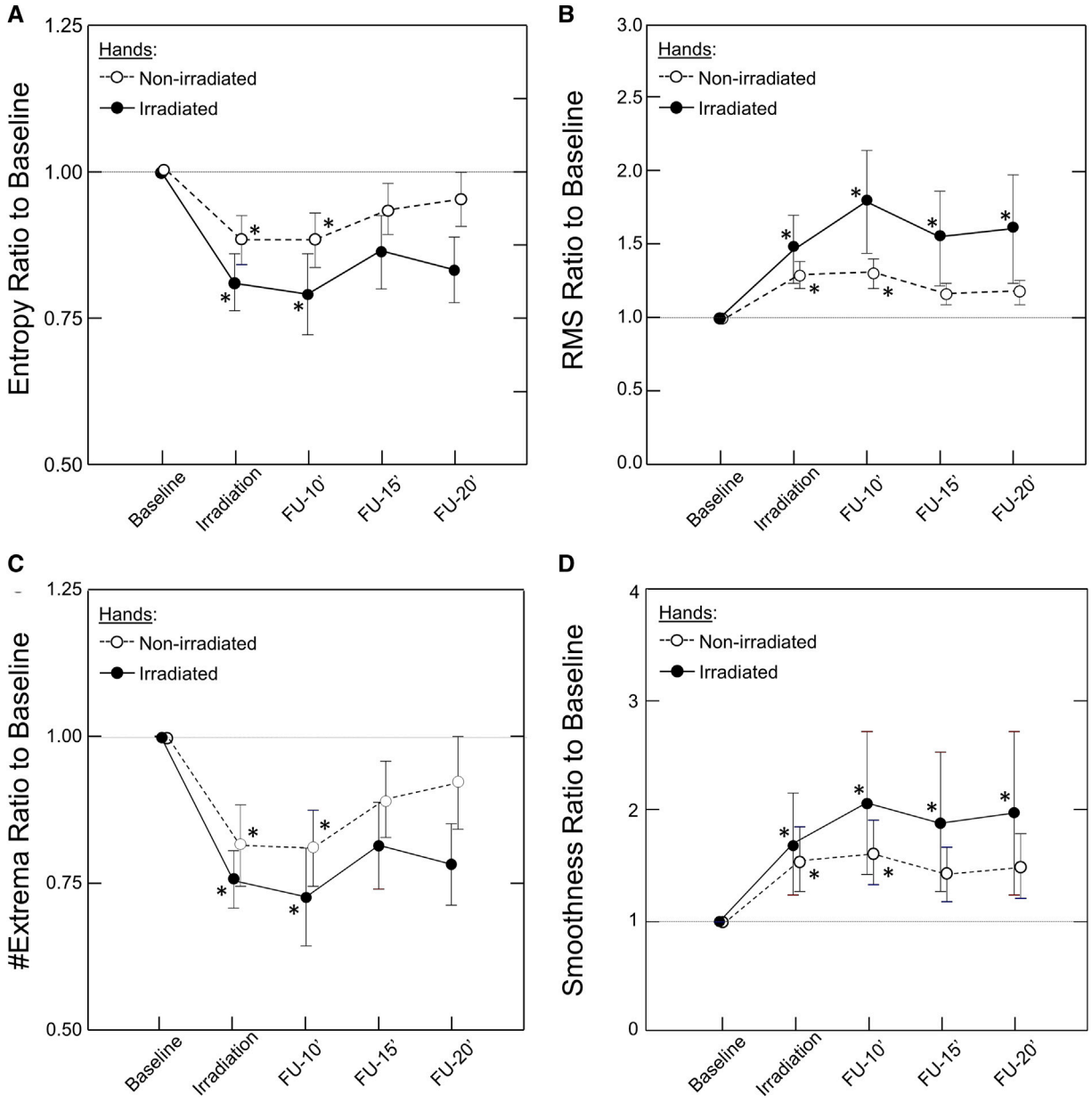

FIGURE 4
Kinetics of the Bilateral Response of Morphological Features of the PPG Signal to Unilateral Photobiomodulation. Note the significant change post irradiation for both hands that remained significant throughout the experiment in the irradiated hand but only up to 10 min in the non-irradiated hand. Also note that the response was larger in the irradiated than the non-irradiated hand. Data points and error bars represent mean ± SEM by time point for the irradiated hands (closed circles, solid line) and non-irradiated hands (open circles, dashed line) of responders to PBM (n = 12) for **(A)** Entropy; **(B)** Root Mean Square (RMS); **(C)** #Extrema per beat; and **(D)** Smoothness. *$p < 0.05$ by Friedman's test with multiple comparisons and Holm's modification of Bonferroni's correction.

3.1 Bilateral effect

Unilateral irradiation resulted in a bilateral response, but the response of the contralateral, non-irradiated hand was shorter in duration, persisting for only 10 min, and lower in magnitude (Figure 4). The correlation between irradiated and non-irradiated hands in Entropy, #Extrema, and RMS was moderate before irradiation and strong post-irradiation (Table 1). This was not the case with Smoothness since the correlation was already strong at baseline (r_s = 0.86). The strongest improvement of correlation after irradiation between irradiated and contralateral, non-irradiated hands was seen in the #Extrema feature (r_s, baseline vs. post-irradiation: 0.566 vs. 0.923, p = 0.018).

4 Discussion

In recent years, photoplethysmography (PPG) has become very widely used for non-invasive monitoring instruments particularly in the healthcare arena. This has included its use as a basis for a rapidly

expanding variety of wearable devices (Singh et al., 2021; Charlton and Vaidotas, 2022). The implementation of advanced methods of PPG signal processing, including advanced morphological analysis, has expanded the capabilities, accuracy, and usefulness of this technology in various fields of physiology and pathology such as cardiovascular function, sleep studies, pregnancy, pain, and mental health (Hickey et al., 2015; Qawqzeh et al., 2020; Ahmed et al., 2022; Allen, 2022; Allen and Fei, 2022; Mejia-Mejia et al., 2022).

Previously we found, using laser Doppler and thermal imaging, that PBM induces arteriolar vasodilatation resulting in both immediate and long-lasting increased capillary flow and tissue perfusion in healthy individuals, but not in participants having "cold hands" or "hot hands" (Gavish et al., 2020).

It is important to emphasize that the overall microvascular response to PBM is large in magnitude which is why it can be easily detected even by measurements of skin temperature that are a low-resolution proxy for microvascular blood flow. However, other characteristics of the microvascular response to PBM, for example, change over time or differences between the irradiated limb vs. the contralateral, non-irradiated limb, are much subtler and smaller in magnitude and appear to have a more complex behavior. Hence, an additional direct and more refined method was required.

In the current study, post-acquisitional analysis of advanced (known and novel) morphological features of the PPG waveforms obtained from these three groups was performed to better understand and provide clinically valuable physiological interpretation for the response to PBM. These additional morphological features, or combinations thereof, may be used in the future to improve the ability to identify potential responders to PBM.

The responders were found to have increased amplitude of the PPG signal and decreased level of jaggedness in the PPG waveform, i.e., the signal became smoother.

4.1 Morphological features of the PPG signal

The purpose for detrending the PPG signal was to preserve relevant physiological information and to remove the low-frequency components that were not relevant for the analysis. This involved lower envelope subtraction that is similar to a high pass filter but has some additional advantages. The high pass frequency determination is not required, there are no filter transients in the signal, and the remaining upper envelope clearly manifests the amplitude swing of the PPG signal, since the lower envelope is constant. No additional noise removal filtering was used in order to preserve the relevant information ("jaggedness").

Two common features were used: Root Mean Square (RMS) of the signal and Entropy for the signal shape (Wei et al., 2020; Singh et al., 2021; Mejia-Mejia et al., 2022). Two new features were introduced -- Smoothness and number (#) of local Extrema per PPG beat. The latter are based on the development of a dedicated algorithm for this research that provides more accurate quantitative information regarding the level of jaggedness of the PPG signal. The Smoothness level of a signal is commonly determined by calculating the higher frequency portion of the signal spectrum or calculating the energy after high-pass filtration (Wei et al., 2020; Singh et al., 2021; Mejia-Mejia et al., 2022). These methods require the determination of the cutoff frequency; that is, the frequency bands of the noises and the 'clean' signal. In applying these methods to the PPG signals, the determination of the optimal cutoff frequency was found to be difficult due to the nature of these signals, which are not always fully periodic, and due to the jaggedness of the envelope. To overcome this problem, the RMS value of the PPG signal was calculated after subtracting from the PPG signal its smoothed version obtained by a simple moving-average filter. Following this subtraction, a smooth PPG signal with a very low RMS value was obtained since the signal and its smooth version are similar.

The calculation of derivatives of the PPG signal is often an essential step in pulse wave analysis. For example, several indices of vascular aging can be extracted from the second derivative of the PPG pulse wave (Takazawa et al., 1998; Mejia-Mejia et al., 2022). In this study the number (#) of local Extrema per beat was calculated as another method for describing the jaggedness of the signal: Local Extrema can be easily identified by analyzing the derivatives of the PPG signal. Thus, higher jaggedness will result in a higher count of local Extrema.

4.2 Physiological interpretation of the PPG features

The morphological features of the PPG signal represent characteristics of blood volume changes in a microvascular bed reflecting instantaneous changes in the number of RBCs during the pulsatile blood flow. In the case of constant RBC concentration, the RMS of the signal represents the mean value of the pulsatile component of the blood volume which decreases for smaller diameter and stiffer arteriolar walls (Fusi and Farina, 2020). Thus, in comparison to responders, RMS is expected to be lower in "cold hands" due to vasoconstriction and the elevated wall stiffness associated with increased vascular tone. It should be higher in "hot hands" due to vasodilation.

Entropy represents a measure of fluctuations in the signal structure that reflects its complexity. Thus, Entropy is likely to increase when blood flow is compromised either because of an intrinsic pathology of the vessels themselves or inadequate supply with respect to physiological demand resulting in attempts at compensation. In the case of "cold hands," PBM seems to improve the blood flow resulting in reduction of signal complexity (Entropy) from its baseline level.

Regarding the number of Extrema per beat, the pulse waveform always includes a maximum point at the systolic peak and, frequently, a local minimum at the diastolic phase. Additional Extrema are likely to represent instabilities in the blood flow and dynamic fluctuations in the distribution of RBCs which tend to aggregate at low flow states and in "cold hands" during the diastolic phase (Lipowsky, 2005; Baskurt and Meiselman, 2007). Thus, increased blood flow, as occurs in "hot hands", or upon/after irradiation, is expected to reduce the number of Extrema as observed.

4.3 Clinical considerations

PPG signal processing led to two, clinically important findings: First, the duration of the response to irradiation in the group of

responders lasted for at least 20 min. The second is the synchronized changes in the PPG signal in both hands following irradiation of only one hand. Previous clinical studies conducted with thermography and laser Doppler flowmetry have shown that photostimulation for at least 15 min elicits a response in the non-irradiated side, albeit smaller in magnitude (Schindl et al., 2002; Samoilova et al., 2008a). This bilateral response has importance in clinical practice when the area requiring treatment is not accessible or is too painful to treat. Although the vasodilative response following PBM was shown to depend on local NO synthesis or release (Samoilova et al., 2008b; Keszler et al., 2018; Weihrauch et al., 2021; Keszler et al., 2022), it has been suggested that the bilateral effect may also point to the involvement of neuronal pathways coursing through the central nervous system (Koltzenburg et al., 1999) and/or the systemic release of a humoral mediator. Previous clinical studies using other interventions also observed bilateral effects where local stimulation on one side affected the other side (Koltzenburg et al., 1999; Huang et al., 2007; Ovadia-Blechman et al., 2018; Ovadia-Blechman et al., 2021). Further studies are in order to identify the precise pathway or mediator that can be manipulated, upregulated, or synthesized to simulate, or to improve the efficiency of, the therapeutic effects seen with PBM.

Methods such as time-frequency analysis and machine learning (Allen et al., 2021) should be of additional benefit for enhanced automaticity, standardization of interpretation of PPG morphological data, and more precise prediction of response to PBM.

The main limitation of our study was the small sample size of the "cold" and "hot" groups that prevented appropriate statistical evaluation of the effects of PBM on the morphological features of the PPG signal in these two extreme groups. For this reason, the results of this study were based on the post-acquisitional analysis of the PPG waveform of the responders' group for which adequate numbers were available and reliable statistical separation obtained.

5 Conclusion

This pilot study indicates that post-acquisitional analysis of morphological features of the PPG waveform provides new measures for the exploration of microcirculation responsiveness to PBM. Extraction of morphological features from continuous synchronous bilateral PPG measurements enables additional quantification of the kinetics and magnitude of the local (irradiated hand) and the systemic (non-irradiated) response to intervention. An algorithm for prediction of response to PBM may be developed based on a combination of these features. Application of these advances in waveform analysis to machine learning may improve accuracy, enhance standardization of interpretation, and facilitate automaticity, thereby expanding the usefulness of the rapidly expanding PPG-based non-invasive monitoring technologies for hospital as well as pre-hospital and home care.

Data availability statement

The raw data supporting the conclusion of this article will be made available by the authors, without undue reservation. Requests to access these datasets should be directed to ZOB, zehava@afeka.ac.il

Ethics statement

The studies involving humans were approved by the Afeka Institutional Ethics Review Board. The studies were conducted in accordance with the local legislation and institutional requirements. The participants provided their written informed consent to participate in this study.

Author contributions

ZOB and LG conceived and designed the study; YH, GW, BG, and ZOB were responsible for algorithm development and signal processing; ZOB, LG, YH, and BG were responsible for the analysis and interpretation of the data; LG and YH were responsible for statistical analysis; ZOB, LG, and YH drafted the manuscript; BG, NR, OH, and SG evaluated the data and reviewed the manuscript critically; All authors contributed to the article and approved the submitted version.

Acknowledgments

The authors gratefully acknowledge Professor N. B. Grover for assistance with the statistical analysis and Mr. Yonatan Eavri for organizing the databases for analysis. SDG is the Brandman Foundation Professor of Cardiac and Pulmonary Diseases, Faculty of Medicine, The Hebrew University of Jerusalem. The authors thank the Afeka Research Authority for partial support of these studies. These studies were supported in part by The Stuart Roden Family Research Fund, London, United Kingdom; The Saul and Joyce Brandman Fund for Cardiovascular Research, The Alexander Grass Family Research Fund, The Dr. Bruce and Baila Waldholtz Research Fund, and The Dr. Martin and Grace Rosman Research Fund, Faculty of Medicine, The Hebrew University of Jerusalem, Israel.

Conflict of interest

Author BG was employed by Yazmonit Ltd.

The remaining authors declare that the research was conducted in the absence of any commercial or financial relationships that could be construed as a potential conflict of interest.

Publisher's note

Supplementary material

The Supplementary Material for this article can be found online at: https://www.frontiersin.org/articles/10.3389/fphys.2023.1175470/full#supplementary-material

References

Ahmed, S., Bhuiyan, T. A., and Nii, M. (2022). PPG signal morphology-based method for distinguishing stress and non-stress conditions. *J. Adv. Comput. Intell. Intelligent Inf.* 26 (1), 58–66. doi:10.20965/jaciii.2022.p0058

Allen, J., and Fei, C. (2022). "Low-frequency variability in photoplethysmography and autonomic function assessmen," in *Photoplethysmography - technology, signal analysis and applications*. Editors P. Kyriacou and J. Allen (China: Elsevier).

Allen, J., Liu, H., Iqbal, S., Zheng, D., and Stansby, G. (2021). Deep learning-based photoplethysmography classification for peripheral arterial disease detection: A proof-of-concept study. *Physiol. Meas.* 42 (5), 054002. doi:10.1088/1361-6579/abf9f3

Allen, J. (2007). Photoplethysmography and its application in clinical physiological measurement. *Physiol. Meas.* 28 (3), R1–R39. doi:10.1088/0967-3334/28/3/R01

Allen, J. (2022). "Photoplethysmography for the assessment of peripheral vascular disease," in *Photoplethysmography - technology, signal analysis and applications*. Editors P. Kyriacou and J. Allen 1st ed. (China: Elsevier).

Ammer, K. (2012). Temperature of the human knee - a review. *Thermol. Int.* 22 (4), 137–151.

Avci, P., Gupta, A., Sadasivam, M., Vecchio, D., Pam, Z., Pam, N., et al. (2013). Low-level laser (light) therapy (LLLT) in skin: stimulating, healing, restoring. *Semin. Cutan. Med. Surg.* 32 (1), 41–52.

Baskurt, O. K., and Meiselman, H. J. (2007). Hemodynamic effects of red blood cell aggregation. *Indian J. Exp. Biol.* 45 (1), 25–31.

Charlton, P. H., and Vaidotas, M. (2022). "Wearable photoplethysmography devices," in *Photoplethysmography - technology, signal analysis and applications*. Editors P. Kyriacou and J. Allen (China: Elsevier).

Chen, C. H., Hung, H. S., and Hsu, S. H. (2008). Low-energy laser irradiation increases endothelial cell proliferation, migration, and eNOS gene expression possibly via PI3K signal pathway. *Lasers Surg. Med.* 40 (1), 46–54. doi:10.1002/lsm.20589

Chen, Z., Chen, B., Hu, P., Liu, H., and Zheng, D. (2022). A preliminary observation on rod cell photobiomodulation in treating diabetic macular edema. *Adv. Ophthalmol. Pract. Res.* 2 (2), 100051. doi:10.1016/j.aopr.2022.100051

Chow, R. (2016). "Low-level laser therapy of pain: clinical applications," in *Handbook of low-level laser therap*. Editors M. Hamblin, T. Agarwal, and M. De Sousa (Germany: Jenny Stanford Publishing).

De Brabanter, K., De Brabanter, J., De Moor, B., and Gijbels, I. (2013). Derivative estimation with local polynomial fitting. *J. Mach. Learn. Res.* 14 (1), 281–301. doi:10.5555/2567709.2502590

Dunn, O. J., and Clark, V. (1969). Correlation coefficients measured on the same individuals. *J. Am. Stat. Assoc.* 64 (325), 366–377. doi:10.1080/01621459.1969.10500981

Fusi, L., and Farina, A. (2020). Linear stability analysis of blood flow in small vessels. *Appl. Eng. Sci.* 1, 100002. doi:10.1016/j.apples.2020.100002

Garcia Becerra, A., Olguin Tiznado, J. E., Garcia Alcaraz, J. L., Camargo Wilson, C., Lopez Barreras, J. A., Cano Gutierrez, J. C., et al. (2022). Temperature asymmetry analysis between left and right wrist with sensory and infrared thermography. *Int. J. Environ. Res. Public Health* 19 (16), 10240. doi:10.3390/ijerph191610240

Gavish, L., Asher, Y., Becker, Y., and Kleinman, Y. (2004). Low level laser irradiation stimulates mitochondrial membrane potential and disperses subnuclear promyelocytic leukemia protein. *Lasers Surg. Med.* 35 (5), 369–376. doi:10.1002/lsm.20108

Gavish, L., Gilon, D., Beeri, R., Zuckerman, A., Nachman, D., and Gertz, S. D. (2021). Photobiomodulation and estrogen stabilize mitochondrial membrane potential in angiotensin-II challenged porcine aortic smooth muscle cells. *J. Biophot.* 14 (1), e202000329. doi:10.1002/jbio.202000329

Gavish, L., Hoffer, O., Rabin, N., Halak, M., Shkilevich, S., Shayovitz, Y., et al. (2020). Microcirculatory response to photobiomodulation-why some respond and others do not: A randomized controlled study. *Lasers Surg. Med.* 52 (9), 863–872. doi:10.1002/lsm.23225

Gavish, L., Perez, L. S., Reissman, P., and Gertz, S. D. (2008). Irradiation with 780 nm diode laser attenuates inflammatory cytokines but upregulates nitric oxide in lipopolysaccharide-stimulated macrophages: implications for the prevention of aneurysm progression. *Lasers Surg. Med.* 40 (5), 371–378. doi:10.1002/lsm.20635

Goshvarpour, A., and Goshvarpour, A. (2020). Evaluation of novel entropy-based complex wavelet sub-bands measures of PPG in an emotion recognition system. *J. Med. Biol. Eng.* 40 (3), 451–461. doi:10.1007/s40846-020-00526-7

Hamblin, M. R. (2018). Mechanisms and mitochondrial redox signaling in photobiomodulation. *Photochem Photobiol.* 94 (2), 199–212. doi:10.1111/php.12864

Hauptman, Y., Aloni-Lavi, R., Lapidot, I., Gurevich, T., Manor, Y., Naor, S., et al. (2019). Identifying distinctive acoustic and spectral features in Parkinson's disease. *Proc. Interspeech*, 2498–2502. doi:10.21437/Interspeech.2019-2465

Hickey, M., Phillips, J. P., and Kyriacou, P. A. (2015). The effect of vascular changes on the photoplethysmographic signal at different hand elevations. *Physiol. Meas.* 36 (3), 425–440. doi:10.1088/0967-3334/36/3/425

Huang, L. P., Zhou, S., Lu, Z., Tian, Q., Li, X., Cao, L. J., et al. (2007). Bilateral effect of unilateral electroacupuncture on muscle strength. *J. Altern. Complement. Med.* 13 (5), 539–546. doi:10.1089/acm.2007.6250

Keszler, A., Lindemer, B., Broeckel, G., Weihrauch, D., Gao, Y., and Lohr, N. L. (2022). *In vivo* characterization of a red light-activated vasodilation: A photobiomodulation study. *Front. Physiol.* 13, 880158. doi:10.3389/fphys.2022.880158

Keszler, A., Lindemer, B., Hogg, N., Weihrauch, D., and Lohr, N. L. (2018). Wavelength-dependence of vasodilation and NO release from S-nitrosothiols and dinitrosyl iron complexes by far red/near infrared light. *Arch. Biochem. Biophys.* 649, 47–52. doi:10.1016/j.abb.2018.05.006

Koltzenburg, M., Wall, P. D., and McMahon, S. B. (1999). Does the right side know what the left is doing? *Trends Neurosci.* 22 (3), 122–127. doi:10.1016/s0166-2236(98)01302-2

Kyriacou, P. A., and Chatterjee, S. (2022). *The origin of photoplethysmography*. Germany: Photoplethysmography.

Lipowsky, H. H. (2005). Microvascular rheology and hemodynamics. *Microcirculation* 12 (1), 5–15. doi:10.1080/10739680590894966

Mejia-Mejia, E., Allen, J., Budidha, K., El-Hajj, C., Kyriacou, P. A., and Charlton, P. H. (2022). "Photoplethysmography signal processing and synthesis," in *Photoplethysmography - technology, signal analysis and applications*. Editors P. Kyriacou and J. Allen (China: Elsevier).

Nitzan, M., and Ovadia-Blechman, Z. (2022). "Physical and physiological interpretations of the PPG signal," in *Photoplethysmography - technology, signal analysis and applications*. Editors P. Kyriacou and J. Allen (China: Elsevier).

Ovadia, Z., Kornowski, R., Gavish, B., Chayen, D., Walden, R., Varda-Bloom, N., et al. (1995). Noninvasive evaluation of microcirculatory hemodynamic changes during hemorrhage followed by saline or blood transfusion. *Shock* 4 (2), 96–101. doi:10.1097/00024382-199508000-00003

Ovadia-Blechman, Z., Avrahami, I., Weizman-Shammai, E., Sharir, T., Eldar, M., and Chouraqui, P. (2015a). Peripheral microcirculatory hemodynamic changes in patients with myocardial ischemia. *Biomed. Pharmacother.* 74, 83–88. doi:10.1016/j.biopha.2015.07.011

Ovadia-Blechman, Z., Gavish, B., Levy-Aharoni, D., Shashar, D., and Aharonson, V. (2017). The coupling between peripheral microcirculation and slow breathing. *Med. Eng. Phys.* 39, 49–56. doi:10.1016/j.medengphy.2016.10.009

Ovadia-Blechman, Z., Gritzman, A., Shuvi, M., Gavish, B., Aharonson, V., and Rabin, N. (2018). The response of peripheral microcirculation to gravity-induced changes. *Clin. Biomech. (Bristol, Avon)* 57, 19–25. doi:10.1016/j.clinbiomech.2018.06.005

Ovadia-Blechman, Z., Hoffer, O., Halak, M., Adrai, K., Zimmer, Y., Silverberg, D., et al. (2021). Assessment of blood distribution in response to post-surgical steal syndrome: A novel technique based on thermo-anatomical segmentation. *J. Biomech.* 119, 110304. doi:10.1016/j.jbiomech.2021.110304

Ovadia-Blechman, Z., Meilin, A., Rabin, N., Eldar, M., and Castel, D. (2015b). Noninvasive monitoring of peripheral microcirculatory hemodynamics under varying degrees of hypoxia. *Respir. Physiol. Neurobiol.* 216, 23–27. doi:10.1016/j.resp.2015.05.011

Oyebode, O., Houreld, N. N., and Abrahamse, H. (2021). Photobiomodulation in diabetic wound healing: A review of red and near-infrared wavelength applications. *Cell. Biochem. Funct.* 39 (5), 596–612. doi:10.1002/cbf.3629

Passarella, S., and Karu, T. (2014). Absorption of monochromatic and narrow band radiation in the visible and near IR by both mitochondrial and non-mitochondrial photoacceptors results in photobiomodulation. *J. Photochem Photobiol. B* 140, 344–358. doi:10.1016/j.jphotobiol.2014.07.021

Pastore, D., Di Martino, C., Bosco, G., and Passarella, S. (1996). Stimulation of ATP synthesis via oxidative phosphorylation in wheat mitochondria irradiated with helium-neon laser. *Biochem. Mol. Biol. Int.* 39 (1), 149–157. doi:10.1080/15216549600201151

Qawqzeh, Y. K., Bajahzar, A. S., Jemmali, M., Otoom, M. M., and Thaljaoui, A. (2020). Classification of diabetes using photoplethysmogram (PPG) waveform analysis: logistic regression modeling. *Biomed. Res. Int.* 2020, 3764653. doi:10.1155/2020/3764653

Roy, M. S., Gupta, R., and Sharma, K. D. (2022). Photoplethysmogram signal quality evaluation by unsupervised learning approach. *IEEE Appl. Signal Process. Conf. (ASPCON).*, 6–10. doi:10.1109/ASPCON49795.2020.9276733

Samoilova, K. A., Zhevago, N. A., Menshutina, M. A., and Grigorieva, N. B. (2008a). Role of nitric oxide in the visible light-induced rapid increase of human skin microcirculation at the local and systemic level: I. Diabetic patients. *Photomed. Laser Surg.* 26 (5), 433–442. doi:10.1089/pho.2007.2197

Samoilova, K. A., Zhevago, N. A., Petrishchev, N. N., and Zimin, A. A. (2008b). Role of nitric oxide in the visible light-induced rapid increase of human skin microcirculation at the local and systemic levels: II. Healthy volunteers. *Photomed. Laser Surg.* 26 (5), 443–449. doi:10.1089/pho.2007.2205

Schindl, A., Heinze, G., Schindl, M., Pernerstorfer-Schon, H., and Schindl, L. (2002). Systemic effects of low-intensity laser irradiation on skin microcirculation in patients with diabetic microangiopathy. *Microvasc. Res.* 64 (2), 240–246. doi:10.1006/mvre.2002.2429

Schindl, A., Schindl, M., Schon, H., Knobler, R., Havelec, L., and Schindl, L. (1998). Low-intensity laser irradiation improves skin circulation in patients with diabetic microangiopathy. *Diabetes Care* 21 (4), 580–584. doi:10.2337/diacare.21.4.580

Selfe, J., Whitaker, J., and Hardaker, N. (2008). A narrative literature review identifying the minimum clinically important difference for skin temperature asymmetry at the knee. *Thermol. Int.* 18, 51–54.

Silver, N. C., Hittner, J. B., and May, K. (2004). Testing dependent correlations with nonoverlapping variables: A Monte Carlo simulation. *J. Exp. Educ.* 73 (1), 53–69. doi:10.3200/JEXE.71.1.53-70

Singh, S., Kozłowski, M., García-López, I., Jiang, Z., and Rodriguez-Villegas, E. (2021). Proof of concept of a novel neck-situated wearable PPG system for continuous physiological monitoring. *IEEE Trans. Instrum. Meas.* 70, 1–9. doi:10.1109/TIM.2021.3083415

Suominen, S., and Asko-Seljavaara, S. (1996). Thermography of hands after a radial forearm flap has been raised. *Scand. J. Plast. Reconstr. Surg. Hand Surg.* 30 (4), 307–314. doi:10.3109/02844319609056409

Takazawa, K., Tanaka, N., Fujita, M., Matsuoka, O., Saiki, T., Aikawa, M., et al. (1998). Assessment of vasoactive agents and vascular aging by the second derivative of photoplethysmogram waveform. *Hypertension* 32 (2), 365–370. doi:10.1161/01.hyp.32.2.365

Vasyltsov, I., and Lee, S. (2020). Entropy extraction from bio-signals in healthcare IoT. *1st ACM Workshop on IoT privacy. Trust, Secur.*, 11–17. doi:10.1145/2732209.2732213

Vladimirov, Y., Borisenko, G., Boriskina, N., Kazarinov, K., and Osipov, A. (2000). NO-hemoglobin may be a light-sensitive source of nitric oxide both in solution and in red blood cells. *J. Photochem Photobiol. B* 59 (1-3), 115–122. doi:10.1016/s1011-1344(00)00148-2

Wei, H. C., Ta, N., Hu, W. R., Wang, S. Y., Xiao, M. X., Tang, X. J., et al. (2020). Percussion entropy analysis of synchronized ECG and PPG signals as a prognostic indicator for future peripheral neuropathy in type 2 diabetic subjects. *Diagn. (Basel)* 10 (1), 32. doi:10.3390/diagnostics10010032

Weihrauch, D., Keszler, A., Lindemer, B., Krolikowski, J., and Lohr, N. L. (2021). Red light stimulates vasodilation through extracellular vesicle trafficking. *J. Photochem Photobiol. B* 220, 112212. doi:10.1016/j.jphotobiol.2021.112212

Wilcox, R. R. (2016). Comparing dependent robust correlations. *Br. J. Math. Stat. Psychol.* 69 (3), 215–224. doi:10.1111/bmsp.12069

Zar, J. H. (2010). *Biostatistical analysis*. 5th ed. Upper Saddle River, N.J.: Prentice-Hall/Pearson.

frontiers | Frontiers in Physiology

TYPE Original Research
PUBLISHED 26 October 2023
DOI 10.3389/fphys.2023.1176753

OPEN ACCESS

EDITED BY
Panicos Kyriacou,
City University of London,
United Kingdom

REVIEWED BY
Youngsun Kong,
University of Connecticut, United States
Lisheng Xu,
Northeastern University, China

*CORRESPONDENCE
Serena Zanelli,
zanelli@math.univ-paris13.fr

RECEIVED 28 February 2023
ACCEPTED 05 September 2023
PUBLISHED 26 October 2023

CITATION
Zanelli S, Eveilleau K, Charlton PH, Ammi M, Hallab M and El Yacoubi MA (2023), Clustered photoplethysmogram pulse wave shapes and their associations with clinical data.
Front. Physiol. 14:1176753.
doi: 10.3389/fphys.2023.1176753

Clustered photoplethysmogram pulse wave shapes and their associations with clinical data

Serena Zanelli[1]*, Kornelia Eveilleau[2], Peter H. Charlton[3], Mehdi Ammi[4], Magid Hallab[2,5] and Mounim A. El Yacoubi[6]

[1]Laboratoire Analyse, Géométrie et Applications, University Sorbonne Nord, Villetaneuse, France, [2]Axelife, Saint-Nicolas-de-Redon, France, [3]Department of Public Health and Primary Care, University of Cambridge, Cambridge, United Kingdom, [4]Laboratoire Analyse, Géométrie et Applications, University of Sorbonne Nord, Saint-Denis, France, [5]Clinique Bizet, Paris, France, [6]SAMOVAR Telecom SudParis, CNRS, Institut Polytechnique de Paris, Palaiseau, France

Photopletysmography (PPG) is a non-invasive and well known technology that enables the recording of the digital volume pulse (DVP). Although PPG is largely employed in research, several aspects remain unknown. One of these is represented by the lack of information about how many waveform classes best express the variability in shape. In the literature, it is common to classify DVPs into four classes based on the dicrotic notch position. However, when working with real data, labelling waveforms with one of these four classes is no longer straightforward and may be challenging. The correct identification of the DVP shape could enhance the precision and the reliability of the extracted bio markers. In this work we proposed unsupervised machine learning and deep learning approaches to overcome the data labelling limitations. Concretely we performed a K-medoids based clustering that takes as input 1) DVP handcrafted features, 2) similarity matrix computed with the Derivative Dynamic Time Warping and 3) DVP features extracted from a CNN AutoEncoder. All the cited methods have been tested first by imposing four medoids representative of the Dawber classes, and after by automatically searching four clusters. We then searched the optimal number of clusters for each method using silhouette score, the prediction strength and inertia. To validate the proposed approaches we analyse the dissimilarities in the clinical data related to obtained clusters.

KEYWORDS

PPG, waveform, classification, machine learning, deep learning, unsupervised learning

1 Introduction

The photoplethysmogram (PPG) signal contains precious information about the blood vessels and heart activity. The digital volume pulse (DVP) is defined as the portion of PPG signal corresponding to one cardiac cycle. In young individuals, the DVP exhibits clearly defined systolic and diastolic peaks. The diastolic peak is attenuated with increasing age (Dawber et al., 1973). The systolic peak is related to the forward pressure wave from the heart to the finger. The diastolic wave, also called the reflected wave, depends on the amount of reflection (due to muscular tone) in small arteries (Millasseau et al., 2006). DVP shape changes with age (Allen and Murray, 2003), blood pressure (Millasseau et al., 2006), atherosclerosis (Rozi et al., 2012), and other cardiovascular diseases such as arrhythmia (Sardana et al., 2021) and coronary artery disease (Saritas et al., 2019). DVP wave shapes vary between subjects and with the presence of pathologies. It can be used to assess a

variety of cardiovascular properties, such as estimating blood pressure (Kurylyak et al., 2013), detecting diabetes (Zanelli et al., 2022), or assessing vascular ageing (Charlton et al., 2022). An understanding of typical DVP wave shapes could contribute to the physiological interpretation of wave shapes, and could help in the development of robust DVP wave analysis algorithms. Most of the DVP biomarkers extraction algorithms assume that DVPs have a standardized shape. However real DVPs can show more than one peak. In this case, the biomarker cannot be computed directly but a suitable pre-processing has to be applied to the wave in order to obtain an estimation. For our knowledge very few studies address the DVP shape morphology classification topic.

In 1973, Dawber et al., 1973 defined four classes of DVP shape based on the characteristics of the dicrotic notch (Figure 1). The four classes range from a visible and clearly marked dicrotic notch (Class 1) to a non visible dicrotic notch (Class 4). However, DVPs exhibit far more shape variations than are captured in the characteristics of the dicrotic notch. Other attempts have been made to identify typical DVP wave shapes: frequency analysis to classify the DVPs into three classes based on the age (Sherebrin and Sherebrin, 1990); machine learning and deep learning methods trained over handcrafted features to classify the DVPs shape into the four classes proposed by Dawber et al. (Tigges et al., 2016); and second derivative analysis used to obtain four DVP templates (Takada et al., 1996). Wang et al., 2013 proposed a multi-Gaussian fitting to classify DVPs into five classes. With respect to Dawber et al., they introduced an intermediate class where no notch develops but there is a notable reflected wave in the systolic component of the pulse wave. The main limitation of these studies is the pre-emptive choice of the number of DVP classes.

We used non-supervised approaches to identify clusters of DVP wave shapes as follows. First, we investigated different approaches for clustering DVP waves with the aim of identifying the best approach. K-medoids clustering was used to cluster DVP wave shapes based on: 1) handcrafted DVP features; 2) Derivative Dynamic Time Warping (DDTW) distances; or (iii) features extracted from a convolutional neural network autoencoder (CNN AE). K-medoids was used instead of K-means as it is less affected by outliers, and it guarantees that each medoid (the DVP shape representing the entire cluster) is an actual DVP (Park and June 2009). Second, we investigated whether the optimal number of clusters is four, as suggested by Dawber et al., or a different number. To do so, all the clustering methods were tested when the number of clusters was fixed to four (with and without fixing the medoids to DVP waves typical of Dawber's four classes), and when the optimal number of clusters was determined through one of: the prediction strength method (Tibshirani and Walther, 2005); the silhouette score (Shahapure and Nicholas, 2020); or clusters inertia (Syakur et al., 2018). Third, we investigated whether any of the obtained clusters were clinically relevant. To do so, we analysed the related clinical data for each cluster to assess whether there were significant differences between clusters. The dataset used in this study contained approximately 11,000 DVPs from 300 subjects aged 20–80 years old. Our contributions can be summarized as follows.

- We clustered DVP waves using a K-medoids approach with three different feature sets. We compared the results obtained with 1) a dataset composed by fourteen PPG handcrafted features, 2) a dataset composed by DDTW pairwise distances and 3) a dataset composed by features automatically extracted from a CNN autoencoder.
- We tested the proposed approaches with four clusters to compare the obtained results with the Dawber et al. classes. Then, we investigated the optimal number of clusters using the silhouette score, inertia and the prediction strength methods. The approaches have been also tested by imposing four representative medoids, selected by a human expert.
- We investigate whether or not the obtained clusters are clinically relevant by analysing the distribution of the clinical data associated with each cluster.

2 Material and methods

2.1 Dataset

The dataset used in this study contains PPG signals recorded from 300 different subjects, providing a total of about 11,057 DVPs. Table 1 presents the subject characteristics: the subjects ranged from 19 to 83 years old; and included normotensives, hypertensives and hypotensives. Figure 2 represents the age distribution of the dataset. The PPG signals were acquired at 1 kHz with the pOpmètre device

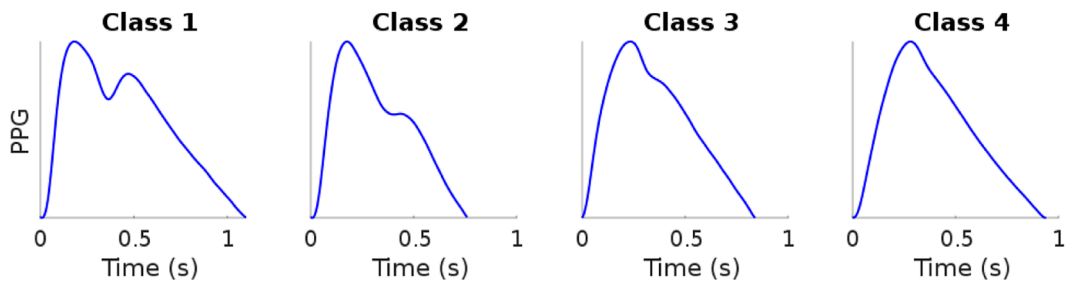

FIGURE 1
Example of digital volume pulse Dawber classes. Data sourced from Charlton et al. (2016). Figure: Classes of photoplethysmogram (PPG) pulse wave shape: Examples of the four classes of pulse wave shape proposed by Dawber et al. Reproduced form https://commons.wikimedia.org/wiki/File:Classes_of_photoplethysmogram_(PPG)_pulse_wave_shape.svg, licensed under CC-BY4.0.

TABLE 1 Clinical data. Mean, standard deviation, minimum and maximum values of the clinical data related to the used DVPs dataset.

Feature	Mean (± std)	Min	Max
Age[years]	44.31 ± 14.34	19.48	83.00
Weight[kg]	74.60 ± 16.99	45.00	180.00
Height[cm]	170.04 ± 8.45	140.00	196.00
PWV[m/s]	7.99 ± 2.91	3.70	26.10
PAS[mmHg]	124.77 ± 16.01	90.00	190.00
PAD[mmHg]	76.10 ± 9.73	48.00	120.00
BMI[kg/m^2]	25.78 ± 5.12	6.00	56.00
BPM[bpm]	71.82 ± 14.89	40.00	185.00

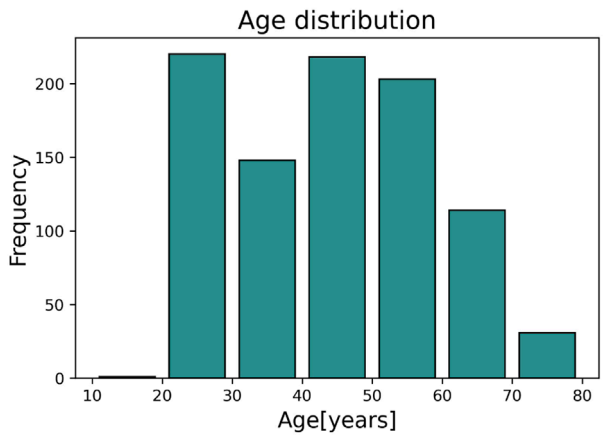

FIGURE 2
Age distribution of the used dataset.

(Axelife, France) (Obeid et al., 2017). pOpmètre is a medical device that measures the pulse wave velocity (PWV) between the finger and the toe in order to assess arterial stiffness. Prior to measurement, subjects were asked to lie down and rest for about 5 min. The device utilizes transmittance PPG with red and infrared light. Each measurement takes up to 14 s to be computed. Some subjects in the dataset had more than one measurement taken. Only the finger signals were used in this study. The quality assessment process described in (Zanelli et al., 2021) was used to select only the high quality parts of the signals. Signals were then segmented into DVPs. DVP waves were normalised in time (100 samples) and amplitude (between zero and one). The employed dataset is composed only of DVP waves without any other information related to the shape. Since no labels are available, we propose an unsupervised approach to cluster the waves, using three different DVP extracted features. This process is further explained in the next section.

The dataset was split into train and test sets using 70% and 30% of the available data respectively. Since one subject can have different DVP shapes along the same measurement, one subject can contribute to the train, validation or test set at the same time. The validation set is composed of 30% of the training test. The same train, validation and test sets were used with all the proposed methods in order to be able to compare the results. The train and validation sets were used to train the CNN AE while the test set was used for clustering.

2.2 Clustering pulse waves

The K-medoids technique was used to cluster DVP waves. K-medoids is a partitional algorithm firstly proposed in 1980 (Rdusseeun and Kaufman, 1987). Its objective is to split a dataset into k clusters by minimising the distance between the center of each cluster and the samples assigned to that cluster. The center of the cluster (also known as a medoid) is defined as the sample in the cluster whose average dissimilarity to all the remaining objects in the cluster is minimal. The chosen medoid is an actual sample of the dataset, in contrast to the k-means algorithm. Furthermore, because k-medoids minimizes the sum of dissimilarities between two samples of the dataset instead of the sum of squared euclidean distances, it is more robust to noise and outliers than k-means (Kaur et al., 2014). In this study, we applied the K-medoids in three ways, as now described.

2.2.1 Using handcrafted features

Clustering was performed using twenty one handcrafted features were extracted from the DVPs contained in the dataset. The features include those proposed in the literature to assess DVP morphology (Tigges et al., 2016), second derivative features (Mouney et al., 2021), and statistical shape features such as kurtosis and skewness. We performed the correlation analysis to identify and remove highly correlated features. This resulted in fourteen handcrafted features being selected, as reported in Table 2. After checking the feature distributions, we applied a logarithmic transformation to three of the remaining features. We then standardized the features by subtracting the mean and scaling to unit variance. The fourteen features were clustered using the K-medoids approach.

2.2.2 Using dynamic time warping

Dynamic Time Warping (DTW) is an algorithm employed to estimate the similarity between two time series (Müller, 2007). DTW was first introduced around 1960 and applied in speech recognition around 1975 (Senin, 2008). Over the years, this algorithm has been demonstrated to be very effective in matching time series of all kinds (Bagnall et al., 2016), such as for handwriting classification (El-Yacoubi et al., 2019). It has already been applied to PPG and ECG signals in various fields to assess signal quality (Li and Clifford, 2012), identify fine finger gestures (Zhao et al., 2018), or for human verification systems (Hwang et al., 2021). We define two time series as $X = (x_1, x_2, \dots, x_n)$ and $Y = (y_1, y_2, \dots, y_m)$.

The DTW similarity measure is computed as the minimal cost of aligning the two time series as described in Algorithm 1 (Sakoe and Chiba, 1978). Several adaptations have been proposed to improve the efficiency and the effectiveness of this algorithm. Local constraints such as the Itakura parallelogram (Itakura, 1975) or the Sakoe-Chiba band (Sakoe and Chiba, 1978) have been

TABLE 2 DVPs features used for clustering with the handcrafted DVP feature approach. Abb: feature name abbreviation.

Feature	Abb	Description
Dicrotic-diastolic notch	DDR	Ratio between dicrotic notch and diastolic peak amplitude. Set to 1.1 if no diastolic point is detected
Relative downslope sum	RDS	Area under the curve from the maximum descendet slope to the end of the pulse
Downslope derivative mean	DDM	Mean value of the pulse derivative after the systolic peak
Skewness	Skew	Measure of the pulse asymmetry
Max second derivative	P_b_2Dev_A	First minimum amplitude of the second derivative
Index min second derivative	P_b_2Dev_i	Index of the first minimum amplitude of the second derivative
Min second derivative	P_a_2Dev_A	Maximum amplitude of the second derivative
Index max second derivative	P_a_2Dev_i	Index of the maximum amplitude of the second derivative
Integral of the curve	S_P_Onde	Total area under the curve
Number of peaks	nbr_peaks	Number of peaks inside the pulse
Logarithm of Rise time	log (RT)	Logarithm of the rise time
Logarithm of Kurtosis	log (Kurt)	Logartimic measure of the "tailedness"
Augmentation index	AI_bin	Augmentation index, binary variable. If augmentation index could be computed the variable has high value
Down slope derivative variance	log (DDV)	Logarithm of the variance of the pulse derivative variance during the down slope

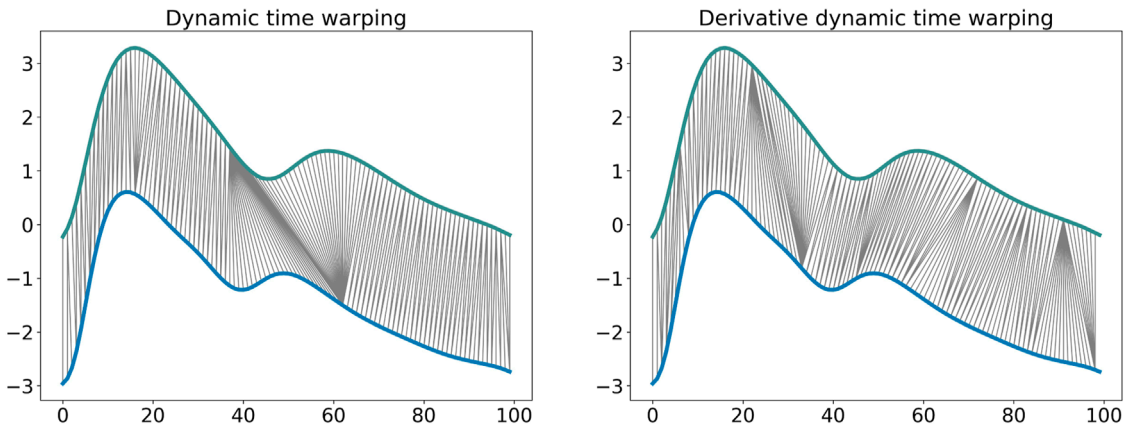

FIGURE 3
Dynamic time warping and derivative dynamic time warping comparison. It is observable how DDTW is able to match the same shape modifications with respect to the DTW that matches points that have low relative distance.

found to reduce the computational complexity of the unconstrained DTW and also improve accuracy when used with a 1 Nearest-Neighbor (1-NN) classifier (Geler et al., 2019). We implemented DDTW using a SakoeChiba window of length $w = 20$ samples. DTW is likely to be successful when applied to two sequences that are similar except for local accelerations and decelerations in the time axis. However, in our case the DVPs differed mostly on the Y-axis. We found that DTW did not provide successful results, as the algorithm matched points with lower mutual distance rather than points with similar shapes. Therefore, we implemented Derivative Dynamic Time Warping (DDTW), in which the time series X and Y are substituted with their derivatives X' and Y'. This takes into consideration the slopes of the DVPs in order to compute the minimal cost (Keogh and Pazzani, 2001). DVPs were further Z-normalised before performing DDTW measures. Figure 3 shows the application of classical DTW and DDTW. The DDTW similarities were clustered using the K-medoids approach.

2.2.3 Convolutional neural network autoencoder

A Convolutional Neural Network (CNN) AutoEncoder model was used to automatically extract features from DVP waves (Chafik et al., 2019). CNNs are widely employed in biomedical signal processing (Alaskar, 2018) since they are capable of extracting features by exploiting the convolution operation between the input

```
Require: n,m ≥ 0
 int DTW[0..n, 0..m]
 int i, j, cost
 s: array [1..n], t: array [1..m]
 for i := 1 to n do
   for j := 1 to m do
     DTW[i, j] := infinity
   end for
 end for
 DTW[0, 0] := 0
 for i := 1 to n do
   for j := 1 to m do
     cost:= abs(s[i] - t[j])
     DTW[i, j] := cost + minimum(DTW[i-1, j ],
      DTW[i , j-1], DTW[i-1, j-1])
   end for
 end for
 return DTW[n, m]
```

Algorithm 1. Calculating the dynamic time warping (DTW) distance between time series.

and learnt filters (Li et al., 2017). The autoencoder is trained to extract features from the input (performing a dimension compression step) and reconstruct it using the learnt features by minimising the Mean Squared Error (MSE) between the reconstructed input and the actual input. The model is composed of 6 convolutional layers and three dense layers. A flattening layer is added after the last convolution in order to reduce the dimensions and pass the feature maps to the fully connected layer. Relu activation functions inside CNN layers were used, while a sigmoid activation function was used for the reconstruction layer. The model architecture is represented in Table 3. We optimize the bottleneck layer size, the learning rate and λ L2 regularisation factor using Autonomio Talos python tool (Talos, 2019). The optimal model was chosen as a trade-off between validation loss and bottleneck layer size. A latent size of eight was chosen, indicating that eight features were extracted from DVP waves. This provided the smallest bottleneck layer size that performed well enough compared to the best validation loss obtained. Once the autoencoder is trained, only the encoder part is used to extract features from the DVPs. The eight features were clustered using the K-medoids approach.

TABLE 3 CNN AutoEncoder architecture.

Layers	Output shape
Encoder	
Input layer	(None, 100)
Convolution layer	(None,100,32)
MaxPooling	(None,50,32)
Convolution layer	(None,50,32)
MaxPooling	(None,25,32)
Convolution layer	(None,25,32)
MaxPooling	(None,13,32)
Flatten	(None,416)
Dense	(None,8)
Decoder	
Dense	(None,8)
Dense	(None,416)
Reshape	(None,13,32)
Convolution layer	(None,26,32)
Cropping	(None,25,32)
UpSampling	(None,50,32)
Convolution layer	(None,50,32)
UpSampling	(None,100,32)
Convolution layer	(None,100,32)
Flatten	(None,3,200)
Dense	(None,100)

2.3 Investigating the optimal number of clusters

We employed three different methods to investigate the optimal number of clusters: the silhouette score (Rousseeuw, 1987), the prediction strength (Tibshirani and Walther, 2005), and the cluster inertia (Syakur et al., 2018). These are now described.

The silhouette score is calculated by taking into account the mean intra-cluster distance a, and the distance between a sample and the nearest cluster that the sample is not a part of b. The silhouette score s for a sample is:

$$s = (b - a)/max(a, b). \tag{1}$$

The score is then averaged over all samples. This score measures how well a dataset sample i matches the chosen clustering scheme. A score of 1 means the samples are correctly clustered, a score of 0 means the samples could belong to other clusters, and a score of −1 means that the cluster contains the wrong samples.

The prediction strength of the clustering $C(X_{tr}, k)$ is a defined as:

$$ps(k) = \min_{1 \le j \le k} \frac{1}{n_{k,j}\left(n_{k,j} - 1\right)} \sum_{i \neq i' \in A_{kj}} D[C(X_{tr}, k), X_{te}]_{ii'}, \tag{2}$$

where $n_{k,j}$ is the number of observations in the jth cluster, $D[C(X_{tr}, k), X_{te}]$ is the co-membership matrix of size (X_{tr} (train set), X_{te} (test set)) and $C(X_{tr}, k)$ is the clustering algorithm fitted to the training set. In other words, for each test cluster, the proportion of observation pairs in that cluster that are also assigned to the same cluster by the training set centroids is computed. The prediction strength is the minimum of this quantity over the k test clusters. The maximum number of clusters for which the prediction strength is above a certain threshold is then chosen. Although the experiments ran by the authors suggest 0.8–0.9 as a good value for the threshold, the latter may be interpreted on a case-by-case basis.

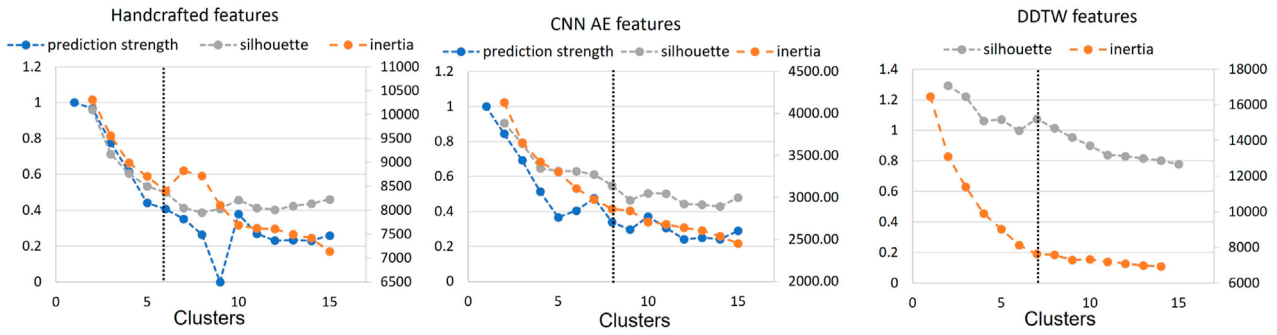

FIGURE 4
Prediction strength, inertia and silhouette score for clusters k = [1,15] for handcrafted and CNN AE approach. Inertia and silhouette score for clusters k = [1,15] for DDTW approach. Black dotted line: chosen number of clusters.

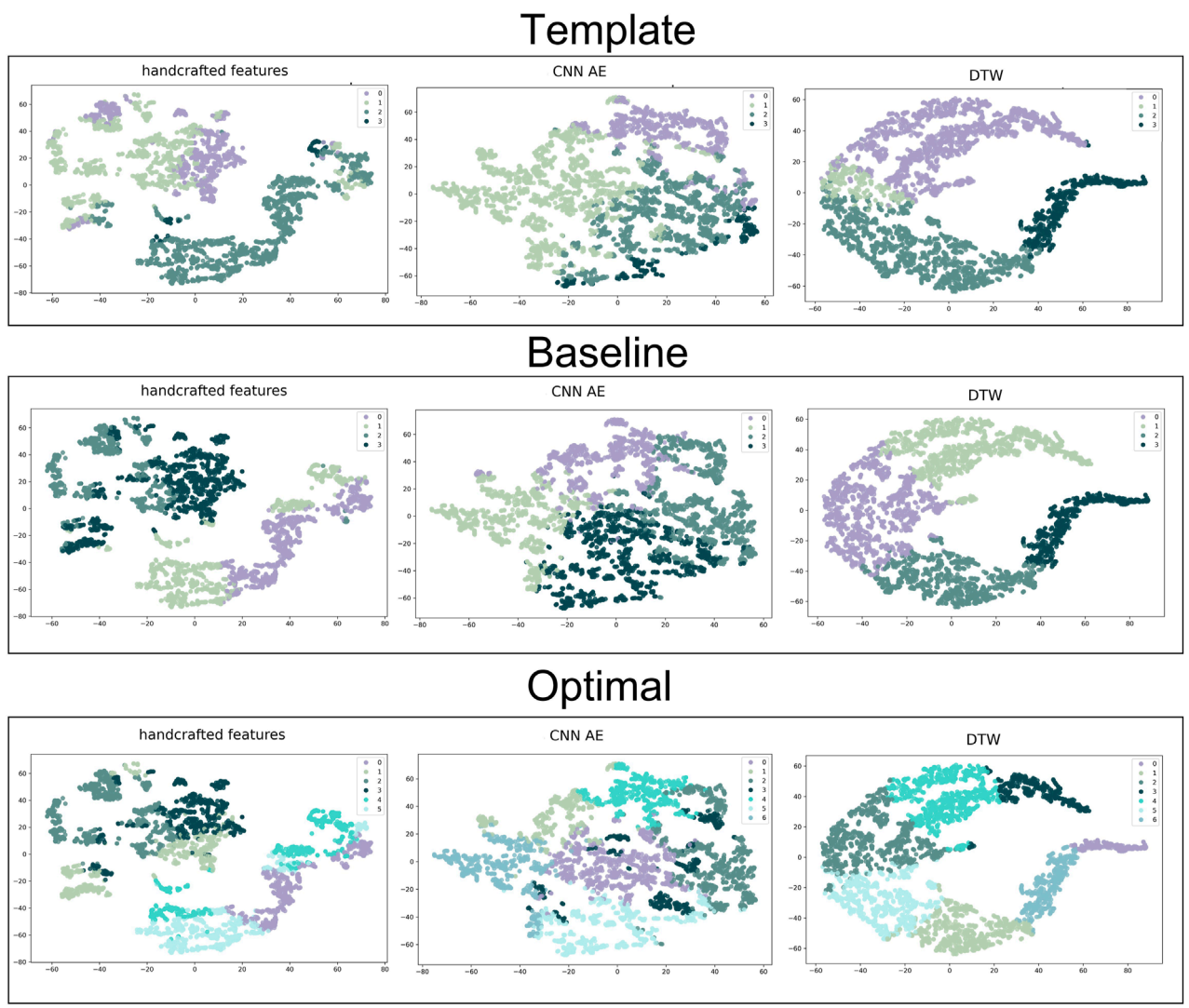

FIGURE 5
t-SNE clustering representation of all the proposed approaches. From the top to the bottom: template, baseline and optimal approach. From the left to the right: handcrafted, CNN AE and automated features.

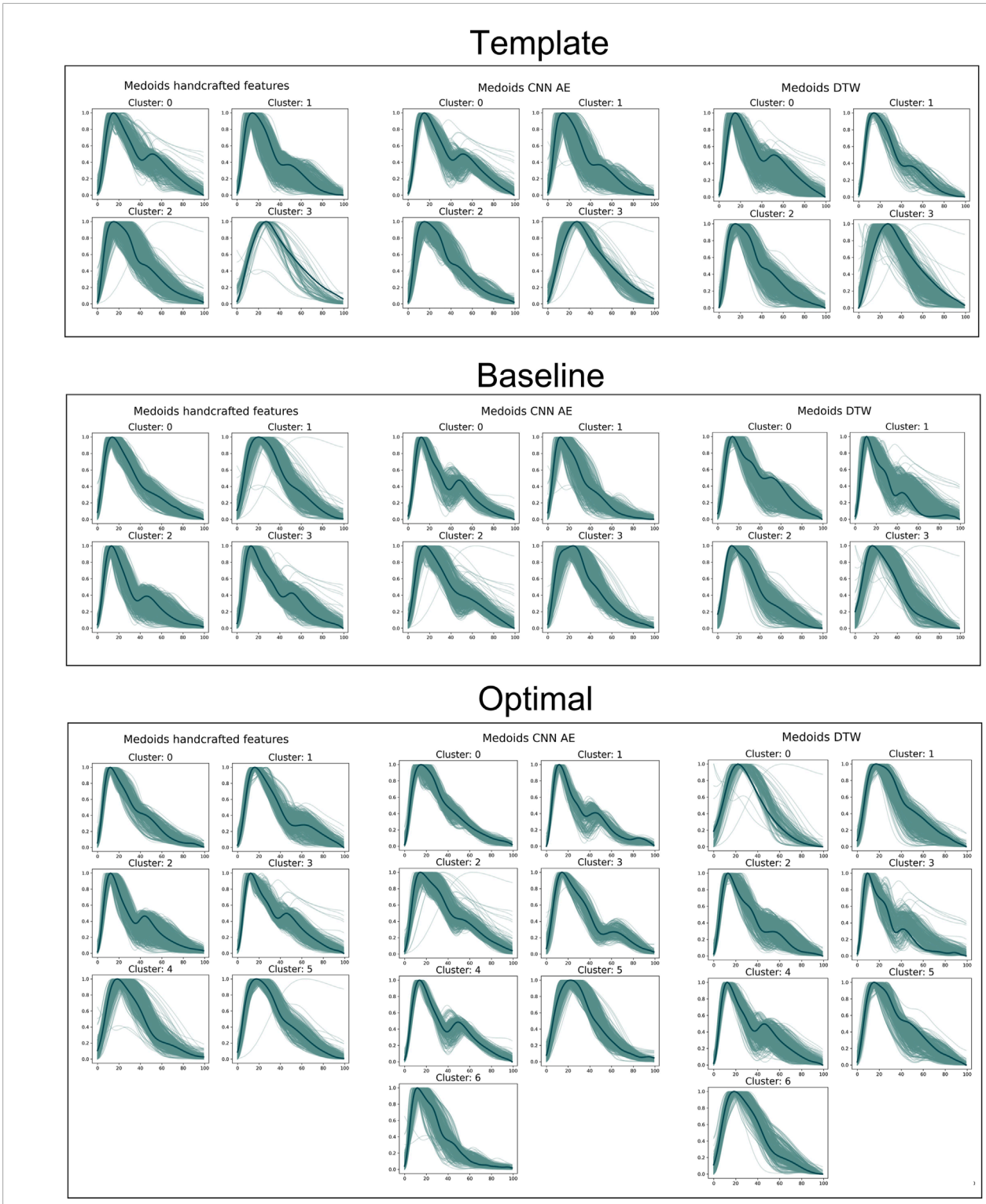

FIGURE 6
Medoids (dark green) and DVPs (light green) for all the proposed approaches. From the top to the bottom: template, baseline and optimal approach. From the left to the right: handcrafted, CNN AE and automated features.

The cluster inertia was computed as follows:

$$\sum_{i=1}^{N}(x_i - C_k)^2, \tag{3}$$

where N is the number of samples within the data set and C is the center of a cluster. It computes the sum of squared distance of each sample in a cluster to its cluster center.

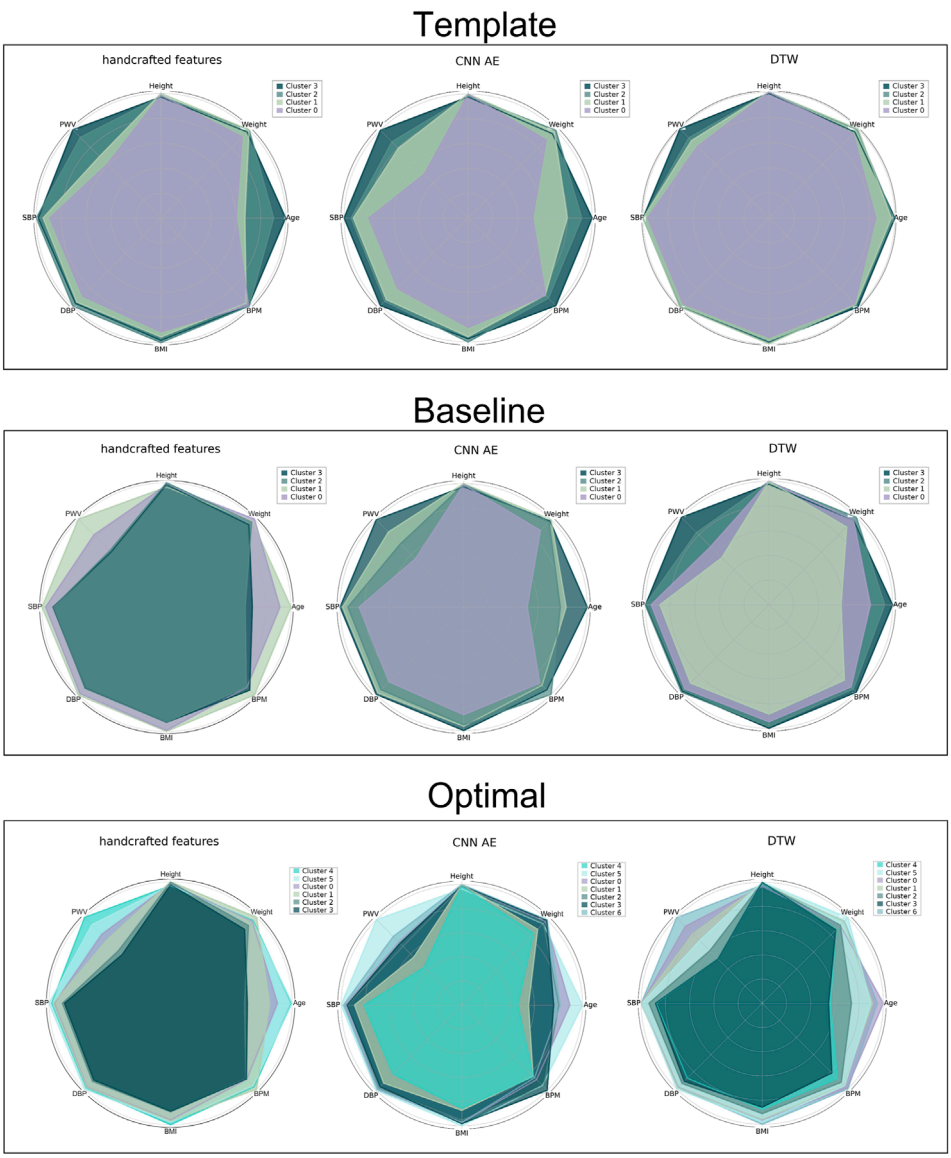

FIGURE 7
Radar plot for all the proposed approaches representing the average value of the clinical data related to the clustered DVPs. From the top to the bottom: template, baseline and optimal approach. From the left to the right: handcrafted, CNN AE and automated features.

We have to highlight that, although we tested three different methods to investigate the optimal number of clusters, the final choice of the optimal number of clusters is still affected by personal interpretation.

2.4 Investigating the clinical relevance of obtained clusters

The clinical relevance of the clustering was investigated as follows.

The Kruskal Wallis test (McKight and Najab, 2010) was used to assess whether there was a significant difference between the values of each clinical parameter between the clusters found using each clustering approach (template, baseline, and optimal). In the case of significant differences, the null hypothesis that the mean ranks of the groups are the same was rejected, and the Welch test (Alekseyenko, 2016) was used to identify the clusters for which the differences were significant.

Since significant differences were found between the clinical parameters of different clusters when using all the clustering approaches, we also conducted a more in-depth analysis of differences. Here, we propose a technique to identify which methods better discriminate the clinical data distribution among the clusters. Inspired by core shape modelling (Boudaoud et al., 2010), we assessed the intrinsic shape variations of the clinical data probability density functions (PDFs) across different clusters. This method assesses the dissimilarity between cluster PDFs by computing the distance between the relative reversed cumulative distribution function. The CSM objective is to remove the shape

modification related to the x-axis shift and focus only on the shape. Differently from the original approach, we did not want to remove the x-axis shift. Thus, we computed the distances between the reversed cumulative distribution function taking into consideration the possible x-axis shift. Probability density functions (PDFs) of the clinical data related to the clusters were computed for each of the proposed methods. From the reversed cumulative distribution function it is now possible to compute the euclidean distance. This measure gives an index to quantify the similarity between two PDFs. The larger it is, the better the method is able to cluster waves in a clinical relevant manner. The averaged distance d that we propose is computed as follows:

$$d = \frac{1}{k(k-1)} \sum_{i=1}^{k} w_i \sum_{i \neq j}^{k} w_j dist(i,j) \tag{4}$$

where $w_n = \frac{N_{DVP_n}}{N_{DVP}}$ is a weight that penalises clusters composed of fewer DVPs computed as the ration between the number of DVP contained in the cluster n and the total amount of DVP in the dataset and $dist(i,j) = |CDF_i^{-1} - CDF_j^{-1}|$ is the distance between two reserved cumulative distribution functions.

3 Results and discussion

In this section we present and discuss the obtained DVP clusters. First, we compare results obtained using the baseline approach and the template approach to understand whether the clusters of DVP waves are similar to Dawber's classes. Second, we present the results obtained using each of the three methods for identifying the optimal number of clusters. Finally, we assess the clinical relevance of the obtained clusters.

Clusters were visualised using a nonlinear dimensionality reduction method: the t-Distributed Stochastic Neighbor Embedding (t-SNE) (Van der Maaten and Hinton, 2008). This method provides a faithful lower-dimensional representation where the distribution of the original data is conserved also in the lower dimension representation. It achieves this by modeling the dataset with a dimension-agnostic probability distribution, finding a lower-dimensional approximation with a closely matching distribution (Li et al., 2017). In order to visualise the clinical data among the different clusters we present, for each proposed method, a radar plot representing the clinical data normalized averages among the clusters. Figure 5, Figure 6 and Figure 7 respectively represent the t-SNE cluster representation, the medoids and the PPG waves attributed to each cluster; and the radar plot of the clinical parameters.

3.1 Comparing with Dawber's classes

This section presents the results of clustering the dataset into four clusters using each of the three clustering methods: handcrafted features, CNN AE automated features, and the DDTW similarity matrix. We chose four clusters to allow comparison with the DVP shapes proposed by Dawber et al. In a first (baseline) approach each method was used to automatically identify the four clusters. In a second (template) approach, the medoids of the four clusters were imposed as DVP waves selected by an expert to correspond to the four classes identified by Dawber et al. We iteratively computed the assignments of the pulses to the clusters.

The results are shown in Figure 6, where the top row shows the template approach, and the middle row shows the baseline approach. Dawber's classes (top row) were designed based on differences in dicrotic notch characteristics. The medoid DVP waves automatically identified in the DDTW baseline approach are most similar to Dawber's classes: cluster 1 (corresonding to the youngest subjects as observed in Figure 7) exhibits a marked dicrotic notch (similar to Dawber's class 1), which gradually disappears in older subjects (clusters 0, 2, and 3 respectively, corresponding to Dawber's classes 2, 3, and 4) (see Figure 6). The clusters automatically identified when using the CNN autoencoder method are less similar to Dawber's classes, and those identified when using handcrafted features are even less similar still.

The number of DVP waves in each cluster was less balanced when imposing Dawber's classes as medoids than when automatically identifying medoids (see Table 4). For instance, when using handcrafted features, the proportion of DVP waves allocated to each cluster ranged from 3% to 43% when prescribing Dawber's template classes, compared to 20%–33% when allowing cluster medoids to be identified automatically. There were similar imbalances when using CNN autoencoder features, and DDTW.

The clusters identified using DDTW not only exhibited differences in dicrotic notch characteristics (similarly to Dawber's classes) but also exhibit changes in the characteristics of the systolic portion of the DVP wave (see Figure 6): the systolic peak becomes wider with age (i.e., from cluster 1 to 0, 2, and 3), and the secondary systolic wave disappears with age. This secondary systolic wave could be a reflected wave caused by the elasticity of the artery (Luo et al., 2014) or the reflection of the forward wave at the renal artery branch (Nagasawa et al., 2022).

3.2 Determining the optimal number of clusters

In order to determine the optimal number of clusters, we computed the silhouette score, the inertia and the prediction strength of the proposed approaches (see Section 2.3). Whilst these methods do require some subjective interpretation, using multiple methods allowed us to reduce the level of subjectivity. The computational cost of applying the prediction strength to the DDTW matrix was found to be high resulting in an extremely long runtime (>10 days) requiring, in our opinion, a non-justifiable amount of resources (Patterson et al., 2021). Therefore, the silhouette score and inertia were used to select optimal numbers of clusters. Where available, the result was then compared with the prediction strength.

Figure 4 shows the results for the three approaches when varying the number of clusters from 1 to 15. Silhouette score and inertia have been used jointly to select the optimal number of clusters. We searched in the results a number of cluster k, for which the obtained silhouette score was close to 1 and the inertia presented an elbow. The selected number of clusters was then compared with the obtained prediction strength analysis. Based on these results, we chose not to use a threshold of 0.8 for the prediction

TABLE 4 Number of DVPs in each cluster and for each proposed method.

Features	Handcrafted	CNN	DDTW	Handcrafted	CNN	DDTW	Handcrafted	CNN	DDTW
Approach	Template			Baseline			Optimal		
Cluster 0	746	656	1,506	803	701	1,161	495	714	172
%	20	18	41	22	19	32	14	20	5
Cluster 1	1,230	1,602	247	920	854	1,087	584	351	601
%	34	44	7	25	23	30	16	10	16
Cluster 2	1,580	1,151	1,354	734	998	878	743	642	780
%	43	32	37	20	27	24	20	18	21
Cluster 3	87	234	536	1,186	1,090	520	606	342	345
%	2	6	15	33	30	14	17	9	9
Cluster 4	-	-	-	-	-	-	539	452	725
%							15	12	20
Cluster 5	-	-	-	-	-	-	676	579	635
%							19	16	17
Cluster 6	-	-	-	-	-	-	-	563	388
%								15	11
Total waves	3,643	3,643	3,643	3,643	3,643	3,646	3,643	3,643	3,646

strength because it would have been too restrictive. The optimal number of clusters was determined as 6, 7, and 7 clusters for the handcrafted feature, the CNN AE, and the DDTW approaches respectively.

3.3 Determining the optimal clustering method

The t-SNE visualisations (Figure 5) help determine which clustering approach best separates DVP waves into clusters. The DDTW approach appears to better separate the clusters when using the template, baseline, or optimal approaches. However, we can observe from the medoids plot (Figure 6) some clusters appear to be very similar in all of the three proposed approaches. We used the intra-cluster inertia to further investigate the performance of different clustering approaches (see Figure 4). The intra-cluster inertia was lowest for the DDTW approach (approximately 0.2), and substantially higher for the other approaches (approximately 0.4 for the CNN autoencoder approach, and 0.5 for the handcrafted features approach). Based on this, we suggest that the DDTW clustering approach performed best in this study.

3.4 Investigating the clinical relevance of clusters

Clustering a dataset composed of real DVPs with no prior information about the possible optimal number of clusters, can be challenging. The main difficulty is represented by the impossibility of validating a certain approach. In this work, we used the clinical data related to the DVPs to validate and score the proposed approaches. To visualize the clinical data related to the clustered DVPs, we employed the radar plot in Figure 7. These plots represent the average value of each clinical parameter for each cluster. From visual inspection it is clear that almost all the clustering approaches result in clusters which are associated with differences in clinical parameters. To quantify this, we first performed statistical tests to assess whether there were significant differences between the clinical data for each cluster. Significant differences were found between clusters obtained using all the approaches. To investigate which method is able to better differentiate the clinical data related to the clusters we implemented a modified version of the CSM approach (Boudaoud et al., 2010). For each clinical data contained in the dataset and for each method, we assessed the capability of the latter to cluster waves in a clinical relevant manner. Table 5 reports the obtained results. Depending on the considered data, the method that obtained the largest distance changes. When clustering with with the optimal approach, the distances are smaller. This finding is logic, since the starting support space is unaltered. The CNN and DDTW approaches (template and baseline) seem to always score large distances among all the clinical data. Age and transit time appear to have the largest difference, perhaps being the primary determinants for DVPs shape. Clusters appear to correspond to different clinical characteristics, and could provide insights into a subject's vascular age as they are most strongly influenced by age and pulse transit time. This finding is in accordance with several studies (Alty et al., 2007; Brillante et al., 2008; Yousef et al., 2012). Physiologically, the aging process leads to increasing arterial stiffness (Bortolotto et al., 2000) which is reflected on the DVP shape as a less marked backward wave and dicrotic notch (Dawber et al., 1973). Arterial stiffness is

TABLE 5 PDF distances for each clinical data for each proposed method. The larger is the scored distance the better the method is able to cluster DVPs in a clinical relevant manner. The methods are scored, for each clinical data, from the best to the poorest.

Variable	Distance	Method	Variable	Distance	Method	Variable	Distance	Method
Age	0.19	CNN AE baseline	0.05	BMI	CNN AE template	0.05	BPM	CNN AE baseline
Age	0.18	DDTW baseline	0.05	BMI	CNN AE baseline	0.04	BPM	DDTW baseline
Age	0.17	CNN AE template	0.05	BMI	DDTW baseline	0.04	BPM	CNN AE template
Age	0.17	Handcrafted template	0.04	BMI	Handcrafted template	0.03	BPM	Handcrafted template
Age	0.17	Handcrafted baseline	0.04	BMI	Handcrafted baseline	0.03	BPM	Handcrafted baseline
Age	0.08	DDTW template	0.03	BMI	DDTW template	0.03	BPM	DDTW template
Age	0.07	Handcrafted optimal	0.02	BMI	Handcrafted optimal	0.02	BPM	Handcrafted optimal
Age	0.05	CNN AE optimal	0.01	BMI	CNN AE optimal	0.01	BPM	CNN AE optimal
Age	0.05	DDTW optimal	0.01	BMI	DDTW optimal	0.01	BPM	DDTW optimal
Height	0.06	Handcrafted baseline	0.08	PAD	CNN AE template	0.09	PAS	CNN AE baseline
Height	0.06	CNN AE baseline	0.08	PAD	CNN AE baseline	0.09	PAS	CNN AE template
Height	0.06	CNN AE template	0.07	PAD	Handcrafted template	0.08	PAS	DDTW baseline
Height	0.06	Handcrafted template	0.07	PAD	DDTW baseline	0.08	PAS	Handcrafted template
Height	0.05	DDTW baseline	0.06	PAD	Handcrafted baseline	0.07	PAS	Handcrafted baseline
Height	0.02	Handcrafted optimal	0.03	PAD	DDTW template	0.03	PAS	DDTW template
Height	0.02	DDTW template	0.03	PAD	Handcrafted optimal	0.03	PAS	Handcrafted optimal
Height	0.02	CNN AE optimal	0.02	PAD	CNN AE optimal	0.02	PAS	CNN AE optimal
Height	0.01	DDTW optimal	0.02	PAD	DDTW optimal	0.02	PAS	DDTW optimal
TT	0.17	DDTW baseline	0.09	PWV	DDTW baseline	0.05	Weight	DDTW baseline
TT	0.17	CNN AE baseline	0.09	PWV	CNN AE baseline	0.05	Weight	CNN AE template
TT	0.16	Handcrafted template	0.09	PWV	Handcrafted baseline	0.05	Weight	CNN AE baseline
TT	0.16	CNN AE template	0.09	PWV	CNN AE template	0.04	Weight	Handcrafted template
TT	0.15	Handcrafted baseline	0.08	PWV	Handcrafted template	0.03	Weight	DDTW template
TT	0.07	DDTW template	0.04	PWV	DDTW template	0.03	Weight	Handcrafted baseline
TT	0.06	Handcrafted optimal	0.03	PWV	Handcrafted optimal	0.02	Weight	Handcrafted optimal
TT	0.05	DDTW optimal	0.03	PWV	DDTW optimal	0.02	Weight	CNN AE optimal
TT	0.05	CNN AE optimal	0.03	PWV	CNN AE optimal	0.02	Weight	DDTW optimal

directly correlated to the transit time. The more rigid the arteries, the smaller is the transit time due to a physiological loss of compliance of the arteries with the age (Nitzan et al., 2001). The obtained clusters seem to be able to differentiate among DVP related to subjects with different levels of arterial stiffening. The obtained clusters exhibit differences in dicrotic notch characteristics and also in the shape of the systolic portion of the DVP (see Figure 7). The systolic peak becomes wider with age and the diastolic wave disappears with age (Figure 6). However, further studies are needed to better understand the relation between the obtained clusters and their physiological meaning.

4 Conclusion

In this work we investigated several unsupervised approaches to cluster DVPs. We wanted to address whether or not a dataset composed of real DVPs can be described by 4 classes based on the dicrotic notch position, as previously reported by Dawber et al.

Our results indicate that DVP wave shapes do differ due to their dicrotic notch characteristics. However, there are additional differences such as width of the systolic peak and the strength of a secondary systolic wave. Investigating the optimal number of clusters with the help of methods such as inertia, silhouette score and prediction strength, we found 7 clusters of DVP wave shapes. Whilst these methods do require some subjective interpretation, using multiple methods allowed us to reduce the level of subjectivity.

The DDTW clustering approach performed best in this study, providing better separation between clusters than using either handcrafted features, or a CNN autoencoder approach. The DDTW approach takes into account the shape of the DVP wave by applying DTW to the first derivative of the DVP wave, and may therefore

confer benefit over the previously proposed approach of applying DTW to the original DVP wave.

The different clusters of DVP waves correspond to different clinical characteristics. The clustering revealed that DVP wave shape was primarily associated with pulse transit time and age, which is in accordance with other studies Yousef et al. (2012); Alty et al. (2007); Brillante et al. (2008). Therefore, these clusters may provide insight into a subject's vascular age. However, further studies are needed to better investigate the relationship between PWV and age and its effect on the DVP morphology. However, further studies are needed to better understand the relation between the obtained clusters and their physiological meaning.

Further improvements will focus on improving the measure of similarity d to assess differences in the probability density function by taking into consideration the distance between the averaged clinical values, the standard deviation and the variability among clusters. Other methods such as Gaussian and exponential modelling will be taken into consideration to extract relevant features from the DVP. In order to test the presented approach on a public dataset for comparison, it would be very helpful if public PPG datasets were created which contain PPG signals alongside reference cardiovascular measurements such as systolic blood pressure, pulse wave velocity and generic data such as age, weight and BMI.

Data availability statement

The datasets presented in this article are not readily available because they are private datasets. Requests to access the datasets should be directed to magid@axelife.com.

Ethics statement

The studies involving humans were approved by the cohort register referenced BS-004—University Hospital of Nice. The studies were conducted in accordance with the local legislation and institutional requirements. The participants provided their written informed consent to participate in this study.

Author contributions

SZ, KE, ME, MA, and MH contributed to conception and design of the study. SZ performed the clustering and wrote the manuscript. KE performed the statistical analysis. PC selected the DVPs templates and helped with the physiological interpretation of the results. ME confirmed the results and shaped the article's focus. All authors contributed to the article and approved the submitted version.

Acknowledgments

PHC acknowledges funding from the British Heart foundation [FS/20/20/34626]. This article is based upon work from COST ACTION "Network for Research in Vascular Ageing" CA18216 supported by COST (European Cooperation in Science and Technology): www.cost.eu.

Conflict of interest

KE was employed by Axelife. SZ collaborates with Axelife, a company that designs and develops PPG-based medical devices. MH has authored patents used by Axelife and was the president of Axelife.

The remaining authors declare that the research was conducted in the absence of any commercial or financial relationships that could be construed as a potential conflict of interest.

Publisher's note

References

Alaskar, H. (2018). Convolutional neural network application in biomedical signals. *J. Comput. Sci. Inf. Tech.* 6, 45–59. doi:10.15640/jcsit.v6n2a5

Alekseyenko, A. V. (2016). Multivariate welch t-test on distances. *Bioinformatics* 32, 3552–3558. doi:10.1093/bioinformatics/btw524

Allen, J., and Murray, A. (2003). Age-related changes in the characteristics of the photoplethysmographic pulse shape at various body sites. *Physiol. Meas.* 24, 297–307. doi:10.1088/0967-3334/24/2/306

Alty, S. R., Angarita-Jaimes, N., Millasseau, S. C., and Chowienczyk, P. J. (2007). Predicting arterial stiffness from the digital volume pulse waveform. *IEEE Trans. Biomed. Eng.* 54, 2268–2275. doi:10.1109/tbme.2007.897805

Bagnall, A., Bostrom, A., Large, J., and Lines, J. (2016). *The great time series classification bake off: An experimental evaluation of recently proposed algorithms.* extended version. arxiv 2016 *arXiv preprint arXiv:1602.01711*

Bortolotto, L. A., Blacher, J., Kondo, T., Takazawa, K., and Safar, M. E. (2000). Assessment of vascular aging and atherosclerosis in hypertensive subjects: second derivative of photoplethysmogram versus pulse wave velocity. *Am. J. Hypertens.* 13, 165–171. doi:10.1016/s0895-7061(99)00192-2

Boudaoud, S., Rix, H., and Meste, O. (2010). Core shape modelling of a set of curves. *Comput. Statistics Data Analysis* 54, 308–325. doi:10.1016/j.csda.2009.08.003

Brillante, D. G., O'sullivan, A. J., and Howes, L. G. (2008). Arterial stiffness indices in healthy volunteers using non-invasive digital photoplethysmography. *Blood Press.* 17, 116–123. doi:10.1080/08037050802059225

Chafik, S., El Yacoubi, M. A., Daoudi, I., and El Ouardi, H. (2019). Unsupervised deep neuron-per-neuron hashing. *Appl. Intell.* 49, 2218–2232. doi:10.1007/s10489-018-1353-5

Charlton, P. H., Bonnici, T., Tarassenko, L., Clifton, D. A., Beale, R., and Watkinson, P. J. (2016). An assessment of algorithms to estimate respiratory rate from the electrocardiogram and photoplethysmogram. *Physiol. Meas.* 37, 610–626. doi:10.1088/0967-3334/37/4/610

Charlton, P. H., Paliakaitė, B., Pilt, K., Bachler, M., Zanelli, S., Kulin, D., et al. (2022). Assessing hemodynamics from the photoplethysmogram to gain insights into vascular age: A review from vascagenet. *Am. J. Physiology-Heart Circulatory Physiology* 322, H493–H522. doi:10.1152/ajpheart.00392.2021

Dawber, T. R., Thomas, H. E., and McNamara, P. M. (1973). Characteristics of the dicrotic notch of the arterial pulse wave in coronary heart disease. *Angiology* 24, 244–255. doi:10.1177/000331977302400407

El-Yacoubi, M. A., Garcia-Salicetti, S., Kahindo, C., Rigaud, A.-S., and Cristancho-Lacroix, V. (2019). From aging to early-stage alzheimer's: uncovering handwriting multimodal behaviors by semi-supervised learning and sequential representation learning. *Pattern Recognit.* 86, 112–133. doi:10.1016/j.patcog.2018.07.029

Geler, Z., Kurbalija, V., Ivanović, M., Radovanović, M., and Dai, W. (2019). "Dynamic time warping: itakura vs sakoe-chiba," in 2019 IEEE International Symposium on INnovations in Intelligent SysTems and Applications (INISTA), 1–6. doi:10.1109/INISTA.2019.8778300

Hwang, D. Y., Taha, B., Lee, D. S., and Hatzinakos, D. (2021). Evaluation of the time stability and uniqueness in ppg-based biometric system. *IEEE Trans. Inf. Forensics Secur.* 16, 116–130. doi:10.1109/TIFS.2020.3006313

Itakura, F. (1975). Minimum prediction residual principle applied to speech recognition. *IEEE Trans. Acoust. speech, signal Process.* 23, 67–72. doi:10.1109/tassp.1975.1162641

Kaur, N. K., Kaur, U., and Singh, D. (2014). K-medoid clustering algorithm-a review. *Int. J. Comput. Appl. Technol.* 1, 42–45.

Keogh, E. J., and Pazzani, M. J. (2001). "Derivative dynamic time warping," in Proceedings of the 2001 SIAM international conference on data mining (SIAM), 1–11.

Kurylyak, Y., Lamonaca, F., and Grimaldi, D. (2013). "A neural network-based method for continuous blood pressure estimation from a ppg signal," in 2013 IEEE International instrumentation and measurement technology conference (I2MTC) (IEEE), 280–283.

Li, Q., and Clifford, G. D. (2012). Dynamic time warping and machine learning for signal quality assessment of pulsatile signals. *Physiol. Meas.* 33, 1491–1501. doi:10.1088/0967-3334/33/9/1491

Li, W., Cerise, J. E., Yang, Y., and Han, H. (2017). Application of t-sne to human genetic data. *J. Bioinforma. Comput. Biol.* 15, 1750017. doi:10.1142/S0219720017500172

Luo, F., Li, J., Yun, F., Chen, T., and Chen, X. (2014). "An improved algorithm for the detection of photoplethysmographic percussion peaks," in 2014 7th International Congress on Image and Signal Processing (IEEE), 902–906.

McKight, P. E., and Najab, J. (2010). "Kruskal-wallis test," in *The corsini encyclopedia of psychology*, 1.

Millasseau, S. C., Ritter, J. M., Takazawa, K., and Chowienczyk, P. J. (2006). Contour analysis of the photoplethysmographic pulse measured at the finger. *J. Hypertens.* 24, 1449–1456. doi:10.1097/01.hjh.0000239277.05068.87

Mouney, F., Tiplica, T., Fasquel, J.-B., Hallab, M., and Dinomais, M. (2021). A new blood pressure estimation approach using ppg sensors: subject specific evaluation over a long-term period, *Int. Summit Smart City* 360. Springer, 45–63.

Müller, M. (2007). "Dynamic time warping," in *Information retrieval for music and motion*, 69–84.

Nagasawa, T., Iuchi, K., Takahashi, R., Tsunomura, M., de Souza, R. P., Ogawa-Ochiai, K., et al. (2022). Blood pressure estimation by photoplethysmogram decomposition into hyperbolic secant waves. *Appl. Sci.* 12, 1798. doi:10.3390/app12041798

Nitzan, M., Khanokh, B., and Slovik, Y. (2001). The difference in pulse transit time to the toe and finger measured by photoplethysmography. *Physiol. Meas.* 23, 85–93. doi:10.1088/0967-3334/23/1/308

Obeid, H., Soulat, G., Mousseaux, E., Laurent, S., Stergiopulos, N., Boutouyrie, P., et al. (2017). Numerical assessment and comparison of pulse wave velocity methods aiming at measuring aortic stiffness. *Physiol. Meas.* 38, 1953–1967. doi:10.1088/1361-6579/aa905a

Park, H.-S., and Jun, C.-H. (2009). A simple and fast algorithm for k-medoids clustering. *Expert Syst. Appl.* 36, 3336–3341. doi:10.1016/j.eswa.2008.01.039

Patterson, D. A., Gonzalez, J., Le, Q. V., Liang, C., Munguía, L.-M., Rothchild, D., et al. (2021). *Carbon emissions and large neural network training. ArXiv* abs/2104.10350

Rdusseeun, L., and Kaufman, P. (1987). "Clustering by means of medoids," in Proceedings of the statistical data analysis based on the L1 norm conference, switzerland (neuchatel) 31.

Rousseeuw, P. J. (1987). Silhouettes: a graphical aid to the interpretation and validation of cluster analysis. *J. Comput. Appl. Math.* 20, 53–65. doi:10.1016/0377-0427(87)90125-7

Rozi, R. M., Usman, S., Ali, M. M., and Reaz, M. (2012). "Second derivatives of photoplethysmography (ppg) for estimating vascular aging of atherosclerotic patients," in 2012 IEEE-EMBS Conference on Biomedical Engineering and Sciences (IEEE), 256–259.

Sakoe, H., and Chiba, S. (1978). Dynamic programming algorithm optimization for spoken word recognition. *IEEE Trans. Acoust. speech, signal Process.* 26, 43–49. doi:10.1109/tassp.1978.1163055

Sardana, H., Kanwade, R., and Tewary, S. (2021). Arrhythmia detection and classification using ecg and ppg techniques: A review. *Phys. Eng. Sci. Med.*, 1–22.

Saritas, T., Greber, R., Venema, B., Puelles, V. G., Ernst, S., Blazek, V., et al. (2019). Non-invasive evaluation of coronary heart disease in patients with chronic kidney disease using photoplethysmography. *Clin. kidney J.* 12, 538–545. doi:10.1093/ckj/sfy135

Senin, P. (2008). *Dynamic time warping algorithm review*, 855. USA: Information and Computer Science Department University of Hawaii at Manoa Honolulu, 40.

Shahapure, K. R., and Nicholas, C. (2020). "Cluster quality analysis using silhouette score," in 2020 IEEE 7th international conference on data science and advanced analytics (DSAA) (IEEE), 747–748.

Sherebrin, M., and Sherebrin, R. (1990). Frequency analysis of the peripheral pulse wave detected in the finger with a photoplethysmograph. *IEEE Trans. Biomed. Eng.* 37, 313–317. doi:10.1109/10.52332

Syakur, M., Khotimah, B., Rochman, E., and Satoto, B. D. (2018). "Integration k-means clustering method and elbow method for identification of the best customer profile cluster," in IOP conference series: materials science and engineering (IOP Publishing) 336, 012017

Takada, H., Washino, K., Harrell, J. S., and Iwata, H. (1996). Acceleration plethysmography to evaluate aging effect in cardiovascular system. using new criteria of four wave patterns. *Med. Prog. through Technol.* 21, 205–210. doi:10.1023/a:1016936206694

Talos, (2019). Autonomio talos computer software. Available at: http://github.com/autonomio/talos.

Tibshirani, R., and Walther, G. (2005). Cluster validation by prediction strength. *J. Comput. Graph. Statistics* 14, 511–528. doi:10.1198/106186005x59243

Tigges, T., Music, Z., Pielmus, A., Klum, M., Feldheiser, A., Hunsicker, O., et al. (2016). Classification of morphologic changes in photoplethysmographic waveforms. *Curr. Dir. Biomed. Eng.* 2, 203–207. doi:10.1515/cdbme-2016-0046

Van der Maaten, L., and Hinton, G. (2008). Visualizing data using t-sne. *J. Mach. Learn. Res.* 9.

Wang, L., Xu, L., Feng, S., Meng, M. Q.-H., and Wang, K. (2013). Multi-gaussian fitting for pulse waveform using weighted least squares and multi-criteria decision making method. *Comput. Biol. Med.* 43, 1661–1672. doi:10.1016/j.compbiomed.2013.08.004

Yousef, Q., Reaz, M., and Ali, M. A. M. (2012). The analysis of ppg morphology: investigating the effects of aging on arterial compliance. *Meas. Sci. Rev.* 12, 266–271. doi:10.2478/v10048-012-0036-3

Zanelli, S., Ammi, M., Hallab, M., and El Yacoubi, M. A. (2022). Diabetes detection and management through photoplethysmographic and electrocardiographic signals analysis: A systematic review. *Sensors* 22, 4890. doi:10.3390/s22134890

Zanelli, S., El Yacoubi, M. A., Hallab, M., and Ammi, M. (2021). "Transfer learning of cnn-based signal quality assessment from clinical to non-clinical ppg signals," in 2021 43rd Annual International Conference of the IEEE Engineering in Medicine & Biology Society (EMBC) (IEEE), 902–905.

Zhao, T., Liu, J., Wang, Y., Liu, H., and Chen, Y. (2018). "Ppg-based finger-level gesture recognition leveraging wearables," in IEEE INFOCOM 2018 - IEEE Conference on Computer Communications, 1457–1465. doi:10.1109/INFOCOM.2018.8486006

frontiers | Frontiers in Physiology

TYPE Original Research
PUBLISHED 26 February 2024
DOI 10.3389/fphys.2024.1228439

OPEN ACCESS

EDITED BY
Panicos Kyriacou,
City University of London, United Kingdom

REVIEWED BY
Sebastian Zaunseder,
University of Augsburg, Germany
Manuela Ferrario,
Polytechnic University of Milan, Italy

*CORRESPONDENCE
Philip J. Aston,
P.Aston@surrey.ac.uk

RECEIVED 24 May 2023
ACCEPTED 17 January 2024
PUBLISHED 26 February 2024

CITATION
Pettit C, Charlton PH and Aston PJ (2024), Photoplethysmogram beat detection using Symmetric Projection Attractor Reconstruction.
Front. Physiol. 15:1228439.
doi: 10.3389/fphys.2024.1228439

Photoplethysmogram beat detection using Symmetric Projection Attractor Reconstruction

Callum Pettit[1], Peter H. Charlton[2] and Philip J. Aston[1]*

[1]Department of Mathematics, University of Surrey, Guildford, United Kingdom, [2]Department of Public Health and Primary Care, University of Cambridge, Cambridge, United Kingdom

Many methods have been proposed to detect beats in photoplethysmogram (PPG) signals. We present a novel method which uses the Symmetric Projection Attractor Reconstruction (SPAR) method to generate an attractor in a two dimensional phase space from the PPG signal. We can then define a line through the origin of this phase space to be a Poincaré section, as is commonly used in dynamical systems. Beats are detected when the attractor trajectory crosses the Poincaré section. By considering baseline drift, we define an optimal Poincaré section to use. The performance of this method was assessed using the WESAD dataset, achieving median F_1 scores of 74.3% in the Baseline phase, 63.0% during Stress, 93.6% during Amusement, and 97.7% during Meditation. Performance was better than an earlier version of the method, and comparable to one of the best algorithms identified in a recent benchmarking study of 15 beat detection algorithms. In addition, our method performed better than two others in the accuracy of the inter-beat intervals for two resting subjects.

KEYWORDS

photoplethysmography, beat detection, symmetric projection attractor reconstruction, PPG signals, attractor, poincaré section, inter-beat intervals

1 Introduction

Photoplethysmogram (PPG) signals are now widely measured both by consumer smartwatches and by clinical pulse oximeters for unobtrusive physiological monitoring. A key step in many PPG signal processing tasks is detecting heartbeats in the PPG signal: this can form the basis for heart rate monitoring; it is fundamental to extracting inter-beat intervals (IBIs) from which to assess autonomic function through pulse rate variability analysis (Mejía-Mejía et al., 2020); and is often a precursor to estimating blood pressure from PPG pulse wave morphology (Mejía-Mejía et al., 2022). Therefore, accurate PPG beat detection algorithms are of the utmost importance in the field.

Beat detection in photoplethysmogram (PPG) signals is not a straightforward task. First, PPG signals are highly susceptible to noise and in particular motion artifact. Second, PPG signals do not exhibit a prominent feature indicating a heartbeat, in contrast to electrocardiogram (ECG) signals which contain a high-frequency R-wave each heartbeat. Third, the morphology of PPG signals can vary from one beat to the next. PPG beats are commonly detected using some form of either peak or trough detection (Charlton et al., 2022). However, peaks or troughs in the PPG are not always clearly defined, particularly in the presence of noise. Furthermore, PPG signals sometimes exhibit two peaks

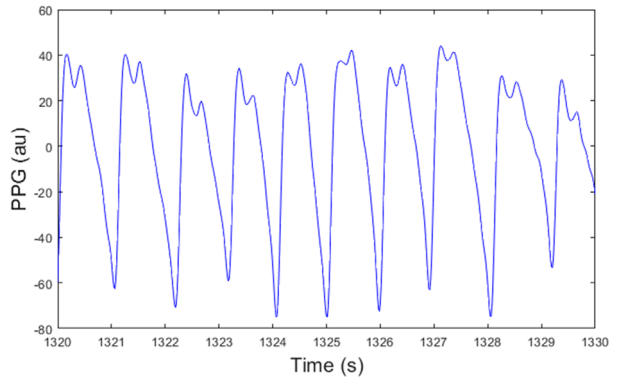

FIGURE 1
A PPG signal for subject S4 with double peaks.

per heartbeat, with the first being the highest for some beats and the second being the highest for other beats (see Figure 1), which can introduce timing errors into beat detection.

In this study we propose a novel beat detection algorithm for PPG signals based on the generation of Symmetric Projection Attractor Reconstruction (SPAR) attractors (Aston et al., 2018; Lyle and Aston, 2021). The SPAR method derives attractors from signals using a number of equally spaced points running through the signal to generate a bounded attractor in a two-dimensional phase space. In this work, we use a SPAR attractor as previously defined and combine it with the concept of a Poincaré section, a line which cuts through the attractor that is a concept borrowed from dynamical systems theory (Wiggins, 2003), to detect beats from SPAR attractors. The beat detection algorithm presented in this paper has been refined since an early version of the method was presented in Charlton et al. (2022). Thus, we present new results on the performance of the SPAR beat detector and compare its performance with the best methods in Charlton et al. (2022).

Our novel beat detection algorithm may be applied not only in heart rate monitoring, but also for applications requiring accurate inter-beat interval estimation such as heart rhythm assessment, heart rate variability analysis, and stress monitoring. The algorithm may be particularly useful for wearable devices such as smartwatches, smart rings, and earbuds, due to its low computational complexity and its ability to handle baseline wander.

Heart Rate Variability (HRV) analysis (Acharya et al., 2006) consists of deriving a range of useful measures from the IBIs, which are obtained from the distances between successive R peaks of an ECG signal. Similarly, Pulse Rate Variability (PRV) (Mejía-Mejía et al., 2020) performs a similar analysis using the IBIs derived from a PPG signal. It has been concluded that PRV is a valid surrogate for HRV for healthy, resting subjects (Mejía-Mejía et al., 2020). Thus, we also compare the accuracy of the SPAR beat detector IBIs and two other PPG beat detection algorithm IBIs against the ECG RR intervals for two resting subjects which have no artefacts in their PPG signals.

2 Methods

2.1 Dataset

The dataset used in this study was the Wearable Stress and Affect Detection (WESAD) dataset from the UC Irvine Machine Learning Repository (Schmidt et al., 2018). This dataset includes: i) PPG signals recorded from an Empatica E4 wrist-worn device at a sampling frequency of 64Hz; and ii) ECG signals recorded simultaneously from a RespiBAN chest-worn device at 700Hz. For each of the 15 subjects there is around 100 min of data. Each subject followed a protocol including five phases: Baseline, Amusement, Stress, Meditation 1, and Meditation 2. We considered all phases in our analysis.

2.2 Symmetric Projection Attractor Reconstruction

The Symmetric Projection Attractor Reconstruction (SPAR) method converts the PPG signal, which is measured over time, into an attractor in a bounded domain, by plotting its trajectory in three-dimensional phase space and then projecting it onto a particular plane, as described in Aston et al. (2018). The process of obtaining an attractor from a PPG signal is summarised in Figure 2, and the remainder of this section provides further mathematical details.

Using Takens' method for reconstructing attractors using time delay coordinates (Takens, 1981), an attractor can be reconstructed in an N-dimensional phase space from a single signal $x(t)$ by using a vector of delay coordinates given by

$$[x(t), x(t-\tau), x(t-2\tau), \ldots, x(t-(N-1)\tau)]$$

where $\tau > 0$ is a fixed delay and $N \geq 2$ is the embedding dimension. The embedding dimension was initially chosen as $N = 3$ for ease of visualisation in Aston et al. (2018) although this was later generalised to any embedding dimension $N \geq 3$ in Lyle and Aston (2021).

For the case $N = 3$, we define the new variables

$$y(t) = x(t-\tau), \quad z(t) = x(t-2\tau)$$

where the time delay τ is chosen to be one-third of the average cycle length (Aston et al., 2018). The trajectory can then be plotted in a three-dimensional phase space as shown in Figure 2B. Projecting the three-dimensional attractor onto a plane perpendicular to the vector (1,1,1) reduces the effect of baseline wander and gives a two-dimensional attractor with approximate three-fold rotational symmetry (Aston et al., 2018). For this, we define the new variables

$$\begin{aligned} u &= \frac{1}{3}(x+y+z) \\ v &= \frac{1}{\sqrt{6}}(x+y-2z) \\ w &= \frac{1}{\sqrt{2}}(x-y) \end{aligned}$$

and then the (v, w) plane is perpendicular to the vector (1,1,1), (Aston et al., 2018). The resulting attractor in the (v, w) plane is shown in Figure 2C where the trajectory runs in a clockwise direction and each loop of the attractor corresponds to one cycle of the PPG data.

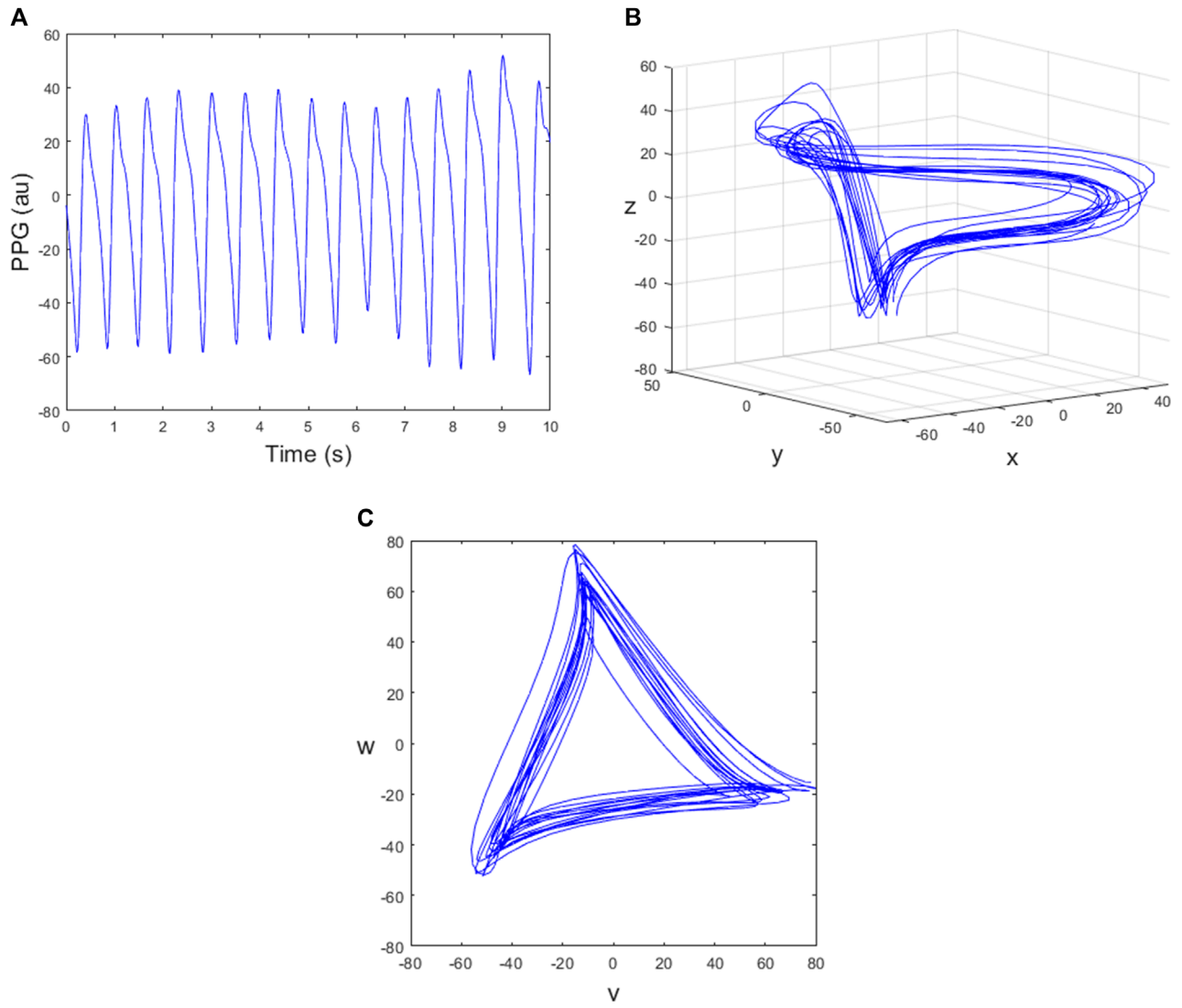

FIGURE 2
The steps used to generate a two-dimensional attractor using the SPAR method. The data is 420–430 s of subject 13. **(A)** A sample of PPG signal; **(B)** The trajectory plotted in three dimensional phase space; **(C)** The corresponding attractor in the (v,w) plane.

2.3 Using a Poincaré section for beat detection

In dynamical systems, described by a system of ordinary differential equations, a Poincaré section that intersects the flow in phase space transversely can be used to convert a continuous dynamical system into a discrete dynamical system (Wiggins, 2003). Here we are working with data, not a dynamical system, but we similarly define a Poincaré section that intersects our attractor as a means of detecting individual beats. The section should be transversal to the flow ideally, which of course can never be guaranteed for data-defined trajectories. Due to the approximate three-fold symmetry of the attractor, there are three natural choices of the Poincaré section, as shown by the black, red and green lines in Figure 3A.

In practice, we define a fixed Poincaré section by the horizontal line $w = 0$, $v > 0$ and rotate the attractor appropriately. The timestamps at which the section is crossed are found by checking the conditions $w_i > 0$ and $w_{i+1} < 0$. Note that these conditions also specify the direction of crossing, namely, from above to below the line. When these conditions are satisfied, linear interpolation is used to find the time t^* of the crossing more accurately and then the further condition $v\,(t^*) > 0$ is also checked. If required, IBIs can be obtained by finding the difference between consecutive times at which the attractor intersects a particular Poincaré section.

2.4 Varying the embedding dimension *N*

The description of the SPAR method for generating attractors (in Section 2.2) considered an embedding dimension $N = 3$. More

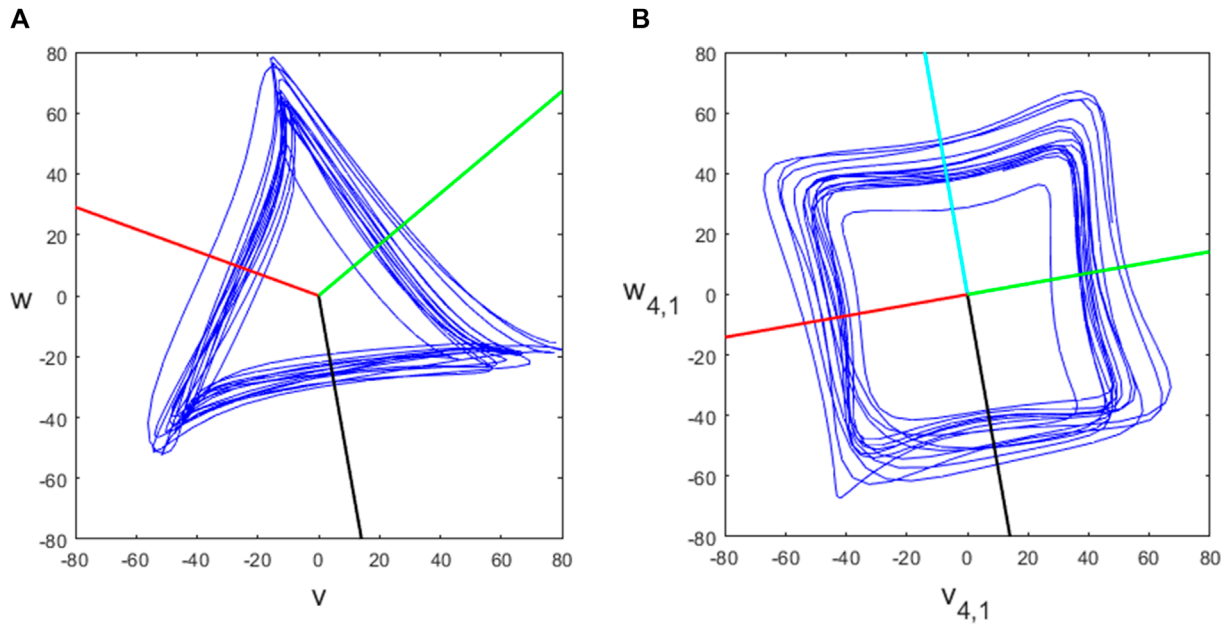

FIGURE 3
The **(A)** N = 3 and **(B)** N = 4 attractors and chosen Poincaré sections.

generally, the embedding dimension can be set to any integer $N \geq 3$. Lyle and Aston (2021) showed how to generate similar two-dimensional attractors $(v_{N,k}, w_{N,k})$, but with multiple attractors for each dimension $N > 4$ which we call projections, indexed by $k = 1, \ldots, \lfloor (N-1)/2 \rfloor$. The (N,k) attractor has an approximate m-fold rotational symmetry where $m = N/\gcd(N,k)$. The attractor for the PPG signal shown in Figure 2A for $N = 4$ is shown in Figure 3B and for $N = 5,7,9$ is shown in Figure 4, all with projection $k = 1$. We investigated using higher projections $k > 1$ but found that they were not suitable as the attractors were more variable in these cases. Therefore all of our examples use projection $k = 1$. Similarly to the $N = 3$ case, we used 4 equally spaced Poincaré sections in approximately the middle of each side of the $N = 4$ attractor, as shown in Figure 3B, to give multiple estimates for individual beats and IBIs.

For higher dimensions, the attractors become more circular in nature (Lyle and Aston, 2021) which is an advantage. However, if N is too large, there may be very few data points between each of the delay coordinates if the sampling frequency of the data is relatively low and so there may be a mismatch between the expected positions of the delay coordinates and data points available.

2.5 Finding the optimal Poincaré section

We now consider whether there is an angle for the Poincaré section that consistently gives the best accuracy. An example when finding the errors for the section at all possible angles for the $N = 3$ attractor is shown in Figure 5, where the distance from the centre of the plot indicates the mean absolute error. As might be expected, the errors are high if the section is positioned at the corners of the attractor and is much lower when positioned in the middle of the straight sides of the attractor. However, this pattern is not repeated for higher values of N, when the attractor becomes more circular, as is also shown in Figure 5. The optimal angle seems to be always in the first quadrant and has an increasing angle as N increases.

We conjecture that the optimal angle of the section is related to baseline wander in the signal and so we consider the effect of linear baseline drift on the attractor by considering the function

$$x(t) = x_0(t) + ct \tag{1}$$

where $x_0(t)$ is an approximately periodic function which has linear drift added to it, where c is a constant.

When $N = 3$, the v attractor coordinate is given by

$$\begin{aligned} v(t) &= \frac{1}{\sqrt{6}}\left(x(t) + x(t-\tau) - 2x(t-2\tau)\right) \\ &= \frac{1}{\sqrt{6}}\left(x_0(t) + x_0(t-\tau) - 2x_0(t-2\tau) + ct \right. \\ &\quad \left. + c(t-\tau) - 2c(t-2\tau)\right) \\ &= v_0(t) + \frac{3}{\sqrt{6}}c\tau \end{aligned}$$

where $v_0(t)$ is the v coordinate generated from the signal $x_0(t)$. Similarly, the w attractor coordinate in this case is given by

$$\begin{aligned} w(t) &= \frac{1}{\sqrt{2}}\left(x(t) - x(t-\tau)\right) \\ &= \frac{1}{\sqrt{2}}\left(x_0(t) - x_0(t-\tau) + ct - c(t-\tau)\right) \\ &= w_0(t) + \frac{1}{\sqrt{2}}c\tau \end{aligned}$$

where $w_0(t)$ is the w coordinate generated from the signal $x_0(t)$.

Thus, the baseline drift added to the signal results in a translation of the (v_0, w_0) attractor which is proportional in magnitude to the

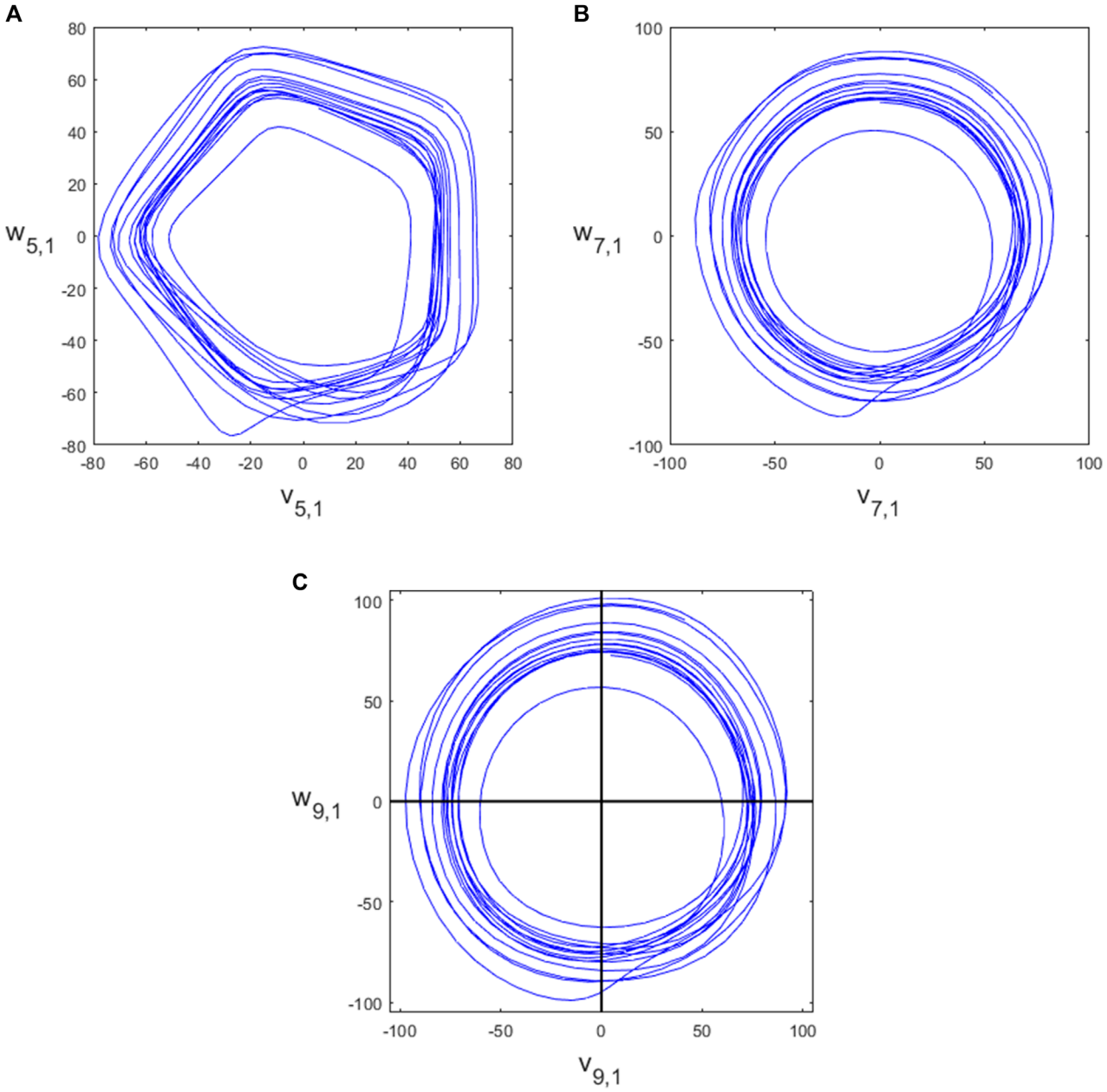

FIGURE 4
The attractors for **(A)** $N = 5$, **(B)** $N = 7$, **(C)** $N = 9$.

slope c of the drift. The direction of movement in the (v, w) plane is in a direction θ defined by

$$\tan\theta = \frac{c\tau/\sqrt{2}}{3c\tau/\sqrt{6}} = \frac{1}{\sqrt{3}}$$

which is independent of c. In this case, we have $\theta = \pi/6$ if c is positive or $\theta = -5\pi/6$ if c is negative. The angle $\theta = \pi/6$ is shown as a red line on the $N = 3$ plot in Figure 5 and it can be seen that this is very close to the optimal angle in this case.

We can generalise this result to any value of $N \geq 3$.

Supplementary Theorem S1.

The (N, k) attractor for $k = 1 \ldots, \lfloor (N-1)/2 \rfloor$ generated from an approximately periodic signal $x_0(t)$ with superimposed linear drift given by Eq. 1 *is related to the (N, k) attractor generated from the signal $x_0(t)$ only by a translation in the direction $\theta_{N,k}$ where*

$$\theta_{N,k} = \frac{\pi}{2} - \frac{\pi k}{N} \quad (c > 0), \quad -\frac{\pi}{2} - \frac{\pi k}{N} \quad (c < 0)$$

The magnitude of the shift is proportional to the slope c of the drift but the direction of the shift is independent of c.

The proof of this result is given in the Supplementary Material.

We note that as $N \to \infty$ for fixed k, $\theta_{N,k} \to \pm\pi/2$. Also, for $k = 1$ and $N = 3, 5, 7, 9$, we have $\theta_{N,k} = 30°, 54°, 450/7 = 64.29°, 70°$ respectively. These angles are shown as red lines on the respective plots in Figure 5 and give good agreement with the minimum error in each case.

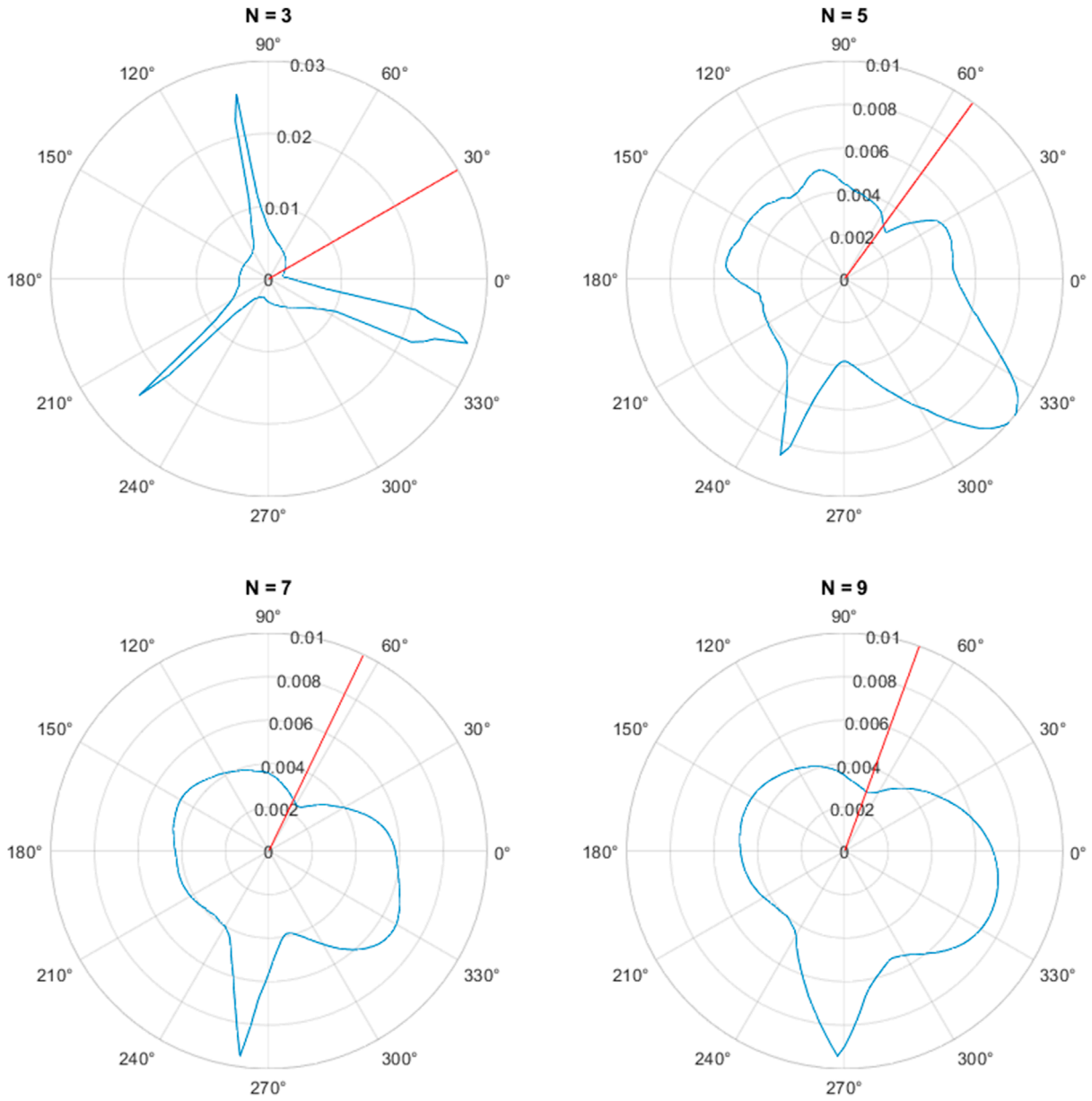

FIGURE 5
The mean absolute error of the inter-beat intervals for varying angle of the Poincaré section (in degrees) applied to the PPG signal shown in Figure 2A for the attractors with **(A)** $N = 3$, **(B)** $N = 5$, **(C)** $N = 7$, **(D)** $N = 9$. The optimal angle of Supplementary Theorem S1 is depicted by the red lines.

We conjecture that the angle given in Supplementary Theorem S1 is optimal because baseline drift on the signal moves the attractor in the direction of the section and so has no effect on the time for each cycle whereas, if the direction of translation is not aligned with the section, the IBIs will be increased or reduced by the translation of the attractor.

2.6 Algorithm implementation

The SPAR beat detector was implemented as follows. Signals were segmented into 20 s windows with a 5 s overlap. For each window, the time delay parameter τ was found by: i) filtering the signal using a fourth order Chebyshev II filter to remove baseline wander, as recommended in Liang et al. (2018) ii) identifying the average cycle length (*i.e.*, the average IBI); as the cycle length which produced the maximum autocorrelation value for the filtered signal (limited to a search between and 0.4 s and 1.5 s, corresponding to a heart rate range of 40–150 bpm); and iii) calculating τ as $1/N$ times this average cycle length. The attractor trajectory was then generated from the raw PPG signal using this value for τ. Individual beats were then detected as the times at which the attractor trajectory crossed the optimal Poincaré section as given in Supplementary Theorem S1. Multiple embedding dimensions were investigated.

A further step was included to account for noisy signals. The autocorrelation function provides values between −1 and 1, with

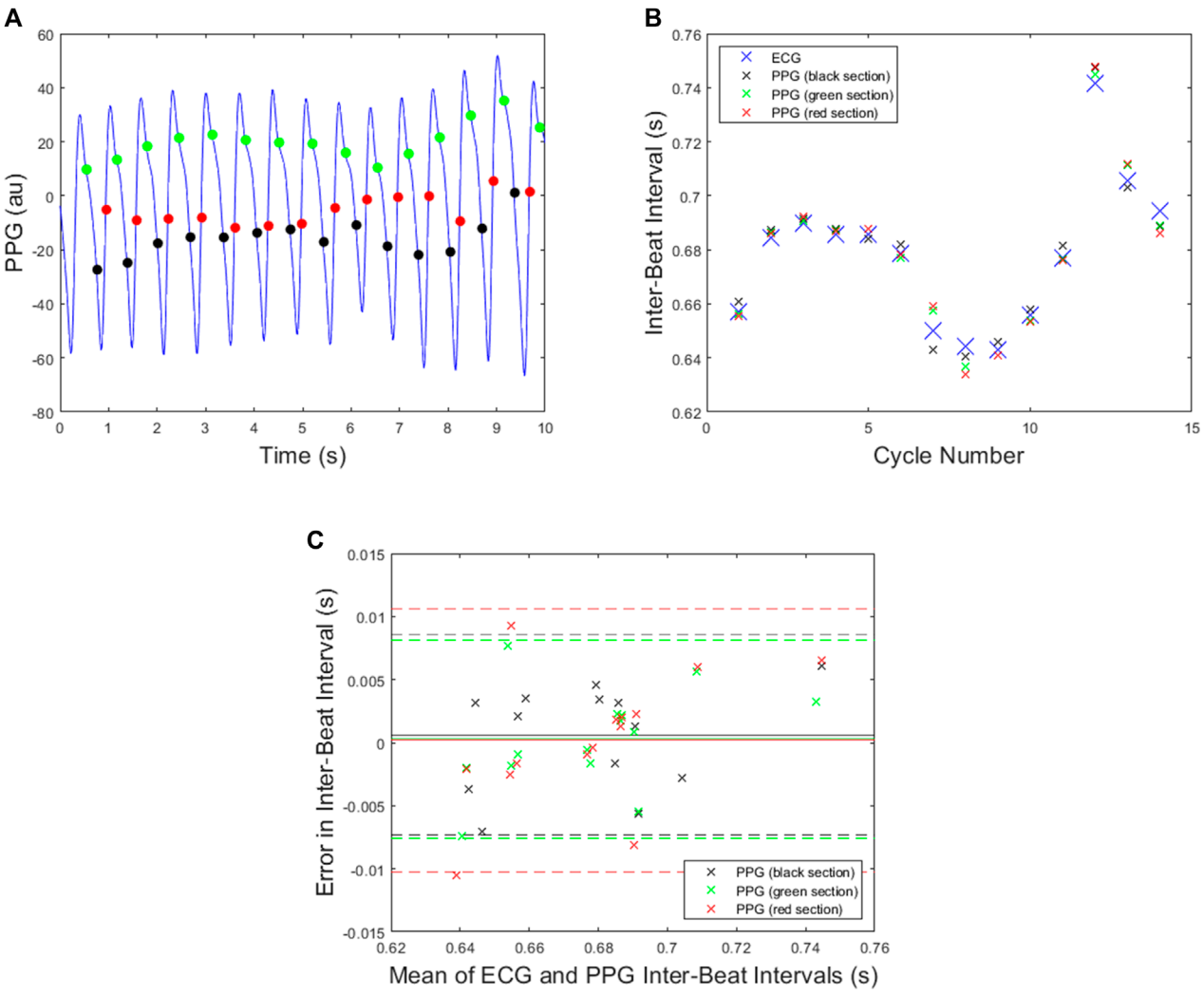

FIGURE 6
All plots are for the PPG data shown in Figure 2A and the $N = 3$ attractor. **(A)** The beats detected when the delay coordinate x lies on either the green, black or red sections shown in Figure 3A. **(B)** The ECG inter-beat intervals together with the PPG inter-beat intervals for each section. **(C)** A Bland Altman plot for each section with mean indicated by solid lines and mean plus/minus 1.96 x standard deviation indicated by dashed lines.

1 indicating perfect correlation. Through a manual inspection, a threshold of the maximum autocorrelation value of 0.4 was identified to distinguish between clean and noisy signals. Windows with values of <0.4 were deemed noisy, and so the window was divided in half and the cycle length corresponding to the highest maximum of the autocorrelation function from the two-halves of the window was used as the average cycle length. This worked well where there was high quality signal at the start or end of the window.

In the periods of overlap between consecutive 20 s windows, beats were duplicated but were not necessarily identified at the exact same times, due to a difference in the time delay τ for the two windows. The smallest error between the duplicated beats was found and this beat was the last one used from the earlier window before swapping over to the beats in the new window.

Following beat detection, missed or false beat detections were corrected as follows. Missed beats were detected by checking for IBIs greater than the median IBI plus a tolerance of 0.35IBI. The number of missing beats was determined from the IBI divided by the median IBI and the corresponding number of evenly spaced beats was inserted. Similarly, if two beats were closer than the median IBI minus a tolerance of 0.3IBI then the beat closest to its other neighbour was removed.

2.7 Performance assessment

The performance of the SPAR beat detector was assessed in three ways: i) PPG-derived IBIs and reference ECG-derived IBIs were compared for short time intervals for illustrative purposes;

TABLE 1 The mean absolute error for the inter-beat intervals of the PPG signal shown in Figure 2A.

N	Section	Mean absolute error (s)
3	black	0.0036
3	green	0.0031
3	red	0.0039
4	black	0.0045
4	green	0.0031
4	cyan	0.0045
4	red	0.0041

ii) the accuracy of beat detection was assessed against reference beats identified in the ECG signal using the F_1 score and iii) PPG IBIs were compared with ECG-derived IBIs for two subjects during the Meditation 1 phase. These three approaches are now described.

First, IBIs obtained from PPG signals using the SPAR beat detector were compared to reference IBIs obtained from ECG signals. To do so, beats were detected in PPG signals using the SPAR beat detector, and then IBIs were calculated as the time differences between consecutive beat detections. R-peaks were detected in the ECG signals, manually checked, and corrected where necessary (for the whole dataset). ECG-derived IBIs were then calculated as the time differences between consecutive R-peaks. Performance was expressed as the mean absolute error between PPG- and ECG-derived IBIs.

Second, the performance of the SPAR beat detector was assessed against reference ECG beats using the F_1 score, which is the harmonic mean of the recall (*i.e.*, sensitivity, the proportion of ECG beats which were correctly detected in the PPG) and the precision (*i.e.*, positive predictive value, the proportion of PPG beat detections which were correct). The F_1 score simplifies in this context to

$$F_1\,(\%) = \frac{2n_{\text{correct}}}{n_{\text{PPG}} + n_{\text{ECG}}} \times 100$$

where n_{correct} is the number of correct beats, n_{PPG} is the number of PPG beats and n_{ECG} is the number of ECG beats. The number of correct PPG beats was determined as in Charlton et al. (2022) by finding the nearest PPG beat to each ECG R peak and designating it as correct if the absolute time difference between the two was <150 ms. The results were reported as median (lower - upper quartiles) F_1 scores on a per subject basis. The performance of the present SPAR beat detector algorithm was compared with that of an earlier version of the algorithm, which was described in Charlton et al. (2022).

It was important to synchronise the timings of ECG and PPG signals since they were measured using different devices. To do so, PPG beats were aligned with ECG R-peaks using the time delay which resulted in the highest number of correct beats (with candidate time delays of between −10 s and 10 s in steps of 10 ms investigated).

Finally, we compared PPG-derived IBIs found using the SPAR beat detector with the ECG-derived IBIs and did a similar comparison with the qppg and MSPTD beat detection algorithms, which were the top two methods for beat detection in Charlton et al. (2022). The sequences of IBIs derived from the ECG and PPG signals can only be compared if they have detected the same number of beats. Also, if the PPG beat detector missed a beat which has then been estimated, this beat is likely to have a larger error which will dominate any errors from correctly detected beats, thus distorting the results. Thus, we chose subjects from the WESAD data using the Meditation 1 phase for which there were no noisy intervals in the signal so that all the beats are detected by the PPG beat detectors. In particular, we chose subjects S9 and S10. (The exception to this was the qppg beat detector which incorrectly detected a few beats at the start for subject S9 and so for this case, we excluded the first 14 s of data, which should have little influence on the results.) The Meditation 1 phase for both of these subjects was 400 s long and consisted of 475 beats for subject S9 and 501 beats for subject S10. The IBIs were found using the three PPG beat detectors (using $N = 3, \ldots, 10$ for the SPAR beat detector) and from the corresponding ECG signals. Each sequence of PPG-derived IBIs was aligned with the ECG-derived IBIs by finding the minimum of the mean absolute error with a shift of ±5 IBIs. We then report the mean absolute error of these aligned sequences of IBIs.

3 Results

3.1 Illustrative examples

Illustrative examples of PPG beat detection using the SPAR beat detector are now presented. Figure 6A shows the PPG beats detected using an $N = 3$ attractor for the signal in Figure 2A, where the points shown are the position of the leading delay coordinate, x, when the attractor trajectory crosses each of the three sections. The corresponding IBIs obtained are shown in Figure 6B while the Bland Altman plot in Figure 6C shows the errors when compared to the ECG-derived IBIs. This plot shows that the mean of the errors is smallest for the red and green sections, while the standard deviation is the smallest for the black and green sections, thus suggesting that the results obtained from the green section are the best. The mean absolute error for each section is given in Table 1 from which we can see that in this particular case the best results were also obtained for the green section.

In the case of $N = 4$, similar results are shown in Figure 7, and the corresponding mean absolute errors are shown in Table 1. The green section again gave the best results with the smallest standard deviation in the Bland Altman plot and the same error as for the green section with $N = 3$.

3.2 The accuracy of the SPAR beat detection

Results relating to the accuracy of the SPAR beat detector are now presented, expressed as the F_1 score. Accuracy was assessed

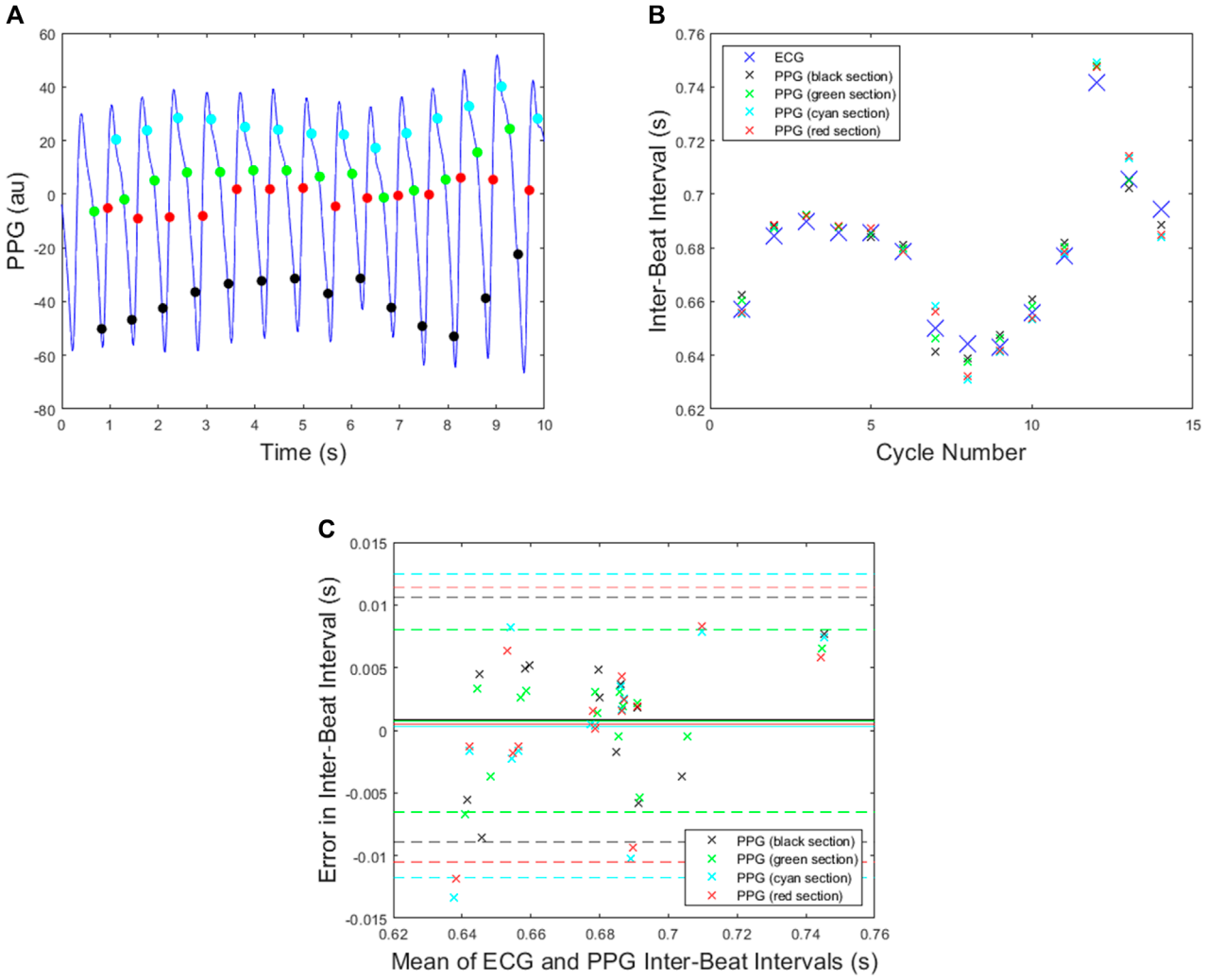

FIGURE 7
All plots are for the PPG data shown in Figure 2A and the N = 4 attractor. **(A)** The beats detected when the delay coordinate x lies on either the green, black, red or cyan sections shown in Figure 3A. **(B)** The ECG inter-beat intervals together with the PPG inter-beat intervals for each section. **(C)** A Bland Altman plot for each section with mean indicated by solid lines and mean plus/minus 1.96 x standard deviation indicated by dashed lines.

over each of the five protocol phases, and using a range of attractor embedding dimensions: $N = 3,5,7,9$. Box plots were used to summarise these results for all the subjects, as shown in Figure 8. There was only a small difference in the median F_1 scores for the different values of N. The best median score was obtained with $N = 3$ for three of the five phases (Stress, Amusement and Meditation 2). $N = 3$ also provided good performance in the other phases, being the second best performer in the 'Meditation 1' phase, and the third best performer in the 'Baseline' phase (where the median F_1 score with $N = 3$ was 1% lower than that of the best performer, $N = 7$).

For comparison, results obtained using the previously reported SPAR method are shown in Figure 9. It can be seen that the new SPAR method gives significantly improved results compared with the previous method.

3.3 The accuracy of the SPAR inter-beat intervals

The mean absolute error between the ECG-derived IBIs and the PPG-derived IBIs was found for the SPAR, MSPTD and qppg beat detectors for subjects S9 and S10 during the Meditation 1 phase. These errors are shown in Figure 10.

For subject S10, the SPAR errors are much smaller than those for the other two algorithms. The reason for this is that there are quite a few double peaks in this PPG signal and the second peak is sometimes the highest, resulting in inaccurate IBIs. A sample of the signal with the detected peaks and the IBIs calculated using the qppg algorithm are shown in Figure 11. The results for the MSPTD method are similar. We also note that the error for the SPAR method with $N = 4$ is much larger than the other

10.3389/fphys.2024.1228439

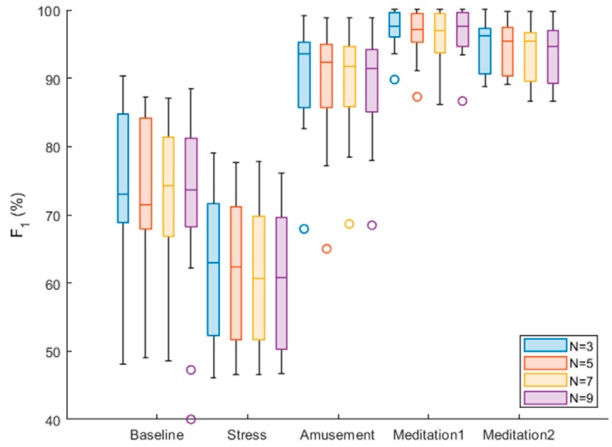

FIGURE 8
Box plots of the F_1 scores for each of the five conditions and for $N = 3,5,7,9$.

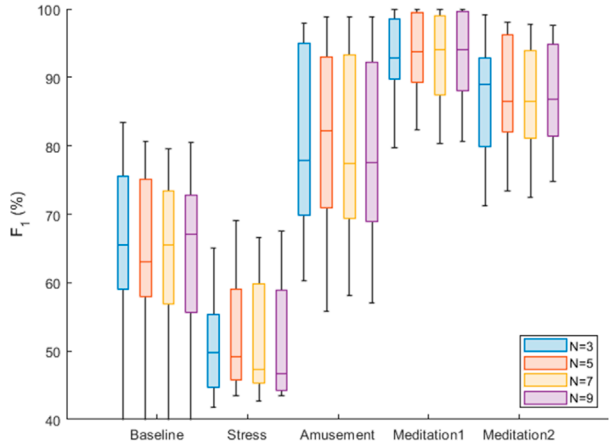

FIGURE 9
Box plots of the F_1 scores for each of the five conditions and for $N = 3,5,7,9$ using the earlier SPAR method that was used in Charlton et al. (2022).

SPAR errors. The reason for this is that this method misses one beat in approximately the middle of the data, and so the second half of the IBIs are out of synch with the ECG IBIs. For the SPAR method, the smallest mean absolute error of 0.0061 was obtained for $N = 3$.

There is no problem with double peaks for subject S9, but here also the SPAR method with $N = 3$ has the lowest mean absolute error of 0.0052 as compared to 0.0103 for MSPTD and 0.0089 for qppg.

The simplest variability metric that is derived from the IBIs is the standard deviation, which is usually referred to as SDNN. The percentage error between the ECG-derived and PPG-derived SDNN is shown in Table 2 for both subjects S9 and S10.

TABLE 2 Percentage errors in calculating SDNN compared to the ECG-derived value for subjects S9 and S10.

	S9 (%)	S10 (%)
SPAR ($N = 3$)	2.22	2.16
MSPTD	8.52	42.67
qppg	4.59	45.39

4 Discussion

This study has presented a novel algorithm for detecting beats in the PPG signal which is not based on peak detection. The algorithm involves representing the PPG signal as an attractor in phase space using the SPAR method, and identifying beats as the times at which the attractor trajectory intersects the optimal Poincaré section. The algorithm showed good performance on a dataset of PPG signals acquired from a wrist-worn device across different phases of a mental stress protocol.

We now compare our results with those reported in Charlton et al. (2022) for the WESAD dataset and in particular, with the qppg algorithm from the prior study. For the 'Baseline' phase, the median F_1 score for qppg was 74.2%, in comparison to the SPAR beat detector's performance of 74.2% ($N = 7$). For 'Stress', the SPAR beat detector achieved 62.6% ($N = 3$), which was a little worse than qppg which achieved 68.7%. For 'Amusement', the SPAR beat detector achieved 93.6% ($N = 3$) which was marginally better than the 92.8% achieved by qppg. For 'Meditation 1', the SPAR beat detector achieved 97.7% ($N = 9$) which is slightly lower than the 98.3% obtained by qppg. The 'Meditation 2' data was not considered in Charlton et al. (2022) so a comparison is not possible in this case. In summary, the new SPAR methodology performed similarly to qppg, which was one of the two best-performing algorithms identified in Charlton et al. (2022). We note that there are some differences in the algorithm assessment methodologies used between these studies, introducing some uncertainty into the above comparison. Nonetheless, in this study the SPAR beat detector demonstrated a clear improvement in performance when compared to an earlier version of the SPAR beat detector.

The calculation of the IBIs for the SPAR method with $N = 3$ outperformed both the MSPTD and qppg algorithms, which were the top two best performing algorithms in Charlton et al. (2022), for two subjects during the Meditation 1 phase. Poor results were obtained for the IBIs for subject S10 due to the regular occurrence of a second peak being the highest, but the SPAR method also performed best for subject S9 where there were no such problems. In the calculation of SDNN, the SPAR method with $N = 3$ had an error of just 2.2% relative to the ECG-derived value for both subjects, whereas the other methods had an error in excess of 40% for subject S10, due to the double peaks, but also had higher errors (8.5% for MSPTD and 4.6% for qppg) for subject S9. Thus, we conclude that the SPAR method is clearly the best performing of the

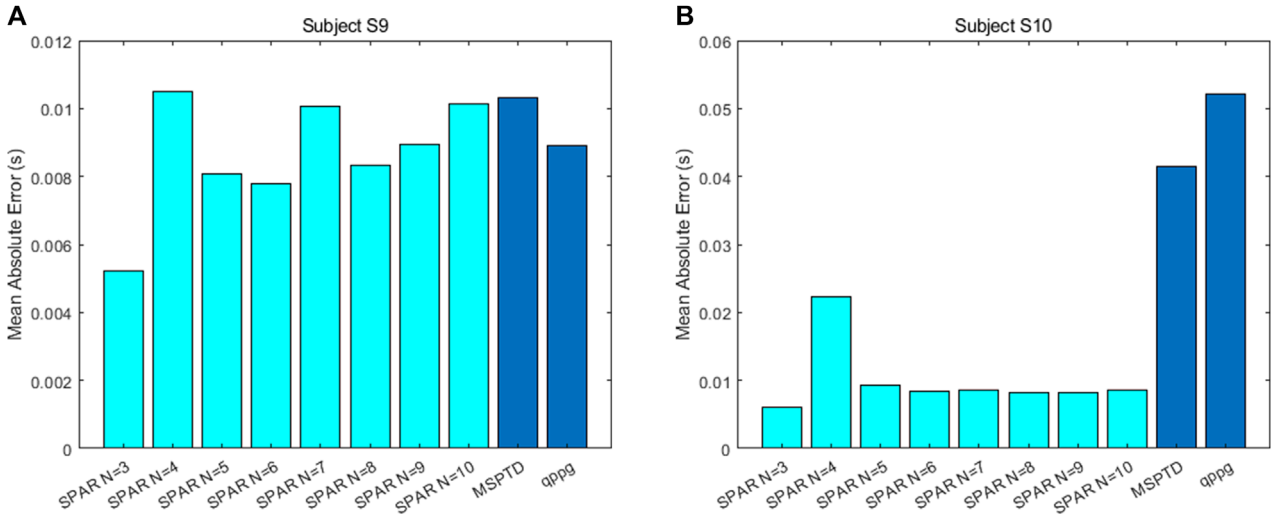

FIGURE 10
The mean absolute error between the ECG-derived IBIs and the PPG derived IBIs for **(A)** subject S9 and **(B)** subject S10 during the Meditation 1 phase.

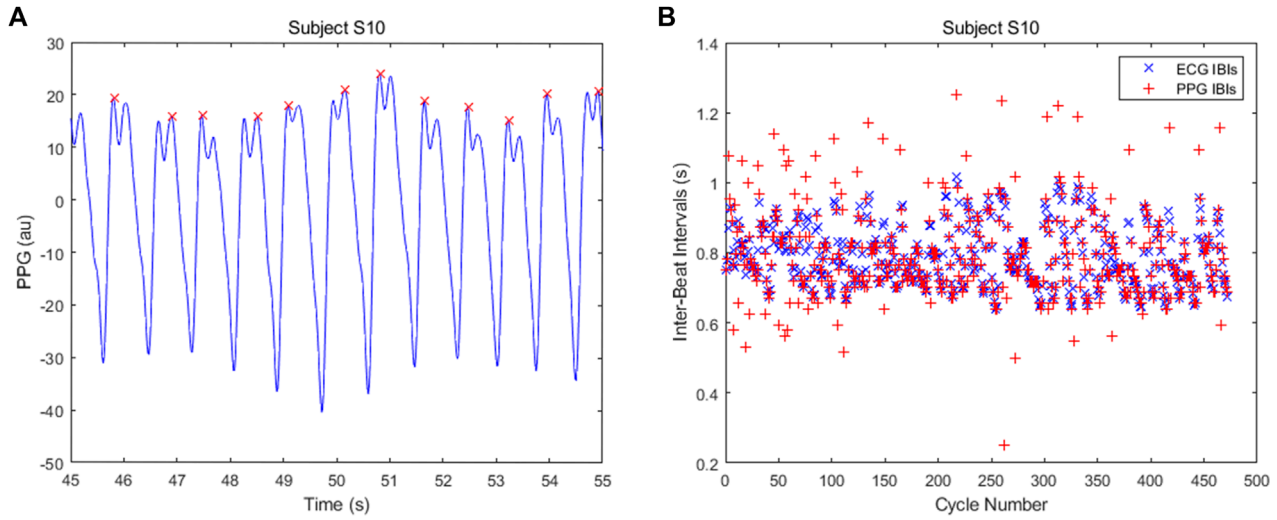

FIGURE 11
(A) Some of the detected beats showing alternation between which of the double peaks is the highest and **(B)** the IBIs calculated by the qppg algorithm for subject S10.

methods considered for calculating the IBIs that are required for HRV/PRV analysis.

In conclusion, the novel SPAR PPG beat detection algorithm presented in this study was found to perform well with wrist PPG signals. The algorithm methodology differs greatly from previously proposed PPG beat detection algorithms as it does not depend on detection of peaks or troughs in the signal but instead calculates times at which the orbit in reconstructed phase space intersects a Poincaré section. These intersections typically occur well away from the peaks and troughs and so are not dependent on the clarity of the peaks and troughs. Future work should investigate how the algorithm performs across different subject groups. Future work may also consider extending the method to detect beats in other cardiovascular signals such as the electrocardiogram, and also to detect events in any approximately periodic data, such as breaths in respiratory signals.

Data availability statement

Publicly available datasets were analyzed in this study. This data can be found here: https://archive.ics.uci.edu/ml/datasets/WESAD+%28Wearable+Stress+and+Affect+Detection%29 WESAD dataset.

Ethics statement

Ethical approval was not required for the study involving humans in accordance with the local legislation and institutional requirements. Written informed consent to participate in this study was not required from the participants or the participants and legal guardians/next of kin in accordance with the national legislation and the institutional requirements.

Author contributions

This study was conceived and designed by PA and then coded in Matlab by CP. CP also wrote the first draft of the paper. PA refined both the code and the paper. PC aided with study design and drafting and refining the paper. All authors contributed to the article and approved the submitted version.

Funding

The author(s) declare financial support was received for the research, authorship, and/or publication of this article. PC acknowledges support from the British Heart Foundation, grant FS/20/20/34626.

Conflict of interest

PA has a patent (WO2015121679A1 "Delay coordinate analysis of periodic data"), which covers the foundations of the SPAR method used in this paper.

The remaining authors declare that the research was conducted in the absence of any commercial or financial relationships that could be construed as a potential conflict of interest.

Publisher's note

All claims expressed in this article are solely those of the authors and do not necessarily represent those of their affiliated organizations, or those of the publisher, the editors and the reviewers. Any product that may be evaluated in this article, or claim that may be made by its manufacturer, is not guaranteed or endorsed by the publisher.

Supplementary material

The Supplementary Material for this article can be found online at: https://www.frontiersin.org/articles/10.3389/fphys.2024.1228439/full#supplementary-material

References

Acharya, U., Joseph, K., Kannathal, N., Lim, C., and Suri, J. (2006). Heart rate variability: a review. *Med. Bio. Eng. Comput.* 44, 1031–1051. doi:10.1007/s11517-006-0119-0

Aston, P., Christie, M., Huang, Y., and Nandi, M. (2018). Beyond HRV: attractor reconstruction using the entire cardiovascular waveform data for novel feature extraction. *Phys. Meas.* 39, 024001. doi:10.1088/1361-6579/aaa93d

Charlton, P., Kotzen, K., Mejia-Mejia, E., Aston, P., Budidha, K., Mant, J., et al. (2022). Detecting beats in the photoplethysmogram: benchmarking opensource algorithms. *Phys. Meas.* 43, 085007. doi:10.1088/1361-6579/ac826d

Liang, Y., Elgendi, M., Chen, Z., and Ward, R. (2018). An optimal filter for short photoplethysmogram signals. *Sci. Data* 5, 180076. doi:10.1038/sdata.2018.76

Lyle, J., and Aston, P. (2021). Symmetric Projection Attractor Reconstruction: embedding in higher dimensions. *Chaos* 31, 113135. doi:10.1063/5.0064450

Mejía-Mejía, E., Allen, J., Budidha, K., El-Hajj, C., Kyriacou, P., and Charlton, P. (2022). Photoplethysmography signal processing and synthesis. *Photoplethysmography*, 69–146. doi:10.1016/b978-0-12-823374-0.00015-3

Mejía-Mejía, E., May, J., Torres, R., and Kyriacou, P. (2020). Pulse rate variability in cardiovascular health: a review on its applications and relationship with heart rate variability. *Phys. Meas.* 41, 07TR01. doi:10.1088/1361-6579/ab998c

Schmidt, P., Reiss, A., Duerichen, R., Marberger, C., and van Laerhoven, K. (2018). "Introducing WESAD, a multimodal dataset for wearable stress and Affect detection," in Proceedings of the 20th ACM International Conference on Multimodal Interaction, New York, USA, 400–408.

Takens, F. (1981). "Detecting strange attractors in turbulence," in *Dynamical Systems and Turbulence, Warwick 1980, Lecture Notes in Mathematics*. Editors D. Rand, and L. S. Young (Berlin, Heidelberg: Springer) 898. doi:10.1007/BFb0091924

Wiggins, S. (2003). *Introduction to applied nonlinear dynamical systems and chaos*, Vol. 2. New York: Springer. Texts in Applied Mathematics.

Frontiers in Physiology

Understanding how an organism's components work together to maintain a healthy state

The second most-cited physiology journal, promoting a multidisciplinary approach to the physiology of living systems - from the subcellular and molecular domains to the intact organism and its interaction with the environment.

Discover the latest Research Topics

See more →

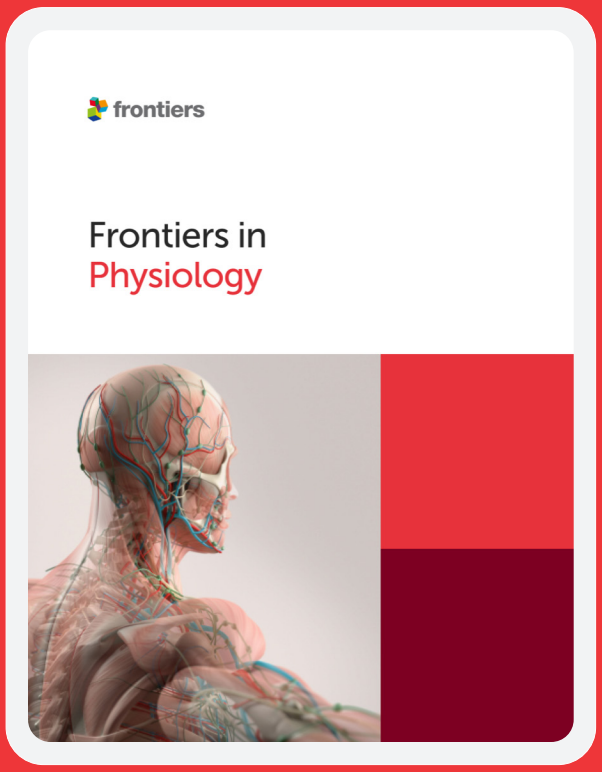

Frontiers

Avenue du Tribunal-Fédéral 34
1005 Lausanne, Switzerland
frontiersin.org

Contact us

+41 (0)21 510 17 00
frontiersin.org/about/contact